Diandong Ren

Storm-triggered Landslides in Warmer Climates

Springer

Storm-triggered Landslides in Warmer Climates

Diandong Ren

Storm-triggered Landslides in Warmer Climates

Springer

Diandong Ren
Curtin University of Technology
Perth, WA, Australia

ISBN 978-3-319-08517-3 ISBN 978-3-319-08518-0 (eBook)
DOI 10.1007/978-3-319-08518-0
Springer Cham Heidelberg New York Dordrecht London

Library of Congress Control Number: 2014947106

© Springer International Publishing Switzerland 2015
This work is subject to copyright. All rights are reserved by the Publisher, whether the whole or part of the material is concerned, specifically the rights of translation, reprinting, reuse of illustrations, recitation, broadcasting, reproduction on microfilms or in any other physical way, and transmission or information storage and retrieval, electronic adaptation, computer software, or by similar or dissimilar methodology now known or hereafter developed. Exempted from this legal reservation are brief excerpts in connection with reviews or scholarly analysis or material supplied specifically for the purpose of being entered and executed on a computer system, for exclusive use by the purchaser of the work. Duplication of this publication or parts thereof is permitted only under the provisions of the Copyright Law of the Publisher's location, in its current version, and permission for use must always be obtained from Springer. Permissions for use may be obtained through RightsLink at the Copyright Clearance Center. Violations are liable to prosecution under the respective Copyright Law.
The use of general descriptive names, registered names, trademarks, service marks, etc. in this publication does not imply, even in the absence of a specific statement, that such names are exempt from the relevant protective laws and regulations and therefore free for general use.
While the advice and information in this book are believed to be true and accurate at the date of publication, neither the authors nor the editors nor the publisher can accept any legal responsibility for any errors or omissions that may be made. The publisher makes no warranty, express or implied, with respect to the material contained herein.

Printed on acid-free paper

Springer is part of Springer Science+Business Media (www.springer.com)

Contents

Notation

α	Slope angle
α_s	Compressibility of bulk soil
α_w	Compressibility of water voids
S	Stability parameter
μ	Internal friction coefficient
C_{eff}	Effective cohesion
ϕ	Internal frictional angle
P_r	Precipitation
P	Porosity
T_{r}	Soil transmissivity
ρ	Bulk density
$\vec{V}$	Velocity vector
u	Zonal (east component) velocity
v	Longitudinal velocity
w	Vertical velocity
V	Speed of Sound
σ	Internal stress tensor
F	The body force
ν	Viscosity
ν_{p}	Poisson's ratio (unitless)
S_p	Spherical part of the stress tensor σ
$\lvert\dot{\varepsilon}_e\rvert$	Effective strain rate
I	Inertial number
d	Particle diameter
ρ_s	Particle density
c	Heat capacity
T	Temperature

κ	Thermal conductivity
K	Hydraulic conductivity
σ_{eff}	Effective stress
$h(x,y)$	Surface elevation
h_m	Head due to pore water pressure
h_g	Head due to gravity
h_o	Head due to osmosis
h_v	Head due to kinetic energy
ϕ	Gravitational potential
δ_E	Pressure perturbation caused by earthquake or human-induced disturbances
Subscript 'f'	Means failure
λ	Longitude
θ	Latitude
(λ, θ)	Longitude/longitude location on spherical earth
h	Distance from the sliding material surface to the Earth's center
r	Variable location within sliding material domain in the radial direction of (λ, θ)
H	The local sliding material thickness
t	Time
R	Earth's radius
σ^+	Root mechanical reinforcement
C_{smc}	Soil moisture control factor (0-1)
σ_{veg}	Strength of xylem of roots
NPP	Net primary production
P_a	Annual precipitation
T_{air}	Annual mean air temperature
$\hbar$	Hydrostatic pressure (in slope model)
CCCMA-cgcm, CSIRO-mk30, GFDL_CM2.1, GISS_e_h, GISS_e_r, GISS_aom, MIROC3.2_hires, MIROC3.2_midres, MIUB_echog, MPI_echam5, MRI_cgcm2.3, NCAR_ccsm3, and UKM_HadCM3	Are coupled general circulation climate model acronyms as defined by CMIP project (http://cmip-pcmdi.llnl.gov/cmip5/)
Elastic moduli E	Young's modulus
ν_p	Poisson's ratio
K	incompressibility

Megajoule (MJ) $= 10^6$ Joules
Terajoule (TJ) $= 10^{12}$ Joules
Petajoule (PJ) $= 10^{15}$ Joules

Chapter 1
Introduction

As the failure mechanism of sloping earth materials driven by gravity, landslides are one of the most widespread and effective agents in shaping the Earth's surface (Eckel 1958, p. 1), through redistributing earth material from uplands into river systems. They occur in all mountainous regions of the Earth, in response to a wide variety of natural conditions and triggering processes (see for example Figs. 1.1 and 1.2). These triggers include windstorms and rainstorms, earthquakes, and the numerous consequences of human activity, such as the rapid increase in size of areas that have been rendered vulnerable to large-scale soil erosion. Landslides in the USA, particularly in southern California, are severe hazards that cause substantial human and economic losses, estimated at an annual average of 25–50 deaths, and a financial cost of approximately $1 billion to $3 billion per year (NRC 2008). In addition, globally, they cause both significant environmental damage and societal disruption (Dai, personal communication 2012), and affect developing countries disproportionately.

Landslides are part of the natural erosion process, which is an ongoing levelling of the surface features of the Earth, both on land and beneath the sea. They can assume the forms of rockfalls, land slumps and slides, and debris flows (Cruden 1991; Cruden and Varnes 1996). Current risk analysis techniques remain simple, and largely are descriptive. Landslides occur irregularly, so present and future research is concerned with generating more accurate predictions about their timing (when, or under what circumstances they occur), location (where, geological features, material properties, and ecosystem configuration), size (how large), and how sliding materials redistribute, and in developing procedures that convey timely and accurate risk and warnings to the public, to mitigate loss of life and damage to infrastructure and ecosystems (van Asch et al. 2007; Casadei et al. 2003). Such an effort is critical, particularly when tied to the anticipated impacts of climate variability and change on areas already prone to slope instability.

Successfully answering the above four questions of when, where, what (size), and how (mass is redistributed), is a prerequisite for a "complete" landslide model, and forms the basis of quantitative risk analysis (Hungr et al. 2008). This review

© Springer International Publishing Switzerland 2015

D. Ren, *Storm-triggered Landslides in Warmer Climates*,
DOI 10.1007/978-3-319-08518-0_1

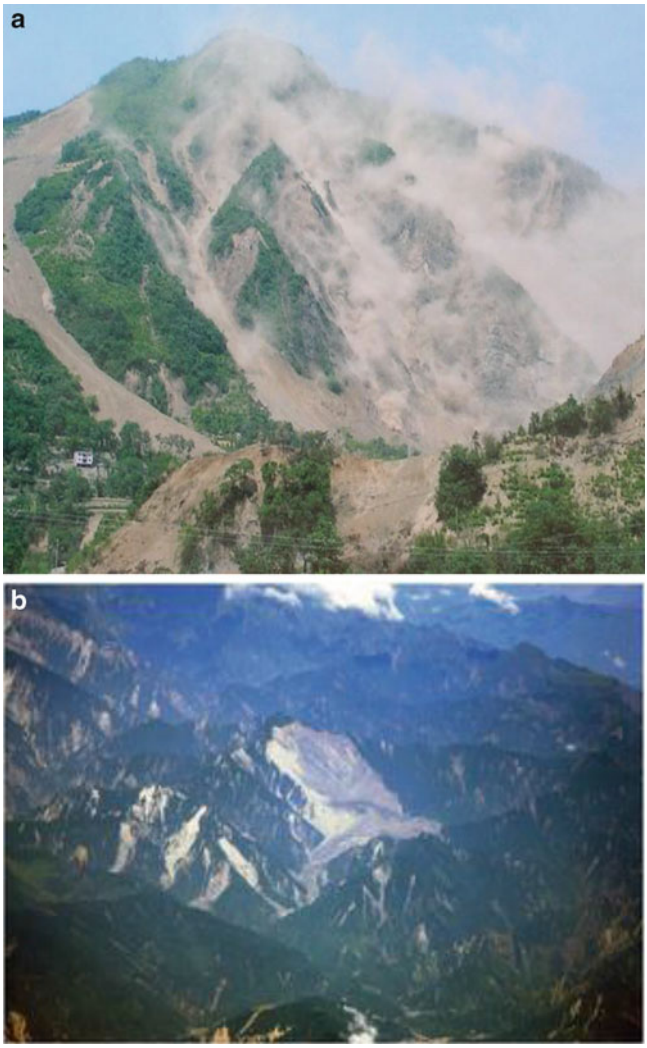

Fig. 1.1 Earthquake triggered landslides: Wenchuan, China (**a**). The Daguangbao Landslide (**b**), with a volume of 1.16×10^9 m^3 (Huang and Fan 2013), was the largest landslide that occurred at the time of the May 2008 Wenchuan earthquake. Figure is partly adapted from Huang and Fan (2013)

aims to provide a greater quantitative understanding of the fundamental physical processes associated with landslides, in order to predict their occurrence, locations, evolution once triggered, and likely ecological and societal impacts. There is an urgent need for increased quantitative investigation of the coupling and feedback between the Earth's crust, the atmosphere and the vast number and range of ecosystems, initially in the context of past and present climate conditions for validation purposes, and then in a range of possible warming future climate

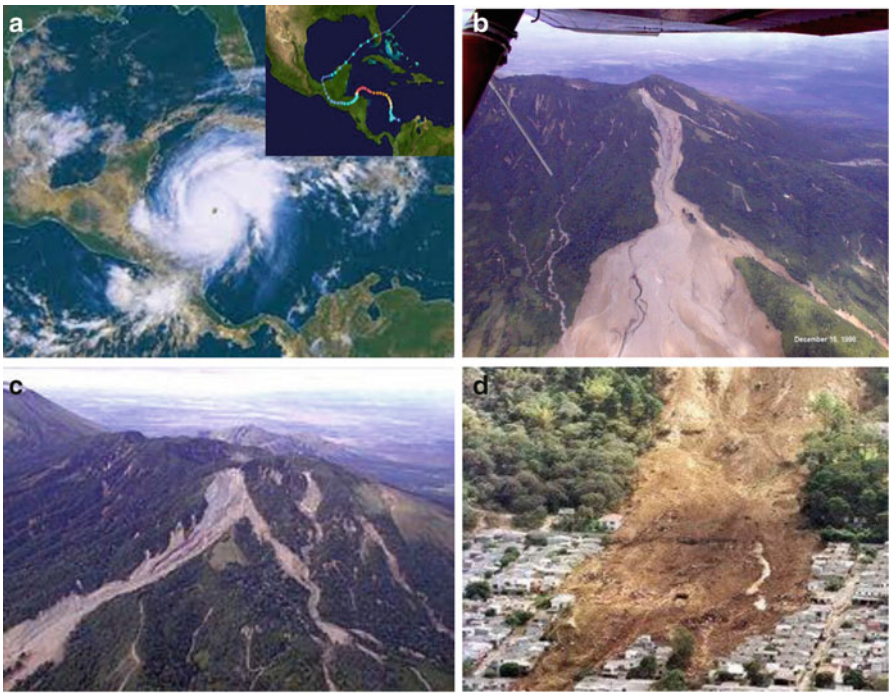

Fig. 1.2 Example of storm-triggered landslides. Hurricane Mitch 1998 (**a** is a satellite imagery of Mitch right before its landing at Honduras, and the *inset* is the storm's track from Oct 18 to Nov 5, 1998. It gained the hurricane status around Oct. 24) and the landslide scarps it left near Vulcan Casita, Nicaragua (**b**–**d**). Panels (**b**) and (**c**) are from different view angles. (**d**) is a zoomed-in view of a populated area. *Sources*: NASA (**a**) and USGS ((**b**) and (**c**))

scenarios. This review complements that of Dietrich and Perron (2006), where "life's footprints" on the Earth's topography are discussed in terms of two competing physical processes: advection and diffusion. Their conclusion was that life activity alone is not responsible for topographical features of a large enough scale and in the time frame of climate. Here, the discussion focuses on the effects of landslides on ecosystems. The review is organized as follows.

Firstly, there is a succinct summary of ecosystems on sloping terrain. In Chap. 3, it is pointed out that the global distribution of landslides correlates strongly with biomass production, indicating the interdependency of biological and physical worlds. This results from the dual role of landslides in ecosystem disturbances. Landslide is a "fatigue" of granular slopes, the general theories on material properties apply but need proper modifications. To provide a proper basis for landslide dynamics and the ensuing numerical modelling of landslides, basic strain–stress theory and yielding criteria are described in Chap. 4. This chapter systematically introduces existing theories on fatigue of brittle material and the various yielding criteria based on effective strain distribution or from the density of mechanical energy considerations. In Earth environment, landslides are complicated by the

intersection with hydrosphere (intervene of soil moisture) and biosphere (root system of living vegetation). To properly implement their effects, the yielding criteria take a generic form of the summation of the gravitational potential, the effective cohesion, the internal friction and the pressure perturbations caused by earthquakes or of human origin. Chapter 4 also forms the theoretical basis for numerical modelling of landslides on various degree of complexity. Chapter 5 provides a general overview of landslide dynamics and concentrates on storm-triggered landslides (debris flows). Sliding materials involved in landslides fall under the general category of granular material. Compared with its non-fractured source material, granular material has a larger surface area and occupies a larger space. Rheologically, it is similar to the mother material but with a certain level of fluidity. An objective measure of destructivity from sliding granular material is introduced. Destructive potential must be quantified according to magnitude, moving speed of the landslide, and granular dimensions. The interstitial moisture increases cohesion, but primarily dissolves the bonding substance and reduces shear strength of potential sliding material. Erosion potential of runoff flow is reviewed in the general context of entrainment and detrainment/deposition. The four major influences from live vegetation are summarized in this section. Chapter 5 also presents an application of the generic fracture theories on Earth slope granular material. Section 5.2 reviews the present models for debris flows including, in order: empirical statistical models; slope stability models; and fully three-dimensional (3D) mechanistic modelling systems. This also is the temporal order of numerical model development, driven by improved understanding of this phenomenon and the rapidly burgeoning, less expensive computational capabilities. The water dissolve of inter-particle bonds is so effective in reducing the shear strength and hence resistive stress. The intensity-duration empirical schemes thus keep only this first order relation (soil moisture directly relates to infiltration and percolation of surface runoff, which in turn are proportional to precipitation rate and duration) and it suffices especially for debris flows and shallow landslides. One level up is the 1D slope stability models, which define a stability index, usually as the ratio of driving and resistive stress. Simplified forms of Richards' equation are usually used to diagnose the soil moisture vertical distribution. Soil moisture reduction to resistive stress is then implemented. Aside from utilizing the full form of Richards' equation, 3D landslide models systematically attend the root system effects in slope hydrology and in the mechanical reinforcement. A recently developed dynamical system, which conserves mass, momentum, and energy, then is introduced in Chap. 6. This model was developed by the author and is known as the scalable, extensible geo-fluid model, or SEGMENT-Landslide (Ren et al. 2008, 2009; Ren et al. 2011). It has been used in a number of studies of past, present, and future landslides. Empirical and slope stability modelling systems are reduced forms of this framework, developed under special assumptions of simplified geometry and/or lateral boundary conditions. A generic energy bundle form, which facilitates describing the full life cycle of debris flows, is introduced. In the physical parameterization of the numerical modelling system, only the relevant, recent improvements that have occurred after the review by Iverson (1997) are addressed.

These include a parameterization of granular viscosity that accounts for multi-body solids, reinforcement of slope strength by distributed vegetation roots, and gravitational sedimentation underlying the sorting of granular material in downslope movement, which is a mechanism underpinning the formation of fertile alluvial fans.

For root fortification, an allometric formula is proposed that facilitates using remotely sensed biomass to estimate root volumetric density. Using a reference map of vegetation type, the strengthening of the slope by roots is estimated. For idealized geometry, four numerical experiments are described using the SEGMENT-Landslide model. These related experiments are used to illustrate that: (1) precipitation has a decisive role in the formation of alluvial fans, because gravity sedimentation tends to have coarser granular material (pebbles and boulders) outrunning finer material when the sliding material is dry; and (2) small landslides or rock falls, which are stopped at mid-slope, add to future, more destructive debris flows when storms reactivate these deposits. Point (2) is confirmed by the devastating case of 2010 in Zhouqu, China (Sect. 6.3). Section 6.3 is a real case simulation of the Zhouqu landslides, which are archetypal examples of debris flow. In the Zhouqu debris flow, model features including granular rheology, vegetation effects, and runoff advection all were activated. Model calculation of total sliding material involved is very close to that estimated from observations. However, many modelled features still cannot be verified. Importantly, the SEGMENT-Landslide model suggests strongly that future sliding still is very likely in the forthcoming 10 years, if there is no significant increase in vegetation cover. Comparisons with peer models are discussed in the application of SEGMENT-Landslide to a large, repeatable (reactivation of previous landslide scarps) landslide along the Changjiang River. These exemplary applications of SEGMENT-Landslide over various climate zones indicate its potential as a component in earth system modelling. The case study of Zhouqu shallow landslides fully indicated that debris flows are the "predictable" type of landslides because of the strong correlation with extreme precipitation. The following subsections (Sects. 6.4.1–6.4.3) dedicate to the mid-latitude frontal system, the cause of Zhouqu 2010 extreme precipitation. Same year 2010 in May, Central-Southeast USA also suffered flash floods caused by frontal system with strong low level jets (LLJs) as a conveyor belt for atmospheric vapor. The concept of atmospheric river and LLJ is introduced in describing the frontal system (Sect. 6.4.1). Blocking mechanisms that slow down the evolution of the precipitation systems are described (Sect. 6.4.3). Since landslides are specific to mountainous region (narrow valleys also worsen the flash floods), orographic enhancement effects on local precipitation are addressed (Sect. 6.4.2). An advanced numerical weather prediction model is used to investigate the May 2010 US extreme precipitation (Sect. 6.4.4). Other conditions favoring extreme precipitation over the US Appalachians are investigated and future landslide events are projected (Sect. 6.4.6).

We feel it is necessary to dedicate an entire chapter (Chap. 7) to systematically review the extreme precipitation under a future warming climate. Commencing in Chap. 7, another focus of this book is addressed: changes in extreme precipitation in a future warming climate and consequences on storm-triggered landslides.

Firstly, a perspective is given on extreme precipitation that has relevance to debris flow, in a warming climate context. This is based on possible rainfall morphological changes in climate model projections. The consequences of debris flows for ecosystems can clearly be seen. The review suggests that, based on the modelling results, there is an urgent need for the development of an accessible, worldwide landslide ecosystem knowledge-based (or "intelligent") archive system that is updated regularly as landslides occur. It should include estimates of risk factors for as many susceptible locations as possible. In the Earth's atmosphere, there are large-scale, persistent patterns as major rainmakers: monsoons (Sect. 7.3), El Niño and Southern Oscillations (ENSO, Sect. 7.1), and tropical cyclones (Sect. 7.2). Chapter 7 discusses these rainmakers in detail, using recent state-of-the-art numerical models and remote sensing data where necessary. Their possible climate warming responses are addressed. For tropical cyclones, as their activities are basin specific, cases from different basins are compared to draw generally applicable conclusions. At the end of Chap. 7 (Sect. 7.4), changes in southern California's storm-triggered landslides are projected for the twenty-first century. Similar analyses can be performed for other mountainous regions on Earth. In addition to the direct effects felt by the mountainous region dwellers, landslides also can affect coastal populations through their sea level rise contribution.

Chapters 8 and 9 focus on ecosystem impacts from landslides. In addition to perturbing local ecosystem and especially affect biodiversity, landslides also may have global sea level consequences, through mechanisms not apparent to most readers. Chapter 8 presents a case where the West Antarctic Ice Sheet's (WAIS) disintegration as a result of warming climate may have landslide consequences that positively feedback through an elevated eustatic sea level. This case has indirect environmental consequences through the possible slope movement under the present WAIS and its possible sea level change effects. In addition to displaying the adaptability of SEGMENT-Landslide and similar fully 3D hydraulic landslide models, the case of the WAIS places landslide consequences in the larger arena of public concerns. Regions of systematic landslides, for example, those occurring on the earthquake belts, usually signify an increased soil porosity (shallower level) and bedrock cravasses (deeper levels). This may contribute a lowering of sea level through enhanced precipitation infiltration and runoff water percolation into groundwater reservoir. Chapter 9 presents a case study of the peri-Himalayan region. It turns out that the contribution from this region can completely cancel the sea level rise increase caused by groundwater overtap by the desert countries. More importantly, this negative source tapers off slowly (compared with man-made hydraulic reservoirs). Landslides always go hand in hand with other ecosystem disturbances such as wild fires (Chap. 9).

Chapter 10 specifically provides a perspective on using remotely sensed signals from gravity changes to identify a larger background indicator of slope instability. Storm-triggered landslides are, partially, an upscaling process, residing in a geologically unstable background and locally enhanced by extreme precipitation. We are living in a remote sensing era and the satellites can provide us with valuable information on both triggering of precipitation and changes in the longer term ground water level.

To mitigate the landslide disaster, the establishment of a knowledge archive system is very important. Chapter 11 specifically addresses debris flows and is organized around the theme of constructing a storm-triggered landslide knowledge archive system. As storm-triggered landslides result from extreme precipitation events, knowledge of changes in weather extremes is one perspective from which to view landslide-generated ecosystem disturbances, while a physically based dynamic landslide model offers another. Technical details of the landslide intelligence system are also overviewed in this chapter. Chapter 11 also provides a view point for future research directions. Because debris flows are caused by extreme precipitation, a topic being actively pursued in climate research, collaborations between climatologists and geologists are necessary for further progress in predicting storm-triggered landslides. To make optimal use of this research, regional, national, and international collaborations are necessary since disastrous debris flows are still infrequent natural hazards and, if possible, all cases should be archived. All debris flow events should be studied and catalogued as observational and computational resources are distributed in discord with the global distribution of landslides. Preventative measures potentially can save more global resources than aftermath financial aids. Although this review is concerned almost entirely with the scientific aspects of landslides, given that an increased occurrence of devastating storm-triggered landslides is anticipated in a warming climate, their destructive financial and emotional impacts can be reduced, and even eliminated in some cases, by deploying landslide mitigation and climate adaptation strategies. These strategies require access to the global knowledge archive suggested above. Another key requirement is a society of informed citizens, communities, businesses, and emergency managers who know how to use the intelligence. Thus, there are educational aspects of the proposed approach that are required to enable the global community to cope with a warmer future world, with its associated enhanced hydrological cycle.

To facilitate graduate students to follow the derivation procedure in constructing the full 3D landslide dynamic model, Chap. 12 lists all involved numerical steps and mathematical formulae for tensor and vector operations. A general curvilinear coordinate system is also introduced to project physical space into the calculation space. To facilitate further study/research of interested readers, five topic-oriented Appendices are furnished: Appendix A addresses pressure fields within granular media. This essay reveals that there generally no hydrostatic balance within granular media. The formation of compression struts within can even result in regions free of stress. Instead, a "region of influence" may be a convenient roundabout for understanding the stress structure within granular lumps. Appendix B is a statistical tool for cluster analysis. Landslide scarps are usually sporadic in geographical distribution. To quantify changes in landslide activities, cluster analysis may fit in many circumstances. Appendix C investigates what factors control the magnitude of a landslide. Appendix D actually is for Chap. 11. The advanced tensor-operation tools may facilitate the reader to follow the derivations in Chaps. 4 and 11. Appendix E presents an advanced analysis method for extreme precipitation. This method works on daily precipitation. The critical values for extreme precipitation

can be objectively defined for regions of interest. Once the shape and scale factors determined, Return periods for extreme events (with daily precipitation exceeding the critical value) can then be estimated accordingly. This book also serves as a practical reference book. For this purpose, there is sample code (Appendices F–G) and the entire SEGMENT-Landslide system is available per request to the author. There are also animations for illustrating several ideal cases of slope instability (because of the large image size, available only as supplementary material).

References

Casadei M, Dietrich W, Miller N (2003) Testing a model for predicting the timing and location of shallow landslide initiation in soil-mantled landscapes. Earth Surf Processes Landf 28:925–950

Cruden DM, Varnes DJ (1996) Landslides types and processes. In: Schuster RL, Krizek RJ (eds) Landslides investigation and control, Special report 247. Transportation Research Board, Washington, DC, pp 36–75

Cruden D (1991) A simple definition of a landslide. Bull Int Assoc Eng Geol 43:27–29

Dietrich W, Perron J (2006) The search for topographic signature of life. Nature 439:411–419

Eckel E ed. (1958) Landslides and engineering practice: National Research Council, Highway research Board Special report, 29, 232 p

Huang R, Fan X (2013) The landslide story. Nat Geosci 6:325–326

Hungr O, McDougall S, Wise M, Cullen M (2008) Magnitude–frequency relationships of debris flows and debris avalanches in relation to slope relief. Geomorphology 96:355–365

Iverson R (1997) The physics of debris flows. Rev Geophys 35:245–296

NRC (2008) Origin and evolution of earth-Research questions for a changing planet. National Academy Press, Washington, DC

Ren D, Fu R, Leslie LM, Dickinson R (2011) Predicting storm-triggered landslides. Bull Am Meteorol Soc 92:129–139. Doi: 10.1175/2010BAMS3017.1

Ren D, Leslie LM, Karoly DJ (2008) Landslide risk analysis using a new constitutive relationship for granular flow. Earth Interact 12:1–16

Ren D, Wang J, Fu R, Karoly D, Hong Y, Leslie LM, Fu C, Huang G (2009) Mudslide caused ecosystem degradation following Wenchuan earthquake 2008. GRL 36, L05401. doi:10.1029/2008GL036702

van Asch T, Malet J, van Beek L, Amitrano D (2007) Techniques, issues and advances in numerical modelling of landslide hazard. Bull Soc Gol Fr 178:65–88

Chapter 2
Ecosystem of Sloping Terrain, Soil, and Vegetation

Failure of sloping earth materials falls within the general form of fatigue. However, the involved material is not a single solid specimen; rather, a multiple-body of countless degree of freedom is involved: a lump of granular material, with rocks at the coarse end of grain size and sandy loam soil at the fine end of grain size. Under the unique processes of Earth environments, the mechanical strength of the granular material is further altered by the presence of vegetation roots (fortification effects) or tunnels of subterranean animals (weakening effects). A further degree of complexity that acts on slope stability within the ecosystem of a sloping terrain is the effect on the granular material's moisture content, through slope hydrology.

2.1 The Biological and Physical Worlds Are Interdependent

A unique feature of terrestrial ecosystems is that vegetation acquires its resources from two very different environments; air (for CO_2) and soil (for inorganic minerals of nutrients). Landslides cause disturbances to ecosystem productivity by displacing the soil mantle. In addition to being the medium in which most decomposers and many animals live, the physical soil matrix provides a source of water and nutrients to plants and microbes, and is the physical support system in which terrestrial vegetation is rooted. For these reasons, landslide displacement of the soil mantle has severe ecological consequences (Fig. 2.1).

Sloping terrain creates unique patterns of microclimates, through surface energy budgets, hydrology and availability of nutrients. For example, slopes facing the equator receive more solar radiation than opposing slopes and, hence, usually experience warmer and drier conditions. In colder or moister climates, the warmer microclimate of the equator-facing slopes provides conditions that enhance productivity, decomposition, and other ecosystem processes (including the formation

© Springer International Publishing Switzerland 2015

D. Ren, *Storm-triggered Landslides in Warmer Climates*,
DOI 10.1007/978-3-319-08518-0_2

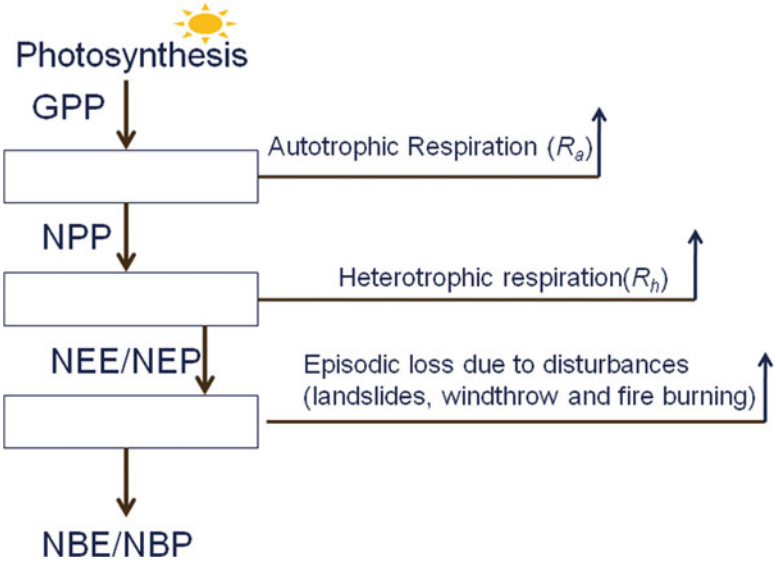

Fig. 2.1 Diagrammatic representation of the major terms describing system carbon balances. *Arrows* indicate that gross primary production (GPP) and net primary production (NPP) are always positive (carbon gains by the system), net ecosystem exchange (NEE) is usually, but not always, positive, and net biome exchange/products (NBE/NEP) is the net carbon fixed and can be positive or negative. Role of landslides in the carbon cycling is as an episodic disturbance. Total global GPP is estimated to be about 120 GtC/year (Gifford 1982; Bolin et al. 2000)

of soils). Conversely, in dry climates, the low moisture levels on these slopes limit such production. Furthermore, microclimatic variations associated with slope and aspect allow stands of a particular ecosystem type to exist hundreds of kilometers beyond its major zone of distribution. These outlier populations are important sources of colonizing individuals during times of rapid climate change and are, therefore, important in understanding species migration and the long-term dynamics of ecosystems. Topography also influences climate through the drainage of cold, dense air in the form of katabatic winds that form strong near surface air temperature inversions. Inversions are climatologically important because they increase the seasonal and diurnal temperature extremes experienced by ecosystems in low-lying areas. In cool climates, inversions greatly reduce the length of the frost-free growing season. The third aspect of the impact of sloping surfaces on ecosystems is surface hydrology. The surface runoff on sloping surfaces is much larger than over flat terrain. For dry climates, this places severe water limitations on production. Before addressing the slope effects on nutrients, the soil formation process must be reviewed.

Soils are the substrate where plants roots grow and many soil animals burrow. The characteristics and qualities of soil determine its ability to retain water and to supply minerals required by plant growth. Thus, its variation provides a key to understanding the productivity of biological communities and spatial distribution of

plant species. Unfortunately, soil is difficult to define exactly. Commonly, it refers to the porous material that overlies unaltered bedrock. It includes minerals derived from the parent rock, altered minerals formed by weathering, organic material contributed by plants, air and water within the pores of soil, living roots of plants, microorganisms, and the larger worms and arthropods that dwell inside soil. Generally, soil is determined by factors such as climate, parent material (underlying rock), vegetation, local topography, and age after the formation moment from newly exposed rocks (Brady 1974). Specifically, the activities of organisms within soil affect the arrangement of particles and the size and degree of pores in the soil as well as its chemical characteristics (e.g., Oades 1993; Gonzalez-Prieto and Carballas 1995). Thus soils have vertical stratifications: soil horizons. A simplified, generalized soil profile has five major divisions (from top to bottom): O, A, E, B, and C horizons. Landslides disturb the division arrangement and cause nutrients unavailable to plants. Soil develops initially from the weathering of three types of parent rock found in the earth's crust. Igneous rock (e.g., granites) is formed when the hot magma of the earth's mantle rises to near the surface and cools. Igneous rock is composed of primary minerals, products of the original rock formation, such as olivine and plagioclase. Sedimentary rock (e.g., limestone and shale) is formed when deposits of materials in lakes and oceans accumulate and merge over thousands of years, and are pushed to the surface by geologic activity. They are composed of secondary minerals, which are the products of weathering. When either igneous rock or sedimentary rock is subjected to the intense heat and pressure of the earth's deep environment, the minerals in those rocks melt, forming new material, called the metamorphic rock. Weathering is the process whereby parent rock is broken down by physical and chemical processes. Scouring by wind, repeated freezing and thawing of water in rock crevices, and the physical and chemical actions of roots are the chief modes of weathering. Initial chemical weathering occurs when water dissolves some of its more readily soluble constituent minerals (esp. $CaSO_4$ and NaCl). We here leave more detailed discussion on soil formation to ecology textbooks (e.g., Stiling 2011) but emphasize that the displacement of oxides minerals by hydrogen ions is the key step and the process is a continuing one that constantly evolves. Hence, soils are dynamic, changing from the moment they begin to develop on newly exposed rocks. But even after soils achieve stable properties, they remain in a constant state of flux. Groundwater removes some material; other material enters the soil from vegetation, in precipitation (lightning produces absorbable nitrates), as dust from the air, or by further weathering of rock from below. Again because the critical role of the hydrogen bond, arid region typically have shallow soils, with bedrock lying close to surface. On the other extreme, weathering proceeds rapidly in parts of the humid Tropics, where chemical alteration of parent material may extend to depth of 100 m (Eyre 1968). Most soils in temperate climate zones are intermediate in depth, ~1.2 m global average. At a place, soil is a result of dynamic balance of production and erosion. Thus, soils may not form at all where weathered material and detritus erode as rapidly as they form. Soil development also stops short over alluvial deposits, where fresh layers of silt deposited each year by floodwaters bury weathered

material. At this locations, soil thickness increases but it is by advection from upstream regions rather by local soil formation! In this sense, landslides also play a dual role in soil formation rate: by exposing the scarp region, increasing the weathering rate, but reducing the soil formation rate in the alluvial areas.

Under a given climatic regime, soil properties are the major form of control over ecosystem processes. Soils are the regions where geological and biological processes intersect. Soils mediate many of the key reactions within the giant global reduction–oxidation cycles of carbon, nitrogen, and sulfur, and provide essential resources to biological processes that drive these cycles. As the intersection of the terms bio-, geo-, and chemistry in the term biogeochemistry, soils play such an integral role in ecosystem processes that it is impossible to separate the study of soils from that of ecosystem processes. Soils are formed from weathered metamorphic rocks. The presence of living organisms accelerates the soil formation processes. Water is a pathway for nutrients entering an ecosystem and, also, is crucial in determining whether the products of weathering accumulate or are lost from a soil, especially the soluble minerals. Topsoils generally are more fertile because weathering rates usually are larger at the surface. Moreover, leaching processes tend to transfer soluble ions (e.g., chelated complexes of organic compounds, iron or aluminum ions from precipitation or released in the weathering of upper layers of soil) downwards. During the downward movement, they can react with ions encountered at depth under new chemical environments (e.g., increased pH value), or may precipitate out of the system when dehydration occurs (e.g., water is evaporated in semiarid or arid climate zones). Consequently, the concentrations of silica and base cations in the secondary minerals usually increase with depth, resulting in a nutrient poor, deeper soil horizon. As iron and aluminum ions dissolved in the soil water move downward, slight changes in ionic content and the microbial breakdown of the organic matter both can cause the metal ions to precipitate as oxides. The deeper soil horizon containing iron-rich minerals usually is hardened irreversibly. These layers can impede water drainage and root growth. This is the case for tropical iron-rich soils, and similar processes exist for calcium (or magnesium) soils of arid and semiarid temperate climate zones. The hard calcic horizon at depth is formed when calcium carbonate precipitation occurs under conditions of increased pH, or under saturation concentrations of carbonate with evaporation of soil moisture. If a debris flow removes the fertile topsoil, then the deeper horizon is exposed and this layer has poor water retention ability and also is nutrient-poor. Moreover, roots cannot develop within it and thus cannot support regrowth. Even for the depositional alluvial fans, the exposed deep soil and deep buried top soil is a nutrient sink for the ecosystem, as the majority of the roots can use nutrients only in the upper one or two meters. Thus, landslides remove nutrients from the rhizospheric layer by burying nutrient-rich soil and unearthing nutrient-poor deep soil.

Following sections intend to build up proper background for understanding root reinforcement of slopes and their unique role in slope hydrology. Distribution of roots in soil represents the plants' strategy to maximize the use of available soil moisture under climatologically normal condition.

2.2 The Ability of Soil to Retain Water Is Related to the Size of Soil Particles

Most terrestrial plants obtain the water they need from the soil. The amount of water that soil holds, and its availability to plants, vary according to the physical structure of the soil particles. Soil consists of grains of clay, silt, and sand, as well as particles of dead and decomposing organic matter, called "detritus." Grains of clay (particles smaller than 0.002 mm according to USDA classification), produced by the weathering of minerals in certain kinds of bedrocks, are the smallest; grains of sand (particles larger than 0.05 mm), derived from quartz crystals that remain after minerals more susceptible to weathering dissolve out of rock, are often the largest; silt particles are intermediate in size. Collectively, these particles make up the soil skeleton. The soil skeleton is an imaginary stable component that influences the physical structure of the soil and its water-holding ability, but does not play a major role in chemical transformations.

Plants obtain water from the soil. The availability of water in the soil is only partly determined by the amount of water present. It is also determined by how tightly the water is held in the soil. The concept of water potential (to be detailed in Chap. 5, e.g., Sect. 5.1.3), which is central to the dynamics of water, plants, and soil, needs to be established to understand water movement within the soil–plant–atmosphere. The water potential of a system is a form of Gibbs free energy of solvent water in the system. It is usually measured in units of pressure (e.g., MPa, KPa, and GPa). In case of solutes diffuse, water moves down a gradient of water potential (moving from higher water potential to lower water potential) to arrive a uniform solute concentration. Apparently, pure water has the highest water potential and adding in impurities lower the water potential. Since water potential is a form of compressive tensor, there apparently are gravitational potential components (generally compressive pressure components) in the total water potential, in addition to the component determined by solute concentration (osmotic component for plant cell). Thus, a cell surrounded by pure water will gain water through osmosis. On the other hand, if it is surrounded by water of higher ions concentration, it may lose water. By convention, the water potential of pure water at 1-atmospheric pressure is zero.

A comparison of the water potential of the soil, the atmosphere, and various parts of the plants help us understand how water moves from the soil to the upper portions of a plant, a topic that we will discussed more in Sect. 5.1.3 below and have direct influence in slope hydrology for vegetated slopes.

2.3 The Movement of Water from Soil to Plant to the Atmosphere Depends on Transpiration and the Cohesive Properties of Water

Typically, water potential is lowest (most negative) in the atmosphere and highest in the soil. Leaves, stems, and other parts of a plant usually have water potentials in between. This difference creates a downward water potential gradient from the soil to the leaves and out to the atmosphere, which helps move water through the plant. The water potential of a plant is affected mainly by the concentration of solutes inside and tension applied to some parts of the plant. Water potential in the soil, at least for parts of the soil that are above the water table, is usually not affected as much by pressure components. Water is held in soil by capillary action resulting from adhesion of the water to the elements of the soil skeleton. This capillary action holds water in the soil with a force equivalent to a pressure of about 0.01 Mpa (~1 m water column). Water that is draw to soil particles with a vertical *continuous* column length greater than 1 m will drop the extra as ground water. Water within the spaces between soil particles is held by cohesion, which generates pressures of about −15 KPa (field capacity tension). Water in large pores inside the soil, at a distance from the surfaces of soil particle, is held with pressure less than −15 KPa (e.g., −17 KPa), and usually drains through the soil under the pull of gravity. The tendency of soil to hold additional water molecules is referred to as its matric potential. The matric potential equals to the average strength with which the least tightly held water molecules are held. The matric potential of a soil contributes to its total water potential. For example, if the soil is very dry, the matric potential may be extremely low (e.g., −200 MPa or lower). This will lower the water potential of the soil, thereby making the water potential gradient from soil to plant weaker.

As soil water is depleted, the remainder is held by increasingly strong forces, because a greater portion of the water lies close to the surfaces of soil particles. There are empirical relationship between water content and water potential (Brady 1974). For a soil of porosity 45 % (loamy soil), the saturation moisture content is 45 %. The field capacity of this soil may be only 34 %. Thus, at field condition, when the loam soil is saturated, about 11 % of the water will be lost to ground water by gravity. The wilting point—the minimum water content of the soil at which plants can no longer obtain water—may be 7 % volumetric soil moisture. The difference between the field capacity and the wilting point, about 27 % for this loam soil, measures the water available to plants. Of course, plants obtain water more readily when soil moisture is close to the field capacity. In clayey soils with predominantly smaller particles, the soil skeleton has a relatively large surface area; such soils hold a larger amount of water at both the wilting point and the field capacity, and a correspondingly larger proportion of soil water is held by forces greater than −15 KPa. On the other hand, sandy soils with predominantly larger skeletal particles have less surface area and larger interstices between particles. Most of the soil water is held loosely and is thus available to plants, but such soils

have lower field capacities due to higher drainage. Plants can obtain the most water from soils having a variety of particle sizes between sand and clay.

In order to live, terrestrial plants must obtain water from the soil and transport it to all areas of the plant where cellular function is ongoing. This transport mechanism must include a way to get water from the soil into the roots, and a means to move that water from the roots to the topmost parts of the plant, all against the gravity and the resistance exerted by the structures through which the water moves. Xylem is the tissue primarily responsible for the transport of water in plants. Xylem is composed of dead cells in the stems of the plant. In addition to water transport, xylem also provides support for the plant and is the major contributor to root tensile strength. We are not going to discuss the details of the upward water transfer here but would like to emphasize that active transpiration ("transpiration pull") is critical for sending water to tree tops over 50 m tall. Xylem sap's concentration changes also are responsible for maintaining the downward water potential inside stems. Thus, the cohesive properties of water, and the fact that the xylem tissue creates a continuous column of water from root to leaves, explain the movement of water. When tension is applied to the top of the column by transpiration, the entire water column is pulled upward.

Plants obtain water from soil by osmosis, so the ability of their roots to take up water depends on their osmotic pressure. Osmotic pressure, in turn, is a function of the concentration of dissolved molecules and ions within the root cells. By manipulating the osmotic pressure of their root cells, plants can alter their ability to remove water from the soil. Plants growing in deserts and in salty environments can increase the water potential of their roots by as much as −6 MPa by increasing the concentration of amino acids, carbohydrates, or organic acids in their root cells. There certainly is a metabolic price to pay to maintain such high concentrations of dissolved substances. Soil to root water transfer also is necessary because life requires inorganic nutrients and the mineral nutrients (nitrogen (N), phosphorous (P), sulfur (S), potassium (P), calcium (C), magnesium (M), and iron (I)) must be obtained from water as dissolved forms (Chapin 1980). For low level concentration nutrients that limits growth (e.g., potassium), active uptake of that nutrient by increasing the extent of the root system, or the absorptive surface of the roots. The active absorption requires the expenditure of energy as the root tissue moves ions against a concentration gradient. Plants may also respond to decreased soil nutrient availability by increasing root growth at the expense of shoot growth—allometrically.

2.4 Plants Can Control the Energy and Material Fluxes Between Their Internal and External Environments

Crops and wild species growing on fertile soils have greater capacity to absorb nutrients across their root surfaces, and their growth rates vary in response to variations in soil nutrient levels. Species adapted to nutrient-poor soils are much more conservative in increasing their rate of growth (Chapin 1980) and cope with nutrient-limitation by allocating a large proportion of their biomass to roots; by growing slowly and retaining leaves for longer periods, thereby reducing nutrient demand; or even establishing symbiotic relations with fungi, which enhance mineral absorption. In response to nutrient flush, their roots absorb more nutrients than the plant requires and store them for subsequent utilization when the nutrient status of the soil decreases. Different species relate differently to their environments because many physical and physiological processes vary out of proportion to size. In ecology (Ricklefs and Miller 2000), this is referred to as allometry. The above adaptation to environments by roots can be described by allometric relationships.

Water is the basic medium of life. The chemical, physical, thermal, and mechanical characteristics of water result from the nature of the covalent bonds between hydrogen and oxygen and the weak hydrogen bonds between water molecules. This also explains its "lubrication effects on granules." Live vegetation, by transpiration, alters the soil moisture level and indirectly affects slope stability.

References

Bolin B, Sukumar R, Ciais P, Cramer W, Jarvis P, Kheshgi H, Nobre C, Semenov S, Steffen W (2000) Global Perspective. In: RT Watson, I. Noble, B. Berlin, N. Ravindranath, D. Verardo, and D. Dokken (eds) Special Report on Land Use, Land-Use Change and Forestry. Cambridge Univ. Press, Cambridge, UK, pp 23–51

Brady N (1974) Nature and property of soils, 8th edn. Macmillan, New York, NY

Chapin FS III (1980) The mineral nutrition of wild plants. Annual Rev Ecol Syst 11:233–260

Eyre S (1968) Vegetation and soils: a world picture, 2nd edn. Aldine, Chicago, IL

Gifford RM (1982) Global photosynthesis in relation to our food and energy needs. In: Govindjee (ed) Photosynthesis: Development, Carbon metabolism and plant productivity, Vol. 2, New York, Academic Press, pp 459–495

Gonzalez-Prieto S, Carballas T (1995) N biochemical diversity as a factor of soil diversity. Soil Biol Biochem 27:205–210

Oades J (1993) The role of biology in the formation, stabilization and degradation of soil structure. Geoderma 56:377–400

Ricklefs R, Miller G (2000) Ecology, 4th edn. Freeman and Company, New York, NY, 822 p

Stiling P (2011) Ecology: global insights and investigations. McGraw-Hill Education, New York, NY, p 656

Chapter 3
Landslides Are a Double-Edged Sword

The surface of the Earth, both on land and beneath the oceans, is continually modified by mass movements responding to gravitational forces. In this sense, landslides reduce the hill slopes to stable angles. Landslides can assume the forms of rockfalls, slumps and slides, and debris flows (Cruden and Varnes 1996; Cruden 1991; Iverson 1997). Here, landslide refers to downslope movements at a variety of scales and velocities, and also those related to vegetation cover. Storms are the primary cause, and storm-triggered landslides (debris flows, Fig. 1.2) are the emphasis of this book, because of their relatively frequent occurrence and their particularly high destructive potential (tending to travel extended distances at high speeds). Dense and diluted debris flows (e.g., an equal amount or more water and poorly sorted solid sediment, Iverson (1997)) are not differentiated except when it is absolutely necessary.

Topography influences soil through its effects on climate and the differential transport of fine soil particles (Amundson and Jenny 1997). Characteristics such as soil depth, texture, and mineral content vary with hillslope position. Erosion processes, such as infiltration-excess surface runoff, preferentially move fine-grained materials downslope and deposit them at lower locations. Depositional areas at the bases of slopes and in valley bottoms, therefore, tend to have deep, fine-textured soils with high organic content and high water-retaining capacity. These areas also supply more soil resources (water and nutrients) to plant roots and microbes, and provide greater physical stability than do higher slope positions. Thus, alluvial fans at valley bottoms typically exhibit higher rates of most ecosystem processes than do ridges or shoulders of slopes. In brief, soils in lower slope positions have greater soil moisture, more soil organic matter content, and higher rates of nitrogen mineralization and gaseous losses than upslope soils (Matson et al. 1991; Matson 1991).

In addition to soil media, water supply is vital for an ecosystem. The surface water channelling system may start from landslide scars (Montgomery and Dietrich 1988). The fact that, with the same topographic gradient, a drier region tend to have a larger source area (of sliding material), indicates the importance of storm-

© Springer International Publishing Switzerland 2015

D. Ren, *Storm-triggered Landslides in Warmer Climates*,
DOI 10.1007/978-3-319-08518-0_3

triggered landslides (debris flows) as the primary channel makers. In creating channels, landslides themselves are not shelf-perpetual. Suppose there is a scarp left by a landslide. This scarp, eventually will be filled in by the surrounding area through diffusion processes (micro-scale landslides), unless loose material falling into this scarp is regularly removed through advective processes such as runoff or Aeolian processes. In exactly the same way that removal of sawdust facilitates further cutting of a piece of wood, effective removal of the loose granular cover on a scarp further exposes the slope to erosion and development of crevasses (Fig. 3.1). This positive feedback is composed of the relay of advective processes and diffusion processes, and landslides are the nexus. Therefore, on geological timescales, landslides help to produce stable land (Rinaldo et al. 1995) suitable for agricultural and habitation (and, for tropical islands, tourism) and they provide materials that form fertile plains and valleys, beaches, and barrier islands. However, on the scale of a human life span, the benefits accruing from landslides are overshadowed by their destructive characteristics; they are hazards that should be understood and mitigated as much as possible. This nature of being a double-edged sword partially explains their frequent intersections with human activities. Landslides are among the most costly natural hazards in terms of human life and economic losses, particularly because they tend to repeat (their repeatability nature). Non-systematic, individual landslides are inefficient in stabilizing/levelling a region. Previous landslides leave morphologic and geologic features prone to future landslides. For example, once atmospheric conditions are favorable, renewed deformation is likely for many dormant slides in the Mediterranean climate zone. Even those inactive (fossil, Varnes 1978) ones can be reactivated once the precipitation climatology changes (Ren et al. 2011), or when human activities, such as reservoir construction, alters their topographic or hydrologic conditions.

While it is reasonable to generalize that landslide activity is important, studies of landslide phenomena in regard to deforestation are, along with ecosystems in general, not well addressed. The following comments are not an exhaustive review but aim to indicate the relevance of landslides to deforestation.

The main geological hazards of volcanic activity, earthquakes, and landslides are commonly, but not entirely, associated with processes occurring in areas near subduction zones. This is, because it is there that elevation gradients are large enough to generate instability and, also, sources of hazardous agents are abundant. This explains why the "landslide belt" coincides with the Earth's major earthquake belts. The Himalayan Mountain range, for example, is a hot spot (Fig. 3.2). Figure 3.2 shows the primary landslides that are up to 2.5 m thick and contain $>10^5$ m^3 of solid material, enough to cause vegetation damage. Plotted are the cases for years 2003–2007. Landslides are one type of geological hazard. Geological hazards become so only where population, services or structures are at risk. In this sense, although northwestern China is a hot spot for landslides, the low population, by itself, reduces the hazard to a vanishingly small likelihood. In contrast, India and Indonesia both have large populations under the threat of storm-triggered landslides. As the population increases, previously unoccupied alluvial fans are used for habitation (e.g., the Zhouqu County in China) and landslide events therefore have a

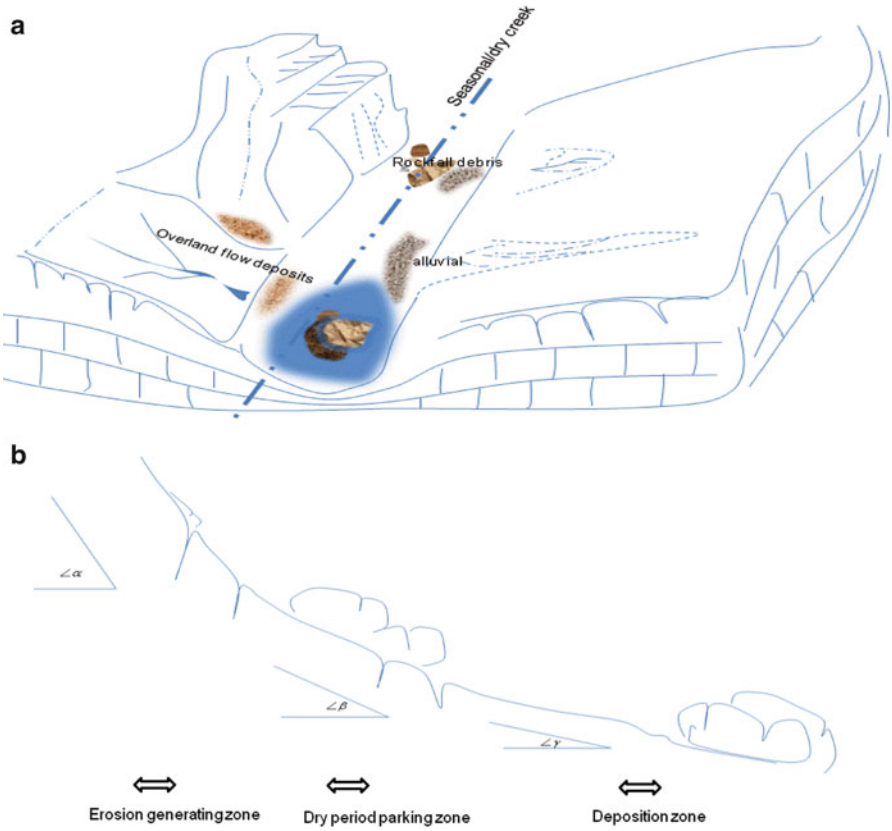

Fig. 3.1 Repeatability of landslides prone region. During relatively dry conditions, agitated sliding material (with the reduction of strength as a result of erosion or liquefied by seismic shaking) on the banks of a dry creek usually stop mid slope (at short distance down slope from their scarps, panel (**a**)), because the bed rock slope becomes gentler downward to the toe (**b**). Following storms collect these debris deposits and entrain them down the creek (progressive bulking). 1D slope model is unsuitable for the progressive bulking type of slides because the agitated material is not resting on one uniform slope. The sliding material is laterally confined before being displaced (wash) out and flow into the creek. If the fallouts debris is not removed by rainfall, the slope of the bank reduces and following slides are harder to occur—a cold trace left by previous slides. Effective removal of the deposits facilitates future slides the same way removing saw dust facilitates the cutting process of a piece of wood. The growth of the dry creek is a positive feedback favored by nature in regions of repeated landslides because it is an effective relay between slow diffusive processes (working on large area) and concentrated quick advective processes (rainfall water entrainments). Panel (**b**) is a cross-sectional view along the *dashed line* along the center of the dry creek. Graded sloping feature are shown (slope angle gets gentler down slope). Accumulation of sliding material related to the fatigue of the bank slopes and the production rates increase under cyclic forcing conditions such as wet–dry and freeze–thaw cycles. Thus the illustration is a common mode of repeated landslides over mid-latitude as well as permafrost regions. For the latter, thawing period corresponds to wet period when removal of the accumulated debris is scheduled to happen

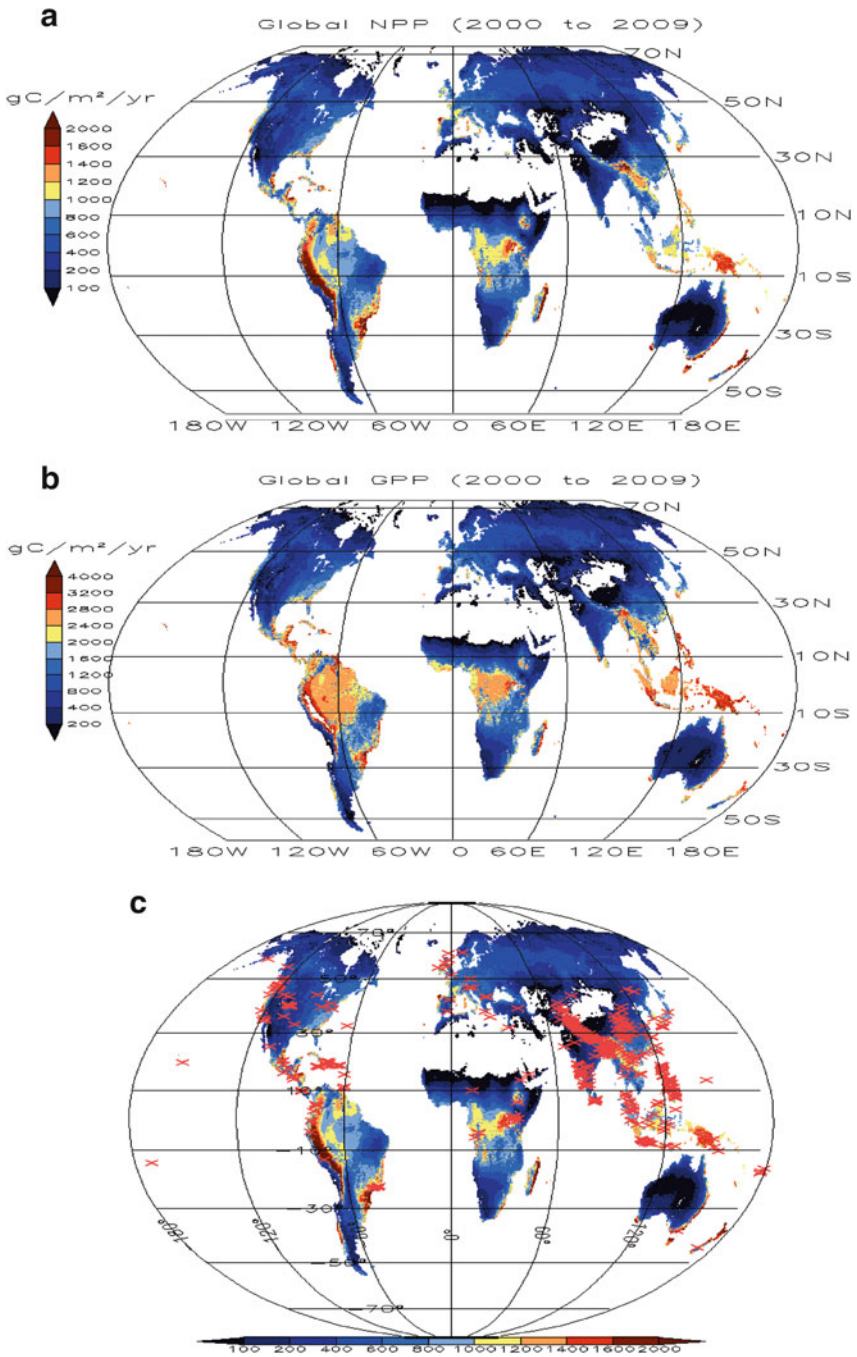

Fig. 3.2 Global distribution of Net Primary Production (NPP, (**a**)) and GPP (**b**) from MODIS NDVI products (color shading, in g/m^2/year). Data credit: M. Zhao (U. Montana). Panel (**c**) shows occurrence (*red crosses*) of storm-triggered landslides (2003–2008)

greater potential to impact human settlements or activities. The state of California is a locality where the combined effects of earthquakes and landslides have been documented. The precipitation of this region, being regularly affected by El Niño and Southern Oscillation (ENSO, Neelin et al. 1998; McPhaden 2002) and potentially also sensitive to climate change, as it lies in Mediterranean climate zone, possesses large uncertainty in the future occurrence of storm-triggered landslides (Ren et al. 2010).

From Fig. 3.2, there are very few landslide hazards for regions with net primary production (NPP) <200 g/m^2/year, indicating that soil, vegetation and landslides are closely linked in the Earth's environmental system. The landslide-free areas exist, either because of limited liquid precipitation (deserts and polar regions), or because of a lack of soil mantle. In both cases, the annual net primary productivity is low. For vegetated slopes, landslides give an edge to those survivors (usually shallow rooted, grassy plants) in nutrition sequestration. For those species that have a disadvantage in the competing in sunlight, landslide-created scars provide a chance for them regain predominancy. In this sense, landslides disturbances may improve species diversity. The chances for landslides to selectively destroy a certain species are slim. In addition, landslides are a challenge for plant adaptation in a warming future climate. In summary, landslides are disturbances to ecosystems, and ecosystems are the material foundation for our human society. It is imperative to establish an intelligence network to handle landslide disasters: to monitor the historical and present situations to understand the conditions causing slope instability; and to project their occurrence to make informed decisions on infrastructure investment and assistance, as well as establishment of evacuation routes in case of a disaster. Landslides, because they are caused by unfortunate combinations of several extreme events, are low-frequency phenomena. However, a major landslide at one location should not be forgotten after the media coverage ceases. Knowledge gained from one case may have application in mitigating disasters at other locations. To evaluate the consequences of landslides on ecosystems, it is necessary to understand why landslides occur. The possibility of a landslide depends on the balance between the driving forces for downslope movement and the forces that resist this movement. Uneven topography caused horizontal stress gradients are the driving stress for sliding. At the stationary phase, the cohesion between soil particles acts as the resistive force. Once sliding starts, the resistive force associated with flow shear is then the primary stress that eventually stops the flow.

References

Amundson R, Jenny H (1997) On a state factor model of ecosystems. Bio Sci 47:536–543

Cruden DM, Varnes DJ (1996) Landslides types and processes. In: Schuster RL, Krizek RJ (eds) Landslides investigation and control, Special report 247. Transportation Research Board, Washington, DC, pp 36–75

Cruden D (1991) A simple definition of a landslide. Bull Int Assoc Eng Geol 43:27–29
Iverson R (1997) The physics of debris flows. Rev Geophys 35:245–296
Matson P (1991) Trace gas emissions by plants: a summary. In: Sharkey T, Holland E, Monney HA (eds) Trace gas emission by plants. Academic, San Diego, CA, pp 341–343
Matson P, Volkmann C, Coppinger K, Reiners W (1991) Annual nitrous oxide flux and soil nitrogen characteristics in sagebrush steppe ecosystems. Biogeochemistry 1:1–12
McPhaden MJ (2002) Mixed layer temperature balance on intraseasonal timescales in the equatorial Pacific Ocean. J Climate 15:2632–2647
Montgomery D, Dietrich W (1988) Where do channels begin? Nature 336:232–234
Neelin J et al (1998) ENSO theory. J Geophys Res 103:14,262–14,290
Ren D, Fu R, Leslie LM, Dickinson R, Xin X (2010) A storm-triggered landslide monitoring and prediction system: formulation and case study. Earth Interact 14:12. doi:10.1175/2010EI337.1
Ren D, Leslie L, Fu R, Dickinson R (2011) Predicting storm-triggered landslides and ecological consequences. Bull Am Meteorol Soc 92, 129–139. DOI: 10.1175/2010BAMS3017.1
Rinaldo A, Dietrich W, Rigon R, Vogel G, Rodriguez-Iturbe I (1995) Geomorphological signatures of climate. Nature 374:632–635
Varnes D (1978) Slope movement types and processes. In: Schuster RL, Krizek RJ (eds) Landslide analysis and control, Transportation Research Board Special report 176. National Academy of Sciences National Research Council, Washington, DC, pp 11–33

Chapter 4
Strain and Stress

The mathematical theories of elasticity, viscosity, and plasticity all follow the same course in continuum mechanics. Firstly, the notions of stress and strain are developed; secondly, a stress–strain relationship between these quantities or their derivatives is assumed which idealizes the behavior of actual materials; and finally, using this relationship, equations of motion or equilibrium are set up which enable the state of stress or strain to be estimated when a body is subjected to prescribed forces. In this chapter the analysis of stress and strain will be developed in detail. We will start with three dimensional theories and leave the 2D theories to classical textbooks such as Jaeger (1969a, b). The three dimensional theory in Sect. 4.3 leads to the Mohr's representation, which provides a simple geometrical construction for the stress across any plane. The analysis of strain is essentially inherited in the deformation of granular material: an assemblage of particles of multiple dimensions. We will start from elastic (infinitesimal strain) theories and evolve to finite strain theory, applicable to brittle upper tectonic materials on slopes which experience large strain.

In Fig. 4.1, we used simplified geometry to illustrate the equilibrium requirements of a set of identical blocks. There is no cohesion among them, just friction. The maximum available friction is proportional to normal stress (pressure). From Newton's Third Law, the forces (also pressure, because the interface are identical) in the horizontal direction are identical at every interface. However, the required vertical "lift" is different for each block, with the central block requiring the least and the two boundary blocks the most, increasing linearly. Suppose the frictional coefficient is a constant, in equilibrium, all interior interfaces can provide more than enough lifts to counter the block weights. In other words, the interior section is farther away from the critical yielding condition. If, for some reason, the horizontal pressure is reduced, the blocks near the boundary will slide first and yield the maximum displacement (compared to the previous equilibrium configuration, Fig. 4.1c). This is also why the arch bridges need to be fortified at the ends and can use less material at the center (bottom panel in Fig. 4.1, i.e., Fig. 4.1d). In textbooks, failure properties of actual materials are derived from carefully prepared

© Springer International Publishing Switzerland 2015

D. Ren, *Storm-triggered Landslides in Warmer Climates*,
DOI 10.1007/978-3-319-08518-0_4

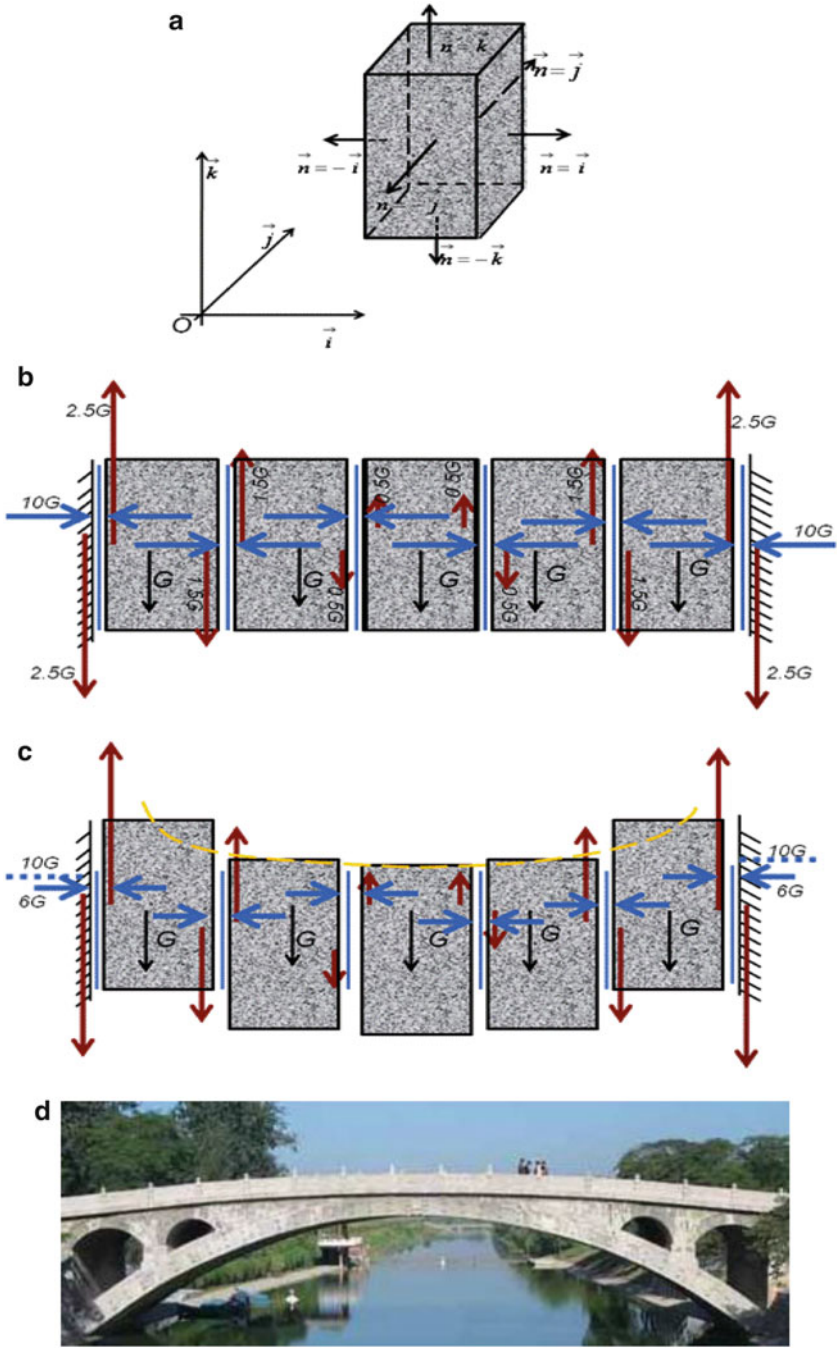

Fig. 4.1 Panel (**a**) shows out normal of the surfaces of a block of weight G. In Panel (**b**), *vertical red arrows* indicate how the forces are balanced for each block. The *horizontal blue arrows* indicate the compressive force at the interface and the *vertical bars* are the potential (maximum) vertical friction corresponding to the horizontal compress. Panel (**c**) (*yellow dashed lines*) shows

specimens. For granular earth material, many aspects are complicated by the complex configuration and geometry. Failure usually manifests in the form of relative displacements among granules. In general, the soil material above the water table can resist more pressure than tension, and can be fairly adequately represented by the straight line Mohr envelope (c.f. Sect. 4.3). Around a vertical crevasse, the horizontal pressure between the two regolith layers can be very small (if filled by water, just the hydrostatic pressure of the liquids). Inside the regolith, the vertical direction may satisfy the hydrostatic relation very well. The horizontal direction can be very far from being in hydrostatic equilibrium. If a regolith is surrounded by cracks (crevasses), small changes in liquid depth can set it into motion, because the neighboring regolith may be of minimal assistance in balancing this extra horizontal pressure (Jaeger 1969b).

There are several working hypotheses on stress distribution within granular slope soil material. The interested reader should refer again to Chapter IV of Jaeger (1969a). Following is a description of the yielding (ductile material)/fracture (brittle material) criteria and their proper implementations with regard to vegetated slopes. To ease the interested readers to follow the derivations in this chapter, Chap. 12 provides the necessary mathematical skills used here for tensor analyses.

4.1 A Simple "Cantilever Beam" Approximation

When being put under stress, the behavior of general material has the following stages: Elastic region, permanent damage starts after reaching yield point, plastic deformation, and necking and separation. Within elastic range, the fatigue caused by external stress is minimal and reversible after the load is removed. Maximum strain when entering from the elastic region to the plastic region is a good measure for brittle and ductile material. The limit usually is set at 10^{-3}. After each such strain cycle, unit-cells' orientation is "trained" by the external stress and becoming better organized. The following cycle usually has a raised yielding point (the so-called strain-hardening). Many measures such as Young's modulus (E), Poisson ratio (ν), modulus of rigidity (G), and incompressibility (K, bulk modulus) are elastic moduli (and indicate the nature of material in the elastic range). An important property of bed rock that is important for geohazard modelling is its brittle to ductile transformation if confining pressure reaches ~0.5 GPa, equivalent to be burying 20 km down into earth. This is not considered in our landslide modelling system because the largest elevation on earth is smaller than this magnitude.

Fig. 4.1 (continued) the vertical deflections when the horizontal compressive force is relaxed (from 10G to 6G, assuming a frictional coefficient of 0.25). Stresses are force per unit normal area. We follow the convention of Jaeger (1963 throughout this volume). Panel (**d**) is Zhaozhou Bridge of China (*source*: http://kaleidoscope.cultural-china.com)

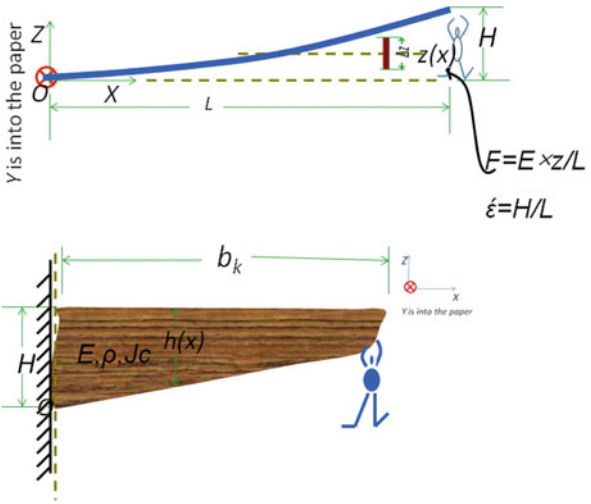

Fig. 4.2 Cantilever beam approximation. *Upper panel* is the mechanical energy storage estimation when an elastic splinter is deflected from one end. *Lower panel* is an idealized model for limiting length of a cantilever beam of brittle material

The granular materials involved in landslides are safely considered to be elastic granules of brittle nature.

Before reviewing more generally applicable recent yielding theory, we now discuss a simplified elastic model, the cantilever beam model, suitably explains the Karst caves geometry and limit depth before being self buried (material peeling off the ceiling and side walls having larger porosity (i.e., void space between granules) when being granularized and quickly filling up the cave) by falling debris. Yielding/fracture is actually a gauge of how much mechanical energy per unit of material can store, an energy form of measure of fatigue resistance capability. As shown in the simplest one dimensional form (Fig. 4.2), if an elastic splinter (of Young's modulus E and length L) is deflected upward by an amount H, the work needed to be done (also the mechanical energy stored in the system), can be obtained by a simple integration:

$$W = \int_0^H F(z)dz = \int_0^H E\frac{z}{L}dz = \frac{E}{2L}H^2 = \frac{E}{2}\left(\frac{H}{L}\right)^2 L = 0.5E\left(\overset{\bullet}{\varepsilon}\right)^2 L, \qquad (4.1)$$

where W is mechanical energy, F is force, and other variables are as in the illustration. Per unit length, the density of mechanical energy is $0.5E\left(\overset{\bullet}{\varepsilon}\right)^2$. This energy intensity expression is applicable for three dimensional form. More interestingly, this expression has formal similarity for fluids, and can be formally extended to describe granular material and viscoplastic material as well (to be shown later). For example, in the case of fluids, E is in the form of viscosity and $\overset{\bullet}{\varepsilon}$ is the strain rate expressed in the form of flow shear. Returning to the discussion of a simple yielding model, as indicated in the lower panel of Fig. 4.2, the material is

assumed to be stiff and the deflection in the z direction is sufficiently small that linear deformation theory for elastic material holds. It is further assumed that the cross section is rectangular to simplify the derivation by removing variations in the y-direction and working only in the x-z plane (the convention for moment and torque are all in the right-handed coordinate system, as in Fig. A.1). It is further assumed that the beam material has an elastic modulus E and density ρ. Other geometrical parameters are as labelled in the figure.

As the cross section is assumed to be rectangular, the area moment of inertia is $I = \frac{1}{12}H^3$ at point O. The momentum around O exerted by the self-weight of the beam and an external loading (analogous to tides and other random factors), T, located at the tip end of the shelf can be expressed as:

$$M = \int_0^{b_k} x\rho g h(x)dx + T \bullet b_k, \tag{4.2}$$

where g is gravitational acceleration (9.8 m/s^2), and M is the moment in the positive y-direction. In a static state, the resistance moment should be in the $-y$ direction and of the same magnitude. As a result of moment drive, there is potential energy stored around the cross section passing through O:

$$W = \frac{2E \bullet I}{H \bullet r} \tag{4.3}$$

where r is the curvature of the beam at O. At the yielding condition, $f_c = \frac{E}{r}$ is the tensile strength of ice. In Eq. (4.3), the factor of 2 appears because mass conservation is assumed, so that the cross-sectional area experiencing compression and the area experiencing expansion are the same. The relation between strain and Young's modulus are applied, producing the factor of 2. The stored potential energy and the moment should be the same. That is,

$$2f_c \bullet I = H \bullet M \tag{4.4}$$

Equation (4.4) also is the key equation for obtaining the limiting length of ice shelf before a systematic attrition.

For example, assuming a linear ice thickness profile:

$$h(x) = H - kx, \text{ where } k = \frac{H}{b_k}\frac{\rho_i}{\rho_w}, \tag{4.5}$$

where ρ_w and ρ_i are respectively the density of water and ice. Substituting into Eqs. (4.2) and (4.3), and using the relationship of Eq. (4.4) gives:

$$b_k = \frac{-3T}{2a} + \left(\frac{9T^2}{4a^2} + \frac{c}{a}\right)^{0.5}, \tag{4.6}$$

where $a = \rho_i g H\left(1 - \frac{\rho_i}{\rho_w}\right)$, and $c = -\frac{f_c H^2}{2}$. For the case without external loading, $b_k = [f_c H/(2\rho_i g(1 - \rho_i/\rho_w))]^{0.5}$. This is the expression for the limiting length for a uniform material uniform geometrical beam hanging horizontally. Several application of this expression can be found in Karst cave life cycle studies. For example, as the cave size expands, the peel off of material at the central section is largest and decrease gradually to peripheral region. The falling out debris, has larger void space (porosity) and tends to fill up the cave, if there is no currents to take them away, the cave quickly fills up because the horizontal expansion must be outpaced by the central section peeling off speed, governed by the limiting length expression. If there are currents effectively wash the debris off, then the cave will eventually have a sky-window (e.g., natural "bridges" in southern Texas) when the central section all falls down. This formula has relevance in the application of slow creeping of deep-seated landslides.

4.2 The Griffith Theory and Possible Application in Stability Developments for Fractured Slopes

It is well known that attempts to calculate the tensile strengths of simple crystals give results very much higher than those observed experimentally. Griffith hypothesized this is because of the presence of a large number of minute cracks, known as Griffith cracks, inside the material. Here, it is not intended to repeat the sophisticated derivations, which include algebraic skills. The gist/essence of the Griffith theory is that particles are confined in an energy trap within a certain range of the equilibrium position. Depending on the bonding, this can be determined by magnetic/electronic forces and/or van der Waals–London forces. Very similar to the free-length theory in turbulent fluid dynamics, once a particle can move away from the equilibrium position farther than the inter-particle average spacing, fluidity appears and macroscopically manifests itself as a fracture or yield. Thus, there are two rival players in the further development of an existing crack: one is the release of potential energy (W, as in Eq. 4.1) but the other is the increase in surficial energy (creating new interfaces). Assume, on a flat plate, there is an elliptical hole of major axis $2l$ and subject to an average tensile stress σ (Fig. 4.3). The concentration of stress at the acute tip is $\sigma* = 2\sigma\sqrt{l/r}$, where r is the inverse curvature at the ends of the major axis. Taking r as the intermolecular spacing a, the crack will spread if $\sigma*$ reaches σ_m, the maximum tensile stress which can be sustained by the material without cracking. To estimate the value, the process of cracking must be considered: this produces two new surfaces within the material with a distance apart of the order of the intermolecular spacing a, and with each possessing surface

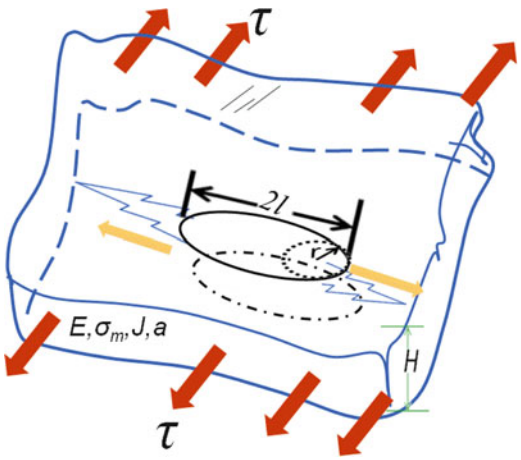

Fig. 4.3 Illustration of Griffith theory on fracture propagation. A brittle plate of uniform thickness H and elastic material parameters E (elastic modulus), σ_m (strength), J (surface energy) and a (unit cell dimension) put under external tension (τ). The oval indicates a minute crack with long axis $2l$ and curvature of the acute tip of $1/r$. Whether or not the crack can progress depends on the relative magnitude of the increased surface energy and the released strain energy, with the further growth of the crack

energy J per unit area which is an intrinsic and measurable property of the material. The released strain energy must exceed this surface energy for cracking to proceed. Using the same concept as in Eq. (4.1) and applying a linear strain–stress relationship, the amount of strain (mechanical) energy is $\frac{\sigma_m^2}{2E}a^2$. The critical requirement for cracking to proceed is $2JaD = \frac{\sigma_m^2}{2E}Da^2$, where D being the uniform depth of the plate. That is, $\sigma_m = \sqrt{4JE/a}$. Equating this with the above $\sigma*$ expression, the uniaxial tension in the direction perpendicular to the crack is obtained as $\tau = \sqrt{JE/l}$, which is of the same order as results from experiments with ceramics and glasses. This expression also explains the accelerating characteristic of crack propagation before being arrested by another crack.

From Griffith's energy criteria, further cracks develop if the elastic energy released from further cracking exceeds the required surface energy (e.g., 30 mJ/m^2 for solid ice and 140 for some upper crust lithospheric rocks) to propagate the crack. Application of this criterion to the problem at hand with weathered regolith is complicated by it being a multiple-body problem. It can only be assumed that a slope contains a large amount of randomly oriented incipient cracks and that the cracks proceed in the direction of the highest local stress (tip ends of longest cracks). The most dangerous configuration is that of a crack heading to and merging with a "parallel" one. At the other extreme, resting of a crack happens when two perpendicular cracks meets and releases the concentrated stress, as depicted in Fig. 4.3.

4.3 Mohr's Theory of Fracture and von Mise's Criteria

Fracture/yield is, in essence, a fatigue process. It happens when the mismatch between stresses in different principal directions is so great that it exceeds the tolerance level of the material. Fracture is process specific and usually no two fractures are the same. Cyclic processes hasten the fatigue processes because defects inside the material develop coherence with cyclonic forcing (otherwise, cracks arrest cracks and stable configuration develops within the fabric and delays the fatigue process). Macroscopically, developing coherence creates distortional strain energy. Mohr's theory assumes that, at failure across a plane the normal and shear stresses across the plane, σ and τ, are intrinsically connected by some form of generic functional relationship, $\tau = f(\sigma)$, characteristic of classes of material. Since changing the sign of shear stress only changes the direction of failure but not the condition for it, the curve must be symmetric about the σ axis. Because tests of experimental specimen are undertaken in conditions with symmetry in one principal direction, the 2D Mohr envelope is used in the following discussion (Fig. 4.4, a special form of $\tau = f(\sigma)$). Any state can be represented by a Mohr circle on the (τ, σ) plane. If the circle lies wholly within the curve $ABA'B'$, nowhere does the stress involved attain the critical value: if any portion lies outside this curve, the material cannot withstand the stresses. The limiting case is that of a circle, such as those of centers C1–C3, which just touches the curve AB. In the case of C1, failure will take place under conditions corresponding to the point P1, that is, over planes whose normals are inclined at angles of half the angle P_1C_1D to the direction of the greatest principal stress. The curve $\overset{\frown}{A}\overset{\frown}{B}$ will be the envelope of all the circles corresponding to all conditions at which fracture takes place, and for this reason is known as the Mohr envelope. To construct the Mohr envelope, three special circles can be relatively easily identified (blue circles in Fig. 4.4) through simple experiments of compression, simple shear and tension, respectively for those centered at C4, O, and C3. In practice, it is difficult to perform shear or tensile tests on rock material, and the triaxial test is preferred. In this, the specimen is subjected to axial compression and to hydrostatic pressure in the perpendicular directions. By varying the hydrostatic pressure, any number of circles, all to the right (since compress is negative) of the τ axis, can be plotted. Since increasing the hydrostatic pressure in general increases the resistance to fracture, it seems probable that the Mohr envelope is open to the right. In this case, for sand stone, the Mohr's envelope seems to fit the straight line Coulomb–Navier theory, $\tau = \pm(\tau_1 - \mu\sigma)$. The angle between the direction of the greatest principal stress and the out normal of the plane of fracture makes an angle $0.5a \tan(1/\mu)$. Actually, shear strength of most bedrock can be determined quite accurately using this approximation through triaxial testing. Mohr's theory, as detailed above, is an empirical attempt to set up a criterion which gives not only the stress necessary to cause fracture but also the direction of fracture: it has the merit that the quantities involve both the mean stress and the maximum shear. Many important results regarding slope material follow from the geometry of the Mohr envelope. For convenience of the algebraic

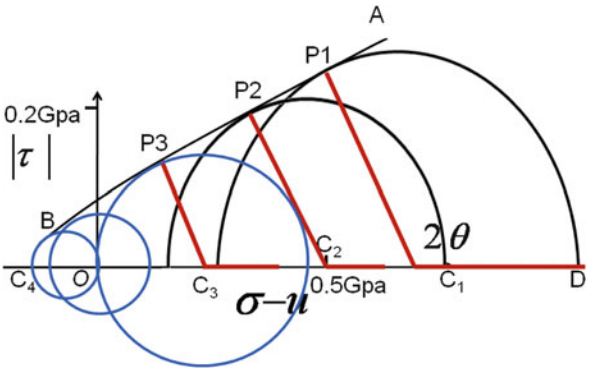

Fig. 4.4 Mohr's envelop for failure of sandstone under triaxial conditions including pore-pressure u. Adapted from Hubbert (1959), proving the validity of Coulomb–Navier criterion for earth material

expression, we now use a more generic form of the Mohr curve as in Fig. 4.5 (combining p and u into $-\sigma$). Since slope soils cannot sustain tension, only the compressive stresses are of concern. We write $\sigma_1 = -p_1, \sigma_2 = -p_2$ for the principal stresses so that the lengths OP1 and OP2 are p1 and p2. Also, it is convenient to introduce as a new parameter the angle α defined by $2\alpha = \phi + \pi/2$ so that the angles (Fig. 4.5) BCP_2 and BAP_1 are both 2α. That is, when failure takes place, the plane of sliding will make an angle α with the direction of lesser compression. It follows immediately that $c\tan(\phi) = -\tan(2\alpha) = \frac{2\tan(\alpha)}{\tan^2(\alpha)-1}$.

Now, from the geometry in Fig. 4.5,

$$p_2 = 2c \times \tan(\alpha) + p_1 \tan^2\alpha. \tag{4.7}$$

Equation (4.7) is a fundamental relationship which connects the principal stresses at which failure takes place with the properties of the material (repose angle ϕ). The repose angle is also obtainable via triaxial testing, in which the soil/rock specimens are formed into a finite cylinder that is enclosed in a waterproof cover and subjected to external hydrostatic pressure p_1 and an axial load p_2 which increases until the specimen yields. With the linear envelope assumption, two such experiments suffice to determine both cohesion c and repose angle ϕ. Or a series of such experiments at different values of p_1 yield the actual form of the Mohr envelope for the soil/rock under consideration, which certainly will slightly deviate from the straight line assumption.

Another use of Eq. (4.7) is in estimating the lateral "earth pressure" which shows the potentially complex stress regime within granular sliding material. Suppose AB is the upper horizontal surface of a mass of soil (of uniform density ρ), Fig. 4.5b, and that we wish to find the horizontal pressure which must be applied at each point of a vertical wall of a trench AC to prevent the soil from slipping into the trench. Suppose p is the required pressure at depth h. Then $-p$ and $-\rho gh$ are the principal stresses which, by symmetry, must be horizontal and vertical. Using $p_1 = p$ and $p_2 = \rho gh$ in Eq. (4.7), we obtain $p\tan^2\alpha = \rho gh - 2c \times \tan(\alpha)$. If a pressure prescribed by this expression is exerted on the side wall, the lump of soil is in a state

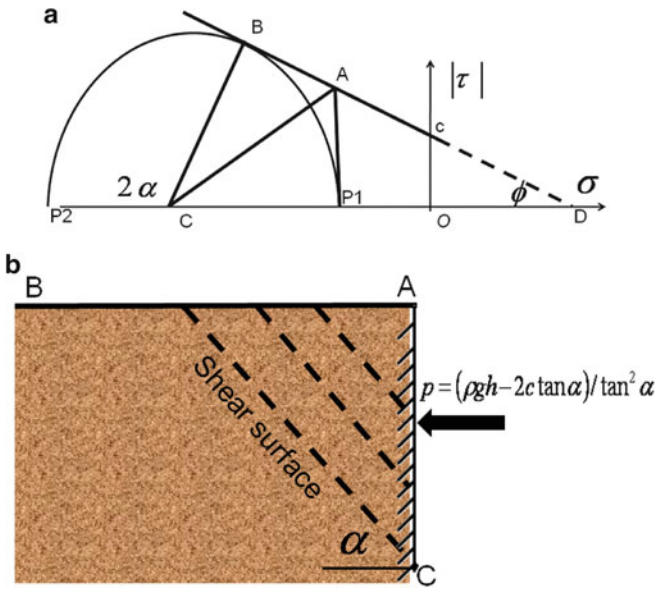

Fig. 4.5 Theoretical basis for triaxial experiments (**a**) and Rankine state of plastic equilibrium (**b**). In (**a**), c is cohesion, the shear stress material can sustain with zero normal stress, ϕ is called repose angle or internal frictional angle, α is related to frictional angle as shown in (**a**) and is introduced for convenience. Lengths of OP1 and OP2 corresponds to the maximum and minimum principal stresses and other capital letters are for geometry labelling of the compressive linear Mohr envelope

of incipient slip down, along the dotted plane in Fig. 4.5b, which is inclined at angle α to the horizontal direction. This can be used to verify sophisticated numerical models for landslides.

Since the slope material composition is complicated, the granular sands and clay have very different rheologies and, especially, yielding criteria. In addition to the above elaborated Griffith theory on brittle strength, it is necessary to briefly discuss the yielding criteria that are generally applicable in slope stability modelling—the von Mise yielding criteria. Hydrostatic pressure alone does not cause appreciable plastic deformation in crystalline rocks. Thus, in developing criteria for yielding, it is usual to subtract a spherical part (mean normal stress, $S = (\sigma_1 + \sigma_2 + \sigma_3)/3$) from the actual full stress, calling the remainder a stress deviation ($\sigma^* = \sigma - S$). It is assumed that it is stress deviation alone that is responsible for yielding and the proposed yielding criterion should be a function of it. Modern yielding criteria are constructed on the invariants of the deviation stress tensor. For example, for mass continuity, it is the trace of this matrix $I_1 = 0$. $I_2 = tr(\sigma^* \sigma^{*T}) = 0.5(\sigma_1^{*2} + \sigma_2^{*2} + \sigma_3^{*2})$, and I_3 are similarly second and third order measures of the shear and normal stress components. Neglecting density changes within specimen, a yielding criterion must be expressible in terms of the invariants I_2 and I_3, in the form of $f(\sigma_0^*, I_2, I_3) = 0$, with σ_0^* a constant of material mechanical property. Using the aforementioned strain

energy per unit volume concept that was introduced in deriving the Griffith theory, it is straightforward to see that the following combination is a qualified candidate:

$$2\left(\sigma_0^*\right)^2 = \left(\sigma_2^* - \sigma_3^*\right)^2 + \left(\sigma_1^* - \sigma_3^*\right)^2 + \left(\sigma_2^* - \sigma_1^*\right)^2 \tag{4.8}$$

Equation (4.8) is the von Mise criterion which is probably the most concise and easy to use, and the consequences of which have been most studied. Numerical models usually are not constructed on principal stresses. A linear transformation usually is involved in its application to the simulation of slope stability.

Thus, landsliding is partly an upscale process, with localized disturbances adding instability, by adding fluids of reducing root reinforcement, to preexisting weathered regolith and granular soil particles spreading on slopes in a region predisposed to geo-hazards (extreme precipitation and freeze–thaw cycles and earthquakes). Granular rheology features such as "loose assemblage of multi-body elastic particles," "resilience to pressure and weakness for tension," and "semifluidity and degree of hydrostatic are sensitive to moisture content" are central in the provision of upscale positive feedback.

References

Hubbert MK, Rubey WW (1959) Role of fluid pressure in mechanics of overthrust faulting. I. Mechanics of fluid-filled porous solids and its application to overthrust faulting. Bull Geol Soc Amer 70:115–166

Jaeger JC (1963) Fracture of rocks. Tewksbury Symposium on Fracture 268–283

Jaeger J (1969a) Elasticity, fracture and flow. Methune & CO. Ltd, New Fetter Lane, London

Jaeger J (1969b) The stability of partly immersed fissured rock masses and the vaiont rockslide. Civil Eng Public Works Rev 1204–1207

Chapter 5
Landslide Dynamics

Slope movements occur when down-slope driving stress dominates resistive stress (strength), as a result of stress build up from mechanical processes (e.g., seismic shaking, asteroid impacts and extremely strong gales), reduced shear strength (e.g., weathering, developments of slickensides, and creeping), or phenomena affecting both. For example, increased soil moisture content, vegetation loading, and tensile cracking and shrinkage caused loss of tensile strength and mass redistribution, to name just a few, can enhance driving strength and simultaneously reduce material strength. All presently existing landslide models try to answer (or partially answer) the full start–slide–stop cycle. The following review is organized in the order of triggering of a slide (Sect. 5.1) to the ensuing flow and mass redistribution (Sect. 5.4). Along these lines, there are physically based slope stability models to simulate the transient dynamic response of pore pressure to spatiotemporal variabilities in rainfall (e.g., Transient Rainfall Infiltration and Grid-based Regional Slope-Stability Analysis—TRIGRS, Baum et al. 2002, 2008); commercially available numerical modeling codes for geotechnical analysis of soil, rock, and structural support in three dimensions (e.g., FLAC-3D, www.itascacg.com/flac3d); and fully three dimensional, full Navier–Stokes and multi-rheological modeling systems, such as SEGMENT-Landslide (Ren et al. 2008a, b, 2010, 2011c).

5.1 Failure Criteria

For a chemically uniform specimen, fracture and failure occur when stress applied in one principal direction cannot be effectively balanced by the other two principle directions. Mechanical strength (τ_f) is the physical property quantifying the degree of stress imbalance that the material can tolerate. For landslide studies, the sliding material as a lump of granular material has a tremendous degree of freedom and defies analytical forms of universally applicable criteria for failure description. Gross stress–strain relationships are still applied to try to quantify the failure state.

© Springer International Publishing Switzerland 2015

D. Ren, *Storm-triggered Landslides in Warmer Climates*,
DOI 10.1007/978-3-319-08518-0_5

Furthermore, the definition of the strength of hillslope materials varies widely depending on the discipline and perspective (Selby 1993). The different stages of a landslide and the conception of strength also vary, in accordance with the changes in rheological properties. For example, for methods interested in the triggering (initiation) of a landslide, the ability of materials to resist deformation by compressive, tensile or shear stresses are ideal. For the following stage of downward and outward movement of the detached surficial soil and rock, the ability of materials to resist being transported by fluid is desirable. For estimate the fluvial deposits, the ability of the sliding material to entrain creek bank may also be required. In this section, material strength is for the landslide initiation thus the strength of sliding granular material refers to the ability to resist strain arise from tensile, compressional, and shear stresses.

5.1.1 A Generic Form of Internal Stress

The full internal stress tensor is bundled as

$$\sigma = \phi + C + S_p\mu + \delta_E, \tag{5.1}$$

Where $\phi = \rho g h$ is the gravitational potential, C is effective cohesion (also called "apparent cohesion" or "interlocking cohesion",[1,2] i.e., the shear stress which the material can sustain at zero normal stress), and δ_E is the pressure perturbation caused by earthquake or human-induced disturbances at that location. $\mu < \mu_I = tg\phi$, with ϕ granular repose angle (i.e., angle of friction). It, is found experimentally that the behavior of soil materials above the water table can be adequately represented by the Coulomb–Navier fracture criterion (the middle two terms in Eq. 5.1). The Coulomb–Navier criterion is a special case of Mohr theory with the straight-line, tangential to the circles of tension-simple shear-compression, Mohr envelope. For conditions with ground water, hydrostatic pressure (pore pressure) is usually included in S_p for convenience. Except around cavities, where the so-called "bridge effects" distort the stress fields, S_p is close to loading pressure. The extreme values of the middle two terms on the right hand side are the yielding strength (shear strength) of the sliding material $\tau_f = C + S_{p,f}\mu$, with subscript "f" meaning failure. This is the Navier-modified Columb criterion. C and μ are functions of soil

[1] Also called inter-particle locking. Contacts among granular particles are area-to-area contacts rather than point-to-point contacts. Even in the absence of normal stress, shear resistance does not reduce to zero. Reflected on the Mohr circle, there is some non-zero residual intercept of the failure envelope on the shear stress axis.

[2] Under constant pore-pressure conditions (e.g., saturated drained condition), 'drained cohesion' simply is shear strength at the state that internal friction no longer matters. In other words, it is in a state that water molecules perfectly amended the defects of the inter-particle contacts and point-to-point contacts hold universally.

moisture, soil chemical components, and also of shear stress (e.g., Schofield and Telford 2006). For soils at depths deeper than 10 m, the dependence of μ on stress is minimal and the Navier modified Coulomb criterion is more applicable than for shallower soils (i.e., smaller S_p, Kenney 1984; Townsend and Gilbert 1973). When being applied to shallow shear surfaces, volume change and dilation within the shearing soil have an apparent nonlinear influence on μ. For sandy soils, the friction angle increases with increasing confining pressure (Cornforth 2005; Lu and Godt 2008). For an extremely deep shearing zone (>200 m), von-Mise's criterion is a closer approximation because the plasticity of earth material becomes more salient.[3,4]

For non-fractured bedrock, C is the dominant term, usually three orders of magnitude larger than the remaining three terms together. For most of the soil (except pure sandy soil), cohesion and internal friction are both important in maintaining stable slopes. For fractured rocks and sandy soils, the internal friction becomes the dominant term, although it is not necessarily larger than the gravitational potential. This is because the horizontal gradient of the gravitational potential causes motion instead of the bulk term. For natural slope soil, both the cohesion and friction components of the strength are sensitive to clay particle content. On the one hand, development of cohesion is enhanced by the large surface area provided by the clay minerals. On the other hand, the interlocking[1] friction is weakened. In shear box tests, interlocking friction is a measure of the amount of deviation required for particles at the shear surface to move past each other. A soil dominated by clay particles requires very little deviation to shear. In north western Europe, there is a type of "quick" clay. The soluble ingredients in the solids structure makes its rheological properties even more sensitive to moisture contents.

[3] Failure criteria are forms of representation of the peak strength in terms of principal stresses (the degree of tolerance to their imbalance). Different materials, or the same material with different formation workmanship have different stress–strain graphs. For the surfacial material (with overlain loading level of < 1Mpa), its brittle nature is apparent and Mohr–Coulomb failure envelope suffices. If the granular material is buried further down, plasticity appears and the von-Mise criterion, a square root mean of the principal deviatoric stress tensor, is a better approximation.

[4] Before the occurrence of fatigue, general material under tension/compression has an elastic range (the unitcell skeleton deforms but can fully recover once loading is removed), followed by plastic or permanent strain that will be observed upon unloading (some skeleton in the open and refabricated to form a new interface within the original regular structure). The following stage of deformation is strain hardening (strain–stress hysteresis stage, or necking stage, with quick reduction of Young's modulus and increase of brittleness). With further strain (after reaching the peak strength point), the material may release mechanical energy that is applied (creeping). This continues until the material has only its residual strength/ultimate strength (to a state where the units are now composed of multiple previous unit-cells, each with surficial fabrication. The bonding between these units is much weaker than the original bonding. This is a viscous state of material).

5.1.2 *Fortification of Shear Strength Through Distributed Plant Roots*

Plant roots play a significant role in storm-triggered landslides because of their effects on hill slope hydrology and the reinforcement of the near surface soils in which they reside. Live vegetation modifies slope hydrology because the plants must transpire to utilize minerals dissolved in soil water. During precipitation, the canopy also can intercept droplets and hence prevent their direct impact on the slope. In certain extremely stressed conditions (Ren et al. 2004), vegetation roots also can reserve soil moisture. Changing soil moisture conditions is an effective way of changing granular viscosity (Appendix A). Mechanically, plants exert tensile strength to resist tensile cracking. As a distributed source, the tensile strength of roots can be converted to shear strength to resist driving shear stress. The role of vegetation in improving slope stability is well recognized (Wu and Sidle 1995; Coder 2009; Morgan and Rickson 1995 and references therein; Wu and Watson 1998) and shear tests have been carried out in the laboratory (Gray and Ohashi 1983), in the field (Abe and Iwamoto 1988) and even retrieved from failed slopes containing a root membrane (Riestenberg 1994). Coder (2009) tabulated root strength for a variety of plants.

The scientific community generally agrees that the contribution to soil strength from the root structure/network is an extra term in the effective/apparent cohesion (in Eq. 5.1). To develop a quantitative framework that includes the contribution to shear strength from plant roots lies with parameterization of the mobilization of root tensile stress and its conversion to shear strength of hill slope granular material. A single, supple root has only tensile strength. However, distributed and structured roots, under slope environments, project portions of the tensile strength to shear strength. In this sense, the tensile strength of plant roots is the common origin of both the tensile and shear strength contributed. The conversion (efficiency) of the tensile strength of roots to shear strength contribution to granular soil depends on various factors such as soil type (granular friction angle), geomorphologic and climatic setting (slope angles, stratigraphy, soil moisture and plant morphology), and plant species. Only for 2D slope models, the differentiation of tensile and shear stress from roots is necessary (Waldron 1977). Theoretical development starts from a "fully mobilization" assumption, assuming there is no root slip-out during stress and, thus, roots and surrounding granular material yield simultaneously. As a natural extension, degree of mobilization is a measure of how much of the tensile strength of a root can be effectively exerted. This usually is a matter of soil moisture content. In 3D models, under the isotropic root distribution assumption (i.e., all roots are distributed evenly in all directions), the degree of mobility and the ensemble mean root tensile strength are the only parameters that matter.

In a 2D slope model framework, Gray and Ohashi (1983) proposed that the shear resistance arising from a single root, in terms of shear stress along the local slope, is linearly proportional to the fully mobilized root tensile strength, with a coefficient called "root shear strength conversion factor." The conversion factor depends on

root orientation and soil frictional angle and, hence, is root specific. The proposed method for up-scaling to all roots is simply by summing over all roots. To simplify the procedure of quantifying the conversion coefficient, root structures are assumed to be of simple form (e.g., perpendicular to slope rather than being upright, Wu et al. (1979)). Laboratory experiments with sandy soil and fiber (to mimic roots) support the assumption that shear strength contribution from roots varies with orientation of roots with respect to the surrounding granular material, as well as the internal friction of the granular soil (Jewell 1980; Gray and Ohashi 1983). The sandy soil, because of its relatively small cohesion against roots, were pulled out of intact with the granular, apparently violating the full mobilization assumption by Waldron (1977) and Wu et al. (1979). Also, this line of reasoning does not consider the fact that, for a certain type of vegetation, roots have information (determined by their ecosystem functioning) that can be utilized. For example, their environment-determined allocation into coarse structural roots and fine absorbent roots, leads to quite different mechanical properties. Following is an introduction to a recent study by Ren et al. (2013) that proposed an approach for evaluating root strength contribution. This method, although still belongs to a type of "fiber bundle model" (Pollen and Simon 2005), facilitates the use of increasingly available remote sensing data.

Roots from the same plant behave differently: elastically for thinner ones (diameter < 3 mm for boreal pine trees) and elastoplastically for thicker ones. The maximum strength of roots depends primarily on the fiber content in the xylem. Thus, ephemeral, absorbing roots have very different strength than structural roots. The same types of root of different thickness have similar tensile strengths per unit cross-sectional area (Table 5.1). The structural roots of the Swiss Stone Pine of thickness 12.6 mm and 13.9 mm have similar tensile strengths, respectively, of 12.9 MPa and 13.5 MPa. Because different vegetation types, or the same vegetation in different growing stages or in different climate zones, can have different root mass density (or even different orientation) within their ranges of influence in the soil, generic schemes are still lacking a method for estimating root strength, both regionally and globally. Because roots occupy a small fraction of the soil volume, root reinforcement can be factored in as an added stress over the case of no roots (Fig. 5.1b). As not only tensile strength but also the cross-sectional areas (thickness of roots) are critical, the following "allometric" approach is proposed that uses "root weight density" and vegetation type to characterize the addition of tensile strength to the soil medium shear strength and elevated yielding criterion.

$$\sigma^{+} = C_{smc} \times \sum_{i=1}^{3} \sigma_i \times F_i\left(NPP, I_{veg}, Pa, T_{air}\right) \tag{5.2}$$

where σ^{+} is the root mechanical reinforcement (kPa), C_{smc} is soil moisture control (0–1), index i differentiates woody transport roots, woody supporting roots, and ephemeral absorbing roots, σ_i (kPa) is a root species-dependent reference value (i.e., tensile strength of xylem of roots, varying from 10 to 30 MPa for most plants),

Table 5.1 Root strengths of two plants growing in similar environmental conditions (Cartina, personal communication 2012)

	Root type	Diameter (mm)	Failure tensile force (kg)	Deformation ratio (%)	Tensile strength (MPa)
Juniper	Ephe. Absorb	2.9	1.9	3.9	2.87
	Woody trans.	8.6	140	3.7	24
	Structural	12.1	130	2.8	11.3
Swiss Stone Pine	Ephe. Absorb	5.1	21.6	3.6	10.5
	Woody trans.	9.3	120	6.8	17.6
	Structural	12.6	169	2.8	13.5
	Structural	13.9	195	8.8	12.9

Samples are taken at Duron Valley (46° 29′37″ N, 11° 39′25″ E) of Italy

NPP is net primary production (kg/m^2/year), P_a is annual precipitation, T_{air} is annual mean air temperature, and I_{veg} is the species-dependent reference *NPP* value. F varies from 0 to 1 and represents the weight fraction of roots in a unit volume of soil, within the range of influence of the roots. The value of F usually is close to 0.2 %. The functional form of C_{smc} is tabulated according to soil type. The modifications due to climate conditions are necessary because the same plants can have very different strategies in allocating biomass when present in different climate zones. For example, leaves tend to be thin and wide when growing in moist tropical rainforests. The same plant, when growing in drier locations, tends to have smaller leaves and a more extensive root system to better use the limited water resources. A positive side of this formula is that root volumetric (or mass) density is obtained remotely using satellite data (Zhang and Kondragunta 2006). Summarization over root species according to their ecosystem functions is also presented by Waldron and Dakessian (1981), who proposed that root tensile strength depends exponentially on root diameter. Ziemer (1981) first suggested that the gross tensile strength of vegetated slopes is proportional to root biomass. Wu and Sidle (1995) and Sidle and Ochiai (2006) elevated the discussion of the effects of vegetation on slope stability to include land use.

Soil moisture content is the key factor affecting root-soil bond strength and, hence, in deciding whether or not roots can fully mobilize their strength at slope failure. As roots with different functions differ greatly in their tensile strengths (Table 5.1, Juniper roots) and the root-soil interactions (i.e., root-soil bonds) are not that different, it is possible that, under the same soil moisture conditions, some roots stretch, other roots slip and another group of roots simply break. Because woody transport roots have the highest percentage of xylem cells to transport water, this is the strongest type of root. At the other extreme, ephemeral absorbing roots have higher concentrations of phloem and cambium cells, making them the weakest category. Cambium cells are a cell layer in thickness; thus, the thinner the root, the

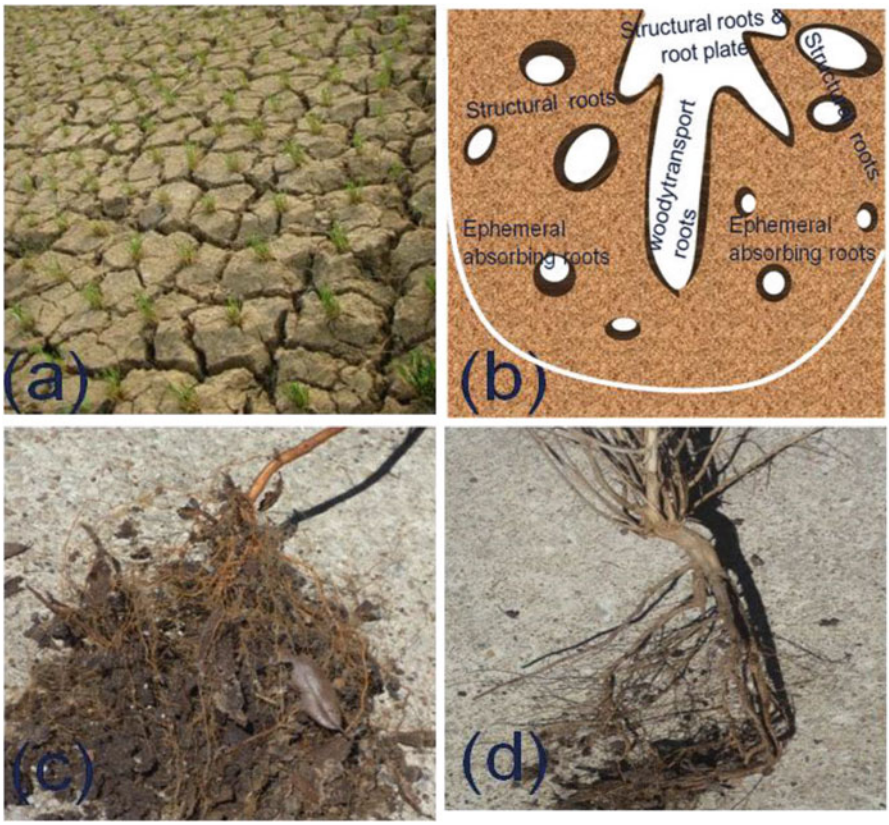

Fig. 5.1 The effect of roots is to unite soil within the extending range (influence range). Panel (**a**) is a rice paddy during an extended drought period. The crevasses are in a pattern centered on the bundles of sprouts, demonstrating the mechanical reinforcement from roots. Panel (**b**) is a schematic cross section within the soil, defining area density of roots. The *oval circles* represent root cross sections. The *inner white section* is xylem. The surrounding *dark area* represents skin (inner bark and cambium cells). The reinforcement effect is proportional to the total area of the *white oval circles* in (**b**). Thus the root volumetric density determined by allometric method (analogous to the definition of drainage density of a basin, root volumetric density is defined as the volume of roots in a unit volume soil) forms a suitable metric to measure the reinforcement effects of roots. For natural temperate plants, the net gain for the strength of soil is around 3–6 kPa. The above is suitable assumption for clay soils under relatively dry conditions, where slope failure involves breaking roots. For sandy soils, or when the soil moisture content is high, cohesion between root surface (cortex) and surrounding soil is less than root strength. In the case of slope failure, roots slip out of the soil medium rather than broken (**c** and **d**; Wu and Watson 1998). Panels (**c**) and (**d**) show two different plants taken out of the same patch of sandy soil. There are no apparent root damages. Soil moisture plays a decisive role in soil-root mechanical interactions. The *white bold line* in panel (**b**) outlines the influence range of the roots of the plant in question. Cross sections of roots (*ovals*) show also the position and orientation of the root system

higher its proportion of these cells. Equation (5.2) thus can explain why large roots usually are pulled out during soil slipping, whereas thin roots, which generally form a network in the soil, are often broken (Schmidt et al. 2001). There still is room for improving Eq. (5.2), the amount of soil reinforcement provided by roots. In future improvements to the parameterizations of mechanical reinforcement of roots to soil, what needs to be considered is that roots, as the extensions of stem, have the function of supporting as well as transporting nutrients and water. Climate and soil affect the allocation of biomass in roots of different functionalities to maximize growth competition (Sect. 2.4).

Soil strength that results from plant roots is dynamic (Sidle 1992), especially for timber-harvesting sites (Schmidt et al. 2001) and those affected by wild fires. While the exponential decay in tensile strength after clear-cut harvesting (proposed by Sidle (1992)) is a good approximation, the recovery of root tensile strength for some species is not unimodal and assumes a form similar to the sigmoidal curve proposed by Sidle (1992). Research on root strength recovery for fire-affected sites is still lacking. Montrasio and Valentino (2008) noticed the prevalence of holes in the shear zone soil, caused by living organisms, and the possible effects on soil shear strength. Parameterization schemes addressing this phenomenon are not available yet. The parameterization of root strength may shed light on evaluation of the reduction in granular strength caused by the hollow channel structures left by subterranean animals.

5.1.3 Soil Moisture on Slopes

In the standstill stage, effects of soil moisture on the internal stresses are generally defined as suction stress or, more generically, the chemical potential of water molecules. Using chemical potential makes the inclusion of cementation cohesion into the apparent cohesion term equally as convenient as the inclusion of capillary cohesion. As aforementioned, granular material lumping together forms a porous media for soil moisture. Because of the critical role played by soil moisture in determining the rheological properties of granular sliding material, all models of slope stability need to address the participation of precipitation water into runoff, infiltration and evapotranspiration. In addition to these rhizospheric hydrological processes, the ground water table, when it is shallower, also needs to be taken into account.

Fluid flow and moisture content in hilly environments vary spatially and temporally, due to time-dependent environmental changes (e.g., precipitation, solar radiation, transpiration of vegetation through distributed roots), and the storage capacity of porous granular soils. In modeling, the time-dependent environmental changes are usually treated as boundary conditions of distributed forcing terms, whereas the soil hydrologic property-determined soil storage is usually cast in the flow laws. Considering a representative soil volume (RSV, Fig. 5.2), this RSV is of arbitrary volume and arbitrary surface area Ω with an outward pointing normal unit

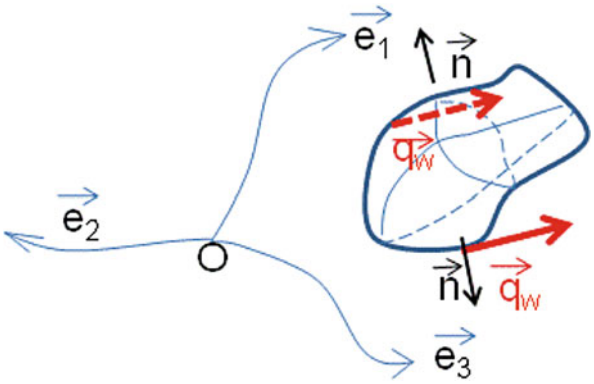

Fig. 5.2 Elemental soil volume showing in generalized orthographic coordinates. The mass continuity requirements is $\iiint \nabla \bullet \left(\rho_w \vec{q}\right) dv = \iint \vec{q} \bullet \Omega \vec{n} dA \equiv \iiint \frac{\partial \rho_w w_c}{\partial t} dv$. This relationship holds for arbitrary elemental soil volume so that the first and the third terms has point to point correspondence (equality holds for each points in the 3D space (Green's first theorem, Appendix D.4, c)

vector $\vec{n}$. We assume the soil porosity is P (maximum of the volumetric water content, w_c) and moisture flux is $\vec{q}$.

From Green's First Theorem (Eq. A.97) and mass continuity,

$$\nabla \bullet \left(\rho_w \vec{q}\right) = \vec{q} \bullet \Omega \vec{n} = \frac{\partial \rho_w w_c}{\partial t} \tag{5.3}$$

Equation (5.3) holds everywhere inside the porous media. From Darcy's Law, soil water flux (kg/s) is proportional to hydraulic conductivity (K) and total hydraulic gradient (h_t):

$$\vec{q} = -K \nabla h_t \tag{5.4}$$

where h_t usually is assumed to be the sum total of matric potential (h_m, head due to pore water pressure), head due to gravity (h_g), head due to osmosis (h_o), and head due to kinetic energy (h_v, negligible). Darcy (Henry Darcy, in 1857) first realized that the total energy of the system stored in the form of the total water potential is always lost during flow through the porous material, and the amount of energy loss depends on the material. This actually is a manifestation of the Second Law of Thermodynamics. In general, the energy stored or released by an element of soil due to change in the fluid mass can be related to the hydraulic head (Freeze and Cherry, p. 51, 1979).

$$\frac{\partial \rho_w w_c}{\partial t} = {\rho_w}^2 g(\alpha_s + P\alpha_w)\frac{\partial h_m}{\partial t} \tag{5.5}$$

Where α_s is the compressibility of bulk soil and α_w is compressibility of water voids. The $(\alpha_s + P\alpha_w)$ term is also the mean compressibility of wet soil (1/Pa). Whereas the compressibility of water under earth surface environment is close to a constant value of about 4.4×10^{-10} (1/Pa), the compressibility of clay soil ranges from 10^{-6} to 10^{-8}, for sandy soil from 10^{-7} to 10^{-9}, and 10^{-8} to 10^{-10} for pebbles/gravels. Assuming constant water density in Eq. (5.3), and substituting in Eqs. (5.4) and (5.5), gives:

$$\nabla \bullet (-K\nabla h_t) = \rho_w g(\alpha_s + P\alpha_w)\frac{\partial h_m}{\partial t} \tag{5.6}$$

Equation (5.6) is applicable for both saturated and unsaturated flows and is the most general form of Richards equation. For unsaturated situations, the compressibility of the bulk soil usually is smaller than the compressibility of the fluid voids, so the void compressibility dominates the average compressibility. By definition

$$P\alpha_w = \frac{P}{V_v}\frac{\partial V_w}{\partial(\rho_w g h_m)} \tag{5.7}$$

Substituting Eq. (5.7) into Eq. (5.8) and rearranging gives:

$$\nabla \bullet (-K\nabla h_t) = \frac{\partial w_c}{\partial t} \tag{5.8}$$

In the absence of osmotic head, the total head comprising only matric suction head and geopotential, gives the most common form of Richards equation (3D hydraulic conductivity in the component form):

$$\frac{\partial}{\partial x}\left(K_x\frac{\partial h_m}{\partial x}\right) + \frac{\partial}{\partial y}\left(K_y\frac{\partial h_m}{\partial y}\right) + \frac{\partial}{\partial z}\left(K_z\frac{\partial h_m}{\partial z}\right) + \frac{\partial K_z}{\partial z} = \frac{\partial w_c}{\partial t} \tag{5.9}$$

For 3D landslide models, the land surface model subcomponent needs to solve the Richards equation in a full 3D setting (Eq. 5.9). For example, SEGMENT-landslide includes SHEELS (Ren et al. 2004) as a subscheme to simulate the soil moisture content. To suit the application in 2D (x-z plane) slope models (e.g., TRIGRS, Fig. 5.3, Baum et al. (2002, 2008)), Richards equation in hill slope settings is proposed based on Philip's (1991) assumption, although several recent theoretical and experimental studies question the validity of this assumption (e.g., Jackson 1992; Philip 1993; Sinai and Dirksen 2006). It is beneficial to introduce two analytical solutions to the Richards equation because of their value in dealing with flux boundary conditions. The Green–Ampt (1911) infiltration model is an analytical solution for flow into an initially dry, uniform column of soil. Although

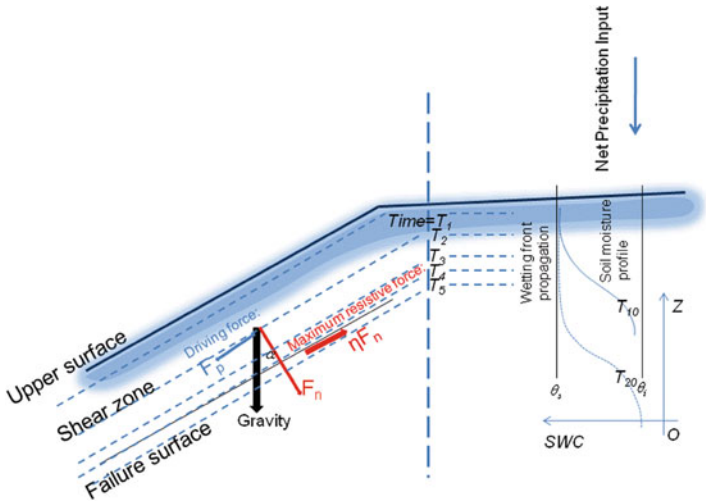

Fig. 5.3 TRIGRS. Diagram of a contemporary slope model. It considers the shear zone sliding material as a cohesive solid body sitting on an uniform slope bedrock (α). The gravity is decomposed into a slope-normal component (F_n) and a slope parallel component (the driving force, F_p). At the interface (failure surface), the maximum resistive force can be provided is proportional to the normal stress (ηF_n, red arrow pointing upslope). Once the slope-parallel component exceeds this maximum resistive force, sliding occurs. The reason of the excess of driving force can be caused by an increase in loading, a reduction in frictional coefficient (η), or both. A common cause of reduction in η is increased soil moisture contents, following intense precipitation events (as shown in the *right* portion of the diagram). Slope model usually do not solve the full form of Richards equation. In this diagram, Green–Ampt (1911) infiltration scheme is shown. The advancing of wetting front and the soil moisture profile evolves according an analytical solution. Sliding occurs usually when wetting front closes (e.g., at T_4)

not a direct analytical solution of the Richards equation, it has the essence by two assumptions arising from observations of wetting fronts during infiltration: (1) the soil suction beyond (ahead of) the wetting front is constant in space and time, and (2) the water content and the corresponding hydraulic conductivity of the soil behind the wetting front (the wet portion of the soil column) also are constant in space and time. For some efficient land surface schemes, this relationship is utilized for unsteady rainfall flux upper boundary conditions (e.g., Chu 1978). The infiltration scheme inside TRIGRS is also a unique analytical solution of the Eq. (5.9). It is based on a Gardner (1958) linearization of a 1D Richards equation (keeping only the z-coordinate of Eq. 5.9) applied to a water table (origin at water table and positive above). An analytical solution for transient infiltration above the ground water table is thus obtained. Interested readers are referred to Srivastava and Yeh (1991) and Baum et al. (2008). Suction head and soil moisture profiles, as functions of vertical elevation above water table and of time, are standard outputs of this type of model. With some extension, TRIGRS used the analytical solution as described in Srivastava and Yeh (1991) to link to a stability factor to assess landslide potential

over broad geographic areas. Further improvements in efficiency can be achieved by applying the time compression approximation to Philip's equation (Famiglietti et al. 1992), which depends on the accumulated rainfall and the soil volumetric water content at saturation. Once rainfall is infiltrated, it adds to the soil water, which is either lost to evapotranspiration or subject to drainage and percolation into macro-crevasses. The transpiration effects from live roots can be factored into the matric head h_m in Eq. (5.9), or treated as a forcing term, as in Ren (2006). In the first treatment, care is needed because roots occupy only a small portion of space and they, essentially, form a distributed source for soil moisture extraction. The treatment of root moisture extraction as an external forcing term is advantageous in dealing with seasonality (and even daily cycles, Ren et al. (2004)) of the water utilization activities of vegetation. The transpiration process, once extracted as a separate process, is exactly the Penman–Monteith formulation (e.g., Allen et al. 1998).

$$LE = \Delta(R_n - G) + \frac{\rho C_p}{r_a} D / \left(\Delta + \gamma \frac{r_s}{r_a} \right) \tag{5.10}$$

where r_s is the bulk stomatal resistance of the entire canopy, γ is the psychrometric constant ($\gamma \approx 66$ Pa/K), r_a is aerodynamic resistance (s/m), D is the vapor pressure deficit or vapor partial pressure (Pa), Δ is rate of change of saturation specific humidity against air temperature, or slope of the saturation vapor pressure curve (Pa/K), $R_n - G$ is the available energy to be partitioned into sensible and latent heat, ρ is air density (kg/m), and c_p is the specific heat of dry air (J/kg/K). Equation (5.10) takes this form because the transpiration's energy source is photosynthesis demands. The so-called resistance is a fundamentally rooted in the root's selective absorption of ions and leaves' guard cells' control of CO_2 absorption. The water escaping from leaves as stomata open is eventually removed from the roots. The resistance at the root ends is grossly accounted for in the r_s coefficient. In the present modeling community, there are two related but different approaches to the treatment of r_s: the Jarvis (1976) and the Ball-Berry (Ball et al. 1987) schemes. The Jarvis approach assumes a minimum resistance $r_{s,min}$ (corresponding to the ideal case when there is limitations from water content, photosynthetically active radiation (PAR), and life activity-related environmental parameters such as air temperature, humidity and leaf area index). An exemplary summary of this approach can be found in the PILPS project (Henderson-Sellers et al. 1996; Shao and Henderson-Sellers 1996). The Ball-Berry scheme, in a gas exchange model, simulated the stomatal resistance as $R_s = 1/\left(b + a h_s p_s \frac{A_n}{C_s}\right)$, where a and b are linear coefficients based on gas exchange considerations, h_s is relative humidity at leaf surface, p_s is surface atmospheric pressure, A_n is net CO_2 assimilation or photosynthesis rate, and C_s is CO_2 concentration at the ambient of leaves (immediately surrounding the leaves). The fundamental difference between the two approaches is that, in the Ball-Berry scheme,

Table 5.2 Basic vegetation parameters in SEGMENT-Landslide

Vegetation Type *a*	Albedo factor Z_0	Roughness resistance	Shading deficit	Stomatal control	Radiation stress factor	Vapor pressure factor (Jarvis)
		(m)		(s/m)	UNITLESS	W/m^2
Impermeable (urban)	0.15	1.0	0.1	200.0	N/A	N/A
Cropland/ pasture	0.19	0.07	0.8	40.0	100.0	36.25
Cropland/ grassland	0.19	0.07	0.8	40.0	100.0	36.25
Cropland/ woodland	0.19	0.15	0.8	70.0	65.0	44.14
Grassland	0.19	0.08	0.8	40.0	100.0	36.35
Shrubland	0.25	0.03	0.7	300.0	100.0	42.0
Savanna	0.20	0.86	0.5	70.0	65.0	54.53
Decid. Broad-leaf Forest	100.0	0.80	0.12	0.8	30.0	54.53
Decid. Needleleaf Forest	0.11	0.85	0.70	150.0	30.0	47.35
Evergr. Broad-leaf Forest	0.11	2.65	0.95	150.0	30.0	41.69
Evergr. Needleleaf Forest 0.10		1.09	0.70	125.0	30.0	47.35
Mixed Forest	0.12	0.80	0.80	125.0	30.0	51.93
Water Bodies	0.19	0.001	0.0	100.0	30.0	51.75
Barren and Spar. Vegted	0.12	0.01	0.01	N/A	N/A	N/A
Herbaceous Tundra	0.16	0.04	0.6	150.0	100.0	42.0
Wooded Tundra	0.16	0.06	0.6	150.0	100.0	42.0
Mixed Tundra	0.16	0.05	0.6	150.0	100.0	42.0
Snow or Ice	0.7	0.001	0.0	N/A	N/A	N/A

evaporation is viewed as an "inevitable cost" that foliage incurs during photosynthesis, or the carbon assimilation process. At present, SEGMENT-Landslide has implemented only the Jarvis type of r_s parameterization. The involved parameters are listed in Table 5.2. At flow stage, there is an advection term in the soil moisture equation. This term will be further discussed in the numerical solution section (Chap. 12 and Appendix F).

The effect of changes in pore pressure (h_m) in the development of landslides is so important that merits some deliberation. Generally, any mechanism which

increases pore pressure represents a potential hazard. Pore pressure changes can be of natural (seasonal water table fluctuation) origin or of man's activity (e.g., engineering projects that alter the natural hydrological pattern of the region of interest). A slope that has been stable for a long time under existing load and water-table conditions can be rendered unstable by a change in the drainage patterns in the surrounding area. For example, the construction and occupation of houses at the top of a hillside area may cause changes in the groundwater conditions through drainage collection systems, watering of lawns, and through changes in natural runoff and drainage patterns of the hillside through the presence of paved streets and roofs. In southern California, it is not uncommon failures of hillsides with occupied houses. In many cases, although difficult to investigate, most probably are due to changes in the amount of soil water present in the normally arid hillsides. Pore pressure also plays a critical role in the liquefaction of quick clay (in this type of clay, increase in soil moisture will meltdown the skeleton of the soil and it is liquefied). As described in Appendix A, adding water is an effective way to liquefy granular slope material. Repeated shaking (also in Appendix A) is yet another effective way for liquefaction. These two mechanisms work in synergy to destabilize slopes during earthquakes. In an earthquake the soil below the ground surface is subjected to alternations of shearing stress at irregular frequency and random amplitudes. Since an earthquake is of relatively short duration, only soil of fine enough grain size, and thus of low permeability, will be effectively liquefied because the soil cannot effectively drain during the vibrations. Thus pore pressure may build up. If the earthquake vibrations are sufficiently intense or the duration of the shaking is sufficiently prolonged in relation to the soil properties, liquefaction spread to coarser grained granular material distributed on slopes. As fine-grained soils in near-saturated state are so widespread in their distribution, and earthquake vibrations extend over such large areas, that liquefaction phenomena have been a part of virtually every major earthquake. For example, it was the primary cause in damage and destruction in the 2008 Wenchuan earthquake. In the San Fernando, California earthquake of Feb. 9, 1971, liquefaction of material in the San Fernando dam caused a landslide of the upstream portion of the dam structure (Plate 4.3 in Bolt et al. 1975).

In summary, land surface subcomponents in a landslide model should effectively simulate how a catchment filters rainfall inputs into runoff (stream flow), infiltration (increasing soil moisture content or percolated into macro-crevasses), and evapotranspiration losses into the atmosphere. Both infiltrated water and the surface runoff have direct landslide consequences. Depending on the region of interest, a properly weighted land surface scheme is critical for the efficient performance of the entire landslide modeling system. For example, if the study region is over tropical islands, the snow pack thermodynamics will be irrelevant and should be hang-up. On the other hand, if we are dealing with polar environments, the transpiration scheme can be ignored and the growing season snow melt and consequent flash floods are a major concern for triggering slope instability. Actually, in the flow stage, soil moisture effects on granular viscosity are critical for sliding material redistribution.

5.1.4 Full Three Dimensional Mechanics Approach

The physics of storm-triggered landslides (debris flows) has been systematically discussed in Iverson (1997). In the following discussion, emphasis is on recent significant progress in the research field, such as the parameterizing of reinforcement from vegetation roots using remotely sensed biomass information and allometric methods, which makes global estimates a possibility, formation of a shear zone of weaknesses, and an energy bundle formulation that unifies the full range of descriptions of granular material movement from sliding initiation to deposition (Eq. 5.1). Following is the introduction of a generic dynamic scheme that governs the sliding material's mobilization and redistribution.

By estimating a slope stability parameter, two dimensional slope stability models answer the first of the four major questions on landslides, namely, where will they occur? When being applied to a regional area, it is simply a repeated run for isolated grids and the order of execution on these spatial grids does not matter, either. The models have difficulty in implementing realistic lateral boundary conditions and can be "fooled" by extended (e.g., several km long) gentle slopes with well-weather surface cover and are laterally bounded by trenches (dry creeks) left by previous heavy rainfall runoff (see the Yangjiashan example in Chap. 5). In contrast, three dimensional models allow for all the known physical processes and can be applied to regional areas. Lateral boundary conditions can be sensed by inner grids because there are dynamic links between spatial grids. To describe the physics involved in Fig. 5.4, the following equations are used in full 3D landslide models in slightly different form. The governing equations of SEGMENT-Landslide, a recently established 3D dynamics model for studying storm-triggered landslides, are outlined below. Successfully solving these governing equations is a prerequisite for a "complete landslide model" aiming to explain their timing, location, magnitude and ensuing mass redistribution. As will be revealed later, the slope stability models and empirical storm intensity-duration schemes are a reduced form of this generic dynamic system.

For the sliding material, a coupled system is solved for conservation of mass:

$$\nabla \cdot \vec{V} = 0 \tag{5.11}$$

and momentum:

$$\rho\left(\frac{\partial \vec{V}}{\partial t} + \nabla \bullet \left(\vec{V} \otimes \vec{V}\right)\right) = \nabla \bullet \sigma + F \tag{5.12}$$

under the multiphase rheological relationships for water, condensed mud, and wet sliding granular materials, with granular viscosity parameterized as:

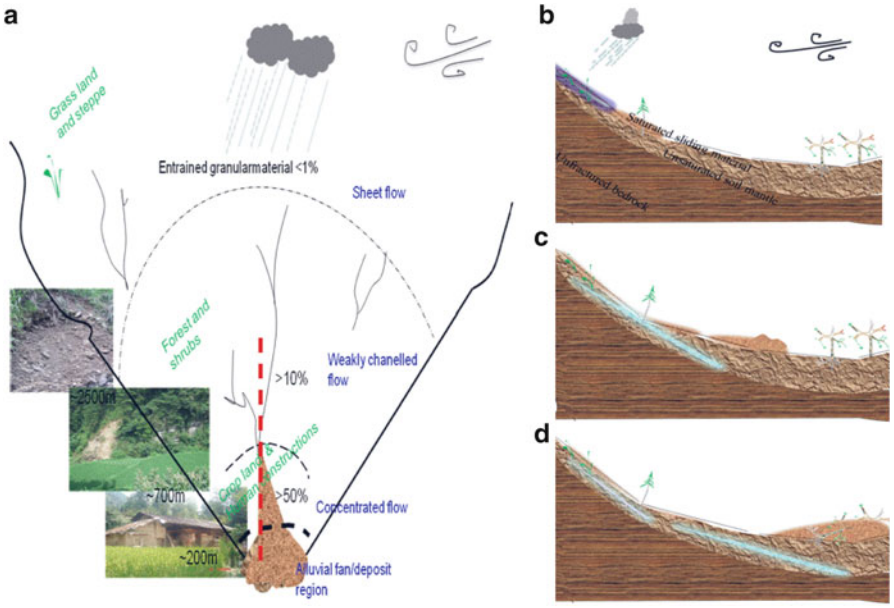

Fig. 5.4 A characteristic storm-triggered landslide (debris flow). Panel (**a**) is a "bird's eye" view of the entire (solid material) collection basin. The elevation divisions are only for reference. The section with concentrated solid material creeping is only a small portion of the entire area. This means of mass redistribution is referred as "progressive bulking." Vegetation mortality is caused by that portion with >50 % granular material concentration, especially when boulders are entrained. Panels (**b**), (**c**) and (**d**) illustrate a full life cycle of the debris flow: (**b**) is initiation, (**c**) is sliding, and (**d**) is cessation. Precipitation generated surface runoff washes the fine-grained material further downslope. Because the steepness of the slope is graded (steeper at top and gentler at the toe), granular material (saturated soils) are thicker toward the toe of the slope. As the sliding material run downslope, it entrains the pebbles and small stones (granular material) at the bottom. This significantly changes its rheological properties as it becomes drier and more viscous. The sliding material eventually ceases at places with gentle slopes, or where the slope angle reverses

$$v = \left(\mu_0 + \frac{\mu_1 - \mu_0}{I_0/I + 1}\right)\frac{S_p}{\left|\dot{\varepsilon}_e\right|} \tag{5.13}$$

Where ρ is bulk density, $\vec{V}$ is velocity vector, σ is internal stress tensor, and F is the body force (e.g., gravity $\rho\vec{g}$). Here ν is viscosity, $S_p = (R_{kk} - \rho g(h-z))/3$ is the spherical part of the stress tensor σ, μ_0 and μ_1 are the limiting values for the friction coefficient μ, $\left|\dot{\varepsilon}_e\right|$ is the effective strain rate and $\left|\dot{\varepsilon}_e\right| = \left(0.5\,\dot{\varepsilon}_{ij}\,\dot{\varepsilon}_{ij}\right)^{0.5}$, I_0 is a constant depending on the local slope of the footing bed as well as the material properties, and I is the inertial number defined as $I = \left|\dot{\varepsilon}_e\right| d/\left(S_p/\rho_s\right)^{0.5}$, where d is particle diameter and ρ_s is particle density. Actually, $\mu_0 = \mathrm{tg}\,(\Phi)$, with Φ the repose

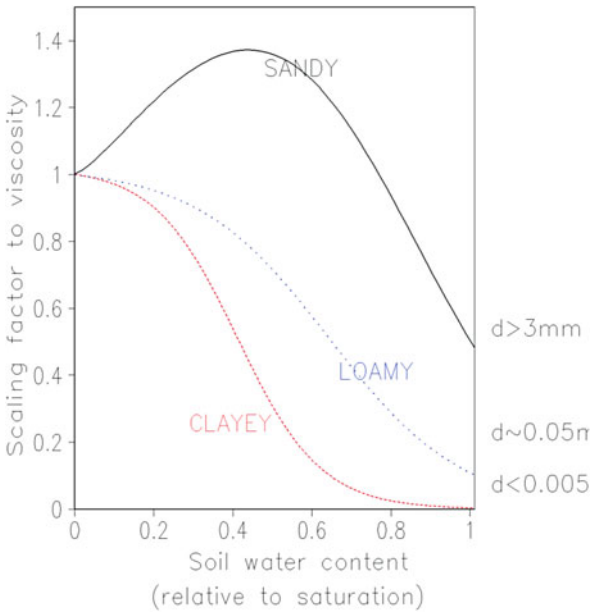

Fig. 5.5 Illustration of soil moisture effects on granular viscosity. The range of particle size (**d**) is labelled to the right. The six-parameter sigmoid function form follows Sidle (1992)

angle of granular material. In Eq. (5.13), the dense granular sliding material is treated analogous to incompressible fluid. The soil moisture enhancement factor for viscosity is assumed to vary according to a sigmoid curve formally as in Eq. (9) of Sidle (1992) but with the time decay term replaced by relative saturation. The general form of this controlling curve is presented in Fig. 5.5. The sigmoidal curve behavior of the viscosity's soil moisture content dependency is rooted in the Van der Waals force among particles. Soil moisture content is obtained by solving Eq. (5.9).

As derived from Eq. (5.11), the prognostic equation for surface elevation, $h(\theta, \phi)$, is

$$\frac{\partial h}{\partial t} + \left(\vec{V} \bullet \nabla_H\right)\Big|_{top} h - w|_{top} = 0 \tag{5.14}$$

where $X|_{top}$ indicates evaluation at the free surface elevation. In the case of slope movements, Eq. (5.14) is solved regularly to update the sliding material geometry. The w terms may include sedimentation rate and entrainment rate for clear debris flows. Once the material is entrained inside the sliding material, it changes the rheological properties of the medium and is advected within the sliding material.

The viscous term in Eq. (5.12) implies an energy conversion from kinetic energy to heat. To make a full closure of energy, the following thermal equation is required:

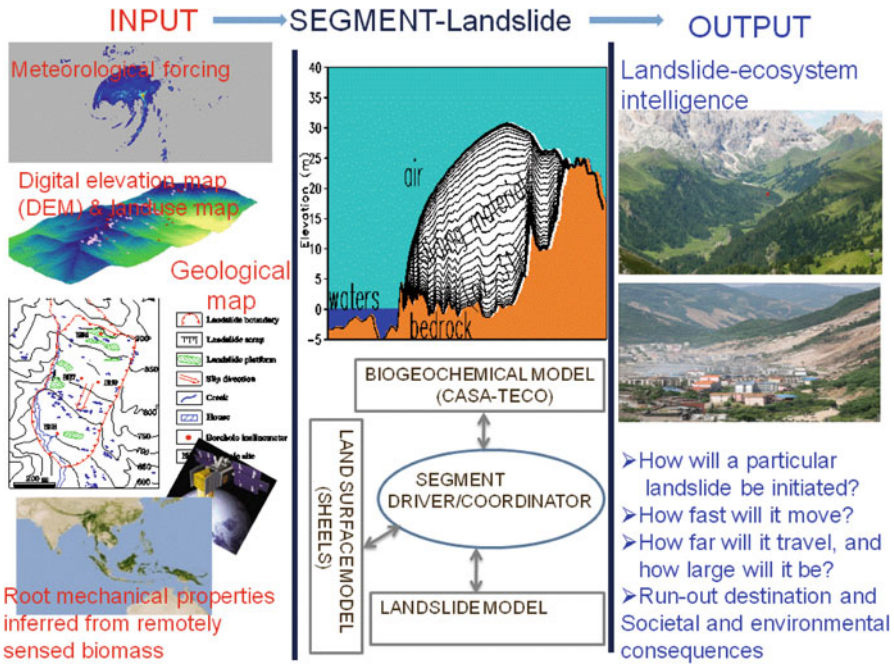

Fig. 5.6 Conceptual framework of SEGMENT-Landslide for the projection of storm-triggered landslides. The numerical techniques, model physics, input and output parameters are described in Ren et al. (2008a, b, 2011b). The model has wide applications to many other geophysical flows including glaciers and ice-sheets, snow and mud avalanches, soil and coastal erosion, sea level change following ocean bottom tsunami, and pyroclastic flows such as magma from volcanic eruptions. The land surface model component considers hydrological processes of soils and vegetation. The mechanical properties of roots and the biomass loading also are implemented in the landslide subcomponent

$$\rho c\left(\frac{\partial T}{\partial t}+\left(\vec{V}\cdot\nabla\right)T\right)=k\Delta T+\frac{2}{\nu}\cdot\sigma_{eff}^{2} \tag{5.15}$$

where c is heat capacity (J/kg/K), T is temperature (K), κ is thermal conductivity (W/K/m), and σ_{eff} is effective stress (Pa). The last term is "strain heating," which is the conversion of work done by gravity into heat affecting the sliding material by changing the viscosity, or causing a phase change. Numerical solving of diffusion equation is further addressed in Chap. 12. Sample code can be found in Appendix G. The above is the landslide component of SEGMENT-Landslide. Other components are shown in Fig. 5.6.

The energetics of a landslide is that all its potential energy reduction, ultimately, will be converted into heat. If the heat is uniformly distributed within the sliding material, as concluded in Iverson (1997), a 1,000 m descent of the flow increases the debris flow mixture temperature by only about 5 °C; assuming no evaporation of the soil moisture and a gross heat capacity of 2×10^3 J/kg/K, with volumetric heat

capacity of about 3.4 MJ/m^3/K for a gross density of 1,700 kg/m^3. In reality, in open, outdoor environments, latent heat fluxes caused by vapor evaporation consume most of the heat converted from release of potential energy, and, consequently, the temperature increase of the sliding mass is even smaller. This reasoning is close to reality for progressively bulking types of diluted debris flow. However, for landslides with a well-formed bottom sliding surface (i.e., those with well-formed shear zones before sliding, like the Yangjiashan creeping slope, to be detailed), the strains and hence frictional heating are concentrated near the bottom (Heim 1932). In this case, there are strong temperature gradients in the vertical profile of the sliding material. Bottom temperatures can reach ~100 °C. For example, this is the case for landslides accompanying earthquakes. The huge amount of heat interacts with local convective processes and produces thunderstorms. The thunderstorms then feedback positively, causing ensuing debris flows. In moist tropical region, landslides caused evaporation can send vapor to the atmosphere and form a special type of clouds: landslide clouds. For the cases with well-formed shear zones, bottom frictional heating also increases the travelling distance of the sliding material. Water is a common factor in failed landslide masses, and it often contributes to the initial failure. Quick evaporation of the interstitial moisture produces an air cushion beneath the undisturbed sliding material because of its low permeability. The air cushion, moving with the sliding mass, greatly reduces the bottom friction and increases the run-out distance (De Blasio 2008; Habib 1975; Goguel 1976).

While the horizontal grid stencil is regular lat/lon (λ, θ) in spherical earth surface, SEGMENT-Landslide uses a terrain following vertical coordinate system, the sigma coordinate system, z, defined as $z = (h - r)/H$, where h is the distance from the sliding material surface to the Earth's center, r is a variable location within the sliding material domain in the radial direction of (λ, θ), and H is the local thickness of the sliding material.

Here, it is timely to give some guidelines for input data for such generic modeling systems as those presented above (applicable for SEGMENT-Landslide and similar 3D process modeling systems). The model simulation domain should contain all possible sliding material (the entire soil layer) and one bedrock layer as the bottom model sublayer. For 3D distributed process modeling, the following input parameters are generally required: initial moisture content of the failed slab, soil material properties, vegetation root depth and distribution morphology such as root length density and root strength, and initial bedrock topography (high-resolution elevation data). High-resolution elevation data are needed because the driving force for sliding is the uneven surface. It is surface elevation gradients that drive downward motion. There are various sources for high-resolution digital elevation maps (DEMs). For example, the National Aeronautic and Space Administration (NASA) Shuttle Radar Topography Mission (SRTM; USGS 2004) provides DEMs in the order of 10 s-m resolution. From the governing equations, it is apparent that soil mechanical, as well as hydrological, properties are needed. For storm-triggered landslides, the focus is on mechanical properties of the soil particles. Many rheological features and hydromechanical properties of granular

material originate from the particle interlocking, which relies on soil particle size distribution. Ideal soil classification should classify soils such that their hydromechanical properties could be similar within the same classification. A number of soil classification systems are available, depending on the disciplines and their general engineering or scientific objectives. Some of the most widely used classification systems in the USA are US Department of Agricultural (USDA, Eswaran et al. 2002), International (Buol et al. 2003), Unified Soil Classification System (USCS, ASTM 1985), and American Association of State High and Transportation Organization (AASHTO, Hogentogler and Terzaghi 1929). The commonality among these systems is the use of soil particle sizes in dividing soils into different categories of clay, silt, sand, gravel, and large-sized materials, although the boundaries for each of these systems are somewhat different (see Soil Survey Division Staff (1993) for more details). This study uses the USDA classification system. Soil chemical composition also is important for their hydromechanical properties. Unfortunately, none of the four classifications are based on soil chemical compositions. In setting up the spatial variable soil mechanical properties, not only the USDA soil map was used, but also references was made to the STATSGO (Web site and Fig. S2) soil data for its wealth of vertical profile information. The general ranges of soil mechanical properties are listed in Table 5.3.

These soil mechanical properties (Table 5.3) are used to parameterize the granular viscosity of the sliding material according to the formula in Eq. (5.13). The setting of the bedrock mechanical properties always references to the published geological map of the region of interest. However, care needs to be exerted because the documented mechanical strength and viscosity values usually are laboratory testing results for non-fractured specimens. If there are cracks, the actual values can have orders of magnitude differences. Everything else remaining the same (e.g., same lithology, same resting slope, same above ground loading and similar shearing zone depth), scarp sizes of deep-seated, rotational landslides are proportional to the degree of fracture. This is, again, a granular size issue in a more general sense and follows the similar sigmoid curve in its "ensemble" rock size dependence. In this sense, existing landslide inventories can assist in objectively determining the degree of fracture of the bedrock. If circumstances permit, boreholes should be taken from the sites and the samples should be tested at loading pressures they would experience in reality. The mechanical properties obtained in this way should be much more representative than from civil engineering handbooks. In setting up the bedrock mechanical strength, the burying depth, in addition to the geologic unit reflecting lithology, should be taken into consideration to reflect an increasing strength of rock with confining pressure. For vegetated surfaces, especially those affected by fires, representing soils as purely mineral (e.g., sand, silt and clay classifications) is inadequate (DeBano 2000; Moody and Martin 2001; Smith et al. 2002). For previous fire sites within the last decade, a parameter f_i should be introduced to represent the fraction of soil sublayer i) that is organic matter. The thermal and hydraulic parameters for organic soil are weighted averages of the corresponding mineral soil and those of humus, using an empirical relationship (Lawrence and Slater 2008; Letts et al. 2000).

Table 5.3 Soil parameters in SEGMENT-Landslide (partially adapted from Soil Survey Division Staff 1993 and partly from FAO)

Soil type	Particle diameter mm	Bulk density kg/m^3	Field capacity m^3/m^3	Porosity fraction	Saturated hydraulic conductivity cm/h	Cohesion kPa	Dry frictional angle degree drained-cementation
Sand	2	1,490	0.12	0.34	38.41	2–8	38–42
Loamy loam	1.2	1,520	0.15	0.42	10.87	5–10	27–30
Sandy loam	1	1,570	0.21	0.43	5.24	4–8	28–36
Silt loam	0.6	1,420	0.32	0.46	3.96	6–12	23–25
Silt	0.05	1,280	0.28	0.48	8.59	6–12	23–30
Loam	0.004	1,490	0.29	0.43	1.97	7–40	21–24
Sandy clay loam	0.0035	1,600	0.27	0.39	2.4	8–50	18–22
Silt clay loam	0.003	1,380	0.36	0.46	4.57	36–82	16–17
Clay loam	0.002	1,430	0.34	0.45	1.77	20–50	18–22
Sandy clay	0.0015	1,570	0.31	0.41	1.19	7–42	21–24
Silty clay	0.001	1,350	0.37	0.47	2.95	20–40	17–20
Clay	0.001	1,390	0.36	0.45	3.18	30–50	15–18
Soil type	Thermal diffusivity	Wilting point (volumetric)	Saturation water diffusivity	Soil quartz content	Matric potential at saturation	Clapp–Hornberger *b*	
	W/(m K)	m^3/m^3	10^{-6} m^2/s	fraction	kPa	Unitless	
Sand	0.15–0.3	0.01	0.61	0.92	0.069	2.79	
Loamy loam	1.04	0.028	5.1	0.82	0.036	4.3	
Sandy loam	0.57	0.047	8.05	0.60	0.141	4.7	
Silt loam	0.16	0.084	24.0	0.26	0.759	5.3	

(continued)

Table 5.3 (continued)

Soil type	Particle diameter mm	Bulk density kg/m^3	Field capacity m^3/m^3	Porosity fraction	Saturated hydraulic conductivity cm/h	Cohesion kPa	Dry frictional angle degree drained-cementation
Silt	0.17	0.084	24.1	0.15	0.759	5.4	
Loam	0.33	0.067	14.3	0.4	0.355	5.2	
Sandy clay loam	1.5	0.069	9.9	0.55	0.135	6.7	
Silt clay loam	1.12	0.12	23.7	0.1	0.617	8.5	
Clay loam	1.29	0.1	11.3	0.32	0.263	8.2	
Sandy clay	3.2	0.1	18.7	0.52	0.098	10.7	
Silty clay	1.91	0.13	9.6	0.1	0.324	10.4	
Clay	2.14	0.15	11.2	0.17	0.468	11.55	
Organic material	0.33	0.06	14.3	0.06	0.355	5.2	

Compared with the physical properties of hill slopes that affect the potential for landslides, vegetation and rainfall are far more temporally variable. Choices for land cover maps are: the USGS National Land Cover Dataset 2001 (NLCD 2001, Homer et al. (2004)), the International Geosphere-Biosphere Programme Data and Information System's DISCover (IGBP-DISCover, Belward 1996), or the U. Maryland 1 km (Hansen 2001) land cover maps. Although both the latter two are derived from the 1992–1993 Advanced Very High Resolution Radiometer (AVHRR) data (Fig. S1), the two have slightly different classifications. Fortunately, the differences are primarily around Polar Regions and do not affect landslide research. In situ archiving of biomass usually is limited to forests with commercial value (e.g., California). In addition to being cost-effective, remote sensing provides the best spatial and temporal coverage of terrestrial biomass. Usually, foliage biomass can be estimated from the Moderate Resolution Imaging Spectroradiometer (MODIS) leaf area index (LAI) products. Aboveground biomass residing in branches and stems is then derived from generalized, diameter-based allometric methods (Zhang and Kondragunta 2006), with reference to the land use map. For example, a unique feature of SEGMENT-Landslide is its treatment of the root properties relevant to storm-triggered landslides according to ecosystem functioning, directly based on root mass allocation of vegetation in the residing climate zone. The partitioning of supporting roots, nutrient absorption roots and moisture tapping roots affects soil moisture content as well as the mechanical reinforcement effects. In addition, total biomass loading also is supposed to be proportional to aboveground biomass. With these pieces of information and the potential magnitudes of landslides, damage to terrestrial ecosystems also can be estimated.

For different research purposes, meteorological inputs can come from many different sources. For example, to investigate the long-term suitability for infrastructure, atmospheric parameters from high-resolution climate models may suffice. For real time operation and monitoring, precipitation products from weather models (e.g., Weather Research and Forecasting (WRF), Advanced regional Prediction System (ARPS) and Rapid Update Cycle (RUC)) or precipitation estimates from National Weather Service radar products can be used as input to landslide models. From the general diagram (Fig. 5.6), to estimate the socio-ecological consequences of storm-triggered landslides, population maps and infrastructure layouts also are required information. These types of information also are regularly used by the GIS systems.

5.2 Contemporary Slope Stability Models

Slope stability models are based on the following reasoning. On a sloping surface, the gravitational force can be partitioned into a component normal to the slope (F_n), contributing to friction that resists sliding erosion, and a component parallel to the slope (F_p) that promotes sliding (Fig. 5.3). A stability parameter, S, is defined as $S = F_n \times \eta / F_p$, where η is the internal friction coefficient. This is the general form of S,

but there are many specific forms, based on the fact that, landslides, as the movement of a mass of rock, debris or earth downslope (Cruden 1991; Dai and Lee 2002), occur when shear stress (F_p) is higher than shear strength (i.e., when $S < 1$). For example, the stability factor can be defined as $(S \times G - C_{eff} L \sin\alpha)/(\cos\alpha + tg\phi \sin\alpha/S)tg\alpha = C_{eff}L + (S \times G - C_{eff}L \sin\alpha)/(S \times \cos\alpha + tg\phi \sin\alpha)tg\phi$ (derivations to be detailed), where G is the total weight of the sliding mass, L is the slope length, α is the slope angle (of the sliding surface), C_{eff} is effective cohesion (mechanical property of soil and weathered rock), and ϕ is the internal frictional angle, a mechanical property of sliding material. If a slope is composed of several segments of sub-slopes with very different mechanical properties, this expression can be summed to obtain the gross stability of the entire slope. If the iteratively obtained value of S is 1, it is assumed that the slope is in a critical-stable condition. As a slope stability model, TRIGRS considers soil moisture effects on cohesion and saturated soil layer depth.

Rather than using land surface schemes to diagnose the depth of sliding material, recent slope stability models, to facilitate global implementation, have further simplified the infiltration scheme (e.g., Rui 2004; Montrasio and Valentino 2008). For example, the SHALlow landsliding STABility model (SHALSTAB, Montgomery and Dietrich 1994) is a physically based stability model, which couples the steady state hydrologic model TOPOG (O'Loughlin 1986) with the infinite slope stability equation. This model assumes that steady state rainfall and soil transmissivity control the slope-parallel fluctuations of the water table, whereas the failure plane is located at the interface between soil and bedrock, parallel to the ground surface. The model requires few input parameters: a digital elevation model, soil properties (bulk density, and effective friction angle), soil thickness, saturated hydraulic conductivity and the rainfall amount. The factor of safety in SHALSTAB follows Henkel and Skempton (1954). The output is further transformed into a shallow landslide susceptibility map, in which the instability is expressed as the ratio between the critical precipitation P_r and the soil transmissivity T_r. The hydrological ratio (P_r/T_r) is used to assign the relative landslide hazard potential. SHALSTAB also is known to be sensitive to topographic data.

SHALSTAB was originally designed for soil-mantled hilly terrains with impermeable bedrock and alluvial deposits, an assumption not applicable for areas with a long glacial history, rocky terrain, terrain dominated by deep seated landslides, and areas with deep groundwater flows and emergent springs. Simplicity of mathematical formulation and requirements for a small number of input parameters make this model suitable for diagnosing the susceptibility of shallow landslides at regional scales. Overall, the model tends to have a high false alarm rate, and, more problematically, the steady state hydrological assumption limits its application to generic slope conditions (Casadei et al. 2003).

There are several other slope stability models that are widely used among European groups. For example, Stability Index MAP (SINMAP, Pack and Tarboton 2004) has theoretical assumptions similar to SHALSTAB, but allows for spatial variability of soil strength parameters and accounts for roots and soil cohesion. The probability of a given slope being unstable is expressed trough the stability index.

In estimating the stability index, the uncertainties of the soil strength parameters are modeled, providing upper and lower limits along with their uniform probability distributions.

The GEOtop-FS is a distributed slope stability model designed to analyze the probability of occurrence of shallow landslides and debris flows (Simoni et al. 2008). The likelihood of slope failure, or the safety factor, is estimated using a probabilistic approach. GEOtop-FS was developed on GEOtop, a small scale distributed hydrological model, which solves the surface energy balance equation accounting for water and energy budgets on a real topography (Bertoldi et al. 2006). Unlikely many other stability models, which rely on steady state hydrological assumptions, the hydrological analysis (water content and suction dynamics) is computed using an approximation of the 3D Richard's equation which allows water to redistribute laterally and even move uphill or exfiltrate according to local suction (Rigon et al. 2006). The required input parameters are a digital elevation map and those atmospheric parameters commonly required by a land surface scheme. Soil parameters are assigned using a statistical distribution, in order to account for the spatial variability of these values. Additional modules can be implemented in the analysis, accounting for snow accumulation and melt (Zanotti et al. 2004), freezing and thawing processes in the soil (Dall'Amico et al. 2011) and spatial patterns of ground thaw and runoff generation in permafrost terrains (Endrizzi et al. 2011).

Although a wide range of geomorphological, geomechanical, hydrological and atmospherical parameters can be taken into account, false alarms are inevitable for slope stability models of debris flow, primarily because the lateral support in 3D configuration is nonexistent (Fig. 3.1). Besides being unable to rigorously treat lateral support of a channel, slope stability models have no real projection ability. The stability parameter is intended to diagnose when the sliding initiates. Because only static mechanical properties are included, a slope stability model does not include the sliding process and how the sliding material is redistributed after sliding ceases. Table 5.4 summarizes the relationship between slope stability schemes and full 3D process-based landslide models.

5.3 Slope Stability Model Is a Special Case of the Generalized Unified Landslides System

The system described by Eqs. (5.11–5.15) is suitable for investigating a wide spectrum of landslides, particularly shallow or storm-triggered debris flows. It also is convenient to investigate the positive feedback between deforestation, land use changes, undercutting of slope for road construction and expansion of settlement areas and landslides. For example, the effects of vegetation can be fully considered in this modeling system. The weight loading is set as an upper stress boundary. The hydrological effects are manifested in the parameterization of viscosity. For example, soil water dissolves certain chemical bonds in clay soils,

Table 5.4 2D slope stability model vs. 3D process-based landslide models

Model type	2D Slope stability model (e.g., TRIGRS, SLIDE)	3D process-based landslide models (e.g., FLAC^{3D}, SEGMENT-Landslide)
Governing equation for motion	Systematically solving the conservation equations for mass, momentum and energy (thermodynamic equations)	Mohr–Coulomb criterion in the apparent cohesion form. Frictional resistance vs. Gravitational shear driving stress.
		Assume constant slope angle and well-defined sliding surface (shear zone)
Slope hydrological processes	Solving 3D Richards equation	Solving simplified Richards equation. Some use the Green–Ampt (1911) infiltration model, which is an analytical solution of Richards equation
Capability	Having the potential to describe the full landslide cycle and the spread of the sliding material (hence the ecosystem and societal consequences)	Providing slope safety index

and affects on cohesion and internal friction for sandy soils. The pore pressure adjustments of the spherical part of the stress tensor, and (minor) changes to the loading corresponding to the soil water weight (Smith et al. 2009) can be implemented conveniently. The mechanical properties of the roots can be implemented in the effective cohesion. The water distribution effects of vegetation roots are parameterized in a land surface sub-model. This sub-model provides the soil moisture conditions for the sliding sub-model. These explain how antecedent rainfall influences the saturation of soil and ground water level for a vegetated slope and its instability (Crosta 1998; van Asch et al. 1999) and provide a sound basis for discussing deforestation effects on landslides, and the positive feedbacks that lead to further deforestation. However, to mechanistically quantify these complex processes (material entrainment, incision/undercutting of gully banks and occlusion of channel by debris) detailed digital elevation mapping to represent bank geometry is needed, along with strength provided by vegetation roots, and stratification of the sliding layer. An absence of these parameters makes the problem intractable.

Interestingly, the ID empirical approach and the slope stability models are various reduced forms of the above equation set. For example, if the time dependence is neglected and three dimensional topography reduced to only including x-z plane, the governing equations can be written as (in component form):

$$\begin{cases} \dfrac{\partial \sigma_{xx}}{\partial x} + \dfrac{\partial \sigma_{xz}}{\partial z} = 0 & (5.16) \\ \dfrac{\partial \sigma_{xz}}{\partial x} + \dfrac{\partial \sigma_{zz}}{\partial z} - \rho g = 0 & (5.17) \end{cases}$$

Further simplifying the slope geometry to be of constant bedrock slope (α), uniform sliding material thickness (thus, surface slope also is α), and a stable bed, the volume integration of Eqs. (5.16) and (5.17) yields

$$\begin{aligned}&\left(G - C_{eff}L\sin\alpha/S + u \times tg\phi\sin\alpha/S - \Sigma_v\right)/(\cos\alpha + tg\phi\sin\alpha/S) \times \sin\alpha - \\ &\left(C_{eff}L + \left\langle\left(G - C_{eff}L\sin\alpha/S + u \times tg\phi\sin\alpha/S - \Sigma_v\right)/(\cos\alpha + tg\phi\sin\alpha/S) - u\right\rangle \times tg\phi\right)/S, \\ &\times\cos\alpha + \delta E + \Sigma_h + \hbar = 0\end{aligned} \tag{5.18}$$

where $\hbar$ is the hydrostatic pressure from ground water, Σ_v is the net vertical support at top and toe (determined by boundary conditions), Σ_h is the horizontal support evaluated at top and toe, and δE is the horizontal force exerted during earthquake. Equation (5.18) indicates that slope stability is influenced by various factors, such as slope gradient (α), soil properties (implicit in G, C_{eff} and α), ground water table and geomorphology ($\hbar$ and the boundary conditions). As for the triggering mechanism, it includes not only the storm (excessive rainfall), but also earthquake and volcanic activity (δE).

In the case without ground water and no effects of earthquake, Eq. (5.18) takes the form $(S \times G - C_{eff}L\sin\alpha)/(\cos\alpha + tg\phi\sin\alpha/S)tg\alpha = C_{eff}L + (S \times G - C_{eff}L\sin\alpha)/(S \times \cos\alpha + tg\phi\sin\alpha)tg\phi$, as discussed in the review of slope stability model in the previous subsection. This is an extension of Eq. (5.15) of Takahashi (1978), as he made the further assumption that sliding material is resting on a stable bed of cohesion-less material.

Similarly, rainfall intensity-duration methods (IDs henceforth) are based on the soil moisture sensitivity of the resistive terms (the middle two terms on the right hand side of Eq. 5.1). Sliding material is a structured mixture, with particular spacing patterns and arrangements, of solid particles, pore-water and, in some cases, cementitious material accumulated at particle–particle contacts. In addition to factors such as the electrical charge of the particles, and the chemistry of pore water, the chemical bonds are the key to the soil yield strength. As an example, there are the cementation-particles connected through a solid substance, such as recrystallized calcium carbonate formed in dry climates when seeping water experiences/encounters new environments of high pH value and (or) the solvents are evaporated, as aforementioned in Chap. 2. Cementation cohesion (the effects can be explicitly implemented in Eq. (5.1) in the cohesion term) can also be a part of soil animal's biological chemical processes or a resultant of wild fire burning. During dry conditions, tensile strength resulting from cementation varies in magnitude and could reach 0.2 Mpa in soils, substantially increasing the stability of shallow material on hill slopes (Sitar and Clough 1983; Collins and Sitar 2008). Soil water, especially if it is acid (pH value <6), can dissolve these chemical bonds.

Increased pore pressure also tends to reduce the effective spherical pressure and reduces the yield strength of the sliding material. Comparatively, the extra loading of the water mass is insignificant for increasing slope instability. Unfortunately, IDs do not employ a processed modeling of the relationship. Rather, they have empirical/statistical

relationships constructed between precipitation and occurrence of sliding. In addition to shortcomings already discussed in the previous subsection, or lacking necessary time varying features in its empirical coefficients, current IDs do not take rainwater acidity and soil profile properties into account. The empirical parameters therefore are sensitive to changes in climate and soil/vegetation/land use.

Because of their relatively frequent occurrence, storm-triggered shallow landslides/debris flows have been actively studied using myriad approaches suitable for many situations. Empirical and descriptive landslide models have contributed much to public awareness of landslide hazards and have led to valuable accumulated experience in identifying the key causal factors (Caine 1980; Cannon and Ellen 1985; Sirangelo and Versace 1996; Godt et al. 2006). As the pioneer of Ids, Caine (1980) proposed the seminal rainfall intensity-duration threshold line, above which shallow landslides may occur (the ID method), based on 73 landslides worldwide. In intensity-duration thresholds, a dataset consisting of rainfall intensity (I, mm/day) and rainfall duration (D, h) of landslide events is first prepared. A scatter graph is then generated with rainfall duration as x-axis and rainfall intensity as y-axis. The equation for the rainfall threshold is a power-law curve that fit the points in the scatter plot (actually a lower envelope in that if a point lies to the right upper of the curve, landslides may occur), usually take the form $I = aD^{-b}$, where a and b are positive constants that vary with soil, vegetation and land use. For fire-burn cites, the indirect effects of precipitation through reducing cementation cohesion may be implicitly implemented into future ID methods through a elevating the "a" parameter. Not surprisingly, the IDs are also used actively in flash floods research, because flash floods and debris flows occur concurrently and sometimes the damages by debris floods are ascribed to flash floods and vis-versa.

Godt et al. (2006) suggested that landslide-triggering rainfall must be considered in terms of its relationship with antecedent rainfall. For example, a heavy rainfall event within a dry period is not likely to trigger shallow landslides, while the opposite is true for lighter rainfall within a wet period. As it directly affects soil moisture conditions, Godt et al. (2006) correctly claim that antecedent rainfall must be included in an empirical model's assessing of a rainfall's potential in causing landslide. Godt et al. (2006) therefore is a significant improvement over Caine's (1980) seminal rainfall intensity-duration threshold line approach. The antecedent rainfall index is usually defined as a red noise of the accumulative rainfall amount 3 days (for tropics) and 7 days (temperate climate zones) prior the landslide event. Hong and Adler (2008) further adapted the empirical rainfall intensity-duration thresholds technique for global assessment of storm-triggered landslide hazards, by using remotely sensed precipitation rather than ground-based observations. Remotely sensed precipitation has near-global coverage and is available almost in real time. Hong and Adler (2008) is thus another significant improvement of the traditional empirical intensity-duration threshold method. Recent empirical methods also compile many soil hydrological parameters by using water-balance models with little physical basis but are convenient for estimating soil moisture conditions. For example, Godt et al. (2006) uses a detailed assessment of rainfall triggering conditions, hill slope hydrologic properties, soil mechanical properties,

and slope stability analyses. The accumulation of sliding material is a slow process, compared with sliding, whether they are rockfalls (Ma and Qi 1997), aeolian processes (Okin et al. 2011), or damaging erosion processes from weathering (Anderson 2006; Cutler 2006). Previous sliding will reshape the sliding material profile and may even completely remove the sliding layer. These will increase the stability of the slope and a similar rainfall amount may cause sliding on a reduced scale, or not at all. Thus, the empirical parameters (a and b) in the ID approach vary not only spatially but also temporally. In this sense, all present ID approaches still lack the important time varying features.

Hungr et al. (2008) found that the magnitude–frequency relationship also obeys a power law relationship. For debris flows and avalanches, the coefficient is a function of slope length, that is, relief, rather than being a universal statistical quantity. They used a data set compiled entirely from ground investigations and their conclusions therefore have a high level of credibility. A notable development in the empirical approach is that GIS information is used to form predictors (e.g., Dai and Lee 2002). Based on the ID method, NASA now provides routine services on landslide estimates, constructed primarily on rainfall amounts and intensities obtained from the real-time Tropical Rainfall Measuring Mission (TRMM) multi-satellite precipitation analysis (TMBA Web site). Although it is of considerable value, it is not a true intelligence system of landslides because its basis, the projection component, is empirical. Debris flows or storm-triggered landslides represent formidable forecast challenges because they are not caused uniquely by meteorological phenomena. They occur when favorable meteorological, hydrological, geographical, and geological circumstances coexist. For example, although heavy rainfall is necessary, a given amount and duration of rainfall may or may not result in a debris flow, depending on the hydrologic characteristics of the watershed where rainfall accumulates. Same amount of infiltration-excess infiltration may entrain very different amount of debris, depending the soil type and vegetation cover of the basin. Even same amount of debris material is involved, the severity of the mudslide may be further confined by the basin geometry. The forecast challenge is further augmented by urbanization component of the physical character of the basin.

A synthetic consideration of both preparatory and triggering factors, demands a more comprehensive modeling of the physical processes involved in landslides (Costa 1984; Iverson 1997). The overview by Iverson (1997) suggested several criteria for dynamic landslide models, including that a model should be capable of simulating the full start–movement–spread–cessation cycle of the detached material, and should cover a wide spectrum of debris flows. With continued growth and expansion of human population, rain-triggered shallow landslides result in increasing loss of life and economic cost. From an ecological viewpoint, landslides are important factor in desertification over mountainous regions because they are very effective at transferring biomass from live to dead respiring pools (Ren et al. 2009). Along these lines, there are physically based slope stability models to simulate the transient dynamical response of pore pressure to the spatiotemporal variability of rainfall (e.g., TRIGRS, Baum et al. 2002); commercially available numerical

modeling codes for geotechnical analysis of soil, rock and structural support in three dimensions (FLAC-3D, www.itascacg.com/flac3d); and three dimensional, full physics multiple rheological modeling systems (Ren et al. 2008a, b, 2010).

5.4 Flow and Redistribution of Sliding Material: Several Measures of Landslide Destructivity

Empirical and statistical I.D. models and slope stability models aiming at the initiation of slides are not belonging to this category. The following sections summarize the current knowledge and the state of modeling ability in a full spectrum simulation of landslides.

As remarked above, a complete landslide model needs to include mechanisms explaining their timing, location, magnitude (size), and ensuing mass redistribution. To answer these needs, we need geographically detailed information of material elasticity, creeping (strain hardening and necking), fracture, and flow (Iverson 1997). As earth surface materials are mostly brittle, the elastic range is rather short on a strain–stress graph. As measurement of strain is the traditional approach for geological studies of landslides, the short elasticity range of natural rocks contributes to their abruptness of the occurrence. As uneven surface topography, or more accurately, the uneven horizontal stress caused by uneven loading, is the ultimate driver for sliding, landslides occur only in mountainous regions. The lateral accelerations of an earthquake can also supply the uneven horizontal stress and thus also is a mechanism for sliding. As landslide occurs as a result of mismatch between the downslope driving stress and maximum shearing resistance of the slope material, a slope failure may develop without any change in the driving stress, if the slope material strength decreases for any reason. For example, the maximum shear resistance may be altered by chemical processes as a consequence of weathering, or decreased by physical reasons such as pore pressure in cracks or fissures or in the voids of the soil material. Also, granular particles from brittle rock are shear thinning-shearing strength goes down as being sheared. This apparently is a shelf-perpetual unstable behavior in that initial distortions cause a reduction in strength, which leads to further distortions and still lower strength. Different types of soils/rocks have very different shear strengths, and pinpointing the failure location requires analysis of the three dimensional stress distributions together with the corresponding detailed material properties. For landslides, even with detailed density profiles (thus gravity loading information), differences in material rheological properties at very short distance can result in very different fracturing structure. Sliding material redistribution after slope failure is a “fluid” flow governed by granular rheology (Jaeger 1969).

Rheological properties are macroscopic manifestation of chemical bonds and particle interactions. Following is a brief discussion of the chemical bonds involved in landslides. Non-fractured rocks contain very strong ionic and covalent bonds and

are not going to yield under normal stress conditions experienced shallower than upper mantle depth. When being weathered, especially when soluble substances (inorganic or organic) of aeolian origin are involved (Okin and Gillette 2001), the much weaker hydrogen bonds are involved and fracture becomes a possibility. After experiencing repeated wet–dry cycles, the material accumulated in the crevasses can be very strong when being dry (ionic bonds or those of carbon-rings as in commercial glues) and strength diminishes when being wet. This is because as the cementing material is dissolved by rain, randomly oriented weak intermolecule hydrogen bonds replace the previously strong ionic bonds. This usually is how rainfall weakens shear strength and facilitates slope instability. A shared property with other forms of fatigue is that cyclic forcing is the most effective way to cause landslides. Interestingly, most of the cyclic forcing involve changing in hydrogen bonds (e.g., repeated wet–dry cycles in lower latitudes and freeze-melt phase change cycles in polar regions both are most common landslide trigger,[5]). It has been observed in laboratory tests of the shearing strength of soil that under repetitive shear-stress loading, certain soils can develop a somewhat lower shear strength than when they are loaded once only to their maximum value; thus the "dynamic" shear strength is lower than the static value. Consequently, a potential landslide mass which is stable under static conditions may fail after a number of cycles of vibration caused by an earthquake. In extreme cases, usually involving fine grained sands of loamy soils saturated with water, the interaction of the cyclic shearing stresses with the hydraulic properties of the soil can result in liquefaction of the soil on slopes during the earthquake (e.g., the case discussed in the Sect. 5.1.3).

Most frequent and of most ecological consequence are movements of soil-mantled slopes. Sliding materials involved in landslides fall under the general category of granular material. In addition to the canonical definition of Campbell (1990), the concept of granular material needs to be extended to include discrete solids (units that do not break during sliding and collision with peer particles or bedrock or lateral banks) of a wide size spectrum. The size that a solid body is classified as a granule is arbitrary and relative to the dimension of the slope it resides. In the following discussion, the granular particle size should be six orders (10^6) of magnitude larger than molecular (nano-) scale and at least three orders of magnitude smaller than the slope length it resides upon. Suppose a three dimensional solid is composed of uniform molecules. At its inner domain, the lattice is very regular so each molecule vibrates around its equilibrium position. Near the surface, however, forces from inside neighbors are not going to be exactly balanced the same manner by the environmental particles or fields. The lattice near the surface is distorted under boundary effects. Two solid bodies of identical macroscopic feature and matching interface therefore cannot be put together and stay

[5] Causal factors of landslides cover a wide range of timescale. If a causal factor is so effective in initiating a landslide motion, it is called a trigger. Common triggers are heavy rainfall, earthquake shaking or volcanic eruption.

together because, at the interface, restoring the lattice structure to resemble the inner domain needs phase change (to drastically increase the diffusivity). The healing process may increase under high pressure and temperature, depending on $\exp(-A/kT)$, where T is the absolute temperature, A is a constant of material under question, and k is Boltzmann constant. In the Earth surface environment, the healing of brittle rocks is beyond the timeframe of interest here. Breaking of boulders into small granules tremendously increases the surface area and the boundary effects. The occupied gross volume also increases because contacts between granules are incomplete due to their different macroscopic geometric features (Fig. 5.7). As subdivision continues, the bulk density first decreases and then increases to approach that of the original boulder. With the increased degree of freedom, granular material has a certain fluidity, while still resembling the mother material in its mechanical features. In fact, Johnson (1965) and Yano and Daido (1965) realized independently that wet granular materials exhibit rheological properties of both viscous fluids and plastic solids. However, as a multi-body, loose lump of solid granules (e.g., the solid particles that have same chemical composition and physical properties, such as elastic modulus, as their non-fractured mother material), granular material is not true fluid and the stress fields inside is highly isotropic and locally non-hydrostatic (Appendix A). For true fluids, the particles (molecules) can freely exchange locations without causing heat increase. Granules do not have such freedom (the free path of granule is usually on the same order of its dimension) thus horizontal pressure component is always orders of magnitude smaller than vertical pressure component. Shaking can increase the free-path length of granules and increase the fluidity. This is the fundamental reason why earthquake causes landslides and enhances the magnitude of landslides. Another way for increasing the fluidity if add liquids into granular lump. The interstitial fluids lubricate the granules and reduces the energy loss (transform through friction into heat) when exchanging locations. This actually explains why increased water table, melting snow drainage, and storms trigger landslides. As to response to loading, unlike solid, which can localize the lift to very limited (contacting surface) areas, granular media have to mobilize all granules within a certain range (domain of influence, as defined in Appendix A) to act in synergy to counter the load's weight. The source of lifts, as indicated in Fig. A.1, include bottom and lateral boundary lifts. This is unlike true fluids, which particle has high degree of freedom in exchanging location so that the internal stress is isotropic (equal in all directions). The lift for a load merged in liquid is only the "bottom" type (for irregular solid body, the integrated net results are "bottom" type of vertical lift). For granular media to behave similar to fluids, the granules must be in point-to-point contact (i.e., non-cohesive) at most and must be truly smooth so that there is no friction among them no matter how large the compressive normal pressure (near zero repose angle). The landslide materials apparent do not meet these criteria. Thus, in reality, the influence domains are much irregular and can be very polarized in certain direction. This is the underlying fundamental physics for the existence of shear zone or sliding surface on weathered slopes. As an introduction to the interested readers, we provided Appendix A to explain why there is no hydrostatic

relationship within even much ideal granular media. The concept of "influence domain," the existence of minimum set-in depth, and internal bridging phenomenon are introduced. Unitless scaling invariants are introduced for a full spectrum coverage of granular flow regimes.

A strict definition of granular flow allows only interstitial soil moisture content. Following the terminology of Bagnold (1954) and Iverson (1997), the "inertial" stress exerted on bedrock or lateral confining boundaries are through granular collision and are proportional to flow shear in the direction normal to the boundary. This is analogous to Prandtl's mixing length theory (Wallace and Hobbs 2006). As shown in Figs. 5.7 and 5.8, the overall rheological properties of granular material resemble that of the original solid material but with fluidity, as a consequence of increased degree of freedom of a multi-body system. In most cases, the attractions between particles are minimal (like liquids) but the frictional interaction, as measured as granular viscosity (to be detailed), depends also on normal pressure (unlike liquids). As shown in Fig. 5.7, the movement of one granular particle affects its non-neighboring particles anisotropically, yet another feature resembling fluid advection. Tracing each particle is thus impractical mathematically. However, the macro-properties such as average mixing length, repose angle and granular viscosity can all be determined experimentally (e.g., Jop et al. 2006). The effects of moisture content are also being actively studied experimentally (Tegzes et al. 2002). Thus it is reasonable to put the sliding problem of granular substance into a 3D modeling system that rigorously treats the evolution of temperature, velocity, and thickness profiles.

Many factors influence the yield strength of a soil mass (Selby 1993). These include the sliding friction between the material and some well-defined yield plane (i.e., the movement of coarser soil over a saturated clay layer), but most commonly the internal friction caused by the friction among individual grains within the soil matrix. Cohesion among soil particles is sensitive to soil moisture/water content. For sandy soil, a small amount of water enhances cohesion among particles, whereas high water content reduces the frictional strength through increased pore pressure. The situation for clay soil is a simple reduction of strength as moisture content increases (Ren et al. 2004). From the perspective of a dry internal frictional angle, coarse-textured soils have lower slope thresholds of instability and are more likely to lead to slope failure than are fine-particle soils (Fig. 5.8). The situation is further complicated by the hydrological processes and the presence of vegetation (Fig. 5.4).

As illustrated in Fig. 5.4, the presence of aboveground vegetation introduces the following effects: aboveground biomass loading (gravitational), growing season soil moisture extraction by live roots (hydrological), fortification of the soil within its extension range (mechanical), changing chemical environment of the soils through life processes (e.g., respiration, absorption of minerals selectively, and secretion of organic substances) and therefore the bond strength among unit cells (chemical), and wind stress loading (meteorological). The overall effects are the interaction of the above factors and it is difficult to generalize before a detailed analysis is carried out that is specific to a certain situation. For example, the

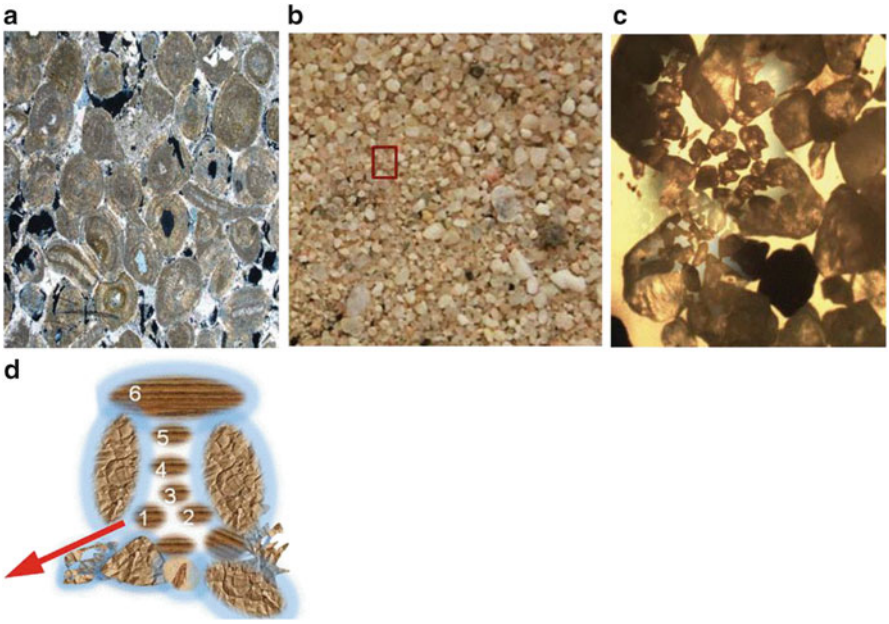

Fig. 5.7 Granular material. (**a**) is non-fractured source material (microscope image). (**b**) is regular image of palm sand and (**c**) is a microscope image of (**b**), zoomed in the *red box* in (**b**). Panel (**d**) is a schematic vertical cross section of a representative segment of an idealized granular particle lump. Within this segment, if grain 1 exits as a result of its gaining momentum through interactions with the underlying bed (the *red arrow* is a possible passage for it to exit), or with neighboring grains, weight centers of particles 3, 4, and 5 all adjust accordingly. Particle 6, being supported by two underlying particles, will not be able to freely lower its weight center in response to particle 1's absence. Apparently, every particle's free mixing length is different. It therefore is impossible in practice to track individual particles. It is necessary to consider the ensemble mean free mixing length: that is, the distance a particle travels on average before it collides with other particles. Photo credit of (**a**)–(**c**): Kongyang Zhu (Dept. Applied Geology, Curtin University). Cross-polarized light with a field width of 4.9 mm is used in producing (**a**)–(**c**)

fortifying roots have yield strength larger than dry soils and the existence of roots is commonly thought to increase the resistance of soils. However, the presence of roots, especially when there is precipitation, also facilitates water channelling into deeper depths. After the soil is moistened, the cohesion between soil and the root surface is reduced greatly (to negligible strengths <0.001 Mpa, Lawrance et al. 1996) and the root strength cannot be effectively exerted. Also, the effect of roots is to "unify" the soil particles within root distribution range (Fig. 5.1a). Once the entire rhizosphere soil layer is saturated, the fortifying effects will be totally lost. Thus, a more accurate statement would be "the reinforcement effects from roots are an effective mitigating factor for shallow storm-triggered debris flows." It is known that shallow interlocking root networks can contribute to mechanical reinforcement to soils (Sidle et al. 1985; Selby 1993; Lawrance et al. 1996). For a pasture species, Selby (1993) estimated the "additional" cohesion ranging from 0.1

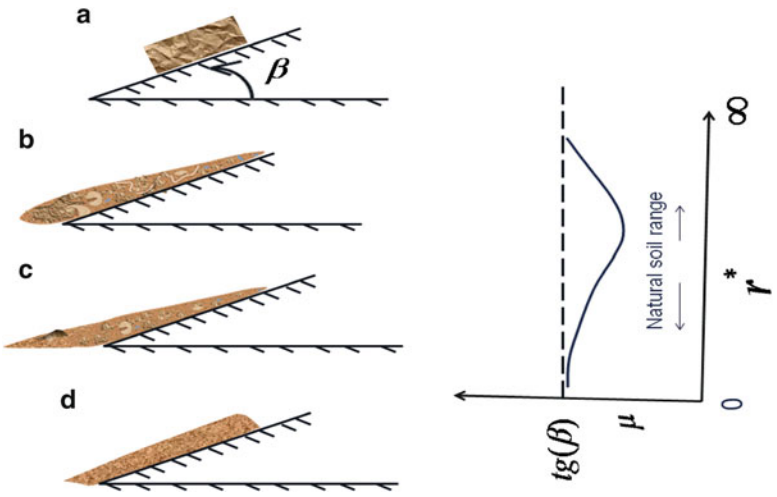

Fig. 5.8 Vertical cross section of a corn slope composed of the same material as the sliding material. It shows the rheological effects when a large piece of solid is divided into granular particles. From (**b**) to (**d**), the particle size becomes gradually finer. When divided into smaller parts, the surface area increases. In the inner domain of a solid, the lattice of fundamental particles is very regular. The surface particles are relatively irregularly arranged. It is in principle impossible to make the reverse process of putting smaller parts together without liquefying the solid (increasing the diffusion). This implies that granular particles are not in full contact, and the tensile strength is miniscule compared with the original solid before it is broken into granular particles. In static state and without lateral confining, they form a cone of a repose angle internally linked to, but smaller than, the maximum/critical friction angle (β in Panel (**a**)) when the original solid is placed on a slope composed of the same material under the same environmental conditions. As the granular particle size get finer and finer (**b**–**d**), the free repose angle first decreases and then increases. In the *right panel*, inertial number μ is plotted against particle size (r^*). This physical property is at the basis of gravity sorting as debris flows rush down a slope: the surge front is composed of large boulders and the tail is composed of finer grained granular debris. When soil moisture is involved, the van der Waals attractive forces interferes with electric double layer forces, capillary suction/repel and surface tension, composes the primary cohesion among granular particles. The repose angles for clayey soil is sigmoid (resemble dry power example showing here), whereas the sandy and silty soils peaks at ~50 % relative saturation (Godt et al. 2009; Ren et al. 2008a, b)

to 9.8 kPa, with changes in soil moisture. There also are experimental tests of root strength for a variety of species (Table 5.1). While the parameters obtained from in situ sampling are sufficient as input for slope stability models. The root strength parameters are desired for a larger regional or even global scale for 3D mechanistic models.

The wind stress and the biomass loading will further deteriorate the situation. For example, in addition to the disturbance to the upper boundary stress conditions, falling trees may join the sliding mass. Therefore, effects of roots depend on precipitation rate in specific cases and on meteorological conditions in general. The hydrological and chemical effects are not expanded upon here but for interested readers details can be found in Ren et al. (Ren and Henderson-Sellers 2006; Ren and Leslie 2011). Following are some details that are highly relevant for

"progressive bulking" type of landslides, such as the pathways by which water leaves the landscape and the erosion ability of running surface water.

Water typically leaves a landscape by one of several pathways: groundwater flow, shallow subsurface flow, or overland flow (when precipitation rate exceeds infiltration rate). The relative importance of these pathways is strongly influenced by topography, vegetation, and material properties such as the hydraulic conductivity of soils. Drainage (ground water) and shallow subsurface flow dissolve and remove ions and small particles that cement large soil particles when being dry. Overland flow (runoff, a driving factor for debris entrainment) causes erosion primarily by surface sheet wash, rills and rain splash. Runoff is strong for bared ground (e.g., arid soil-mantled landscapes) or disturbed ground (e.g., by soil animals or human construction). Runoff of 3 mm/s suffices to suspend clay and silt particles and move them downhill (Selby 1993). As water collects into gullies, its velocity, and therefore erosion potential, increases. For not-so-dense debris flow, erosion potential can be approximated as $P = C_1(gh)^{1/2}\alpha^{1/3}(D/D_0)^{0.27}$, where C_1 is a coefficient depending on vegetation condition, α is slope angle, D is particle size, and D_0 is a reference particle size, h is runoff water depth, and g is gravity acceleration. Vegetation and litter layers level the peak of runoff and increase infiltration and drainage through reducing velocity with which raindrop hit the soil, thereby preventing surface compaction, and through the interconnected channels webbed by roots and soil animals. For progressive bulking debris flows, these are apparent preventative features.

Size of a landslide has direct relevance to its ecosystem consequences. The debris flow magnitude is rarely determined by the volume of the initiating landslide (Jacob and Hungr 2005). Usually, debris flows start as small landslides and, through entrainment of material along the path to depositional area, become several orders of magnitude larger in volume. The entrainment usually takes the form of bed and bank erosion (Pierson et al. 1990). For example, the largest natural debris flow observed in Hong Kong, which was the 1990 Tsing Shan debris flow (King 1996), which transported over 20,000 m^3 of sliding material to its depositional area, started only as a small slip of 400 m^3. Entrainment processes of uniform sliding material have been extensively discussed by Jacob and Hungr (2005). In addition to bulk density of the sliding material, draining conditions are identified vital to the stability of the bed and, in the unstable case, the unstable layer depth. Entrainment's counterpart, namely deposition, usually occurs when sliding material further mixes with stream water (Pierson and Scott 1985).

It is apparent that the disturbance of landslides to ecosystem is through displacement of the fertile topsoil layer. Whether the existing vegetation can be destroyed depends on the severity of the landslide. The severity of a landslide depends on its size, velocity and material composition. The first two points are obvious. The composition of the sliding material is important for landslide destructive potential primarily because the effective size of granular material. If the debris flow entrained big boulders during its downslope movement, the destructive potential to trees and buildings will be much greater than similar debris flows containing only sand and silt. It is the efficiency of the entrainment that primarily determines the total volume

of a debris flow and its ecosystem consequences. In line with the concept of "bulking" in the terminology of Iverson (1997), the drag of debris flows to obstructions can be expressed as $\eta_{eff}\frac{\partial U}{\partial Z}$, where U is flow velocity (m/s), η_{eff} is effective dynamic viscosity (Pa s). Since η_{eff} is also a function of particle density, particle size and normal confining pressure, the drag can be expressed in a quadratic form in granular particle size and vertical flow shear, as proposed by Iverson (1997). The formulation was recently confirmed as relevant in experiments using a vertical rotating drum apparatus (Hsu et al. 2008). For a fast moving debris flows (3 m/s) and 50 % solid material sludge of about 2 m depth, the stress exerted on obstacles is of order 10^5 Pa. When a large boulder encounters an obstacle, the energy is transformed primarily in the form of longitudinal waves (similar to acoustic waves in the air). The impact pressure on the obstacle is $0.5\rho_b UV$, with V the sound wave speed in solids, and ρ_b is the boulder's density. Sound speed varies with obstacle medium. At standard pressure of 1 atm and temperature 25 °C, it is about 4,500 m/s for bridges and concrete-steel buildings. In contrast to turbid sludges, a boulder of about 2 m^2 cross-sectional area (assuming this also is the area of simultaneous contact with an obstacle), of bulk density of 2.7×10^3 kg/m^3, can exert 10^8 Pa pulse pressure, which is three orders of magnitude larger than the sludge. This explains the results of Stock and Dietrich (2006), who identified that for boulder debris flow, the coarse, fluid poor snout exerts the greatest collisional stress on the underlying bedrock, whereas the relatively fine grained tail is less important for channel wear. As landslides rush down valleys, the entrainment of loose material and, in the case of runoff flow, detrainment/deposition of the sliding material are the primary terms for total mass balance. In addition to those studies cited in Iverson (1997), recent developments are summarized in Jacob and Hungr (2005, Chapter 7) and references therein. The mechanical reinforcement from vegetation roots (Sidle 1992) will be detailed in the section on a scalable, extensible and adaptable geo-fluid model for environmental studies (SEGMENT-Landslide, Ren et al. 2008a, b).

Figure 5.4 is a conceptual sketch of storm-triggered landslides/debris flows. There is usually a large collection region, providing solid material for the downstream area. The collection region is usually two orders of magnitude larger than the channelled, streaming, concentrated flows of the dense mud. Along the flow, the sliding material becomes denser and viscosity becomes larger. At the spread region, because of the kinetic energy gain, the sliding will not cease, even the slope angle now is less than the repose angle. In actuality, it continues to spread until the speed is reduced to zero, usually at bed slopes much smaller than the stable repose angle. In Fig. 5.4, panel (a) is a "bird's eye" view of the mass collecting region, and panels (b) to (d) illustrate the life cycle of a debris flow. The solid material is a mudslide, formed by surface runoff from a much larger area than seen with the naked eye. The portion with direct ecosystem damage primarily is the region with concentrated stream flows, typically constituting only about 2 % of the entire collecting area.

The August 8 (August 7, 16UTC), 2010 Zhouqu (China) landslide is a characteristic "progressive bulking" type of debris flow (Ren 2014). On August

7, Zhouqu's Beishan slope received over 80 mm of rain within 2 h, leading to widespread shallow landslides and debris flow generation. The town of Zhouqu is built on the sloping surfaces of previous debris fans formed at the base of steep rocky hillslopes. The debris fan at the mouth of the rocky creek, Sanyanyu, is usually stable because of the elaborated root system laced through the stony, loose soil. Prior to the intense cloudbursts, there was a long period of drought in the region and the ground surface was cracked, especially the mid-slope (1,200–2,500 m elevation range). In addition to causing rock falls (providing more solid sliding material), the Wenchuan earthquake that occurred barely 2 years earlier, deepened the bedrock crevasses. Consequently, the drought stressed vegetation cover had little ability to intercept the rainfall and dampen the peak runoff. Much of the runoff water was channelled directly into the crevasses and deepened the shear zone. As the runoff water flowed down slope, it progressively increased the solid material contents (as a result of entrainment) and also its ability to further entrain. This positive feedback continues and at elevation of 2,500 m, the turbid mud can pick up large boulders of 1 m diameter. As water filled the crevasses, patches of soil layers up to 4 m were made unstable and were scoured out and descended as rock-filled creeks. The scoured area was generally still dry, and only the surface several centimeters was saturated. As it ran down the steep canyon, it further picked up debris as it travelled at ~5 m/s. By the time it reached lower, gentler slopes (~1,200 m elevation), its mass had increased by one order of magnitude, but the overall water content was still low. Some parts, the finer granular components, simply came to a halt. The coarse granular material and boulders continued their motion and demolished constructions at the mouth of the rocky creek. Subsequently, material disturbed by the slide, including wood and constructions, was washed by following slides and moved down the Sanyanyu creek, depositing debris all the way to the Bailongjiang River. This tragedy, and others in the previous rainy seasons following the Wenchuan earthquake, led to an awareness of the need to develop warning intelligence systems, compile hazard maps, and adopt legislation concerning forest practice and soil preservation, for regions on or near active faults.

In summary, a soil in its natural field environment is different from a soil sample, even taken from the same site. In practice, it is difficult to perform shear or tensile tests on rock material, and the triaxial test is preferred. In this method, the material is subjected to axial compression and to hydrostatic pressure in the perpendicular directions. By varying the hydrostatic pressure, the Mohr envelope is obtainable (usually only the section to the left of the strain axis suffices). For any one such experiment, axial loading pressure is increased gradually until specimen fails. The problem lies with the preparation of the specimen. The rock/soil usually is in the form of a finite cylinder enclosed/wrapped in a waterproof cover and subject to external hydrostatic pressure p_1 and axial load p_2, which is increased until the specimen fails. For rock sample taken out from a borehole, the original confining pressure (compares to p_2) can be deduced from its burying depth. As long as the original structure is not disturbed in the specimen preparation process, triaxial tests

give representative characteristics of cohesion and internal friction angle. During the process, elastic moduli such as Young's modulus E, Poisson's ratio ν_p, and incompressibility K are also obtainable. Soil samples usually are sieved before being wrapped into cylinder box and placed in the test machine. Roots and some organic impurities are removed for results to be more "representative." A common problem is that values of cohesion (clay soils) and repose angle (sandy soils) provided by the test are higher than reality. For example, experiments with Eutric Podzols soil (Endoskeletic, according to the FAO protocol, Allen et al. (1998) in FAO 1998, IUSS Working Group WRB 2006, Fig. S3) of Duron Valley (46° 29′37″ N, 11° 39′25″ E) of Italy indicate large over estimation of the repose angle. The primary reason for this inaccuracy likely is that the natural soil, especially topsoil, is not as regularly structured as that being sieved. There are numerous micro-crevasses/cracks that reduce the contact surfaces of the soil particles. The effect of a crack is to produce a very high concentration of stress at its edges. The crevasses can be a result of soil animal's activity, of dead roots, of a result of earthquake, or from human disturbances to the slopes. To play a significant role, the dimension of these cracks needs to be of the order of granular particle diameter, or larger. Suppose the length density of such crevasses is l, the shear box testing results need to factor in $l^{-2/3}$, based on analysis of the data collected on a site near Apennines, Italy, where landslides are quite frequent and most of them are located on deforested soils (Ren 2012, unpublished material). Very recent studies for areas in Sichuan, China (Xiang, personal communication) indicate that the power index may vary from -0.5 to -0.7, closely related to organic contents in the soil. The lower boundary envelope of the cracks usually is the sliding surface where liquefaction, the most drastic form of bed material destabilization, occurs (Sassa 1985).

For historical reason, empirical method and 2D slope stability models appeared earlier than full physics 3D dynamic models. This was not because early researchers did not have the stress–strain based landslide concept at their disposal; rather it was primarily from a more pragmatic philosophy and the limited information on mechanical property of slope material. The 3D model certainly benefited from recent advance in understanding stress fields inside granular material and the rheological properties of granular material. Almost half a century passed but the concept of "pore pressure build up enhances fluidity of granular material (making the stress fields inside granular material more hydrostatic)" is still paramount to our understanding of slope stability. This explains why the "rainfall intensity–duration" relationship, which recognizes the amount of soil moisture inside the sliding material as the first order importance factor for slope stability, so strongly shaped the landslide science. Nevertheless, we are now entering a data rich remote sensing era and time is mature to considering more complete physics in landslide models. Super computers running parallelism also make execution of such numerical models feasible. These two (i.e., developments in computation facility and remote sensing measurements) give shape and direction to contemporary landslide research.

References

Abe K, Iwamoto M (1988) Preliminary experiment on shear in soil layers with a large direct-shear apparatus. J Jpn Forest Soc 68:61–65

Allen RG, Pereira L, Raes D, Smith M (1998) Crop evapotranspiration – guidelines for computing crop water requirements, FAO Irrigation and drainage paper 56. Food and Agriculture Organization of the United Nations, Rome, Italy. ISBN 92-5-104219-5

Anderson S (2006) Impact of mineral surface area on solute fluxes at Bench Glacier, Alaska. In: Knight PG (ed) Glacier science and environmental change. Blackwell Science Ltd., Malden, MA, pp 79–81

ASTM (1985) Standard test method for classification of soils for engineering purposes. Am. Soc. for Testing and Mater., ASTM Designation D 2487-83, Annual book of ASTM standards, Sec. 4, Vol. 04.08. Soil and Rock Building Stones: Geotextiles. ASTM, West Conshohocken, PA, pp 395–408

Bagnold R (1954) Experiments on a gravity-free dispersion of large solid spheres in a Newtonian fluid under shear. Proc R Soc Lond Ser A 225(1160):49–63

Ball JT, Woodrow IE, Berry JA (1987) A model predicting stomatal conductance and its contribution to the control of photosynthesis under different environmental conditions. In: Biggins J (ed) Progress in photosynthesis research, vol 4. Martinus Nijhoff, The Netherlands, pp 221–224

Baum R, Savage W, Godt J (2002) TRIGR-a Fortran program for transient rainfall infiltration and grid-based regional slope-stability analysis. U.S. Geological Survey Open File report, 02-424

Baum R, Savage W, Godt J (2008) TRIGR-a Fortran program for transient rainfall infiltration and grid-based regional slope-stability analysis, version 2.0. US Geological Survey Open-File Report, 75 pp

Belward AS (Ed) (1996) The IGBP-DISGlobal 1 km Land CoverData Set 'DISCOVER': proposal and implementation plans. Report WP No. 13, IGBP-DIS, Stockholm, Sweden

Bertoldi G, Rigon R, Over T (2006) Impact of watershed geomorphic characteristics on the energy and water budgets. J Hydrometeorol 7(3):389–403

Bolt B, Horn W, Macdonald G, Scott R (1975) Geological hazards. Springer, New York, NY, p 328

Buol S, Southard R, Graham R, McDabiel P (2003) Soil genesis and classification, 5th edn. Iowa State Press, Blackwell, Ames, IA

Caine N (1980) The rainfall intensity-duration control of shallow landslides and debris flows. Geografisker Annaler Series A 62:23–27

Campbell CS (1990) Rapid granular flows. Annu Rev Fluid Mech 22:57–92

Cannon S, Ellen S (1985) Rainfall conditions for abundant debris avalanches. San Francisco Bay Region, California. Cal Geol 38:267–272

Casadei M, Dietrich W, Miller N (2003) Testing a model for predicting the timing and location of shallow landslide initiation in soil-mantled landscapes. Earth Surf Processes Landf 28:925–950

Chu S (1978) Infiltration during an unsteady rain. Wat Resour Res 14:461–466

Coder K (2009) Root strength & tree anchorage. University of Georgia Warnell School of Forestry & Natural Resources monograph publication WSFNR09-1, pp 63

Collins B, Sitar N (2008) Processes of coastal bluff erosion in weakly lithified sands, Pacifica, California, USA. Geomorphology 97:483–501

Cornforth D (2005) Landslides in practice: investigation, analysis, remedial/preventative options in soils. John Wiley and Sons, New York, NY

Costa JE (1984) Physical geography of debris flows. In: Costa JE, Fleisher PJ (eds) Developments and applications in geomorphology. Springer, New York, NY, pp 268–317

Crosta G (1998) Regionalization of rainfall threshold: an aid to landslide hazard evaluation. Environ Geol 35:131–145

Cruden D (1991) A simple definition of a landslide. Bull Int Assoc Eng Geol 43:27–29
Cutler P (2006) Modelling impact of glacier-permafrost interaction on subglacial water flow. In: Knight PG (ed) Glacier science and environmental change. Blackwell Science Ltd., Malden, MA, pp 67–68
Dai F, Lee C (2002) Landslides on natural terrain-Physical characteristics and susceptibility mapping in Hong Kong. Mount Res Dev 22(1):40–47
Dall'Amico M, Endrizzi S, Gruber S, Rigon R (2011) A robust and energy-conserving model of freezing variably-saturated soil. Cryosphere 5:469–484
Debano L (2000) The role of fire and soil heating on water repellency in wild land environments: a review. J Hydrol 231–232:194–206
De Blasio FV (2008) Production of frictional heat and hot vapour in a model of self-lubricating landslides. Rock Mech Rock Eng 41:219–226
Endrizzi S, Quinton W, Marsh P (2011) Modelling the spatial pattern of ground thaw in a small basin in the arctic tundra. Cryosphere Discuss 5:367–400
Eswaran H, Rice T, Ahrens R, Stewart B (eds) (2002) Soil classification: a global reference. CRC Press, Boca Raton, FL
Famiglietti J, Wood E, Sivapalan M, Thongs D (1992) A catchment scale water balance model for FIFE. J Geophys Res 97:18,997–19,007
Freeze R, Cherry J (1979) Groundwater. Prentice Hall, Englewood Cliffs, NJ
Gardner W (1958) Some steady-state solutions of unsaturated moisture flow equation with application to evaporation from a water table. Soil Sci 85:228–232
Godt J, Baum R, Chleborad A (2006) Rainfall characteristics for shallow landsliding in Seattle, Washington, USA. Earth Surf Process Landform 31:97–110
Godt J, Baum R, Lu N (2009) Landsliding in partially saturated materials. Geophysical Res Lett 36, L02403
Goguel J (1976) Geothermics. McGraw-Hill, New York, NY
Gray D, Ohashi H (1983) Mechanics of fiber reinforcement in sand. J Geotech Eng 109:335–353
Green W, Ampt G (1911) Studies on soil physics, Part I. The flow of air and water through soils. J Agricult Sci 4:1–23
Habib P (1975) Production of gaseous pore pressure during rock slides. Rock Mech Rock Eng 7:193–197
Hansen DT (2001) Defining cooperative geospatial projects between organizations. In: Hansen DT, Singhroy VH, Pierce RR, Johnson AI (eds) Spatial methods for solution of environmental and hydrologic problems: science, policy, and standardization, ASTM STP 1420. West Conshohocken, PA, American Society for Testing and Materials
Heim A (1932) Bergsturz und Menschenleben. Fretz und Wasmuth, Zurich
Henderson-Sellers A, McGuffie K, Pitman A (1996) The project for intercomparison of land-surface parameterization scheme (PILPS) 1992-1995. Climate Dyn 12:849–859
Henkel D, Skempton A (1954) A landslide at Jackfield, Shropshire, in an over-consolidated clay. Proceedings European conference on stability of earth slopes, vol 1. Stockholm, Sweden, pp 90–101
Homer C, Huang C, Yang L, Wylie B, Coan M (2004) Development of a 2001 National Landcover Database for the United States. Photogr Eng Rem Sens 70:829–840
Hong Y, Adler R (2008) Predicting landslide spatiotemporal distribution: integrating landslide susceptibility zoning techniques and real-time satellite rainfall. Sp Iss Int J Sedim Res 23 (3):249–257
Hogentogler C, Terzaghi K (1929) Interrelationship of load, road and subgrade. Pub Road 10:37–64
Hsu L, Dietrich W, Sklar L (2008) Experimental study of bedrock erosion by granular flows. J Geophys Res 113:F02001. doi:10.1029/2007JF000778
Hungr O, McDougall S, Wise M, Cullen M (2008) Magnitude–frequency relationships of debris flows and debris avalanches in relation to slope relief. Geomorphology 96:355–365
Iverson R (1997) The physics of debris flows. Rev Geophys 35:245–296

Jackson CR (1992) Hillslope infiltration and lateral downslope unsaturated flow. Wat Resour Res 28:2533–2539
Jacob M, Hungr O (2005) Introduction. In: Jacob M, Hungr O (eds) Debris flow hazards and related phenomena. Praxis-Springer, Berlin
Jarvis P (1976) The interpretation of the variation in leaf water potential and stomatal conductance found in canopies in the field. Phil Trans Roy Soc Lond B 273:593–610
Jaeger J (1969) Elasticity, fracture and flow. Methune & CO. Ltd, New Fetter Lane, London
Jewell RA (1980) Some effects of reinforcement on the mechanical behaviour of soils. PhD Thesis, University of Cambridge, Cambridge, UK, 320 p
Johnson G (1965) A model for debris flow. PhD dissertation, PA State Univ., State College
Jop P, Forterre Y, Pouliquen O (2006) A constitutive law for dense granular flows. Nature 441:727–730
Kenney C (1984) Properties and behaviours of soils relevant to slope instability. In: Prior DB, Brunsden D (eds) Slope instability. John Wiley, Chichester
King J (1996) The Tsing Shan debris flow, special project report SPR6/96. Geotechnical Engineering Office, Civil Engineering Department, Hong Kong
Lawrance C, Rickson R, Clark J (1996) The effect of grass roots on the shear strength of colluvial soils in Nepal. In: Anderson MG, Brooks SM (eds) Advances in hillslope processes. John Wiley, Chichester
Lawrence D, Slater A (2008) Incorporating organic soil into a global climate model. Climate Dyn 30:145–160
Letts M, Roulet N, Comer N, Skarupa M, Verseghy D (2000) Parametrization of Pearland hydraulic properties for the Canadian land surface scheme. Atm Ocean 38:141–160
Lu N, Godt J (2008) Infinite slope stability under unsaturated seepage conditions. Water Resour Res 44:W11404
Ma D, Qi L (1997) Study on comprehensive controlling of debris flow hazards in Sanyanyu Gully. Bull Soil Wat Conserv 17:26–31
Moody JA, Martin D (2001) Hydrologic and sedimentologic response of two burned watersheds in Colorado. USGS Water Resources Investigations Report
Montgomery D, Dietrich W (1994) A physically-based model for the topographic control on shallow landsliding. Water Resour Res 30(4):1153–1171
Montrasio L, Valentino R (2008) A model for triggering mechanisms of shallow landslides. Nat Hazard Earth Sys Sci 8:1149–1159
Morgan R, Rickson R (1995) Slope stabilization and erosion control. E and FN Spon, London
O'Loughlin E (1986) Prediction of surface saturation zones in natural catchments by topographic analysis. Water Resour Res 2(2):794–804
Okin GS, Gillette DA (2001) Distribution of vegetation in wind-dominated landscapes. Implications for wind erosion modeling and landscape processes. J Geophys Res 106:9673–9683
Okin GS, Bullard JE, Reynolds RL, Ballantine JAC, Schepanski K, Todd MC, Belnap J, Baddock MC, Gill TE, Miller ME (2011) Dust: small-scale processes with global consequences. Eos Trans AGU 92(29):241–242. doi:10.1029/2011EO290001
Pack R, Tarboton D (2004) Stability index mapping (SINMAP) applied to the prediction of shallow translational landsliding. Geophys Res Abst 6:05122
Philip J (1991) Hillslope infiltration: planar slopes. Wat Resour Res 27:109–117
Philip J (1993) Comment on "Hillslope infiltration and lateral downslope unsaturated flow" by C. R. Jackson. Wat Resour Res 29:4167
Pierson T, Janda R, Thouret J, Borrero C (1990) Perturbation and melting of snow and ice by the 13 November 1985 eruption of Nevado del Ruiz, Colombia, and consequent mobilization, flow, and deposition of lahars. J Volcanol Geotherm Res 41:17–66
Pierson T, Scott K (1985) Downstream dilution of a lahar: transition from debris flow to hyperconcentrated streamflow. Water Resour Res 21:1511–1524
Pollen N, Simon A (2005) Estimating the mechanical effects of riparian vegetation on stream bank stability using a fiber bundle model. Wat Resour Res 41:W07025. doi:10.1029/2004WR003801

Ren D (2001) Scaling issues in the calculation of surface latent and sensible heat fluxes at Blue River Basin using SHEELS model. University of Oklahoma, Norman, OK, p 86
Ren D (2004) 4DVAR retrieval of prognostic land surface model variables for ARPS. PhD Thesis, University of Oklahoma, Norman, OK, pp 236
Ren D (2014) The devastating Zhouqu Storm-triggered debris flow of August 2010: Likely causes and possible trends in a future warming climate. J Geophys Res 119:3643–3662
Ren D, Fu R, Leslie LM, Dickinson R, Xin X (2010) A storm-triggered landslide monitoring and prediction system: formulation and case study. Earth Interact 14:12. doi:10.1175/2010EI337.1
Ren D, Leslie LM, Karoly D (2008a) Mudslide risk analysis using a new constitutive relationship for granular flow. Earth Interact 12:1–16
Ren D, Leslie L, Karoly D (2008b) Greenland ice sheet response to transient climate change: consensus between two CGCMs. Geophys Res Abstr 10, EGU2008-A-12412
Ren D, Leslie L, Karoly D (2007) Sensitivity of an ecological model to soil moisture simulations from two different hydrological models. Meteorol Atm Phys 100:87–99
Ren D, Wang J, Fu R, Karoly D, Hong Y, Leslie LM, Fu C, Huang G (2009) Mudslide caused ecosystem degradation following Wenchuan earthquake 2008. Geophys Res Lett 36, doi:10.1029/2008GL036702
Ren D, Leslie L, Fu R, Dickinson R (2011a) Predicting storm-triggered landslides and ecological consequences. Bull Am Meteorol Soc 92:129–139. doi: 10.1175/2010BAMS3017.1
Ren D, Fu R, Leslie LM, Karoly DJ, Chen J, Wilson C (2011b) A multirheology ice model: formulation and application to the Greenland ice sheet. J Geophys Res 116:D05112. doi:10.1029/2010JD014855
Ren D, Leslie L (2011) Three positive feedback mechanisms for ice sheet melting in a warming climate. J Glaciol 57:206
Ren D, Fu R, Leslie LM, Dickinson R (2011c) Modeling the mudslide aftermath of the 2007 southern California wildfires. J Nat Hazard 57:327. doi:10.1007/s11069-010-9615-5
Ren D, Henderson-Sellers A (2006) An analytical hydrological model and its implication in scaling issues for land surface modeling. J Earth Interact 10(20):1–24
Ren D, Xue M, Henderson-Sellers A (2004) The effects of hydraulic lift in simulating superficial soil moisture for vegetated surfaces under dry conditions. J Hydrometeorol 5:1181–1191
Ren D, Xue M (2004) An improved force-restore model for land-surface modeling. J Appl Meteorol 43:1768–1782
Ren D (2006) A modified Richards' equation, its adjoint, and a new perspective on land data assimilation. Meteorog Atmos Phys 92:25–32
Ren D (2001) Scaling issues in the calculation of surface latent and sensible heat fluxes at Blue River Basin using SHEELS model. MS Thesis. University of Oklahoma, Norman, Oklahoma, 236 pp
Ren D, Leslie L, Lynch MJ, Duan Q, Dai Y, Shangguan W (2013) Why was the August 2010 Zhouqu landslide so powerful? Geography, Environment Sustainability 1:67–79
Riestenberg M (1994) Anchoring of thin alluvium on hill slopes by roots of sugar maple and white ash. Landslides in the Cincinnati area. USGS, Bulletin 2059E
Rigon R, Bertoldi G, Over T (2006) GEOtop: a distributed hydrological model with coupled water and energy budgets. J Hydrometeorol 7:371–388
Rui X (2004) Theory of hydrology, vol 386. Waterpub, Beijing, pp 90–91
Sassa K (1985) The mechanism of debris flows. Proceedings, XI international conference on soil mechanics and foundation engineering, San Francisco, CA, USA, 12-16 August, vol. 1, pp 1173–1176
Schofield A, Telford T (2006) Disturbed soil properties and geotechnical design. Thomas Telford Publishing, London. ISBN 0-7277-2982-9
Schmidt K, Roering J, Stock JD, Dietrich W, Montgomery D, Schaub T (2001) The variability of root cohesion as an influence on shallow landslide susceptibility in the Oregan Coast Range. Can Geotech J 38:995–1024

Selby M (1993) Hillslope materials and processes, 2nd edn. Oxford University Press, New York, NY, 451 pp
Shao Y, Henderson-Sellers A (1996) Validation of soil moisture simulation in land surface parameterization scheme with HAPEX data. Global Planet Change 13(1):11–46
Sidle R, Pearce A, O'Loughlin C (1985) Hillslope stability and land use. American Geophysical Union, Washington, DC
Sidle R, Ochiai H (2006) Landslides: process, prediction, and land use. AGU, Washington, DC
Sidle R (1992) A theoretical model of the effects of timber harvesting on slope stability. Water Resour Res 28:1897–1910
Simoni S, Zanotti F, Bertoldi G, Rigon R (2008) Modelling the probability of occurrence of shallow landslides and channelized debris flows using GEOtop-FS. Hydrolog Process 22(4):532–545
Sinai G, Dirksen C (2006) Experimental evidence of lateral flow in unsaturated homogeneous isotropic sloping soil due to rainfall. Wat Resour Res 42:W12402
Sirangelo B, Versace P (1996) A real time forecasting model for landslides triggered by rainfall. Meccanica 31:73–85
Sitar N, Clough G (1983) Seismic response of steep slopes in cemented soils. J Geotech Eng 109:210–227
Smith R, Smettem K, Broadbridge P, Woolhiser D (2002) Infiltration theory for hydrologic applications, Water resources monograph, 15. American Geophysical Union, Washington, DC
Smith J, Schneider S, Oppenheimer M, Yohe G, Hare W, Mastrandrea M, Patwardhan A, Burton I, Corfee-Morlot J, Magadza C, Füssel H, Pittock A, Rahman A, Suarez A, van Ypersele J (2009) Assessing dangerous climate change through an update of the Intergovernmental Panel on Climate Change (IPCC) "reasons for concern". Proc Natl Acad Sci 106:4133
Soil Survey Division Staff (1993) Soil survey manual, UDSA Handb. No. 18. GPO, Washington, DC
Srivastava R, Yeh T-C (1991) Analytical solutions for one-dimensional, transient infiltration toward the water table in homogeneous and layered soils. Wat Res Res 27:753–762
SRTM, http://www2.jpl.nasa.gov/srtm/
Stock JD, Dietrich WE (2006) Erosion of steepland valleys by debris flows. GSA Bull 118(9/10):1125–1148
STATSGO, http://water.usgs.gov/GIS/metadata/usgswrd/XML/ussoils.xml
Takahashi T (1978) Mechanical characteristics of debris flow. J Hydraulic Div 104(8):1153–1169
Tegzes P, Vicsek T, Schiffer P (2002) Avlanche dynamics in wet granular materials. Phys Rev Lett 89:094301
TMBA, http://trmm.gsfc.nasa.gov/publications_dir/potential_flood_hydro.html
Townsend F, Gilbert P (1973) Tests to measure residual strengths of some clay shales. Geotechnique 23:267–271
van Asch T, Buma J, Van Beek L (1999) A review on some hydrological triggering systems in landslides. Geomorphology 30:25–32
Waldron L (1977) The shear resistance of root-permeated homogeneous and stratified soil. J Soil Sci Soc Am 41:843–849
Waldron L, Dakessian S (1981) Soil reinforcement by roots: calculation of increased soil shear resistance from root properties. Soil Sci 132:427–435
Wallace JM, Hobbs PV (2006) Atmospheric science: an introductory survey, 2nd edn. Elsevier, Inc., Oxford, UK, 483 pp
Wu W, Sidle R (1995) A distributed slope stability model for steep forested basins. Water Resour Res 31:2079–2110
Wu T, McKinnell W, Swanton D (1979) Strength of tree roots and landslides on Prince of Wales Island, Alaska. Can Geotech J 16:19–33
Wu T, Watson A (1998) In situ shear tests of soil blocks with roots. Can Geotech J 35:4, ProQuest Science Journals, pg. 579

Yano K, Daido A (1965) Fundamental study on mud-flow. Bull Disast Prev Res Inst Kyoto Univ 14:69–83

Zanotti F, Endrizzi S, Bertoldi G, Rigon R (2004) The GEOTOP snow module. Hydrolog Process 18:3667–3679. doi:10.1002/hyp.5794

Zhang X, Kondragunta S (2006) Estimating forest biomass in the USA using generalized allometric models and MODIS land products. Geophys Res Lett 33:L09402. doi:10.1029/2006GL025879

Ziemer R (1981) Roots and the stability of forested slopes. IAHS Pub 132:343–361

Chapter 6
SEGMENT-Landslide and Applications to Various Climatic Zones

Different landslide models implement the master equations (Eqs. 5.11–5.15) differently. Following is SEGMENT-Landslide's implementation and stress decomposition. In SEGMENT, the momentum equations are prototyped in the rotating earth reference system (Fig. 6.1). The numerical model is a discretized representation of the governing partial differential equations. The equations are in generalized curvilinear coordinates. In discretizing the model horizontal domain, SEGMENT-Landslide takes the Earth's curvature into consideration. The horizontal grid is a regular latitude (λ)–longitude (θ) grid. Uneven spacing in latitude/longitude allows higher resolution for marginal areas. The governing equations are, in spherical coordinates:

$$\begin{cases} \dfrac{\partial u}{\partial t}+\dfrac{u}{r\cos\lambda}\dfrac{\partial u}{\partial \theta}+\dfrac{V}{r}\dfrac{\partial u}{\partial \lambda}+w\dfrac{\partial u}{\partial r}-\dfrac{tg\lambda}{r}uV+\dfrac{uw}{r} \\ \quad =\dfrac{1}{R\cos\lambda}\dfrac{\partial \Re_{\theta\theta}}{\partial \theta}+\dfrac{1}{R}\dfrac{\partial \Re_{\theta\lambda}}{\partial \lambda}+\dfrac{1}{R^2\cos\lambda}\dfrac{\partial \Re_{\theta r}}{\partial r}-\dfrac{g}{r\cos\lambda}\dfrac{\partial r}{\partial \theta} \qquad (6.1) \\ \dfrac{\partial V}{\partial t}+\dfrac{u}{r\cos\lambda}\dfrac{\partial V}{\partial \theta}+\dfrac{V}{r}\dfrac{\partial V}{\partial \lambda}+w\dfrac{\partial V}{\partial r}+\dfrac{tg\lambda}{r}u^2+\dfrac{Vw}{r} \\ \quad =\dfrac{1}{R\cos\lambda}\dfrac{\partial \Re_{\lambda\theta}}{\partial \theta}+\dfrac{1}{R}\dfrac{\partial \Re_{\lambda\lambda}}{\partial \lambda}+\dfrac{1}{R^2\cos\lambda}\dfrac{\partial \Re_{\lambda r}}{\partial r}-\dfrac{g}{r}\dfrac{\partial r}{\partial \lambda} \qquad (6.2) \\ \dfrac{\partial w}{\partial t}+\dfrac{u}{r\cos\lambda}\dfrac{\partial w}{\partial \theta}+\dfrac{V}{r}\dfrac{\partial w}{\partial \lambda}+w\dfrac{\partial w}{\partial r}+\dfrac{tg\lambda}{r}u^2-\dfrac{u^2}{r}-\dfrac{V^2}{r} \\ \quad =\dfrac{1}{R\cos\lambda}\dfrac{\partial \Re_{r\theta}}{\partial \theta}+\dfrac{1}{R}\dfrac{\partial \Re_{r\lambda}}{\partial \lambda}+\dfrac{1}{R^2\cos\lambda}\dfrac{\partial \Re_{rr}}{\partial r} \qquad (6.3) \end{cases}$$

© Springer International Publishing Switzerland 2015

D. Ren, *Storm-triggered Landslides in Warmer Climates*,
DOI 10.1007/978-3-319-08518-0_6

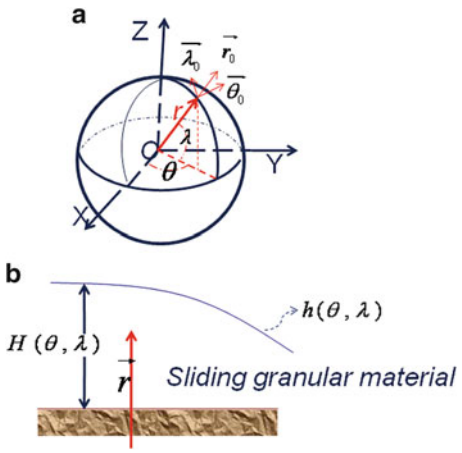

Fig. 6.1 The general curvilinear system in SEGMENT-Ice. (**a**) the spherical rotating earth reference system, and (**b**) the terrain-following sigma coordinate system transfer. Operations resulted from general curvilinear system: $x = r\cos\lambda\cos\theta$; $y = r\cos\lambda\sin\theta$; $z = r\sin\lambda$. Consequently, the first order derivatives (Jacobians) involves the following Lame operations: $H_r = 1$; $H_\lambda = r$; $H_\theta = r\cos\lambda$ $\frac{\partial\vec{\theta_0}}{\partial\theta} = \sin\lambda\,\vec{\lambda_0}$; $\frac{\partial\vec{\lambda_0}}{\partial\lambda} = -\vec{r_0}$; $\frac{\partial\vec{r_0}}{\partial\lambda} = \vec{\lambda_0}$; $\frac{\partial\vec{r_0}}{\partial\theta} = \cos\lambda\ \vec{\theta_0}$; $\frac{\partial\vec{\lambda_0}}{\partial\theta} = -\sin\lambda\ \vec{\theta_0}$. The viscous term (Laplacian) involves the second order derivatives (Hessians) as in Eq. (6.4). Operations resulted from vertical terrain following system (sigma–coordinate) are as in Eqs. (6.6)–(6.11)

where t is time, R is the Earth's radius, θ is longitude, λ is latitude, u and V are the horizontal velocity components and w is the vertical velocity component. In Fig. 6.1, variable r is the distance from the point of interest to the Earth's center. Here, R is much larger than the granular material thickness, so r can be replaced by R. Stress decomposition into resistive ($\Re$) and lithostatic ($L = -\rho g(h-r)$) stresses follows van der Veen and Whillans (1989). Unit vectors are indicated by the superscript "0" in Fig. 6.1a. The right hand side of Eqs. (6.1)–(6.3), when expanded, involves viscous terms in the form of vector Laplacians in the spherical coordinate system. When expanded, using Eq. (6.1) as an example, it becomes:

$$\frac{1}{R^2\cos^2\lambda}\frac{\partial^2 u}{\partial^2\theta} - \frac{2\sin\lambda}{R^2\cos^2\lambda}\frac{\partial v}{\partial\theta} + \frac{2}{R^2\cos\lambda}\frac{\partial w}{\partial\theta} - \frac{tg^2\lambda}{R^2}u - \frac{1}{R^2}u + \frac{1}{R^2}\frac{\partial^2 u}{\partial\lambda^2} - \frac{tg\lambda}{R^2}\frac{\partial u}{\partial\lambda} + \frac{\partial^2 w}{\partial r^2} + \frac{2}{R}\frac{\partial w}{\partial r} \tag{6.4}$$

In practice, the calculation domain contains only the media of interest (e.g., sliding material, or at most limited additional domains that contain the sliding material). The terrain-following sigma coordinate system, s, (Fig. 6.1b), is:

$$s = \frac{h - r}{H} \tag{6.5}$$

where h is the distance from the ice surface to the Earth's center and H is the local ice thickness. In SEGMENT-Ice, discretization of the vertical coordinate has irregular spacing, as flow vertical shear is greatest near the bottom, while temperature fluctuations are larger near the ice's upper surface interface between ice and air. Levels are spaced most closely near the surface and the base of the ice sheet.

The Jacobian involved for transferring between two coordinates is, for any function F:

$$\left(\frac{\partial F}{\partial \theta}\right)_{s,\lambda} = \left(\frac{\partial F}{\partial \theta}\right)_{r,\lambda} - \frac{1}{H}\left(\frac{\partial F}{\partial s}\right)_{\theta,\lambda} \Delta s_\theta \tag{6.6}$$

$$\left(\frac{\partial F}{\partial \lambda}\right)_{s,\theta} = \left(\frac{\partial F}{\partial \lambda}\right)_{r,\theta} - \frac{1}{H}\left(\frac{\partial F}{\partial s}\right)_{\theta,\lambda} \Delta s_\lambda \tag{6.7}$$

$$\left(\frac{\partial F}{\partial s}\right)_{\theta,\lambda} = -H\left(\frac{\partial F}{\partial r}\right)_{\theta,\lambda} \tag{6.8}$$

Here, Δs_θ is short-hand for the r-contour's slope in θ direction, and similarly Δs_λ is the slope of r-contour surface in the λ direction. In the new, general curvilinear coordinate system, they are:

$$\Delta s_\theta = \left(\frac{\partial h}{\partial \theta}\right)_\lambda - s\left(\frac{\partial H}{\partial \theta}\right)_\lambda \tag{6.9}$$

$$\Delta s_\lambda = \left(\frac{\partial h}{\partial \lambda}\right)_\theta - s\left(\frac{\partial H}{\partial \lambda}\right)_\theta \tag{6.10}$$

The transfer Hessian terms (second order derivatives) can be similarly defined. For example,

$$\left(\frac{\partial^2 F}{\partial \lambda \partial r}\right) = -\frac{\partial}{\partial \lambda}\left(\frac{1}{H}\frac{\partial F}{\partial S}\right) - \frac{\Delta s_\lambda}{H^2}\left(\frac{\partial^2 F}{\partial s^2}\right) \tag{6.11}$$

The deviatoric stress ($\mathfrak{R}_d$) is related to strain rate by a rheological relationship (Eq. 5.13). The strain rate, in turn, is calculated from the first order derivatives of velocity. Thus, Eqs. (6.1)–(6.3) have second order derivatives. The Hessian terms (Eq. 6.11) come into play when making generalized coordinate transform. Five options are available for the lateral boundary conditions in SEGMENT-Landslide: Wall (mirror) boundary conditions; periodic boundary conditions; zero-normal gradient conditions; radiative boundary conditions; and specified boundary conditions. Advantage of using the general curvilinear coordinate system will be clearly

shown for its application to large regional areas, for example the West Antarctic Ice Sheet's disintegration and following landslides on sea level rise.

By implementing 3D dynamics and the known soil physics/chemistry (Eqs. 5.11–5.15), SEGMENT-Landslide is a recently developed and thoroughly tested mechanistic, process-based modeling system for monitoring and predicting storm-triggered landslides and their ecosystem implications. It is a tool for investigating the roles of triggering factors in sliding, and offers a unique opportunity for regional scale assessment.

In SEGMENT-Landslide, landslides are simulated using a full 3D Navier–Stokes solver. This is necessary because, as a mechanism for releasing unevenly concentrated stress, landslide occurrence at a specific location affects the stability of adjacent areas. "Legacy effects" (Casadei et al. 2003) is one example. While tending to miss landslides without a historical precedent, many empirical and theoretical procedures at present tend to over-predict the area that may fail in a given rainstorm (Casadei et al. 2003; Wooten et al. 2008; Hong and Liao 2010, personal communication). The over-estimation tendency occurs because many empirical models employ indices based on historical events. However, the occurrence of a slide, by releasing the stress buildup, makes the surrounding area more stable and less likely to experience future sliding.

There are situations when previous landslides do assist subsequent landslides. Individual landslides transform limited amounts of potential energy into heat (Eq. 5.15). Sliding can cause intense heating inside the material, especially near the bottom. This can be a positive feedback mechanism that accelerates sliding, by further reducing the shear band of loose granular media material strength. In the case of earthquakes, the heat released by thousands of simultaneous landslides is significant enough to interact with local convective processes. The intense storms that follow may cause widespread landslides in the same area. It was illustrated well by the Wenchuan earthquake, which induced over 5,000 landslides and ~3,600 rock falls. The massive amount of potential energy was transferred into heat and enhanced local convection. The following storms incurred ~358 debris flows, resulted in a direct economic loss of near $US60 billion. SEGMENT-Landslide thus simultaneously solves the thermal equation, the dynamic equations, and the surface kinematic (continuity) equations.

SEGMENT-Landslide, because it synthetically simulates landslides over a continuous regional area, can, in principle, minimize the false-alarm tendency of most empirical procedures. Against the 2007 wild fire-burn background, using the observed precipitation, SEGMENT-Landslide simulated the landslide cases during year 2008 for a region with documented landslides (Ren et al. 2010a; 2011). Inserting the landslide model component into a scalable and extensible system (SEGMENT, Fig. 5.6) also makes implementation of newly identified physical processes more convenient. This advantage is apparent in a recent simulation of Zhouqu landslides, where SEGMENT satisfactorily demonstrated why rainfall intensity is such a critical factor affecting slope stability for cracked slopes.

According to Iverson (1997), SEGMENT-Landslide belongs to the hydraulic modeling of debris flows. It is a state-of-the-science, full 3D model of landslides in that it fully implements the momentum, mass and energy differential equations. The vertical layer division makes it possible to implement soil and vegetation profile properties, required by its hydrological scheme, entrainment scheme, and the ecosystem scheme. Precipitation can be realistically proportioned into runoff and infiltration into different soil depths to increase soil moisture. Soil moisture information is parameterized in the rheological properties of granular material, so are reinforcement effects of live vegetation roots. Figure 5.6 is a diagram showing the SEGMENT-Landslide being used to investigate environmental issues.

6.1 SEGMENT-Landslide's Application to Two Theoretical Questions

Factors that complicate landslide research in real situations are intricate lateral and bottom boundary conditions and heterogeneous sliding material. For any dynamic model, the example of an idealized slope and uniform sliding material is a necessary test case. The easiest case is to assume a finite source of sliding material resting on a uniform slope. Based on this setting, the effects are added of nonuniform sliding material and more sophisticated boundary conditions. The following idealized cases illustrate the underlying physics of landslides: gravity sedimentation and the potential energy minimization principle.

6.1.1 Uniform Sliding Material

Suppose we have a lump of dry sand of dimension 8 (depth) $\times$ 24 (wide) $\times$ 55 m (length) resting on a slope of 30° composed of exactly the same type of material (sand of 1 mm diameter, 2.7×10^3 kg/m^3 density and 35° dry repose angle). Because the 30° slope angle is smaller than the dry repose angle, the slope itself is stable when dry. The slope is of infinite width and sufficient length so that this lump of sand, after sliding, will rest on the slope. In the numerical setting, there is an assumed slope length of 2,400 m, and a width of 500 m. For this finite source, uniform slope case, numerical simulations indicate that the sliding material will stop at mid-slope (Fig. 6.2, upper panel) after travelling only about 120 m. It spreads into a "fan" shaped area with only one convex lobe. The contour lines are simulated sliding material depth (m). The lateral spreading is almost perfectly confined by two straight lines with an angle of ~70°, close to the theoretical value for cohesion-less dry granular material. Along the centerline of the "mini" alluvial fan, however, because of the kinetic energy gained from the release of potential energy, the slope angle of the tail end section is less than the dry repose angle

(only ~5°). However, the slope of the head section is close to the dry repose angle. Although the spreading area resembles an equilateral triangle in a plane view, the mass of the sliding material is distributed primarily in the bowed head sector, as indicated by the contour lines of thickness (red lines in upper panel of Fig. 6.2).

6.1.2 Mixing of Two Types of Granular Material

Now assume the same configuration, but with the sliding material changed into sand mixed with pebbles (particle density is similar to sands but bulk density is smaller, about 2×10^3 kg/m^3, because of the larger void space). As expected from Fig. 5.8 (right panel), the pebble has slightly smaller dry repose angle than the sand but still is larger than the slope angle (30°). Model simulations indicate that, if pebbles were used in the same experiment, the lateral spreading will be narrower but longer in the centerline direction (i.e., more elongated). It stops at a greater distance than the case with sand as sliding material. To quantify mixing of two granular materials, mixing ratio m is defined as m weight of pebbles mixing with $(1 - m)$ weight of sand to obtain a unit weight of mixture. Volumetric mixing ratio is not used because, as sand can enter the space between pebbles, the mixture's volume is less than the total volume of the two components before mixing. Figure 6.2, lower right panel, is a schematic representation for the case of $m = 0.5$. SEGMENT-Landslide does not trace single particles. It regularly updates the components within a vertical profile of a grid point (the value of m). The location of $m = 0.5$ is shown as the interface in the sliding material. Upon stopping, the two components are not distinctively separated, as intuitively might be expected from their respective sliding experiments. This is because the inter-pebble sand retards the forward moving of pebbles. Or put in another word, pebble motion enhances sand motion. The interface between the two is not clear cut ($m = 1$ on one side and $m = 0$ another side), but slanted toward sandy side. Interestingly, the depositing of the sliding material is correlated with m (more vertical as m increases) but in a nonlinear manner.

Natural landslides seldom occur on indefinitely wide flat slopes. Usually valley banks laterally confine them. Sliding material will deposit more longitudinally and slide farther before stopping. In reality, sliding material is a mixture of more than two components. Usually there lacks clear boundaries. The rule of thumb is that coarser material resides in the head sector and finer material with larger repose angle resides in the tail sector of the deposits. Sedimentation is an issue with debris flow because it is as important as entrainment. Unfortunately, our understanding is not yet complete so far and more research is needed on this aspect. In SEGMENT-Landslide, one grid allows only two types of particle and the sedimentation is parameterized as depending on particle relative size and respective density, and on the mixture's viscosity. Various realistic boundary conditions are supported in SEGMENT-Landslide and multi-rheology for the sliding material components also is allowed.

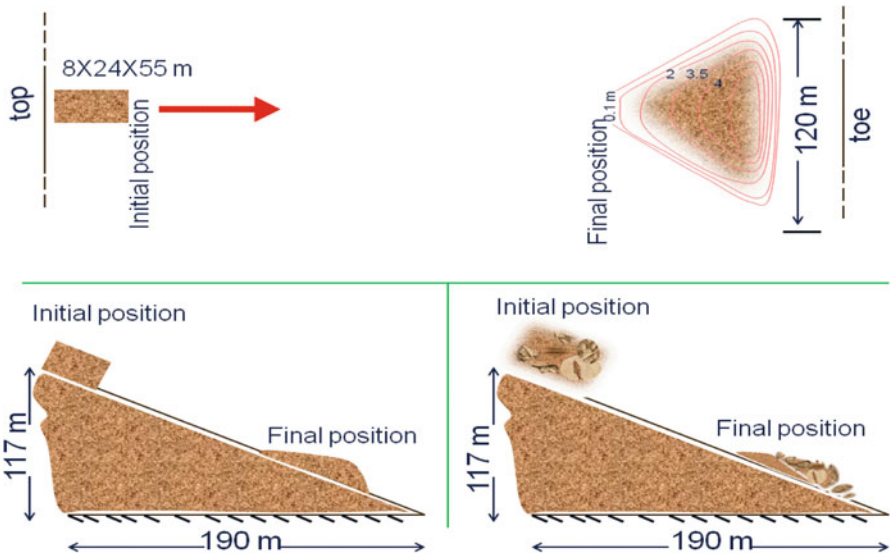

Fig. 6.2 Idealized infinitely wide uniform slope experiments. *Upper panel* is a plane view (left end is slope top). Sliding spread area is labeled with SEGMENT-Landslide simulated thickness of sands (1.5 mm average diameter). *Lower left panel* is a schematic cross section along the center line (*red arrow* on the *upper panel*). When sliding ceases (in this case at mid-slope), most sliding material has slope angles less than the dry repose angle. Only the front part is close to the repose angle, due primarily to the momentum it possessed before stopping. The case with mixed pebbles and sand is qualitatively similar to what is seen here, except for the gravity sedimentation effects (*lower right panel*), which produce a head section with more coarse granular material (in this case pebbles of effective diameter 1 cm). Finer granular material, in this case sand, falls behind and below the pebbles

In this set of dry sliding material experiments, sliding material stops mid-slope, as the slope angle is less than the dry repose angle. The sliding material parked mid-slope can be fuel for a future, larger scale slide when conditions are mature, usually when there are significant changes in soil moisture conditions. For example, when saturated by rainstorms, further movement is possible. This situation is common for debris flows in reality, which will be detailed in the Zhouqu case study below in Sect. 6.3.

As mentioned, in reality landslides usually are triggered by changes in hydrogen bonds. Effects of soil moisture content on soil rheological properties are discussed in Ren et al. (2008). In summary, for sandy soil, the repose angles first increase and then decrease as soil moisture approaches saturation. For most clay soils, it steady decreases with increasing soil moisture. Soils are different not only in particle size but, more importantly, in chemical components. For same chemical component, the finer the particle size, the more sensitive are its rheological properties are to soil moisture content. These are the underlying reasons why during alluvial fan formation, rainfall plays a decisive role. For dry granular material, pebbles and boulders

have lower repose angles and run out farther than fine particles, forming natural "dams" for the latter. When saturated by rainfall, the situation reverses because boulder/pebble repose angles are not as sensitive as fine-particles to soil moisture content. Fine particles then pass through the space between boulders and lead the way in running further down slope or spread ahead of the coarser pebbles and boulders on hill toe or valley bottoms (wherever the slope reverses or significantly reduces). Thus, storm-triggered landslides/debris flows are very effective at producing alluvial fans.

A case study is now discussed of a landslide triggered by thawing of frozen soil versus being saturated by heavy storms (figures not shown), with the configuration of infinite wide uniform slope and the same sliding material as previous experiment with sands mixing with pebbles. Note that the start position of the sliding material is the end position of the dry experiments. For the frozen soil case, it is supposed that the initial temperature of the sliding material is −5 °C and the material is frozen to the bedrock. The ambient air temperature is 2 °C and warming is in the form of sensible heat flux, as diagnosed by the land surface scheme in SEGMENT-Landslide. There is no evaporation so the medium is always saturated. The layer near the upper surface thaws and slides first. The exposed layer thaws and this pattern continues down to the bottom layer. In the case of storm-triggered landslides, it is assumed that the shearing zone (sliding surface) is the interface between the sliding material and the bed, which is stable during the entire rainfall process. Neglecting the rainfall's impact and the Horton overland flow, the spreading patterns of the two are very similar, despite the very different times needed to complete the sliding-stop process. In this case, it is assumed that thawing of the frozen soil provides enough water to saturate the sliding material. In reality, this usually is not the case. Thus, in general, storm-triggered landslides run faster and farther from the source region and spread in a more elongated pattern. If evaporation from the frozen material is allowed, by assuming a 2 m/s ambient wind and 14 g/kg ambient vapor mixing ratio (Fig. 6.3), the material distribution is quite different between these two cases. The runout depositional area for the storm triggered sliding covers a larger area and the maximum depth of the material is much smaller. The parking region is also farther away from the source region than the case with thawing of frozen soil, which is a slow process that gives enough time to deplete its soil moisture and increase the viscosity.

A slightly more sophisticated case is that the entire slope (340 m) is covered by sliding material of uniform depth (1 m). The slope transforms into flat ground at the toe. Suppose the flat ground is composed of the same material as the slope bed. The sliding material is of limited width (50 m). The slope angle (24°) is larger than the granular dry repose angle (22.5°). The sliding material is hold at the initial configuration (Fig. 6.4) and suddenly the imaginary cover is removed and the sliding material is free to flow in all directions (primarily down slope). Figure 6.4 is SEGMENT-Landslide simulated evolution of the sliding material thickness profiles at regular intervals (5–10 s) after the commencement of sliding (t = 0 s). At the early stage, there are dynamic mass build up at the leading front section, due primarily to the higher resistance when sliding on flat ground and the slow down

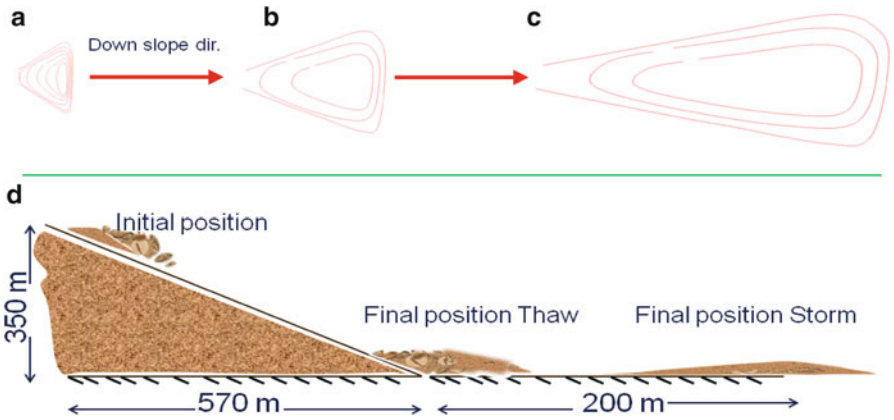

Fig. 6.3 Differences in depositional areas between storm-triggering and thaw-triggering of debris flow. Panel (**a**) shows the initial configuration of the sliding material, if the sliding material is initially saturated and frozen to the bedrock. The depositional area of sliding material under a natural thawing process with evaporation is in (**b**), and saturated by a rainstorm in panel (**c**). *Red arrows* show the down slope direction. Contour lines are sliding material thicknesses. The outermost contour is 0.1 m. Panel (**a**) is as in the *upper panel* of Fig. 6.2. Panel (**b**) shows the 1.0 and 1.5 m contours and panel (**c**) shows the 0.5 and 1.0 m contours. *Bottom panel* (**d**) is a schematic of vertical cross-sectional view. With the assistance from water, finer grained material runs faster down slope and at the depositional area, usually spread ahead of the coarse components. If the sliding material is at the point of slope change (toe), as in the frozen soil thaw case, future runoff water entrainment helps to further sort the particles and forms fertile alluvial fans that leave coarser components behind

due to the diminishing of the driving stress once leave the slope. Thus, there are mass convergence for the front section of the sliding material and thinning of the rear section. The peak value of the thickest is about 3.5 m (along the center line), achieved at ~10 s at a location ~60 m above the toe. The first 20 s of the sliding is steady acceleration (see the steady thinning of the tail section) and the sliding material achieves a maximum speed of 35 m/s. While the sliding material keeps moving forward after leaving the slope, the moving speed slows down quickly. The trailing granular particles become obstacles of the following/trailing particles. Thus the forward sloping is gentler than the backward sloping. This tendency starts at around 25 s (c.f. profiles of 25 and 35 s and note the front advancing is slower than the trailing tails advancing). This vividly illustrates that the granular motion is a multi-body interaction, a concept that will be further discussed in Appendix A. The sliding material stops at a profile to the rightmost (after about 1 min). The center (maximum sliding material thickness) is just <500 m away from the toe of the slope. As sliding material also spread sidewise so the area under the curves steadily decreases but at the tempering rate (e.g., the maximum depth is ~0.27 m when stops). Due to the conversion of potential energy into kinetic energy, sloping in all directions are significantly less than the dry repose angle, especially the forward sloping. Difference in potential energy of the initial

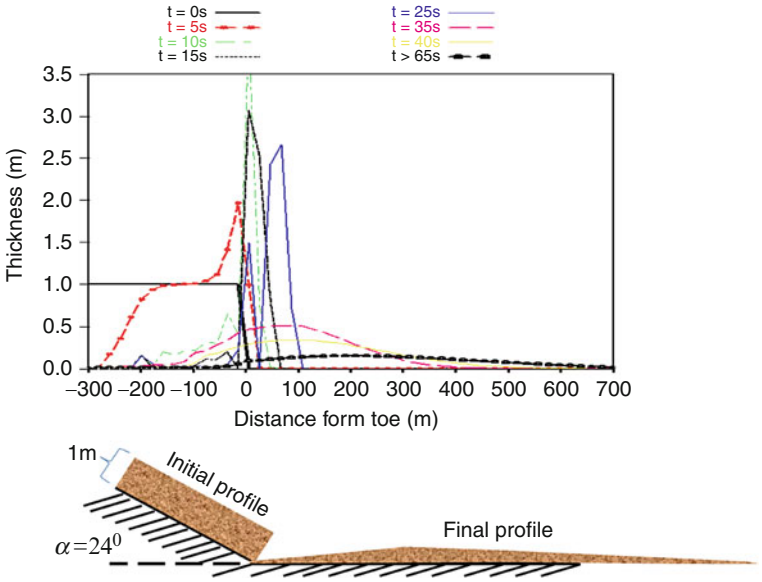

Fig. 6.4 SEGMENT-Landslide simulated complete slide-stop cycle when slope transforms from 24° into flat ground. *Lines* are evolution of sliding material thicknesses along the center line of the sliding material, which initially assume the geometry of a cube of 420 m × 50 m × 1 m and is hold in still by an imaginary cover. The imaginary cover is lifted at time zero. Changes in the sliding material thickness (rather than showing the entire slope) are shown because sliding material is merely a thin layer (1 m in this case) spreading on a hundreds meter tall slope. If the entire run of the slope is plotted, it is hard to discern the thickness change. *Lower panel* schematically show the initial and final configurations of the sliding material. Sliding material in this case has a dry repose angle of 22.5°. From this experiment, it is clear that granular material sliding is a multiple-body motion (further discussed in Appendix A) and the leading particles, when stop, become obstacles for the following ones. This results in an asymmetric sloping for the forward and backward facings of the deposit (forward direction has a gentler sloping than the backward face, as illustrated in the final profile)

and final configuration is dissipated into heat during the process. Reasonably simulating the entire life cycle of the sliding material is a prerequisite for a dynamic landslide model. SEGMENT-Landslide is robust in this aspect. In addition, we also performed experiments try to mimic the situation of sliding material move in creek tunnels and other more sophisticated lateral boundary conditions and satisfactory results are obtained.

Over 70 % of landslides are reactivation of previous landslides. Smaller landslide and rock falls that stopped mid-slope (illustrative animation available by request) provide material for future, larger and more destructive storm-triggered debris flows (as the case with Zhouqu 2010 debris flows to be discussed in Sect. 6.3). The above discussions are idealized situations to test the physics in SEGMENT-Landslide. The following is a real case application of SEGMENT-Landslide to a disastrous debris flow.

6.2 Comparison of a Slope Model and Two Full 3D Dynamics Models for the Yangjiashan Landslide

While 2D slope stability models may be equally valid in answering "where" and "when" of most shallow landslides, they may have difficulty in handling the "progressive bulking" type of loose debris flows. In "progressive bulking" type of debris flows, there usually is a widespread upstream collecting area, where infiltration excess surface runoff entrains debris and carry them to creeks/valleys. Then the accumulated material slides down as visible debris flows. For the upstream collecting area, the slope safety factors usually are larger than unity ($S > 1$). In another word, slope stability model is more suitable for the case where sliding material is locally scooped out from the residing slope, where as the full 3D model can handle the case where the sliding material is transported from elsewhere. In the following example, another shortcoming of slope stability model is present: no ability to transfer boundary information to interior grids.

SEGMENT-landslide uses the data typically required by a sophisticated land surface scheme. In addition to a surface elevation map and bedrock topography, the model also requires as input various geomechanical parameters such as cohesion, angle of repose (dry), density, porosity, field capacity, and saturated hydraulic conductivity. SEGMENT-landslide also requires a vegetation weight mask and a root distribution profile. Detailed geological surveys are conducted only for areas with important infrastructure in danger of destruction by natural hazards. Fortunately, we have access to one such geological dataset for a small region along the Qingjiang River, a tributary of the Changjiang River. The Yangjiashan creeping slope (YC) in China, is located at 29°50′ N and 109°14′ E (see Fig. 6.5). In addition to a recently detailed geological map, we also performed an engineering study of the soil and rock profiles from bore-hole drilling, extracting soil samples for laboratory testing (Table 6.1), and continuous displacement measurements within the creeping zone. The shear strengths of the various materials present in the region also have been obtained. Both drained and non-drained shearing tests are carried out on the soil specimens (Table 6.1). In addition to recovering creeping zone rock and fluid for laboratory analyses, intensive down-hole geophysical measurements and long-term monitoring provided the following information: the composition and geomechanical properties of active creeping zone rocks; the nature of the stresses responsible for sliding; and the role of pressurized water in controlling landslides recurrence, for field conditions with a wide dynamic range. Displacement surveys have been carried out continuously since July 2007, using the RST-IC3500 digital inclinometer. Displacement data from five boreholes (see Fig. 6.5, BH6-9) are analyzed in this study. The boreholes are labeled BH6, BH7, BH8, BH8-1, and BH9. Using YC as test bed, we run SEGMENT-Landslide, FLAC3D, and TRIGRS and compare the results.

The YC region has a subtropical moist climate, with a typical monsoonal precipitation pattern. The annual mean precipitation ranges between 1,100 and 1,900 mm. This section of the Yangjiashan Mountains, because of its proximity

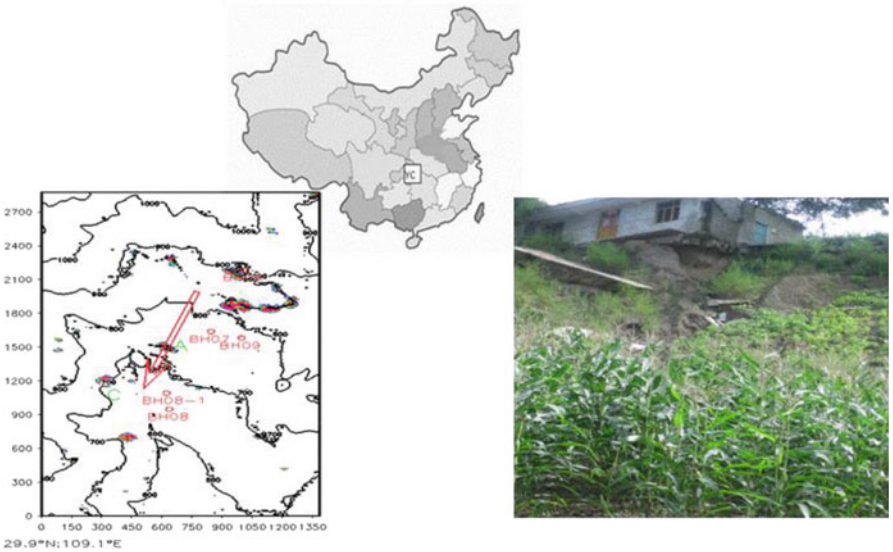

Fig. 6.5 Topographic map of Yangjiashan Creeping (YC) slope (the *upper map* shows its location in China). Contours are surface elevation (m). Borehole locations are labeled with a *red circle* (e.g., BH06-9). *Color shading* indicates surface maximum attainable creeping speeds larger than 1 mm/s, after a 50-year recurrence storm event. The primary sliding direction (*red arrow*) is determined according to subsiding and swelling belts. The X- and Y-axis are distances from the SE corner (29.9N, 109.1E). The *lower right panel* is picture taken south-west of BH08. Repeated sliding makes vegetation recovery difficulty (c.f. the maize field on the alluvial fan)

Table 6.1 Geomechanical observations and parameters obtained by field surveys and laboratory tests of saturated specimens

Material category	Young's modulus E (GPa)	Poisson's ratio ν_p (unitless)	Bulk density ρ (kg/m^3)	Cohesion (C, in MPa)	Repose angle φ (°)
Loamy soil with pebbles (in situ rock and soils)	0.2/0.16	0.3/0.24	2,050/2,150	0.48/0.38	25
Sliding zone (slip-surface material)	0.04/ 0.032	0.4/0/32	1,850/1,950	0.05/0.04	20/16
Shale (middle/lightly weathered mudstone)	2/1.6	0.24/0.2	2,500/2,600	2/1.6	35/28

Rock strength and deformation properties are obtained from triaxial compression tests using INSTRON-1346. Four saturated specimens of each layer were tested. During tests, confining pressure was applied stepwise in 3 MPa increment (i.e., 3, 6, 9, and 12 MPa), and vertical load are applied at displacement rate at 0.1 mm/s. Mechanical parameters of the sliding material under dry conditions also are listed (preceding the saturated ones)

to a dam, is well-instrumented and thus is an ideal region to verify the numerical model, which calculates the roles of pore pressure, biomass loading and root distribution, and the intrinsic friction of the stress distribution. In this region the major slides are preceded by creeping movements. Since the 1960s, the YC slope has experienced repeated failures, as a result of exceptionally heavy rainfall periods in 1960, 1980, and 1997. During a storm in July 1997, very heavy rainfall fell over 2–3 days and caused substantial erosion in one small canyon. Field studies indicate that after a major rainstorm toe-slope failure occurs first, reducing the stability of the upper slope, and the failure then moves gradually to the upper slopes. The scenario therefore is that towards the end of a heavy rain storm, a block of material was undercut by the stream and moved into the canyon, its downhill movement left an unsupported upslope block which followed the movement. This, in turn, was followed by a third block as the movement retrogressed up the slope.

The Yangjiashan community is situated on hills composed of inter-bedded siltstones and sandstones, occasionally interspersed with altered clay layers. The rocks range from highly to completely weathered at the ground surface. The weathered rocks date from the Paleozoic and Mesozoic eras, the 200–900 m thick yellowish interbedded sandstone and siltstone dates from the Silurian period, and the grey siltstone is from the Triassic period. The infiltration of rainfall through macro-pores, which are well developed in the soil and rock mass, plays a critical role in slope stability. The hills intersect with canyons in which increased erosion takes place during the spring and fall rainy seasons. Although many of the drainage patterns in this region have been altered by human activity, thereby increasing the slope stability, some remain unchanged, even in the inhabited areas (eastern part of the slope).

The Triassic siltstone of YC is especially sensitive to pore pressure changes. Because of the complicated stratification, SEGMENT-Landslide and FLAC-3D are initialized with five borehole soil/rock profiles (18–50 m depths within the granular soil mantle), with a horizontal resolution of 10 m in delineating the 3,000 m by 5,500 m simulation domain. Because FLAC 3D is a finite element model, its gridding scheme is out of the context of this review. Figure 6.6 provides a glimpse into the grid setting in the vertical dimension of FLAC3D by ANSYS pre-processing tool. In order to reduce spurious numerical boundary effects, the horizontal simulation domain encompasses the entire region shown in Fig. 6.5. The sliding material forms a characteristic alluvial fan, that is, with the down-slope section thicker than the upslope section. A thin plate splines (Burrough and McDonnell 2004) interpolator is used to obtain a sliding mass depth distribution over the grid. The TRIGRS model shares the same digital elevation map with the two 3D models. It considers vegetation roots effects using a look up table according to vegetation classification (Schmidt et al. 2001). Vegetation effects in SEGMENT-Landslide is more sophisticated and is described in Ren et al. (2007). For vegetation loading information, there is onsite collected values as input to SEGMENT-Landslide for the YC slope.

The SEGMENT-Landslide uses three model sublayers to delineate the sliding mass, and one layer to represent the montmorillonite, within which sublayers 10–12

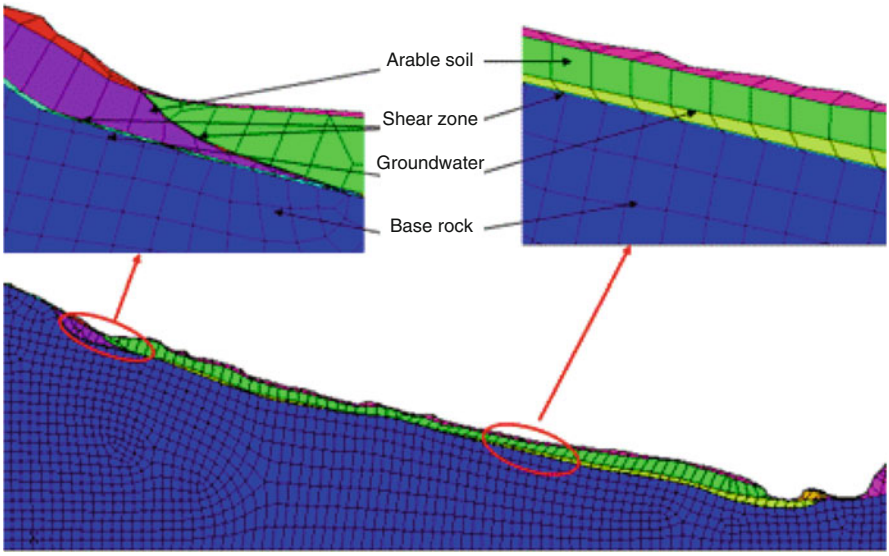

Fig. 6.6 Vertical cross-sectional of the Yangjiashan Creeping (YC) slope in FLAC 3D finite element model. The cross section is along the primary sliding direction indicated in Fig. 6.5 (the *red arrow*)

are assumed to define the slip surface. This is further supported by the creep monitoring data (Figures not shown). This layer has the same chemical composition as the overlying layer but is physically fractured. We use three sublayers to delineate the regolith layer because, although only ~1 m deep, it is the critical layer controlling water infiltration into the creeping slide mass. As it represents granular material under high confining pressure, the viscosity of this thin bed of finer-grained materials is smaller than that of the adjacent layers. The deep underlying rock layer is divided into seven sublayers, with mechanical properties specified from laboratory test results.

Using mean annual soil moisture conditions (obtained from NCEP/NCAR reanalyses, http://www.cdc.noaa.gov/data/gridded/data.ncep.reanalysis.surfacefluxes.html), a creeping rate is simulated using the SEGMENT model near BH8 of 17 mm/year, 17.2 mm/year, 16.2 mm/year, 8.5 mm/year, 5.2 mm/year, and 3.1 mm/year respectively at 1.5 m, 3 m, 10 m, 30 m, 40 m, and 45 m depths, agreeing well with the observed measurements. The root mean squared error, when compared with the 108 measurement data grids, is overestimated by only 0.42 mm/year, well within instrumental error range. The depth of the sliding surface (49 m at this location) is accurately delineated. Sliding will eventually accelerate along this plane of weakness, which is composed of highly fractured sandy shale. FLAC 3D behaves equally well, after converting the simulated horizontal displacement vectors to the corresponding locations.

Three historical landslides (1960, 1980, and 1997) reported in the YC study area are separated by ~20 years (Fig. 6.7). In 1960 and 1997, high annual precipitation

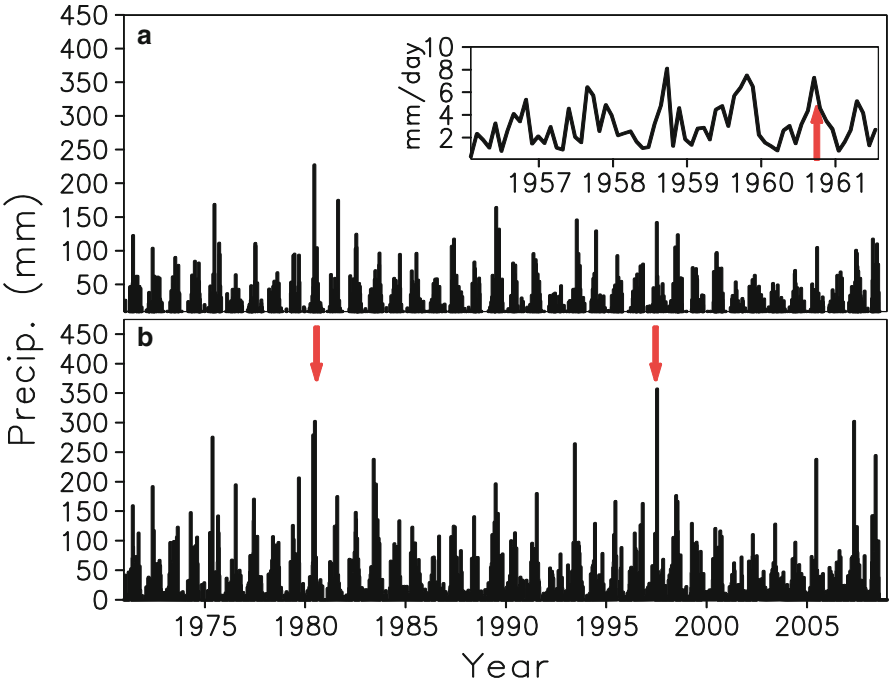

Fig. 6.7 (**a**) Daily precipitation and (**b**) rain event analyses, with the three major historical landslides indicated by *red arrows*. In panel (**a**) the daily rainfall time series reveals that that the 1997 event was not an intense rainfall event but was composed of two consecutive rainfall events over several days. In panel (**b**), rainfall totals are plotted for each rain event, by calculating the cumulative rainfall for each rain event and placing the total at the center of the start and end times. In panel (**b**), it is clear that both the 1980 and the 1997 events correspond to large total rainfall events. However, large rainfall totals alone do not necessarily trigger slope movements but, as discussed in the text, result from the combined effects of a number of factors. There is a lack of observed daily precipitation prior to 1970 to perform similar analyses. The *inset* of panel (**a**) is the NCEP/NCAR reanalysis monthly precipitation data. For example, the year 1960 not only had intense August precipitation, it also followed immediately after 1959, which was a very wet year

values of 1,819 mm and 1,771 mm, respectively, were recorded. However, 1980 was relatively dry with 1,200 mm total precipitation compared to 1,600 mm and 1,360 mm respectively for 1979 and 1981. Examination of the daily precipitation series from 1979 to 1980 indicates that in 1979 over 90 % of the annual precipitation occurred in the latter half of the year, with no significant precipitation before June. Although the total precipitation for 1980 is small, the heavy precipitation in January 1980 immediately following the previous year's precipitation events formed an extended wet period. There was a significant precipitation event in January, reaching a rate of 58.3 mm/day that lasted 4.7 h on January 15. As a result, the deep soil moisture (0.23 volume per total volume) remained relatively high for the remaining several months. What triggered the landslide was a very

heavy precipitation event of a 100-year recurrence frequency, with a single day precipitation of 230 mm on June 11th.

For the YC, heavy precipitation is both an enhancement factor, and a determining factor, in triggering landslides. However, current observational data of displacements are less than 2 years long, which is far too short to unambiguously resolve this hypothesis. SEGMENT-landslide simulations indicate that, under long term mean soil moisture conditions, the creeping will achieve a near-surface movement rate of 0.1 mm/day near the head of the slope, sometime within the next 40 years. Ironically, this creeping rate may never have been realized during the previous half-century. It has been interrupted by heavy rain storms and, consequently, slides have occurred before this movement rate ever was reached.

For a storm with a 50-year recurrence frequency (~170 mm/day) more than 80 % of the total water mass is channeled to the sliding surface through macro-pores, so movement rates can become dramatic toward the end of such a storm. The areas of significant deformation (i.e., maximum attainable surface sliding speed greater than 1 mm/s) after a 50-year storm are shown in Fig. 6.5 (with color shades). Thus far, the geological survey team has identified at least ten landslide scars and slide debris deposits, all within the color shaded areas in Fig. 6.5. For example, there are obvious landslide platforms near BH8 and another major one near the position labeled point "A". A shear surface exists at point "A" with a depth of about 70 m. When water drains down to this surface, the material strength at the shear surface is reduced to its residual value. The artesian pressures along the failure surface add to the instability of the sliding mass.

During heavy rainfall periods, water penetration reduces the strength of materials. In addition, hydrodynamic pressure along the slip surface further reduces stability of the sliding mass. The model simulations indicate that point C is highly unstable under an extreme precipitation event. Failure will occur around this point first, triggering a failure of the upper portion. The sliding mass spreads about 50 m downslope and was brought to rest by the lateral stress from the walls of the V-shaped gully which parallels the 750 m elevation contour. The sliding material can become up to 20 m thick in the lower elevations. The accumulated material also can block the gullies and enhance infiltration of rainfall into deep layers and cause pore water pressure increases, which is a lubricating effect in the model parameterization. This is especially important for the land segment lying between the 700 m and 600 m elevation, which is where the primary human residential areas are located. To obtain additional information for verifying the model credibility for slope stability at Point C, several more bore-holes are required in slopes adjacent to the gully on the west bank.

In the above scenario, a volume of 6.3×10^7 m^3 of soil and rock is estimated to be creeping, a value agreed upon by SEGMENT-Landslide and FLAC3D. The TRIGRS only output a slope stability factor. If we summarize those grid points with safety parameter less than unity (unstable region), the total volume is significantly smaller than this value. It is find that the slope model only identified the unstable grid points along the dry creek (to the west of the simulation domain). For the neighboring area, it show stability factor well above unity (stable). It is clear that

the slope model "cut" the creeping of those location off the dry creek with its surroundings. This shortcoming cannot be corrected by setting model parameters. It is rooted in the fact that 2D slope stability model sees the grid points as unrelated isolated islands (model running order among the grids does not matter for slope stability models but matters for full 3D dynamic models). The situation in YC slope reminds us the importance to look landslides in a wider horizontal context. Unstability of a spot has consequences on its neighbor—not only immediate neighbor but also "remote" ones. In retrospect, it appears landslides have been occurring in this region at intervals through history; but only part of the total creeping mass is involved in any particular landslide. Specifically, one portion may slide, causing a reduction in the stability of an adjoining portion; then, years, decades or even centuries later, a subsequent landslide will occur. As a consequence, the topography of the area is hilly and highly uneven. What determines the creeping rate of a slope is the material viscosity. We examined the modeled viscosity change near BH8 (Figures not shown). Because the rocks are heavily weathered, the viscosity is on the order of 10^{16} Pa s, which is two orders of magnitude smaller than for the same material in an undisturbed state. So, when dealing with fractured rocks as a whole, they must be viewed as granular material. The viscosity of granular material changes as strain accumulates. In this case, the viscosity is reduced substantially with time at all levels (e.g., it is reduced by >40 % from year 2007 to 2008). This explains why the creeping tends to accelerate with time.

During high flood levels or storms, the creek's rapid removal of material at the base, which helps to stabilize the soil and rock mass of the kilometer-long slope, leads to instability. This is a repeatable slope steepening process. The slide material from one slope failure temporarily stabilizes the area, but is removed by currents and further instability develops, and this debris is, in turn, removed. A salient proof of ongoing of this mechanism, in addition to eye-witness accounts, is the existence of scarps where subsurface material is revealed by the removal of sliding debris. Vegetation recovery is extreme difficult and thus the scarp takes a fresh appearance and are discontinuous with the general run of the hillside (Fig. 6.5, right panel).

Figure 6.8 shows SEGMENT-Landslide modeled creeping velocities for January 2012. A vertical cross section is provided along the direction of the primary sliding direction, located near the demarcation line in Fig. 6.5, for the current geometry and a climatological mean soil moisture conditions. Because the sliding material depth is only one-tenth of the slope dimension, for a more effective display the flow field is transformed into terrain-following sigma coordinates. The surface corresponds to $\sigma = 0$ and the bottom of the sliding mass corresponds to $\sigma = 1$. For clarity, the portion with flow speeds less than 0.3 m/year is filtered out. The formation of the local maximum speed "core" (the band along the $\sigma = 0.8$ level) near the bottom (Fig. 6.8b) is attributed to movement within the fractured layer. Varying the soil moisture conditions indicates that the movement of this layer is most sensitive to changes in soil moisture conditions. Any factors preventing surface water entering the ground will help reduce the acceleration of the sliding mass and delay future landslides. The landslides are sensitive to soil moisture conditions, but a qualitatively persistent feature is that the maximum strain area is located upslope, as

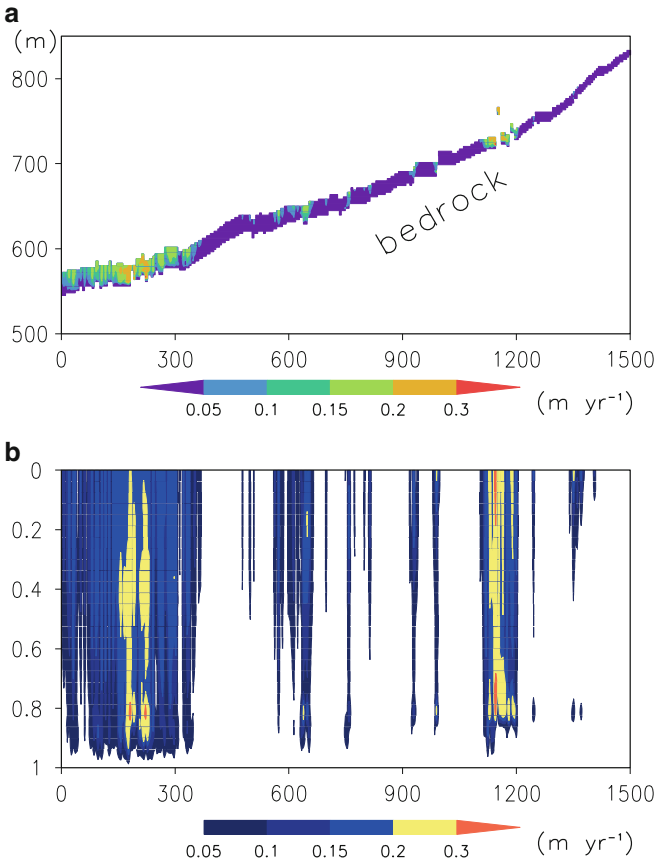

Fig. 6.8 Creeping speed for January 2012, within a vertical cross section (along the *red arrow* in Fig. 6.5) under climate mean soil moisture conditions. The *top panel* is displayed in physical space (vertical axis is elevation; horizontal axis is distance from the origin). The *bottom panel* is displayed in the σ terrain-following coordinate system. So $\sigma = 0$ corresponds to the surface and $\sigma = 1$ corresponds to the bottom of the sliding mass. The color shading is the magnitude of the full 3-D velocity. In panel (**b**) maximum cores (roughly at the $\sigma = 0.8$ level) corresponding to the "creamy" basal sliding layer

shown by the warm color shading near ~750 m elevation in Fig. 6.8a. At present there are crevasses with openings wider than ~5 cm of horizontal displacement. That the maximum speed cores are relatively isolated indicates that the sliding surface is not fully connected. In the upcoming 10 years, the causal mechanism for major slides remains the same, namely, the storm charging of the artesian aquifer and the lubrication of the granular layer by drainage water. A parallel experiment with FLAC 3D shows qualitatively the same pattern of instability (Fig. 6.9).

Slope stability model, when applied to real 2D topography, also runs on each grid point. However, there is no inter-grids connection, even the neighboring grids. In the

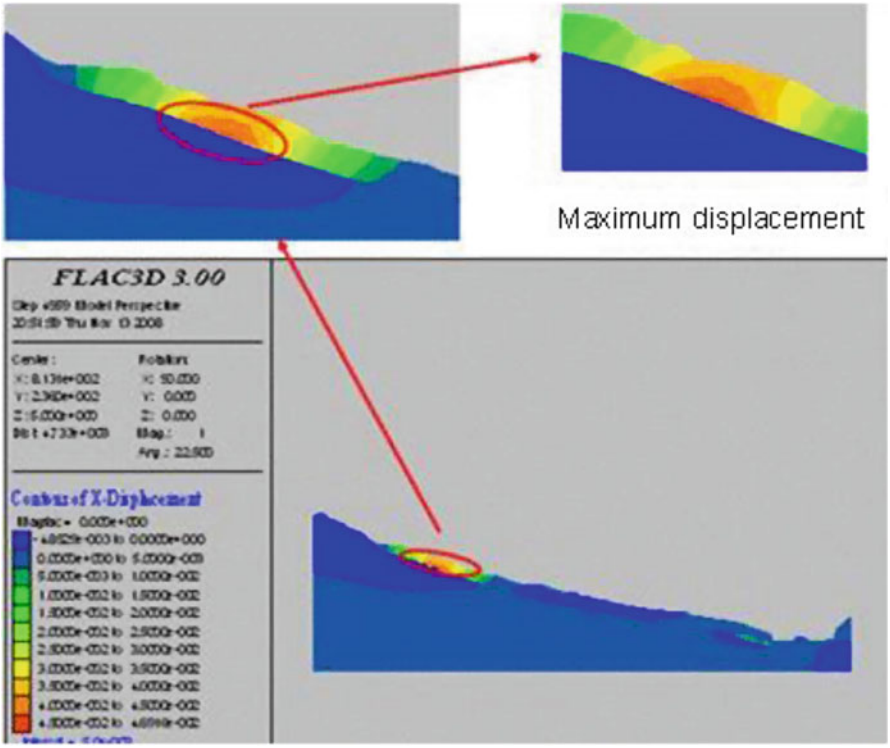

Fig. 6.9 FLAC 3D simulated x-direction displacement of Yangjiashan landslide. The identified unstable locations from top to toe regions are close to the three "hot spots" identified by SEGMENT-Landslide

case of Yangjiashan creeping, it is the lower boundary condition (a dry creek) that matters for the entire 3-km long slope stability. In a sense, the sliding body moves in harmony (a domino-like series of movements after extremely strong storms). Slope stability model (in this case TRIGRS), only indicates that the lower boundary section of the slope is unstable, the remainder are stable. The three dimensional dynamics model, in this case FLAC3D, does not suffer this shortcoming.

6.3 Case Study for the August 8, 2010 Zhouqu Landslide: Why Was it So Powerful?

On August 8, 2010 in the northwestern Chinese province of Gansu, rainstorm-triggered debris flow devastated the small county of Zhouqu. A modeling study, using SEGMENT-Landslide suggests that the cause is the result of an intersection of several events. These were a heavy rainstorm, not necessarily the result of global

warming, which triggered the landslide and followed a drought that created surface cracks and crevasses; the geology of the region, notably the loess covering heavily weathered surface rock; and the bedrock damage, which deepened the surface crevasses, inflicted by the 7.9 magnitude Wenchuan earthquake of May 12, 2008. Deforestation and topsoil erosion also contribute. The modeling results underscore the urgency for a high priority program of re-vegetation of Zhouqu county, without which the region will remain exposed to future disastrous, "progressive bulking" type landslides.

The storm season of 2010 saw landslides in many regions, including Zhouqu, China (August 8), Sikkim, India (August 27), Guatemala (September 3), and Patong, Thailand (Dec 22–23), to name just a few. The question is are these events a bellwether of an intensified water cycle as a consequence of climate warming (blogs.nature.com/news/thegreatbeyond/2010/08/mudychinafacingmorelandsl.html)? Or does the cause lie elsewhere? A version of the SEGMENT modeling system, SEGMENT-Landslide, was used to investigate the cause of the Zhouqu debris flow and possible future preventative actions. The Zhouqu landslides were preceded by an extreme precipitation event that occurred around midnight of August 7, 2010 (Fig. 6.10). Both the precipitation intensity of 77.3 mm/h near 104.42E, 33.78N, and total rainfall amount of 96.3 mm in 24 h are the highest recorded for the period since the May 2008 Wenchuan magnitude 7.9 earthquake. From a longer perspective, the Zhouqu rainfall event had a 20-year probability of occurrence under the present climatology, considering ongoing, significant climate change. The hills around Zhouqu have been well known for their long history of landslides (http://news.sciencenet.cn/htmlnews/2010/8/235921-1.shtm; Ma and Qi 1997; p. 187 of Bolt et al. 1975). However, this event is unique in its unprecedented magnitude, involving ~2.05 million cubic meters of sliding material. Because the landslide produced significant loss of life and great economic cost, it has generated intense discussion about the possible cause of the slide. Climate warming often is seen as the major cause, by contributing to the severity of the rainstorm; others argue that it was the recent drought, which produced cracks in the soil mantle. In addition to its geological uniqueness, because it occurred so soon after the 2008 Wenchuan earthquake, the presence of earthquake-broken bedrock also is cited as a factor contributing to the size of the landslide. A number of factors other than extreme precipitation therefore have been suggested as responsible for magnifying the Zhouqu landslide to its unexpected great size (Yu et al. 2010).

To investigate quantitatively the relative importance of these possible causal factors, SEGMENT-Landslides model was applied, with a wide variety of input variables, such as land cover, land use and geological data, which were provided by a research group of Beijing Normal University. SEGMENT-Landslide is a fully three-dimensional dynamical landslide model that incorporates not only soil/rock mechanical properties but also the hydrological and mechanical effects of vegetation on storm-triggered landslides (Sects. 5.1.2 and 5.1.3). The digital elevation data were from the Shuttle Radar Topography Mission (SRTM), at 90 m resolution. To reproduce historical landslides, we used a non-hydrostatic, full physics weather precipitation model—the Weather Research and Forecasting (WRF, Skamarock

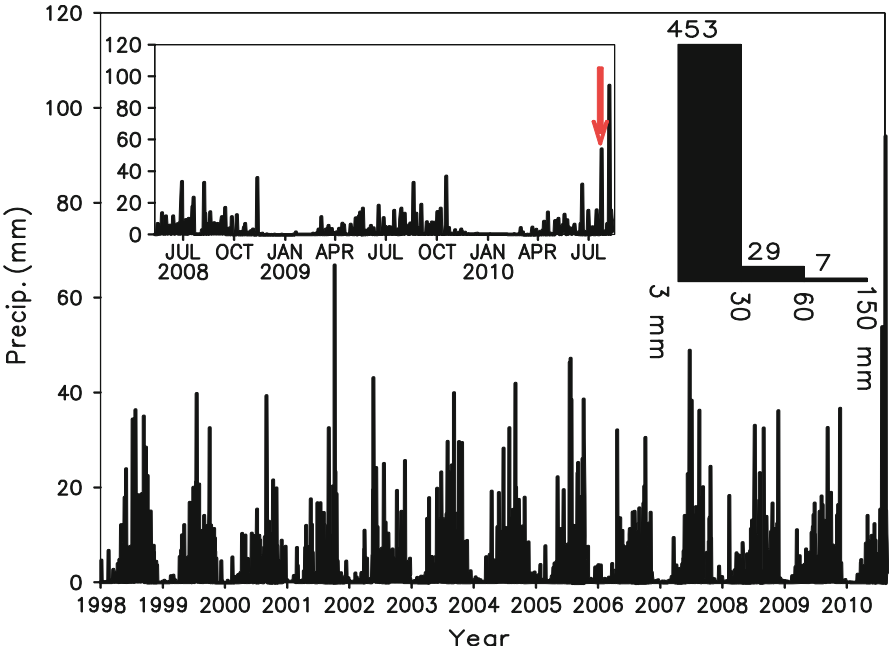

Fig. 6.10 The daily precipitation time series for Zhouqu (33.875N; 104.375E), for the period January 01, 1998 to August 20, 2010. These are estimated from NASA/TRMM (3B42V6, microwave-IR mixed products) 3-hourly precipitation. The last 2 months are from rain gauge measurements. The *left inset* is a zoomed view for the period after the 2008 Wenchuan earthquake. The *right inset* shows the rainfall histogram based on the landslide triggering rain event analyses proposed by Ren et al. (2011). Rain events with rainfall totals >30 mm can trigger significant landslides in the Zhouqu region (see *inset histogram*). Moreover, in that period, there are seven events with rainfall totals >60 mm, which therefore are rainstorms as intense as that which preceded the August 7, 2010 Zhouqu mudslides (the event indicated by the *red arrow* in the *left inset*). Thus, extreme precipitation alone does not explain the magnitude of the Zhouqu mudslide

et al. 2008) model. Compared with the satellite-based NASA/TRMM, which has 3-hourly data on a 0.25 by 0.25° resolution grid, WRF model can output on more flexible (usually finer) time steps. More importantly, the model can be used in multiple nested domains, hence progressively higher spatial resolutions, to better simulate the convective precipitation system. For this research, we used a three-layer nesting (Fig. 6.11), with inner-most domain (domain 3) using a 1 km resolution. The model is run for an extended period covering April to September of 2010.

Because of the complex terrain around Zhouqu (34.19°N; 104.41°E, lies in a northwest-southeast oriented narrow valley. Surface elevation to the west are generally above 3,000 m, ~800 hPa), there is no closed surface lows and only a 700-mb shear zone present. This is a belt of cyclonic vorticity. The low level jet, frequently accompany extreme precipitation is also absent due to the complex terrain and high average elevation. Precipitation is thus very patchy, associated with a series of meso-γ scale cyclones. From the circulation fields, it can be

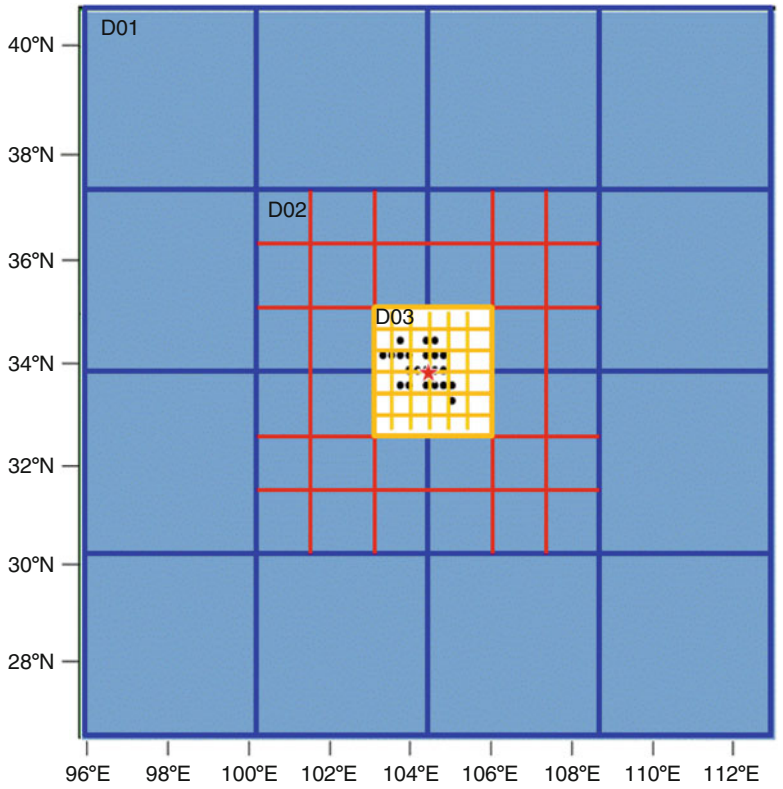

Fig. 6.11 The WRF nested domain configuration for Zhouqu regional precipitation simulation. Grid lines illustrate the relative grid sizes of the nesting domains. The coarsest, intermediate and inner domains are respectively of 9-km, 3-km and 1-km resolution. The *red star* labels Zhouqu city. The *black dots* represent 42 automatic weather stations

identified that there are a series terrain forced of meso-γ scale cyclones developing around Zhouqu. These features are identifiable from the MODIS cloud top imageries at around 0635 UTC 7 aboard the NASA EOS Aquasatellite (Fig. 6.12). River evaporation apparently also contributed because the clouds as a group align the valley direction. As these meso-γ scale cyclones develops, strong, local precipitation was produced.

Figure 6.13a illustrates the WRF simulated precipitation total amount in Domain 3 (contour lines) during May 01–Sept. 1, 2010. The records at automatic stations (numbers in mm around black dots) support this spatial pattern. The WRF captured the apparent orographic features in the spatial precipitation distribution. The primary rainmaker for this region is the vortices off the southern branch of the circum-Tibetan Plateau flow. When getting off the plateau, they intensify and cause severe weather. Prevailing winds are westerly so the leeway side has rain shadows. Figure. 6.13b is a zoomed-in look at the red-box defined region in (a), for the 07–08 August, 2010 precipitation events that directly caused the debris flows. It is

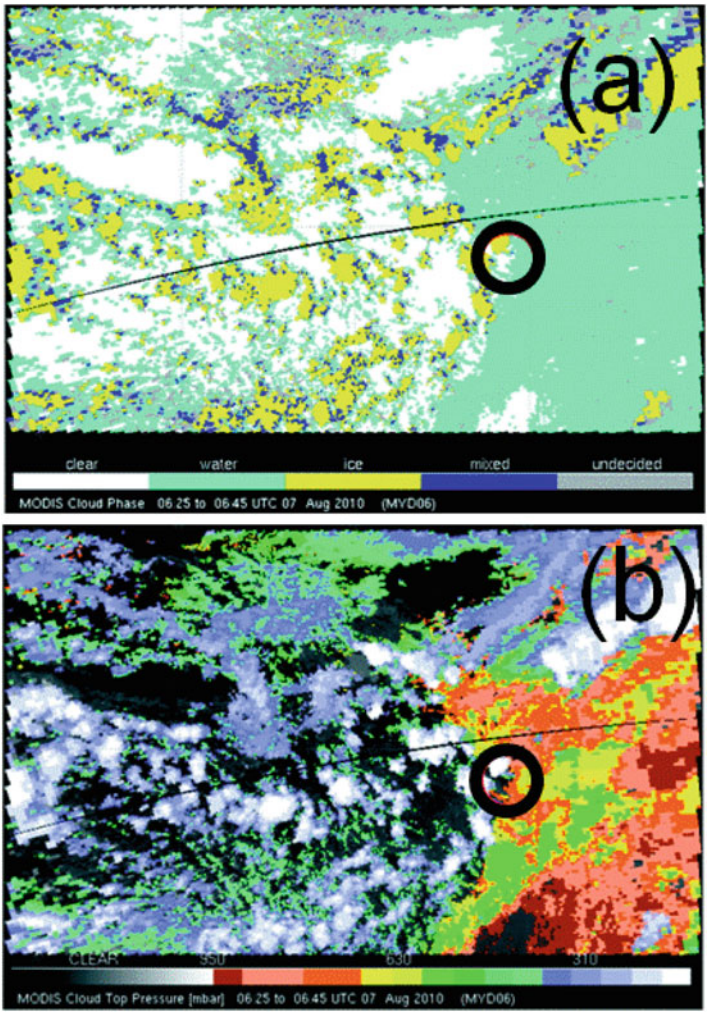

Fig. 6.12 MODIS cloud phase (**a**) and cloud-top pressure (**b**) from 0625 to 0645 UTC, August 7, 2010. The NASA EOS Aqua satellite's overpass time is at about 0635 UTC on 7 August 2010 over the Zhou Qu area (*circled*). Meso-γ scale cyclones associated with 700-hPa shear zone are shown as a band of cloud clusters. The areas east of Zhouqu are covered by low water clouds, while most areas to the west are mostly clear sky with some isolated high ice clouds (with cloud tops higher than 300 hPa)

apparent that the precipitation is highly concentrated (corresponding to the size dimension of those convective cells of $<$10 km). Without high-resolution model simulation, it is difficult (e.g., from using statistical downscaling), and almost impossible to capture the detailed precipitation features like these. Verification of the modeled precipitation is not easy. Fortunately, there are ten automatic stations within this small area (set up in 2003 by hydrologists) and some of them recorded

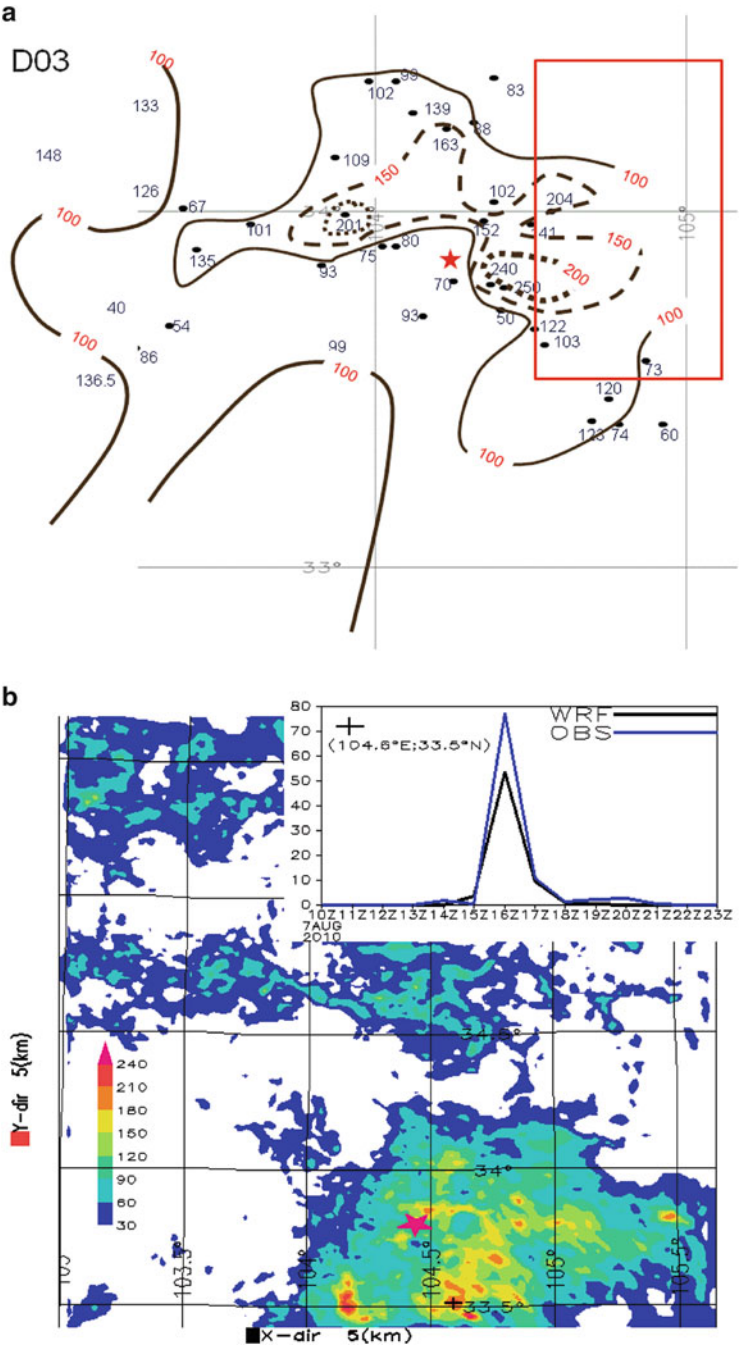

Fig. 6.13 The WRF simulated precipitation total amount in domain 3 (contour lines, in mm water) during May 1–Sept. 9, 2010. Numbers are total precipitation by automatic stations (*black dots*). *Color shading* is high resolution (1″) digital elevation maps. The WRF captured the apparent orographic features in the spatial precipitation distribution. Prevailing winds are westerly so the leeway side has rain shadows. Panel (**b**) is a zoomed-in look at the *red-box* defined region in (**a**),

the strongest precipitation events. Inset in (b) is a comparison between WRF simulated and automatic station measured precipitation rates (mm/h). There almost no phase/timing error from the model. The magnitude is slightly lower than reality (resulting in <5 % rainfall total in error). Other nine stations within this small area, for those recorded significant precipitation, also agrees well (not plotted for clarity). At stations with weaker precipitation, phase- (timing) and magnitude-errors/differences become significant. Compared with TRMM measurements, which tend to smear the rainfall over a larger area and the magnitudes are significantly lower (several folds lower) than reality, the WRF provided more satisfactory driving meteorological parameters for our landslide model. Both the rainfall total and the temporal structure (intensity and duration) are critical for an accurate projection of ensuing landslides. In this sense, WRF simulation quantifies to provide the atmospheric forcing for SEGMENT-Landslide.

For surface biomass loading, we used the Moderate Resolution Imaging Spectroradiometer (MODIS) products (Zhao and Running 2010; Zhang and Kondragunta 2006). A team survey of the area also provided a 300 m resolution vegetation mask. To investigate possible mechanisms, we performed several sensitivity experiments with assumed vegetation conditions. Our selected region is 33.66–34.06°N; 104.26–104.66°E. The hilly terrain of this area is composed mainly of metamorphosed limestones, interspersed with altered clay layers. The ground surface rocks range from highly to completely weathered. The weathered rocks date from the Paleozoic (primarily the Permian period) and Mesozoic eras, the yellowish inter-bedded sandstone and siltstone date from the Silurian period, and the grey limestones dates from the Triassic period. The infiltration of rainfall through macropores, which are well-developed in the soil and rock mass of the Zhouqu region, plays a critical role in slope stability. The hills intersect with canyons in which increased erosion occurs during the highly regular rainy season.

6.3.1 Collection Areas and Hotspots of Failure

Figure 6.14a shows model simulated unstable areas, as indicated by the maximum obtainable surface sliding speed. Under the current vegetation regime, the most significant scar is that near the Sanyanyu Valley (33.81–33.87N; 104.36–104.42E). The particular sliding is a characteristic "progressive bulking" type (Fig. 5.4). The accumulation area spreads up to 3,500 m elevation, in a fan shape with the fan "handle" extending down to the Bailongjiang River. The surface runoff essentially

Fig. 6.13 (continued) for the 07–08 August, 2010 precipitation events that directly caused the debris flows. *Inset* in (**b**) is a comparison between WRF simulated and automatic station measured precipitation rates (mm/h). Other nine stations within this small area, for those recorded significant precipitation, also agrees well (not plotted for clarity). At stations with weaker precipitation, phase- (timing) and magnitude-errors become significant

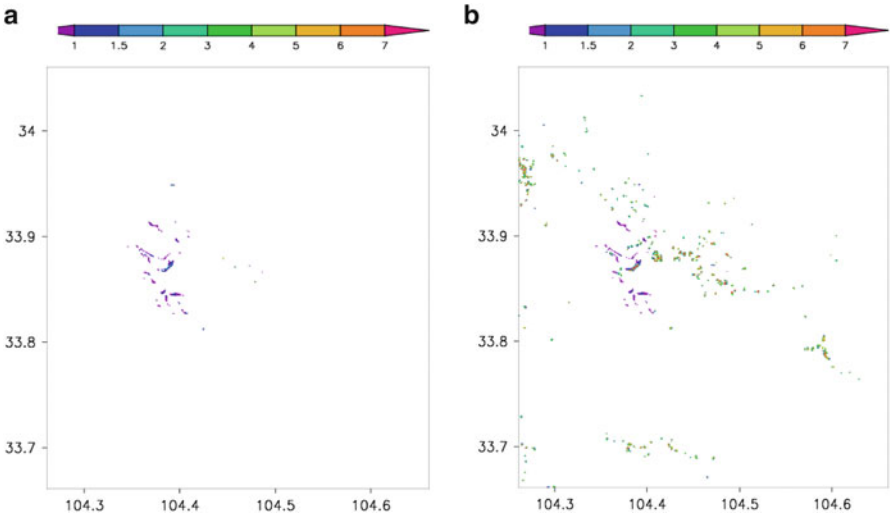

Fig. 6.14 A detailed comparison of the unstable areas identified by the landslide model. These are areas for which the model sliding speeds (m/s) exceeded the threshold value. Panel (**a**) is with current vegetation. Panel (**b**) is with vegetation removed. Under current vegetation conditions, only the Sanyanyu area is unstable. When the vegetation is removed, there are many other unstable areas. Moreover, the landslide flow magnitudes are larger than for the vegetated case

is clear water above the 3,500 m elevation contour, but at lower elevations gradually becomes turbid and entrains small stones and coarse granular material into the slide streams. These creeks are usually dry except during rainy periods. Figure 6.15 is an enlargement of the Sanyanyu gully, showing the surface elevation changes at two times in the sliding process: the beginning (Fig. 6.15a) and the cessation (Fig. 6.15b). At the cessation, the areas indicated by the two red arrows have little elevation change, despite the massive total mass in the slide. They acted like a pathway for the sliding materials at higher elevations. For example, at point A there is a break in the slope where some of the sliding material originated. Over 70 % of the sliding material came from the gully banks. Below 2,300 m, the solid form of sliding material is continuous in nature and the entrainment effects are so significant that boulders (>50 cm in diameter) are relocated down the slope. The thick mud has a viscosity of about 100 Pa s and the peak sliding speed reaches as high as 2 m/s. A total of 2.05×10^6 m^3 of solid sliding material was involved in this slide and was spread over an area of about 3.2×10^6 m^2.

Figure 6.15 uses the actual vegetation coverage of the area. If we assume the entire region is bare of vegetation, SEGMENT-Landslide identifies the following "hot-spots" as unstable (Fig. 6.14b): (33.773N, 104.375E); (33.347N, 104.412E); (33.77, 104.35), (33.79, 104.38) ,and (33.965, 104.105). In reality, only the Sanyanyu Valley slid significantly. The model makes it clear that the light vegetation cover over Sanyanyu is the main reason for such a large scale outbreak of debris flows. In turn, the light vegetation cover may have arisen from a positive

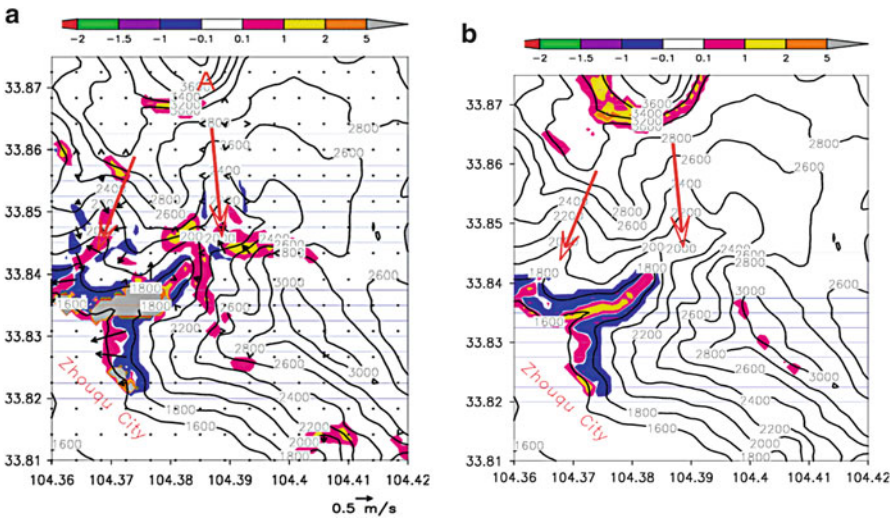

Fig. 6.15 The Sanyanyu gully area. Panel (**a**) shows the elevation changes (m) in color, at 9 min after the August 7th heavy rainfall event. Mud sources are clearly shown in the *left panel*. Its final deposition is shown in Panel (**b**) approximately an hour later. The flow has ceased and the deposition is in the Zhouqu city area, via the two parallel gullies. Elevation changes of the creeks (*two red arrows*) are small and act primarily as pathways for the sliding material. Note the break/failure of the 3,400 m elevation contour, indicating the provision of sliding material for the next sliding cycle

feedback inherent in successive historical landslide deforestation (e.g., Sidle 1992; Bolt et al. 1975). Repeated landslides, usually of smaller scale, were investigated in SEGMENT-Landslide simulations using historical WRF-simulated precipitation. They show that the rainy seasons of 1998, 2001, 2008 and 2009 all produced landslides capable of destroying the existing vegetation cover. Lighter vegetation cover lowers the criteria for subsequent landslides. This self-propagating mechanism has no lower limit before leveling the slope to below the granular material's repose angle.

In the Zhouqu area, the shear zone depth is variable and depends on the quantity of water penetrating into the crevasses. For bare ground (e.g., covered by previous landslide deposits or rockfalls caused by historical earthquakes), runoff readily drains into the crevasses, moistens the granular material and forms a shear zone at the bottom (the lowest reaches of the crevasses). Vegetation cover reduces surface runoff through canopy interception. Roots also assist in the retention of water within the rhizosphere. Thus, with vegetation cover, runoff water cannot be effectively channeled into the crevasses and much less sliding material will be involved in the landslide (Fig. 6.16). The cohesion of the granular particles (loam soil, pebbles from fractured grey limestones, and sands) are of order 0.1 KPa, far less than the root strength. Thus the mechanical effects of the roots also contribute to slope stability. We performed an additional set of sensitivity experiments to further investigate the importance of vegetation in reducing the magnitude of landslides. If

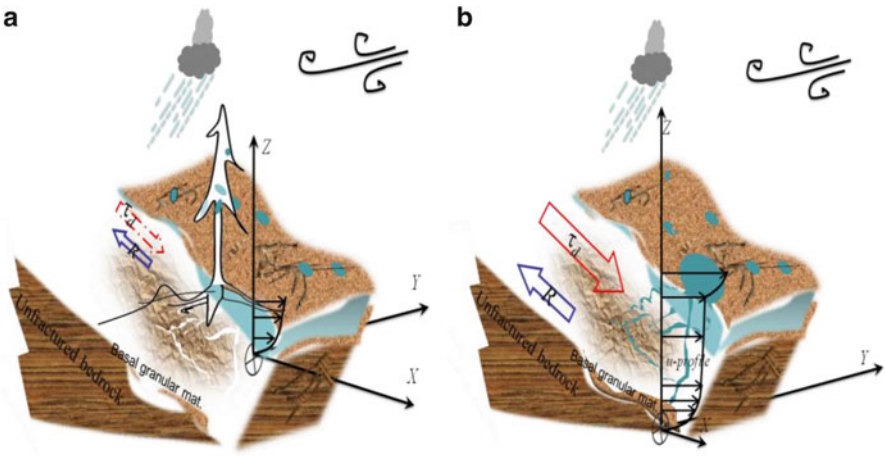

Fig. 6.16 Diagram showing the vegetation effects on storm-triggered landslides. Panel (**a**) is the case with vegetation and panel (**b**) is the case void of vegetation. All else being equal, in the vegetation case a proportion of rainfall goes into canopy interception (canopy runoff); and runoff and surface ponding are reduced as a consequence. Vegetation also effectively prevents water infiltration into deeper depth. Thus less sliding mass is involved in the vegetated case (the *blank arrows* show the magnitude of bulk resistive and driving stresses)

the Sanyanyu Basin had been covered 70 % by shrub of negligible biomass loading, with a root strength of 0.1 Mpa, and coarse root (diameter > 1 mm) density of 2 m^{-2} all residing within the top 2 m of soil, the amount of sliding material would be only 1.1×10^6 m^3, or about half the actual volume involved. If there is a closed cover (that is, 1.0 vegetation fraction), the sliding material can be further reduced to 10^4 m^3, and primarily involves only pebbles and protruding boulders at lower elevations. These experiments underline the critical role of vegetation in reducing the magnitude of the "progressive bulking" types of storm-triggered landslides.

Importantly, loss of vegetation has occurred not in recent 10 years and there actually are clear signs that local vegetation cover has been increasing (Fig. 6.17, also in Zhao and Running 2010). Because the 2008 Wenchuan earthquake has deepened the crevasses within the soil mantle and the bedrock, the criteria for storm-triggered landslides are significantly lowered. Large landslides did not occur before 2008 because, previous storms, although can be equally intense and have even larger total amount (e.g., Sept. 4, 2001), could not infiltrate into deeper shear zone, without the help of the earthquake's tearing of the bedrocks. Large landslides did not occur during the past 2 years because the threshold precipitation intensity and total were not reached (the past 2 years are relatively dry as indicated by total annual precipitations: 500 mm for 2008 and 480 mm for 2009 respectively, see Fig. 6.10). The landcover in August 2010 therefore was unable to prevent landslides caused by an intense rainstorm, owing to the legacy of the 2008 Wenchuan earthquake. The sealing of the cracks caused and/or deepened by the Wenchuan earthquake is slow process occurring on a timescale of several decades. Thus, a

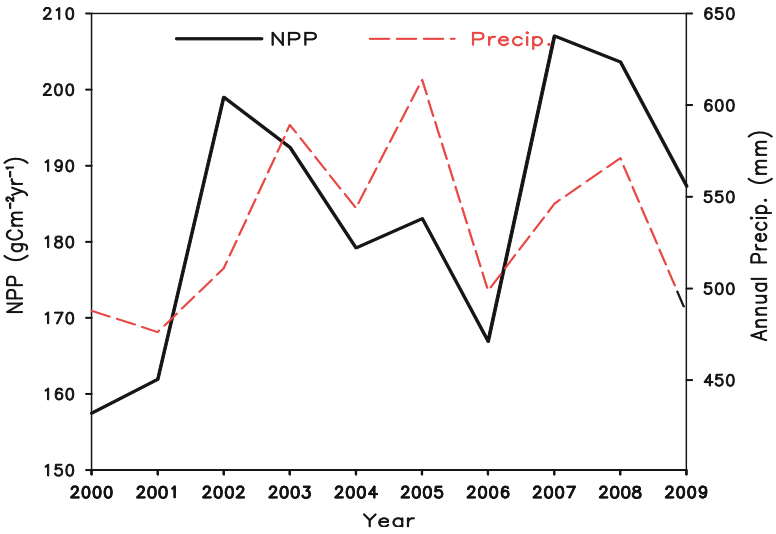

Fig. 6.17 The annual Net Primary Production (NPP) and precipitation over the past decade for the region of interest (33.66–34.06N; 104.26–104.66E). The 1 km resolution MODIS NPP products are obtained from M. Zhao. Precipitation data is from gauge station near Zhouqu (data obtained from Beijing Normal University). NPP quantifies the amount of atmospheric carbon fixed by plants and accumulated into ecosystem as biomass. An upward trend in NPP indicates a healthy ecosystem (i.e., vegetation is getting denser or is in a growing stage) or climate constraints getting relaxed. As expected, NPP matches closely with annual precipitation. Discordances in 2002 and 2008 may correspond to landslide disturbance of the vegetation. The 2008 perturbation possibly is related to the Wenchuan earthquake. In the past decade, the NPP has a rising trend, indicating the vegetation cover is gradually becoming denser

program of rapid restoration of the vegetation cover over the Zhouqu area is urgently required for rebuilding that region. The climate of that region, with an annual precipitation over the last 40 years is only 435 mm/year, suggests that the priorities are the restoration of forest on the north-facing slope and of a seamless grass cover for the south facing slopes.

The Sanyanyu deep valley has much coarse granular sliding material, particularly stones and boulders, because of a self-accumulation mechanism originating from its specific topographical features and because its loamy soil mantle is more easily dissected by running water. Topographically, the creeks in the valley have "graded beds" because the upper parts (near peaks) are steeper than the lower parts (close to the toes). Thus the upper river bed slopes are larger than the lower river bed slopes. For lighter precipitation events, the stones and pebbles cannot roll directly to the toe, stopping at mid-slope and creating natural barriers to the sliding material that follows (see the red blobs in Fig. 6.15). These accumulations apply to small slides, typically caused by low to moderate precipitation events. They have occurred at least five times during the past 2 years: in August, 2008; May, 2009; June, 2009; July, 2009; and September, 2009. However, when intense precipitation occurs, as in August 2010, all accumulated material will be activated

and a disastrous event will be generated. Recent studies (Ma and Qi 1997; Yu et al. 2010) indicate that granular material accumulated after the 1879 Wenxian earthquake (Bolt et al. 1975) was involved as the major debris. This supports the progressive bulking mechanism. Because previous landslides, lacked the unfortunate combination of the rainfall intensity, earthquakes and poor vegetation coverage, fail to move the solid material of the Wenchuan earthquake to the Bailongjiang River.

6.3.2 *Insights into the Next Series of Debris Flows If Vegetation Conditions are Not Improved*

On August 8, 2010 in the northwestern Chinese province of Gansu, 1,765 people died or were lost when a debris flow devastated the small county of Zhouqu. Our modeling study suggests that the cause is the result of an intersection of natural and human-induced events. The natural events include: a heavy rainstorm, not necessarily the result of global warming, which triggered the landslide and followed a drought that created surface cracks and crevasses; the geology of the region; and the bedrock damage, which deepened the surface crevasses, which was inflicted by the 7.9 magnitude Wenchuan earthquake of May 12, 2008. The human contribution was historical (before 1990) deforestation and topsoil erosion. Consequently, Zhouqu became vulnerable to a devastating rainstorm-triggered landslide. The model confirmed the cause of the landslide by producing a rain-triggered mudslide far larger than historical landslides. The landslide was magnified by prior vegetation loss and by water penetration deep into the cracks and crevasses created by the Wenchuan earthquake. The recent findings (Ma and Qi 1997; Yu et al. 2010) that solid granular material from a historical earthquake 130 years ago was involved in the debris flows further confirm our hypothesis. It was not that the rainfall intensity was of 100 year recurrence frequency (it actually is only of 20 year recurrence frequency, according the Generalized Extreme Value (GEV, Chapter 4 of Wilks 2011) approach, the likelihood of 42 % occurrence in the upcoming 10 years), but because the combination of strong precipitation with poor vegetation and recent earthquake enhancement of the crevasses is lacking in the past century. Previous debris flows, of smaller scale, failed to transport the granular deposits to stable locations. It also reflects the difficulty in re-vegetating the landslide scarps and even the granular deposits for the region, due to the climate of the region.

The massive Zhouqu landslide of August 2010 was caused by an extreme precipitation event, but was magnified by the Wenchuan earthquake of May 2008 that greatly deepened the preexisting cracks (either from historical earthquake or more gradual erosion processes) in the ground surface. For such surfaces, intense precipitation events favor the channeling of runoff water to greater depths than usual, creating sliding surfaces at those depths. Thus, more sliding material was

involved than for a less intense rainstorm. Vegetation is very effective at holding drainage water in the rhizosphere and reducing drainage into deeper levels, but the severe vegetation loss in the Zhouqu region prevented the vegetation cover from playing a protective role in reducing the critical impact of the hydrological process of deep level drainage.

The modeling results underscore the urgency for a high priority program of the re-vegetation of Zhouqu County, without which the region will remain exposed to future disastrous, "progressive bulking" type landslides. A direct cause of the large magnitude of the 2010 debris flow is the loss of historical deposits and the undercutting of loose gully beds. Re-vegetation of the areas with historical deposits is a priority. Thus, engineering approaches, such as installing check dams, slope protectors, and leveling gullies, should be followed by re-vegetation, because, restoring the current vegetation cover to its natural, much denser state is the most effective long-term approach to landslide mitigation. The Zhouqu 2010 landslides occurred in the remote sensing era and the records are valuable both for social and scientific purpose. These information contain important clues necessary for scientific appraisal of the cause, nature, and consequences of the natural phenomenon itself. After the landslides, there are expended efforts over the past several years by geologist, geophysicists, engineers and meteorologists/hydrologists to extract the maximum knowledge from the calamity.

The Earth's climate currently is in an interglacial period that possibly will continue for another 50k years (Berger and Loutre 2002) without human alteration. Since the 1970s, however, the Earth's climate has steadily warmed and shows no signs of slowing. With the enhanced hydrological cycle (Trenberth 1999; Ren et al. 2011), more extreme weather conditions are expected. The precipitation happened at Zhouqu has a 20-year recurrence frequency, as calculated from projected climate change. A disaster of the same magnitude as 2010 is expected within ~20 years if no effective counter measures are taken.

6.4 Debris Flows Are the "Predictable" Type of Landslide

As the concentration here is storm triggered landslides, knowing the changes in weather extremes (rainfall morphology) offers one lens for viewing landslide-caused ecosystem disturbances; a physically based, well-tested dynamics landslide model offers another. The following discussion centers on SEGMENT-Landslide, while noting that other recent fully 3D, hydraulic models of landslides follow a similar approach.

If a slope is littered with debris (e.g., those after wild fires or harvesting of timber) or being covered by soils, surface runoff can easily entrain them down slope. Through a gradually increasing positive feedback process (the more debris is involved, the more destructive it becomes), the sliding material's volume drastically increases in the process. The sliding material is so diluted that it has all the

features of a "flash flood".[1] By stating that it is more predictable we are trying to mean that the triggering factor, the spatial distribution of the mobilized source material and the tracking of the sliding material all are strongly correlated with intense rainfall that caused flash floods. Any available procedures in predicting flash floods can be used for this type of landslides.

Regardless of which definition is applied, the distinctive characteristics of debris flow mean that forecasting processes are quite different for this landslide type than for other types of landslides. The focus for predicting this type of slide, apparently, should focus on increased accuracy in quantitative precipitation estimation, desirably on spatial scales to represent individual slopes and temporally scales of several minutes.

In Earth atmosphere, there are two primary rainmakers that may result in extreme precipitation: the extratropical cyclones (associated with frontal system, baroclinic) and tropical cyclones (barotropic in nature). The discussion of tropical storms will be left with Chap. 7. Following subsections address the structure of frontal system, topographic influence in cyclogenesis, how climate change may affect the structure of the frontal system. A case study of the south-central US flood of May 2010 will be discussed as an example of how zonal index adjustment, hence blocking system can slow down the evolution of the frontal system and produce extreme amount of precipitation.

At present, the routine practical prediction of weather in general and extreme precipitation in specific depends on a relay between a medium-range global model and a regional atmospheric model. The Bureau of Meteorology (BoM/Australia) has developed the Global Analysis and Prediction (GASP), a full global model just like the European Centre for Medium-Range Weather Forecasts (ECMWF), or the National (USA) Center for Environmental Prediction's Global Forecasting System (GFS, Kalnay et al. 1990). These global models provide weather prediction out to 2 weeks ahead right around the world and forecast wind, temperature and humidity at ~100 km horizontal resolution and vertically containing ~50 vertical level to differentiate the atmosphere. The ~100 km resolution is insufficient for dealing with flash floods and weather-related natural hazards (Ren et al. 2010b; 2011). The fine resolution regional models, such as the Weather Research and Forecasting (WRF),

[1] A flash flood is generally defined as a rapid onset flood of short duration with a relatively high peak discharge (World Meteorological Organization). The American Meteorological Society defines it as a "flood that rises and falls quite rapidly with little or no advance warning, usually as the result of intense rainfall over a relatively small area."

The U.S. National Weather Service employs a more detailed definition as:

"A rapid and extreme flow of high water into a normally dry area, or a rapid water level rise in a stream or creek above a predetermined flood level, beginning within six hours of the causative event (e.g., intense rainfall, dam failure, ice jam)". However, the actual time threshold may vary in different parts of the country. Ongoing flooding can intensify to flash flooding in cases where intense rainfall results in a rapid surge of rising flood waters. Flash floods can be triggered by a variety of events including intense rainfall, failure of a natural (e.g., glacial lake debris) or manmade (e.g., dam, levee) structure that is impounding water, or the sudden impoundment of water upstream of a river ice jam.

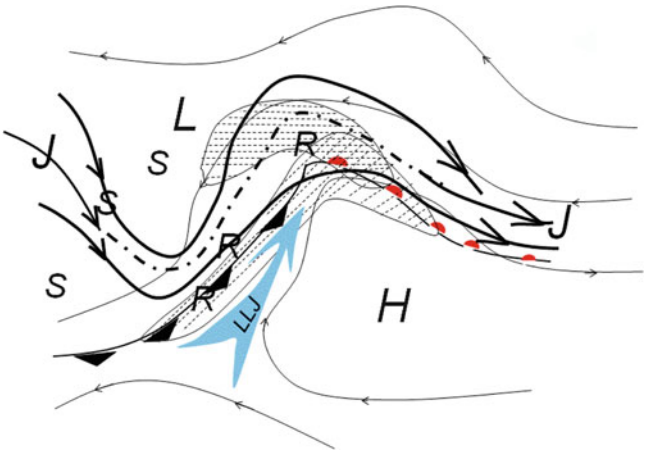

Fig. 6.18 Schematic diagram of hypothesized synoptical structure of air flows inside a mature stage extra-tropical cyclone (*L* at surface). *Thin lines* are lower tropospheric stream lines (primarily from east to west); the upper tropospheric flow (*thick lines*) are primarily westerly. *J* stands for upper level jets and *LLJ* is pre-cold-frontal low-level jet. Significant ascending and descending regions are labeled *R* and *S* respectively. There are two cloud systems corresponding respectively to warm conveyor belt (*vertical hatch*) and cold conveyor belt (*horizontally hatched*). They compose the "λ" shape clouds in satellite imageries. In a certain sense, in a frontal system, the cold airmass forms a shallow plate that holds the warm airmass as "water" content

the Regional Atmospheric Modeling System (RAMs, Pielke et al. 1992), and the Advanced Regional Prediction Systems (ARPs, Xue et al. 2003) will be embedded in such global weather models to simulate the atmosphere to sub-kilometer grid spacing, suitable for providing atmospheric parameters to natural hazard modeling systems such as SEGMENT-Landslide.

6.4.1 Synoptic Scale Flows Inside a Frontal System: Warm Conveyor Belt and Cold Conveyor Belt

Figure 6.18 is the flow structure of a mature mid-latitude frontal system (Northern hemisphere). This concept originates from the 1970s (e.g., Harrold 1973; Browning and Pardoe 1973). There are two warm moist airstreams, both originating from planetary boundary layer and have high specific humidity, that are decisive for the synoptic scale cloud/precipitation distribution. One is the warm conveyor belt (also referred to as the atmospheric river, Newell et al. 1992). It (the warm conveyor belt) intakes warm and moist air from the warm sector of a frontal system. In a frontal system, the cold air form a baskin (border of very gental slope) that "hold/confine" the warm air. Or the warm air as water inside a plate composed of cold air. It will

spill in all directions. The ascending of moist warm air along the cold front, most of them reaching the upper troposphere and form stratus (high) clouds. It is primarily an anticyclonic pattern when reaching the cold air in front of the warm front (hatched sector in Fig. 6.18).

The air mass of the warm conveyor belt usually originate from the peripheral of the surface high to the south east (of the cold front). The planetary boundary layer air over there has higher temperature and composes the western boundary of the warm air mass. Next adjacent to this air stream is the cold air. In contract, the eastern boundary of the warm air is not that clear (gradients are much smaller than the western boundary). From thermal wind relationship and the baroclinic structure as shown in Fig. 6.18, a pre-cold-frontal low-level jet (*LLJ*) usually forms (or, *the warm conveyor belt usually manifests as a pre-cold-frontal low-level jet*). The maximum wind core inside the *LLJ* usually are associated with the maximum in pseudo-equivalent potential temperature (θ_w), and the maximum of the thickness field (or, a ridge in the 1,000–700 mb thickness field). The fact that the daily cycle is not apparent for the synoptic scale (100–200 km wide and 1–2 km thick off the surface depression center and can reach 2.5 km as approaching the frontal region) *LLJ* indicates that there is a sustaining mechanism explainable from the recent proposed hypothesis (positive feedback from condensational latent heat release, Lackmann 2013). As *LLJ* is a region of high concentration of moisture, momentum and heat, the likely location of *LLJ* is the peripheral of subtropical highs. Subtropical highs can provide a clear sky condition that favors evaporation. The predominantly subsiding motion favors keeping the high moisture air at lower levels. More importantly, because of the temperature gradients, air at lower latitude has higher specific humidity and poleward transport of this moist layer can cause convective instability (causing lower level moist and warm configuration). Only the west peripheral region of subtropical high simultaneously meet the above three requirements. This explains the climatological location of Southern Great Plain (USA) *LLJ* that drains the Gulf of Mexico warm pool; the Somali (East Africa) *LLJ* that is trans-equatorial (going north along coast of East Africa, passing Madagascar and turning north east and reaching maximum wind speed to the south east of the Arab peninsular (15–20 m/s) at about 1.5 agl); and the eastern route *LLJ* that affecting central China. The formation of *LLJ* thus is forced primarily by the advection of potential vorticity (PV), whereas the path of the *LLJ* is also strongly modified by the land–sea contrasts and the orientation of coastal mountains (*LLJ* cannot surpass mountains that are higher than 3 km and has to circumvent them).

Another branch is the so-called "cold conveyor belt." It is not that the airmass is cold, it is rather because it extends a northern pass. It originates as anti-cyclonic airstream from north eastern sector of the surface high. Relative to the east motion of the frontal system, the air mass in the cold-conveyor belt lies under the airmass of the warm-conveyor belt. It moves westward along the edge of surface warm front and ascending slowly, reaching 500 mb at the top of the warm sector. The ascending of the cold-conveyor belt air near the surface warm front is of dynamic forcing. The ageostrophic motion associated with cyclonic vorticity inside the surface layer

causes air convergence and then upward motion (for mass continuity). To the north east of the cold-conveyor belt, the upward motion is weak and may even be slow downward motion.

It needs to be reminded that the airmass inside the warm and cold conveyor belts are interchangeable (they meet at the western edge of the warm conveyor belt at about 600 mb, northeastern direction of the surface low) and can be reorganized by the anticlonic upper stream to join the warm conveyor belt. Thus, warm and cold conveyor belts and the upper level jets are salient synoptic features of a cold frontal system. The upper level jets, because of the baroclinicity, lags at different degree to the *LLJ*. At early stage, the downward motion (of dynamic origin of a stream tube) of the exit region of upper level jet may inhibit the convective motion associated with the *LLJ*. Once the upper level jet further moves ahead, the secondary circulation associated with it assists the convective developments associated with *LLJ*. From a different view angle, upper level jet prevents premature development of convective activity and accumulates moisture for later, larger scale explosive development of precipitation events. The upper jets is in faster motion than the *LLJ* and, at a moment, they will cross (spatially still one above another, but cross in plane view) and the region west of upper level jet and east of *LLJ* will be the region of strongest precipitation. The *LLJ* signifies a mechanism for tapping moisture form source regions. Since the moisture source regions are geographically fixed. For example, for central and eastern USA, the Gulf of Mexico Warm Pool is usually the moisture source region. For Eastern China, there are three main source regions: the western route that originates from Indian Summer Monsoon; the central route that originates from trans-equatorial monsoon flow from southern hemisphere, originating from northern Australia over the Holloway Current/South Equatorial Current, passing equator between Kalimantan Island and Singapore, then meandering north through Southern (China) Sea reaching eastern China. This also is a mass exchange corridor between the two Hemispheres. It is however weaker than the other corridor, the Somali trans-equatorial flow, which can reach 700 mb; and eastern route originating from the southern edge of the Western Pacific subtropical high. On 850 mb, these moisture corridors are apparent on the time-longitude (Muller) graphs of the north-wind component (v), based on daily atmospheric data over summer months (e.g., May–August for Northern Hemisphere). The geophysical locations of the *LLJ* also are more or less fixed. Thus, the *LLJ* can only be a transient feature of the moving frontal system (moving flows on surface pressure maps). Some weaker frontal systems even do not form an effective *LLJ*. However, for those caused significant amount of precipitation, the existence of a well organized *LLJ* seems to be a common feature. The two conveyor airstreams are fundamental for the formation of the clouds and precipitation regions, especially the warm conveyor belt, which also is responsible for poleward and vertical upward transportation of vapor, heat, and positive momentum, is the most salient upward motion in the large (synoptic) scale baroclinic convective system. The distribution of the precipitation, to a large extent, reflects how the moisture are transported, rather than the local configuration of the frontal system. In fact, local

precipitable water, or the total moisture contained in the atmospheric column, is only a small friction of the total precipitation. Most of the precipitation, in another word, is transported from source region by *LLJ* to the region in question. Conveyor belt can be very different. For example, Harrold (1973) presented six different types of conveyor belts. At different stages of developments, the conveyor belt also changes. In frontal system, factors affecting extreme precipitation are primarily those affecting the vertical motion of air mass in the warm conveyor belt. These can be synoptic scale motion, mesoscale circulation and microscale convective activities. The most strong upward motion section in Fig. 6.18 also may nest mesoscale convective clouds (MCCs).

Baldwin et al. successfully simulated the pre-cold frontal *LLJ* developments. They emphasized the importance of latent heat release from atmospheric moisture. The ageostrophic wind (perpendicular to the cold front) increases with latent heat release, especially within the boundary layer of the warm sector, or the source region of the warm conveyor belt. In a comparison, strong *LLJ* develops in the model allowing condensation. In contrast, the "dry" model only produces a weaker *LLJ*. This study also has implications for investigating climate warming sensitivity of *LLJ* (to be detailed in Sect. 6.4.4). It should be noted that convective instability in the frontal system is potential instability ($\frac{\partial \theta_w}{\partial z} < 0$ but $\frac{\partial \theta}{\partial z} > 0$). As the cold front (also warm front) is of very gentle slope and the warm air generally floating above the cold air. The required "dry, cold upper and moist, warm lower" unstable configuration generally is nonexistent from surface until the top of the warm conveyor. To realize the potential instability, gradual, frontal lift (to condensation level) is an inefficient mechanism. The usual situation is that above and to the west of the *LLJ*, there exists a "dry" tongue resulted from the sinking of dry cold air from upper level trough. This configuration of "dry tongue" overlain moist conveyor air forms potential instability (usually exist between 700–500 mb). Release of the potential energy causes convection. This upward motion caused by "differential-advective" among vertical layers usually still is small (<1 m/s). Squall lines share some similarities with frontal system but have usually a temperature inversion or a dry cover that makes the unstable energy release in a more "explosive" manner. The role of vertical wind shear and the tilting of horizontal vorticity also work effectively only for squall lines. Rotunno et al. (1988) suggested that squall-line strength and longevity is most sensitive to the strength of the component of low-level (0–3 km agl) ambient vertical wind shear perpendicular to the squall line orientation. Dry lines and squall lines are important extreme precipitation systems over Southern Great Plains of USA as well as the equatorial islands such as Indonesia and are major players for causing flash floods and landslides. Mechanical forcing such as the tilting of horizontal vorticity by topograph is also possible for frontal system, but only in the limited warm sector within the warm conveyor belt with well mixed (from surface to 2 km agl), almost saturated planetary boundary layer.

6.4.2 Topographic Effects on Cyclogenesis

Landslides are mountainous phenomena. Our attention to orographic effects on cyclogenesis is natural. Orlanski (1982) pointed out that the topographic effects on cyclogenesis and developments depends not only on mountain geometry, geographic location, and extension range but also on the large scale meteorological patterns. He further pointed out that there are two basic processes that may result in cyclonic vorticity and vortices: the instability of air when ascending along the slopes and the effects of topography on mobile frontal systems. Krishnamurti (1968), in diagnosing a north American developing wave cyclone, also realized that the leeway descending motion bears the mountain effects, especially the early stage of cyclogenesis. The topographic effects are local to lower levels and disappearing quickly above 500 mb. Also, surface friction is the primary mechanism causing cyclolysis (the filling up of the low pressure and decease of a cyclone, Darnard 1971). Frontal system travelling in mountains of similar scale apparently suffers stronger surface friction. However, surface friction also is a mechanism for causing strong upward motion and resulting stronger mid-tropospheric vertical speeds. These explain that, it is common that precipitation does not weakens or even increases at the very beginning of cyclolysis. Topography also has effects on long wave radiation, another factor that affects cyclogenesis, especially at stages after the formation of the "λ" clouds.

In a certain sense, topography has effects on all factors in cyclogenesis (i.e., advection of vorticity, temperature, latent heat release, radiative balance, and friction). However, different mountain systems affect through different mechanisms and not affecting these factors evenly. For example, the north–south oriented Rockies and the east–west oriented Alps affect cyclogenesis differently. Because the Rockies are large-scale primarily north–south oriented, there usually forms cyclones downstream (lee way side) when westerlies circumventing through. In detail, when air streams pass through Rockies, at the eastern side (half wave length away) there forms a steady low-level leeway trough, which produces positive vorticity. If the upper level trough approaches, the closed vortice can be produced. This situation is similar to the case an upper level trough deepens surface frontal area, a region with cyclonic vorticity. Because the surface elevations of Rockies are only reach 850 mb, a significant amount of air just over-pass (rather than circumventing). This determined that the leeway wave exist only in low levels.

In contrast, the Tibetan Plateau is on average 4,000 m (reaching above 600 mb on average), most air mass circumvent. There are two wave trains (one corresponds to the southern branch of the diverted air stream and one corresponds to the northern branch) downstream to the eastern side (Fig. 6.19). The large west–east dimension (regions above 1.5 km covers 50 longitudinal grids vs. barely 20 longitudinal grids for Rockies) also explains the two wave trains associated with Tibetan Plateau.

Figure 6.19 illustrates the annual mean cyclone counts/occurrence frequency at leeway side of the Tibetan Plateau. There are two maxima: one to the north east and one to the south east. The north east center has apparent seasonal cycle (i.e., move to the coast of East Asia in winter time, corresponding to the well-known East Asia

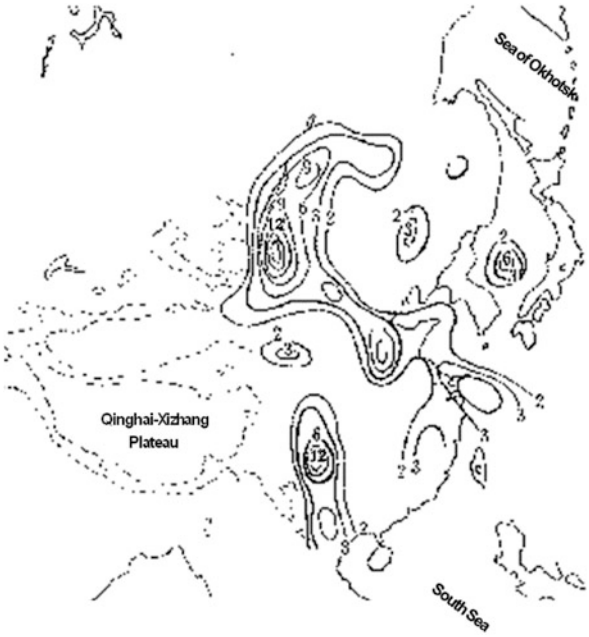

Fig. 6.19 Cyclone counts in 1958 for East Asia. Sampling region is (2.5 by 2.5 lat/lon). Tracker scheme is applied on NCEP/NCAR reanalysis. Adapted from Ding (1991)

Trough), resulting apparently from the seasonal cycle of the base currents flow through the plateau. The south east wave train in early summer season brings copious of precipitation along its path and are responsible for most recent landslides/debris flows over the Wenchuan earthquake affected region. The effects from Southern Hemisphere's Andes Mountains on cyclone development can be found in Orlanski (1982). If the mountain range is much smaller but surface elevation is significant, and are primarily west–east orientation, the effects on cyclogenesis and development will be different from the case of Rockies and Andes. For example, the European Alps (with an average elevation of 2.5–3 km, sloping to SSE) has significant effects on cyclogenesis at the Mediterranean region. The effect of Alps is to deform the thermal fields and the flow patterns of the cold surges associated with explosive expansion of the anticyclones to the north or northwest. The Alps forms a semicircular obstacle to prevent a direct southward invasion. Thus, on the southern side, there is a surface depression and, reflected thermally, a ridge in the thickness fields (the thickness between two pressure levels). Winter is the rainy season for the region and the Alp aided surface cyclone and the associated frontal system is the primary rainmaker for the region. Many landslides are triggered by the wave train straddling along the peripheral of Alps. For example, over 50 % of storm-triggered landslides in Italy and Greece are in winter season (October–March) and have direct relation with this type of weather pattern.

6.4.3 Mechanisms for System Persistence: Blocking Mechanisms and Index Circulation

As described in Sect. 6.4.1, the pre-cold-frontal low-level jet, often located at the western boundary of the cyclonic warm sector of a frontal system, accompanies a warm, moist airstream referred to as the warm conveyor belt. The *LLJ* is a region of highly concentrated vapor, momentum, and heat. The role of *LLJ* (with maximum wind speed >16 m/s) in heavy precipitation has been studied extensively (e.g., Eckhardt et al. 2004; Field and Wood 2007; Berry et al. 2011; Knippertz and Wernli 2010). In general, *LLJ* is the primary mechanism for providing water vapor and momentum to mid-latitude extreme precipitation events. The correlations between *LLJ* and extreme precipitation events can exceed 0.8. The precipitation region usually is located at the left front of the maximum wind speed core of *LLJ* (i.e., the sector where upper level jet's secondary circulation positively feedbacks to *LLJ*). The establishment of *LLJ* and the following extreme precipitation can be separated by 2–3 days. The *LLJ* can be strengthened by condensational heating and lower-tropospheric cyclonic potential vorticity (PV) generation in cold-frontal precipitation to the west (e.g., Lackmann 2002), suggesting a positive feedback between condensational heating and enhanced poleward vapor transport in the *LLJ*.

As discussed in previous two sections, more favorable situation for precipitation is that upper level jet and *LLJ* properly locked at certain phase ranges. For extreme precipitation to occure, the motion/evolution of upper level trough and associated jet should slow down (being blocked) or similar patterns become fast repeated (index circulation enters high zonal index regime, Namias 1950). Extreme precipitation, especially those last 2 days or longer, usually are controlled by planetary scale circulation environments. Extreme precipitation usually occurs during stagnant stage of perturbation on mass field, usually right after an adjustment of flow pattern (i.e., from high index to low zonal index). Right before or shortly after the beginning of an extreme precipitation event, planetary scale circulation will have an apparent adjustment. After the adjustment, the background flow becomes extraordinary stable. Extreme precipitation resulted because the conditions allow the convections to be organized and to sustain for an extended period of time. Another situation is that planetary systems keep repeating a certain configuration and cause perturbations on mass fields (e.g., at high zonal index periods). Planetary scale system indirectly control extreme precipitation through determining the motion speed of synoptic scale systems and their repeatability, longevity, and the coupling of upper and lower levels.

Figure 6.20 gives two situations that extreme precipitation tends to occur, corresponding too blocking situation at low index stage (large amplitude ridges and troughs on the 500 mb height maps) and frequent small perturbations on essentially zonal background currents (Fig. 6.20b). The longitudinal pattern usually results in precipitation distribution South West to North East along the low pressure corridor defined by the three rather stable surrounding highs. Notice that the ridge of the subtropical high is at a more southern location and can be cut through

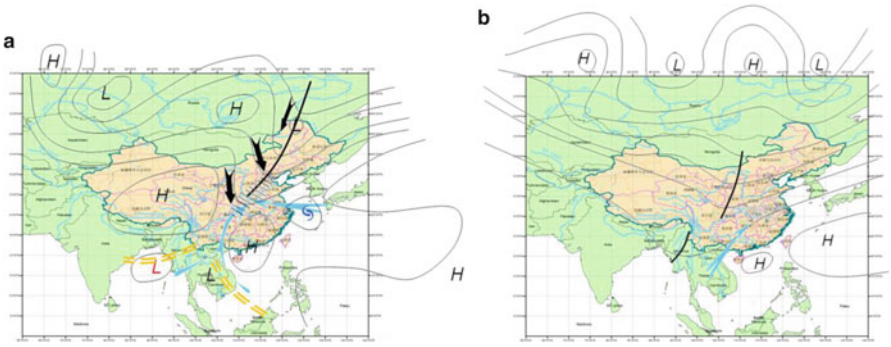

Fig. 6.20 Schematic 500 mb geopotential heights during longitudinal (**a**) and latitudinal (**b**) blocking in extreme precipitation events. The *blue arrow* is the warm conveyor belt, *hatched region* are surface precipitation areas. *Black arrows* are cold air streams from trough pouches. *Yellow dashed lines* are shear lines in flow field. Other symbols follow meteorological conventions

occasionally by a tropical cyclone. Depending on the track of the tropical cyclone, it may follow the existing low pressure corridor or creating a new warm moist airstream path. The most intense precipitation are expected below the cross-point of the two warm moist conveyor airstreams. For China, the Meiyu season (March–May) over Chang Jiang and Huai He region's extreme precipitation is mostly latitudinal pattern, or the high zonal index stage. The blocking highs are at higher latitudes (in this case the Okhotsk sea area) and the zonal airstreams over Asia is shifted south and give birth to a series of shallow troughs (the middle-level rain makers). In both pattern, the source of cold air is from the pouches of the mid-level trough. Persistent provision of cold air is a necessary condition for extreme precipitation and the efficiency of precipitation (moisture cannot be completely condensed and precipitated out the clouds).

In summary, blocking conditions allow the convections to be organized and to sustain for an extended period of time. As a result, torrential rains can occur repeatedly for several days, resulting in wide spread landslides and flash floods. In the case of high zonal index, MCCs may be involved and their replacements form a semi-stand still precipitation system and result in extreme large amount of rainfall.

6.4.4 Effects of Background Warming on Frontal Systems

The effects of diabatic processes within extratropical cyclones have been extensively investigated from theoretical (e.g., Montgomery and Farrell 1991), observational (e.g., Tracton 1973; Schafler et al. 2011) and modeling (e.g., Stoelinga 1996; Didone 2006) perspectives. Latent heat release has often been considered to be an important factor in cyclogenesis (e.g., Sanders and Gyakum 1980; Davis

et al. 1993; Zhu and Newell 1994; Wernli et al. 2002) and may even take a leading role in some cases, serving as a surrogate for a surface temperature gradient. For example, Baldwin et al. experiment revealed the critical role of condensation in the establishment of *LLJ*. Given the role of condensation in *LLJ*'s positive feedback scenario (Lackmann 2002), increased future water vapor content associated with climate warming could strengthen this feedback mechanism (Fig. 6.21). The strengthening of the *LLJ* in response to warming would lead to precipitation increases beyond the thermodynamic effect, due to increased horizontal moisture flux and flux convergence associated with the strong ageostrophic winds. A stronger *LLJ* could also potentially increase the threat of severe convective storms due to increased lower-tropospheric wind shear, considering the theory of Rotunno et al. (1988). Such a change could alter transient meridional transports in the mid-latitude storm tracks (Held and Soden 2006). Changes to upper-tropospheric jets could also result from increased heating and the associated secondary circulation may couple stronger with *LLJ*, inducing stronger convective activities. To test the hypothesis that a diabatically driven moisture-transport feedback (Fig. 6.21) feedback would amplify with climate warming, Lackmann (2013) first run the Advanced Research Weather research and Forecasting (WRF) model (Skamarock et al. 2008), with initial and boundary condition data from Global Forecast System (GFS, Kleist et al. 2009) final analyses on a 1° latitude–longitude grid, for the May 4, 2010 extreme precipitation event over south-central USA. Then the initial and lateral boundary conditions are perturbed by thermodynamic changes computed from a small ensemble of IPCC AR4 GCM output for the A2 emission scenario. He intend to prepare a simulation of a future, highly similar synoptic pattern to the control (2012 case) simulation, but with a warming thermodynamic environment. The comparison essentially proved the validity of the hypothesis.

Anthropogenic climate change has the potential to increase the severity of both droughts and floods because of changes in the hydrologic cycle (e.g., Trenberth 1999; Allen and Ingram 2002; Ren et al. 2011). Increased atmospheric water vapor is a straightforward thermodynamic consequence of warming, and as expected, general circulation models consistently indicate a robust vapor increase in future projections of a warmer climate. This increase in consistent with the Clausius–Clapeyron equation, which yields roughly a ~7 % specific humidity increase per degree Celsius of warming for typical lower-tropospheric temperatures (e.g., Pall et al. 2007). Larger water vapor content results in strengthened upward vapor flux even with the same upward vertical motion. The increase in lower-tropospheric water vapor that accompanies climate warming can lead to precipitation increases in many types of precipitating weather systems (e.g., Trenberth 1999), however the overall precipitation increase may grow at a lower rate than vapor increases, from energy balance consideration (Allen and Ingram 2002; Wentz et al. 2007; Stephens and Ellis 2008). An overall tendency for increased frequency of heavy rainfall has been documented in both numerical and observational studies (e.g., Karl and Knight 1998; Semenov and Bengtsson 2002; Groisman et al. 2005).

In addition to the thermodynamic effects (primarily the specific humidity dependence on temperature), there are several proposed dynamic mechanisms that justify

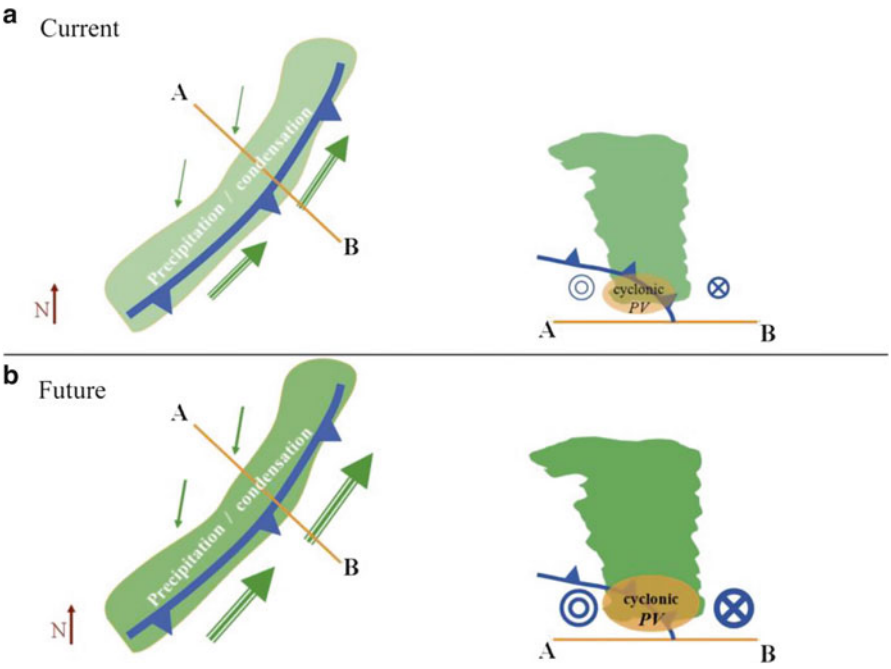

Fig. 6.21 Schematic diagram of hypothesized changes in an idealized cold-frontal zone in (**a**) current and (**b**) future conditions. (*left*) Plan projections showing region of cloud and precipitation (*green shading*), cold front, and lower-tropospheric wind vectors. (*right*) Corresponding cross section; location and strength of diabatically produced cyclonic PV features added. From Fig. 1 of Lackmann (2013)

the intensification water cycle hypothesis. For convective storms, enhanced convective available potential energy (CAPE) that is expected to accompany climate warming (Trapp et al. 2007) may lead to strengthened convective updrafts. Synoptic-dynamic research has established the importance of condensational heating to the dynamics of extratropical cyclones and frontal systems. This role has been quantified using potential vorticity inversion (Davis and Emanuel 1991). Back to the mid-latitude frontal system and *LLJ*. The *LLJ* can be strengthened by condensational heating and lower-tropospheric cyclonic potential vorticity generation in cold-frontal precipitation to the west (e.g., Brennan et al. 2008), suggesting the above mentioned positive feedback between condensational heating and enhanced poleward and upward moisture transport in the *LLJ*. Given the role of condensation in this scenario, increased future water vapor content associated with climate warming could strengthen this feedback mechanism. The strengthening of the *LLJ* in response to warming (Fig. 6.21) would lead to precipitation increase beyond the thermodynamic effect, due to increased horizontal moisture flux and flux convergence (increased ageostrophic winds). A stronger *LLJ* could also potentially increase the threat of severe convective storms due to increased lower-tropospheric wind shear (Rotunno et al. 1988). Such a change could alter transient

meridional transports in the mid-latitude storm tracks (Held and Soden 2006). Further, considering the upper-tropospheric jets can couple into different configurations to affect precipitation pattern, changes to upper-tropospheric jets could also result from increased heating and have significant consequences on extreme precipitation.

6.4.5 *A Case Study of the 2010 US Floods Using the WRF Weather Prediction Model*

For the 2010 extreme precipitation affected Appalachian plateau, there are places with colluvial soils as thick as 20 m along the valley walls. Also, some valleys are extremely narrow and still are habitated. In case of extreme precipitation (e.g., of a common blocking form as reported in Lackmann 2013), flash floods are foreseeable. To make situations worse, Karst landform are rather common, providing a non-local link for extreme precipitation and the scene for flashflood and landslide disasters.

The flash floods over South Central USA in (May 4) is followed by landslides in Zhouqu China (August 8, 2010), Sikkim, India (August 27), and Guatemala (September 3). An obvious question is whether or not these events a bellwether of an intensified water cycle, as a consequence of a warming climate?

To answer this concern, we first reproduce the 2010 extreme precipitation using a high resolution Advanced Research Weather Research and Forecasting (WRF, Skamarock et al. 2008) simulation. To resolve the mesoscale evolution of this event, the model domain features a larger outer domain with 20-km grid spacing, along with a 1-km nested innermost domain. Vertically, the model uses the default 28-level configuration with the model top set at 50 hPa. The Betts–Miller–Janjic convective parameterization scheme was used on the 20-km domain only. All domains employed the WRF single-moment 6-class microphysics scheme, the Yonsei University PBL scheme, and the National Oceanic and Atmospheric Administration (NOAH) land surface model. Long wave radiation was handled with the Rapid Radiative Transfer Model (RRTM) scheme, and shortwave radiation was the Dudhia scheme. Initial and lateral boundary condition data were based on Global Forecast System (GFS) final analyses on a 1° latitude–longitude grid; simulations were initialized at 00 UTC 24 April 2010 run for 10 days. For the nested domains, the parent domain provides lateral boundary conditions and one way nesting is used.

Figure 6.22 is model simulated precipitation total (mm) in the 50-km middle nested domain. The precipitation pattern compares quite well with TRMM measurements. However, compared with the in situ measurements at the KY-Mesonet stations (red dots on the background map), the intensity has a tendency of being weaker than reality.

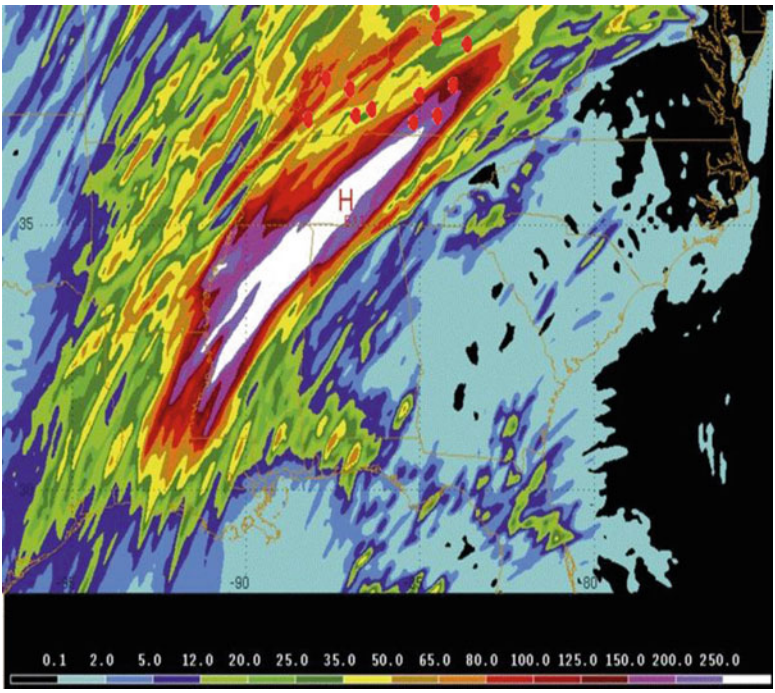

Fig. 6.22 WRF model simulated precipitation for the middle nested domain of 50 km resolution (mm, *shaded*). *Red dots* are where we have in situ measurements from the KY-Mesonet

To investigate the changes in precipitation characteristics (amounts and geographical distribution patterns) in a future warming climate, sensitivity study using "pseudo climate change" is performed exactly as proposed by Lackmann (2013). In detail, for simulating future (years 2060–2080) landslide events, the WRF model is used in the same pseudo-global warming approach proposed by Lackmann (2013). There is no simple means of anticipating how future synoptic pattern changes might influence the frequency and severity of those extreme precipitation events that trigger landslides. The experimental design for simulating future extreme precipitation events addresses this issue by replicating the synoptic pattern that caused the May 4th precipitation, but imposing possible future large-scale thermodynamic changes. While it is acknowledged that an identical synoptic pattern will not occur in the future, it is reasonable to assume that a similar pattern could occur. Because the model simulation is allowed to evolve dynamically for the duration of the synoptic event, the resulting changes, brought about by imposing thermodynamic perturbations, can also induce dynamical changes. Quantification of projected thermodynamic changes due to increased anthropogenic greenhouse gases is accomplished using an ensemble of Intergovernmental Panel on Climate Change (IPCC) Fourth Assessment Report (AR4) general circulation model (GCM) simulations of monthly temperature, sea surface temperature and mixing ratio

values. Experiments using the A1B scenario are used. The May monthly fields were averaged over a subset of 5 GCMs for which reliable temperature data are available at all vertical levels: the Bjerknes Centre for Climate Research Bergen Climate Model version 2 (BCCR BCM2), the Centre National de Researches Meteorologiques Coupled Global Climate Model version 3 (CNRM-CM3), the Institute of Numerical Mathematics Coupled Model version 3 (INM-CM3.0), the Max Planck Institute (MPI) ECHAM5, and the third climate configuration of the UK Met Office Unified Model (HadCM3). A two-decade average temperature change was then computed from the May monthly averages from the 5-member GCM ensemble for the periods (2000–2020) and (2060–2080). Similarly, sea surface temperature, air temperature at 2 m, and all available variables on isobaric levels were averaged. These spatially varying average fields were interpolated to the same 1° US global forecast system (GFS) grid and used for the initial and lateral boundary conditions in the control (2010) simulation. Differences between the 2060s and 2000s decades were computed for each grid cell, and these changes were subsequently added to the original GFS analyses. Given that the landslide event in question took place in May 2010 and that a change is added that was calculated from a 60-year difference, the future simulation can be interpolated as approximating the thermodynamic conditions around the year 2060 that would arise from anthropogenic greenhouse gas forcing alone, under the A1B scenario. The same synoptic weather pattern from May 2010 also characterizes the future simulation, and this fictitious date does not correspond to a specific date in future GCM projections. To resolve the mesoscale evolution of this event, the model domain features a larger outer domain with 20-km grid spacing, along with a 90-m nested innermost domain within which SEGMENT-Landslide is actually run.

As discussed in Lackmann (2013), there are overall increase in precipitation (Fig. 6.23, reproduced from Fig. 10 in Lackmann 2013), due to the diabatic (vapor condensation) heating caused intensification of ageostrophic wind around the cold front in a frontal system and the subsequent intensification of the low level jet (LLJ, a synoptic scale conveyor belt for vapor, momentum and heat). Since, for extreme precipitations, the vapor is mostly non-local and transported from source region. The LLJ plays a critical role in current and future extreme precipitation, by slowing down the evolution of the blocking system (Fig. 2a of Lackmann 2013).

With remote sensing information (land cover and vegetation maps as input to SEGMENT-Landslide are remote sensing products) and an advanced modeling system, we are able to provide an updated map of potential areas in such kind of danger. Especially, the southeast of the Appalachian plateau, the flanks of the Appalachian ridges and the Blue Ridge, as well as the Karst-land form, Bowling Green side of the clay pockets all are prone to slope instability (Fig. 6.24). For this region (Central South USA), observational study by Groisman et al. (2012) find that, on average, more than 70 % of annual precipitation falls during ~25 % of days with intense precipitation and about half of intense precipitation totals comes from moderately heavy events that comprise more than 70 % of all days with intense precipitation, during the past half century. In the last three decades, only 0.1 % of intense rain days were 6-inchers and they brought ~0.8 % of intense precipitation in

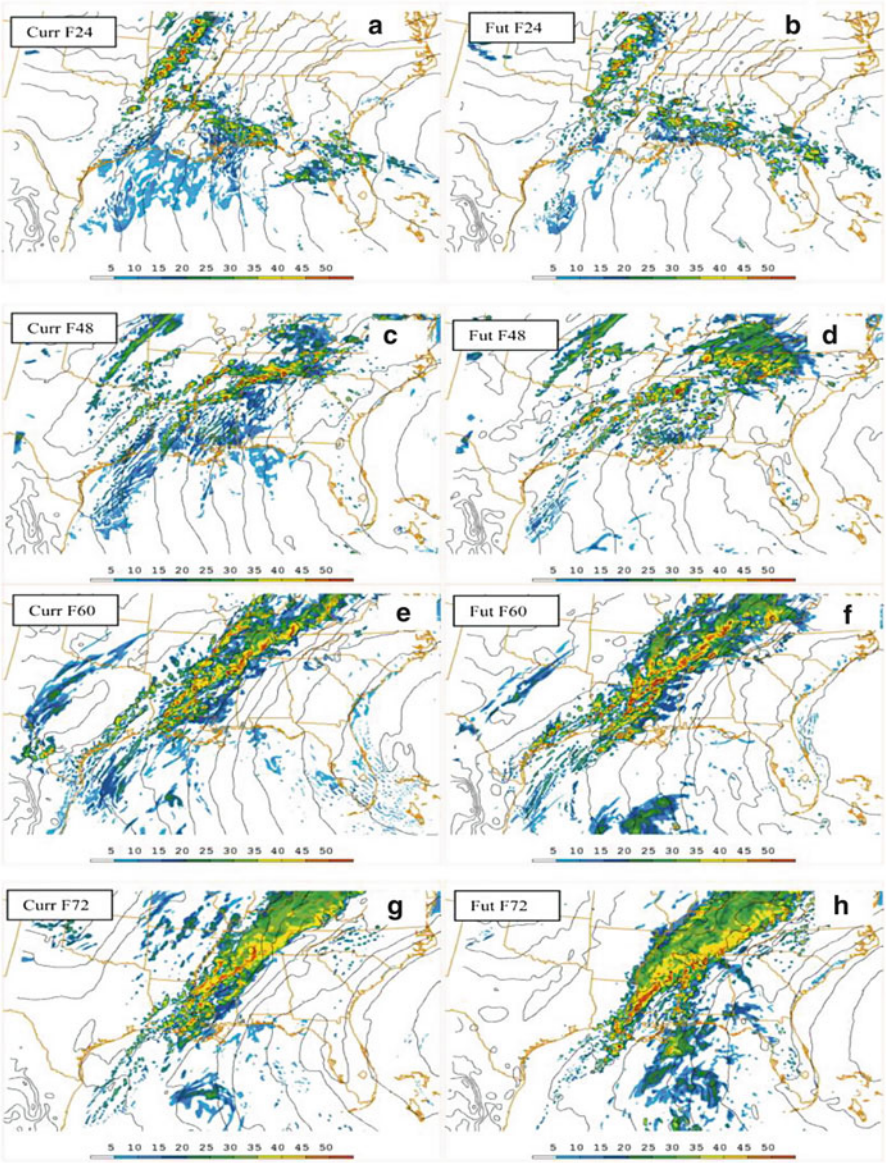

Fig. 6.23 Comparison of control (current) and future A1B simulation of simulated composite reflectivity (*shaded*) and sea level pressure (contour interval 2 hPa) for a subset of the 5-km WRF domain: present-day simulation hours (**a**) 24, valid 0000 UTC 1 May; (**c**) 48, valid 0000 UTC 2 May; (**e**) 60, valid 1200 UTC 2 May; and (**g**) 72, valid 0000 UTC 2 May. The (**b**), (**d**), (**f**), (**h**) as at *left*, but corresponding to the simulation hours of the present-day simulation but modified with thermodynamic changes from the A1B climate change scenario. Courtesy AMS

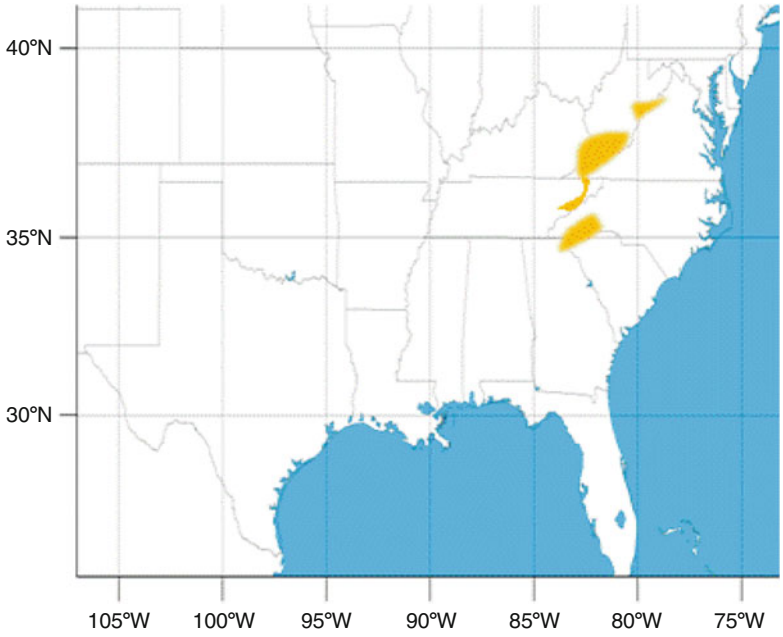

Fig. 6.24 Unstable areas (*Yellow shades*) once a May 2010 type of storm occurs after 2060

the last decades (vs. 40 years ago they brought only ~0.6 %). And, most strikingly, almost all trends in very heavy precipitation during the past 119 years are ascribed to the 1948–2010 period. If this 60-year period is halved, the second 30-year accounts a much larger share. This trend likely continues into the future.

Along this line, we analyzed several (5) CGCM future scenario runs under the A1B emission scenario. For the central USA, which comprises >35 % of the contiguous USA, there is a significant increase in very heavy and extreme precipitation. There exist invariants in the current intense precipitation changes over all regions of conterminous United States. For example, the maximum hourly rainfall intensity does not change with increase of the frequency of intense rain events. There is a statistically significant redistribution among the intense precipitation days and multi-day events: while moderately intense precipitation events (in the range from 12.7 to 25.4 mm per day or per multi-day event, decided by the Generalized Pareto Distribution method, GPD, Li et al. 2005) did not appreciably change, the fraction of very heavy and extreme precipitation days and events increases.

6.4.6 *Storm-Triggered Debris Avalanches in the Appalachians*

Weather and climate related hazards are causing more damage than in the past (e.g., Kunreuther and Michel-Kerjan 2009). Recent years have seen a steep rise in economic and insured losses from weather and climate related hazards, largely due to a significant increase in exposure. This study focuses on storm-triggered landslides/debris flows over the US Appalachians. The landslides prone regions can be identified from the geological, geographical, and extreme precipitation characteristics, using the extensively tested SEGMENT-Landslide. One of the focus regions is the central Virginia Blue Ridge area, which in 1969 experienced slope failure as a result of extreme precipitation from Hurricane Camille 1969, which recharged the area's hillslope soil. A SEGMENT-Landslide case study of the August 1969 Camille (Fig. 6.25) was planned using model simulated atmospheric parameters from the Advanced Research version of the Weather Research and Forecasting (ARW-WRF or, simply, WRF; Skamarock et al. 2008). This event indicates that the

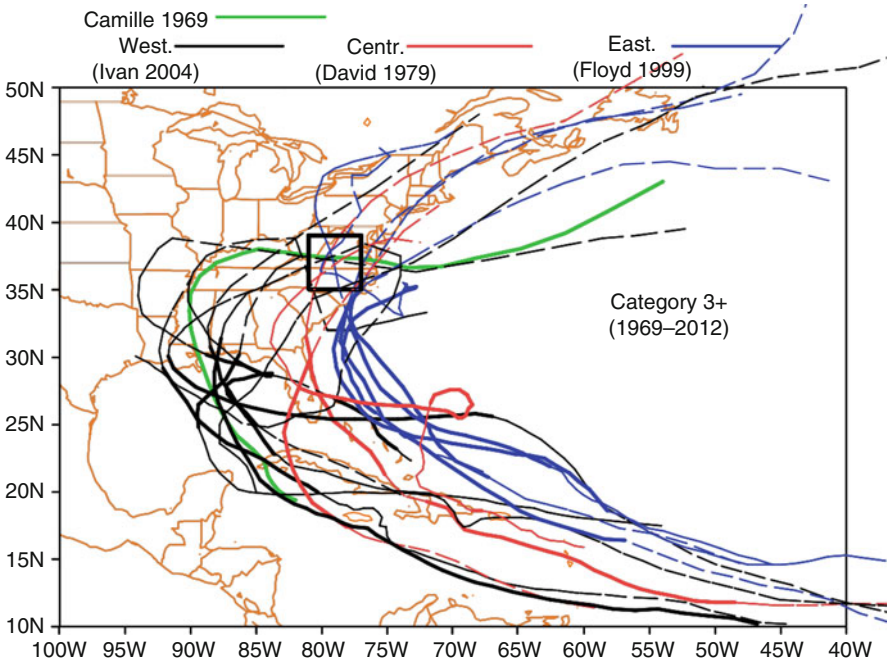

Fig. 6.25 In addition to the warm conveyor belt mechanism, tropical cyclones are major contributor to extreme precipitation over the Appalachians. Seventeen severe (Category 3 and above) hurricanes have affected the region of interest since Camille, over the period 1969–2012. They follow three general paths: western path such as Ivan (2004), central path (David 1979), and eastern path (Floyd 1999). The region of interest is defined by the $3^\circ \times 3^\circ$ black box centered on Nelson County, Virginia. Except for Camille and Eloise (1975), all remaining 15 hurricanes occurred during the satellite era and the available IBTRACS data are regarded as reliable

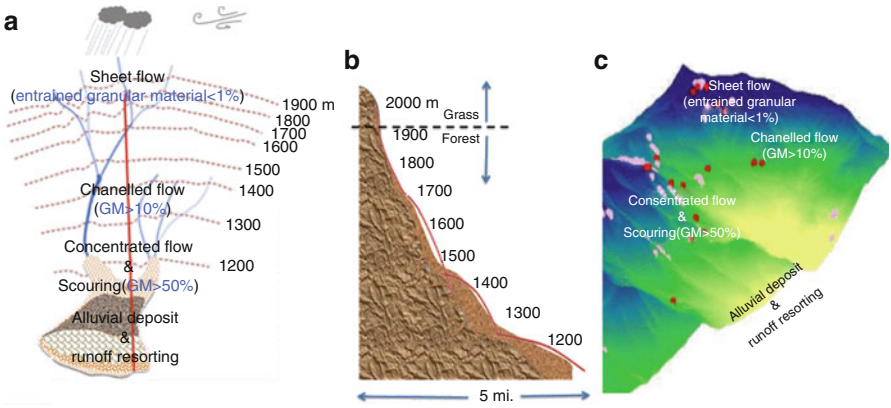

Fig. 6.26 A characteristic storm-triggered landslide (a debris flow). Left panel (**a**) is a plane view of the entire (solid material) collection basin. The elevation divisions are only for reference in the Black Mountain Range. The section with concentrated solid material creeping is only a small portion of the entire area. This means of mass redistribution is referred to as "progressive bulking" (Iverson 1997). Center panel (**b**) is a cross-sectional view along the *red line* (on panel (**a**)), showing graded slope feature: upper segment is steeper than the toe section. Depending on the orientation (azimuth) of the slope and climate zone, the forest line may fluctuate. This is based on the J-shaped semicircle defined by the Black Mountain, NC (panel (**c**)).

entrainment of vapor remnants from a hurricane by mid-latitude vortices can be a cause of extreme precipitation. The Camille occurred in a pre-satellite era and we can only verify the reproduced heavy rainfall event with witness accounts and indirect observation from drawn birds and the extremely fast increasing water levels in the creeks. The model simulated dynamic and thermodynamic features, however, are convincing and form the basis for a series of experiments on climate sensitivity using the hypothesis of Lackmann (2013). As the climate warms, extreme precipitation events are likely to become more common (Trenberth 1999), and future recurrence frequencies of such events therefore must be estimated and included in the forcing of the landslide model. Another focus region is North Carolina. Macon County has mapping (by USGS offices) completed for landslide hazards (www.geology.enr.state.nc.us). These maps are very helpful for studying potential and known landslide hazards. The Black Mountain Range (Buncombe County) is identified by SEGMENT-Landslide as another unstable region that is not mapped yet. This region satisfies the confluence of surface runoff and graded sloping and very prone to progressive bulking type of debris flows (Fig. 6.26a).

Landslides are partly upscale processes, with localized disturbances enhancing instability by adding fluids or reducing root reinforcement of pre-existing weathered regolith and granular soil particles spreading on slopes in regions predisposed to geo-hazards. Remotely sensed observations (e.g., the Gravity Recovery And Climate Experiment, GRACE) over the past decade provide an opportunity to examine the bedrock cracking conditions over the Appalachians, which includes both Nelson County and the surrounding areas affected by significant Karst

development. By identifying regions suffering steady mass gain/loss over the past decade and knowing the precipitation trends over the same period, it is possible to deduce the sources of increasing/decreasing groundwater. Regions with increased partitioning of precipitation into groundwater may be linked with a corresponding increase in bedrock crevasses. Climate change will impact the Appalachian region's extreme precipitation and storm-triggered landslides. The modeling approach in this study extracts information from the historical landslide cases (e.g., lesson learned from the 1969 hurricane Camille case). The predictability of future landslide events by SEGMENT-Landslide provides additional information for mitigation planning of resource and infrastructure protection.

Landslides involve weathered rock material, generally referred to as granular material (GM), which spreads on graded mountain slopes (Appendix A). GM has unique mechanical properties (e.g., viscosity, cohesion, and dry repose angle/frictional angle). Effects from moisture content, vegetation roots, and external loading (earthquakes, wind loading through canopy, or direct impact from raindrops of a storm) all need to be considered in the context of granular material. Which process that dominates depends not only on the soil and vegetation conditions, but also on the precipitation morphology. An advanced 3-D numerical model is like SEGMENT-Landslide thus is required to evaluate slope stability, and here it is used to investigate historical debris flow of Nelson County on August 19–20, 1969, particularly its cause and its role in assisting in deciding upon possible future preventative actions. The Nelson County landslides were preceded by an extreme precipitation event that brought over 600 mm rainfall within a narrow 8-h window, on August 19–20, 1969 (Fig. 6.27). Both the (WRF reproduced) precipitation intensity, which peaked at a rate of 1,400 mm/h near 79°W, 37.78°N on the south-eastern slopes of the Blue Ridge Mountain, and a total rainfall of ~900 mm in 24 h, are the highest recorded in the region. From a longer perspective, the rainfall event had a 100-year probability of occurrence under the present climatology, as determined by, for example, a generalized Pareto distribution (GPD) analysis (Coles 2001; Balkema and e Haan 1974), considering ongoing, significant climate change. The Blue Ridge has a long landslide history (Pileke et al. 1993). There is no dispute on causal factor of the 1969 slides (Williams and Guy 1973; Gryta and Bartholomew 1989). Because the 1969 landslide produced significant life and economic losses, it is of great practical importance to investigate the possible future possibility of such events. Climate warming is seen by some as the major cause, by contributing to the severity of the rainstorm (Chapter 14 in IPCC AR5, 2013), whereas others argue that it is the expanding of population into naturally unstable areas and disturbing the land cover and land use that might be the main factor in the future for storm-triggered landslides.

6.4.6.1 Special Attention to SST in WRF Setup for This Pre-satellite Era Case

In this study, WRF (release 3.5) is used to reproduce the historical 1969 Camille precipitation and to project changes in similar events under future climate. WRF is

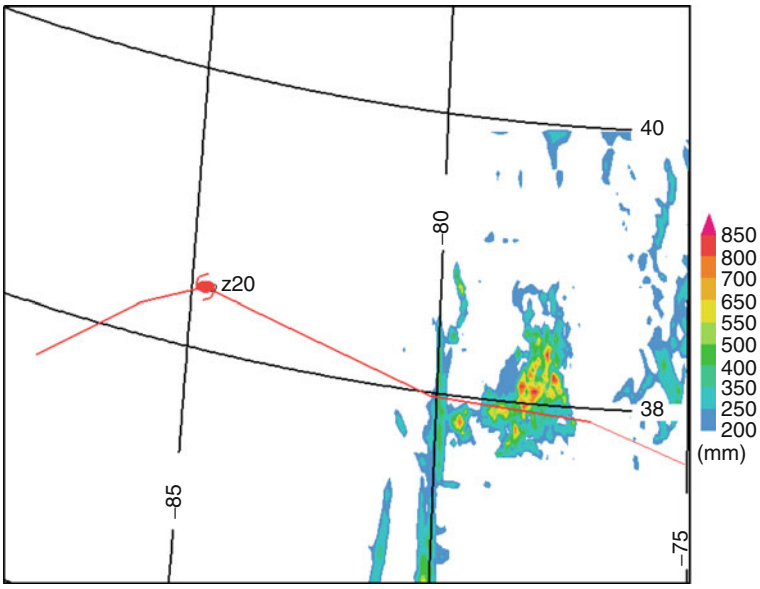

Fig. 6.27 Accumulated precipitation over Domain 2 up to 00Z 20 August 1969. The primary precipitation occurred during 19–20 August. WRF captured the apparent orographic effects in the spatial precipitation distribution. The eastern side of the Blue Ridge Mountains received up to 900 mm of rain in that period. Major precipitation centers are along a line north of the hurricane track and perpendicular to the Blue Ridge Mountains. There were recorded sightings of animals drowning in trees and people had to cup their hands around their mouth and nose to breathe (Roger A. Pielke, Personal communication 2014).

a fully compressible non-hydrostatic, primitive-equation model with multiple-nesting capabilities to enhance resolution over the area of interest, fully use the available computational resources on super computer centers (e.g., iVEC in this study). This version of the WRF model uses the Eulerian mass coordinate and is referred to as ARW-WRF. Over Nelson County, five nested domains are configured as shown in Fig. 6.28a. Domain 1 is the coarsest mesh and has 501×462 grid points in the south-north and west-east directions, respectively, with a horizontal grid spacing of 27 km, comfortably cover the region tracked by Camille during its entire life cycle. During our 10-day simulation, boundary condition setting matters because the spurious calculation waves bounced back into the simulation domain (e.g., Vaidya and Kulkarni 2007). Radiative boundary conditions are used to minimize the impact of domain size and boundary conditions. Domain 2 is nested with 720×600 grid points at 9 km grid spacing. This domain covers the oceanic period of the Camille's life cycle. Domain 3 covers the Blue Ridge region and is parallel to Domain 2 but with 400×380 grid points. To facilitate providing precipitation to SEGMENT (which runs on 90 m resolution DEMs/topography), two further nested domains (Domains 4 and 5) were employed within Domain 3, with nesting ration of 3 in cascading, producing grid spacings of 3 and 1 km, respectively.

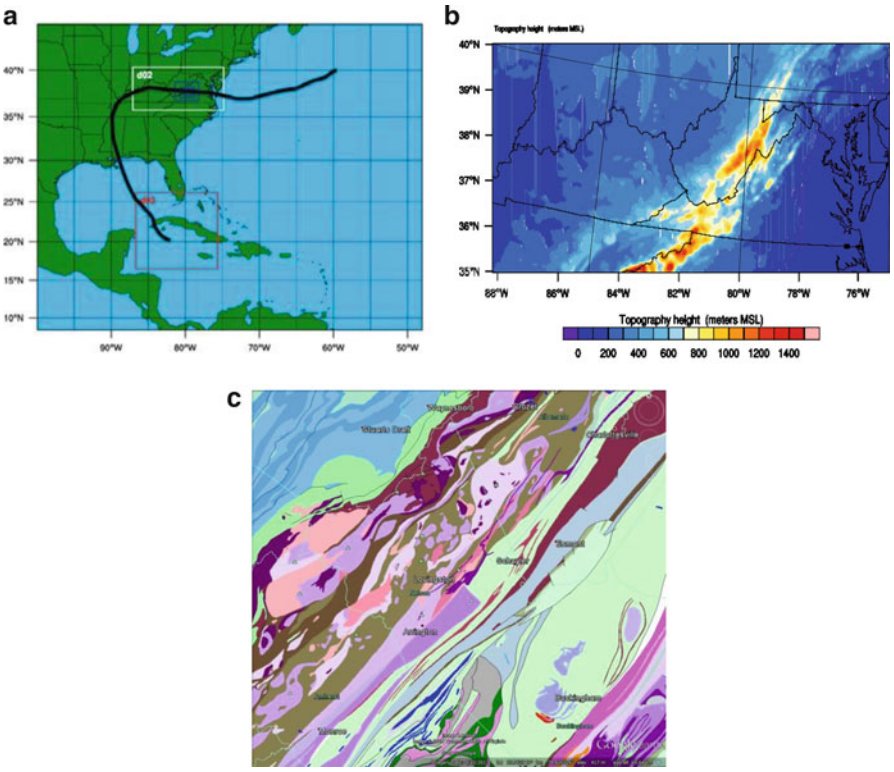

Fig. 6.28 Panel (**a**) shows the selected WRF domains and the nested domain. Domain 1 is of 27 km resolution. The innermost (Domain 5) is of 90 m resolution. *Color shadings* in panel (**b**) are the shaded relief images of the 90-m digital elevation map in Domain 3. Panel (**c**) is the geological map of Blue Ridge Mountains. Source: Google Earth. Dr. Kongyan Zhu assisted in obtaining this map

Running WRF for the Camille 1969 case has an important technical issue; a lack of SST information in the reanalysis data. Tropical cyclones are very sensitive to sea surface temperature (SSTs, Ren et al. 2014). For this historical case, which occurred before the remote sensing era, the Hadley Centre Global Sea Ice and Sea Surface Temperature (V1.1) is used, interpolated to daily intervals from monthly means. Similarly, all the simulations use the same initial and boundary conditions, as derived from the coarse resolution NCEP/NCAR reanalysis (2.5° rather than the 1° FNL analysis, which starts well after 1969). The NNRP Variable Table is used in the pre-processing stage (*WPS* and *REAL* in the WRF setup). The analyses are interpolated to the WRF–model grid to provide the initial conditions for 00UTC 14 August 1969, as well as 6-hourly lateral boundary conditions for the 27-km outermost domain. All domains 1–3 start from 00 UTC 14 August 1969. Domains 4 and 5 start 2 days later to give enough time for model spin-up. This model configuration is referred to as control-run (CTRL). The WRF run is initialized at

00 UTC 14 August 1969 and integrated 196 h until 00 UTC 23 August 1969. The model's initial and lateral conditions are taken from the NCEP reanalyses with outermost lateral boundary conditions updated every 6 h, and the SST products are interpolated and the sea surface boundary conditions updated.

6.4.6.2 Multiple Nesting Instead of Downscaling in Matching Up Atmospheric Parameters with DEMs

To quantitatively investigate the relative importance of the various possible causal factors, the SEGMENT-Landslide model was applied to the event. SEGMENT-Landslide requires a wide range of input variables such as land cover, land use, and geological data, all of which were provided by a University of Oklahoma group associated with CIMMS and Department of Civil Engineering. The digital elevation data were obtained from the Shuttle Radar Topography Mission, SRTM (http://srtm.mgs.gov/), at ~90 m resolution (Fig. 6.28b) over Nelson County (VA). For Macon County (NC), we have DEMs at ~6 m horizontal resolution (color shades of Fig. 6.29). To reproduce historical landslides, precipitation forcing

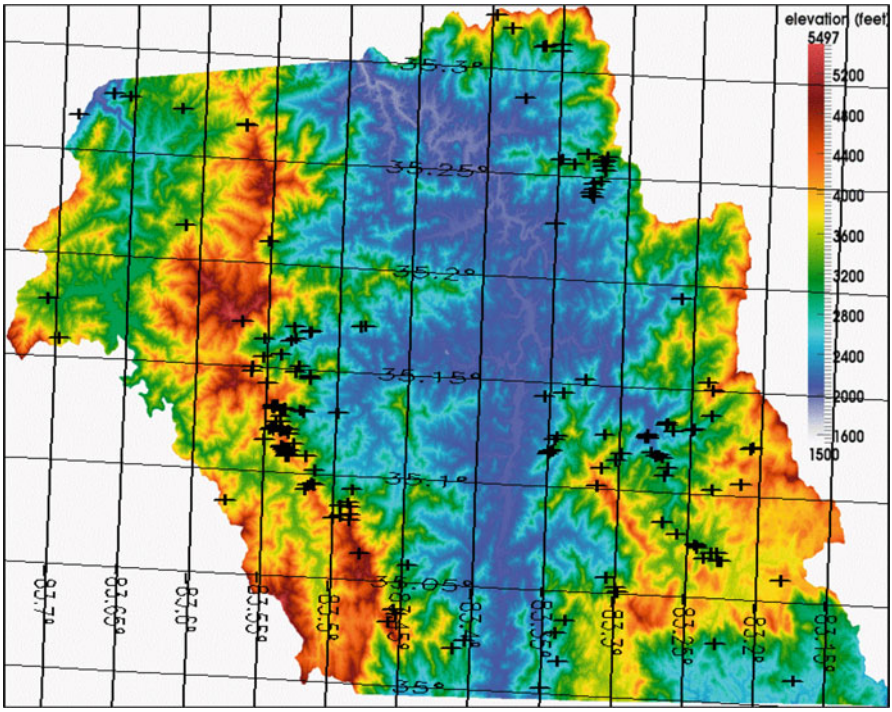

Fig. 6.29 The SEGMENT-Landslide simulation of the Macon County area under a 15 mm uniform precipitation when soil moisture is set at annual mean values. The *cross marks* indicate the landslide-prone areas

was derived from the ARW-WRF in a one-way nested mode with the innermost domain having a horizontal resolution close to the DEM, which is 90 m. The Macon County 6 m DEMs also use 1 km precipitation (i.e., no further downscaling performed). The multiple-level nesting approach circumvents the necessity of dynamic (Pielke et al. 2012) or empirical (Yang et al. 2013 and references therein) downscaling procedures, in order to match the resolutions of model precipitation and topography. The output frequency of WRF is hourly. The Moderate-resolution Imaging Spectroradiometer (MODIS) products (Zhao and Running 2010) provided surface biomass loading. To investigate possible mechanisms, several sensitivity experiments were made with a range of specified vegetation conditions.

6.4.6.3 Technical Skill in the "Pseudo-global Warming" Experiments for Warming Scenario

For simulating future (years 2060–2080) landslide events, WRF is used in the same "pseudo-global warming" approach proposed by Lackmann (2013). There is no simple means of anticipating how future synoptic pattern changes might influence the frequency and severity of those extreme precipitation events that trigger landslides. The experimental design for simulating future extreme precipitation events addresses this issue by replicating the synoptic pattern that caused the August 19–20th precipitation, but imposing possible future large-scale thermodynamic changes. While it is acknowledged that an identical synoptic pattern will not occur in the future, it is reasonable to assume that a similar pattern could occur. Because the model simulation is allowed to evolve dynamically for the duration of the synoptic event, the resulting changes, brought about by imposing thermodynamic perturbations, can also induce dynamical changes. Quantification of projected thermodynamic changes due to increased anthropogenic greenhouse gases is accomplished using an ensemble of Intergovernmental Panel on Climate Change (IPCC) Fourth Assessment Report (AR4) general circulation model (GCM) simulations of monthly temperature, SST, and mixing ratio values. Experiments using the moderate IPCC SRES A1B scenario are used. The August monthly fields were averaged over a subset of five GCMs for which reliable temperature data are available at all vertical levels. These models are: the Bjerknes Centre for Climate Research Bergen Climate Model version 2 (BCCR BCM2), the Centre National de Researches Meteorologiques Coupled Global Climate Model version 3 (CNRM-CM3), the Institute of Numerical Mathematics Coupled Model version 3 (INM-CM3.0), the MaxPlanck Institute (MPI) ECHAM5, and the third climate configuration of the UK Met Office Unified Model (HadCM3). A two-decade average temperature change was then computed from the August monthly averages from the five-member GCM ensemble for the periods (1960–1980) and (2060–2080). Similarly, SST, air temperature at 2 m, and all available variables on isobaric levels were averaged. These spatially varying average fields were interpolated to the same 1° US Global Forecast System (GFS) grid and used for the initial and lateral boundary conditions in the control simulation.

Differences between the 2060s and 1960s decades were computed for each grid cell, and these changes were subsequently added to the original GFS analyses. Given that the landslide event in question took place in August 1969 and that a change is added that was calculated from a 100-year difference, the future simulation can be interpolated as approximating the thermodynamic conditions around the year 2060 that would arise from anthropogenic greenhouse gas forcing alone, under the A1B scenario. The same synoptic weather pattern from August 1960 also characterizes the future simulation, and this fictitious date does not correspond to a specific date in future GCM projections. To resolve the mesoscale evolution of this event, the model domain features a larger outer domain with 27-km grid spacing, along with a 900-m nested innermost domain within which SEGMENT-Landslide is actually run. Vertically, the model uses the default 28-level configuration, with the model top set at 50 hPa. The Betts-Miller-Janjic convective parameterization scheme was used only for the outermost domain. All domains employed the WRF single-moment 6-class microphysics scheme, the Yonsei University PBL scheme, and the National Oceanic and Atmospheric Administration (NOAH) land surface model. Longwave radiation was handled with the Rapid Radiative Transfer Model (RRTM) scheme, and shortwave radiation was the Dudhia scheme. Initial and lateral boundary condition data are from the GFS final analyses on a 1° latitude–longitude grid; simulations were initialized at 00 UTC 14 August 1969 and run for 10 days. For the nested domains, the parent domain provides lateral boundary conditions and one-way nesting is used.

6.4.6.4 Extreme Precipitation Under Future Climate

The present knowledge base of extreme precipitation and its change in a warmer climate is summarized in Appendix B. For storm-triggered landslides, extreme precipitation can be either severe storm (high precipitation rate) lasting several hours, or can be a moderate rain rate lasting several consecutive days. In estimating the recurrence frequency of extreme precipitation from climate model simulations, the definition of extreme precipitation in Ren et al. (2011) is followed. For individual extreme precipitation events such as that of Camille 1969 over Nelson County and its future alike, the precipitation pattern will be compared with its historical precedent. Because hurricanes can play such important roles in this region's extreme precipitation events, future changes in hurricanes that take a similar route as Camille 1969 are investigated in detail.

6.4.6.5 Input DATA over US Appalachians as Required by the Landslides Casual Triads

To account for the stability of slopes, only a full-physics numerical model such as that employed in this study, SEGMENT-Landslide, a surface transport type of model in geomorphology term, is not adequate. Knowledge of the slope material

properties over a large enough neighboring region also is a prerequisite. The following subsections are organized according to the triads of storm-triggered landslide: geological condition, surface loading and vegetation roots, and extreme precipitation.

High-Resolution Digital Elevation Maps (DEMs)

High-resolution elevation data are needed because the ultimate driver for sliding is the uneven surface elevation, as surface elevation gradients generate downward motion. There are various sources for high-resolution DEMs. For example, the National Aeronautic and Space Administration (NASA) Shuttle Radar Topography Mission (SRTM, USGS 2004) provides DEMs of order 10-m resolution. Especially for dynamical simulation of landslides, we expect high-resolution DEMs to represent individual slopes, preferably the graded slope feature for extended slopes. The steepest slope that can be represented by a DEM of 6, 60, 90, 900, 5,000, and 20,000 m resolution are, respectively, 89.77°, 87.71°, 86.56°, 59.0°, 16.7°, and 4.3°. That is to say, it is almost impossible to use DEMs of 1,000 m or coarser to reasonable identify unstable slopes on earth. The landslides of most concern are in the range 100–1000 m. The 90-m ASTER DEMs generally suffice, although they cannot realistically represent the steep upper portion of may extended slopes, which have steep upper slopes and gentle toe slopes (Fig. 6.26b). For the four surveyed counties in North Carolina, 6-m resolution InSAR data is available, which can represent slopes as high as 84°. Over Macon county, the 6-m resolution lidar DEM identified the steepest location as 84.73° at (83.59385 °W, 35.02944 °N), a 1,500 m long slope facing east (most part are >45°). The scarp drops by 66 m in just 6 m distance, forming a cliff. For the InSAR data, a mask is applied to filter out the built-up regions and lakes.

Bedrock Geology

Unlike other forms of natural hazards, landslides are highly multidisciplinary. In addition to surface relief, the bedrock chemical components, foliage, and fabric conditions all are critical for the slope stability. The surface soil and granular debris are primarily from the weathering of bedrock, whereas the portion advected from remote places by runoff or Aeolian processes is minor. If the bedrock contains graphite, the weathered granular material will possess viscosity several orders of magnitude smaller than material not containing these components. The scarp size and orientation of debris flows are co-controlled by chute density and its distribution, and the precipitation morphology. In general, anticlinorium ridges in fault zones containing mesoproterozoic crystalline rocks (biotite augen gneiss, granulite, amphibolite, anorthosite, granite, granodiorite, charnockite, etc.) in its core and flanked by younger gneiss are locations prone to sliding. The rock units with massive or poorly developed in biotite foliation usually are stable bedrocks. Rock

units with a biotite or amphibole foliations (especially larger specs on the cross-sectional surface when broken) and/or gneiss textures are highly susceptible to slope susceptibility. Not only the crops along the Blue Ridge satisfy the required geological conditions, all hills are weathered sufficiently and have plenty of sliding material.

Nelson County is located in the Blue Ridge province, which is a rugged area in central Virginia. As shown in Fig. 6.28c, the Blue Ridge province is an anticlinorium containing Mesoproterozoic crystalline rocks (biotite augen gneiss, granulite, amphibolite, anorthosite, granite, granodiorite, charnockite, etc.) in its core (Rader and Evans 1993). The Blue Ridge province thrusted northwestward over the Paleozoic carbonate rocks of Valley and Ridge and is thrusted by the Piedmont province in the southeast (Bloomer and Werner 1955). Mapped mylonites, anastomosing around lenses of less-deformed or undeformed rocks, represent fault zones with multiple movements (Rader and Evans 1993). In the study region, it is shown that the rock units with a moderate to low susceptibility are massive or poorly developed in biotite foliation. Those with a high susceptibility generally have a biotite or amphibole foliations and/or gneissic textures (Gryta and Bartholomew 1989).

GRACE Measurements

The bedrock crevasses are both pathways and "containers" for fossil ground water. The groundwater changes are measurable by gravity satellites (e.g., Famiglietti and Rodell 2013). It is convenient to discuss the global land water cycle from a net precipitation approach (precipitation minus evaporation), which usually has river runoff getting back to oceans to close the hydrology cycle. However, a small fraction also seeps through the soil and bedrock layers to recharge groundwater aquifers. As bedrock cracks open wider, more runoff will be diverted into drainage percolation and saved in groundwater reservoirs (Eq. 1 in Scanlon et al. 2012). Because the surface runoff to the sea has a turnover time scale of less than a week, this increased replenishment of groundwater is accompanied by local mass variations detectable by gravity satellites such as the GRACE (Voss et al. 2013). Aside from net precipitation and drainage, other factors also may cause perturbations on regional gravity, for example, irrigation projects (Scanlon et al. 2012) and large-scale population and animal migrations. The region of interest has not been affected by these factors during the past several decades. The same precipitation total may mobilize very different amounts of sliding material, as indicated in Fig. 6.30. The density of macroscopic crevasses (an indicator of the bedrock's degree of fracture) is critical in partitioning the received precipitation. However, as a rhizosphere layer generally overlies these cracks, there is no simple means for direct measurements of bedrock crevasses/cracks. The present remote sensing era provides an opportunity to indirectly deduce the bedrock-fracturing situation in the region of interest.

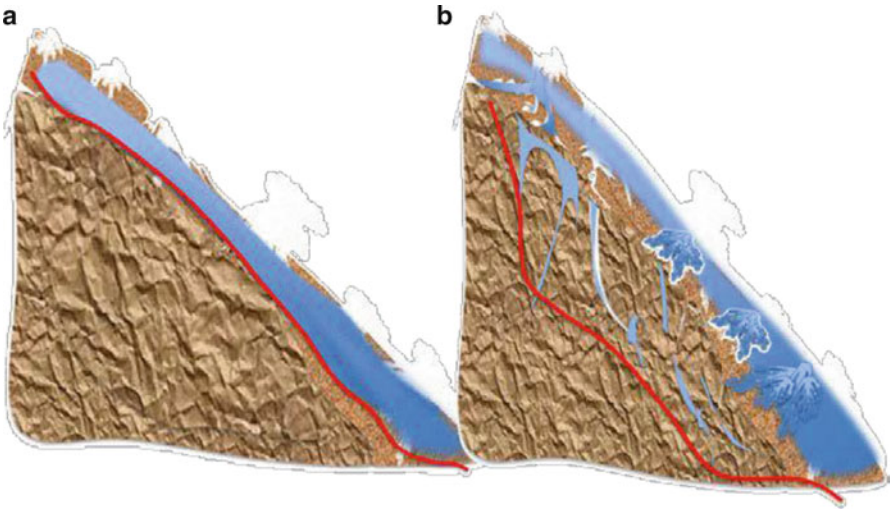

Fig. 6.30 Effects of bedrock cracking. Bedrock crevasses under rhizosphere are usually filled with fine weathered soil (**b**). *Cyan* indicates wet soil and accumulated groundwater. Panel (**a**) illustrates a vertical cross section of a slope, with least fractured bedrock. The shear surface (*red thick line*) is just within the rhizosphere parallel to the saturation front. Panel (**b**) illustrates the situation with same rainfall morphology but underlain by a fractured/cracked bedrock. Through the presence of cracks, the rainfall can saturate a much deeper depth than uniform saturation, so the shear surface is much deeper than in (**a**)

Soil and Vegetation Conditions

For storm-triggered landslides, ideal soil classification should classify soils such that their hydro-mechanical properties could be similar within the same classification. A number of soil classification systems are available, depending on the disciplines and their general engineering or scientific objectives. Some of the most widely used classification systems in the United States are from the U.S. Department of Agricultural (USDA, Eswaran et al. 2002), International (Buol et al. 2003), Unified Soil Classification System (USCS, ASTM 1985), and the American Association of State Highway and Transportation Organization (AASHTO, Hogentogler and Terzaghi 1929). The commonality among these systems is the use of soil particle sizes in dividing soils into different categories of clay, silt, sand, gravel, and large-sized materials, although the boundaries for each of these systems are somewhat different (see Soil Survey Division Staff (1993) for more details). This study uses the USDA classification system. Soil chemical composition also is important for their hydro-mechanical properties. Unfortunately, none of the four classifications are based on soil chemical compositions. In setting spatial variable soil mechanical properties, not only the USDA soil map was used, but also reference was made to the STATSGO soil data for its wealth of vertical profile

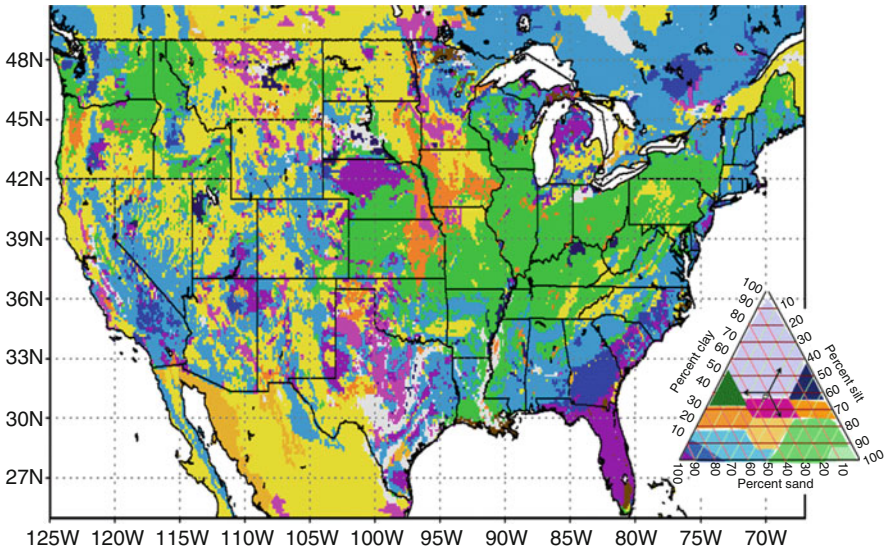

Fig. S2 The predominant surface soil texture obtained from STATSGO. The *inset* is a ternary diagram showing the soil classification as relative percentages of sand, silt, and clay in the basic textural classes. For any point on this phase diagram, the percentages are shown in the three directions (120° in between any two directions), adding to unity. The STATSGO classification includes soil stratigraphy information, which is not shown here as this is just the surface layer

information (Fig. S2). The general ranges of soil mechanical properties are listed in Table 5.3.

The soil mechanical properties are used to parameterize the granular viscosity of the sliding material according to a formula (Ren 2014a). The setting of the bedrock mechanical properties always references the published geological map of the region of interest. However, care needs to be exerted because the documented mechanical strength and viscosity values usually are laboratory-tested results for non-fractured specimens. If there are cracks, the actual values can have orders of magnitude differences. All else being equal (e.g., same lithology, same resting slope, same above ground loading, and similar shearing zone depth), scarp sizes of deep-seated, rotational landslides are proportional to the degree of fracture. This, again, is a granular size issue in a more general sense and follows the similar sigmoid curve in its "ensemble" rock size dependence. In this sense, existing landslide inventories can assist in objectively determining the degree of fracture of the bedrock. If circumstances permit, boreholes should be taken from the sites and the samples tested at loading pressures they would experience in reality. The mechanical properties obtained in this way should be much more representative than from civil engineering handbooks. In setting up the bedrock mechanical strength, the burying depth, in addition to the geologic unit reflecting lithology, should be taken into consideration to reflect the increasing strength of rock with confining pressure.

For vegetated surfaces, especially those affected by fires, representing soils as purely mineral is inadequate (DeBano 2000; Moody and Martin 2001; Smith et al. 2002). For previous fire sites within the last decade, a parameter f_i should be introduced to represent the fraction of soil sublayer "i" that is organic matter. The thermal and hydraulic parameters for organic soil are weighted averages of the corresponding mineral soil and those of humus, using an empirical relationship (Lawrence and Slater 2008).

Compared with the physical properties of hill slopes that affect the potential for landslides, vegetation is far more temporally variable. Choices for land cover maps are: the USGS National Land Cover Dataset 2001 (NLCD 2001; Homer et al. 2004), the International Geosphere-Biosphere Programme Data and Information System's DISCover (IGBP-DISCover, Belward 1996), or the University of Maryland 1 km (Hansen 2001) land cover maps. Although the latter two are derived from the 1992–1993 Advanced Very High Resolution Radiometer (AVHRR) data (Fig. S1), they have slightly different classifications. Fortunately, the differences are primarily around the Polar Regions and do not affect landslide research. In situ archiving of biomass usually is limited to forests with commercial value (e.g., California). In addition to being cost-effective, remote sensing provides the best spatial and temporal coverage of terrestrial biomass. Usually, foliage biomass can be estimated from the Moderate Resolution Imaging Spectrodiometer (MODIS) leaf area index (LAI) products. Aboveground biomass residing in branches

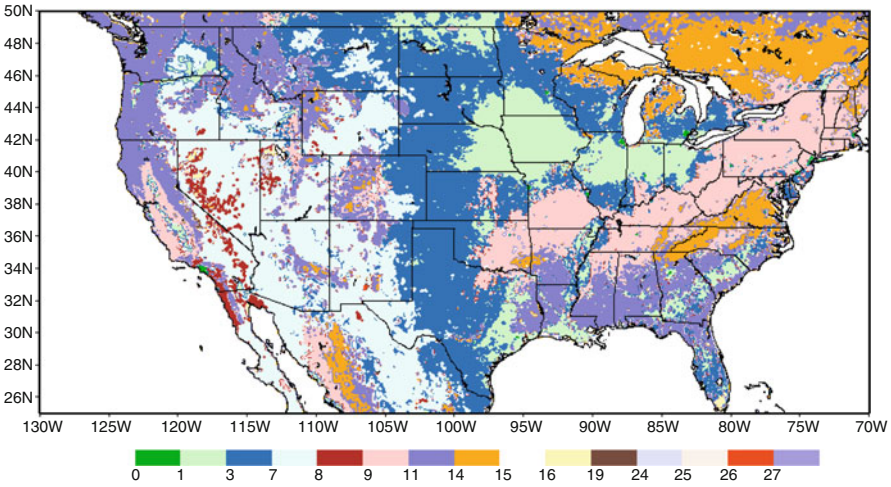

Fig. S1 USGS/EROS 1 km vegetation type. AVHRR products (Townshend 1992). (1) Urban Impenetrable surfaces; (2) Dryland Cropland and Pasture; (3) Irrigated Cropland and Pasture; (4) Mixed Dryland/Irrigated Cropland; (5) Cropland/Grassland Mosaic; (6) Cropland/Woodland; (7) Grassland; (8) Shrubland; (9) Mixed Shrubland/Grassland; (10) Savanna; (11) Deciduous Broadleaf; (12) Deciduous Needle-leaf; (13) Evergreen Broadleaf; (14) Evergreen Needle-leaf; (15) Mixed Forest; (16) Water Surface; (17) Herbaceous Tundra; (18) Wooded Wetland; (19) Barren; (20) Herbaceous Tundra; (21) Wooded Tundra; (22) Mixed tundra; (23) Bareground Tundra; (24) Glaciated; (25) Playa; (26) Lava; (27) White Sand

and stems is then derived from generalized, diameter-based allometric methods (Ren et al. 2009), with reference to the land use map. For example, a unique feature of SEGMENT-Landslide is its treatment of the root properties relevant to storm-triggered landslides according to ecosystem functioning, directly based on root mass allocation of vegetation in the residing climate zone. The partitioning of supporting roots, nutrient absorption roots, and moisture tapping roots affects soil moisture content as well as the mechanical reinforcement effects. In addition, total biomass loading also is assumed to be proportional to aboveground biomass.

As a salient example of the critical role of soil, adding water to sandy soil significantly reduces the ID size (see the Appendix A) and creates a shear surface (the interface between compact, more coherent wet sands and adjacent dry loose sands), thus making the slopes slide-prone. Vegetation effects on slope stability are multifaceted. During the growth season, evapotranspiration and canopy interception of rainfall significantly influence the soil moisture content. Vegetation roots, on the one hand, produce a distributed reinforcement web of the soil particles but, on the other hand, facilitate water (surface runoff) discharge into deeper depths. It is thus likely liquefying a larger volume of sliding material than would result from a uniform saturation from the surface. In SEGMENT-Landslide, these effects are parameterized.

6.4.6.6 Reproducing the 1969 Camille Precipitation

For reproducing the 19–20 August 1969 debris flows that occurred in Nelson County (37.79°N; 78.88°W), spatially distributed, high-resolution precipitation rates are a prerequisite. Because of the complex terrain (a southwest–northeast oriented range. Surface elevations to the west are generally above 3,000 m, i.e., ~800 hPa), precipitation is very patchy. In situ measurements typically are unable to identify the "hot spots" (i.e., locations with extreme precipitation and may have debris flow hazards). Remotely sensed precipitation products were not available in 1969. Nested runs of WRF, with the innermost domain set at 900 m resolution, is the best available approach for that time period.

As shown in Fig. 6.27 (color shading over Domain 3), Camille's rain swath is oriented perpendicular to the Blue Ridge and is exceedingly narrow. There were east-west assembled rainfall maxima, located respectively on the southeast-facing slopes of the Appalachians and the Blue Ridge. This is a result of upslope flow of moisture. Over Nelson County, there was a perfect alignment of the extreme precipitation triads. The low levels accumulated a thick moisture "pool" because of (1) the higher antecedent soil moisture (the summer of 1969 was wet, and at least four periods of intense rainfall occurred over this area from May to early August) and thus strong land surface evapotranspiration; and more decisively, (2) the remnant vortex of Camille produces low-level water vapor convergence, in a similar manner to a low-level jet. The vigorous ascent of moist low-level air is from the synergetic lifting of the remnant vortex, a cold front, and the local topography. During 19–20 August, a cold front passed through central Virginia.

Thick vapor collected south of the cold front, and the along slope uplift was the main factor that organized the aforementioned precipitation pattern. In the intersection of the Blue Ridge and the cold front, moisture was funneled rapidly upward, due to orographic effects. The thunderstorm complex is formed and received a steady, strong moist inflow from the southeast, at low levels. The repeated passage of cloudbursts across Nelson County formed a train of cells sustaining the most intense 6-h precipitation. Within the thunderstorm complex, each individual storm cell has its own life cycle of maturation, movement away from the mountain range, and dissipation. Then new cells formed immediately upwind. This genesis point over Nelson County remained locked to the terrain, for hours. The combination of large-scale atmospheric processes and local topography led to an unprecedented period of heavy rain along the Blue Ridge Mountains.

Primarily because of the severe precipitation, the hills of Nelson County were essentially liquefied. The role of vegetation was minimized. The chute density and distribution determines the scarp size and sliding material redistribution. The generation of sliding material is partly from surface runoff advection, according to the progressive bulking process described by Iverson (1998), but primarily through water percolation in crevasses and scouring out a slope material up to a depth deeper than uniform saturation (i.e., destabilizing a large chunk of slope material through increasing pore pressure). Also noteworthy is that the scarps have no preferred azimuthal orientation (Fig. 6.31).

Using the high spatial and temporal resolution precipitation rates of Camille 1969 provided by the WRF simulation, Fig. 6.31 shows the SEGMENT-Landslide simulated unstable areas, as indicated by the maximum surface elevation changes larger than 2 m. The red marks are archived observations. Under the current vegetation regime, the most significant scar is that near Spicewood cabin (37.84°N; −79.05°W). This particular sliding is a characteristic "progressive bulking" type of debris flow (Iverson 1997). The accumulation area spreads up to 3,600 ft elevation, in a fan shape with the fan "handle" extending downslope. The surface runoff essentially is clear water above the 2,500-ft elevation contour, but at lower elevations it gradually becomes turbid and entrains small stones and coarse granular material into the slide streams. These creeks are usually dry except during rainy periods. Almost all major valleys, with surface opening 10 m or wider, experienced sliding. Also, landslides know no County borders and there is a scarp right across to the south (37.74°N; 79.14°W). Similar scarps are also found for the southeast-facing Three Ridge slopes. However, most of the eastern slopes of the Blue Ridge Mountains suffered deep-seated slides, resulted from rainfall percolation to deeper depth along crevasses (mechanism illustrated in Fig. 6.30). The pattern of the scarps indicates the dual control from precipitation and chute distribution. For example, three southeast-facing slopes near the Lesesne State Forest, Massies Mill, VA (37.845°N, 78.98°W) clearly experienced creek bank failure. While the hardest hit slopes, or those near Dillard Creek (37.79°N, 78.89°W), are a mixture type of progressive bulking and deep-seated sliding. Wherever the surface topography favors runoff convergence, the greater the volume of sliding material volume. Within a ~70 km^2 region (37.75–37.85°N; 78.85–78.96°W), the total

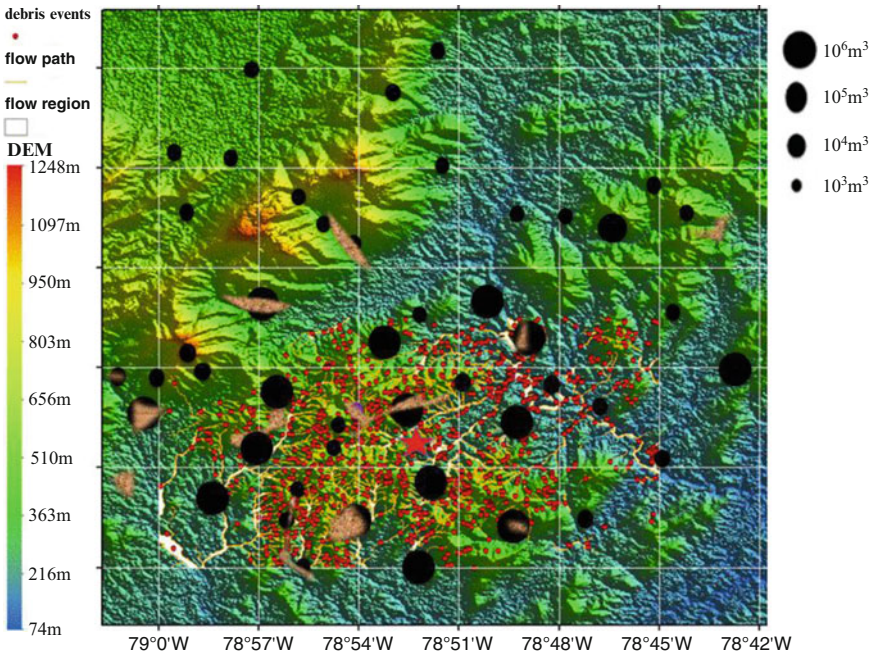

Fig. 6.31 SEGMENT-Landslide simulated landslides after Camille 1969. Red star is the cluster center of the identified scarps. The sizes of the *black dots* are proportional to the volume of the involved sliding material. The *red marks* are archived observations. Scarps are still identifiable are shown as tapered shades. Courtesy Drs. Xiyi Shen at University of Oklahoma and Frank Yu at Curtin University

sliding material involved is about 4.7×10^6 m^3. While critical for major landslides, crevasses underneath the rhizosphere are challenging for in situ surveys, because they are obscured by surface soils and vegetation. These crevasses are also the major pathways for recharging ground water. Gravity measurements from GRACE can be used to deduce the underground chute condition. If local mass changes closely follow the precipitation changes and there is no major earthquake jolt and major infrastructure construction, the underground chute system is stable. Because of the rainfall's patchiness, especially over complex terrain (Orlanski 1982), even dense observational stations cannot guarantee the representativeness of the measurements. The annual net primary production (NPP) over a large area, however, is a good indicator of annual precipitation (Zhao and Running 2010). The area average annual NPP also serves as a smoother/filter for the spatial rainfall heterogeneity and reflects the changes in area total precipitation accurately. In the following analysis, the annual area averaged NPP time series is used as surrogates for precipitation variations over the past decade, to close the dominant term in regional mass balance.

The GRACE measurements (2003-present) over the region of interest (82–75°W; 35–41°N, framed in Fig. 6.32a) show systematic and 100-km spatial

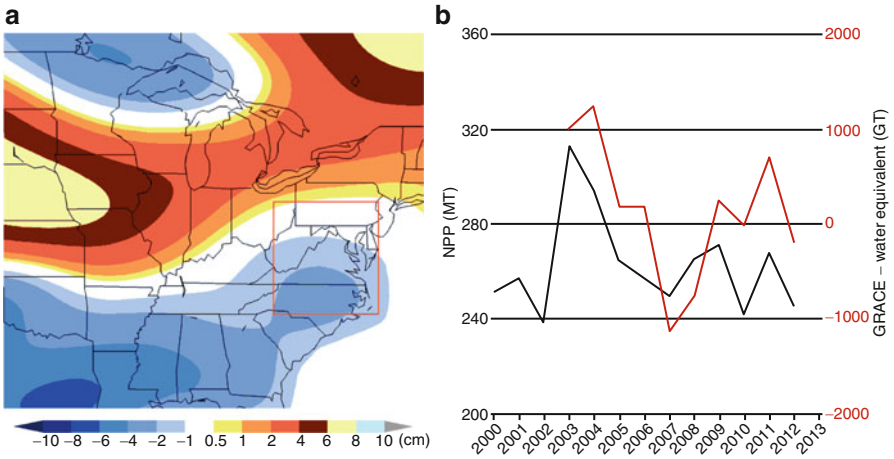

Fig. 6.32 Mass changes from GRACE over the 2003–2013 period (in water depth equivalent, cm). For convenience, it is subdivided into two 5-year periods. The differences between the two periods are plotted, that is (2009–2013) minus (2003–2008) values. The region of interest shows moderate mass change signals. Panel (**b**) shows (*red line*) area averaged mass changes (in GT, or 10^{12} kg), relative to 2003 levels, for the Virginia region of interest. A good indicator of precipitation, the Net Primary Production (NPP), is plotted (*black lines*) to show possible trends in precipitation. This region's mass changes have strong correlations with precipitation

scale consistent signals of mass loss (blue colors in Fig. 6.32a) and mass gain (red colors). The surrounding regions experienced slight mass losses during the past decade. There also have been no large-scale population and animal migrations in the past decade, and there are no large hydraulic projects that can persistently affect the region of interest. The only possible cause of regional mass fluctuation (as sensed by GRACE) is in the water/fluids mass changes. The GRACE measurements follow closely the NPP curve (Fig. 6.32b), indicating that the portion going to drainage from total precipitation is approximately constant. This is a clear indication of the stability of the chute system. Without external causal factors such as earthquakes that might further disintegrate the bedrock over the region, the key reason to remain alert for possible subsequent natural hazards is impending extreme precipitation events. The past decade is a relatively dry period over the region of interest. The increasing precipitation, and hence the increasing fluids accumulated as groundwater, will make future landslides more severe and more frequent. Looking further ahead, the pattern of mass changes creates a saddle structure in the vicinity of Nelson County. The exerted stress might cause strain build up and cause further crack development.

There are 6-m DEMs over the Nelson County. A sensitivity experiment is performed, assuming a uniform 15-cm rainfall in a day precipitation scenario. The cross marks are places that will suffer significant mass changes. The USGS surveyed present scarps, primarily those left by hurricane Ivan (Sept. 15–18) and Frances (Sept 5–8, 2004), are a subset of the marked unstable slopes. The slopes that can be represented by the 6-m DEM have no preferred north-orientation

Table 6.2 Azimuth angle (counterclockwise from due east) and slope angle from the 168 scarps

Azimuth angle											
0–30	30–60	60–90	90–120	120–150	150–180	180–210	210–240	240–270	270–300	300–330	330–360
27	8	9	14	9	8	7	3	6	8	7	11
Slope angle											
0–18			18–42			42–66			66–90		
25			13			71			8		

components. However, the slopes prone to slide have an apparent azimuthal preference (Table 6.2). Over 70 % of the unstable slopes have a north-facing component. The most unstable slope segments are those with repose angles between 42° and 66° (for deep-seated large-scale scarps) and less than 18° for progressive bulking-type slides/debris flows. The orientation preference results from vegetation roots preventative effects. In this moist climate zone, north-facing slopes tend to be grass slopes.

Outside this domain, we have only ~90-m ASTER DEMs. Similar experiments identify the Black Mountain Valley as very unstable. The Black Mountain forms a U-shaped semicircle that opens to the northwest. This configuration, in addition to the orographic effects on precipitation, also favors surface runoff confluence and the collection of debris and granular sliding material (Fig. 6.26a). At present, it is well covered by forest (firs at higher elevation and Eastern Hemlock trees at lower elevation) and this is a stable effect as only <0.01 % of the slope area is unstable at present for extreme precipitation, mostly northeast-facing slopes. In the future, removal of these trees either by insects or by deforestation associated with rapid population growth may significantly increase the landslide threats. The Black Mountain form of landslides is not unusual for progressive bulking type of landslides. A configuration even more favorable for sliding is that such a geographical feature is further nested in a larger range that also has strong orographic enhancement to precipitation.

6.4.6.7 Future Camille-Like Extreme Precipitation Events and Landslide Scarps

Compared to the washout rate, the accumulation rate of granular sliding material is much slower. The availability of granular material on the slopes is the first prerequisite for landslides. Thus, steep slopes are at one end and the weathered granular mantle is at the other end for slope instability. Because the region of interest has no lack of sliding material, and the chute system and underground crevasses are in a stable state, future storm-triggered landslides depend primarily on changes in extreme precipitation. How much sliding material can be mobilized on an unstable slope is co-determined by slope hydrology and precipitation morphological characteristics (i.e., total amount as well as intensity distribution). For thoroughly

fractured slopes, how much rainfall is infiltrated or drained into the ground is a key parameter for estimating the landslide magnitude (Ren 2014b). For the case of intense bursts, there is insufficient time to infiltrate. The surface runoff, when it enters crevasses, percolates to greater depths, creating a shear zone much deeper than uniform wetting can reach. The landslide magnitude thus is much larger for the intense storm case. The weight of rainfall is negligible in aiding the driving stress. However, if it can be effectively channeled into the interface between non-fractured bedrock and the overlain granular lump, the effect on reducing the maximum resistive stress is significant. In addition, the concentrated water column inside the crevasses will exert a hydrostatic horizontal direction differential pore pressure, aiding the driving stress in overcoming the resistive stress. Once the driving stress and the differential pore pressure together exceed the reduced (by drainage lubrication) maximum available resistive stress, the entire layer is set into motion; even through most of the soil inside this layer still is dry. In contrast, if the precipitation is retained entirely in the upper shallow layer and does not discharge into a deeper layer, only a very shallow layer is mobilized and this layer, by entraining drier material, quickly loses its fluidity and might stop mid-slope. Thus, any future changes in precipitation morphology and structure characteristics can have direct effects on storm-triggered landslides. This especially is the situation for graded slopes (those extended slopes as illustrated in Fig. 6.26b). There are also examples in which medium followed by severe rainfall intensity maximizes the sliding material gain. For example, for nonuniform graded slopes, at medium rainfall rates, sliding material cannot slide all the way to toe, and stops mid-slope. The next intense rainfall event then is capable of sending the material to the toe, entraining along the way at a significantly larger rate, because the entrainment process is nonlinearly related to the instantaneous amount of sliding material.

To estimate possible changes in future extreme precipitation events, WRF was run with thermodynamic changes computed from the small five-member IPCC GCM ensemble output, under the A1B emission scenario applied to the initial and lateral boundary conditions for this event. The resulting simulation is a replication of a highly similar synoptic pattern to that of the control simulation, but within a projected future thermodynamic environment. Over the region of interest, the increased atmospheric water vapor as a direct thermodynamic consequence of warming, or a robust vapor increase consistent with the Clausius-Clapeyron relationship, still holds (Karl and Knight 1998; Semenov and Bengtsson 2002; Groisman et al. 2005). In addition, precipitation in the Appalachians also is strongly influenced by orographic effects, which was the case for the precipitation pattern from Camille 1969.

Figure 6.33 is the resulting precipitation changes. Figure 6.33a is the WRF simulated Camille 1969 like extreme precipitation event caused total precipitation over Domain 3 under a warming climate condition, the SRES A1B scenario in the 2060–2080 time frame. Compared with the actual Camille 1969 event, future such events are expected to have similar spatial patterns (c.f. Figs. 6.27 and 6.33a). Compared to the control run (Fig. 6.27, under current climate), the spatial maximum value has increased from 850 to 900 mm. The grid point that receives this

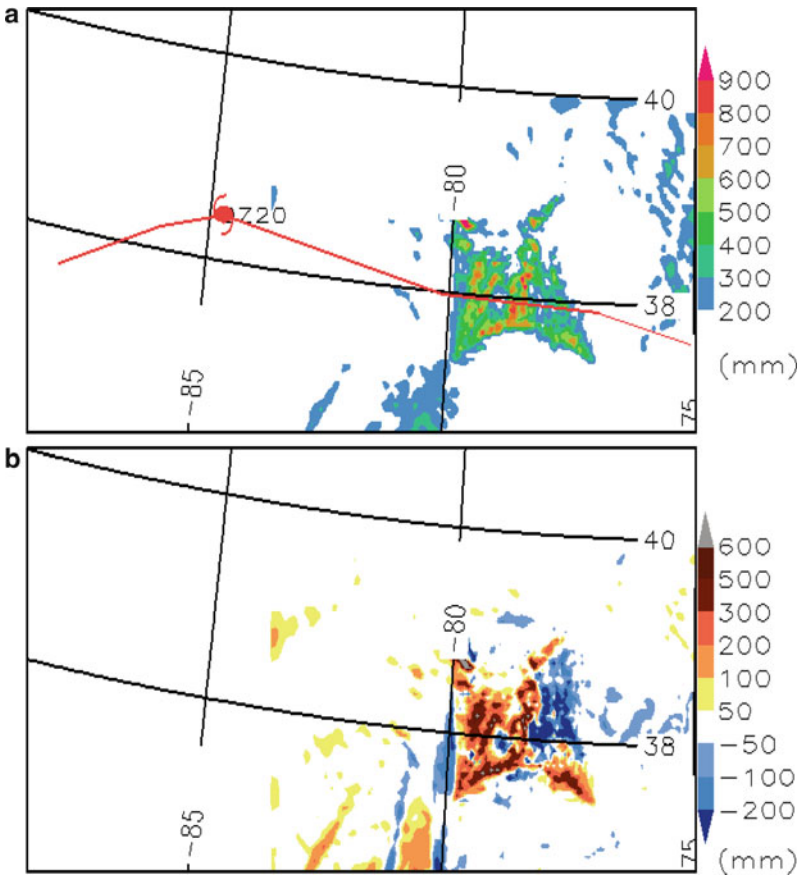

Fig. 6.33 WRF simulated total precipitation over Domain 3 under a warming climate scenario (Panel a, SRES A1B scenario) from a Camille (1969)-like extreme precipitation event. Panel (**b**) is the differences between SRES A1B and current climate (Fig. 6.27, Control). Comparison of (**a**) with Fig. 6.27 indicates that the maximum value has increased from 850 to 900 mm. However, panel (**b**) indicates that the increase does not occur over the entire domain, as there are locations that received less rainfall. Compared with the Control run, the rainfall distribution is more concentrated and has shifted westward

maximum rainfall amount does not always correspond to the same geographic location. Also, the increase in precipitation amount does not occur throughout the domain, and there are places receiving decreased rainfall as the climate warms (blue color shades in Fig. 6.33b). The time series of accumulated total precipitation amount (in 10^9 m^3, figure not shown) in Domain 5 indicates that total precipitation differs less than 2 %. At the time of slope liquefaction the difference in the total amount of rainfall in the simulation domain is not significant. Zooming into the slope of interest, however, reveals that the precipitation doubles, reaching ~200 mm in the first hour. Compared with the control case, the distribution is more

concentrated and shifted westward. The cluster center of future landslide scarps also shifts northwestward accordingly about 30 km. Thus, a warmer climate might signify a more spatially concentrated rainfall distribution, with important landslide consequences.

The above results are in general agreement with the Allen and Ingram (2002) hypothesis regarding the climate response of extreme precipitation to increased air temperature resulting from increased atmospheric concentration of greenhouse gases. While frontal passages are regular events, hurricanes are more irregular and bring moisture into the region of interest. Extreme precipitations over Appalachians are frequently affected by TC remnants (from those in the north Atlantic Basin, Fig. 6.25). It is notable that TC remnants can, on the one hand, enhance instability by moistening the low level and, on the other hand, the cyclonic vorticity input to the upper-level circulation also is a lifting mechanism (contributing to slantwise instability). In Fig. 6.25, tracks of 17 severe (Category 3 and above) hurricanes, which brought extreme precipitation over the region of interest, defined by a $3^\circ \times 3^\circ$ black box centered at Nelson County, Virginia, since Camille (i.e., for the period 1969–2012), are plotted. They generally follow three paths: western paths such as Ivan (2004), central paths (David 1979), and eastern paths (Floyd 1999). Except for Camille and Eloise (1975), all 15 remaining hurricanes occurred during the satellite era and the International Best Track Archive for Climate Stewardship (IBTrACS, Kruk et al. 2010; http://www.ncdc.noaa.gov/oa/ibtracs/) data are reliable. To estimate future changes in the TC tracks, a tracker scheme is used (Ren et al. 2014) to identify TCs from the climate model simulated atmospheric fields. The changes in hurricane activity in the Atlantic basin also are examined. As the climate warms, the frequency of occurrence does not wary much but the intensity increases systematically with time. Under the current climate, it is very rare that two hurricanes occur simultaneously and travel north to affect the region of interest. Under a future warming climate, the changes are such that the trailing vortex of the major hurricane also develops into a categorical tropical cyclone. The major TC takes the west route and the secondary one takes the east route and heading north simultaneously. This situation causes very strong precipitation and the resultant landslides also are of larger scale. Although the overall TCs do not have significant increase in occurrence frequency, it is found that the "western path" category has a significant increase, especially after 2040 when approximately every 5 years will experience such a TC. This primarily is caused by the expansion of subtropical high.

Table 6.3 lists all the potential landslide scarps identified by SEGMENT-Landslide under a similar precipitation scenario as Camille 1969 but occurring in the 2060–2080 time range. These locations have thus far not recorded storm-triggered landslides, but this study suggests that they be earmarked for future attention. Among these listed scarps, the valley near Shenandoah National Park (38.3°N, 78.7°W) has perfect condition for storm-triggered landslides.

Table 6.3 The most endangered locations in the Appalachians during the 2060–2080 time frame

Lat	Lon	Lat	Lon
36.925	−80.176	37.85	−81.87
36.82	−80.31	36.12	−83.16
38.455	−78.437	36.08	−83.07
38.45	−78.44	35.4	−80.0
38.6	−78.34	35.998	−82.689
38.228757	−78.693	36.01	−82.676
38.314	−78.58	35.96	−82.657
37.933	−78.92	35.928	−82.622
37.74	−79.14	35.6272	−82.25
37.84	−79.0	35.625	−84.14
37.677	−79.588	36.382	−81.945
37.62	−79.64	38.782	−79.297
37.37	−80.2	38.12	−76.79
37.62	−80.01	39.10	−84.822
37.61	−80.0	40.387	−79.756
38.44	−78.35	37.83	−79.0
38.42	−78.36	37.8	−78.9
38.46	−78.44	37.85	−78.98
38.5	−78.35	37.845	−78.97
38.05	−81.96	37.74	−79.14
38.08	−81.98	37.83	−79.55
37.76	−81.736	37.38	−80.17
37.42	−80.22	37.48	−80.13
37.35	−80.4	38.30	−78.70
38.81	−78.5	38.91	−78.37
37.3	−80.79	37.4	−80.48

6.4.6.8 Perspective of the Future Appalachian Storm-Triggered Landslides

The Camille event occurred in the pre-satellite era and the simulated rainfall can only be verified with local witness accounts, media reports, and indirect observations and the extremely fast increasing water levels in the creeks. The model simulated dynamic and thermodynamic features, however, are convincing and form the basis for a series of experiments on climate sensitivity using the hypothesis of Lackmann (2013). The experiments conducted with WRF model suggest that this type of highly localized, heavy rain, as a result of an interaction of synoptic-scale weather systems with the mesoscale tropical cyclone and topographical features, will be enhanced in magnitude in a warmer climate.

Because the well-developed chutes and gullies in the Blue Ridge and Appalachian Mountains, storm-triggered landslides can take the form of progressive

bulking or of deep-seated, large-scale slope instability, depending on the morphology of extreme precipitation. Land cover plays an important preventative role for the progressive bulking form of landslides. Very large drainage/percolation may render the protective roots ineffective. This also explains why, although the slopes in general are randomly oriented, the unstable slopes tend to have a north-facing component for the northern portion of the Appalachians and also tend to have a southerly component for the Black Mountains and the hills within Macon County. In a future warmer climate, extreme precipitation tends to have larger magnitude and may also occur more frequently. As a result, more frequent occurrence of storm-triggered landslides can be expected. The cluster center of the landslide scarps shifts westward, as a result of the shift of the hurricane storm tracks. As karst landform is common over the region, even neighborhoods outside historical or geological river channels are no longer safe. Reducing global wide GHGs emission is an approach generally accepted as most likely to mitigate such anticipated disasters.

In summary, in the US Appalachians, concave valleys that favor the convergence of surface runoff are the primary locales for landslides. If the slopes are weathered to the same degree and have the same vegetation coverage, slope orientation (azimuthal) is not critical for slope stability. However, it is found that for the region south of the Black Mountains (North Carolina), north-facing slopes are more prone to slide, because the northern slopes usually are grass slopes for the regions not limited by annual precipitation (water availability). For the slopes of the Blue Ridge Mountains, south-facing slopes are more prone to slide. Deforestation and topsoil erosion are critical contributors to the massive sizes of the debris flows. Gravity measurements over the past decade reveal that geological conditions, the chute system, and underground cracks over the region are stable, and sliding material is plentiful. Future changes in storm-triggered landslide frequency are primarily controlled by changes in extreme precipitation. Thus, a series of ensemble climate model experiments is carried out of possible changes in future extreme precipitation events, using the WRF model forced by temperature perturbations. The focus is the impact on storm-triggered landslides, and over 50 locations are identified as prone to future landslides. In a future warmer climate, more severe extreme precipitation events are projected because of increased vapor content and more frequent passage of tropical cyclone remnants. There also is a likely shift of tropical cyclone tracks and associated extreme precipitation, and the Appalachians scarps cluster center is expected to move westward.

References

Allen M, Ingram W (2002) Constraints on future changes in climate and the hydrologic cycle. Nature 419:224–232

Balkema A, de Haan L (1974) Residual lifetime at great age. Ann Probab 2:792–804

Berger A, Loutre M (2002) An exceptionally long interglacial ahead? Science 297:1287–1288

Berry G, Reeder MJ, Jakob C (2011) A global climatology of atmospheric fronts. Geophys Res Lett 38:L04809. doi:10.1029/2010GL046451

Bloomer RO, Werner HJ (1955) Geology of the Blue Ridge region in central Virginia. Geol Soc Am Bull 66:579–606
Bolt B, Horn W, Macdonald G, Scott R (1975) Geological hazards. Springer, New York, NY, 328 pp
Brennan MJ, Lackmann GM, Mahoney KM (2008) Potential vorticity (PV) thinking in operations: the utility of nonconservation. Weather Forecast 23:168–182
Browning K, Pardoe C (1973) Structure of low-level jet streams ahead of the mid-latitude cold fronts. Q J Roy Meteorol Soc 99:619–638
Burrough P, McDonnell R (2004) Principles of geographical information systems: spatial information systems and geostatistics. Oxford Univ. Press, Oxford
Casadei M, Dietrich W, Miller N (2003) Testing a model for predicting the timing and location of shallow landslide initiation in soil-mantled landscapes. Earth Surf Processes Landf 28:925–950
Coles S (2001) An introduction to statistical modeling of extreme values, Springer Series in Statistics. Springer, New York, NY, p 224. ISBN ISBN-10: 1852334592
Darnard B (1971) A numerical study of the effects of long wave radiation and surface friction on cyclone development. Mon Weather Rev 99:831
Davis C, Emanuel KA (1991) Potential vorticity diagnostics of cyclogenesis. Mon Weather Rev 119:1929–1953
Davis C, Stoelinga M, Kuo Y (1993) The integrated effect of condensation in numerical simulations of extratropical cyclogenesis. Mon Weather Rev 121:2309–2330
Debano L (2000) The role of fire and soil heating on water repellency in wild land environments: a review. J Hydrol 231–232:194–206
Didone M (2006) Performance and error diagnosis of global and regional NWP models. PhD thesis, Swiss Federal Institute of Technology (ETH) Zurich. 124 pp
Ding Y (1991) Advanced synoptic meteorology. China Meteorologocal Press, Beijing, p 792
Eckhardt S, Stohl A, Wernli H, James P, Forster C, Spichtinger N (2004) A 15-year climatology of warm conveyor belts. J Climate 17:218–237
Field PR, Wood R (2007) Precipitation and cloud structure in midlatitude cyclones. J Climate 20:233–254
Groisman PY, Knight RW, Easterling DR, Karl TR, Hegerl GC, Razuvaev VN (2005) Trends in intense precipitation in the climate record. J Climate 18:1326–1350
Groisman PY, Knight RW, Karl TR (2012) Changes in intense precipitation over the Central United States. J Hydrometeor 13:47–66
Gryta JJ, Bartholomew M (1989) Factors influencing the distribution of debris avalanches associated with the 1969 Hurricane Camille in Nelson County, Virginia. Geol Soc Am Spec Pap 236:15–28
Harrold T (1973) Mechanisms influencing the distribution of precipitation within baroclinic disturbances. Q J Roy Meteorol Soc 99:232–251
Held IM, Soden BJ (2006) Robust responses of the hydrological cycle to global warming. J Climate 19:5686–5699
Homer C, Huang C, Yang L, Wylie B, Coan M (2004) Development of a 2001 national landcover database for the United States. Photogr Eng Rem Sens 70:829–840
Iverson R (1997) The physics of debris flows. Rev Geophys 35:245–296
Kalnay E, Kanamitsu M, Baker W (1990) Global numerical weather prediction at the National Meteorological Center. Bull Am Meteorol Soc 71:1410–1428
Karl T, Knight R (1998) Secular trends of precipitation amount, frequency, and intensity in the USA. Bull Am Meteorol Soc 79:231–241
Kleist DT, Parrish DF, Derber JC, Treadon R, Wu W-S, Lord S (2009) Introduction of the GSI into the NCEP Global Data Assimilation System. Weather Forecast 24:1691–1705
Knippertz P, Wernli H (2010) A Lagrangian climatology of tropical moisture exports to the Northern Hemispheric extratropics. J Climate 23:987–1003
Krishnamurti T (1968) A study of developing wave cyclone. Mon Weather Rev 96:208–217

Lackmann GM (2002) Potential vorticity redistribution, the low-level jet, and moisture transport in extratropical cyclones. Mon Weather Rev 130:59–74
Lackmann G (2013) The south-central US flood of May 2010, present and future. J Climate 26:4688–4709
Lawrence D, Slater A (2008) Incorporating organic soil into a global climate model. Clim Dyn 30:145–160
Li Y, Cai W, Campbell E (2005) Statistical modelling of extreme rainfall in Southwest Western Australia. J Climate 18:852–863
Ma D, Qi L (1997) Study on comprehensive controlling of debris flow hazards in Sanyanyu Gully. Bull Soil Water Conserv 17:26–31
Moody JA, Martin D (2001) Hydrologic and sedimentologic response of two burned watersheds in Colorado. USGS Water Resources Investigations Report
Montgomery M, Farrell B (1991) Moist surface frontogenesis associated with interior potential vorticity anomalies in a semigeostrophic model. J Atmos Sci 48:343–367
Namias J (1950) The index cycle and its role in the general circulation. J Meteor 7:130–139
Newell R, Newell N, Zhu Y, Scott C (1992) Tropospheric rivers? - a pilot study. Geophys Res Lett 19:2401–2404
Orlanski I (1982) Orographically induced vortex centers. Proceedings of the First Sino-American Workshop on Mountain Meteorology, May 1982. Science Press, Beijing, 699 pp
Pall P, Allen MR, Stone DA (2007) Testing the Clausius-Clapeyron constraint on changes in extreme precipitation under CO_2 warming. Climate Dyn 28:351–363
Pielke R et al (1992) A comprehensive meteorological modelling system-RAMS. Meteorol Atmos Phys 49:69–91
Ren D, Leslie L, Fu R, Dickinson R (2011) Predicting storm-triggered landslides and ecological consequences. Bull Am Meteorol Soc 91, doi: 10.1175/2010BAMS3017.1
Ren D, Leslie L, Karoly D (2007) Sensitivity of an ecological model to soil moisture simulations from two different hydrological models. Meteorol Atm Phys 100:87–99
Ren D, Leslie LM, Karoly D (2008) Mudslide risk analysis using a new constitutive relationship for granular flow. Earth Interact 12:1–16
Ren D, Leslie L, Fu R, Dickinson R (2011) Predicting storm-triggered landslides and ecological consequences. Bull Am Meteorol Soc 92:129–139. doi:10.1175/2010BAMS3017.1
Ren D, Fu R, Leslie LM, Dickinson R (2011) Modeling the mudslide aftermath of the 2007 southern California wildfires. J Natural Hazards. doi:10.1007/s11069-010-9615-5
Ren D, Wang J, Fu R, Karoly D, Hong Y, Leslie LM, Fu C, Huang G (2009) Mudslide caused ecosystem degradation following Wenchuan earthquake 2008. Geophys Res Lett 36, doi:10.1029/2008GL036702
Ren D, Lynch MJ, Leslie LM, LeMarshall J (2014) Sensitivity of tropical cyclone tracks and intensity to ocean surface temperature: four cases in four different basins. Tellus A 66: 24212. http://dox.doi.org/10.3402/tellusa.v66.24212
Ren D (2014) The devastating Zhouqu Storm-triggered debris flow of August 2010: Likely causes and possible trends in a future warming climate. J Geophys Res 119(7):3643–3662. doi:10.1002/2013JD020881
Rotunno R, Klemp J, Weisman M (1988) A theory for strong, long-lived squall lines. J Atmos Sci 45:463–485
Sanders F, Gyakum JR (1980) Synoptic-dynamic climatology of the “bomb”. Mon Weather Rev 108:1589–1606
Scanlon BR, Faunt CC, Longuevergne L, Reedy RC, Alley WM, McGuire VL, McMahon PB (2012) Groundwater depletion and sustainability of irrigation in the US high plains and central valley. Proc Natl Acad Sci 109(24):9320–9325
Schafler A, Dornbrack A, Wernli H, Kiemle C, Pfahl S (2011) Airborne lidar observations in the inflow region of a warm conveyor belt. Q J Roy Meteorol Soc 137:1257–1272. doi:10.1002/qj.827

Schmidt K, Roering J, Stock J, Dietrich W, Montgomery D, Schaub T (2001) The variability of root cohesion as an influence on shallow landslide susceptibility in the Oregon Coast Range. Can Geotech J 38:995–1024
Semenov V, Bengtsson L (2002) Secular trends in daily precipitation characteristic greenhouse gas simulation with a coupled AOGCM. Climate Dynam 19:123–140
Sidle R (1992) A theoretical model of the effects of timber harvesting on slope stability. Water Resour Res 28:1897–1910
Skamarock WC et al. (2008) A description of the advanced research WRF version 3. Tech. Rep. NCAR/TN-4751STR, 113 pp
Smith R, Smettem K, Broadbridge P, Woolhiser D (2002) Infiltration theory for hydrologic applications, vol 15, Water resources monograph. American Geophysical Union, Washington, DC
Stephens GL, Ellis TD (2008) Controls of global-mean precipitation increases in global warming GCM experiments. J Climate 21:6141–6155
Stoelinga M (1996) A potential vorticity-based study of the role of diabatic heating and friction in a numerically simulated baroclinic cyclone. Mon Weather Rev 124:849–874
Tracton M (1973) The role of cumulus convection in the development of extratropical cyclones. Mon Weather Rev 101:573–593
Trapp RJ, Diffenbaugh NS, Brooks HE, Baldwin ME, Robinson ED, Pal JS (2007) Changes in severe thunderstorm environment frequency during the 21st century caused by anthropogenically enhanced global radiative forcing. Proc Natl Acad Sci U S A 104:19 719–19 723
Trenberth KE (1999) Conceptual framework for changes of extremes of the hydrological cycle with climate change. Clim Change 42:327–339
Van der Veen C, Whillans I (1989) Force budget: I. Theory and numerical methods. J Glaciol 35:53–60
Vaidya S, Kulkarni J (2007) Simulation of heavy precipitation over Santacruz, Mumbai on 26 July 2005, using numerical model. Meteorol Atm Phys 98:55–66
Voss K, Famiglietti J, Lo M, de Linage C, Rodell M, Swenson S (2013) Groundwater depletion in the Middle East from GRACE with implications for transboundary water management in the Tigris-Euphrates-Western Iran region. Water Resour Res 49:904–914
Wentz FJ, Ricciardulli L, Hilburn K, Mears C (2007) How much more rain will global warming bring? Science 317:233–235
Wernli H, Dirren S, Liniger M, Zillig M (2002) Dynamical aspects of the life cycle of the winter storm 'Lothar' (24–26 December 1999). Q J Roy Meteorol Soc 130:405–429
Wilks D (2011) Statistical methods in the atmospheric sciences, vol 100, 3rd edn, International geophysics series. Elsevier, San Diego, CA, 676 pp
Wooten R, Gillon K, Witt A, Latham R, Douglas T, Bauer J, Fuemmeler S, Lee L (2008) Geologic, geomorphic, and meteorological aspects of debris flows triggered by Hurricanes Frances and Ivan during September 2004 in the southern Appalachian Mountains of Macon county, North Carolina (southeastern USA). Landslides 5:31–44
Xue M, Wang D, Gao J, Brewster K, Droegemeier K (2003) The advanced regional prediction system (ARPS), Storm-scale numerical weather prediction and data assimilation. Meteorol Atmos Phys 82:139–170
Yu B, Yang Y, Su Y (2010) Research on the giant debris flow hazards in Zhouqu county, Gansu province on August 7, 2010. J Eng Geol 18:437–444
Zhang X, Kondragunta S (2006) Estimating forest biomass in the USA using generalized allometric models and MODIS land products. Geophys Res Lett 33:L09402. doi:10.1029/2006GL025879
Zhao M, Running S (2010) Drought-induced reduction in global terrestrial net primary production from 2000 through 2009. Science 329:940–943
Zhu Y, Newell R (1994) Atmospheric rivers and bombs. Geophys Res Lett 21:1999–2002

Chapter 7
Changes in Extreme Precipitation in a Future Warming Climate

Using projected meteorological parameters (primarily precipitation) from a weather prediction model, SEGMENT-Landslide (and other 3D hydraulic landslide models) can assist in predicting future storm-triggered landslides. However, mostly, this strong coupling mostly is unnecessary as storm-triggered landslides always are associated with extreme precipitation. Thus, a more efficient strategy is to determine the rainy season for a given region and run SEGMENT-Landslide only for the rainy season. Using SEGMENT-Landslide in this manner is critically important for mitigating landslide damage to existing infrastructure and settlement communities. Another important application of SEGMENT-Landslide is in the planning for future construction of important infrastructure and human settlement, as the population increases.

The first order response to a warming climate from the atmosphere is and uplift of the entire air mass's weight center. Thus, if one examines the geopotential heights (of any pressure level above ground, say 588 dm contour lines for ~500 mb) at two time levels separated by 30 years, one will notice that the area confined by the 588 dm isoline expands. The expansion is a global phenomenon but is not globally uniform (Fig. 7.1). The region shown in Fig. 7.1 is located at remote Southern Hemisphere and "heat-island" effects (from cities) are minimal. The expansion is primarily from anthropogenic warming from CO_2 emission, which is more evenly distributed globally on annual and longer time scales. The changes in air mass redistribution have profound influences on the atmospheric circulation. With the circulation changes, there come many changes in the atmospheric rain makers. For example, with the expansion of the subtropical high, North Western Pacific and North Atlantic tropical cyclone tracks tend to be more inland. Analogously, the first response from ocean to global warming is a general deepening of the mixed layer and the thermocline. This again is a global phenomenon but is also nonuniform for the global basins. For example, due to the limited size, the Walker circulation over Indian Ocean is weaker than that over Pacific Ocean. The primary heating is through turbulent mixing rather than the advective effects from trade winds. From coupled AOGCM runs (J. Luo, personal communication 2012), the

© Springer International Publishing Switzerland 2015

D. Ren, *Storm-triggered Landslides in Warmer Climates*,
DOI 10.1007/978-3-319-08518-0_7

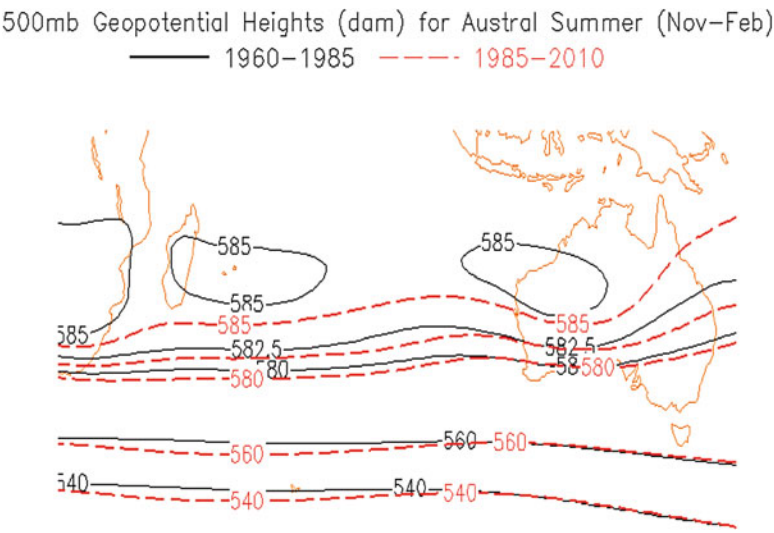

Fig. 7.1 Signs of climate warming during the past 50 years, as indicated by changes of 500 mb geopotential heights for Austral summer. NCEP/NCAR reanalyses

Indian Ocean warms faster than the Pacific Ocean and form salient contrast over the Indonesian Islands (regions frequent by storm-triggered landslides). Because this is also a region of ENSO teleconnection patterns, there is global consequences in the precipitation, especially for the Pacific rims.

Occurrence of extreme precipitation largely is determined by the land surface conditions (ice sheet-ocean-land configuration, vegetation distribution over land, and large hydrologic infrastructures) and the energetics of the atmospheric circulation (e.g., wave-base flow interaction: under certain base-flow pattern, wave perturbation transfers momentum, moisture and heat between different latitudes (longitudinally) and also vertically). For example, a tropical cyclone remnant, combined with a low level jet can cause extreme precipitation for mountainous regions around the world, including southern California and mid-China, which are just two of many locations. The current climate warming necessitates investigating changes in storm-triggered landslides on 50-year (or longer) time scales. The key is precipitation morphological changes relevant to storm-triggered landslides (extreme rainfall events) under a warming climate. It is possible because the overall climate response of the precipitation to increasing atmospheric concentrations of greenhouse gases is proven to be reasonably predictable by current global coupled ocean-atmosphere general circulation models (CGCMs), often simply referred to as climate models, as shown by Allen and Ingram (2002) and the references therein. However, only very heavy or extreme precipitation triggers landslides (Iverson 2000). Although CGCMs are unable to project a specific storm's location and timing, it can provide a statistically accurate rainfall scenario for the region of

interest. For infrastructure construction, the exact timing of landslides is of secondary importance to occurrence frequency and future locations.

There is a large and expanding body of opinion that suggests that the Earth may suffer marked temperature increases over the next 50–100 years (Rind 1984) due to heat retention by the atmosphere caused by increased levels of the greenhouse gases CO_2, CH_4 and oxides of nitrogen. These levels in the atmosphere have increased dramatically in the last 70 years and are expected to continue to rise. Scientific data suggests that the Earth's climate is changing at an unprecedented rate, with instrumental records showing that during the last century the global temperature rose by about 0.6 °C. The warming trend for the last 30 years is roughly three times that for the past 100 years, and it is expected that the global temperature will continue to rise by between 1.4 and 5.8 °C by 2100 due to the emission of greenhouse gases (e.g., McCarthy et al. in IPCC AR4 (2001)). One consequence is an intensified hydrological cycle. Estimates of the effects vary widely but all predict an increase in storm-triggered landslides. However, different regions may respond very differently (Ren et al. 2011a) to intensification of the global hydrological cycle. For example, both monsoonal regions (e.g., Zhouqu in the above case study is located in the Asian monsoonal region) and Mediterranean regions (e.g., California) show significant increases in extreme precipitation, but the average annual precipitation changes are different. Precipitation over the Asian monsoon region increases significantly, consistent with increasing tropospheric specific humidity, as pointed out by Allen and Ingram (2002). In fact, the increase in annual mean precipitation over this region is due mainly to the shift toward heavier precipitation events. The NCAR CCSM3, a coupled climate model of relatively high horizontal resolution of ~1.4° lat/lon, simulated precipitation trend over southern California under the SRES A1B scenario, conversely indicates that total precipitation decreases by more than 0.1 mm/day on an annual basis. However, the southern California storms are expected to become more intense but farther apart in time, favoring a drought-flood bipolar temporal pattern as suggested by Trenberth (1999). Importantly, current climate models show strong inter-model consistency for this finding. Using beads with a fixed number of stones, O.G. Zolina illustrated how we can have in the same region simultaneously increases in prolonged "wet day" and "dry day" periods even with unchanged precipitation totals (Fig. 7.2).

In the case of landslides, there are two differing proposed outcomes of climate change. One possibility is that the debris flows will occur more frequently but on smaller scales. The other, considered more likely by some researchers, is a less

Fig. 7.2 *Red beads* indicate precipitation events, and the *blue segments* indicate "dry period" in between. *Left side* (of the *blue arrow*) indicate present climate and *right side* is a future warmer climate. *Source*: Pavel Ya. Groisman (personal communication, 2013)

frequent but more disastrous occurrence of storm-triggered landslides. However, it is certain that many regions with minor risks could be magnified if the Earth's climate undergoes significant changes over the next 50–100 years, as a consequence of the continued burning of large amount of fossil fuels.[1] The key question is how the precipitation morphology changes. The consensus of scientists is that higher temperatures may lead to a greater proportion of intense precipitation events (Karl and Trenberth 2003; IPCC 2007; NRC 2002; Kharin and Zwiers 2005; Semenov and Bengtsson 2002; Groisman et al. 2004). For most climate zones, increases in extreme precipitation events are a robust constraint to which climate models already have converged (O'Gorman and Schneider 2009). It is an important scientific question of whether or not there are changes in storm-triggered landslides in a warming climate.

CGCMs are well-positioned to answer the question of whether increased temperatures cause increases in precipitation intensity and amount. Climate prediction is concerned with quantifying general trends and not at accurate predictions of specific storm events. This does not devalue the CGCM projections because, for many purposes (e.g., infrastructure construction), interest is not in the exact timing of a mudslide, but rather in the need to know the time frame of its recurrence. The CGCMs, because of their limited horizontal resolution (usually over 100 km but are steadily improving towards a critical resolution of 10 km), are not expected to

[1] Trenberth (1999) has proposed a conceptual model explaining the greenhouse effect on an enhanced hydrologic cycle. An increase in the global mean temperature will increase the water-holding capacity of the atmosphere and thus the available moisture in the atmosphere, from the Clausius–Clapeyron (CC) equation. The CC equation defines the phase change boundary between liquid and gas phases of H_2O and can be used to describe the water-holding capacity of the atmosphere as a function of temperature (the partial pressure contributed by H_2O molecules at saturation is only a function of temperature).

$$\frac{d\ln E}{dT} = \frac{L_{1,2}}{RT^2}$$

where E is the saturation vapor pressure (Pa), T is absolute temperature (K), R is ideal gas constant (8.314 J/mol/K), and $L1,2$ is latent heat of vaporation (energy needed changing from phase 1 (liquid) to phase 2 (gas), 37082 J/mol).

From this expression, at standard atmospheric conditions, 1 degree temperature increase cause the atmosphere holding an additional of 6–7 % of vapor by volume (or partial pressure contribution). The Clausius-Clapeyron relation generally holds for climate model predictions of future changes in extreme daily precipitation (e.g., Allen and Ingram 2002). Hourly rainfall intensities may increase more saliently (Lenderink and Meijgaard 2008). There are observational evidence that daily precipitation extremes have increased over much of North America, with the most significant increases in southern Alaska, western British Columbia, Arctic and southeastern Canada, and the central USA (e.g., Groisman et al. 2005). The changes in heavy precipitation are greater than in precipitation totals. Increases in heavy precipitation occur even where annual totals are decreasing. Time series analysis indicates an increase in the frequency of extended periods (2 months or longer) in the USA (Kunkel et al. 2003). Future climate projection indicate that currently dray regions (e.g., Mediterranean climate region of California) also will experience extreme rainfall increase (Ren et al. 2011a).

resolve individual precipitation events. A reasonable and practical use of a CGCM's projection of precipitation would be for regions with coherent precipitation features, for example, monsoonal and Mediterranean climate regions. That the precipitation signals are strong in these climate zones is probably due, at least in part, to the differential warming in land areas relative to the oceans. Ren et al. (2011a) investigated precipitation morphology for two areas of interest, located respectively in the Asian monsoon area of China and a characteristic Mediterranean climate, in southern California. The following are the primary findings of that research.

Unlike normal precipitation events with life spans of less than a day, extreme precipitation, with total amounts greater than 500 mm for the Asian monsoon region or 70 mm in the southern California region, usually are distributed into groups of consecutive days. For debris flow studies, those precipitation events separated by less than 2 dry days should be considered as one "super" rain event. Thus, unlike many previous studies, such as that of O'Gorman and Schneider (2009) and references therein, which count daily precipitation 1 day at a time, extended-, or super-rain-events are defined as continuous rainfall periods not separated by more than 2 consecutive dry days. Thus, in the following discussion, the "recurrence frequency" of a certain rainfall category is frequently used. For a single model grid, it is defined simply as the total number of occurrence divided by the total number of year. For a regional area, it is the linear average among the model grids involved, i.e., the total number of occurrence divided by grid number and further divided by total number of years.

For the 50–100 mm rainfall category, the CSIRO and IPSL CGCMs, which are models with quite different, relatively coarse spatial resolutions (1.88 by 1.88° lat/lon for CSIRO and 2.8 by 2.8° lat/lon for IPSL), produced similar simulations of pattern changes in precipitation recurrence frequency between (1971–2000) and (2071–2100) (fig. 4 of Ren et al. 2011a). Both indicate an apparent increase (i.e., one or more such rain events every 2 years) in the Asian Monsoon region. Rainfall of that amount occurs less frequently in the Mediterranean climate regions. The increase in frequency is generally less than 1 per 5 years. Other models, under different non-mitigated scenarios, vary only quantitatively and in geographical details. The rainfall morphological changes are a persistent feature across all CGCMs. Below is an investigation of the rainfall morphological changes, according to extended rain events, classifying the rain events in to five categories according to total rainfall amount (Fig. 7.3).

To illustrate the IPCC projected changes of precipitation frequency over the Asian monsoon region, the recurrence frequency during 1971–2000 (horizontal axis in Fig. 7.3) are plotted against the 2071–2100 period (vertical axis). Eight models are represented by eight dots on this plot, for each category. For example, the cyan dots represent the >500 mm category, or, according to the traditional approach, >50 mm/day extreme rainfall for this region of warm temperate mixed forest.

All eight models successfully simulated the observed event frequencies for precipitation intensity less than 50 mm/day events. The hatched dots derived from the observational data are surrounded tightly by the models (numbers of the

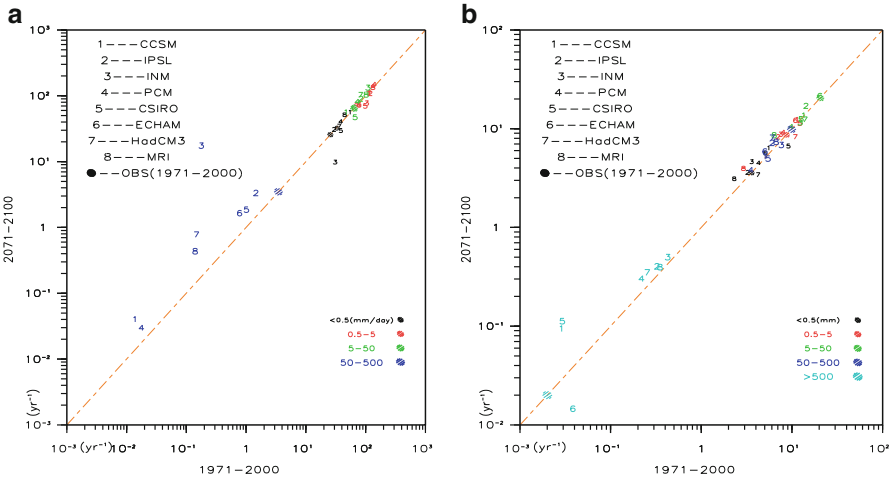

Fig. 7.3 Simulated rain occurrence frequency (year^{-1}) from eight CGCMs, for five different categories: <0.5, 0.5–5, 5–50 interested Asian monsoon region (the framed area near Point A in fig. 4 of Ren et al. (2011a)). Values inferred from 1971 to 2000 are used as x coordinates, while the vertical axis corresponds to the 2071–2100 period (based on the SRES A1B scenario). In each category, estimations based on observations are hatched (the null-hypothesis is there is no change in recurrence frequency, thus all observed lie on the diagonal line). Panel (**a**) is based on the traditional classification of 1 day for each rainfall event, whereas panel (**b**) is according to "super-rain event" classification. This figure is partly adapted from Ren et al. (2011a)

same color). Hence there is no clear overestimation or underestimation tendency among the models. There is, however, a clear tendency to underestimate the extreme events (e.g., MRI and HadCM3 20C3M even fail to identify events with intensities >100 mm/day. Those in the 50–500 mm/day category actually are within 50–100 mm/day category), clearly indicated by the fact that all blue numbers lie to the left of the blue dot (observed occurrence frequency). For rainfall intensity >50 mm/day, however, all indicate an increased tendency over time (the blue numbers lie above the diagonal line in Fig. 7.3a). That all CGCMs shown here underestimate the observed high-end precipitation occurring frequency might suggest that their predictions of future increase in extreme events may also be an underestimation of reality, for the reasons cited in Allen and Ingram (2002). These findings are consistent with many previous studies (Chen et al. 1996; Dai et al. 1999), which conclude that precipitation occurs too frequently and at reduced intensity, in climate models, when compared with observations. In addition, it is found that, for a given climate model, increases of severe precipitation scale with the emission scenario; the greatest increases are achieved under SRES A2, a high emissions scenario, and the smallest increase occurs under SRES B1, a low emissions scenario than SRES A1B.

Examination of the precipitation, based on independent rain events, is then carried out by classifying the rain events into five categories, according to total rainfall amount (Fig. 7.3b). While light rainfalls are close to each other, the extreme

rainfalls stand out separately in the left lower corner. Except for the ECHAM model, all models indicate an increase in extreme rain events (>500 mm). Thus, either examining the problem from a rain intensity histogram or the distribution of rain events according to total precipitation, the models have converged on an increasing extreme precipitation scenario as the climate warms. That models differ only quantitatively indicates that the primary mechanism could be the increase in vapor concentration, as described in O'Gorman and Schneider (2009). Fractional changes in extreme precipitation occurrence (changes of recurrence frequency compared with recurrence frequency extracted from the 1971–2000 period) scale with changes in area mean surface air temperature. When scaled with warming, there is little inter-model scattering in the selected region of interest.

Compared with observations, three CGCMs, the CCSM3, CSIRO, and ECHAM stand out as most closely simulating the extreme rainfall historical occurrence frequency (the x-axis of the cyan numbers in Fig. 7.3b are close to the cyan dots), while the remaining five models significantly overestimate the extreme rainfall's occurrence frequency (as large as two orders of magnitudes, for INM). The models tend to underestimate extreme rainfall intensity but, when divided into individual rainfall events, they also tend to overestimate the rainfall amount of extreme events. Clearly more work is needed in this vital research area. Characteristically, all climate models overestimate the observed high-end precipitation occurring frequency. The truly large (up to 100 times for some models) magnitude of overestimation indicates that the limited observational period (30 years) is not a reason for the low realization of the extreme rainfall events observed in the real world. We set 1 mm/day as the critical value to filter the daily data so "drizzling" of certain CGCMs are not an issue. Coarse grid spacing is also unlikely as an explanation because our region of interest involves at least ten CGCM grids, and the extreme rainfalls show extraordinarily strong spatial coherence over the region. This shared deficiency, fortunately, may not be an indictment of the CGCMs and it is still a valid conclusion that future extreme rainfall events will occur more frequently.

Simulation of the precipitation for the Mediterranean climate zones poses less challenge to CGCMs. There is no systematic overestimation/underestimation for both viewing angles. Some models show great ability in simulating the rainfall morphology. For example, even at a fine bin size of 0.2 mm/day the CCSM3 accurately captures each bin level, when compared with the North American Regional Analysis (NARR) same period observations (figure not shown). For this Mediterranean climate region, precipitation totals >15 mm/day (or total amount greater than ~50 mm) are viewed as extreme precipitation. The model shows a clear increase in its occurring frequency as climate warms. Considering that the model's 20 cm^3 simulation (corresponding to present climate) is close to observations at each bin level, it is highly likely that the increasing trend is viable. The spread in the climate models seems random. Although some models are not as "accurate" as the CCSM3 in simulating the present rainfall histogram, the shared feature of all of the eight climate models is that extreme heavy precipitation will be more frequent as the climate warms.

Although both regions of interest show significant increases in extreme precipitation, the average annual precipitation changes are different. Precipitation over

the Asian monsoon region increases significantly, consistent with an increasing tropospheric specific humidity as pointed out by Allen and Ingram (2002). In fact, the increase in annual mean precipitation over this region is mainly due to the shift toward heavier precipitation. The CCSM3 simulated precipitation trend over the southern California region under the SRES A1B scenario, counter-intuitively indicates that total precipitation decreases by more than 0.1 mm/day on an annual basis. Storms become more intense but farther apart in time, favoring a drought-flood bipolar temporal pattern as foreseen by Trenberth (1999). In addition to the eight CGCMs previously mentioned, we examined also GFDL, IAP-FFOALS, CNRM, and MIROC-hires. The 12 CGCMs models show strong inter-model consistency for this finding.

Thus, a key component of understanding the impacts of human-induced global climate change on landslides is the likely nature of changes in extreme rainfall, rather than the average yearly rainfall total. It therefore is possible that the average annual rainfall for an area might decrease, but the occurrence of landslides increases when rainfall is in more intense bursts. Liu et al. (2009) found that a 1 degree Kelvin increase in global temperature causes a 94 % increase in the most intense rainfall events, with a decrease in the moderate to light rainfall events. Indeed, the median rainfall increased from 4.3 to 18 mm/day. Ren et al. (2011a) further discussed changes in landslide events for the southern California region under a feasible emission scenario. We find that increased infiltration of groundwater into the subsurface from storms increases creeping rates dramatically for weathered slopes. For slopes experiencing repeated failure–restore cycles, increased precipitation amount and intensity under a future warming climate are the two most important factors determining long-term increases in landslide frequency.

Extreme precipitation events of landslide consequences are usually associated with (or nested in) mesoscale or large-scale weather systems with strong seasonality, such as tropical cyclones and monsoons. Landslides occur mostly during monsoonal precipitation in India and Bangladesh. Subtropical islands (including the Taiwan region of China) depend on tropical cyclones for fresh water but also are prone to storm-triggered landslides. Changes in these large scale weather systems, which have high information to noise ratios, contain precious information useful for long-term projection of storm-triggered landslides. The following two subsections review recent progress in trends in tropical cyclone activities and monsoon cycles.

7.1 Trends in Tropical Cyclone (TC) Activity in a Future Warming Climate

Tropical cyclones (TCs) are the most devastating weather systems on Earth. They affect coastal regions or islands directly, as they often generate strong winds, large waves and swell, and severe flooding; and also they affect inland regions by producing lifting mechanism to generate or enhance storms (e.g., the

aforementioned unfortunate combination of the remnant low pressure system with mid-latitude trough and low level jet). Possible changes in TC numbers, intensity, and genesis and decay locations all are relevant for changes in landslide activities. With the copious rainfall in relatively short period of time (usually a couple days), they often generate large number of landslides when they impact mountainous regions. In the USA, TCs that impact the Appalachian Mountains often generate copious rainfall, flooding, and occasionally widespread landslides. For example, Hurricanes Frances and Ivan (Sept. 2004) impacted western North Carolina bring daily rainfall in excess of 200 mm for some locations. The ensuing storm-triggered landslides caused significant loss for the region (Wooten et al. 2008). Many Central American countries experience strom-triggered landslides when being hit by TCs from the North Atlantic basin. Lin and Jeng (2000) reported thousands of debris flows following the landing of Typhoon Herb on northern part of Taiwan island. Possible changes in TC numbers, intensity, and genesis and decay locations all are relevant for changes in landslide activities. For example, if there is an increase in TC numbers then, depending upon their genesis locations, track, and intensity, there is likely more landslide occurrence. The impact of TCs on communities, economic operations and the natural environment also are very sensitive to possible changes in their landing locations. For example, if there is an increase in TC numbers and/or intensities then, depending on their genesis and decay locations, and tracks, there likely are more heavy to extreme rainfall events and hence more landslide occurrences. Over the past decade, the impact on TCs of a future warming climate resulting from increased carbon dioxide has been studied extensively using coupled climate models (see, for example, Sugi et al. 2002; McDonald et al. 2005; Bengtsson et al. 2007; Holland and Webster 2007; Stowasser et al. 2007; Yokio and Takayabu 2009; Knutson et al. 2010; Murakami and Sugi 2010; Murakami and Wang 2010; Ren et al. 2014; Sugi and Yoshimura 2012). The most studied basins are the Atlantic Ocean and the western North Pacific (WNP) Ocean. Although they are TC basin dependent, these projections largely have shown a consistent tendency for a slight decrease in TC numbers, but an increase in the percentage of intense TCs. However, the TC basin should be examined in detail. In the following subsection, we will review the entire TC life cycle from a state-of-the-art numerical weather prediction model and examine the sensitivities of TC activity to sea surface temperature. From the understanding gained from the sensitivity studies, tentative projections will be drawn. Basin-wise investigation based on climate models follows.

7.1.1 TC Genesis, Tracking, and Intensity

TC formation is, in part, an upscaling process, with small convective scale systems (e.g., mesoscale convective systems, or MCSs) adding moisture, energy, and cyclonic vorticity to preexisting disturbances (e.g., Monsoon Trough, easterly waves, MJO/ISO and equatorial Rossby waves) in large scale conditions

predisposed to Tropical cyclogenesis (e.g., SST higher than 26.5 °C, higher relative humidity preventing premature release of convective available potential energy (CAPE), moderate vertical shear of horizontal winds, and upper level divergence for exhaust to escape).

Evaporation at the air–sea interface results in an upward transport of energy in the form of latent heat and, thus, injects water vapor into the atmosphere. This is a major energy source for atmospheric circulation (Schulz et al. 1997). The exchanges of water vapor and heat at the surface take place simultaneously and connect the energy cycle to the hydrologic cycle. As the evaporated moisture reaches the lifting condensation level (LCL), condensation occurs (precipitates) and the released latent heat warms the environment and is critical for tropical disturbances, such as easterly waves, reverse troughs and monsoonal troughs, that become tropical cyclones (Yanai et al. 1973), and especially for the creation of warm-core structures and the maintenance of cyclonic vorticity (Nolan et al. 2007). The warm core establishes a deep layer (700–200 hPa) of air having lower pressure than the surrounding environment and the upper (100 hPa and above) levels sustaining higher pressure than their surrounding, creating low-/mid-level convergence and upper level divergence, act like a chimney. Cyclonic vorticity is generated as a result of maintaining (or attempting to maintain) a hydrostatic and gradient wind balance. This lower level moisture flux is the fuel for this Carnot engine (Emanuel 1986). The surface latent heat flux is estimated from the bulk formula that employs near surface wind speed, air humidity, and sea surface temperature:

$$LE = \overline{\rho} l \overline{w' q_v'} \approx -\overline{\rho} l C_D \left|\vec{V}\right| \frac{\partial \overline{q_v}}{\partial z} \tag{7.1}$$

where LE is latent heat flux (W/m^2), ρ is air density, l is the latent heat of evaporation (J/kg), $\overline{w' q_v'}$ is turbulent covariance of near surface specific humidity (q_v) with a vertical component of velocity (w), which, according to mixing length theory, can be parameterized by a turbulent diffusion coefficient and the vertical gradient of the mean state of q_v. C_D is the drag coefficient, $\left|\vec{V}\right|$ is the near surface wind speed, and over bar identifies the temporal mean state. Once the measurement height is decided, Eq. (7.1) can be rewritten as:

$$LE = -\overline{\rho} l C_E \left|\vec{V}\right| \left(\overline{q_v} - \overline{q_{vs}}(T_s)\right) \tag{7.2}$$

where q_{vs} is specific saturation humidity at the sea surface temperature T_s, and C_E now is the Dalton coefficient (unitless, $\sim 2 \times 10^{-3}$). The latent heat flux causes cooling of the upper layer of the ocean and, through the loss of water, an increase in the salinity of the oceanic mixed layer. For TC research, the changes in salinity are safely neglected. However, the effects of ocean salinity on evaporation cannot be omitted. Salinity can significantly (as high as 70‰, e.g., southern Indian Ocean) lower the saturation vapor pressure at the water surface. Based on the molar Gibbs

free energy criterion, the salinity-dependent parameterization is implemented as follows:

$$LE = -\overline{\rho} l C_E \left|\vec{V}\right| \left(\overline{q_v} - \overline{q_{vs}}(T_s)(1 - \alpha S)\right) = F(T, S) u_* \tag{7.3}$$

where S is salinity in practical salinity unit (PSU), and specific humidity takes the value at the lowest model level (~10 m agl). The ultimate energy source for TCs is the lower surface evaporation. In this study, the WRF scheme is modified to include salinity effects in the bulk formulae. Also, the scheme is applied to the entire simulation domain, not locally to the TC region. It is clear from Eqs (7.1)–(7.3) that the SST and salinity collectively are vital for controlling the magnitude of the surface evaporation: the most important moisture and energy source for TC development and maintenance over the entire lifecycle. Prediction of the TC lifecycle thus depends ultimately on how latent heat flux is represented in numerical weather prediction models (NWPs). In this study, using the forgoing formalism, we modified WRF to include the salinity effect in the bulk formula. Further, the scheme is applied to entire simulation domain, not just locally for the TC region.

An upright "chimney" is not as effective in maintaining the warm-core structure because, as precipitation occurs, the drops-outs (the released water such as hails, snowflakes, and supercooled raindrops) thaw and evaporate (and absorb heat) as they fall, causing "down-drafts." The down-drafts apparently are negative feedbacks that need to be minimized to guarantee further development of the warm-core structure. Weak vertical wind shear can provide a favorable tilted system ("slanted chimney" structure) that takes advantage of the condensation's release of latent heat to warm the air and minimize the cooling of air directly downward of the warm core region. The vertical shear of horizontal winds should be moderate to allow cyclones to develop vertical coherence. The persistent presence of strong shear with thermal winds over the south Atlantic accounts for its lack of TCs. The longevity of the disturbance depends on whether this favorable moisture-providing setting can be maintained. Clearly, this stage of formation is very tricky and slight changes in the environmental conditions (e.g., the push of a subtropical high or the intrusion of a higher latitude disturbance) means a pinch-cut of the moisture source for this tropical disturbance. Most likely, the very first such disturbance following a previous tropical cyclone is not viable. However, it leaves more favorable conditions for the following disturbances: a cyclonic remnant circulation in the mid-/upper-level and a relative moist mid-/low-level atmosphere. Not only does creation of these conditions from scratch require a significant amount of energy, but the latter (moist mid-/low-level atmosphere) also guarantees weaker downdrafts compared to the previous, diminished disturbance, everything else being equal, because the evaporation of the droplets in the moist environment will be less than in a drier environment. Previous disturbances would have left a cold tongue of SST through evaporation and churning of the ocean mixed layer water. Thus, sufficiently high SSTs are critical for a tropical disturbance eventually to become a viable TC (Gray 1968, 1979; Anthes 1982). An ideal condition for TC development is that the

starting region should be a distance away from the poleward turning point, depending on the strength of the westward steering current (e.g., the peripheral winds of subtropical highs), that should allow at least 2 days for the disturbance to gain enough latent heating from the warm ocean surface.

One further mechanism that indicates the critical role of ocean surface evaporation is that, after the passage of a previous disturbance, the vertical stratification of the atmosphere tends to be more stable. In tropical regions (all year round), the mechanism for breaking convective stability is to accumulate more moisture at lower levels. By increasing the stability, a moist middle layer, by preventing a premature release of convectively available potential energy (CAPE), is favorable for the next disturbance because deep convection produced total latent heat release is directly proportional to the moisture content in the deep mid-levels. In other words, the enhanced environmental relative humidity is essential for full-development of clouds, and their upward transport of moist static energy ($c_pT + gz + Lq_s$) from the boundary layer contributes to TC formation (Demaria et al. 2001). Diabatic heating by latent heat release, a leading moist static energy input for the environment, however, is counteracted immediately by adiabatic cooling of the expanding moist air parcel, so the net heating to an air parcel is the residual of the two large terms. However, in this case, as diabatic heating is the "forcing" factor and adiabatic cooling is the "response," as in many dissipative systems, the net result would be heating. In a vertically stratified atmosphere (an environment set by radiative–convective balance), the temperature decreases within the troposphere, but with a reducing lapse rate. At the level of the upper troposphere, the local vertical gradient of moist static energy becomes positive. If an air parcel's condensation occurred at this level, the latent heat release will exceed that required to compensate for the adiabatic cooling caused by expansion and, thus, a net increase in this parcel's temperature is feasible. In reality, deep cumulus clouds can achieve this condition and carry the released latent heat of condensation to the upper troposphere. That the warm core of a TC occurs in such a deep layer clearly suggests a likely association with cumulus towers in the formation and ensuing development of a TC. This also explains why the viable early TC disturbance seeds are selective/picky: normal shallow convections do not qualify as seeding disturbances. Since tropical disturbances are far smaller than the Rossby deformation radius (Gray 1993), mass (pressure) fields adjust to circulation (winds) fields (Nolan et al. 2007; Anthes 1982). Because deep convective towers have strong and easily identifiable remote sensing signatures, assimilation of remotely sensed wind fields is critical for successful TC simulations.

The formation of tropical cyclones (TCs) has long been a major area of research and has resulted in hypotheses such as Convective Instability of the Second Kind (CISK, Charney and Eliassen 1964; Anthes 1982), and the more recent and widely accepted wind-induced surface heat flux (WISHE) theory of Emanuel (1986). These two theories focus on the intensification process of TCs after they have formed, basic structure and, in some cases, the warm-core is already established. The formation of weak and unorganized disturbances into a tropical depression (TD) is thought to be different and more uncertain in nature. Although the

large-scale environmental conditions necessary for TC formation are better known (Gray 1998), the mesoscale and convective-scale mechanisms for unorganized disturbances to develop into a TD are not well understood (Tory and Frank 2010). Nolan et al. (2007) discussed how asymmetric latent heating, in levels of positive gradients of environmental moist static energy, could contribute to the formation of a warm core.

Tropical cyclone motion is primarily caused by advection of the TC by the surrounding environmental flow (Chan and Gray 1982; Flatau et al. 1994; Chan 2005; Leslie and Holland 1995). While there are other mechanisms exist that cause the TC to move independently of this environmental "steering flow" (Wu and Emanuel 1993), the steering of the TC by its environment generally is the dominant contribution, especially for steady TC motion (Chan 2002). This explains why TCs move around the subtropical highs, such as the Bermuda High. However, the relationship of a TC with respect to a complex, dynamically evolving environment, and the process by which the environment steers the TC, have been subjects of modeling research for many years (e.g., Holland 1984; Shapiro 1996; Shapiro and Franklin 1999; Wu and Wang 2004; Chan 2002). By providing high-resolution, 4-dimensional, dynamically consistent atmospheric parameters, NWP model simulations can provide insights into the relative importance (steering-wise) of various synoptic-scale features in the TC environment.

Not only do TCs move toward the direction with largest gradient in increasing cyclonic vorticity, but also that the formation of a TC primarily starts from a cyclonic perturbation in the flow field that initiates the convergence of low level moisture to form convective perturbations. At the initial stage, this may be randomly unorganized tropical depressions (TDs). In practice one TD that dies may left a more favorable circulation environment for the next TD, although the effect on sea surface evaporation is negative (cold trace effect). If SST is sufficiently high, the favorable heritage of the cyclonic vortices may outweigh the cold trace effect and the following TD generally will grower larger in general. After several TDs, typically 3–7 in the North Pacific Basin and less in the South Pacific basin, there will be a viable vortex that is self-sustaining (meets the criteria for self-sustaining and is highly organized) and eventually becomes a tropical cyclone (Montgomery et al. 2006). To investigate the low-level vortex intensification (e.g., TC Glaenda's rapid burst of intense deep convection), the following vorticity tendency equation is a good diagnostic tool:

$$\frac{\partial \varsigma}{\partial t} = -\left(u\frac{\partial \eta}{\partial x} + v\frac{\partial \eta}{\partial y}\right) - w\frac{\partial \varsigma}{\partial z} - \eta\left(\frac{\partial u}{\partial x} + \frac{\partial v}{\partial y}\right) - \left(\frac{\partial w}{\partial x}\frac{\partial v}{\partial z} - \frac{\partial w}{\partial y}\frac{\partial u}{\partial z}\right) + \frac{1}{\rho^2}\left(\frac{\partial \rho}{\partial x}\frac{\partial p}{\partial y} - \frac{\partial \rho}{\partial y}\frac{\partial p}{\partial x}\right) + \left(\frac{\partial F_y}{\partial x} - \frac{\partial F_x}{\partial y}\right) \tag{7.4}$$

where ς is the relative vorticity, $\eta = f + \varsigma$ is absolute vorticity, f is the inertial frequency of the Earth's rotation, u, v and w are the wind components; p is the pressure and ρ is the air density. The right-hand-side terms respectively represent

horizontal advection, vertical advection, stretching, tilting, solenoidal effects and sub-grid-scale flux derivatives. The stretching term indicates that the absolute vorticity is required to be non-zero for low-level convergence to generate relative vorticity. This explains why TCs rarely form within ±5° of the Equator (Gray 1968). The baroclinic term also explains why higher-than-average relative vorticity (e.g., synoptic precursor disturbances) is required for TC cyclogenesis, because this term works more efficiently when the temperature stratification and lower wind field favors harnessing energy released in condensation to strengthen the local cyclonic vorticity, through the generation of potential vorticity.

7.1.2 *State-of-the-Art NWPs Can simulate Details of TC Structure and Complete TC Life Cycles*

Here presented is numerical modeling of two TCs (Fig. 7.4), respectively, over the south Pacific Basin (Larry 2006) and the Atlantic Basin (Katrina 2005). The numerical model used is the advanced, non-hydrostatic full physics Weather Research and Forecast (WRF) model, version 3.4, developed at NCAR (Skamarock et al. 2008). It is used to simulate the entire life cycles of the two selected TCs. To identify the genesis mechanisms (or, processes leading to the formation of a TC), the simulation starts 2 days earlier than the IBTrACS commencement record and

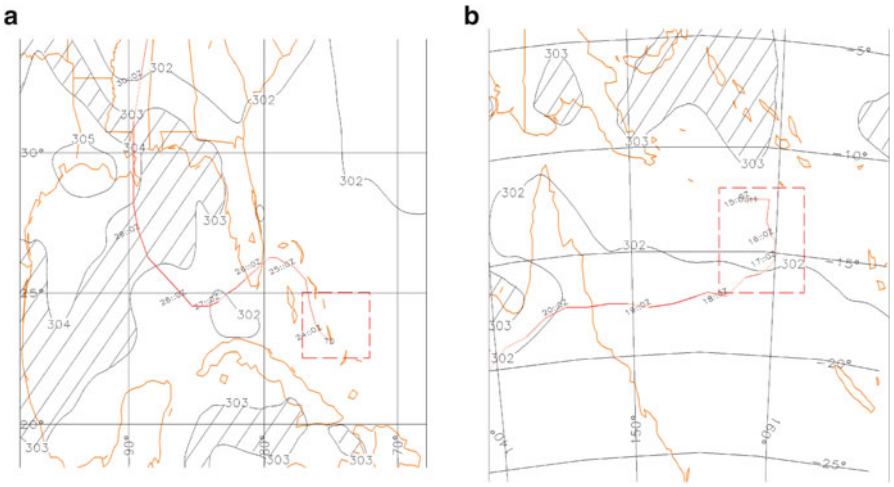

Fig. 7.4 TCs investigated in this study: (**a**) is Hurricane Katrina (21 August to 2 Sept 2005) in the Atlantic Basin, and (**b**) Larry (13–21 March 2006) of the Southern Pacific Basin. The International Best Track Archive for Climate Stewardship (IBTrACS, Kruk et al. 2010; http://www.ncdc.noaa.gov/oa/ibtracs/, at 6-h intervals) traces are plotted as *red lines*. The *contour lines* are environmental SST, with 302–303 K hatched. The region defined by the *dashed lines* is for following vorticity tendency analysis

runs until 1 day after landing. The simulation domains are one-way nested with horizontal resolutions of 20/5 km, and stencil sizes of 168 × 100 and 200 × 150 for the coarse domains of Katrina and Larry, respectively. A 35-level configuration is used, with the model top set at 50 mb. The Kain–Fritsch cumulus parameterization scheme (Kain 2004) is used for the coarse domains and the explicit moisture calculation and micro-physics are used for the 5-km inner domains. Other related packages include the WRF single-moment 6-class microphysics scheme with graupel (WSM6, Hong et al. 2004) and the Yonsei University planetary boundary layer parameterization.

During the ~10 days of integration with 10-s marching steps, the model initial and lateral boundary conditions were taken from the 1° lat/lon NCEP global forecast system final gridded analyses, with the outer lateral boundaries updated every 6-h. The NCEP daily sea surface temperature (SST, of 0.5 degree resolution) field was used to update the lower boundaries. Without data assimilation steps, the simulated TC track for Katrina is off by as much as 1.2 degrees (e.g., to the east of the IBTrACS observations) for Katrina. The locations of the MCSs also do not match well with satellite infrared imageries. To improve the WRF simulation of atmospheric conditions, the NASA's Quick Scatterometer (QuikSCAT) oceanic winds and the Defense Meteorological Satellite Program's Special Sensor Microwave/Imager (SSM/I) oceanic surface wind speed and total precipitable water (TPW) during the first 3 days are assimilated using the WRF-Var 3 with a 6-h assimilation window. The 25-km horizontal resolution, twice daily swath data of QuikSCAT and SSM/I were extracted from the Remote Sensing System (RSS) data archive. This simulation with data assimilation is treated as the control experiment. To verify the model's simulated precipitation, the NASA/TRMM, a joint mission between NASA and JAXA designed to monitor and study tropical rainfall, 3B42RT grid precipitation products (ftp://trmmopen.gsfc.nasa.gov/pub/merged/3B42RT/) were used as an independent source of information.

The genesis positions of the selected TCs are shown in Fig. 7.5. They are either formed in the eastern wave trough (Katrina) or an ITCZ (Larry), both favorable large-scale environments with high humidity and abundant low-level cyclonic vorticity that are shared features for TC formation. For Larry, during mid-March, when it was in its development stage, the integrated amplitude of the first two real-time multivariate Madden–Julian Oscillation (MJO) indices (Wheeler and Hendon 2004) both exceeded one, and the phase of MJO was five in the western Pacific. Therefore, the MJO was in the active (or wet) phase and is considered favorable for TC formation (Maloney and Hartmann 2000).

In addition to the South Pacific Basin Larry 2006, the western North Pacific basin has about 70 % of TCs formed in the monsoon trough (Lander 1996; Mcbride 1995), because the monsoon trough is often associated with a favorable background environment with high relative humidity, cyclonic relative vorticity, convective instability, strong low-level convergence and a broad scale of persistent cloud cluster. It is, thus, not surprising that variability in the monsoon trough substantially impacts the spatial and temporal variations in the frequency of formation of TCs (Chen et al. 2004). Occurrence of MCSs at multiple times was identified during the

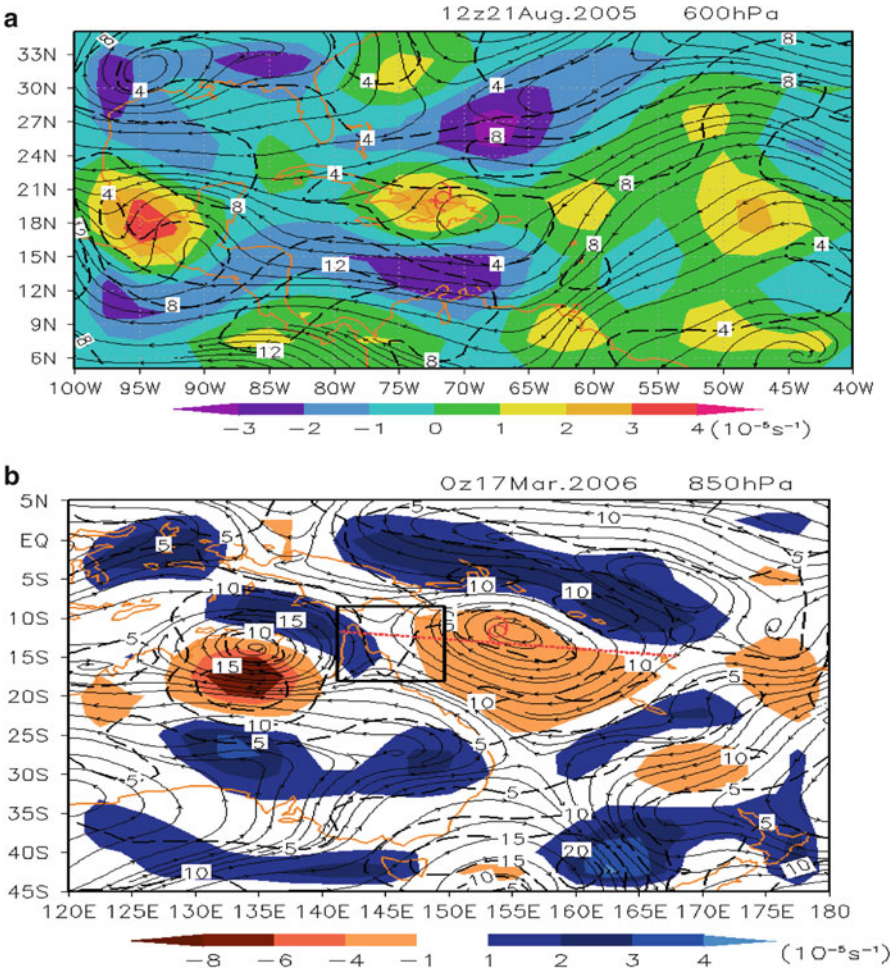

Fig. 7.5 NCEP/NCAR reanalyses of the lower level (600 mb for Katrina and 850 mb for Larry) streamlines, wind speeds (*dashed lines*, m/s) and relative vorticities (*color shades*, 10^{-5} Hz) at 1 day leading time of the TC formation alert (TCFA). The formation environments of Katrina and Larry are different. Katrina forms as a perturbation in the eastern waves, while Larry 2006 was formed inside ITCZ. Larry formed at the maxima southern extension of the ITCZ (*red dashed lines*). The *red dashed lines* are the rough locations of ITCZ

2 days prior to formation of most TCs in the ITCZ and monsoon shear region (Ritchie and Holland 1999). Coexistence of MCSs is common in the monsoon-related synoptic patterns. A middle-level mesoscale convective vortex (MCV) is often generated in active MCSs with severe convection. Once formed, the MCV often outlives its parent MCS. Recent observational and modeling studies have shown mounting evidence of the importance of long-lived MCVs during TC

formation (e.g., Bosart and Sanders 1981; Harr and Elsberry 1996; Ritchie and Holland 1997). Therefore, attention should be paid to the occurrences of MCSs to find viable TC seeds. It is still uncertain as to the mechanisms through which MCSs influence TC formation. Long-lasting MCSs that were developed under substantial low-level vertical wind shear also can have a MCV in the stratiform rain region (Chen and Frank 1993). Over the US Great Plains, a downward extension of MCVs, through vertical advection (Rogers and Fritsch 2001), is critical for the formation of tornados (Maddox 1980; Fritsch and Maddox 1981; Miller and Fritsch 1991). Similar mechanisms, most likely, also are at work in TC formation. Another working hypothesis, the so-called bottom-up hypothesis, is based on the observations of Zehr (1992) that low-level vortex intensification sometimes follows bursts of intense deep convections. Montgomery et al. (2006) suggest that this deep convective, low-level vortex enhancement is taking place within MCSs well before the formation of a self-sustainable system-scale vortex. The system-scale vortex then further intensifies through mechanisms such as CISK and WISHE (e.g., Craig and Gray 1996). Hendricks and Montgomery (2006) further suggested that vertical hot towers (VHTs) with spatial scales of 10–20 km play a critical role during the process. Based on the observational and modeling evidence of VHTs, several recent studies (Reasor et al. 2005; Sippel et al. 2006; Fang and Zhang 2010) indicate that the bottom-up process is a viable pathway to the enhancement of surface vortex during TC formation. With high-resolution modeling with the WRF model, this study investigates the role of MCSs in the formation of weak disturbances leading to hurricanes under basin-specific environmental conditions. Budget analysis for the area-average relative vorticity is performed according to the vorticity tendency equation (Eq. 7.4).

Budget analysis was first performed for area-averaged relative vorticity for the two selected TCs. The regional averages are taken are shown in Fig. 7.4: 22.5–25 N; 77–72 W for Katrina, and 17–12S; 156–162 for Larry. For Larry, at mid-level (5,000 m agl) the vertical advection of vorticity makes a positive contribution to vorticity tendency throughout the entire time period of 2 days leading to its formation, whereas the average tendency of low- to mid-level tilting is always negative (Fig. 7.6b, d), and the two almost cancel each other. Horizontal advection and stretching are the two largest rivals in vorticity generation. There is strong cancellation of the positive tendency from stretching (convergence) and low level horizontal advection. However, the two terms work in synergy at higher levels (above 6,000 m). The stretching term exhibits good timing with development of MCSs, according to satellite imageries. The episodes of strong stretching with apparent daily cycle characteristics (Fig. 7.6c) all correspond to sizable MCS developments which have clear footprints on visible imageries. This supports the bottom-up hypothesis. Atlantic hurricane Dolly (2008) also revealed a similar developing mechanism. However, the situation for Katrina is quite different. For Katrina, the horizontal convergence, or the stretching term, is the dominant vorticity contribution. The frictional term, which always acts to reduce the vorticity (both cyclonic and anticyclonic), is counter to the stretching production of vorticity. Thus, the vorticity is produced in the convergence mid-/lower-layer and is

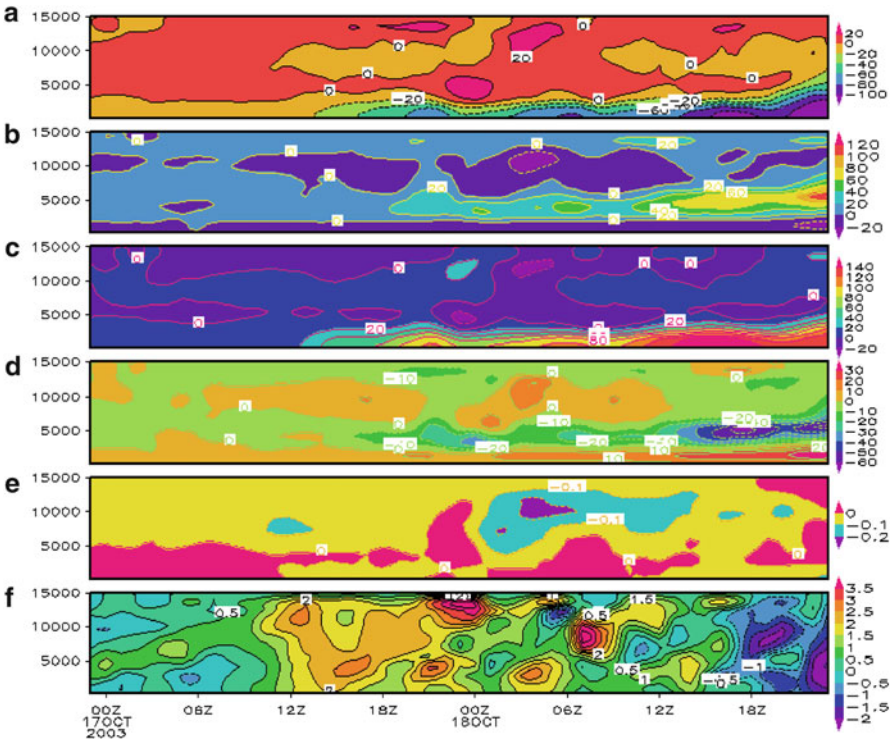

Fig. 7.6 Time-height diagram of the area-average (a sector leading the IBTrACS observed TC location at the formation stage, ~5 by 5° region defined by the *dashed line boxes* in Fig. 7.4) vorticity tendencies (10^{-11} s^{-2}) for Katrina 2005. The panels (from *top* to *bottom*) are organized as (**a**) horizontal advection, (**b**) vertical advection, (**c**) stretching, (**d**) tilting, (**e**) baroclinic, and (**f**) the sum of all above terms. TC moves toward the direction of fastest increasing in cyclonic vorticity. Stretching always is the most important term for positive vorticity production. There is apparent bottom-up tendency in vorticity generation

dissipated at the bottom frictional layer. There is no apparent downward propagation of positive vortices during the initial stage. Larry resembles most West North Pacific Basin TCs in its genesis, except that a local circulation feature between Australia and Indonesia (a saddle structure) produced an input of anticyclonic vorticity at the outer region (10° away to the northwest), which helped to concentrate the cyclonic vorticity regions and better organize the deep convections (VHTs).

Top-down advection is more significant in relative vorticity production for the redeveloping type of TC (which redevelops from a remnant of a preceding TC passing over warm water, such as Glenda 2006 as a redevelopment of Larry 2006, Fig. 7.7). The initial centers of large negative (cyclonic in the Southern Hemisphere) vorticities are located at ~10 km agl and are gradually advected downward, agreeing with the fact that Glenda was a redevelopment of a remnant of Larry, clearly demonstrated in the potential vorticity map generated from reanalysis data

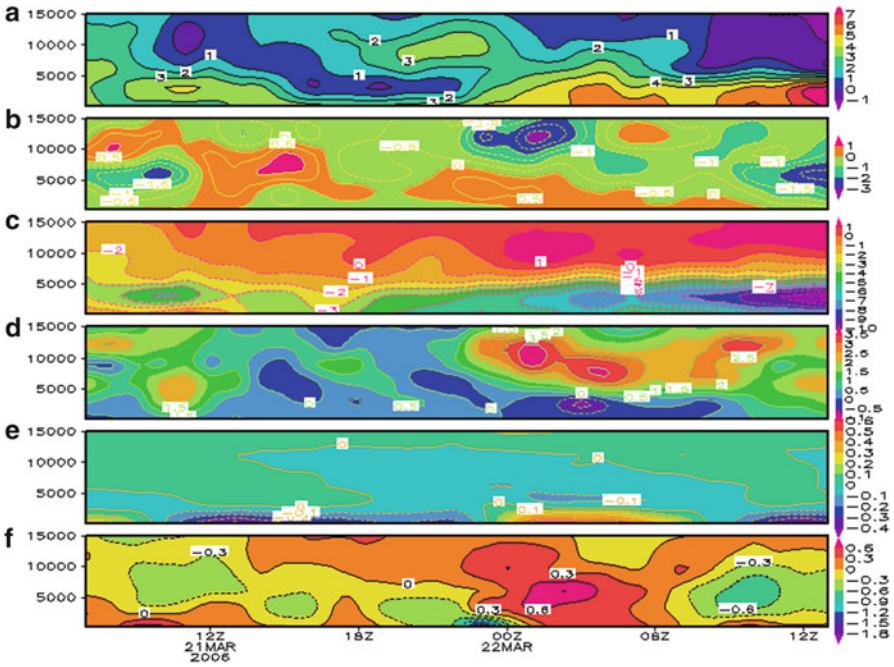

Fig. 7.7 Same as Fig. 7.6 but for Glenda. Unlike Katrina (2005, the last hurricane named Katrina because of its impacts), top-down advection is more significant in relative vorticity production for Glenda. The initial centers of large negative (cyclonic in Southern Hemisphere) vorticities are located at ~10 km and is gradually advected downward, agreeing with the fact that Glenda is a redevelopment of Larry. In this case, tilting works also in synergy with vertical advection. Note that the relative vorticity production is directly proportional to absolute vorticity value, making it impossible for comparison of the magnitude of each term across TCs of different basins

(not shown). In this case, tilting also works in synergy with vertical advection. After landing, Larry dissipated at the lower levels because the moisture input ("fuel" to the hurricane "Carnot engine") was pinch-cut when it traveled over Australia's northern territory. The mid-level/high-level vortex still existed and journeyed quiescently westward until reaching the Hollway currents, where SSTs as high as 31 °C are available (not shown) to provide plenty of moisture for evaporation once the low pressure system passing over. The explosive redevelopment of this vortex into a sizable tropical cyclone needs only one and half days. Throughout the intercomparison, it also is clear that the relative vorticity production is directly proportional to absolute vorticity, hence, the magnitude of each term cannot be compared across TCs of different basins. More importantly, the "bottom-up" and "top-down" may only differ rhetorically. In all cases, no matter how the cyclonic vorticity is brought in, all are accompanied by convective bursts of MCSs (identifiable clearly from satellite imageries) and the latent heat release from precipitation is the energy source for perpetuating the system until it develops into a self-sustainable mode.

Comparison between WRF simulations in the coarsest domain (domain 1's, ~0.18° lat/lon) and the corresponding NCEP/NCAR reanalyses (figures of reanalyses not shown for clarity) indicates that large scale circulations have been simulated satisfactorily, with the WRF providing more details, such as the downdrafts and asymmetric rain bands, near the storm center. Assimilation of QuikSCAT and SSM/I wind information improved the simulation of the low-level cross-equatorial flow, and the location and intensity of the ITCZ. Larry is formed inside the ITCZ, when the ITCZ is at the southern most location (red dashed line in Fig. 7.5). The equator-side strong westerly (reaching 10 m/s steadily at 6° S and 155° E) is key to the creation of cyclonic vorticity at the earliest stage of Larry's development. This is different from the environments of Ketsana 2003 (not shown) in the following two aspects: (1) the subtropical high is at its peak strength (ridge line at ~25° S) and the steering stream advects the young Larry westward; (2) there is a saddle structure (box defined region) that exists for the entire ocean-living period of Larry. At different stages, the role of this saddle structure is different. It is critical for affecting the track of Larry as it is a negative vorticity source (which repels Larry and makes its track deflect southward) and it reinforces the beta-effects in southward deflection. The saddle structure also is a moisture source for Larry, as there exists a strong flow along specific humidity gradients. Larry's development further confirmed low level moisture convergence as the fuel for the CISK and WASHE positive feedback mechanisms that reinforces the warm core and makes the TC self-sustainable against dissipations.

At mature stage, the differences among TCs also are apparent. Only Katrina has a more axisymmetric eye wall structure. The eye region has strong downward motion (Fig. 7.8d) while strongest upward motion is found inside the eyewall. Radially outward, there are thermally indirect, interlaced upward and downward motions. There are clear indications in the humidity (blue dashed lines in Fig. 7.8c) and wind fields (axis-symmetric maximum wind speed cores in Fig. 7.8b ~900 mb, directly above the planetary boundary layer). Larry is less symmetric (not seen). For TCs developed from scratch, the sectors with strongest convective instability (e.g., the sectors with oceanic winds blowing poleward or from ocean to land mass) also tend to have strongest upward motion and associated strongest downward drafts, on a macro-scale, organizing the MCSs into rain bands. For Glenda, the vertical wind shear seems to play an important role for asymmetry in the convective rain bands (land blowing to ocean sector, or south western sector having the strongest precipitation). The moisture contents over land masses are drastically smaller than over oceans (esp. for Glenda, not shown). Measured by the area confined by 1,000 mb contour line (Fig. 7.8a) or from the kinetic energy point of view, Katrina is not outstanding (Glenda 2006 triples Katrina 2005's peak stage kinetic energy). However, in the sense of organization, Katrina is stronger in that it creates an environment with the less Rossby Radius of Deformation (RRD) and the secondary circulation associated with it (to the east), if SST is 2 K warmer in the Atlantic warm pool, would also be a sizable TC (to be further addressed soon).

Precipitation magnitude and structure is a manifestation of TC intensity (Houze 2010; Nolan et al. 2007). Thus, realistic simulation of the precipitation and its

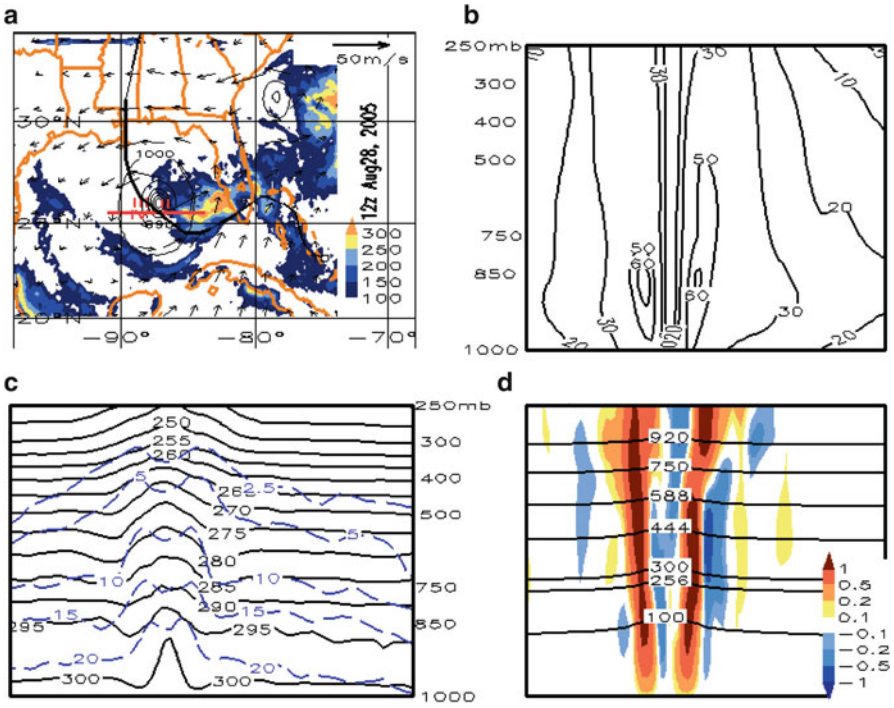

Fig. 7.8 Structure of Katrina (2005) from the WRF-ARW simulation. Typical features necessary for the tracker (to detect TCs) are resolved, including: quasi-axisymmetric shape (**a**), wind speed (**b**) maximum just above the planetary boundary layer (~850 mb), and an upper level (750–200 mb) warm core (**c**). In panel (**a**), *contour lines* are surface level pressure (mb) and *shades* are precipitation (accumulated total amount, mm). The vector fields are 850-mb winds; (**b**) shows the vertical cross section of wind speeds along 25° N (*red line* in panel (**a**)). (**c**) shows the temperature cross section along the *red line* in (**a**). The *dashed blue lines* are specific humidity (g/kg); (**d**) is vertical wind speed along the same cross section. The roughly *horizontal lines* are the geopotential heights (in dm). Model time is August 28, 2005.WRF simulations have more details than NCEP/NCAR reanalyses (not shown). For example, there are downdrafts in the sector with strong precipitation (*blue blob* in (**d**)). The maximum vertical movement occurs around 500 mb (reaching ~5 m/s), agree with the airplane surveys of four Atlantic mature TCs by Jorgensen (1984a, b). Most of the troposphere is warmer than environment (700–200 mb), warm core is around 250 mb. Not shown is the cold core above 100 mb, caused by strong radiative cooling when the convective tower is penetrating above the equilibrium level. Panel (**c**) also indicates that Katrina has a moist core, indicating that the most active convective activity occur inside the 70 km (from center) inner region, becoming close to environmental mean at about 5° latitudinal distance. Outside the ~120 km inside region where upward motion dominates, there are complex alternating patterns of upward and downward (*blue*) regions (**d**)

spatial distribution are a particularly important aspect of the WRF's ability to make accurate TC track and intensity forecasts for the right physical and dynamical reasons.

Figure 7.9 is the comparison between TRMM-measured and WRF-simulated Katrina precipitation rates (mm/h) at three different time levels: 18 z at

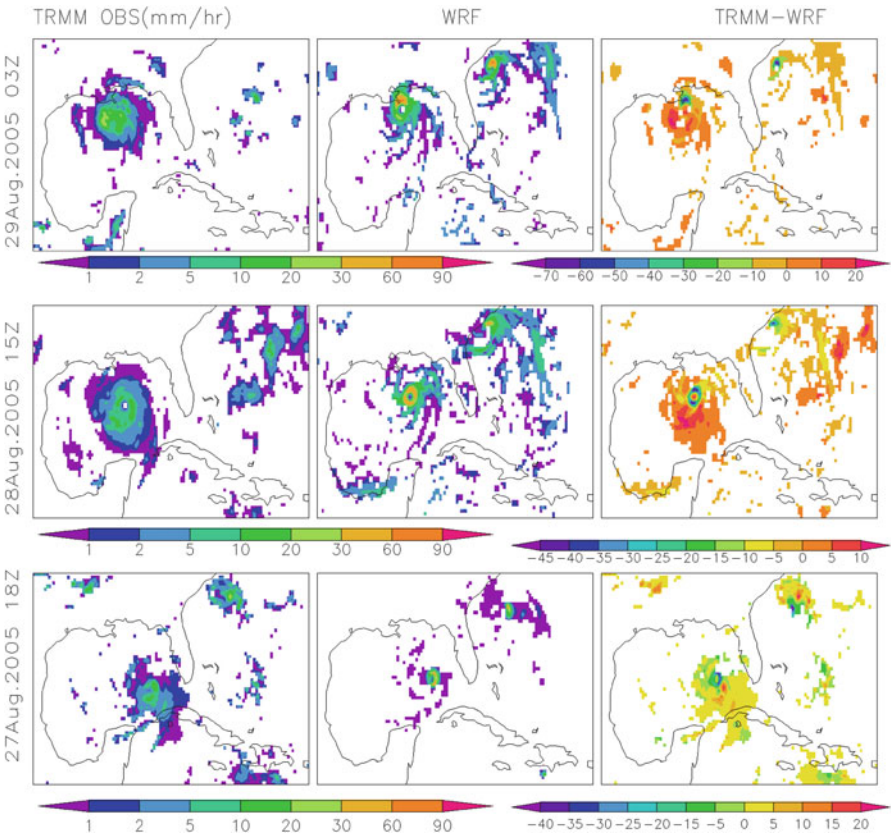

Fig. 7.9 Comparison of Katrina simulated and NASA/TRMM observed precipitation rate (mm/h). *Left panels* are TRMM 3B42RT observations, *middle column* is WRF simulations and *right most column* is the differences between TRMM observations and WRF simulations

August 27, 15 z at August 28 and 03 z at August 29, 2005. Precipitation is very asymmetrically distributed around the eye, and areas with strongest precipitation, located in clusters, can be 200 km away from the TC center. Patterns derived from the radar observations are accurately captured by model simulation (generally less than 1 km). However, quantitative precipitations are quite weak from radar observations and kind of smeared out. While TRMM precipitation provides a good sense of horizontal distribution of precipitation, it lacks the variations in intensity. In contrast, the model prediction yields more details and many strong convective types of precipitation are captured. In this case, it is not certain that TRMM observations are closer to reality or not. From the fact that the precipitation areas are so accurately simulated, higher priority may be given to the concentrated precipitation clusters in the WRF simulation. Upon landing (August 29), the total fallen precipitation and geographical/spatial distribution are vital inputs for storm-triggered landslide and flashflood simulations (Ren et al. 2010a, b). In this sense, as a

high-resolution full-physics model, WRF can play an important role in quantitative precipitation estimates (QPEs, forecasting the heavy precipitation at specific times and locations) and quantitative precipitation forecasts (QPFs) for landfalling cyclones. In this case, WRF performance is very successful. In general cases, to combine numerical model predictions with precipitation patterns derived from radar, satellites and in situ gauges is a viable approach in better estimate rainfall-related natural hazards. For a grid-point trailed by the eyewall, TRMM precipitation concentrates on the 5–20 mm/h bin level, whereas the model-simulated precipitation is much higher at 60–200 mm/h bin level (80 % of precipitation falls into this bin level). The above statements are generically applicable for other TCs (parallel figures are not shown). Precipitation amounts are a good indicator of released latent heat. Actually, only a small fraction of the released latent heating suffices for maintaining the symmetric vortices and warm core structure via transformation into kinetic energy and available potential energy (upper level meso-high and lower level meso-low mass structure). Only with a warm core structure, the cyclonic wind can simultaneously satisfy the gradient wind balance and hydrostatic requirements.

The simulated minimum sea level pressure occurs at different locations with maximum wind speed and cyclonic vorticity. For Katrina, the positions of lowest sea level pressure are close to the IBTrACS positions. However, for Larry, the locations of strongest 850-mb winds are closer to the best-track locations. We applied an automated tropical cyclone detection scheme (TC-tracker) to objectively locate the TC centers. The tracker has to apply a number of criteria to identify candidates from a wide variety of disturbances and then follow the centers to build up a full track. As described by Walsh et al. (2007), a typical tracker starts by locating a localized minimum in surface pressure or maximum in cyclonic vorticity to identify a potential cyclone. Once identified, the system is then filtered by preset values of maximum wind speed, vorticity, duration, and some measure of the presence of a warm core. The modeled tracks for Larry are very close to IBTrACS. For Katrina, the simulated track errors are larger, primarily in the west-bound moving period (e.g., reaching 0.5° persistent to the north at 82–87 W, first 2 days of ocean dwelling period after leaving Florida), while the north-bound stage is free of such large errors. Further research is needed to correct this problem. However, we do not feel that this will affect the following sensitivity studies to SST.

It would cause many inconsistencies if SSTs were directly altered and run the WRF model with otherwise identical initial and boundary conditions. To examine the sensitivity of tropical cyclone tracks and intensities to ocean surface fluxes, several sensitivity experiments with the WRF were performed with SSTs altered uniformly by 0.5,1, 1.5, 2, and 3C for the entire simulation region. Practically, the WRF variational data assimilation system is used to assimilate the altered SST fields. In this way, other atmospheric components still behave based on the same physics implemented in the WRF forward model.

TCs move toward the direction of increasing cyclonic vorticity. Thus, the relative vorticity Eq. (7.4) is equally useful in explaining the TC tracks. For example, the so-called Beta effect is one part of the horizontal advection of absolute vorticity. Advanced numerical model simulation (such as using the WRF here) is

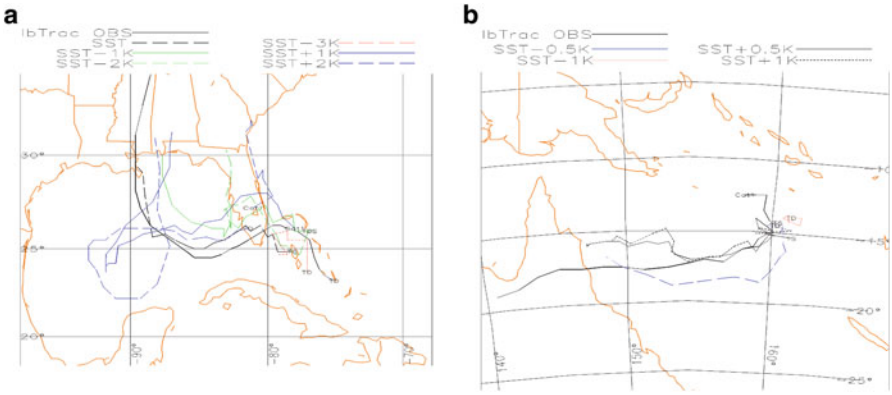

Fig. 7.10 Sensitivity of TC tracks to SST. (**a**) for Katrina, and (**b**) for Larry. For both cases, TCs cannot form if SST were 2 degrees lower than reality. Actually, TCs won't form for a 1 degree colder SST over the southern Indian Ocean basin (case not shown). If temperatures are higher, the tracks tend to turning over sea but spend less overall time before landing (moving faster than the control case). Also, as temperature gets higher, the secondary circulation also tends to form a "weaker" hurricane, for the case of Katrina (there will be another smaller scale one tracing the eastern coast along Florida, *blue dashed curve* in (**a**)). For Larry, stronger TCs tend to take a more northern track, because the Saddle atmospheric circulation (*box* in Fig.7.5b) usually provides anticlonic vorticity that expels the TCs southward (working in synergy with beta effect). The behavior due primarily to stronger steering currents as subtropical heights spreads

the most accurate way to project tracks and investigate the mechanisms for causing particular kinds of track. We should not spend too much in describing mechanisms of TC motion, rather we focus on how the track changes with SSTs. There lacks a unanimous conclusion on track sensitivity to varying SSTs. It seems that increasing SST by 1 °C pushes the track further southward. In the case of a 2 degree increase in SST, the indication is that the TC will wander in the warm pool. Once turning north, it makes a quick landing. In general, increasing SST does not push the track further west. However, reducing the SST produces a more continuous pattern of retracting further east, and more than a 2-degree reduction in SST may not result in a significant categorical hurricane (e.g., the minus 3 °C case simply diminished over the waters, Fig. 7.10a). A point requiring attention is that in the case of 2 degree warming SST, there is a second hurricane to the east (red dashed line as the primary hurricane track), heading north along the Florida coast and reaching category I at the peak stage. This case may have climate warming consequences, demanding further investigation in future work.

Figure 7.10b is the parallel case for Larry. A higher SST forces Larry-like TCs to follow a more northern path, and a lower SST leads Larry-like TCs to a more southern path. This is because the beta effect contests with the negative vorticity input from the saddle structure in the circulation fields, which pushes TCs south. A rise in SST indicates the weakening of the saddle structure (spreading of the subtropical high in the Southern Hemisphere). More TCs are guided to the northern

path. Unfortunately, this type of TC also tends to be like the trans-Australian ones that redevelop at the western coast (e.g., Glenda 2006). Thus, the effects of SST on environmental factors are the primary reasons for the changes in TC tracks. The cases with reduced SST tend to take a more southerly path and bring more precipitation to the eastern coast of Australia. Actually, the vegetation pattern has strong correlation with the post-landing TC tracks. The situation for Glenda is yet another different picture. The cases with higher SST tend to land more southerly, but the cases with reduced SST tend to meander along the coasts. More simple than the result for tracking, the precipitation, in both intensity and amount, is unanimously positively related to SST.

7.1.3 Changes in TC Activity in a Warmer Climate

Climate change likely manifests as a moderate trend (and is increasingly being directly ascribed to an increase of greenhouse gas concentration) and an enhanced natural variability (and thus more frequent extreme weather-related events). Recent "finger printing" attribution research tends to support this hypothesis. As it applies to TC activity, possible consequences can be complicated because the multifaceted nature of TCs and "extreme" may have very different interpretations for their tracking, formation frequency and intensity. It is of practical value to investigate whether or not there is multi-decadal "cycles" in the TC activities over the global basins. To this end, we need to investigate the role of global and regional responses to natural and anthropogenic forcing, and the role of natural oscillations.

Because of the associated natural hazards and their indescribably high social-economic impacts, landfalling TCs have been at the center of discussion of global warming. TC is actually a nexus of multiple research disciplines such as coastal management, flashfloods and landslides, and huge nutrients loss for terrestrial ecosystems. There have been numerous studies projecting the effects of future climate on sea surface temperatures (SSTs, strongly related to all aspects of TCs), based on increased carbon dioxide scenarios. The most studied TC basins are the Atlantic Ocean and the western North Pacific (WNP) Ocean. Although they are TC basin dependent, these projections largely have shown an increase in intensity and a decrease in TC numbers. However, the TC basin inconsistencies between the various model projections are such that the activity in each TC basin should be examined in detail.

The consensus of the theoretical and computer model projections of TCs in the twenty-first century is that TCs may be slightly stronger, by a few per cent, by the end of the twenty-first century, even when it is assumed that strong global warming will occur. The climate models agree in general that the number of TCs will not increase, and in some basins may even decrease by as much as 25 %, largely because of the expected increase in vertical wind shear during the twenty-first century, which will both decrease the genesis rate and increase the decay rate of

TCs in those basins. Two recent studies of the WNP and north Atlantic TC basins illustrate these points.

Over the past decade, the WNP has been the focus of many future projections in TC activity (McDonald et al. 2005; Bengtsson et al. 2007; Stowasser et al. 2007; Yokio and Takayabu 2009; Murakami and Sugi 2010; Murakami and Wang 2010; Murakami et al. 2010). For the WNP TC basin, Murakami et al. (2010) examined future changes in TC track projections over the WNP from the very high (20-km) resolution model, developed by the Japanese Meteorological Research Institute (MRI)-Japan Meteorological Agency (JMA). This study employed the IPCC Special Report on Emissions Scenario (SRES) A1B scenario, which is a commonly employed moderate development scenario. The main assumptions of the IPCC A1B scenario are that of "a future world of very rapid economic growth, low population growth and rapid introduction of new more efficient technology. Major underlying themes are economic and cultural convergence and capacity building, with a substantial reduction in regional differences in per capita income (see, e.g., http://www.ipcc-data.org/ar4/scenario-SRA1B-change.html). One of the key findings of Murakami et al. (2010) was that projected changes in TC activity, including TC frequency, are closely linked with location changes in TC genesis.

In the North Atlantic TC basin, Knutson recently addressed the four most prominent questions concerning the impact of human activity on trends in TC annual numbers and intensities. Knutson suggested that, for the North Atlantic TC basin: (1) it is too early to claim that human activity has already changed Atlantic TC activity; (2) also using the IPCC A1B scenario, climate model projections indicate that human activity will increase TC intensities by the end of the twenty-first century by between 2 and 11 %, and even more so for intense TCs; (3) the increase in intense storm numbers is projected despite a likely decrease (or little change) in the global numbers of all tropical storms; (4) climate models suggest global warming will produce TCs with higher rainfall rates than those of current TCs of about 20 % within ~100 km of the TCs.

Few studies so far have focused on the northwest Western Australia (NWA) TC basin. The second author recently investigated this basin, using high-resolution climate model output for 2000–2060, under the SRES A1B scenario. To identify a TC-like vortex in climate model, a number of criteria were used, because the resolution of climate models still is too coarse to simulate TC vortices in detail. The criteria used were those of Ookuchi et al. (2006), which is designed specifically to extract TCs with genesis in the tropics, and to avoid the extraction of mid-latitude cyclones. Using advanced statistics, it was found that, for NWA basin, there was little difference in the mean TC number over 2000–2060 but there is a statistically significant difference in the mean intensities. There also are significant changes in genesis and decay positions. More importantly, there is a wider longitudinal spread in the genesis and decay positions. These changes have apparent significance for continental shelf slope (under water landslides) for resource rich Western Australia. Considering the sparse population and relatively flat topography, storm-triggered landslides for this region is not a big concern. However, if Leslie's findings are applicable to other basins (e.g., WNP) and take the face value of Murakami

et al. (2010), the implications for storm-triggered landslides over Taiwan region and Japan are potentially harsh. Incidences of intense rainfalls associated with tropical cyclones often cause regolith saturation, especially for the case of shallow regolith overlying an extremely impermeable bedrock surface. In fact, except those immediately following earthquakes, all recorded slope failures in Taiwan area have occurred under conditions of positive pore water pressure. Emanuel (2005) and Webster et al. (2005) show an increase in the frequency of category 4 and 5 TCs in the WNP basin with potential impact on Taiwan. Further, even in areas where the frequency of tropical storms is predicted to decrease, rainfall rates within 100 km of TC center are expected to increase (Knutson et al. 2010). Holland and Webster (2007) found no trend in the mean intensity of Atlantic Basin storms. No consistent trend in the number of TCs in the Atlantic basin can be separated from natural variabilities in number and intensity of TCs (Webster et al. 2005). However, the most sever TCs (category 4 and 5) do have an increasing trend, follow closely the sea surface temperature trend (G. Holland, personal communication, 2012). Synchronize the Knutson et al. (2010) and Holland and Webster (2007) findings, the situation for storm-triggered landslides over the Central American islands are quite severe.

Figure 7.11 shows the changes in return periods of extreme precipitation over Taiwan region. Total precipitation amount over a rainfall period are used in the GEV approach. More sophisticated statistical approaches such as the generalized Pareto distribution (GPD, Coles 2001; Appendix E) give similar values. For each emission scenario, the median value among 13 Coupled General Circulation Models (CGCMs) are picked. For this region affected by tropical cyclone, the return periods for precipitation larger than 100 mm all significantly reduced. For example, the observed return period for 200 mm rainfall events is about 23.7 year. Under scenarios A2, A1FI, A1B, B2, and B1, the return periods are respectively 7.68, 8.05, 12.97, 17.38, and 19.06 years. Lower emission scenarios (e.g., B1) are close to observations but high emission scenarios (e.g., A2 and A1FI) more than halve the observed return period. Put it in another way, the 200 mm precipitation has return period of about 23.7 year return period. If the strong emission scenario A2 realizes in 2100 ($\pm$10 year), the return frequency for this rainfall amount would be only 7.68 year, three time more frequent in recurrence. The likely occurrence possibility in a future 10-year period increases from 40 to ~82 %.

In summary, strong TCs have indescribably destructive strong winds and precipitation. As ocean warms up more TCs may reach higher categories. The tracking and intensity both may change and the latter has more to be expected in improving projection skills. Statistics on losses associated with landslides that coincide with large scale flooding of tropical cyclones are difficult to compile because TCs captures the public attention and official inquiries. However, as human activities continue to expand into landslide-prone environments, the recognition of the scope and magnitude of the hazards has been increased recently.

Extreme rainfall totals can results from TCs making landfall, or moving slowly and parallel to a coastline, particularly if there are coastal mountains or even inland mountains not far from the coast. Prime examples include the Philippines,

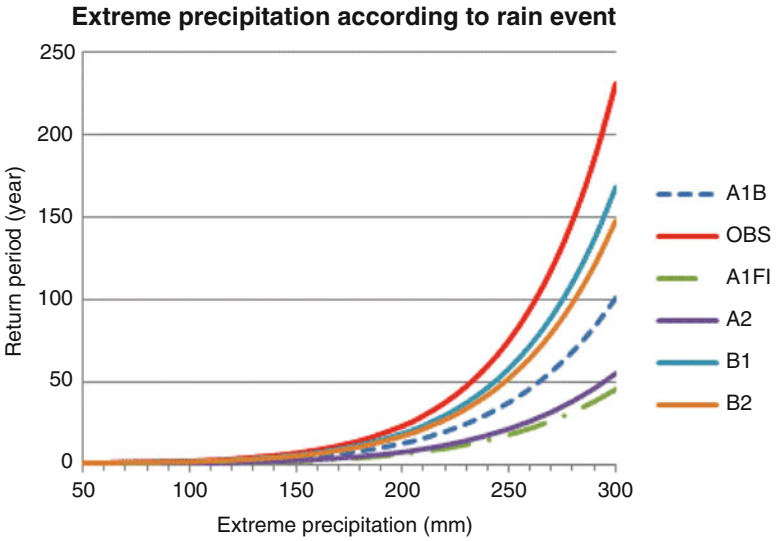

Fig. 7.11 Return periods (year^{-1}) of extreme rainfall over Taiwan area estimated from observations (1960–2009) and SRES scenarios (2000–2100) from 13 CGCMs (CCCMA-cgcm, CSIRO-mk30, GFDL_CM2.1, GISS_e_h, GISS_e_r, GISS_aom, MIROC3.2_hires, MIROC3.2_midres, MIUB_echog, MPI_echam5, MRI_cgcm2.3, NCAR_ccsm3, and UKM_HadCM3), for categories: 50, 100, 120, 140, 160, 180, 200, 210, 220, 230, 240, 250, 260, 270, 280, 290, and 300 mm. The "super-rain event" classification is applied. The GEV analyses are based on each event's precipitation amount. For each emission scenario, the ensemble method simply takes the median of the 13 CGCMs

Taiwan, and northeastern Australia, where totals exceeding 1,000 mm can fall in 24 h and over 3,000 mm in several days (e.g., Chien and Kuo 2011). In the Philippines, Taiwan, because of their high annual TC frequencies of severe TCs, such extreme totals present an annual landslide threat that causes catastrophic loss of life, infrastructure destruction and ecosystem devastation. For example, Hung et al. (2011) examined the nutrient loss to Southern East China Sea (discharging into Taiwan Strait) after Typhoon Morakot 2009. The nutrient loss associated with flashfloods and landslide burial is magnitude of order larger than can be replenished by natural processes such as lightning and legume fixation. In extreme locations, the entire village of Xiaolin was buried by storm-triggered landslides in the southern county of Kaohsiung killing 439 people with many roads left damaged and the landscape changed. Similar damages are caused to Philippines.

Extreme precipitation sometimes is caused by the interactions among several systems of variant spatial scales. For example, the August 7, 1975 extreme precipitation in Henan province, China is caused by mid-latitude trough caused lifting of a TC remnant that landed and slowly moving inland from August 4 to 7, after landing

at Fujian province's coast. During this period, the small amplitude "longitudinal" circulation pattern (high zonal index period) evolved into large amplitude "latitudinal" circulation pattern. Characteristics of this planetary circulation pattern are that a L-H-L "Ω" blocking pattern is formed north of the TC remnant tropical low. Because of the blocking effects, the motion of the TC remnant moves very slowly and the moving direction is diverted to west from the original north east moving direction. Eventually the motion ceases motion for about 20 h, resulting in record high precipitation over the region and several reservoirs was destroyed and flashfloods took hundreds casualties. The case teh August 7, 1975 extreme precipitation apparently belongs to the "latitudinal" type of extreme precipitation in section (Fig. 6.20) but its major vapor source is from a weakened landfalling TC. The narrow valleys over the region also provided lifting mechanisms for enhancing the precipitation.

7.2 Expected Trends in Monsoon Activity in a Future Warming Climate

More than two-thirds of the world's population live in monsoon regions and monsoonal precipitation accounts for a great portion of annual global rainfall (Wang 2006). Monsoon precipitations also contribute the most deadly landslides for India and South America. Monsoon activity is an indicator of large-scale land-ocean thermal contrast. Global warming is a nonuniform warming and usually reduces latitudinal temperature gradients hence reducing land sea thermal contrast for monsoonal region (IPCC, AR4 2007). In the last 50 years, there are reported reductions in number of monsoon depressions and associated monsoon rainfall for the Indian monsoon. Wang and Ding (2006) however found that there is an increasing trend in global monsoon rainfall during the past two decades. Although the global monsoon area may also expanded in the same period (Hsu et al. 2011), the precipitation intensity, defined as global monsoon precipitation amount per unit area, declined. Based on these findings, we still cannot rule out the possibility for regional realization of extreme precipitation, as warming ocean surface temperatures supply higher concentrations of moisture in the low level atmosphere. For similar lifting mechanism, atmospheric energetic allows heavier precipitation to occur. Goswami et al. (2006) examined daily rainfall anomalies during the monsoon season (June 1 to September 30) in central India and identified a significant increasing trend in the variance during the period 1951–2000. Rainfall was gridded on a 1 degree by 1 degree box and heavy rainfall events were defined as more than 100 mm/day and very heavy rainfall as more than 150 mm/day. The increase in extreme events came at the expense of light to moderate rainfall, yielding no overall trend in annual precipitation. The heaviest four rainfall events in each monsoon season have increased ~10 % per decade in precipitation amount over the 50-year record. A recent study (Hsu et al. 2011),

by redefining the global monsoon area as annual range of precipitation and the ratio of summer-to-annual rainfall for each monsoon year, as opposed to traditional definition based on climatologically averaged precipitation information, identified also a statistically significant increase in monsoon rainfall events. These extreme precipitation events are relevant for storm-triggered landslides. As the climate warms, global land surface and ocean temperatures increase unevenly and it is likely that the land-sea thermal contrast also evolves. As a monsoon system is largely attributed to the land-sea thermal contrast, the monsoon range as well as the depressions nested within all may change. Even if the general pattern is that of a weakening system spreading over a larger area, there still exist unfortunate combinations of lifting and transport mechanisms that together produce extreme precipitation events with landslide consequences.

7.3 Trends in ENSO Activity in a Future Warming Climate

Due to the persistent action of trade winds, tropical west Pacific Ocean is a warm pool while the eastern Pacific Ocean is a cold tongue (west coast of south America, in relative sense). Correspondingly, the thermocline is deeper at western Pacific Ocean than the eastern Pacific Ocean and there is an east–west gradient in SST. El Niño (Figs. 7.12 and 7.13) is the periodic warming of the tropical Pacific Ocean that persists for 1 year or longer and occurs every 3–7 years (Neelin et al. 1998; McPhaden 2002). The opposite pattern, a cooling of tropical Pacific Ocean (strengthening of the trade winds) is referred as La Nina (Philander 1990). El Niño and La Nina conditions are dynamically linked to the differences in surface atmospheric pressure over Australia and the eastern tropical Pacific. This pressure oscillation/seesaw is called ENSO (El Niño and Southern Oscillation). Both El Niño and La Nina conditions are associated with changes in weather patterns and, through teleconnections, impact droughts, flooding, and storm-triggered landslides, essentially world-wide. For a theoretical review of ENSO, the readers are referred to Neelin et al. (1998). For the great circle theory, the basis of teleconnection patterns, the readers are referred to Philander (1981, 1985) and Hoskins and Karoly (1981). For observational verification, readers are referred to Wallace and Gutzler (1981). Following is a succinct summary of this phenomenon.

Occurrence of ENSO has been explained as either a self-sustained and naturally oscillatory mode of the coupled ocean-atmosphere system or a stable mode triggered by stochastic forcing. In either case, ENSO involves the positive ocean-atmosphere interactions hypothesized by Bjerknes (1969). After an El Niño reaches its mature phase, negative feedbacks are required to terminate growth of the mature El Niño anomalies in the central and eastern Pacific (called delayed negative feedback). Four negative feedbacks have been proposed so far: reflected Kelvin waves at the ocean western boundary (delayed oscillator theory of 1980s, e.g., Suarez and Schopf 1988; Zebiak and Cane 1987; Battisti and Hirst 1989), a discharge process of upper ocean heat content due to Sverdrup transport (Wyrtki

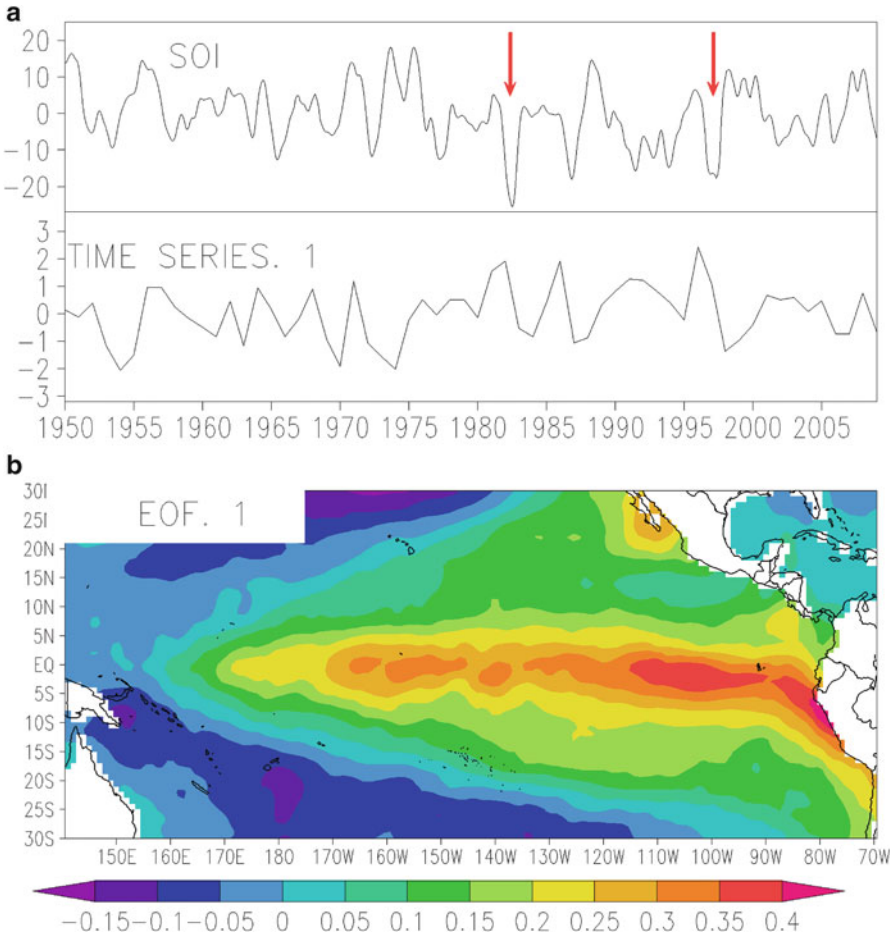

Fig. 7.12 El Niño conditions in the equatorial Pacific, as indicated by the Southern Oscillation Index (SOI) and the empirical orthogonal function (EOF) analysis of Sea Surface Temperature (SST). Panel (**a**) are the time series of the SOI index and the EOF time series for the same 1950–2010 period. The first principle component corresponding to the EOF time series shown in (**a**) and shown as *shaded contours* in (**b**). SOI and the first EOF time series always tend to be out of phase. Pikes in the time series and minimum in the SOI values indicate El Niño conditions. *Red arrows* label two recent strong events, the 1982, 1983 and 1997, 1998 events

1975; Jin 1997a, b; Battisti 1988), western Pacific wind-forced Kelvin waves (Weisberg and Wang 1997), and anomalous zonal advections (Picaut et al. 1997). These negative feedbacks may work together for terminating El Niño, with their relative importance varying with time. Because of different locations of maximum SST anomalies and associated atmospheric heating, El Niño events are classified as

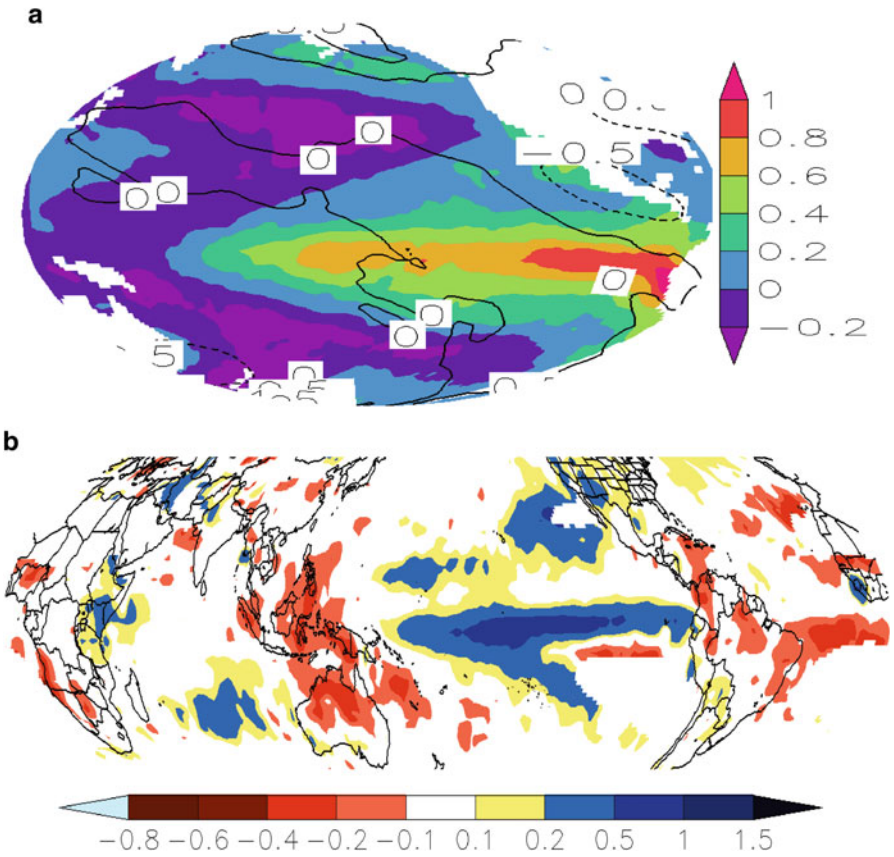

Fig. 7.13 SST and precipitation anomalies associated with El Niño. Panel (**a**) shows El Niño anomalies in SST (*color shading* and *scale* in °C) and surface atmospheric pressure (*contours*) in the Pacific basin. Pressure contour interval is 0.5 mb, with *solid contours* positive and *dashed contours* negative. The El Niño events included in the plotting are: 1957–1958, 1965, 1972–1973, 1986–1987, 1991–1992, 1997–1998, 2003–2003. The 1970–2000 climatic mean is used as reference. During El Niño years, the air mass has a poleward redistribution trend. For example, mid-way between Australia and southern tip of South America, there is a strong anomaly in surface pressure. Similarly, Aleutian low getting weaker because of reduced upper level out flow. Also notice that surface pressure has negative anomalies over southern California region. This has apparent precipitation significances. In (**b**), precipitation anomalies are presented in relative form to the climatic mean values (at each specific location). Precipitation values are based on CPC Merged Analysis of Precipitation (CMAP, http://www.esrl.noaa.gov/psd/data/gridded/data.cmap.html). The El Niño years selected are: 1982, 1983, 1987, 1997, 1998, and 2002. Partly adapted from McPhaden et al. (2006). Mollweid projection is used for preserving area

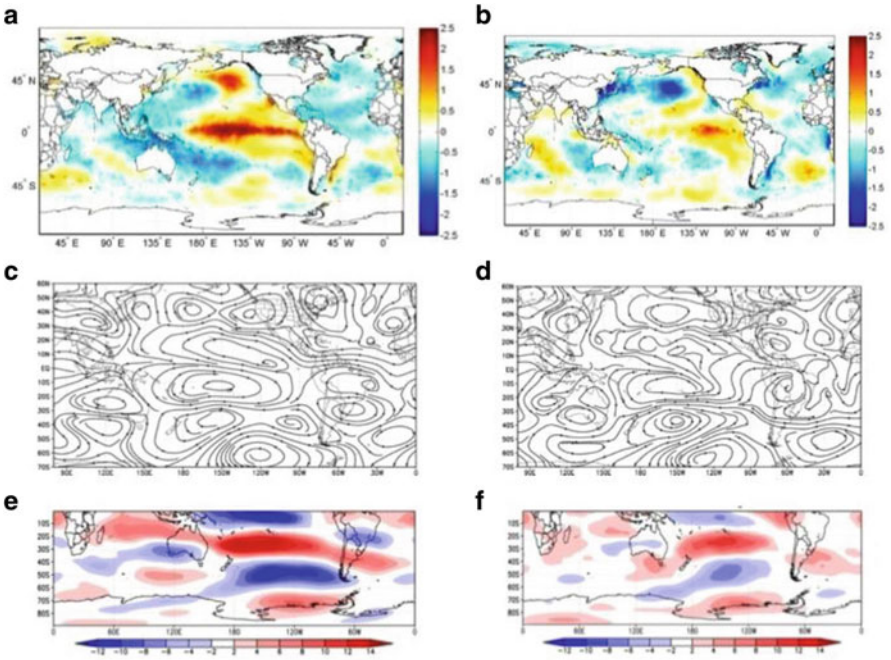

Fig. 7.14 Composite differences in (**a**) the SST (°C), (**c**) 250 hPa streamlines (m/s) (**e**) 250 hPa zonal wind (m/s) between warm and cold SSTA (exceed 1σ) for the CPW years. (**b**) Same as (**a**), (**d**) same as (**c**) and (**f**) same as (**e**) for EPW years during the period of 1979–2002 based on the ECMWF 40-years reanalysis

eastern[2] and central Pacific warming events, EP and CP El Niño respectively. The identification of two distinct types of El Niño offers a new way to examine global impacts of El Niño and to consider how El Niño may respond and feedback to a changing climate (Fig. 7.14).

Rainfall patterns associated with different flavors of El Niños and the Pacific Decadal Oscillation (PDO) had been thoroughly covered in literature (e.g.,

[2] Bjerknes positive ocean-atmosphere feedback: On the Walker Circulation (trade wind is the lower level branch of the Walker circulation) set normal background, a positive perturbation on the equatorial eastern Pacific reduces the east–west SST gradient and hence weakens the Walker Circulation (Gill 1980; Lindzen and Nigam 1987), resulting in weaker trade winds around the equator. The weaker trade winds in turn drive the ocean circulation changes that further reinforce SST anomally. This composes a positive feedback and eventually leads to a warmer state of the equatorial Pacific, i.e., the warm phase of ENSO-El Niño. The maintain of the climate condition of the tropical SST is also referred to as Bjerknes feedback (Cane 2005). The trades normally pile up warm surface water in the western Pacific while upwelling cold water in the east from below the surface along the equator and off the coast of Peru. The resulting east–west (zonal) surface temperature contrast reinforces an east–west air pressure difference across the basin that in turn drives the trades.

Mantua et al. 1997), so are the Pacific-North America patterns (Wallace and Gutzler 1981). Following discussions focus on the South America region. For storm-triggered landslides in the central American islands and South America (e.g., Columbia, Peru, and Brazil), the important role of South America in determining the influence of Pacific SST anomalies on tropical Atlantic climate variability needs to be factored in. Liebmann et al. (2009) have shown that convective coupled Kelvin waves in the equatorial Amazon are generated by three sources of perturbations: (a) northward propagation of the Rossby waves from extratropical South America; (b) preexisting Kelvin waves over the eastern Pacific that propagate eastward into the Amazon; (c) locally generated perturbations. Source (b) has been considered as the primary pathway of ENSO influence on tropical Atlantic (Saravanan and Chang 2000; Chiang and Sobel 2002; Neelin et al. 2003), whereas the roles of (a) and (c), which are influenced both by ENSO and atmospheric and land surface processes within the South America, are still not clear. Previous studies have shown that an increased heating in the central Pacific during an El Niño can weaken equatorward propagation of the extratropical disturbances in South America (e.g., Vera et al. 2004), thus reduce extratropical-forced Kelvin wave activities in the Amazon. El Niños could also cause an earlier northward withdrawal of the Amazon rainfall (Liebmann and Marengo 2001), thus could weaken the locally generated Kelvin waves. These changes could potentially counter the increase of the eastern Pacific-originated Kelvin waves in the Amazon (Liebmann et al. 2009). Hence, the net influence of El Niños on tropical Atlantic climate variability may be modulated by the changes of the extratropical-forced and locally generated Kelvin waves.

It is still not clear what might control changes of Kelvin waves during El Niños? The central Pacific warmings (CPW) El Niños have different impact on atmospheric circulation anomalies in the tropical Atlantic from that of the eastern Pacific warmings (EPW) El Niños (Kim et al. 2009). Analysis in Fig. 7.14 shows a clear Pacific-South America planetary wave train associated with a CPW, but not with an EPW, suggesting different effects on Kelvin waves generated in the extra tropics. Thus, the response of the extratropical-forced Kelvin wave to CPW El Niños could be different from that to EPW El Niños. These two types of El Niños could also have a different influence on the Amazon rainfall withdrawal during boreal spring.

Future research aim to investigate whether or not the influence of Pacific El Niños on the onset of Atlantic Niños is in part controlled by different responses of the extratropical-forced and local generated Kelvin waves in the Amazon, and whether these different responses are primarily linked to El Niño types, is promising (J. Luo and R. Fu, Personal communications 2008 and 2010).

7.4 An Application of SEGMENT-Landslide to California: A Location Susceptible to Threats from Multiplefactors

Extreme precipitation events in California have strong correlations with several teleconnection patterns, on cascading time scales. A high resolution climate model, GFDL/HIRAM, has simulated well the southern (relative to the Aleutian synoptic disturbances) storm tracks in El Niño years and rare, ~27 year recurrence period, hurricane landfalling events. Consequently, the model can be used to simulate the geographical distribution, seasonal cycle, and interannual variability of extreme precipitation (>50 mm) events that may have landslide consequences. Although much less frequent, extreme precipitation constitutes most of the annual total precipitation. There is consistent underestimation of the extreme rainfall (>100 mm), because current climate models do not yet accurately simulate tropical cyclone intensity. However, climate model statistics of extreme precipitation are qualitatively skilful. Changes in storm-triggered landslide activity from an advanced landslide model, SEGMENT-Landslide, driven by climate model projections, are compared for: (1) a twentieth century run (CNTRL); and (2) the moderate IPCC SRES A1B scenario (EGHG). The aims of this study are to determine differences in landslide frequency and magnitude, and test for differences between CNTRL and EGHG projections, using kernel density estimation (KDE) for a cluster analysis of CNTRL and EGHG scarp locations.

It is found that there is an increase in landslide numbers over the period. The CNTRL and EGHG projections differ in mean landslide latitude and longitude positions. The KDE reveals three clusters in both CNTRL and EGHG mean positions. There is an inland shift of ~0.5° and a northward shift of about 1°. The model results can be explained in terms of physical, meteorological, and sea surface temperature conditions.

7.4.1 Overview of the Study Region

How extreme rainfall changes over the next century in mountainous regions has apparent relevance for storm-triggered landslides. In heavily populated regions such as southern California, landslides may have large economic and societal impacts (NRC 2008). This study focuses on the state of California in the USA, a locality where the combined effects of earthquake and landslide have been documented. The precipitation of this region, being regularly affected by El Niño and Southern Oscillation and potentially also sensitive to climate change, as it lies in Mediterranean climate zone and the vegetation is in a retreating (degrading) long term trend, possesses large uncertainty in the future occurrence of storm-triggered landslides (Ren et al. 2010a). In addition, the mountainous ecosystem contains vanguard species of migration in a warming climate. Die-back of certain species as a result of storm-triggered landslides (Ren et al. 2009) may have serious consequences for biodiversity (Chapin et al. 2002).

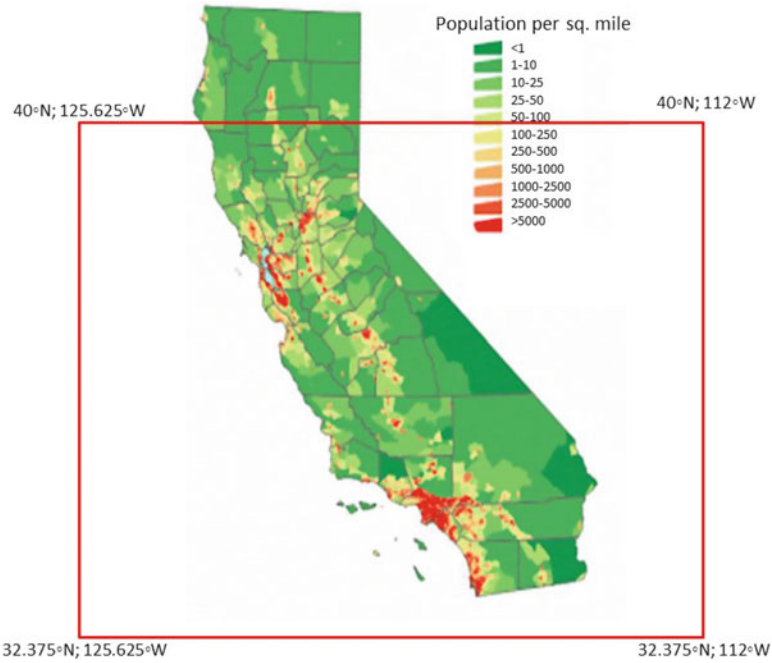

Fig. 7.15 Region of interest (*red box* defined area). Background population density map is from US Census Bureau (Census 2000 summary file) website

In the first part of this study, daily variations in California rainfall associated with teleconnection patterns are investigated. To explore the future change of rainfall along the west coast of the USA, especially the State of California, a high resolution general circulation model, the Geophysical Fluid Dynamics Laboratory High Resolution Atmospheric Model (GFDL/HIRAM, Putman and Lin 2007) simulations are used. The observations over the interested region suffices to validate physical processes in the model that would control the rainfall changes on decadal or longer time scales to increase their credibility for climate projections, if these physical processes are in common with those that control the rainfall changes on seasonal and interannual scales (Palmer et al. 2008). On a cascading time scale, Californian extreme precipitation is highly correlated with the ENSO events, the Pacific decadal oscillation (PDO), and sporadic hurricane landfalls. Faithful simulations of rainfall events associated with the teleconnection patterns and hurricane activities are critical for reliable projections of extreme precipitation in a future warming climate. The GFDL/HIRAM is first verified against observed precipitation morphology. The SEGMENT-Landslide (Ren et al. 2008; Ren 2014), driven by GFDL/HIRAM provided atmospheric fields, then extends our projection ability of future landslides changes in California.

The region of interest (32.375–40° N; 125.625–112° W, Fig. 7.15, spherical area of 1,039,200 km^2 but valid land area is only about 390,000 km^2) comprises several

low mountain ranges in the southwest corner of California, near Los Angeles and San Diego, and the higher, sparsely inhabited Sierra Nevada Mountain Chains to the east. The complex geologic properties of the region of interest support essentially all kinds of landslides as defined in Hutchinson (1968) and Varnes (1978). For example, when the coastal bluffs (of Cenozoic marine sedimentary rocks) are socked with El Niño storms, deep-seated and rotational landslides are likely to occur. For the scars left by wild fires or after limber harvesting, shallow landslides such as the progressive bulking type of debris flows (left panel of Fig. 5.4) are common for intense rainfalls. Land cover and land use are complex and comprise urban, shrub, and forest environments. The dominant vegetation of southern California is a mix of winter deciduous, evergreen, annual grasslands, and some drought resistant deciduous plants. Material properties vary widely, as do local surface relief, vegetation, precipitation climatology, and seismic activity. These factors determine where and when landslides will occur. Previous landslides leave a "cold trace legacy" on future slope stability (Dietrich and Dunne 1978; Dietrich et al. 1995; Crozier and Preston 1999) and detailed process modeling is needed to identify future unstable regions. In this study, the full 3D process-based landslide model is driven by state-of-the-art climate model provided atmospheric parameters in the twenty-first century to make some projections on changes in storm-triggered landslides over southern California. Since SEGMENT-Landslide supports multiple typology of landslides and multiple rheology for sliding material, it hence is capable of investigating all major types of landslides in California.

A range of techniques is employed to analyze the rainfall in California and teleconnection patterns and trends in extreme precipitation. These statistical methods include Monte Carlo based composite analyses (Hendon et al. 2007), scattering analysis (Scott 1992), and nonparametric trend analysis (e.g., Mann-Kendall test, Kendall (1970)). Here, landslide activity is taken as that triggered by extreme rainfall and the mass mobilized varies between 10^3 and 10^6 m^3.

7.4.2 Data Used in the Analyses of Southern California Landslides

The model simulation domain contains all possible sliding material (the entire soil layer) and one bedrock layer as the bottom model sublayer. SEGMENT-Landslides requires the following input parameters: initial moisture content of the failed slab, soil material properties, vegetation root depth and distribution morphology such as root length density and root strength, and initial bedrock topography (high resolution elevation data). This study uses the high-resolution DEMs from the NASA Shuttle Radar Topography Mission (SRTM, http://www2.jpl.nasa.gov/srtm/, USGS 2004). The data set is of ~90-m resolution. The soil characteristics are from the Food and Agriculture Organization of the United Nations (UN/FAO, http://www.fao.org/geonetwork/srv/en/metadata.show?id=14116, Fig. S3). These soil

mechanical properties (Table 5.3) are used to parameterize the granular viscosity of the sliding material according to the formula in Eq. (5.13). Setting of the bedrock mechanical properties always references to the geological map of California. At fracture stage (velocity equals 0 in the governing equations), the static mechanical strength (tensile and shear strength) is set as 30 MPa for the intrusive igneous rocks and other crystalline rocks of Sierra Nevada Range and only 5.6 MPa for the sedimentary rocks at the coasts (e.g., shale and clay stones). Weakly cemented sandstones have an intermediate value of 11.1 MPa. The compressive strengths of rocks are orders of magnitude larger than tensile strengths and rarely are involved in the landsliding events. At flow stages (with apparent velocities of sliding material), the viscosities of the bed rocks also vary from 10^{15} to 10^{9} PaS, depending on lithology and degree of fracture. In setting up the bedrock mechanical strength, burying depth, in addition to the geologic unit reflecting lithology, is taken into consideration to reflect an increasing strength of rock with confining pressure.

Compared with the physical properties of hill slopes that affect the potential for landslides, vegetation and rainfall are far more temporally variable. The USGS National Land Cover Dataset 2001 (NLCD 2001; Homer et al. 2004) provides land cover information. For vegetated surfaces, especially those affected by fires, representing soils as purely mineral (e.g., sand, silt, and clay classifications) is inadequate (DeBano 2000; Moody and Martin 2001; Smith et al. 2002). For previous fire sites within the last decade, a parameter f_i is introduced to represent the fraction of soil sublayer (1) that is organic matter. The thermal and hydraulic parameters for organic soil are weighted averages of the corresponding mineral soil and those of humus, using an empirical relationship (Lawrence and Slater 2008; Letts et al. 2000). A unique feature of SEGMENT-Landslide is its treatment of root properties relevant for storm-triggered landslides. Bedrock rheological properties such as viscosity are set according to published geological map (http://mrdata.usgs.gov/sgmc/ca.html). The atmospheric parameters are provided by the high resolution climate model GFDL/HIRAM.

As a result of the complex geological properties underneath Californian slopes, soil type may vary within the same slope (Segoni et al. 2012; Mahmood et al. 2012). For storm-triggered landslides, we focus on the mechanical properties of the soil particles. Many rheological features and hydromechanical properties of granular material originate from the particle interlocking, which relies on soil particle size distribution. Ideal soil classification should classify soils such that their hydromechanical properties could be similar within the same classification. Among available soil classification systems, we used the USDA classification system. Soil chemical composition also is important for their hydromechanical properties. Unfortunately, none of the four classifications are based on soil chemical compositions. In setting up the spatial variable soil mechanical properties, we not only used the USDA soil map, but also referred to the STATSGO soil data for its wealth of vertical profile information (Table 5.3, Fig. S2).

To study the daily variation in California rainfall associated with the teleconnection patterns such as Pacific North American Pattern (PNA), Pacific Decadal Oscillation (PDO), North Atlantic Oscillation (NAO) and Southern

Oscillation Index (SOI), the North American Regional Reanalysis (NARR) daily composite precipitation is used for the period 1979–2010 (http://www.esrl.noaa.gov/psd/data/gridded/data.narr.html). The indices are obtained from NOAA/NCDC website (http://www.ncdc.noaa.gov/teleconnections/). For the projection of future global warming consequences on storm-triggered landslides, the GFDL/HIRAM, specifically C180 HIRAM2.1 simulations are chosen (over most PCMDI posted climate model simulations for AR4) primarily because of the fine horizontal resolution (~50 km). The GFDL/HIRAM has 32 vertical levels (1/3 more than the GFDL AM2, its predecessor) and covers the entire globe. It utilizes a cubed sphere dynamical core (Zhao and Held 2010) with 180×180 grid points on each face of the cube, resulting in grid sizes ranging from 43.5 to 61.6 km. There are numerous improvements in physical parameterizations to facilitate simulation of the tropical atmosphere, including the Bretherton et al. (2004) shallow convection parameterization and the cloud physics closure. During the twentieth century simulations, the lower boundary sea surface temperatures (SSTs) are observed sea surface temperatures from the Hadley Centre Global Sea Ice and Sea Surface Temperature (HadiSST, V1.1), interpolated to 6-hourly intervals. The twentieth century run is defined as the control run (CNTL). For twenty-first century projection, we only look at the SRES A1B emission scenario runs. The simulations are two continuous 20-year periods: from 1979 to 2000 and 2079 to 2099. The scenario run is referred to as the EGHG run.

7.4.3 Preliminary Results from Model Simulation

The primary source of precipitation over the west coast of the USA is the synoptic troughs traceable to Aleutians lows (Fig. 7.16). The GFDL/HIRAM provides satisfactory simulations of the precipitation events (Fig. 7.16a). However, the precipitation amount and intensity are limited and there usually is limited damage, because the troughs weaken or diminish as they pass over the colder waters of the California Current that flows southward along the California coast. The longer lasting rainfall events are usually associated with ENSO events, which have about a 4–7 year recurrence frequency. These rainfall events (usually of $>$50 mm rainfall) cause most of the observed debris flows in southern California. Closely related to ENSO events, GFDL/HIRAM occasionally produces a southern, subtropical branch of storm tracks in addition to that originating from the Aleutians. This is in response to the unusually warm SSTs in the eastern tropical and subtropical Pacific. This storm track brings tropical moisture to southern California. Figure 7.16b, selected from model year 1982, indicates that GFDL/HIRAM simulations also have ENSO-like precipitation patterns. The most severe rainfall events over southern California are a combination of a mid-latitude trough picking up the moisture remnants of hurricanes that formed in the eastern North Pacific Ocean and traveled northwest far enough. This situation is rare (~27-year recurrence period) but can produce rainfall totals over 200 mm within several days (Blake 1935; Smith 1986; Landsea and

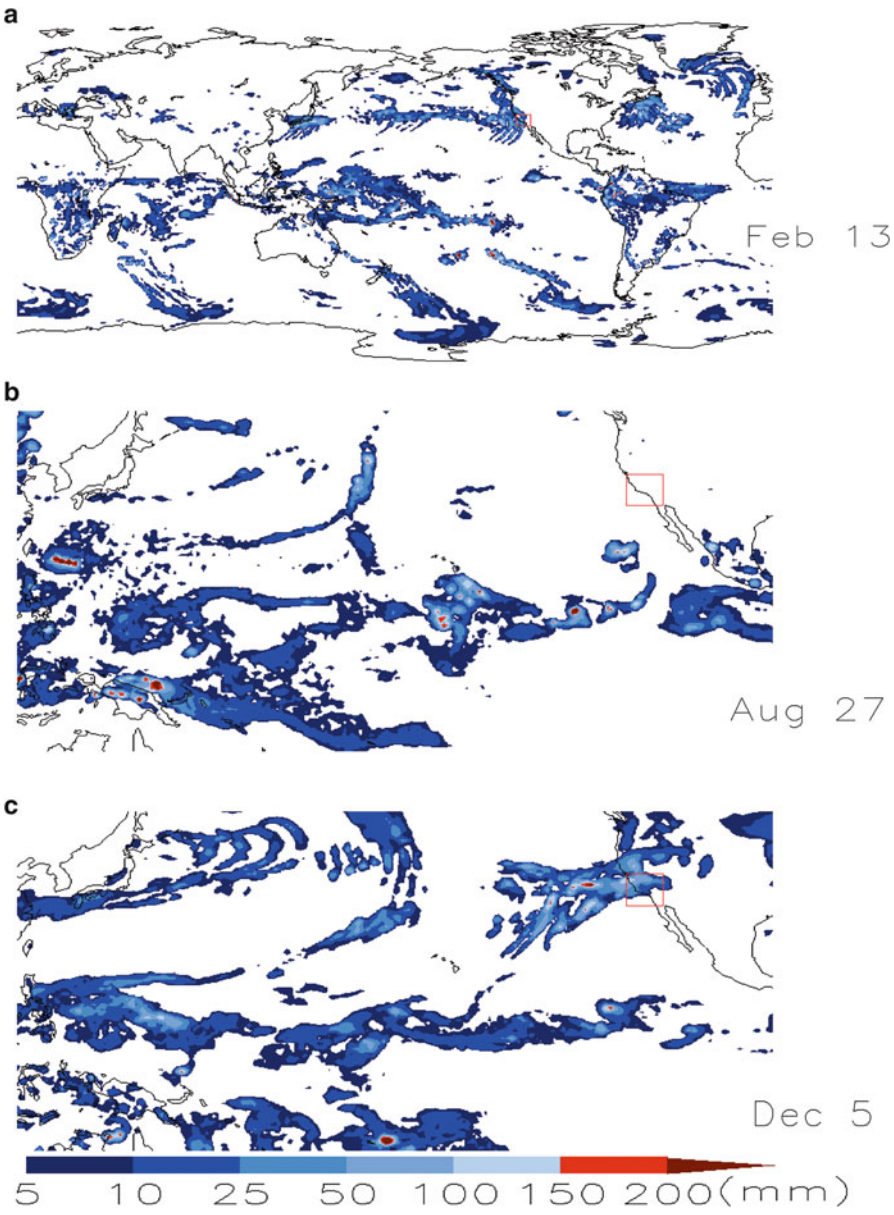

Fig. 7.16 GFDL/HIRAM simulated daily precipitation (mm). The *small red box* is the region of interest. Panel (**a**) shows the most common precipitation system for California, the synoptic scale events originating from the Aleutians. In panel (**b**), a hurricane is approaching the California coast (it made landfall 30 h later). Panel (**c**) shows a south storm track associated with ENSO. This storm track extends from Hawaii all the way to southern California. GFDL/HIRAM satisfactorily simulated these precipitation makers for California

Chenoweth 2004). The climatological statistics of hurricanes simulated in this model, as well as the interannual variability in the model forced by observed SST indicate that it can reasonably simulate the geographical distribution of storm genesis locations, as well as seasonal cycles and interannual variability of hurricane frequencies for the major basins (Zhao et al. 2009). The deficiency of GFDL/HIRAM in simulating the >100 mm category rainfall events over southern California is primarily due to an inability in simulating tropical cyclone intensity (Zhao and Held 2010). Thus, GFDL/HIRAM simulates well the occurrence of this type of event but the simulated intensity and longevity are inadequate as yet. Rescaling the model precipitation empirically (e.g., Zhao et al. 2009) can better fit the observed rainfall morphology. In this study, we do not make such empirical correction because we believe this deficiency should not harm GFDL/HIRAM's ability in indicating the changes of extreme rainfall events as climate warms (i.e., it is still valuable in telling us if there are significant changes in occurrence frequency in extreme rainfalls). Instead, we reclassify the precipitation bin levels as 0–5–20–50–100 mm and we find that the correspondence of the CNTRL period and reality improved significantly (figure not shown).

In addition, the mountainous terrain south of the Peninsular Range and Transverse Ranges also receive some monsoonal rainfall. The GFDL/HIRAM provides satisfactory timing and geographical location of this monsoonal precipitation. Note that the coupled models do not have realistic timing in their simulations, but still can provide statistically reasonable time series to assess the probability of changes in extreme rain events that have landslide consequences.

To investigate the relationship between the daily precipitation variations and the teleconnection patterns, composite maps for the period of 1980 through 2010 were constructed for all days in high index polarity and low index polarity (that is, periods with indices value outside one standard deviation). Composite differences are defined as composite high index minus the composite low map. The natural variability of composite differences, or if the index is completely unrelated to the precipitation variations, is estimated according to a Monte Carlo method (Hendon et al. 2007). For the SOI index, except for spotty areas north of the central valley, all were significant at the 95 % level. The correlations depend on geographical location and can explain up to 17 % of the total variance (e.g., the region containing Yosemite National Park, Mandeville Canyon; Oroville). Similar analyses for the AO and NAO indices show modest correlations. From the composite analyses it is apparent that the most notable precipitation signals on annual time scale across California are from El Niño events, which show an overall positive anomaly over all seven subclimate zones, especially southern California. The composite analysis adapted from Hendon et al. (2007) reveals that as high as 18 % of the variance can be explained by the SOI index. On the longer decadal time scale, the fluctuations in precipitation are related to the PNA patterns. For northern California, it can explain as much as 20 % of the annual variance. Thus, whether GFDL/HIRAM can successfully simulate the El Niño related precipitations is critical in estimating changes in storm-triggered landslides.

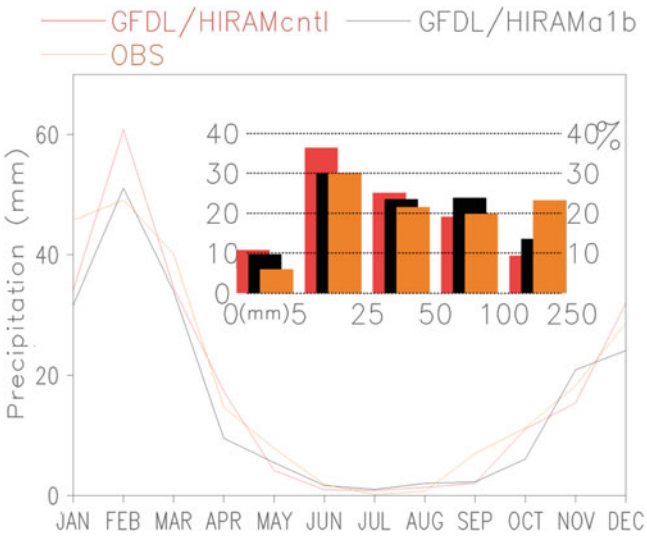

Fig. 7.17 November–March is the rainy season. The *curves* show the annual precipitation distribution. January and February have the largest errors (up to 18 %). The *inset* is rainfall precipitation distribution among rainfall categories. The 100–250 mm extreme rainfall, with a much lower occurrence frequency (e.g., two orders of magnitude lower than the 5–25 mm category), contributes about a quarter of the total precipitation. Model simulations still consistently underestimate this rainfall category

Figure 7.17 shows that, characteristic of Mediterranean climates, the regional average rainfall concentrates within November to March. While the annual mean precipitation is very accurately simulated, the error in February precipitation can reach 18 %. The light precipitation (<25 mm), although occurring most frequently (~70 % of rainfall occurrence), comprised less than 40 % of the annual total rainfall. However, the extreme rainfall (100–250 mm category) occurred 20 times less frequently, contributing about 25 % of the total precipitation. The model significantly underestimates this rainfall category.

Unlike normal precipitation events with life spans of less than a day, extreme precipitation, with total amounts greater than 100 mm in the southern California region, usually are distributed over a couple days in a row, or several nonconsecutive days separated by no more than 2 days. For storm-triggered landslides, those precipitation events separated by less than 2 dry days (as "break") should be considered as one "super" rain event. Thus, unlike many previous studies (e.g., O'Gorman and Schneider 2009 and references therein), which count daily precipitation 1 day at a time, we count those extended super-rain-events, defined as a somewhat continuous rainfall period nowhere separated by more than 2 consecutive dry days (Ren et al. 2011a). Figure 7.18 shows changes in rainfall morphology as the climate warms. Rainfall categories are set according to the extreme rainfall events defined in Ren et al. (2010a). For the control period (x-axis), except for the

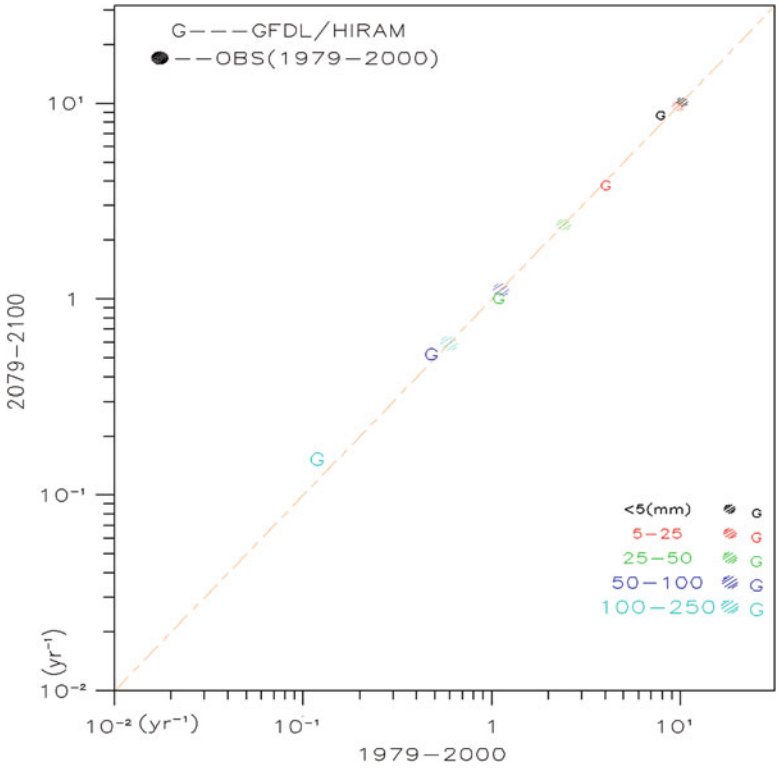

Fig. 7.18 Changes in rainfall morphology as the climate warms. Rainfall categories are set according to the extreme rainfall events (defined in Ren et al. 2011a, b). The occurrence frequencies are in logarithmic scale. The observed occurrence frequencies are plotted on the *diagonal line* for reference. *Letters* (of *different color*, also *font size*) are GFDL/HIRAM simulated rainfall occurrence frequencies in five bin levels. A letter "G" is placed in the figure so that its x-coordinate is the occurrence frequency during 1979–2000 period and its y-coordinate is future occurrence frequency. Thus, lying above the *diagonal line* means this category rainfall increases in occurrence frequency in the future. For the control period (x-axis), except for the <5 mm category, all other categories have clear (2–6 times) errors of consistent underestimation of rainfall occurrence frequency (climate model produces rainfall less frequent than reality). The deficiency in simulating the extreme categories (>100 mm) arises partially from the simulated weaker hurricanes formed in the eastern North Pacific Ocean. The large rainfall categories (50–100 and 100–250 mm categories) have an increased occurrence frequency (figures lying above the *diagonal line*)

<5 mm category, all other categories have apparent (2–6 times) errors of persistent underestimation of rainfall occurrence frequency (climate model produces rainfall less frequent than reality). The deficiency in simulating the extreme categories (>50 mm) arises from the simulated weaker hurricanes formed in the eastern North Pacific Ocean. The deficiency can be corrected by reclassification, or proportionally increasing the modeled precipitation. For example, suppose the 5–10 mm category corresponding to the 50–100 mm category in reality and so on (discussed with

M. Zhao, 2012). The large rainfall categories (50–100 and 100–250 mm categories) have a tendency to increase occurrence frequency (corresponding figure lying above the diagonal line). By looking at three dimensional atmospheric flow fields, it is noteworthy that a broadening of the tropical meridional circulation accompanies the change. By applying a hurricane tracking program (Walsh 2004), the landfalling tropical cyclones significantly increase (reaching about 20 year recurrence period). A clustering analysis (Ren and Leslie 2011) also indicates that the landfalling location is reaching a higher latitude. This alone can explain over 50 % of the extreme rainfall increase. There are negligible changes in the subtropical storm track in El Niño years, for reasons that are not yet clear.

Using GFDL/HIRAM atmospheric fields in the twenty-first century, SEGMENT-Landslides estimated changes in landslide occurrence over California (Fig. 7.19). Because single landslides cover only a very limited area, plotting the individual scar area is hard. The markers of different sizes in Fig. 7.19 indicates the average magnitude of landslides within a grid box of ~2,000 km^2, in the form of amount of sliding material involved. Model grid is 90 m by 90 m but, limited by figure size, a thinning ratio of 50 (skipping every 50 model grids) is applied in each

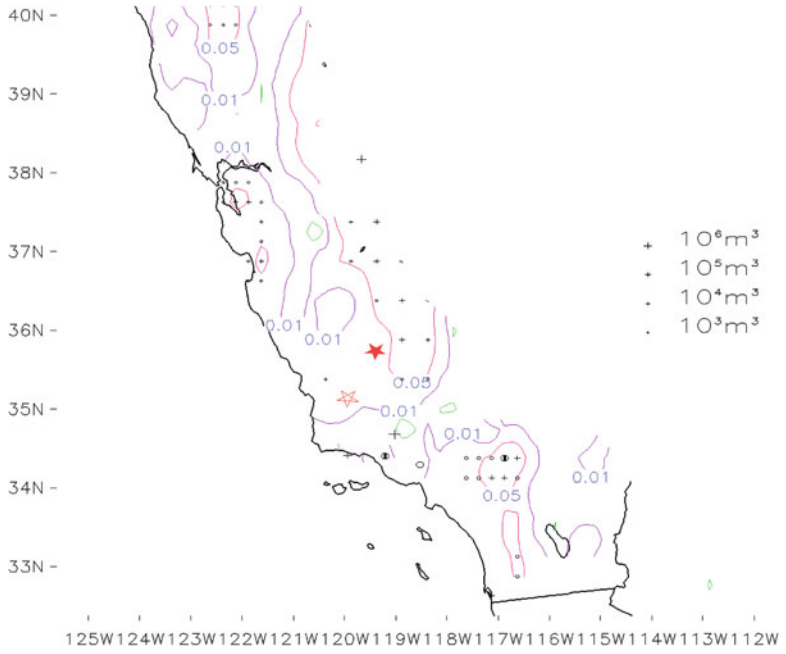

Fig. 7.19 Changes in landslide occurrence over California as the climate warms. *Contour lines* are increases in occurrence frequency (year^{-1}). Marker of *different sizes* indicates the amount of sliding material involved within the 50 km by 50 km grid box. Markers of *different sizes* indicate climatological occurrence of storm-triggered landslides (*cross mark* is 0.25 year^{-1}, *filled round mark* indicates 0.1 year^{-1} and *circle-with-vertical-bar marker* is 0.05 year^{-1}). The *empty star* and the *filled star* indicate the scattering centers, respectively, under CNTL and EGHG runs provided meteorological parameters

direction. Markers of different types indicate climatological occurrence of storm-triggered landslides (cross mark specifies 0.05 year^{-1}, filled round mark indicates 0.1 year^{-1} and circle-with-vertical-bar marker is 0.25 year^{-1}). There are two hot spots along the coastal area: The La Conchita area to the south and the Oakland area (~37.8 N, 122.3 W) to the north. These two areas have the most frequent occurrence of mudslides but the magnitudes are moderate ($<10^5$ m^3 of sliding material is involved for a single event). Precipitation over the Sierra Nevada Mountain chain, especially the western slope, increases significantly during the twenty-first century. However, because the base rocks are primarily least weathered/fragmented granites, the occurrence of debris flow is infrequent. However, for spotty areas covered by volcanic materials (e.g., the north most cross marker on Fig. 7.19), storm-triggered landslides are possible. The increase in occurrence frequency is significant (reaching once per 20 years at some locations), compared to the base occurrence frequency. For these less populated region, the magnitude of landslides, primarily in the form of rockslides, is generally larger than those occurring along the coast.

The KDEs (see Appendix B) were calculated for the CNTRL run landslide locations and the EGHG run landslide locations, for the normal reference 2D bandwidths of (3.95, 1.3) (defined in Eq. A.5). The KDEs led to the conclusion that three clusters are present, corresponding to Sierra Nevada Mountain Range, southern California centered around Malibu and a third one centered around Oakland. The three clusters can also be considered as one disjoint cluster. A spot is defined as the scattering center of landslide scarps if the sum total of the Euclidean spherical distances between this point and all the scarps as a whole is a minimum. Respectively, scattering center of the CNTL run period and the EGHG run period are compared and we find that this center shifted northward by 1 degree and shifted eastward by 0.5 degrees (from (35 N, 120 W) to (35.8 N,119.5 W), the stars in Fig. 7.19). Extreme precipitations associated with ENSO events and, less importantly the northward shifted hurricane tracks, cause more landslides in northern coastal California. This also is reflected in the shape of the *contour lines* in Fig. 7.19. Except for the limited region parallel to the 34.6 N, and the strip portion of the Great Valley, there generally is no safe region (i.e., green lines circled areas). More importantly, very few regions show a decreasing trend of occurrence of landslides.

7.4.4 *Scarp Cluster Centers Shift Inland as Climate Warms*

Simulations on future changes in storm-triggered landslide were carried out over southern California, for the period 2079–2100, using climate model projected precipitation. Projections from two coupled global climate models were assessed. One was a control run (CNTRL) that had prescribed CO_2 levels and SSTs.

The other model run (EGHG) had enhanced CO_2 levels, from the moderate IPCC SRES A1B future scenario. The results of this study are important because any significant trends in landslide activity, and/or changes in the locations of the landslide genesis points, will have major socioeconomic and environmental consequences for southern California.

First, the projected trends in occurrence frequencies and intensities were compared. It was found that there are significant differences in the mean numbers of landslides between the CNTRL and EGHG projections, as well as a notable difference in the mean magnitudes, with the EGHG TCs being larger, at the 95 % statistical significance level. The conclusion, which potentially is critical, is that it is likely that for the southern California area, landslides will become more frequent and more intense.

Second, the locations of the landslides of the CNTRL and EGHG projections were compared. The results from a nonparametric permutation test revealed statistically significant differences between the occurrence locations. The importance of this finding is that the previously stable areas can start to have landslides. This partly is caused by increased storms along the south track as well as tropical cyclones bring moisture to higher latitudes, although a landfalling tropical cyclone is still rare. Further analyses indicate that the landslide activity caused by extreme rainfall events associated with ENSO has not changed significantly. However, the rarest category, that caused by hurricane landfall has a tendency to extend farther north as the climate warms.

To reduce possible contentions on our conclusions, it is emphasized that this study region is very complex. It is affected by triggering factors other than storms. These include, but not limited to wild fire burning of surface vegetation cover, earthquakes, and human activities such as irrigation and construction of hydraulic projects. All are potential contributors to increased landslides but are not addressed in this study.

The above cases focus on lower latitudes. For the high latitude land areas, storm-triggered landslides usually occur concurrently as snow-melt caused flashfloods. Although snow melt by itself often occurs too slow to be considered capable of producing flashflooding, snow and snow melt can contribute to flashflooding and landslides when rain falls on top of snow. Snow melt can also cause antecedent conditions that make an area prone to flashflooding, as soil moisture reservoirs are filled to capacity. By lowering temperature to zero degree, rainfall can cause certain amount of snow to rise zero degree and melt, because the heat capacity of ice is much lower than liquid water. However, a primary amplification to the surface runoff is because snow is porous media and rainfall can penetrate through all the way down. During the melt season, the rainfall may mobilize significant amount of snow mass into motion (the mélange of ice and water from the glaciers or snow packs). While these snow granules are moved down slope and in contact with new land surface environments, accelerated melt is in sight (chapter 12 of Doswell III 2001). This is an amplification filter for the liquid precipitation. As snow environment apparently has lower atmospheric demand (from the Clausius–Clapeyron equation). The evaporation is small and the soils are near saturation. Hence, small

amount of extra melt water matters in generating surface runoff and stream flow. As the melting snow, warm rain water and the entrained debris (and unmelted ice chunks) run into downstream (still) frozen rivers, large chunks of ice may be lifted and increase the solid portion of sliding material and hence potential damages along the path.

Thus, we have seen that landslides over low- and mid-latitudes have direct ecosystem consequences. Landslides occurring in remote, non-vegetated Polar Regions also can have a major societal impact, for example through sea level changes and their consequences. Following is an example of future landslide as the West Antarctic Ice Sheet (WAIS) disintegrates. Melting of the WAIS is not possible in the upcoming centuries, whereas breaking and partial floating of ice is likely, provided the seawater can find pathways to the bottom of ice sectors which have basal elevations below sea level and low free-board potential. If so, the WAIS might disintegrate in a future warming climate. In the following modeling study, the potential contribution to eustatic sea level rise (SLR) from a collapse of the WAIS is reassessed. It is found that previous assessments have overlooked a major contributor: slope instability after the bolstering overlain ice is removed. Overloading ice has a buttressing effect on slope movements in the same way that ice shelves hinder the flow of non-floating coastal ice. The following experiments provide estimates of ~9 mm eustatic SLR contribution from subsequent landslides.

References

Allen M, Ingram W (2002) Constraints on future changes in climate and the hydrologic cycle. Nature 419:224–232

Anthes R (1982) Tropical cyclones: their evolution, structure and effects. Meteorol Monogr Ser (Am Meteorol Soc Boston, MA) 41:298

Battisti D (1988) Dynamics and thermodynamics of a warming event in a coupled tropical atmosphereocean model. J Atmos Sci 45:2889–2919

Battisti DS, Hirst A (1989) Interannual variability in the tropical atmosphere-ocean model: influence of the basic state, ocean geometry and nonlinearity. J Atmos Sci 45:1687–1712

Bengtsson L, Hodges KI, Esch M, Keenlyside N, Kornblueh L, Luo J-J, Yamagata T (2007) How may tropical cyclones change in a warmer climate? Tellus 59A:539–561

Bjerknes J (1969) Atmospheric teleconnections from the equatorial Pacific. Mon Weather Rev 97:163–172

Blake D (1935) Mexican west coast cyclones. Mon Weather Rev 63:344–348

Bosart LF, Sanders F (1981) The Johnstown flood of July 1977: a long-lived convectivestorm. J Atmos Sci 38:1616–1642

Bretherton C, McCaa J, Grenier H (2004) A new parameterization for shallow cumulus convection and its applications to marine subtropical cloud-topped boundary layers. Part I: description and 1D results. Mon Weather Rev 132:864–882

Cane MA (2005) The evolution of El Niño, past and future. Earth Planet Sci Lett 230: 237e240

Chan J (2002) Tropical cyclone motion. Topic Chairman and Rapporteur Rep. 5th WMO international workshop on tropical cyclones (IWTC-V), Cairns, Australia, WMO/TD no. 1136, World Meteorological Organization, Geneva, Switzerland

Chan J (2005) The physics of tropical cyclone motion. Annu Rev Fluid Mech 37:99–128
Chan J, Gray WM (1982) Tropical cyclone movement and surrounding flow relationship. Mon Weather Rev 110:1354–1376
Chapin F III, Matson P, Mooney H (2002) Principles of terrestrial ecosystem ecology. Springer, New York
Charney JG, Eliassen A (1964) On the growth of the hurricane depression. J Atmos Sci 21:68–75
Chen SS, Frank WM (1993) A numerical study of the genesis of extratropical convective mesovortices. Part I: evolution and dynamics. J Atmos Sci 50:2401–2426
Chen M, Dickinson R, Zeng X, Hahmann A (1996) Comparison of precipitation observed over the continental United States to that simulated by a climate model. J Climate 9:2223–2249
Chen TC, Wang S-Y, Yen M-C, Gallus WA Jr (2004) Role of the monsoon gyre in the interannual variation of tropical cyclone formation over the western North Pacific. Weather Forecast 19:776–785
Chiang J, Sobel A (2002) Tropical tropospheric temperature variations caused by ENSO and their influence on the remote tropical climate. J Climate 15:2616–2631
Chien F, Kuo H (2011) On the extreme rainfall of Typhoon Morakot (2009). J Geophys Res 116, D05104. doi:10.1029/2010JD015092
Coles S (2001) An introduction to statistical modeling of extreme values. Springer series in statistics. Springer, New York, p 224. ISBN 1852334592
Craig G, Gray S (1996) CISK or WISHE as the mechanism for tropical cyclone intensification. J Atmos Sci 53(23):3528–3540
Crozier M, Preston N (1999) Modelling changes in terrain resistance as a component of landform evolution in unstable hill country. In: Hergarten S, Neugebauer H (eds) Process modelling and landform evolution. Lecture notes in earth science 78:267–284. Springer, Heidelberg
Dai A, Giorgi F, Trenberth K (1999) Observed and model simulated precipitation diurnal cycles over the contiguous United States. J Geophys Res 104:6377–6402
Debano L (2000) The role of fire and soil heating on water repellency in wild land environments: a review. J Hydrol 231–232:194–206
DeMaria M, Knaff J, Connell B (2001) A tropical cyclone genesis parameter for the Atlantic. Weather Forecast 16:219–233
Dietrich W, Dunne T (1978) Sediment budget for a small catchment in mountainous terrain. Zeitsch Geomorphol Suppl 29:191–206
Dietrich W, Reiss R, Hsu M, Montgomery D (1995) A process-based model for colluvial soil depth and shallow landsliding using digital elevation data. Hydrol Process 9:383–400
Doswell C III (2001) Severe convective storms. Meteorological monographs of American Meteorological Society. American Meteorological Society, Boston, MA, p 02108. ISBN 1-878220-41-1
Emanuel KA (1986) An air–sea interaction theory for tropical cyclones. Part I: Steady-state maintenance. J Atmos Sci 43:585–605
Emanuel K (2005) Increasing destructiveness of tropical cyclones over the past 30 years. Nature 436:686–688
Fang J, Zhang F (2010) Initial development and genesis of Hurricane Dolly (2008). J Atmos Sci 67:655–672
Flatau M, Schubert WH, Stevens DE (1994) The role of baroclinic processes in tropical cyclone motion: the influence of vertical tilt. J Atmos Sci 51:2589–2601
Fritsch JM, Maddox RA (1981) Convective driven mesoscale weather systems aloft. Part I: observation. J Appl Meteorol 20:9–19
Gill AE (1980) Some simple solutions for heat induced tropical circulation. Quart J R Met Soc 106:447–462
Goswami B, Venugopal V, Sengupta D, Madhusoodanan M, Xavier P (2006) Increasing trend of extreme rain events over India in a warming environment. Science 314:1442–1445
Gray WM (1968) Global view of the origin of tropical disturbances and storms. Mon Weather Rev 96:669–700

Gray WM (1979) Hurricanes: their formation, structure and likely role in the tropical circulation. In: Shaw DB (ed) Meteorology over the tropical oceans'. BMS, James Glaisher House, Berkshire, pp 155–218
Gray WM (1993) Seasonal forecasting. In 'Global Guide to Tropical Cyclone Forecasting'. WMO technical document N 560. Tropical cyclone program report N31. UMO, Geneva, pp 5.1–5.21
Gray WM (1998) The formation of tropical cyclones. Meteorol Atmos Phys 67:37–69
Groisman P, Knight R, Karl T, Easterling D, Sun B, Lawrimore J (2004) Contemporary changes of the hydrological cycle over the contiguous United States: trends derived from in situ observations. J Hydrometeorol 5:64–85
Groisman PY, Knight RW, Easterling DR, Karl TR, Hegerl GC, Razuvaev VN (2005) Trends in intense precipitation in the climate record. J Clim 18:1326–1350
Harr PA, Elsberry RL (1996) Structure of a mesoscale convective system embedded in Typhoon Robyn during TCM-93. Mon Weather Rev 124:634–652
Hendon H, Thompson D, Wheeler M (2007) Australian rainfall and surface temperature variations associated with southern hemisphere annualar mode. J Climate 2452–2467
Hendricks EA, Montgomery MT (2006) Rapid scan views of convectively generated mesovortices in sheared Tropical Cyclone Gustav (2002). Weather Forecast 21:1041–1050
Holland GJ (1984) Tropical cyclone motion: a comparison of theory and observation. J Atmos Sci 41:68–75
Holland GJ, Webster PJ (2007) Heightened tropical cyclone activity in the North Atlantic: natural variability or climate trend? Philos Trans R Soc A 365:2695–2716
Homer C, Huang C, Yang L, Wyile B, Coan M (2004) Development of a 2001 National Landcover Database for the United States. Photogramm Eng Remote Sens 70:829–840
Hong S-Y, Dudhia J, Chen S-H (2004) A revised approach to ice microphysical processes for the parameterization of clouds and precipitation. Mon Weather Rev 132:103–120
Hoskins B, Karoly D (1981) The steady linear responses of a spherical atmosphere to thermal and orographic forcing. J Atmos Sci 38:1179–1196
Houze R (2010) Clouds in tropical cyclones. Mon Weather Rev 138:293–344
Houghton JT, Ding Y, Griggs DJ, Noguer M, van der Linden PJ, Dai X, Maskell K, Johnson CA (eds) (2001) Climate change 2001: the scientific basis. Contributions of working group I to the third assessment report of the intergovernmental panel on climate change. Cambridge University Press, Cambridge, UK
Hsu P, Li T, Wang B (2011) Trends in global monsoon area and precipitation over the past 30 years. Geophys Res Lett 38, L08701
Huang CY, Wong CS, Yeh TC (2011) Extreme rainfall mechanisms exhibited by Typhoon Morakot (2009). Terr Atmos Ocean Sci 22:613–632
Hutchinson JN (1968) Mass movement. In: Fairbridge RW (ed) Encyclopedia of geomorphology. Reinhold, New York, pp 688–695
Intergovernmental Panel on Climate Change (IPCC) (2001), Climate change 2001: the scientific basis: In: Houghton JT et al. (eds) Contribution of Working Group I to the Third Assessment Report of the Intergovernmental Panel on Climate Change. Cambridge University Press, New York, NY
IPCC, AR4 (2007) Climate change 2007. The physical science basis. In: Solomon S, Qin D, Manning M (eds) Contribution of working group I to the fourth assessment report of the intergovernmental panel on climate change
Iverson R (2000) Landslide triggering by rain infiltration. Water Resour Res 36:1897–1910
Jin FF (1997a) An equatorial ocean recharge paradigm for ENSO. Part I: conceptual model. J Atmos Sci 54:811–829
Jin FF (1997b) An equatorial ocean recharge paradigm for ENSO. Part II: a stripped-down coupled model. J Atmos Sci 54:830–847
Jorgensen DP (1984a) Mesoscale and convective scale characteristic of mature hurricanes. Part II: inner core structure of hurricane Allen (1984). J Atmos Sci 41:1287–1311

Jorgensen DP (1984b) Mesoscale and convective-scale characteristics of mature hurricanes. Part I: General observations by research aircraft. J Atmos Sci 41:1268–1285
Kain JS (2004) The Kain-Fritsch convective parameterization: an update. J Appl Meteorol 43:170–181
Karl TR, Trenberth K (2003) Modern global climate change. Science 302:1719–1723
Kendall M (1970) Rank correlation methods, 2nd edn. Hafner, New York
Kharin V, Zwiers F (2005) Estimating extremes in transient climate change simulations. J Climate 18:1156–1173
Kim H-M, Webster P, Curry J (2009) Impact of shifting patterns of Pacific ocean warming on North Atlantic tropical cyclones. Science 325:77–80
Knutson TR, McBride JL, Chan J, Emanuel KA, Holland GJ, Landsea C, Held I, Kossin JP, Srivastava AK, Sugi M (2010) Tropical cyclones and climate change. Nat Geosci 3:157–163
Kruk MC, Knapp KR, Levinson DH, Kossin J (2010) A technique for combining global tropical cyclone best track data. J Atmos Ocean Technol 27:680–692
Kunkel KE, Easterling D, Redmond K, Hubbard K (2003) Temporal variations of extreme precipitation events in the United States: 1895–2000. Geophys Res Lett 30, 10.1029/2003GL018052
Lander MA (1996) Description of a monsoon gyre and its effect on the tropical cyclones in the western North Pacific during August 1991. Weather Forecast 9:640–654
Landsea C, Chenoweth M (2004) The San Diego hurricane of October 2, 1858. Bull Am Meteorol Soc 85:1689–1697
Lawrence D, Slater A (2008) Incorporating organic soil into a global climate model. Clim Dyn 30:145–160
Lenderink G, Meijgaard E (2008) Increase in hourly precipitation extremes beyond expectations from temperature changes. Nat Geosci 1:511–514
Leslie LM, Holland GJ (1995) On the bogussing of tropical cyclones in numerical models: a comparison of vortex profiles. Meteorol Atmos Phys 56:101–110
Letts M, Roulet N, Comer N, Skarupa M, Verseghy D (2000) Parametrization of Pearland hydraulic properties for the Canadian land surface scheme. Atmos Ocean 38:141–160
Liebmann B, Marengo J (2001) Interannual variability of the rainy season and rainfall in the Brazilian Amazon Basin. J Climate 14:4308–4318
Liebmann B, Kiladis G, Carvalho L, Jones C, Vera C, Blade I, Allured D (2009) Origin of convectively coupled Kelvin waves over South America. J Climate 22:300–315
Lin M, Jeng F (2000) Characteristics of hazards induced by extremely heavy rainfall in Central Taiwan-Typhoon Herb. Eng Geol 58:191–207
Lindzen RS, Nigam S (1987) On the role of sea surface temperature gradients in forcing low level winds and convergence in the tropics. J Atmos Sci 44:2418–2436
Liu S, Fu C, Shiu C, Chen J, Wu F (2009) Temperature dependence of global precipitation extremes. Geophys Res Lett 36, L17702
Maddox RA (1980) Mesoscale convective complexes. Bull Am Mereorol Soc 16:1374–1387
Mahmood K, Ryu J, Kim J (2012) Effect of anisotropic conductivity on suction and reliability index of unsaturated slope exposed to uniform antecedent rainfall. Landslides. doi:10.1007/s10346-012-0325-9
Maloney ED, Hartmann DL (2000) Modulation of hurricane activity in the Gulf of Mexico by the Madden-Julian Oscillation. Science 287:2002–2004
Mantua NJ, Hare S, Zhang Y, Wallace M, Francis R (1997) A Pacific decadal climate oscillation with impacts on salmon. Bull Am Met Soc 78, 1069e1079
McBride JL (1995) Tropical cyclone formation. In: Elsberry RL (ed) Global perspectives on tropical cyclones, WMO/TD 693. World Meteorological Organization, Geneva, pp 63–105
McDonald R, Bleaken D, Creswell D, Pope V, Senior C (2005) Tropical storms: representation and diagnosis in climate models and the impacts of climate change. Climate Dynam 25:19–36
McPhaden MJ (2002) Mixed layer temperature balance on intraseasonal timescales in the equatorial Pacific Ocean. J Climate 15:2632–2647

McPhaden MJ, Zebiak SE, Glantz MH (2006) ENSO as an integrating concept in Earth Science. Science 314:1739–1745
Miller D, Fritsch JM (1991) Mesoscale convective complexes in the western Pacific region. Mon Weather Rev 117:2922–2978
Montgomery MT, Nicholls ME, Cram TA, Saunders AB (2006) A vortical hot tower route to tropical cyclogenesis. J Atmos Sci 63:355–386
Moody JA, Martin D (2001) Hydrologic and sedimentologic response of two burned watersheds in Colorado, USGS water resources investigations report. USGS, Reston, VA
Murakami H, Sugi M (2010) Effect of model resolution on tropical cyclone climate projections. SOLA 6:73–76
Murakami H, Wang B (2010) Future change of North Atlantic tropical tracks. J Climate 23:2699–2721
Murakami H, Wang B, Kitoh A (2010) Future change of western North Pacific typhoons: projections by a 20-km-mesh global atmospheric model. J Climate 24:1154–1169–2721
Neelin J et al (1998) ENSO theory. J Geophys Res 103:14262–14290
Neelin JD, Chou C, Su H (2003) Tropical drought regions in global warming and El Niño teleconnections. Geophys Res Lett 30(24):2275. doi:10.1029/2003GL018625
Nolan DS (2007) What is the trigger for tropical cyclogenesis? Aust Meteorol Mag 56:241–266
Nolan DS, Moon Y, Stern DP (2007) Tropical cyclone intensification from asymmetric convection: energetics and efficiency. J Atmos Sci 64:3377–3405
NRC (2002) Abrupt climate change. Inevitable surprise. National Academy Press, Washington, DC
NRC (2008) Origin and evolution of earth-research questions for a changing planet. National Academy Press, Washington, DC
O'Gorman P, Schneider T (2009) The physical basis for increases in precipitation extremes in simulations of 21st century climate change. Proc Natl Acad Sci U S A 106:14773–14777
Ookuchi K, Yoshimura J, Yoshimura H, Mizuta R, Kusunoki S, Noda A (2006) Tropical cyclone climatology in a global warming climate as simulated in a 20-km-mesh global atmospheric model: Frequency and wind intensity analysis. J Meteorol Soc Jpn 84:259–276
Palmer T, Doblas-Reyes F, Weisheimer A, Rodwell M (2008) Toward seamless prediction: calibration of climate change projections using seasonal forecasts. Bull Am Meteorol Soc 89:459–470. doi:10.1175/BAMS-89-4-459
Philander S (1981) The response of equatorial oceans to a relaxation of the trade winds. J Phys Oceanogr 11:176–189
Philander S (1985) El Niño and La Niña. J Atmos Sci 42:2652–2662
Philander S (1990) El Niño, La Niña, and the southern oscillation. Academic, London, p 289
Picaut J, Masia F, du Penhoat Y (1997) An advective-reflective conceptual model for the oscillatory nature of the ENSO. Science 277:663–666
Putman W, Lin S-J (2007) Finite-volume transport on various cubed-sphere grids. J Comput Phys 227:55–78
Reasor PD, Montgomery MT, Bosart LF (2005) Mesoscale observations in the genesis of Hurricane Dolly (1996). J Atmos Sci 62:3151–3171
Ren D (2001) Scaling issues in the calculation of surface latent and sensible heat fluxes at Blue River Basin using SHEELS model. M.S. thesis, University of Oklahoma, Norman, OK, p 236
Ren D (2004) 4DVAR retrieval of prognostic land surface model variables for ARPS". University of Oklahoma, Norman, OK, p 236
Ren D (2006) A modified Richards' equation, its adjoint, and a new perspective on land data assimilation. Meteorol Atmos Phys 92:25–32
Ren D (2014) The devastating Zhouqu Storm-triggered debris flow of August 2010: Likely causes and possible trends in a future warming climate. J Geophys Res 119(7):3643–3662. doi:10.1002/2013JD020881
Ren D, Henderson-Sellers A (2006) An analytical hydrological model and its implication in scaling issues for land surface modeling. J Earth Interact 10(20):1–24

Ren D, Leslie L (2011) Three positive feedback mechanisms for ice sheet melting in a warming climate. J Glaciol 57:206
Ren D, Xue M (2004) An improved force-restore model for land-surface modeling. J Appl Meteorol 43:1768–1782
Ren D, Xue M, Henderson-Sellers A (2004) The effects of hydraulic lift in simulating superficial soil moisture for vegetated surfaces under dry conditions. J Hydrometeorol 5:1181–1191
Ren D, Leslie L, Karoly D (2007) Sensitivity of an ecological model to soil moisture simulations from two different hydrological models. Meteorol Atmos Phys 100:87–99
Ren D, Leslie LM, Karoly DJ (2008) Landslide risk analysis using a new constitutive relationship for granular flow. Earth Interact 12:1–16
Ren D, Wang J, Fu R, Karoly D, Hong Y, Leslie LM, Fu C, Huang G (2009) Mudslide caused ecosystem degradation following Wenchuan earthquake 2008. Geophys Res Lett 36:L05401. doi:10.1029/2008GL036702
Ren D, Fu R, Leslie LM, Dickinson R, Xin X (2010a) A storm-triggered landslide monitoring and prediction system: formulation and case study. Earth Interact 14:12. doi:10.1175/2010EI337.1
Ren D, Fu R, Leslie LM, Dickinson R (2010b) Modeling the mudslide aftermath of the 2007 southern California wildfires. J Nat Hazards. doi:10.1007/s11069-010-9615-5
Ren D, Leslie L, Fu R, Dickinson R (2011a) Predicting storm-triggered landslides and ecological consequences. Bull Am Meteorol Soc 91:129–139. doi:10.1175/2010BAMS3017.1
Ren D, Fu R, Leslie LM, Karoly DJ, Chen J, Wilson C (2011b) A multirheology ice model: formulation and application to the Greenland ice sheet. J Geophys Res 116, D05112. doi:10.1029/2010JD014855
Ren D, Lynch MJ, Leslie LM, LeMarshall J (2014) Sensitivity of tropical cyclone tracks and intensity to ocean surface temperature: four cases in four different basins. Tellus A 66:24212, http://dox.doi.org/10.3402/tellusa.v66.24212
Rind D (1984) Global climate in the 21st century. Ambio 13:148–151
Ritchie EA, Holland GJ (1997) Scale interactions during the formation of Typhoon Irving. Mon Weather Rev 125:1377–1396
Ritchie EA, Holland GJ (1999) Large-scale patterns associated with tropical cyclogenesis in the western Pacific. Mon Weather Rev 127:2027–2043
Rogers RF, Fritsch JM (2001) Surface cyclogenesis from convectively driven amplification of midlevel mesoscale convective vortices. Mon Weather Rev 129:605–637
Saravanan R, Chang P (2000) Interaction between tropical Atlantic variability and El Niño-Southern Oscillation. J Climate 13:2177–2194
Schulz J, Meywerk J, Ewald S, Schlussel P (1997) Evaluation of satellite-derived latent heat fluxes. J Climate 10:2782–2795
Scott D (1992) Multivariate density estimation. Wiley, New York
Segoni S, Rossi G, Catani F (2012) Improving basin scale shallow landslide modelling using reliable soil thickness maps. Nat Hazards 61:85–101
Semenov V, Bengtsson L (2002) Secular trends in daily precipitation characteristic greenhouse gas simulation with a coupled AOGCM. Climate Dynam 19:123–140
Shapiro LJ (1996) The motion of Hurricane Gloria: a potential vorticity diagnosis. Mon Weather Rev 124:1497–2508
Shapiro LJ, Franklin JL (1999) Potential vorticity asymmetries and tropical cyclone motion. Mon Weather Rev 127:124–131
Sippel JA, Nielsen-Gammon JW, Allen SE (2006) The multiple-vortex nature of tropical cyclogenesis. Mon Weather Rev 134:1796–1814
Skamarock WC et al. (2008) A description of the Advanced Research WRF version 3. Technical report NCAR/ TN-4751STR, p 113
Smith W (1986) The effects of Eastern North Pacific tropical cyclones on the southwestern United States. NOAA technical memorandum. NWS WR-197, p 229
Smith R, Smettem K, Broadbridge P, Woolhiser D (2002) Infiltration theory for hydrologic applications. Water resources monograph, 15. American Geophysical Union, Washington, DC

Stowasser M, Wang Y, Hamilton K (2007) Tropical cyclone changes in the western North Pacific in a global warming scenario. J Climate 20:2378–2396
Suarez MJ, Schopf P (1988) A delayed action oscillator for ENSO. J Atmos Sci 45:3283–3287
Sugi M, Yoshimura J (2012) Decreasing trend of tropical cyclone frequency in 228 year high-resolution AGCM simulations. Geophys Res Lett 39:L19805. doi:10.1029/2012GL053360
Sugi M, Noda A, Sato N (2002) Influence of global warming on tropical cyclone climatology: an experiment with the JMA global model. J Meteorol Soc Jpn 80:249–272
Tory KJ, Frank WM (2010) Tropical cyclone formation. In: Chan JCL, Kepert JD (eds) Global perspectives on tropical cyclones: from science to mitigation. World Scientific, Singapore, pp 55–91
Trenberth KE (1999) Conceptual framework for changes of extremes of the hydrological cycle with climate change. Clim Change 42:327–339
Varnes D (1978) Slope movement types and processes. In: Schuster RL, Krizek RJ (eds) Landslide analysis and control, transportation research board special report 176. National Academy of Sciences, National Research Council, Washington, DC, pp 11–33
Vera C, Silvestri G, Barros V, Carril A (2004) Differences in El Niño response over the Southern Hemisphere. J Climate 17(9):1741–1753
Wallace JM, Gutzler DS (1981) Teleconnections in the geopotential height field during the northern hemisphere winter. Mon Weather Rev 109:784–812
Walsh K (2004) Tropical cyclones and climate change: unresolved issues. Climate Res 27:77–83
Walsh K, Fiorino M, Landsea C, McInnes K (2007) Objectively-determined resolution-dependent threshold criteria for the detection of tropical cyclones in climate models and reanalyses. J Climate 20:2307–2314
Wang B (2006) The Asian Monsoon. Springer, New York, p 787
Wang B, Ding Q (2006) Changes in global monsoon precipitation over the past 56 years. Geophys Res Lett 33, L06711
Webster PJ, Holland GJ, Curry JA, Chang HR (2005) Changes in tropical cyclone number, duration, and intensity, in warming environment. Science 309:1844–1846
Weisberg RH, Wang C (1997) A western Pacific oscillator paradigm for the El Niño-Southern Oscillation. Geophys Res Lett 24:779–782
Wheeler M, Hendon H (2004) An all-season real-time multivariate MJO index: development of an index for monitoring and prediction. Mon Weather Rev 132:1917–1932
Wooten R, Gillon K, Witt A, Latham R, Douglas T, Bauer J, Fuemmeler S, Lee L (2008) Geologic, geomorphic, and meteorological aspects of debris flows triggered by Hurricanes Frances and Ivan during September 2004 in the southern Appalachian Mountains of Macon county, North Carolina (southeastern USA). Landslides 5:31–44
Wu C, Emanuel KA (1993) Interaction of a baroclinic vortex with background shear: application to hurricane movement. J Atmos Sci 50:62–76
Wu L, Wang B (2004) Assessing impact of global warming on tropical cyclone tracks. J Climate 17:1686–1698
Wyrtki K (1975) El Niño – the dynamic response of the equatorial Pacific Ocean to atmospheric forcing. J Phys Oceanogr 5:572–584
Yanai M, Esbensen S, Chu J (1973) Determination of bulk properties of tropical cloud clusters from large-scale heat and moisture budgets. J Atmos Sci 30:611–627
Yokio S, Takayabu Y (2009) Multi-model projection of global warming impact on tropical cyclone frequency over the western North Pacific. J Meteor Soc Jpn 79:23–25
Zebiak SE, Cane MA (1987) A model El Niño-Southern oscillation. Mon Weather Rev 115:2262–2278
Zehr RM (1992) Tropical cyclogenesis in the western North Pacific. NOAA technical report NESDIS 61, p 181
Zhao M, Held IM (2010) An analysis of the effect of global warming on the intensity of Atlantic hurricanes using a GCM with statistical refinement. J Climate 23:6382–6393
Zhao M, Held IM, Lin S-J, Vecchi GA (2009) Simulations of global hurricane climatology, interannual variability, and response to global warming using a 50 km resolution GCM. J Climate 33:6653–6678

Chapter 8
The Impact of Landslides on Sea Level Rise

Ocean is the largest water reservoir in the Earth's hydrological cycle. Global sea level rise concerns come from the fact that, water kept in the slow cycling reservoirs outside those traditionally defined as hydrosphere, such as cryosphere and the occluded fossil groundwater reservoirs, may release water to the hydrosphere. Following two examples illustrate that landslides can have sea level rise consequences through affecting the container volume (Sect. 8.1) as well as through groundwater pathways (Sect. 8.2).

8.1 The West Antarctic Ice Sheet's Disintegration May Cause Landslides

At present the Earth's climate is in an interglacial period and the interglacial conditions possibly could continue for another 50 kyr (Berger and Loutre 2002). The relative abundance of glaciers, when compared with two of the last three interglacial periods, suggests that there still is room for sea level rise (SLR) from the current cryosphere (Vaughan 2006).

As it is the largest potential contributor to SLR, quantifying the Antarctic ice sheet (AIS, Fig. 8.1a) total mass balance is important in understanding the global hydrological cycle and the fragile polar ecosystem consequences. The AIS, especially the West Antarctica Ice Sheet (WAIS), has been extensively studied (Mercer 1978; Oppenheimer 1998; Vaughan 2006; van den Broeke et al. 2006; Rignot et al. 2008; Bamber et al. 2009; Joughin and Alley 2011). Much of the grounded ice in West Antarctica lies on a bed that decreases inland and extends well below sea level (Fig. 8.1). This bathymetry makes the ice sheet subject to marine-ice sheet runaway instability (Joughin and Alley 2011; Schoof 2007). Complete melting of the WAIS requires ~10^{21} J of energy, enough to quench 30,000 Pinatubo-size volcanoes. Such a large amount of energy cannot be provided under natural

© Springer International Publishing Switzerland 2015

D. Ren, *Storm-triggered Landslides in Warmer Climates*,
DOI 10.1007/978-3-319-08518-0_8

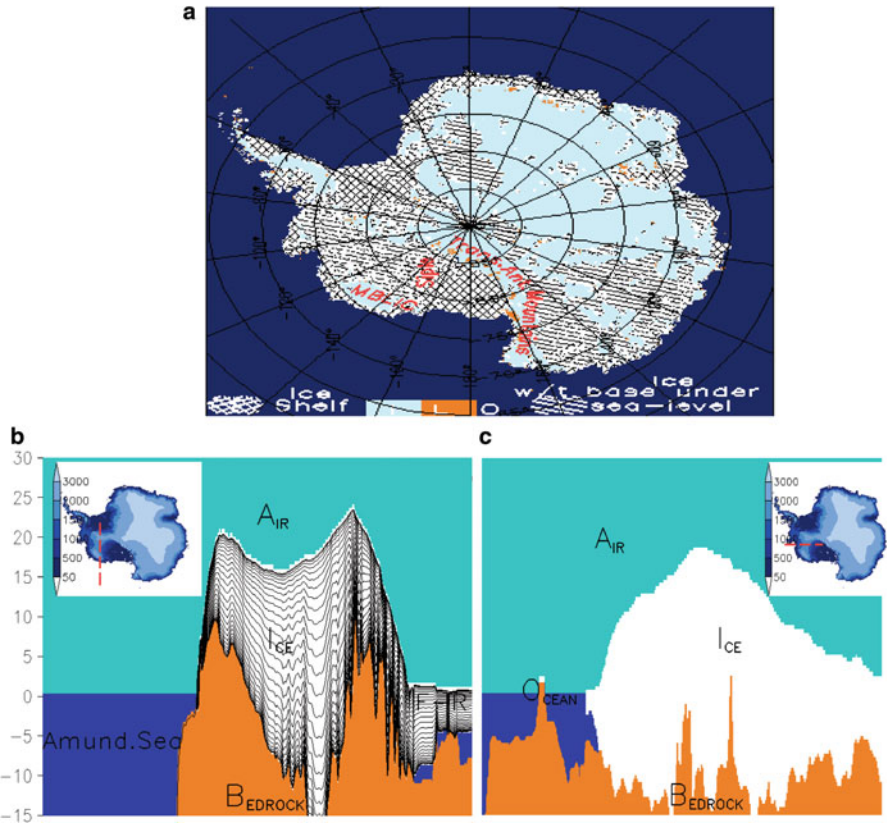

Fig. 8.1 Panel (**a**) The Antarctica land-ice-ocean mask based on SeaRISE 5-km resolution digital elevation, ice thickness and bedrock elevation data. In the *color shading*, *white* is ice, *yellow* (*brown*) is bare ground (L), and *blue* is ocean. The ice shelves are cross-hatched areas; land ice with base under sea level (marine based) is hatched. West Antarctica has more complex ice-water-bedrock configurations than the rest of Antarctica. WAIS is defined as the ice sector confined by the Transantarctic Mountains and 40° W longitude. The Peninsula has a limited ice volume ($<3.3 \times 10^4$ Gt) compared with land-based ice of WAIS ($\sim 2.8 \times 10^6$ Gt). Panels (**b**) and (**c**) are the West Antarctica land-ice-ocean mask based on SeaRISE 5-km resolution digital elevation, ice thickness, and bedrock elevation data. In the *color shading*, *white* is ice, *yellow* (*brown*) is bedrock and *blue* is ocean. The *left panel* is a cross section along the F-R shelf/Amundsen direction, as indicated in the *inset* (*red dashed line*). The *right panel* is along the Siple coast direction, as the *red line* in the *inset*. In a future warming climate, ocean waters likely are entering the WAIS through the Siple coast pathway. The extensive troughs (if ice is removed) can extend to depths of more than 2 km. *Color-shading* in the *insets* is surface elevation over the AIS. Marie Byrd Land Ice Cap (MBLIC) and the Whitmore Mountains ("WM") are labelled for reference in the text

conditions on a century time frame. However, for marine-based ice sheets to have SLR contributions it is not necessary for them to melt completely. It suffices that they are partially afloat, which is viable if basal melt water is connected effectively to the oceans.

At present, the primary factor contributing to the stability of the WAIS is the existence of buttressing ice shelves. Because a significant portion of WAIS's inland ice has basal melting, the gravitational driving stress cannot be balanced locally. Ice-shelves have very flat (upper/sub-aerial) surface elevations and do not need much resistive stress to maintain a balance (except near the tip-end). The hydrostatic pressure from the submerged portion of ice shelves provides the primary resistive stresses for the neighboring coastal land ice, to balance gravitational driving stress arising from uneven surface topography. Warming from underneath the marine-based ice sheet, especially that affecting ice-shelf viability could release this potentially fragile stability and lead to accelerated creeping of the WAIS. Ice is brittle at higher strain rates, especially under tension, because its melting point diffusivity is around 10^{-15} m^2/s, which is much lower than the 10^{-11} m^2/s for elemental metals. Accelerated creeping thus implies breaking of the WAIS. At the same time, after ice shelves are removed, the pathway for seawater to erode marine based ice sheets becomes open. With the breaking of ice, those sectors with thicknesses less than $h_b\rho_w/\rho_i$ (where h_b is the bedrock elevation, $\rho_w = 1028$ kg m^{-3} is the density of seawater and $\rho_i = 918$ kg m^{-3} is the density of ice), can be set afloat and have SLR consequences.

Warming factors can include drastic increases of geothermal activity as a consequence of very large, sustained volcanic eruptions. Although they have a low probability they cannot be discarded because of their feasibly high impact over a short time period. Blankenship et al. (1993) identified what they thought to be a recent active volcano under Ice Stream B (now Whillans Ice Stream) on the WAIS. It has been suggested that subglacial volcanism could accelerate an existing grounding line retreat, promoting WAIS-disintegration. More important is the gradual but widespread oceanic and atmospheric warming driven by anthropogenic greenhouse effects, which is assumed to be salient in the upcoming century (IPCC AR4 2007). The exact timing of a WAIS collapse is not known and this study reexamines the seal level contribution from a collapse of the WAIS, a possibility initially proposed by Mercer (1978).

Mercer's estimate is based on the reasoning elucidated by Oppenheimer (1998). As the WAIS disintegrates, the resulting vacancy, which is the space below sea level that is now fulfilled by solid ice, then will be occupied by seawater. The net amount of the contribution is the water equivalent of the disintegrated ice, adjusted to account for the volume below sea level (V_b) and also for the postglacial rebound of the bedrock (V_r). Fig. 8.2b illustrates the SLR under this theory. The SLR can be expressed as $V_a \frac{\rho_i}{\rho_w} + V_b \frac{\rho_i - \rho_w}{\rho_w} + V_r$, where V_a is the ice volume above sea level. This expression slightly relaxes the free-board condition of Thomas (1973), who assumed that when the summation of the first two terms is positive, it is floatable. A slight surface elevation decrease, either from negative total surface mass balance or accelerated discharge toward the ice-shelves when oceanic interactions make the ice shelf thinner hence reducing the buttressing effects, will set a significant portion of WAIS afloat. Recently, Bamber et al. (2009) made a major advance on the original estimate of Mercer (1978) by using non-static bathymetry from a

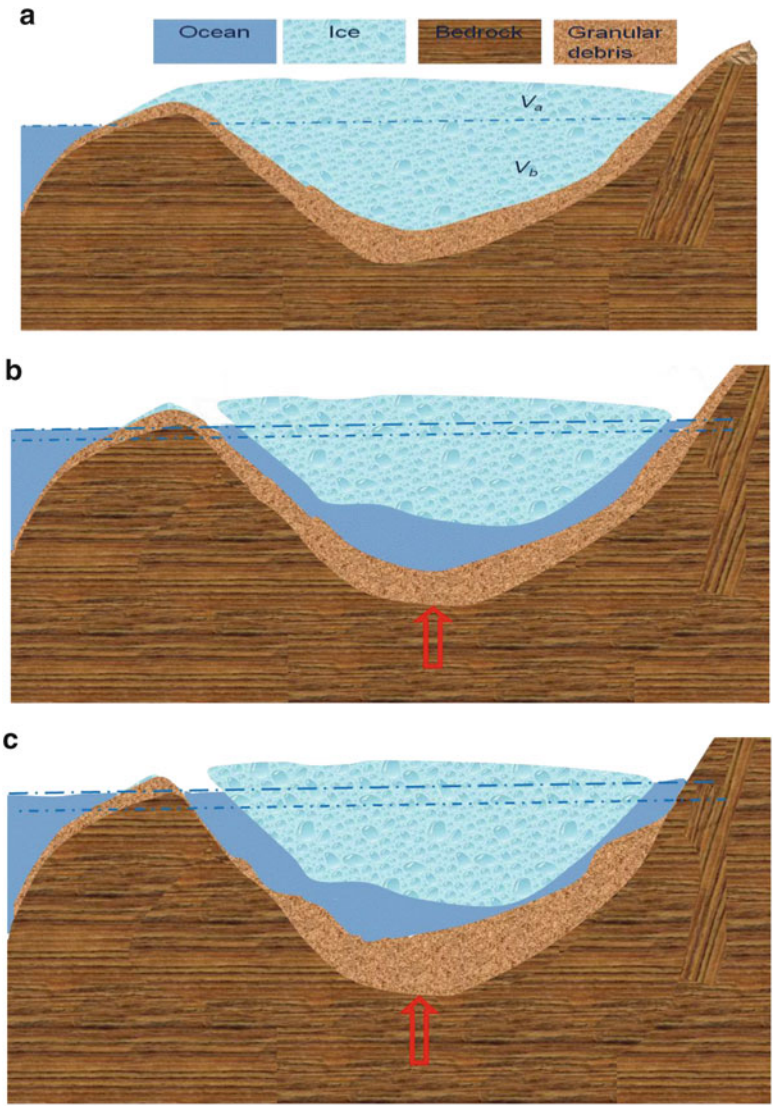

Fig. 8.2 The eustatic sea level rise is shown after disintegration of the WAIS. Panel (**a**) is the ice-bedrock configuration before the WAIS disintegration. As the WAIS is disintegrated, the vacant below future sea level will be occupied by seawater. The net contribution is the water equivalent of the integrated ice adjusted to account for the volume below sea level (V_b) and also for the postglacial rebound of the bedrock (*red arrow*, V_r). Panel (**b**) is the sea level rise under this hypothesis. Sea level rise can be expressed as $V_a \frac{\rho_i}{\rho_w} + V_b \frac{\rho_i - \rho_w}{\rho_w} + V_r$. Inevitably, after the removal of the WAIS, landslides (primarily from Marie Byrd Land), will further change the basin shape (**c**). In principle, only the debris situated originally above sea level has a sea level rise contribution after sliding down-slope to locations below sea level (V_g). Sea level rise then can be expressed as $(V_a + V_b)\frac{\rho_i}{\rho_w} - V_b + V_r + V_g$

sophisticated Earth model, and concluded that only a portion of WAIS satisfies the marine ice sheet instability hypothesis and can become afloat.

However, these studies overlook the fact that ice overlaying bedrock is an ideal configuration for rock erosion and the production of a large amount of granular material, especially beneath Marie Byrd Land and the Siple coast (MacAyeal 1989). Loading of thick ice above slopes reduces landslide occurrence because of the large confining pressure and also because granular debris is effectively cemented by ice crystals. Inevitably, after the removal of the WAIS, landslides will further change the basin shape (Fig. 8.2c) on time scales much shorter than basin rebound. In principle, only the debris sitting originally above sea level has a SLR contribution when it slides to locations below sea level (R. Alley, Personal Communication 2011, V_g). SLR can be expressed as $(V_a + V_b)\rho_i/\rho_w - V_b + V_r + V_g$. V_g is estimated using the SEGMENT-Landslide (Ren et al. 2008, 2009, 2011a, b, c, 2013) model, driven by meteorological parameters from general circulation models.

8.1.1 Data and Methods

The SEGMENT-Landslide model accounts explicitly for soil mechanics, vegetation transpiration and root mechanical reinforcement, and relevant hydrological processes. It considers non-local dynamic balance of the three-dimensional topography, soil thickness profile, basal conditions, and vegetation coverage (Ren et al. 2011a) in determining the prognostic fields of the driving and resistive forces. It also describes the flow fields and the dynamic evolution of thickness profiles of the medium considered. SEGMENT-Landslide is a component of a process-based modeling system for monitoring and predicting landslides and their ecosystem implications (Ren et al. 2009). Applications to the polar environment of the WAIS pose fewer challenges for SEGMENT-Landslide because vegetation processes are not involved. In addition, rainfall morphology, which is critical for storm-triggered landslides, also is not a concern because solid precipitation dominates over the WAIS. Monthly mean atmospheric forcing parameters suffice for driving the temperature solver, which estimates frozen soil mechanical properties. Three independent CGCMs (MPI-ECHAM, NCAR CCSM3, and MIROC3.2-hires, see http://www-pcmdi.llnl.gov/ipcc/about_ipcc.php) are chosen for their relatively fine resolution and for providing all atmospheric parameters required by SEGMENT-Landslide.

The subglacial particle properties of WAIS are specified according to studies using boreholes and seismic methods (Bentley 1991; Englehardt et al. 1990). The rocks are mostly volcanic and the basalt clasts are of sizes ~10 cm. Loose, ice-cemented volcanic debris also is widespread around Mt Waesche (77° S, 130° W) and the northern Antarctica Peninsula and its constituent blocks. In assigning granular particle sizes, geothermal patterns also are referenced because repeated phase changes at the interface of ice/rock arguably are the most efficient means of erosion and reducing the granular particle sizes. A high-resolution digital

elevation map (DEM) is a key input for slope stability analyses. The SeaRISE project (http://websrv.cs.umt.edu/isis/index.php) provides surface DEM at 5 km horizontal resolution on a South Polar Stereographic projection. The actual sphere resolution is higher at the WAIS, but still coarser than 1,000 m. Radarsat-1 SAR sensor via Modified Antarctic Mapping Mission (MAMM, Jezek 2003), as by-product, provides slope information at 200 m resolution. A 200 m resolution surface DEM is obtained by combining the SeaRISE and MAMM data. With these data and assuming no major geothermal disturbance from volcano eruptions, SEGMENT-Landslide simulations indicate that, except for very limited northern areas such as Deception island where avalanches seem likely and involved very limited mass redistribution ($<10^5$ m^3), elsewhere the present WAIS is stable.

In addition to mechanical properties such as particle size, porosity, bulk density, cohesion and repose angle, the thickness of the granular material is critical in determining the magnitude of the landslides. The granular thickness on slopes underneath the present WAIS is inversely retrieved using another SEGMENT component, SEGMENT-Ice (Ren and Leslie 2011; Ren et al. 2011b), constrained by the goodness of fit between model simulated and observed (Jezek 2003) surface ice velocity, over entire AIS. Figure 8.3 is the distribution of the estimated granular material thickness over West Antarctica. This also is the initial sliding material thickness.

Modeling experiments were made to estimate possible landslides contribution to SLR as the WAIS disintegrates. The ice-bedrock configuration of SeaRISE is the same as that of Bamber et al. (2009), except they did not consider the contribution of landslides, but all other factor were included. Their estimate is the most recent for the SLR contribution of the WAIS. The SLR contribution is estimated as follows.

SEGMENT-Landslide uses a terrain following coordinate system, the sigma coordinate system (grid lines in Fig. 8.1a). A vertical integration of the incompressible continuity equation, assuming no external sources of granular material, gives:

$$\frac{\partial h}{\partial t} = -\frac{1}{R\cos\theta}\int_0^1 \left(\frac{\partial u}{\partial \lambda} + \frac{\partial \mathrm{v}\cos\theta}{\partial \theta}\right) H dz - \frac{u_s}{R\cos\theta}\frac{\partial h}{\partial \lambda} - \frac{\mathrm{v}_s}{R}\frac{\partial h}{\partial \theta} + w_b \qquad (8.1)$$

Where t is time, R is the Earth's radius, λ is longitude, θ is latitude, u and v are the horizontal velocity components, and w is the vertical velocity component and is expanded using the continuity equation, assuming incompressible sliding material. The subscripts "b" and "s" mean respectively evaluated at the bottom and upper surfaces. As Eq. (6.1) in spherical coordinate, Eq. (8.1) diagnoses the temporal evolution of the surface elevation and also the sliding material's thickness because

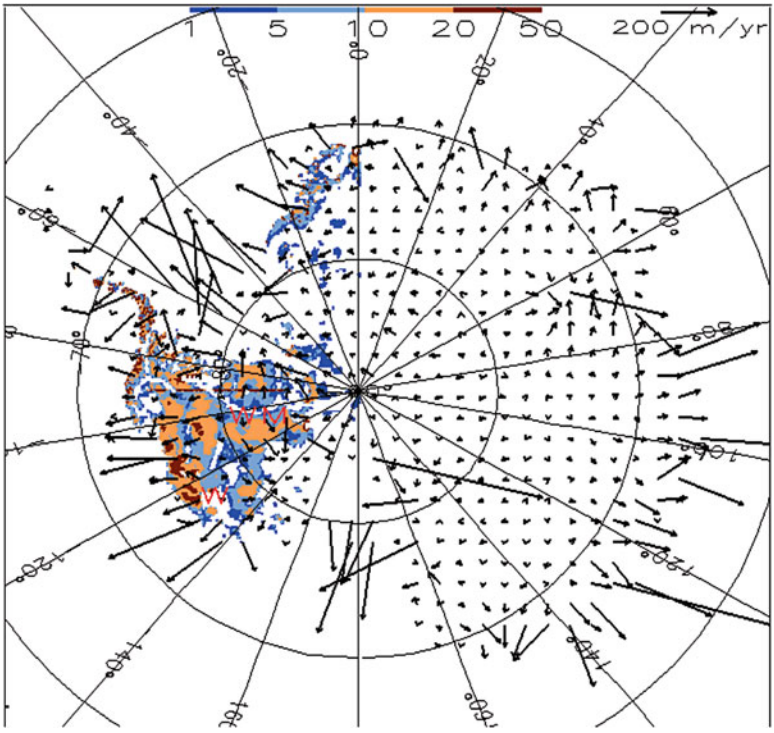

Fig. 8.3 Upon convergence of the optimization procedure, SEGMENT-Ice simulated surface velocities over Antarctica ice sheet (*vector arrows*) and the retrieved granular material depth under the overlain ice (*color shading*, in meters) over WAIS. The *top portion* of Mountain Waesche ("W") and the ridge of Whitmore Mountains ("WM") has shallow debris accumulation (<1.0 m). The retrieval is an optimization process. Magnitudes of surface ice velocity are sensitive to the thickness of basal granular material. Based on this sensitivity relationship, repeated runs of the ice model are performed with present ice geometry and ice temperature profiles, but (automatically) varying granular layer thickness, to best fit the observed surface ice velocities. The metric for goodness of fit of the modelled and observed velocity fields is defined as: $\sum \left\| \overrightarrow{V_{obs}} - \overrightarrow{V_{\text{model}}} \right\| = \sum \sqrt{(u_{obs} - u_{\text{model}})^2 + (v_{obs} - v_{\text{model}})^2 + (w_{obs} - w_{\text{model}})^2}$, where u, v and w are components of the full vector velocity. Subscriptions "obs" and "model" mean respectively observed and modelled velocities. The observed ice velocities are obtained from Radarsat-1 SAR sensor via Modified Antarctic Mapping Mission (MAMM, Jezek 2008). Because the seven regional composite of MAMM do not cover the entire Antarctica Ice Sheet (with a "polar hole"), the summation in the metric is only over regions with MAMM observations. Upon convergence, the overall agreement between modelled and observed velocities is very satisfactorily with correlation coefficients of 0.92 for direction and 0.90 for magnitude, respectively

bedrock is assumed unchanged over the time scale of several hundred years. It varies as a consequence of velocity fields and boundary sources. Changes in surface elevation multiplied by grid area give the mass loss volume for that grid. The total SLR contribution is the sum over all grids with basal elevations above sea level.

8.1.2 Results and Discussion

Figure 8.4 shows the surface elevation changes of the bare slopes and, for areas under seawater, the bedrock elevation changes. Landslides can cause some areas to accumulate more than 200 m of sliding material. The most significant places for volcanic rock and silt debris accumulation are close to Siple coast. However, the source region of the sliding material is primarily the southeast facing slopes of Marie Byrd Land, which contribute ~86 % of the accumulated sliding material. Contributions from the Whitmore Mountains are relatively small (<10 %). This is due primarily to the existing granular material depths on the slopes (Fig. 8.3). The total volume of the scars on the slopes at elevations above sea level, or equivalently the reduction of the basin volume (under sea level part), is 3,220 km^3, is approximately a 0.902 cm eustatic SLR. Although small compared with the ~3.3 m eustatic SLR from the collapsed WAIS, it is added to the eustatic sea level with a very short time delay, closely following the ice disintegration. If the fast scenario (Bamber et al. 2009) is realized, the economic cost to coastally based global cities from the additional 0.902 cm is not a simple linear addition to the 3.3 m SLR. In contrast, the contribution from the rebound of the basin bottom takes over 10,000 years, providing a long period for human adaptation and mitigation measures.

Landslides considered here primarily are associated with granular material as the ice bonds melt and when the solid ice loading is removed. The two most frequent triggering mechanisms for large-scale landslides, rainstorms and earthquakes, both are negligible. The former is apparent from the year round low air temperatures over the WAIS. Earthquakes also are rare in Antarctica and specifically in the WAIS, as the Antarctica plate now has only a very small proportion associated with subduction (Norton 1982) and is bounded by constructive and conservative margins. Thus, the estimates from this study are expected to be highly representative of the SLR caused by the disintegration of the WAIS. The scarp sizes and the maximum attainable sliding speeds both are sensitive to WAIS disintegration scenarios, but the total volume of the sliding material involved are very much a conservative property insensitive to fast/slow scenarios (Bamber et al. 2009).

In 2010 and 2011, extreme events ranged the full gamut from localized brief weather events such as the Zhouqu storms, to regional scale events such as hurricanes and flooding, to climate-scale drought and floods in Australia. These possibly are a harbinger of challenging times ahead for estimating effects from landslides on our society. Above is one example showing the sea level consequence of landslides, among a series of far reaching influences from landslides.

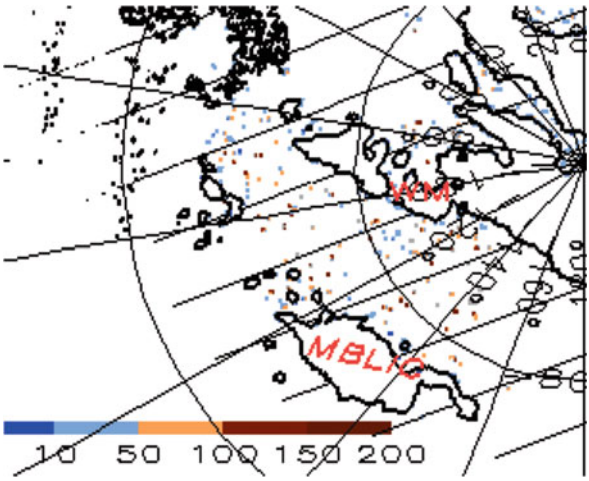

Fig. 8.4 Areas are shown with bedrock elevation increases over 5 m, as a result of landslides accompanying the deglaciation of the WAIS. They are *color shaded* (m). The bedrock zero elevation *contour lines* are shown and areas with bedrock elevations below sea level are hatched. Landslide scars are prominent on the slopes, with localized pairs of elevation increase and decrease. However, regions accumulating most of the sliding material (>5 m depth) are almost below sea level. Marie Byrd Land Ice Cap (MBLIC) and Whitmore Mountains (WM) are labelled for reference. The southeast facing slopes of MBLIC contribute most of the sliding material

8.2 Sea Level Rise from the Wenchuan Earthquake: Groundwater Recharge Aspect

In the global water cycle, evaporation generally exceeds precipitation over the ocean, balanced by precipitation exceeding evaporation over land. Overland, the excess water is the river runoff that closes the hydrological cycle. If this loop is strict, there would be no concerns about steady sea level rise (SLR). In reality, water bodies that are pinch-cut from hydrosphere and stored in solid state (cryosphere), and/or occluded in land reservoirs (e.g., fossil groundwater) may mingles in and make the situation complicated. In the same way increased ice melt from ice sheets and glaciers adds water to the oceans, over-drafting and pumping fossil water increases the total amount of water in the hydrosphere, and may be responsible for up to one quarter of the earth's total sea level rise since the beginning of the twentieth century (Wada et al. 2010). Wada et al (2010) and several recent high profile articles emphasized the issue with ground water depletion and possible SLR consequences. However, the SLR contribution from taping ground water is with large uncertainty (Church et al. 2001). Impoundment by dams and river diverting projects (in China and also in Central Valley of State California) are apparently working in the opposite direction. Impoundments in dams also are associated with recharge of surrounding aquifers. In addition, nature also has its own way increasing the aquifer recharging, or present reservoir capacity is still dynamic.

For example, this study shows that the peri-Himalayan region has an increasing trend in aquifer recharging, i.e., the increased precipitation seepage through soil to recharge the aquifers. And this region alone can cancel global elsewhere's SLR contributions from grounder water usage.

The bedrock crevasses are both pathway and "container" for fossil ground water. The groundwater changes are measured by gravity satellite (e.g., Famiglietti and Rodell 2013). It is convenient to discuss the global land water cycle from the net precipitation (precipitation minus evaporation), which usually as river runoff getting back to oceans to close the cycle. But a small fraction also seeps through the soil and bedrock layers to recharge groundwater aquifers. As bedrock cracks open wider, more runoff will be diverted into drainage percolation and saved in groundwater reservoir (eq. 1 in Scanlon et al. 2012). Because the surface runoff that winds up in the sea has a turnover time scale of less than a week, this increased replenish of groundwater is accompanied by local mass variations detectable by gravity satellites such as the Gravity Recovery And Climate Experiment (GRACE, Voss et al. 2013). Aside from net precipitation and drainage, other factors also may cause perturbations on regional gravity, such as irrigation projects (Scanlon et al. 2012) and large-scale population and animal migrations. The region of interest (Fig. 8.5) is a remote area in China that has not been affected by these factors in the past several decades.

Precipitation also is well known for its patchiness, especially over complex terrains (Orlanski 1982). In situ measurements typically are unable to "catch" the "hot spots". To close this dominant term in regional mass balance, the annual mean Net Primary Production (NPP), because of its high sensitivity to annual precipitation, is used as an indicator for precipitation trends (Zhao and Running 2010). Over the interested region, the near surface air temperature increased $<0.1\ ^{\circ}C$ in the past decade and the changes in evaporation is negligible.

The GRACE measurements (2003–present) over the peri-Himalayas show systematic and 100-km spatial resolution consistent signals of mass loss (blue colors in Fig. 8.6) and mass gain (red colors in Fig. 8.6). First, the significant mass loss from the Himalayan region is from the increased ice mass loss in recent decades. This melt water flows primarily into the rivers and is discharged into the Indian and Pacific Oceans, with a turnover time period generally of less than a week. The three surrounding domains all have significant mass gains, much larger than explained by geological plate movements, which globally are only ~2 Gt magnitude (~1 km^3 in volume), which is three orders of magnitudes smaller than the mass loss. There also have been no large-scale population and animal migrations in the past decade. There also is no river diverting projects or dams. The only possible cause is in the fluids mass changes. Region 3, which is the primary agricultural region of China, with crops comprising the major vegetation over the region, may exhibit strong seasonal fluctuations in its biomass but annual NPP variations still are a good representation of the precipitation amount. Region 2 is an arid region, which is clearly shown in the area total biomass (NPP in Fig. 8.7). Region 2 has a similar total area as Region 3 but the total NPP is two orders of magnitude smaller. Although the total mass in Region 2 significantly increased during the 2003–2012

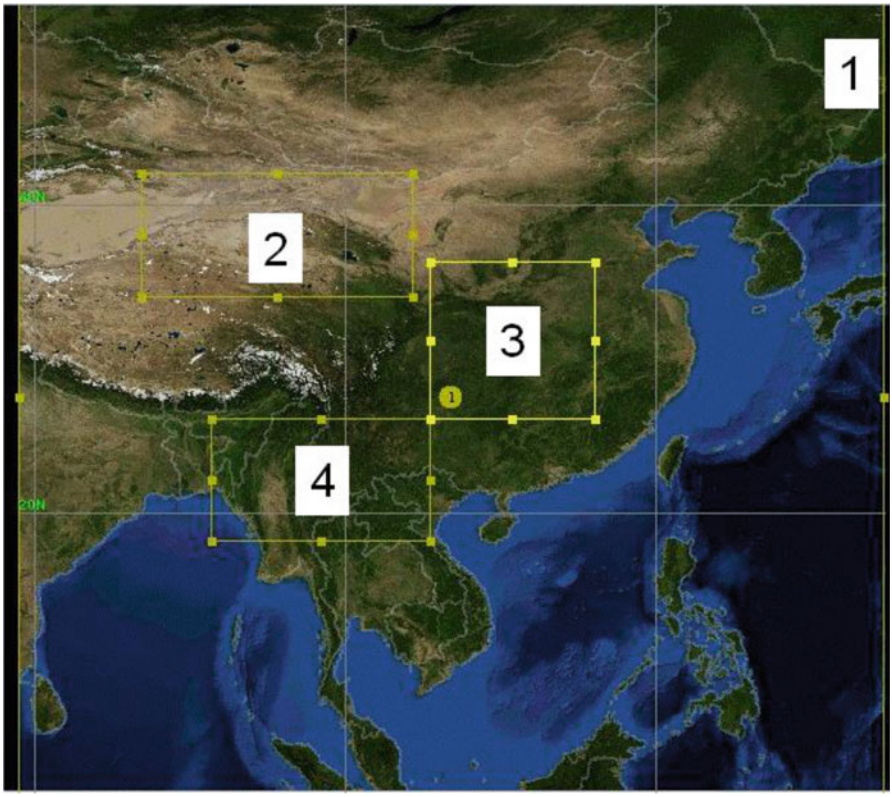

Fig. 8.5 Region of interest, also shows the nested domains. WRF QPF runs are over the subdomains for extended period of 10 years to examine precipitation trends

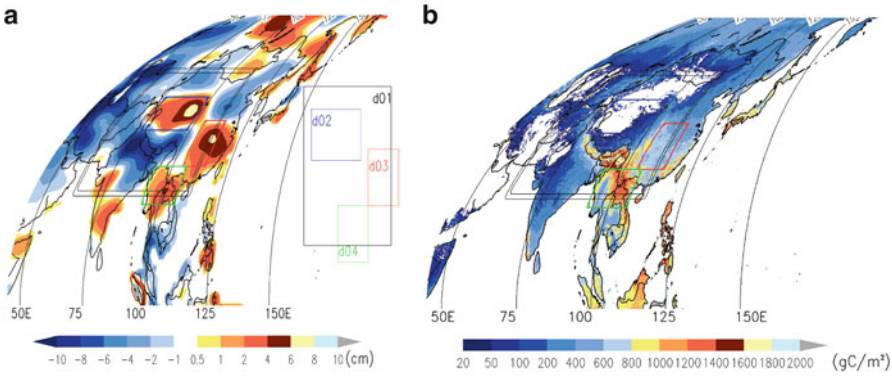

Fig. 8.6 Panel (**a**) is GRACE measured mass changes over 2003–2013 period (in water depth equivalence). Panel (**b**) is vegetation climatology over the same region. For convenience of discussion, it is subdivided into four nested domains (d01–04a). Domains 2,3 and 4 all show significant mass loss signal, for different physical reasons (discussed in the text)

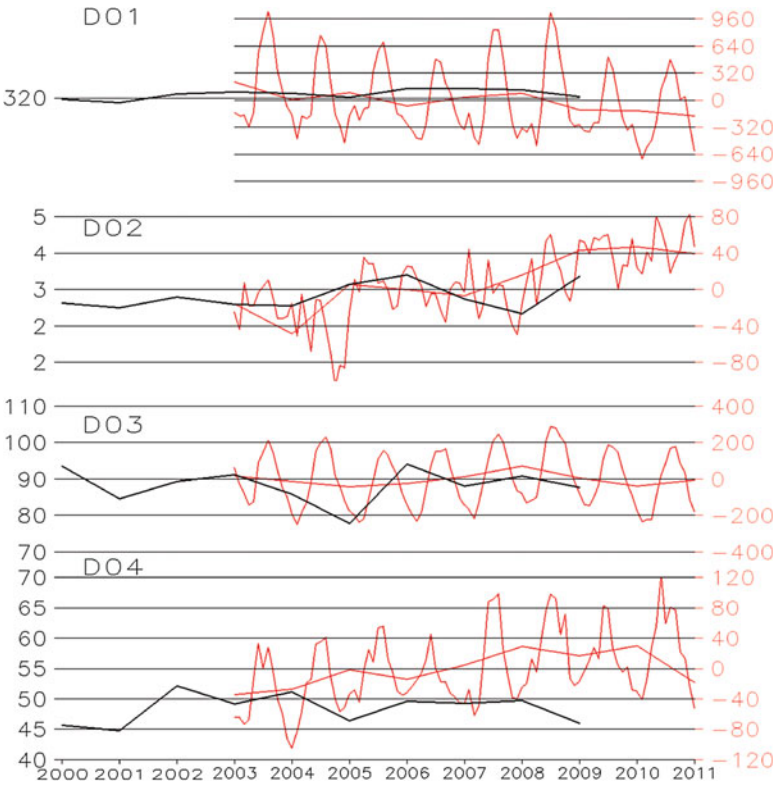

Fig. 8.7 Area averaged mass changes (GT) relative to 2003 levels for the four domains of interest. A good indicator of precipitation, NPP, is plotted (*black lines*) to show possible trends in precipitation. Only domain 3's mass changes has strong correlation with precipitation. Domain 2 and 4 both have upward trend unexplainable by precipitation, which has no apparent trends during this period, as reflected by the NPPs

period, the NPP did not. New data from MODIS indicate a small decreasing trend. In Region 4, the precipitation showed a significant decrease during the past decade 2003–2012, in strong discord with the mass increase trend. The precipitation did not increase for Regions 2 and 4 (it reduced in Region 4), the increased mass can only be explained by an increased proportion flowing into groundwater reserves rather than into runoff. Region 2 is less populated and is not a major agricultural region in China. Irrigation would only cause mass loss, which is the opposite of the observed mass increase and any attempts to recharging the aquifer are not planned. Groundwater recharge/depletion data obtained from M. Bierkens (personal communication, 2013) further asserted this point. This trend possibly can be a result of increased ground disintegration (i.e., crevasses or cracks in bedrocks). The reason is not clear but may also have a natural component after the 2008 Wenchuan earthquake, considering that the signal of a mass increase starts at least from

2003, 5 years earlier. Summarizing up the GRACE measured mass loss rate over the Regions 2, 3 and 4, a rate of 89 km^3/year is obtained, which also is close to the average of SEGMENT-Landslide' estimates driven by 2000–2010 precipitation input from high-resolution WRF simulations.

Reason for increased partitioning of precipitation into groundwater is not entirely clear but an increase in bedrock crevasses is one viable explanation. The reason for increased crevasses may likely be resulted from the active geological activities, manifested as recent earthquakes (2008 Wenchuan earthquake and 2013 Gannan earthquake, both within the region in question). Large scale storm-triggered landslides also indirectly reflecting increased mantle soil and bedrock crevasses, because the August 2010 Zhouqu precipitation is really not an outlier in the extreme precipitation (it has a $<$20 year recurrence frequency). The reason it caused unprecedented magnitude debris-flows is that most precipitation is discharged deeper into the soil and formed a shear zone far deeper than uniform infiltration would achieve.

To worsen the situation, these two regions of ever-increasing fracturing are co-located with the atmospheric baroclinic cyclogenesis basins corresponding to the Qinghai-Xizhang (Tibetan) Plateau (TP hence forth) circumventing airstreams. As climate warms, extreme precipitation events are likely to become more common. The growing bedrock crevasses and the accumulated fluids as groundwater may also have mechanical consequences. Looking further ahead, the pattern of mass changes creates a saddle structure at the vicinity of Region 2. The exerted shear stress may cause strain buildup and cause further earthquakes (by reducing the natural occurrence period). This composes a positive feedback to secondary geo-hazards such as flash floods and debris flows. Further fractured bedrock/soil mantle also increase runoff water percolation, forming a self-sustaining process. Note that the mass gain trend for Region 2 and 4 began well before the 2008 Wenchuan earthquake, even before 2003, the starting time of the GRACE measurements. This points to possible geological causes, because there are no large hydraulic projects that can affect persistently the region of interest.

The same precipitation total may result in different amount of recharging, as indicated in Fig. 8.8. Actual amount of recharging in the region of question is estimated with an advanced numerical system (SEGMENT-Landslide, Ren et al. 2008, 2011a, b). Figure 8.8 illustrates one of the most important mechanisms: Extreme precipitation causes most percolation and recharge. To estimate possible changes in extreme precipitation events, WRF (an advanced numerical weather prediction model, Skamarock et al. 2008) was run with thermodynamic changes computed from the small 5-member IPCC GCM ensemble output, under the A1B emission scenario applied to the initial and lateral boundary conditions for a specific type atmospheric occlusion pattern. Because extreme precipitations are caused by an unfortunate combination of several rain-makers, occlusion pattern slows down the evolving of the circulation pattern and makes the precipitation event lasting longer (Fig. 6.20a).

Detailed setup of the experiment for investigating future extreme precipitation estimate is as follows. Here, using the August 7–8, 2010 Zhouqu extreme

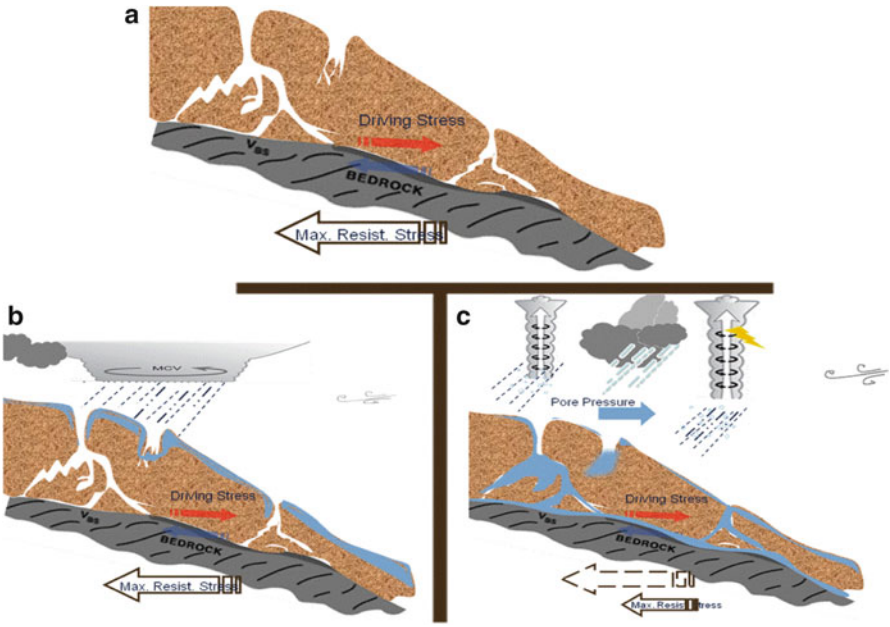

Fig. 8.8 Rainfall characteristics and subsequent distribution. *Cyan color* indicates wet soil and accumulated groundwater. Panel (**a**) illustrates a vertical cross section of a fractured slope, under dry conditions. Panel (**b**) illustrates the situation under stratiform precipitation, where rainfall intensity is low but lasts a longer time. Most rainfall is uniformly infiltrated to the near surface layer. The water may likely be evapotranspired without groundwater consequence. Panel (**c**) is the situation under convective cloudbursts, which have intense precipitation that generate runoff and percolation. Most rainfall is either drained into crevasses or simply lost as surface runoff. Thus, the same precipitation amount, with a different morphology, results in different rainfall distributions within slopes and contributes drastically different amounts of groundwater

precipitation, the quantitative estimation of precipitation using WRF model is outlined. To resolve the mesoscale evolution of this event, the model domain features a larger outer domain with 20-km grid spacing, along with a 4-km nested domain, and a 1 km inner-most domain (Fig. 6.11). Vertically, the model uses the default 28-level configuration with the model top set at 50 hPa. The Betts–Miller–Janjic convective parameterization scheme was used on the 20-km domain only. All domains employed the WRF single-moment 6-class microphysics scheme, the Yonsei University PBL scheme, and the National Oceanic and Atmospheric Administration (NOAH) land surface model. Long wave radiation was handled with the Rapid Radiative Transfer Model (RRTM) scheme, and shortwave radiation was the Dudhia scheme. Initial and lateral boundary condition data were based on Global Forecast System (GFS) final analyses on a 1° latitude–longitude grid; simulations were initialized at 00 UTC 04 August 2010 run for 6 days. For the nested domains, lateral boundary conditions are provided by the parent domain and one way nesting is used.

Nested run of the weather model WRF, for 6 continuous days, starting from 00 UTC 04 August 2010, with the innermost domain set at 1 km resolution (SM) clearly indicates that the strong precipitation is caused by a frontal system that manifest as a 700 mb shear zone. At about 6 UTC August 7, at 700 hPa there is a clear shear zone of significant cyclonic vorticity. From the circulation fields, it is clear that there is a series of terrain forced meso-γ scale cyclones developing around Zhouqu. These features are readily identifiable from the MODIS cloud top imageries at around 0635 UTC August 7 aboard the NASA EOS Aqua satellite (figures not shown). Because Zhouqu is a narrow valley surrounded by high mountains (>3,000 m elevation), low level jets, a frequent companion of extreme precipitation, was absent. In a future warmer climate and an enhanced hydrological cycle (Trenberth 1999; Allen and Ingram 2002; Karl and Knight 1998; Semenov and Bengtsson 2002; Groisman et al. 2005), more extreme weather conditions are expected. Lackmann (2013) presented a method for estimating specific effects from climate warming on a certain pattern of precipitation events.

Future extreme precipitation events can be examined using WRF and a recently developed technique (Lackmann 2013) for perturbing the thermal background, to mimic a warming climate environment. The "pseudo climate change" approach is adopted to estimate possible changes in precipitation in a 2060–2080 time-frame. For simulating future (2060–2080) extreme events, the WRF model is used in the same pseudo-global warming approach as proposed by Lackmann (2013). There is no simple way to anticipate how changes in future synoptic patterns might influence the frequency and severity of extreme precipitations that might have landslide consequences. The experimental design for simulating future extreme precipitation events addresses this issue by replicating the synoptic pattern that caused the August 7–8th precipitation, but with likely future large-scale thermodynamic changes imposed. While it is acknowledged that an identical synoptic pattern would not occur in the future, it is reasonable to assume that a similar pattern could occur. Because the model simulation is allowed to evolve dynamically for the duration of the synoptic event, the resulting changes, brought about by imposing thermodynamic changes, can include dynamical changes as well. Quantification of projected thermodynamic change due to increased anthropogenic greenhouse gases is accomplished using an ensemble of Intergovernmental Panel on Climate Change (IPCC) Fourth Assessment Report (AR4) GCM simulations of monthly atmospheric parameters. Experiments using the A1B scenario are used. The August monthly fields were averaged among a subset of five GCMs for which reliable temperature data are available at all vertical levels: the Bjerknes Centre for Climate Research Bergen Climate Model version 2 (BCCR BCM2), the Centre National de Researches Meteorologiques Coupled Global Climate Model version 3 (CNRM-CM3), the Institute of Numerical Mathematics Coupled Model version 3 (INM-CM3.0), the Max Planck Institute (MPI) ECHAM5, and the third climate configuration of the UK Met Office Unified Model (HadCM3). A two-decade average temperature change was then computed from the August monthly averages from the 5-member GCM ensemble for the periods (2000–2020) and (2060–2080). All available variables on isobaric levels were averaged. These spatially varying

average fields were interpolated to the same 1° GFS grid as used for the initial and lateral boundary conditions in the control (2010) simulation. Differences between the 2060s and 2000s decades were computed for each grid cell, and these changes were subsequently added to the original GFS analyses. Given that the landslide event in question took place in August 2010 and that a change is added that was calculated from a 60-year difference, the future simulation can be interpolated as approximating the thermodynamic conditions around the year 2060 that would arise from anthropogenic greenhouse gas forcing alone, under the A1B scenario. Occlusion patterns are searched in the five climate model run and used the pseudo-climate sensitivity experiments by Lackmann (2013) to estimate changes in extreme precipitation events and these output are used to drive SEGMENT-Landslide to estimate groundwater recharge.

The resulting simulation is a replication of a highly similar synoptic pattern to that of the control simulation, but within a projected future thermodynamic environment. For the interested region, the increased atmospheric water vapor as a straightforward thermodynamic consequence of warming, or a robust vapor increase consistent with the Clausius–Clapeyron relationship, still holds (Karl and Knight 1998; Emori and Brown 2005). In addition, precipitation in Region 2 also is strongly affected by orographic effect. For example, the northern branch of the circumventing Qinghai-Xizhang Plateau airstream adds cyclonic vorticity to the frontal system. Due to the complicated topography and >3,000 m surface elevation, there usually are no closed surface lows and there is only a shear line in the flow fields. The region in question is located within a frequent cyclogenesis region to the east of the TP; there are two such hot spots, and Zhouqu is within the northern one (e.g., Ding 1991, p. 203). Extreme precipitation usually is produced by locally enhanced convective storms. In a larger context, the vapor still eventually comes from the Indian Ocean, following a path illustrated in Fig. 6.20a. The climate warming consequence for "outer" circumstances is that of a warm (and moist) conveyor belt (Harrold 1973) positive feedback by Lackmann (2013).

As a summary, tapping water from the nonrenewable (due to the very slow natural recharging process) groundwater reservoir has the direct concern of sea level rise contribution (Wada et al. 2010; Famiagtte et al. 2013). Some dynamic and engineered reservoirs, such as the California Central Valley, can keep a near balance between extraction and recharge by surface water diversion and dam–reservoir adjustments. The net SLR contributions from these reservoirs are apparently small. For most of the irrigation areas without well designed recharging plans, the depletion rate usually far exceeds the natural recharging rate, including the High Plains of USA (Scanlon et al. 2012). The biggest concerns as to SLR contribution are from those desert Middle East countries that tap fossil groundwater, which has no way to be recharged because of the lack of precipitation and subsequent surface runoff (Fig. 1c of Wada et al. 2010). In this study, we identified a region that may contribute to a net recharging of groundwater due to a natural reason: increased bedrock crevasses due to active geological activity of the Peri-Himalayan region, especially to its north east. This region can well cancel out the next depletion of fossil groundwater from the Middle East countries at present (~90 km^3/year), and,

with an intense surface hydrological as climate warms, may become increasingly important and even exceed the latter and has a negative SLR contribution (-5 km^3/year by 2100, even without new earthquakes and subsequent landslides). This also indicates that near future contributions to global sea level rise may still come from accelerated melting of the cryosphere, another parallel, slow evolving water reservoir that lies also out of the traditionally defined hydrosphere. The IPCC-TAR (Church et al. 2001) realized that the positive contribution (to SLR) of groundwater depletion may be offset by impoundment in reservoirs and associated recharge of surrounding aquifers. Here, the identified increasing in crevasses space of the peri-Himalayan region is yet another such mechanism that persists in the upcoming decades.

References

Allen M, Ingram W (2002) Constraints on future changes in climate and the hydrologic cycle. Nature 419:224–232

Bamber J, Riva R, Vermeersen B, LeBrocq A (2009) Reassessment of the potential sea-level rise from a collapse of the West Antarctic Ice Sheet. Science 324:901–903

Bentley C (1991) Configuration and structure of the subglacial crust. In: Tinguey RJ (ed) Geology of Antartica. Oxford University Press, Oxford, pp 335–364

Berger A, Loutre M (2002) An exceptionally long interglacial ahead? Science 297:1287–1288

Blankenship D, Bell R, Hodge S, Brozena J, Behrendt J, Finn C (1993) Active volcanism beneath the West Antarctica ice sheet and implications for ice-sheet stability. Nature 361:526–529

Church JA et al (2001) Changes in sea level. In: Houghton JT et al (eds) Climate change 2001: the scientific basis. Contribution of working group I to the third assessment report of the intergovernmental panel on climate change. Cambridge University Press, Cambridge, pp 639–693

Ding Y (1991) Advanced synoptic meteorology. China Meteorologocal Press, Beijing, p 792

Emori S, Brown SJ (2005) Dynamic and thermodynamic changes in mean and extreme precipitation under changed climate. Geophys Res Lett 32, L17706. doi:10.1029/2005GL023272

Englehardt H et al (1990) Physical conditions at the base of a fast moving Antarctica ice stream. Science 248:57–59

Famiglietti J, Rodell M (2013) Water in the balance. Science 340:1300–1301

Famiglietti J, Rodell M (2013) Water in the balance environmental science. 340, 1300–130110.1126/science.1236460

Gleeson T, VanderSteen J, Sophocleous AA, Taniguchi M, Alley WM, Allen DM, Zhou Y (2010) Commentary: groundwater sustainability strategies. Nat Geosci 3:378–379. doi:10.1038/ngeo881

Groisman PY, Knight RW, Easterling DR, Karl TR, Hegerl GC, Razuvaev VN (2005) Trends in intense precipitation in the climate record. J Climate 18:1326–1350

Harrold T (1973) Mechanisms influencing the distribution of precipitation within baroclinic disturbances. Q J R Meteorol Soc 99:232–251

IPCC AR4 (2007) Climate change 2007. The physical science basis. In: Solomon S, Qin D, Manning M (eds) Contribution of working group I to the fourth assessment report of the intergovernmental panel on climate change

Jezek K (2003) Observing the Antarctic Ice Sheet using the RADARSAT-1 synthetic aperture radar. Polit Geogr 27:197–209

Jezek K (2008) The RADARSAT-1 Antarctic mapping project. BPRC Report No. 22, Byrd Polar Research Center, The Ohio State University, Columbus, Ohio, p 64

Joughin I, Alley R (2011) Stability of the West Antarctic ice sheet in a warming world. Nat Geosci. doi:10.1038/NGEO1194

Karl TR, Knight RW (1998) Secular trends of precipitation amount, frequency, and intensity in the USA. Bull Am Meteorol Soc 79:231–241
Lackmann G (2013) The south-central US flood of May 2010, present and future. J Climate 26:4688–4709
MacAyeal D (1989) Large-scale ice flow over a viscous basal sediment: theory and application to ice stream B, Antarctica. J Geophys Res 94:4071–4087
Mercer JH (1978) West Antarctic ice sheet and CO2 greenhouse effect – threat of disaster. Nature 271:321–325
Norton I (1982) Paleomotion between Africa, South America, and Antarctica, and implications for the Antarctic Peninsula. In: Craddock C (ed) Antarctic Geoscience. University of Wisconsin Press, Madison, WI, pp 99–106
Oppenheimer M (1998) Global warming and the stability of the West Antarctica Ice Sheet. Nature 393:325–332
Orlanski I (1982) Orographically induced vortex centers. Proceedings of the first Sino-American workshop on mountain meteorology, May 1982. Science Press, Beijing, p 699
Ren D, Leslie L, Lynch MJ, Duan Q, Dai Y, Shangguan W (2013) Why was the August 2010 Zhouqu landslide so powerful? Geography, Environment, Sustainability 1:67–79
Ren D, Leslie L (2011) Three positive feedback mechanisms for ice sheet melting in a warming climate. J Glaciol 57:206
Ren D, Leslie L, Fu R, Dickinson R (2011a) Predicting storm-triggered landslides and ecological consequences. Bull Am Meteorol Soc 92:129–139. doi: 10.1175/2010BAMS3017.1
Ren D, Fu R, Leslie LM, Dickinson R (2011c) Modeling the mudslide aftermath of the 2007 southern California wildfires. J Nat Hazards. doi:10.1007/s11069-010-9615-5
Ren D, Fu R, Leslie LM, Karoly DJ, Chen J, Wilson C (2011b) A multirheology ice model: formulation and application to the Greenland ice sheet. J Geophys Res 116, D05112. doi:10.1029/2010JD014855
Ren D, Leslie LM, Karoly DJ (2008) Landslide risk analysis using a new constitutive relationship for granular flow. Earth Interact 12:1–16
Ren D, Wang J, Fu R, Karoly D, Hong Y, Leslie LM, Fu C, Huang G (2009) Mudslide caused ecosystem degradation following Wenchuan earthquake 2008. Geophys Res Lett 36, L05401. doi:10.1029/2008GL036702
Rignot E, Bamber J, van den Broeke M, Davis C, Li Y, van de Berg W, van Meijgaard E (2008) Recent mass loss of the Antarctic ice sheet from dynamic thinning. Nat Geosci. doi:10.1038/ngeo102
Scanlon BR, Faunt CC, Longuevergne L, Reedy RC, Alley WM, McGuire VL, McMahon PB (2012) Groundwater depletion and sustainability of irrigation in the US high plains and central valley. Proc Natl Acad Sci 109(24):9320–9325
Schoof C (2007) Ice sheet grounding line dynamics: steady states, stability, and hysteresis. J Geophys Res Earth 112:F03S28
Semenov V, Bengtsson L (2002) Secular trends in daily precipitation characteristic greenhouse gas simulation with a coupled AOGCM. Climate Dynam 19:123–140
Skamarock W C, Klemp JB, Dudhia J, Gill DO, Barker DM, Huang XY, Wang W, Powers JG (2008) A description of the advanced research WRF Version 3. NCAR Tech. Note NCAR/TN-475+STR, p 125
Thomas R (1973) The creep of ice shelves: theory. J Glaciol 12(64):45–53
Trenberth KE (1999) Conceptual framework for changes of extremes of the hydrological cycle with climate change. Clim Change 42:327–339
Van den Broeke M, van de Berg W, van Meijgaard E (2006) Snowfall in coastal West Antarctica much greater than previously assumed. Geophys Res Lett 33, L02505. doi:10.1029/2005GL025239
Vaughan D (2006) Recent trends in melting conditions on the Antarctic Peninsula and their implications for ice-sheet mass balance and sea level. Arct Antarc Alp Res 38:147–152

Voss K, Famiglietti J, Lo M, de Linage C, Rodell M, Swenson S (2013) Groundwater depletion in the Middle East from GRACE with implications for transboundary water management in the Tigris-Euphrates-Western Iran region. Water Resour Res 49:904–914

Wada Y, van Beek LPH, van Kempen CM, Reckman JWTM, Vasak S, Bierkens MFP (2010) Global depletion of groundwater resources. Geophys Res Lett 37, L20402. doi:10.1029/2010GL044571

Zhao M, Running S (2010) Drought-induced reduction in global terrestrial net primary production from 2000 through 2009. Science 329:940–943

Chapter 9
Modeling Debris Flows in the Aftermath of the 2007 Southern California Wildfires

In Sect. 5.1.2, we discussed root fortification for slopes. Under natural circumstances, wildfires can cause perturbations on ecosystems and also have landslide consequences. Actually, fires are important in driving land cover change (Fig. 9.1). Decades are needed for damaged forest stands to recover fully and even longer time periods are required for the restoration of soil nutrients.

In this study, an investigation is made of the influence of fire-caused deforestation on precipitation-triggered, shallow landslide susceptibilities in southern California, using the SEGMENT-Landslide, that accounts for soil mechanics, root distribution, and relevant hydrological processes. SEGMENT-Landslide is applicable to variable regional topography, soil thickness profiles, and vegetation coverage.

In this study, for southern California following the 2007 wildfires, three experiments were performed with rainfall recurrence periods chosen to be 2, 10, and 25 years. These intervals correspond to 24-h storm rainfall totals of 17, 25.4, and 33 mm. The model generated landslide stability maps that identified three areas of high instability. These unstable regions are located in the San Fernando Valley, the San Gabriel Mountains, and the Santa Monica Mountains. In each case the vegetation cover had been severely burned during the preceding 2007 wildfires.

The model results showed that burning from wildfires is a major destabilizing factor for southern California. Burn sites are more prone to landslides than vegetated slopes because the soil more readily exceeds its critical moisture content. Severe droughts in a future warming climate are expected to increase the likelihood of more frequent and intense wildfires. Higher temperatures combined with decreased total rainfalls facilitate more intense landslides, including devastating mudslides, following heavy precipitation. Finally, the model is designed to assist in developing timely mitigation measures for post-fire, storm-triggered landslides.

Wildfires that began on October 21, 2007 in southern California, following severe drought and unusually strong winds, resulted in a loss of life and a damage bill over a billion dollars. The fires burned ~2,000 km^2 of land and emitted

© Springer International Publishing Switzerland 2015

D. Ren, *Storm-triggered Landslides in Warmer Climates*,
DOI 10.1007/978-3-319-08518-0_9

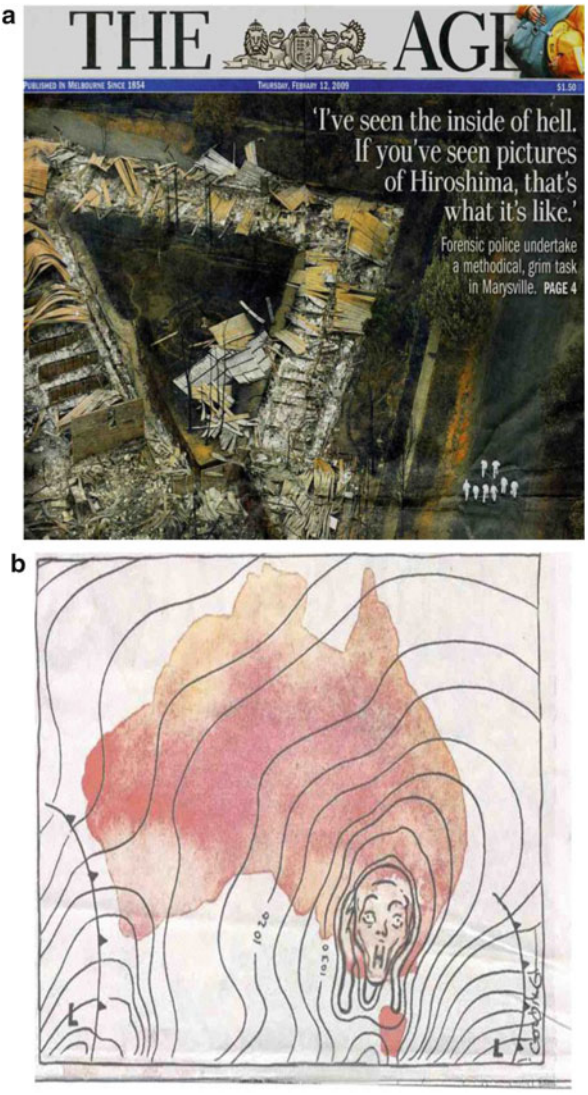

Fig. 9.1 Panel (**a**) Australian bushfires February 7, 2009: over 240 dead, ~1,800 houses destroyed, ~200 businesses and other buildings destroyed, largest natural disaster in Australia's history. Panel (**b**) is an editorial cartoon in Melbourne newspaper the week after the fires indicating Australians know that high pressure in the summer equals extreme heat that is conducive to fires. Context of the Australian bushfire disaster: (1) 8 years of severe drought in southern Australia; (2) record-setting heat wave the week before, 3 days in a row above 43 °C (109 °F); and (3) the day of the fires, Melbourne set an all-time record high temperature of 46.4 °C (115.5 °F) associated with strong high pressure and north winds

~7.9 million metric tons of carbon dioxide in 1 week (Wiedinmyer, personal communication, 2007), so the environmental impacts were long-lasting.

In this study a numerical model (SEGMENT; Ren et al. 2008, 2009) is used to examine rain-triggered shallow landslides, and to determine how the removal of vegetation by fires changes landslide susceptibility, as measured by the following metrics. How will a particular landslide be initiated? How fast will it move, as measured by the maximum achievable speed? How far will it travel, and how large will it be in terms of spillage area, a variable related closely to the maximum achievable velocity of the land mass movements? Most previous discussion has been limited to vegetation effects on landslides (Hutchinson 1988), which also are variously referred to as shallow landslides, mudslides, or debris flow in the literature (Wilford et al. 2005; Iverson 1997). They are landslides that involve near-saturated soils as the slide mass. There are numerous classification schemes for landslide processes, based on an understanding of earth movements (Hungr et al. 2001). For example, the classification scheme developed by Cruden and Varnes (1996) was driven by the need to combine information about the failure forms, the materials involved, and the movement velocity. The phenomena in this study also are described as "soil slip-debris flows" but here the term "landslides" will be used almost exclusively to avoid terminology confusion.

Specifically, this study investigates land cover damage from fires and the consequent effects on infiltration-triggered landslide susceptibilities. The spatial distribution of landslide prone areas is mapped, and a numerical model is used to assess the impacts of intense storms on the slope stability of the burned areas. In southern California, post-fire landslides in the burned areas adjacent to densely populated areas are an annual threat to life, property, and infrastructure. Predicting the locations and timings of landslides, using numerical models with sufficient lead time, is a scientifically challenging problem. However, it is a critical step in mitigating landslide impacts and planning local rescue responses.

Climate model simulations suggest that rainfall events may become less frequent but more intense in a warmer future climate (see IPCC AR4 2007). Consequently, post-burn landslides will present a more acute problem in hilly regions such as southern California, with increased hydrogeological instability. Rapid land development has further increased the risk to life and property. Few studies have addressed the probability of landslides in burned areas (e.g., Cannon et al. 2003, 2004). Increased understanding is needed of the effects of changes in soil mechanical properties (shear strength, viscosity, and elasticity) and hydrological responses (infiltration rate, hydraulic conductivity) of burned areas.

Numerous empirical and descriptive landslide models have been developed for landslide stability analysis and monitoring (Caine 1980; Gritzner et al. 2001; Larsen and Simon 1993; Cannon and Gartner 2005; Godt et al. 2006). They have contributed much to an increased public awareness of these hazards and have provided valuable experience for identifying the key causal factors. For example, Caine (1980) and Larsen and Simon (1993) presented empirical rainfall intensity–duration thresholds for landslide initiation. The work of Godt et al. (2006) uses a detailed assessment of rainfall triggering conditions, hill slope hydrologic properties, soil

mechanical properties, and slope stability analyses. Generally, the models use a subset of all triggering factors, arguing that the data required for a complete landslide susceptibility study is prohibitive. Increased knowledge is required of the preparatory factors (e.g., slope and orientation, soil porosities, grain size, direct and indirect effects of the root system) and of the triggering factors (e.g., earthquakes, rainstorms, melting of frozen soil, accumulated slow crust deformation). Such knowledge is obtainable in part by comprehensive modeling of the physical processes involved in landslides (Costa 1984; Iverson 1997).

9.1 Collecting Input Data for the Fire Sites

Our study region (see location map, Fig. 9.2) comprises several low mountain ranges in the southwest corner of California, near the large cities of Los Angeles and San Diego. Land cover and land use are complex and comprise urban, shrub, and forest environments. The dominant vegetation of southern California is a mix of winter deciduous, evergreen (e.g., cedar and evergreen sclerophyll shrubs), annual grasslands, and some drought resistant deciduous plants. Material properties vary widely, as do local surface relief, vegetation, precipitation climatology, and seismic activity. These factors determine where and when landslides will occur. Previous landslides lower the potential energy of large amounts of material, and change the shape and steepness of hill slopes. They leave a so-called "cold trace legacy" (Dietrich and Dunne 1978; Reneau and Dietrich 1987; Dietrich et al. 1995; Crozier and Preston 1999) on the future slope stability.

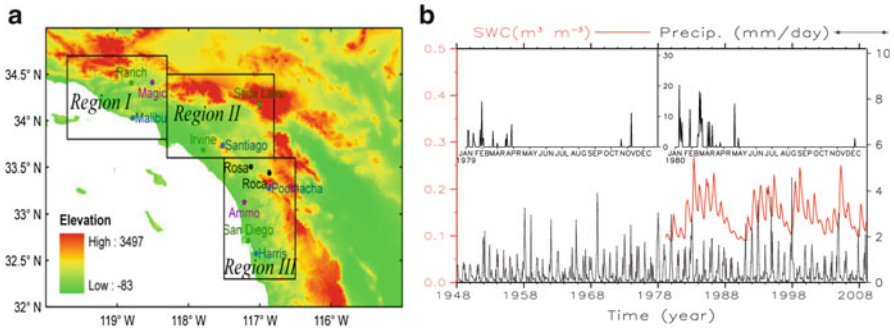

Fig. 9.2 Characteristics of Southern California. Panel (**a**) is the digital elevation map. The major fires are labelled as *color dots*. In this sketch, 1 km low-resolution USGS/GTOPO30 data are used. Fire locations are collected from www.fema.gov. Panel (**b**) is the NCEP/NCAR reanalysis precipitation and soil moisture (0–200 mm average volumetric water content) condition for this region (1948–2000). Two *insets* are monthly precipitation distribution for year 1979 and 1980. Precipitation occurs primarily between November and April, characteristic for Mediterranean climate

High-resolution elevation data are needed to identify unstable slopes. A major advance in remote sensing techniques that assists in determining landslide susceptibility is the high-resolution digital elevation map (DEM) from the NASA Shuttle Radar Topography Mission (SRTM, http://www2.jpl.nasa.gov/srtm/, USGS2004). The dataset, of ~90 m resolution, determines the inclination and orientation of grid cells. These data, together with digital maps of soil characteristics from the Food and Agriculture Organization of the United Nations (http://www.fao.org/AG/agl/agll/dsmw.htm, Fig. S3), provide inputs for the numerical model described in Chap. 6. Compared with the physical properties of hill slopes that affect the potential for landslides, vegetation and rainfall are far more variable. The USGS National Land Cover Dataset 2001 (NLCD2001, Homer et al. 2004) provides pre-fire background land cover information.

The thickness of the failed slab is calculated by the numerical model, which in turn is based on assumptions about precipitation events and land surface processes. The model requires the following input parameters: initial moisture content of the failed slab, soil material properties, vegetation root depth and distribution morphology such as root length density and root strength, and initial bedrock topography. For vegetated surfaces, especially those affected by fires, representing soils as purely mineral (e.g., sand, silt, and clay classifications) is known to be inadequate (DeBano 2000; Moody and Martin 2001; Smith et al. 2002). Here, introduce organic matter content is simulated using the Carnegie Ames Stanford Approach (CASA, Potter et al. 1993) biosphere model with improved soil moisture simulation. A parameter f_i is introduced, representing the fraction of soil sublayer, i, that is organic matter. The thermal and hydraulic parameters for organic soil are weighted averages of the corresponding mineral soil and those of humus, using an empirical relationship (Lawrence and Slater 2008; Letts et al. 2000). DeBano (2000) asserts that organic matter accumulates in the upper soil in the intervals between fires, so parameterizations include the effects of preexisting hydrophobic substances.

Previous studies (e.g., Casadei et al. 2003) have identified the spatial distribution of soil depth as a strong control on local landslides. In mountainous areas, topsoil availability provides yet another limitation on saturated slab thickness. Colluviums form wedge-shaped deposits that are thin on the steeper, higher slopes and gradually thicken near valley bottoms. Therefore the following rules are applied to initializing the sliding mass thickness in our numerical model. If the DEM indicates that the slope is steeper than the dry material repose angle (ϕ), maximum soil thickness is set to zero. Maximum soil thickness also is set to zero initially for impermeable surfaces (e.g., parking lots and pavements) and open water areas. However, as the simulation proceeds, soil thickness can become positive for the impermeable surfaces by advection from neighboring grids.

Because the southern California fires started under very dry conditions, the hydrophobic nature of the top ~5 cm of the sandy soil layer must be considered (Huffman et al. 2001). A burn severity map of the 2007 California fires was obtained from the false-color images of the Advanced Spaceborne Thermal Emission and Reflection Radiometer on NASA's Terra spacecraft (http://www.nasa.gov/vision/earth/lookingatearth/socal_wildfires_oct07.html). The images have three

distinct colors; green for vegetated, blue for unburned and dark red for burned areas. From burn characteristics and root depth, two vegetation categories can be identified: grass and chaparral shrubs, and forests. For the burned grids, we applied the Burned Area Emergency Response Team (BAER of DOI) empirical burn severity classifications (light, medium and severe). The six burn severity categories then become controlling factors on soil hydraulic conductivity, infiltration coefficients, and the upper-most layer (5–10 cm) base viscosity υ_0.

High-resolution simulations of the region require very large in-memory computer processing, limiting the simulations carried out in this study to three domains (Fig. 9.2), covering the major fires. Domain I (34–34.7° N; 119.5–118.5° W) has four significant fire locales (the Buckweed, Ranch, Magic, and Canyon Fires). Domain II (33.8–34.8° N; 118.2–116.5° W) and Domain III (32.8–33.8° N; 118.2–116.5° W), covered the largest fire events, such as the Witch Creek fire, which burned 801 km^2, and the Harris Fire that burned 366 km^2 land cover (http://www.inciweb.org).

The geological structure of the study regions is complex, due to the tectonic interactions of the North American Plate and Pacific Plate, which include periods of folding, faulting, repeated sea level changes, and volcanism. The basal material of the slopes can contain sandstone, granite, shale, and even volcanic rock (i.e., the Santa Monica Mountains). For modeling purposes this region is viewed as underlain primarily by large expanses of weathered bedrock, producing a loamy sand or coarse sandy soil above the bedrock, and possibly exposed core stones on the surface. Most important for modeling shallow landslides in coarse colluviums is that root strength dominates cohesion, so we have a mask of root strength and group distribution profile according to land cover type. Our landslide model component requires above ground surface loading information, so we have produced a vegetation load mask, namely, the weight of vegetation per unit land surface area. For forest areas we follow the method of Chambers et al. (2004) in using a specified vegetation load mask and assuming that the grass weight is miniscule. For regions that lack forest inventory data, an alternative is to obtain aboveground biomass using allometric models driven by remotely sensed land data (Zhang and Kondragunta 2006).

In the past decade, observations of landslides have increased markedly, due to the application of satellite techniques such as geodetic laser scanning and altimetry, together with airborne and ground based observations (Carter et al. 2007).

Hitherto, three general approaches have been used to predict storm-triggered landslides: (1) Empirical analysis of landslide-producing storm characteristics (Campbell 1975; Wilson 2000), which does not account explicitly for soil mechanics, but relies instead on historical records of past storms and landslides; (2) Empirical mapping of the landslide locations (Carrara et al. 1991; Chung et al. 1995), which typically uses GIS-based map overlay techniques, selecting "index predictors" such as topographic gradients, land use, and even distance from faults and ravines. However, neither approach (1) nor (2) predicts timings of events, being based on observed statistics of past landslide events and the assumption that the same conditions hold in time; and (3) mechanistic modeling of hydrology and slope

stability (e.g., Dietrich et al. 2001; Casadei et al. 2003), through coupling of mechanistic slope stability and hill slope hydrological models. Slope stability usually is defined as the ratio of resisting to driving stress for idealized geometry, and a saturated soil slab parallel to bedrock bedding is required. Thus they over-predict the occurrence of landslides, and are sensitive to available topographic data quality. The empirical models have done less well, perhaps due to non-stationarity of the predictors. It is a difficult task to generate a suitable set of a priori, physically based predictors.

9.2 Improved Parameterizations in SEGMENT-Landslide for Fire-Burn Sites

Following the removal of the vegetation canopy and surface organic material, rainfall interception (canopy runoff) is reduced and the bare hill slopes are exposed to unimpeded raindrop impacts. It is known that wildfires alter the hydrologic and erosion responses of watersheds in southern California (Kraebel 1934; Wells 1981; DeBano 2000). Changes in occurrence frequency and strength of mudslides depend on changes in precipitation amount and intensity, and how much water either infiltrates into the soil or becomes runoff (Liu et al. 2001; Zhu et al. 2001; Eagleson 1978). To diagnose the soil moisture variations and the vertical distribution of precipitation, a sophisticated land surface model, the Simulator for Hydrology and Energy Exchange at Land Surface (acronym, SHEELS, Ren 2001) is part of the SEGMENT system. SHEELS is a numerical solution of Richards' equation (Richards 1931), using the Brooks and Corey (1964) relationship for moisture dependent hydraulic conductivity, and a Green-Ampt infiltration scheme. Details of soil moisture are important for determining the potential of shallow landslide/mudslide, and whether it develops into a catastrophic landslide.

Reports by Jibson et al. (1998) and Cannon et al. (2003) have listed slope steepness, the geology, moisture content of sliding material, and burn severity of the surface as first order factors in slope stability. According to DeBano (2000), fires modify the upper soil horizon's water repellence. Burn severity effects are included in SEGMENT through the parameterization of infiltration and the of binding the uppermost layer. The burn impacts on material viscosity are monotonic, whereas the relationship between water repellence and burn severity is more complex. DeBano (2000) points out that there is little change of water repellence for soils heated less than ~175 °C, but water repellence is increased when soils are heated between 175 and 200 °C. Even higher temperatures (280–400 °C) actually destroy the repellence. In the parameterization scheme, the burn effect is a multiplier (F) on the organic soil parameterization. F is defined as:

$$\begin{cases} \mu_0 + (\mu_1 - \mu_0)e^{-R\left(I/I_0\right)}, & \textit{monotonous}\,(\text{i.e., mechanical binding, viscosity}) \\ \mu_1 - \mu_0 R\left(1, -I/I_0\right)^2, & \textit{non-monotonous}\,(\text{i.e., } K_s, \text{ infiltration rate}) \end{cases} \tag{9.1}$$

where μ_0 and μ_1 (20 for viscosity and 8 for infiltration rate) are bounds of the burn effect multiplier. I is proportional to the six burn severity classification; unburned grids have $I = 0$ while severely burned grids have large values of I (~10); I_0 corresponds to the burn severity with maximum enhancement effects on soil water repellency; and R is an empirical numerical magnifier.

SEGMENT explicitly parameterizes soil mechanics, vegetation transpiration and root mechanical reinforcement, and relevant hydrological processes. The parameterization of the root mechanical reinforcing of the soil shear strength achieves the following. For roots of similar strength, a large number of small roots contribute more to soil reinforcement than a small number of thick roots; trees and shrubs reinforce the soil to greater depth than grasses. Moreover, roots within clay soils provide greater reinforcement than those in sandy soils, and the reinforcement effect decreases exponentially with increasing soil moisture content. Tree roots are assumed to extend vertically downwards, not perpendicular to the local slope surface.

For actual landslides, high-resolution real elevation and soil vertical data sets are used. The time step for integration is 10^{-4} s for soil mechanics and 30 min for the hydrological components. Only five vertical soil layers are used, to make the extended integrations achievable in reasonable wall-clock time and to reduce in-memory requirements. In addition, some of the physics in the land surface model component is simplified. Instead of using the implicit solver for soil temperature, we use a force-restore type soil temperature solver (Ren and Xue 2004). Similarly, subroutine for estimating the extra stress on the surface exerted by raindrops falling with terminal velocity is not used. Drag from Horton overland flow is included. The canopy interception of rainfall, runoff and evapotranspiration (ET) processes are retained because of their importance in governing soil moisture regimes, especially for forests. The climate of the region is Mediterranean , with dry warm summers and moist cool winters About 80 % of the ~400 mm annual rainfall occurs between November and March (Wagner and Nelson 1961; see Fig. 9.2b). Wintertime ET is unlikely to be a major controlling factor for the soil moisture regime.

9.3 Sensitivity Studies Over Three Subregions

For the region of southern California studied here, it is assumed that a rainfall event occurs after a near-mean 250 mm antecedent seasonal precipitation, thereby bringing the colluviums' mantle close to field capacity. Three experiments were made with 24 h storm rainfall totals of 33, 25.4, and 17 mm, corresponding to 25, 10, and

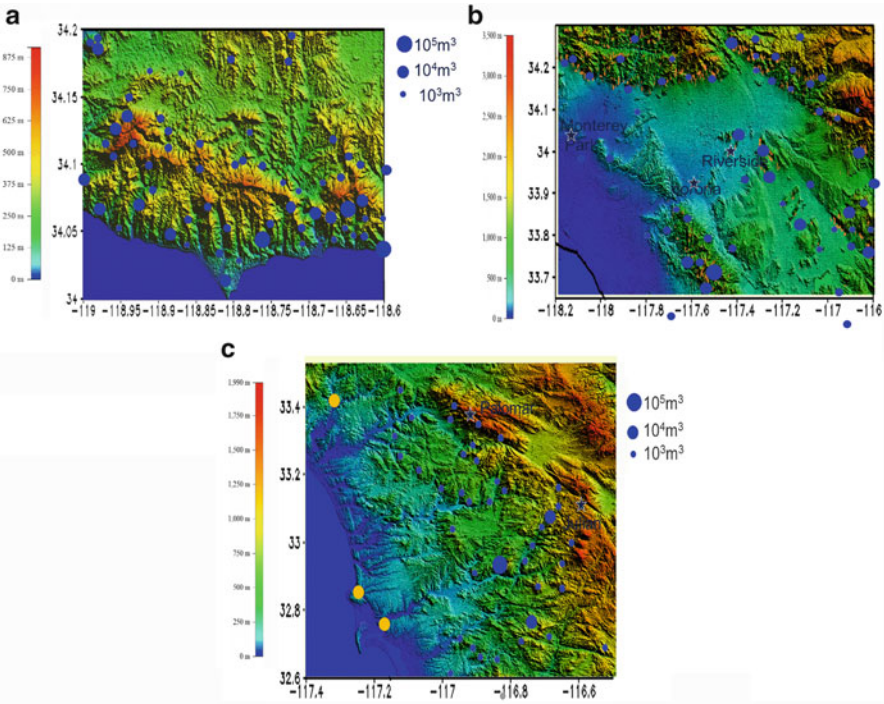

Fig. 9.3 Areas prone to mudslides. The color specs only indicate locations prone to storm-triggered. The ensemble mean of the scarps are indicated by blue dots, which is proportional to the volume of the involved sliding material.

2 year recurrence frequencies, respectively. The precipitation intensity distribution estimates were obtained from intensity–duration graphs of the NCEP/NCAR reanalysis precipitations for 1960–2000.

The focus of the numerical experiments is the consequences of fire-caused deforestation for catastrophic landslides, which in this region often is in the form of mudslides. The landslide metrics are the maximum attainable moving speed, the amount of mud deposited on structures, and total mass loss. A simulation of landslides with original land cover and precipitation is carried out first.

With the original vegetation and a 33 mm precipitation event, model generated maps of landslide potential show the surface elevation changes (Fig. 9.3). The landslides usually are small compared with the slopes on which they reside, so a shaded relief of the topography is the background with soil thickness changes added. Landslide locations are the highlighted, speckled areas. For Region I (Fig. 9.3a), the most unstable area is in the southeast corner and includes the San Fernando Valley, the San Gabriel Mountains, and the Santa Monica Mountains. The most unstable of these is the Santa Monica Mountains national recreational area. Large regions south of the Magic fire site are relatively stable. For Region II, the most unstable region is at the foothills of the San Bernardino Mountains.

The Monterey Park region just north of the Santiago fire site is a highly unstable point. Although its elevation is not high, the Riverside area is prone to slides, because the gradients are large and composed of soft base material. For Region III, the unstable region is an elongated area along the ridge of the Palomar Mountain (33.34° N, 116.91° W), the Cuyamaca Mountains, and a narrow corridor along the San Jacinto fault (between Palm Springs and Hemet). This is an active fault region for earthquakes. The Rosa, Rice, and Witch Creek fire sites are in this area. The locations of landslides frequently are along rivers, at the junctions of ravines and canyons, near the upper points of alluvial fans, or at the foot of steep slopes. Generally, landslides form on steep slopes, but this region is an exception. Despite the steep slopes, most of the peninsular ranges are not prone to mudslides as soil layers are shallow or nonexistent. They are underlain by unfractured granitic rock base, further reducing the possibility of rainfall-triggered mudslides.

The unstable regions are shown in Fig. 9.3. The Santa Margarita Mountains (left upper corner 33.47° N, 117.397° W), due to the light source direction, is not clearly shown on the figure. It is also an unstable region, with maximum moving speeds of the mudslide reaching 2 m/s at several locations. A small, fast-moving landslide (with flow speed >3 m/s, see for example) in a highly populated area may pose a greater threat to public safety than a large, slow-moving landslide (Hungr et al. 2001; Works Bureau 1998). Thus landslide speed is the single most important index of possible destructiveness. By comparing the maximum attainable sliding speed before and after a fire, the effects of burning on slope safety are clear. Locations most likely to experience slope failures are readily identifiable (Fig. 9.4).

For a rainfall threshold of 25.4 mm, there is no significant difference on landslide severity between burned and original unburned situations for Region I. However, the effects remain for Regions II and III, especially for Region II. In Fig. 9.5, two precipitation amounts are compared for Region II, namely 25.4 and 33 mm. Using total mud loss to measure severity of sliding, the mud loss under a 25.4 mm precipitation event is an order of magnitude smaller. For a 33 mm precipitation event, the mud loss difference falls to two orders of magnitude lower. The right y-axis displays the 25.4 mm case. For lighter rainfall events, vegetated surfaces lose far less mud than the post-fire case, indicative of a preventative effect. The situation for heavier rainfall is the converse.

For the 25.4 mm rainfall case, the soil is saturated to a shallower depth and cannot advect the vegetation. Canopy interception reduces the severity of driving stress caused by surface runoff. In contrast, burned surfaces through the formation of the hydrophobic layer concentrate the surface runoff. For a 33 mm rainfall storm, the soil slab is moistened to a greater depth than most vegetation roots and the resistive force of the roots is no longer effective. However, the weight of vegetation and canopy runoff produces additional driving stress exacerbating the sliding. The areas surrounding the Slide Lake fire site and a small area southwest of Riverside are the most sensitive. Region I, which is covered with shallow rooted sage shrub and scattered trees, exhibits preventative effects from vegetation only for light rainfall; at least 6 mm/h is required to trigger landslides. The areas labelled "*V*" in Fig. 9.4 show decreased susceptibility to sliding because the shallow rooted

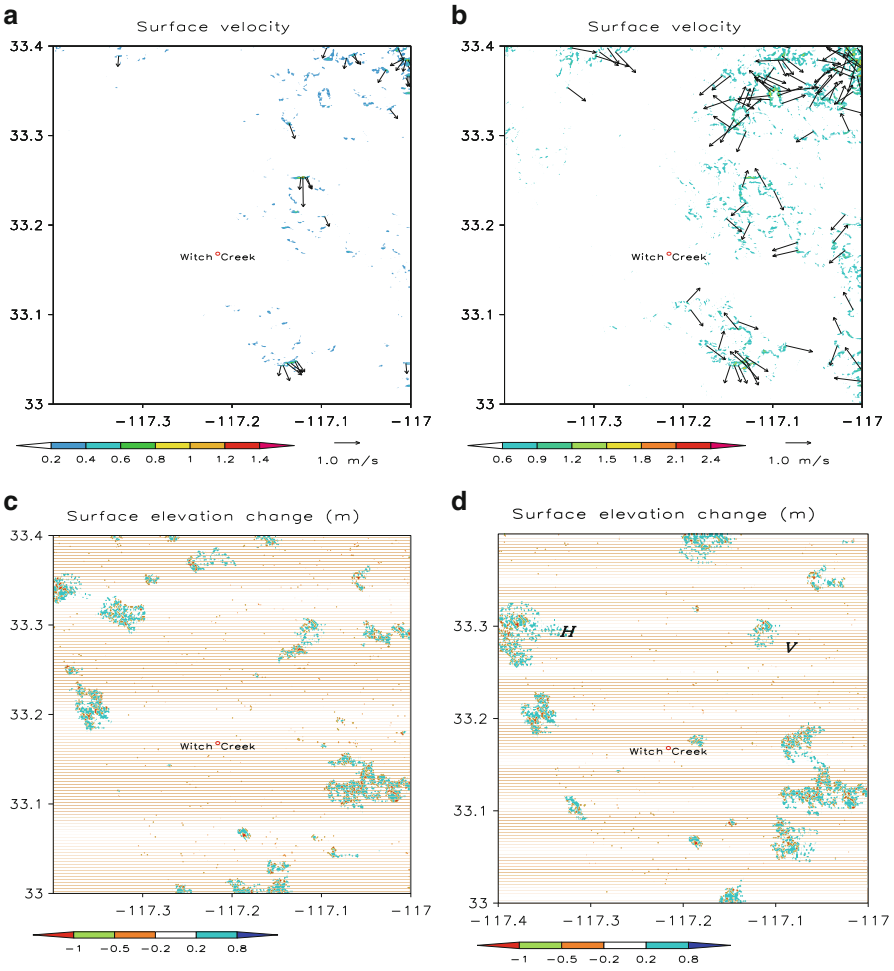

Fig. 9.4 Effects of fire on mudslide susceptibility, indicated by maximal attainable flow speed (panels **a**, **b**) and surface elevation changes (panels **c**, **d**) near Witch Fire. *Left panels* (**a**, **c**) show the original condition. *Right panels* (**b**, **d**) show the post-fire surface situation. In panels (**a**) and (**b**), flow speed greater than 0.2 m/s are shaded. Flow speed greater than 0.5 m/s are further labelled with the (u, v) composed flow vectors

vegetation cover is removed. The increased soil shear strength of the resulting hydrophobic layer now dominates. Regions labelled "*H*" have runoff is diverted to neighboring regions.

For a 17 mm storm threshold, fire removal of vegetation renders an originally stable slope unstable. An exacerbating effect exists for slopes that already are unstable. This applies to all three regions. The Witch Creek fire burned the vegetation of the ocean facing side of the Elsinore Fault, which runs from northwest to southeast through Julian, significantly increases the possibility of mudslides over

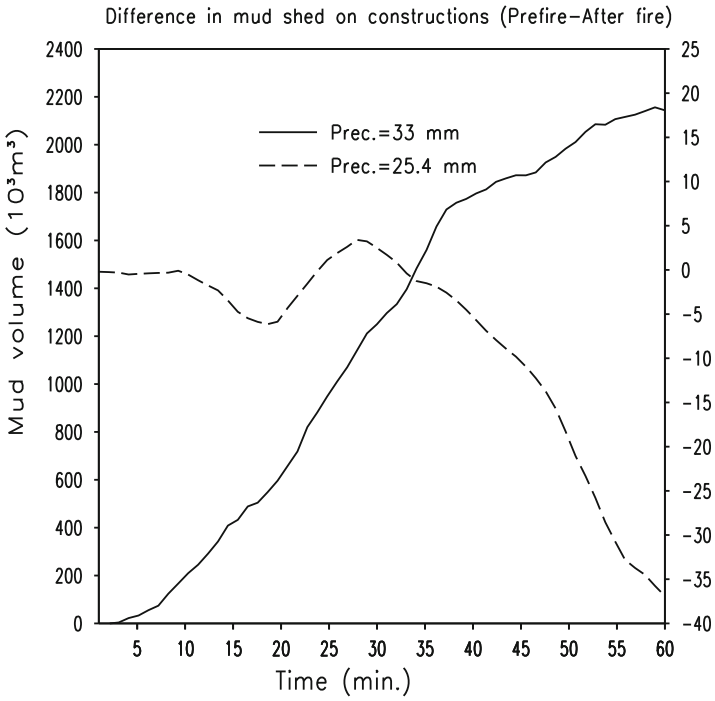

Fig. 9.5 Differences of mud-shed on the impervious surfaces for a portion of Region II (33.65–34.25° N; 118.25–116.8° W). Pre-burn minus post-burn, respectively for 33 and 25.4 mm rainfall amounts. The 25.4 mm precipitation case uses secondary y-axis

this area. In Fig. 9.4, the surface elevation change does not follow the pattern of maximum attainable flow speed, primarily because the soil thickness is nonuniform. To the west of Witch Creek, although the maximum attainable flow speed is generally less than 0.2 m/s, the soil thicknesses all are greater than 1 m, so they are capable of causing significant distortion to topography. The increase in sliding is not uniform over the regions. Some regions show decreases in mud accumulation/reduction. The shaded area in the maximum attainable flow speed maps appears as atolls, because mudslides tend to occur at mid-slope, rather than at the top.

Using the high-resolution land use data as a mask, the model also outputs the total soil mass that spreads to urbanized areas, the total areal coverage, and the total amount of soil loss. For Region III, a 17-mm rainfall threshold event produces ~1.18×10^6 m^3 of mud, covering an area of about 1.1 km^2. The Witch Creek fire mud displacement is about 10 % of the total. For the same precipitation morphology, vegetation removal by fires makes the ensuing slides start earlier, and to shed far more soil mass. The total volume rate also reaches peak values earlier than pre-fire case. For Region II, after fire removal of land cover, a 17 mm rainfall produces ~4×10^5 m^3 of mud.

9.4 Discussion

For typically observed precipitation amounts over southern California, fire-caused deforestation is unusual, compared with barren ground that never was vegetated and has no root distribution, in the following ways. For the first rainy winter season after the fires, the reduced infiltration rate actually reduces the depth of soil saturation and therefore reduces the likelihood of massive mudslides. In the following years, the root remains may starts to erode and hence reduce in strength. However, the complete removal of a tree canopy lessens the driving stress below a full canopy stand and the slopes are still stronger than bare soils without a rooting system. However, in time, sufficient decaying of the roots will lead to increased site susceptibility to failure. For forested grids, the effects of forest dynamics on root strength are included. This time-dependent root strength associated with fire damage is modeled using a root decay model by Sidle (1992). Within approximately 5 years, the strength of the site will be similar to that of bare ground.

Conversely, unburned vegetation plays a two-pronged role in landslides. If the saturated soil is deeper than root depth (the population mean of the vegetation, not just a single tree), the canopy enhances mudslides. Only for weaker storms that saturate a relatively shallower surface soil layer vegetation plays a preventative role.

As anticipated from this study, in the year following the 2007 wildfires, mudslides occurred in southern California in 2008. On July 13, 2008 landslides damaged more than 50 homes in an area scarred by the 2007 wildfires. In September 12, 2008 a mudslide near Pasadena (northeast of Monterey Park, ~34.1° N, 118.0° W) was triggered by a thunderstorm occurring at early stage of the wet season, well before reaching the required antecedent precipitation amount usually required for a pre-burning vegetated condition.

More recently, and significantly, after the present study had been completed, devastating mudslides occurred in southern California on February 6, 2010, when extensive wildfires in 2008 and 2009 were followed by El Nino-related, early wet season rainstorms. California was declared a mudslide disaster area by the Federal Emergency Management Agency (FEMA) on March 6, 2010 (http://www.fema.gov/news/disasters_state.fema?id=6).

Both the 2008 and 2010 mudslides were rainfall-triggered and related to wildfires, as discussed above. The mudslides of 2008 and of 2010 demonstrated two main points. First, if the required precipitation and soil moisture conditions are met, the unstable spots identified in Fig. 9.3 will be realized. Second, if further wildfires are again followed closely by heavy precipitation events, such as the 2008 and 2009 wildfires preceded the El Nino-related heavy rainfall events, mudslides again can be expected to be realized. In fact, the wildfires of 2007 and 2008–2009, followed by heavy rainfall events in 2008 and 2010 respectively, were unusual and relaxed the landslide requirements discussed above owing to their close temporal proximity.

The consensus among climate scientists is that extreme precipitation events are likely to increase more than the mean under future warming climate (IPCC AR4; NRC 2002). Even without any change in total precipitation, higher temperatures may lead to a greater proportion of intense precipitation (Karl and Trenberth 2003).

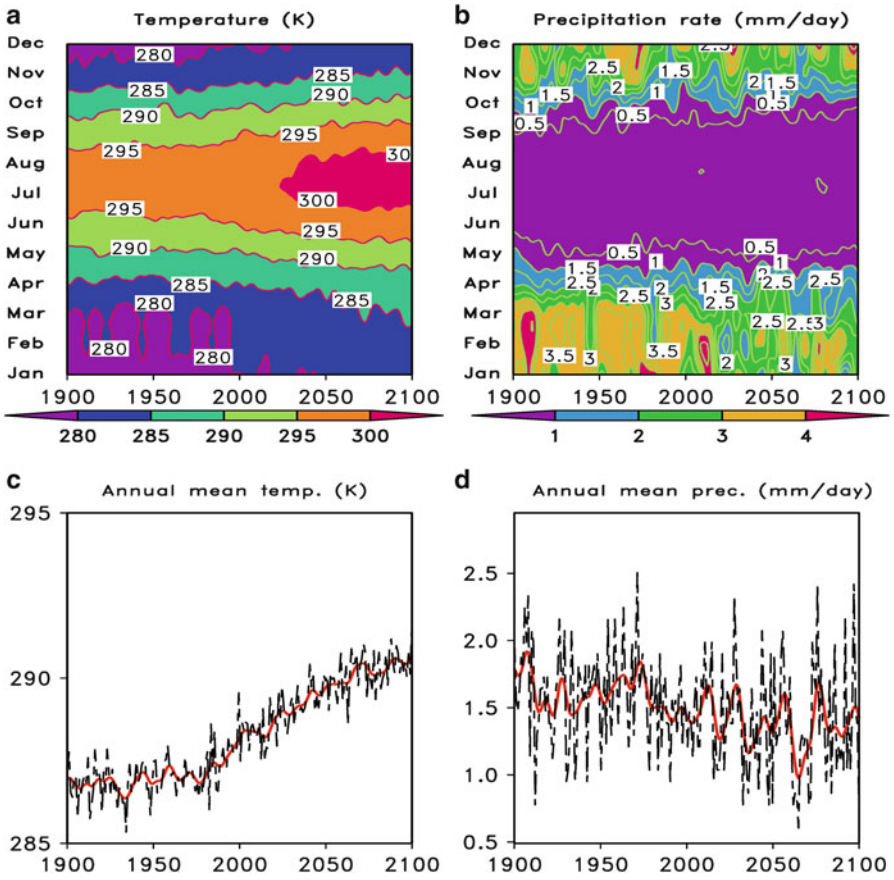

Fig. 9.6 Area-averaged temperature (**a**, **c**) and precipitation rate (**b**, **d**) trends over State California from the CCSM3 model simulation. *Upper panels* show the variations in each month while the *lower panels* are annual-mean time series of the area-weighted (**c**) surface air temperature, and (**d**) precipitation rate. *Thick red curves* in panels (**c**) and (**d**) are 21-year low-pass smoothed representations of the corresponding annual series. Panels (**a**, **b**) illustrate the course of annual values of month-by-month temperature/precipitation rate averaged over State California, putting into a long-term perspective of 200 years. The annual mean temperature (panel **c**) increases by ~3 °C over the next century while the annual mean precipitation (panel **d**) decreases by 0.2 mm/day

Significant increases in observed and simulated extreme precipitation already have been reported for many regions including the USA (Kharin and Zwiers 2005; Semenov and Bengtsson 2002; Groisman et al. 2004; Karoly and Stott 2006).

Observations confirm that the Earth's climate is changing at an unprecedented rate, with instrumental records indicating that over the last century the global temperature rose by about 0.6 °C. The warming trend for the last 30-years is about three times that of the past 100 years (WMO 2002). It is expected that the mean global temperature will continue to rise by between 1.4 and 5.8 °C by 2100 due to the emission of greenhouse gases (McCarthy et al. in IPCC TAR 2001). The climate of the southern California region also is expected to change. In Fig. 9.6,

temperature and precipitation trends are shown from the Community Climate System Model (CCSM3, Collins et al. 2006), with a relatively high horizontal resolution of ~1.4° and using the Special Report on Emission Scenarios A1B scenario (SRES A1B, Nakicenovic and Swart 2000).

The simulations of the twentieth century and the twenty-first century, using the SRES A1B emission scenario forcing, allow us to examine the area-averaged temperature and precipitation rate (Fig. 9.6) within a long-term perspective. The temperature increases during every month of the year (Fig. 9.6a). This summer season (confined by the 295K lines) has been increasing in duration since the 1970s. After 2050, the summer season length should increase rapidly to May–September by 2100. The annual mean temperature (Fig. 9.6c) increases by ~3 °C over the twenty-first century. The annual mean precipitation (Fig. 9.6d) does not increase significantly, on monthly time scales. Another high-resolution general circulation model, the MIROC3.2-hires, produces similar trends to these obtained from CCSM3. However, a statistical analysis of the rainfall extreme frequency indicates that the 33 mm threshold total rainfall within a day is almost a certain event in the upcoming 30 years for the studied regions. Because the storms are more intense but less frequent, this scenario indicates that the droughts will be longer and more severe, favoring conditions that cause wildfires. Combined with the required antecedent soil moisture contents (250 mm seasonal precipitation), there is only a 30 % chance of a 33 mm storm within a single day. So the most likely scenario is that burning will contribute to mudslide generation throughout the entire recovery cycle.

9.5 Tentative Conclusions Drawn from Sensitivity Studies of Fire Burn Sites

In this study a numerical model, SEGMENT, is used to estimate the potential for landslides over a region of southern California. In its application to the post-2007 wildfire areas of southern California, the model produces a range of landslides from slowly streaming sand-rich slurries to surges of boulders and mud. The results provide partial answers to the questions of whether or not the entrainment process will decelerate sliding (p. 249 of Iverson 1997). The design of the sensitivity experiments is in accordance with Iverson's (1997) view of landslides/debris flows, which suggests that debris flows usually start as static, nearly rigid, water filled sedimentary masses situated on sloping land. After the commencement of the landslide, Iverson (1997) states that the original sediment–water fluid mixture becomes a "flowing, liquid-like state."

When applied to the year 2007 southern California fire sites, it was concluded that fire impacts on subsequent landslides are as follows. Vegetation modifies landslides by the following processes: canopy interception of rainfall and the companion reduction to surface runoff; root system reinforcement to soil strength;

and additional loading by stem and canopy weight. The relative importance of these three processes depends on the precipitation amount and the vegetation type and density. The canopy interception contributes to stability, especially for the case of light–moderate precipitation. For precipitation that saturates a relatively shallow layer (less than root depth), vegetation is believed to prevent landslides, in agreement with Campbell (1975). The denser the vegetation, the more effective is this preventative effect. For the Malibu area of southern California, the cliffs are covered with a dense carpet of chaparral and some scattered trees. The root system is shallow and its characteristically thick humus layer increases the amount of rainfall that can infiltrate the surface by holding the water for longer and reduce direct runoff. For Regions I and III (see Fig. 9.3) vegetation effects are found to be negligible for heavy rainfall events, but are significantly preventative for light–moderate rainfall amounts.

Overall, for Region I the most unstable area is the Santa Monica Mountains national park. For Region II, the most unstable region is at the foothills of the San Bernardino Mountains. The Monterey Park region also is highly unstable. For Region III, the unstable region is located along the Palomar Mountain, the Cuyamaca Mountains, and along the San Jacinto fault. Typically, landslides form on steep slopes, but this region is not prone to rainfall-triggered mudslides as the soil layers are shallow or nonexistent, as they have a granitic rock base.

Except for extreme precipitation events that soak the soil slab deeper than the root system, it was found that burning is a destabilizing factor for landslides. Even during the first 1–2 years after the fires, the burn sites are more prone to severe landslides than the previously vegetated situation. A possible explanation is that the water repellent layer intensifies downstream runoff and allows the critical soil moisture content to be exceeded, which might otherwise be unattainable if the rainfall were more evenly distributed. This agrees with the observed watershed scale response of a South African forest (p. 201 of DeBano 2000). At present, the model does not simulate fully some of the more complex infiltration and runoff patterns, as described by DeBano (2000). These include rill formation and fingered infiltration, both of which have are effective erosion processes. These effects will be examined in future work with finer resolution observations.

Under a warming climate, which shifts higher the mean temperature, if we suppose the pdf distribution of the temperature is not affected by warming, then a higher portion of the extreme hot tail is expected (Meehl and Tebaldi 2004, Fig. 9.7). In both the past and present, a warming climate and severe drought are important contributors to major fires (Meyer and Pierce 2003). Future work also is planned to link SEGMENT with models of climate change, dynamic vegetation, and fire modules to provide more timely warnings of devastating landslide hazards.

As a summary to Chaps. 7–9, the above cases cover a wide range of climate zones. A measure of our understanding of slope sliding processes is our ability to predict the future behavior of slopes under a range of conditions. In addition to the above examples, the SEGMENT-Landslide successfully reproduced three historical storm-triggered landslides that occurred during the past half-century, for the Yangjiashan creeping slope (YC) in China (Ren et al. 2010). SEGMENT-Landslide

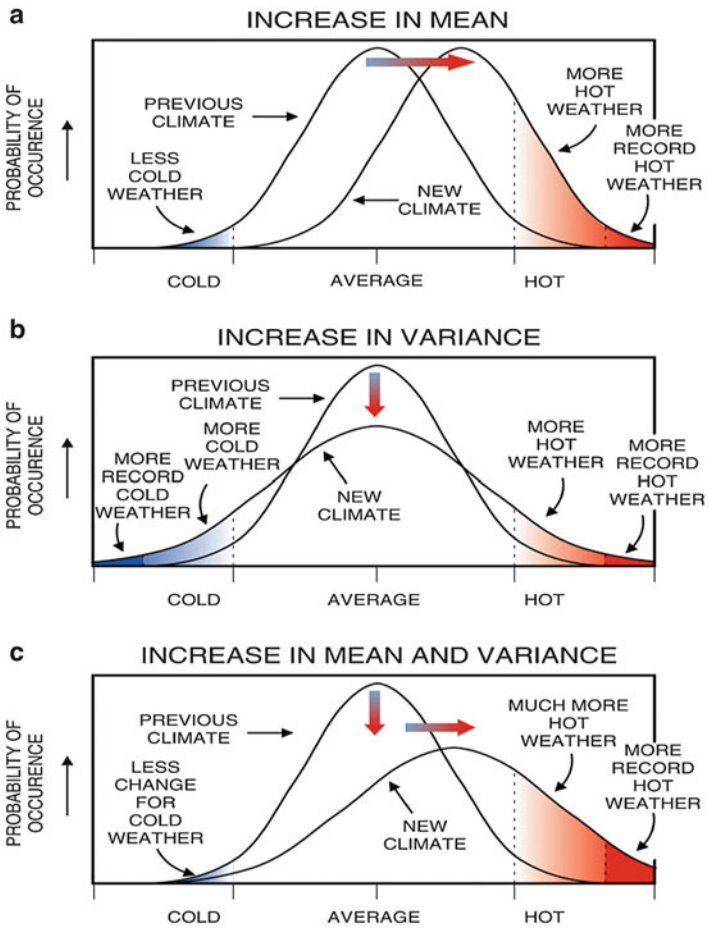

Fig. 9.7 How global warming affects extremes: a relatively small shift in the average temperature produces a very large increase in extreme high temperatures and a decrease in extreme low temperatures. *Source*: Meehl and Tebaldi (2004)

also was used to make one further, long term prediction, for the forthcoming decade, 2010–2019, which quantified the stability of the YC region and showed that slope movements will occur during the next decade and that, even more significantly, a major landslide is imminent if an intense rainstorm with over 150 mm of rainfall occurs at any time in that period, even in the near or immediate future.

The SEGMENT-Landslide landslide modeling system has demonstrated, from numerical experiments carried out over the YC region, that it can anticipate how strain accumulates. For example, it shows how load increases with precipitation and that there is an accompanying decrease in yield strength. SEGMENT-Landslide can

predict when sliding, or rapid slope failure, is probable, given the available meteorological parameters, soil properties and land cover conditions.

For the YC, its particular geological constituents are the main cause of its landslide susceptibility to triggering by storm events. Heavy storms are enhancement as well as triggering factors. Our study points out an aspect that requires close monitoring because it likely is responsible for the upslope cascading of storm-triggered landslides. Model sensitivity experiments established a stability feature not investigated by previous in situ surveys. The model demonstrated that rainstorm generated instability at a given location forms the first sliding block in a sequence, by acting as a trigger for a domino-like slide that moves up the slope.

Landslide perturbations on terrestrial ecosystem can be estimated from the information provided by landslide model, vegetation cover type and biomass, and soil nutrient profile. In situ archive of biomass is limited to forests with commercial value. In addition to being cost-effective, remote sensing provides the best spatial and temporal coverage of terrestrial biomass. Usually, foliage biomass can be estimated from the Moderate Resolution Imaging Spectroradiometer (MODIS) leaf area index (LAI) products. Above ground biomass residing in branches and stems is then derived from generalized, diameter-based allometric methods (Zhang and Kondragunta 2006), with reference to the land use map. Total biomass loading also is supposed to be proportional to aboveground biomass. With these information and the potential magnitudes of landslides, damages to terrestrial ecosystem can be estimated.

References

Brooks R, Corey W (1964) Hydraulic properties of porous media. Hydrology paper 3. Colorado State University, Fort Collins

Caine N (1980) The rainfall intensity-duration control of shallow landslides and debris flows. Geogr Anal A 62:23–27

Campbell R (1975) Soil slips, debris flows and rainstorms in the Santa Monica Mountains and vicinity, southern California. United States Geological Society professional paper 851

Cannon S, Gartner J (2005) Wildfire related debris flow from a hazards perspective, Chapter 15. In: Jacob M, Hungr O (eds) Debris-flow hazards and related phenomena: Springer-Praxis books in geophysical sciences. Springer, New York, pp 321–344

Cannon S, Michael J, Gartner J, Gleason J (2003) Assessment of potential debris-flow peak discharges from basins burned by the 2002 Missionary Ridge Fire, Colorado, open-file report 03-332. US Geological Survey, Denver, CO

Cannon S, Gartner J, Rupert M, Michael J (2004) Emergency assessment of debris-flow hazards from basins burned by the Cedar and Paradise Fires of 2003, southern California, open-file report 2004-1011. US Geological Survey, Denver, CO

Carrara A, Cardinali M, Detti R, Guzzetti F, Pasqui V, Reichenbach P (1991) GIS techniques and statistical models in evaluating landslide hazard. Earth Surf Process Landf 16:427–445

Carter W, Shrestha R, Slatton K (2007) Geodetic laser scanning. Phys Today 60:41–47

Casadei M, Dietrich W, Miller N (2003) Testing a model for predicting the timing and location of shallow landslide initiation in soil-mantled landscapes. Earth Surf Process Landf 28:925–950

Chambers J, Higuchi N, Teixeira L, Santos J, Laurance S, Trumbore S (2004) Response of tree biomass and wood litter to disturbance in a Central Amazon forest. Oecologia 141:596–614
Chung C, Fabbri A, van Westen C (1995) Multivariate regression analysis for landslide hazard zonation. In: Carrara A, Guzzetti F (eds) Geographical information system in assessing natural hazards. Kluwer, New York, pp 107–134
Collins W, Bitz C, Blackmon M, Bonan G, Bretherton C, Carton J, Chang P, Doney S, Hack J, Henderson T, Kiehl J, Large W, McKenna D, Santer B, Smith R (2006) The community climate system model version 3 (CCSM3). J Climate 19:2122–2143
Costa JE (1984) Physical geography of debris flows. In: Fleisher PJ, Costa JE (eds) Developments and applications in geomorphology. Springer, New York, pp 268–317
Crozier M, Preston N (1999) Modelling changes in terrain resistance as a component of landform evolution in unstable hill country. In: Hergarten S, Neugebauer H (eds) Process modelling and landform evolution. Lecture notes in earth science, vol 78. Springer, Heidelberg, pp 267–284
Cruden DM, Varnes DJ (1996) Landslides types and processes. In: Cruden DM, Varnes DJ (eds) Landslides investigation and control. Special report 247. Transportation Research Board, Washington, DC, pp 36–75
Debano L (2000) The role of fire and soil heating on water repellency in wild land environments: a review. J Hydrol 231–232:194–206
Dietrich W, Dunne T (1978) Sediment budget for a small catchment in mountainous terrain. Zeitsch Geomorphol Suppl 29:191–206
Dietrich W, Reiss R, Hsu M, Montgomery D (1995) A process-based model for colluvial soil depth and shallow landsliding using digital elevation data. Hydrol Process 9:383–400
Dietrich W, Bellugi D, Real De Asua R (2001) Validation of the shallow landslide model, SHALSTAB, for forest management. In: Wigmosta M, Burges S (eds) Land use and watersheds: human influence on hydrology and geomorphology in urban and forest areas, vol 2, Water science and application. American Geophysical Union, Washington, DC, pp 195–227
Eagleson P (1978) Climate, soil and vegetation 3. A simplified model of soil moisture movement in liquid phase. Water Resour Res 14:722–730
Godt J, Baum R, Chleborad A (2006) Rainfall characteristics for shallow landsliding in Seattle, Washington, USA. Earth Surf Process Landforms 31:97–110
Gritzner M, Marcus W, Aspinall R, Custer S (2001) Assessing landslide potential using GIS, soil wetness modeling and topographic attributes, Payette River, Idaho. Geomorphology 37:149–165
Groisman P, Knight R, Karl T, Easterling D, Sun B, Lawrimore J (2004) Contemporary changes of the hydrological cycle over the contiguous United States: trends derived from in situ observations. J Hydrometeorol 5:64–85
Homer C, Huang C, Yang L, Wylie B, Coan M (2004) Development of a 2001 national landcover database for the United States. Photogr Eng Remote Sensing 70:829–840
Huffman E, MacDonald L, Stednick J (2001) Strength and persistence of fire-induced soil hydrophobicity under ponderosa and lodgepole pine, Colorado Front Range. Hydrol Process 15:2877–2892
Hungr O, Evans SG, Bovis MJ, Hutchinson JN (2001) A review of the classification of landslides of the flow type. Environ Eng Geosci 7(3):221–238
Hutchinson J (1988) Morphological and geotechnical parameters of landslides in relation to geology and hydrogeology. In: Proceedings of the 5th international symposium on landslides, Lausanne, vol 1, Balkema, Rotterdam, pp 3–35
IPCC, AR4 (2007) Climate change 2007. In: Solomon S, Qin D, Manning M (eds) The physical science basis. Contribution of working group I to the fourth assessment report of the intergovernmental panel on climate change. IPCC, Geneva
Iverson R (1997) The physics of debris flows. Rev Geophys 35:245–296
Jibson R, Harp E, Michael J (1998) A method for producing digital probabilistic seismic landslide hazard maps: an example from the Los Angeles, California area, open file rep. US Geological Survey, Denver, CO, pp 98–113

Karl T, Trenberth K (2003) Modern global climate change. Science 302:1719–1723
Karoly D, Stott P (2006) Anthropogenic warming of central England temperature. Atmos Sci Lett 7:81–85
Kharin V, Zwiers F (2005) Estimating extremes in transient climate change simulations. J Climate 18:1156–1173
Kraebel C (1934) The La Crescenta flood. Am For 40(251–254):286–287
Larsen M, Simon A (1993) A rainfall intensity-duration threshold for landslides in a humid-tropical environment. Geogr Anal A 75:13–23
Lawrence D, Slater A (2008) Incorporating organic soil into a global climate model. Climate Dynam 30:145–160
Letts M, Roulet N, Comer N, Skarupa M, Verseghy D (2000) Parametrization of Pearland hydraulic properties for the Canadian land surface scheme. Atmos Ocean 38:141–160
Liu B, Nearing M, Shi P, Jia Z (2001) Slope length effects on soil loss for steep slopes. In: Stott D, Mohtar R, Steinhardt G (eds) Sustaining the global farm. pp 784–788. http://topsoil.nserl.purdue.edu/nserlweb-old/isco99/pdf/ISCOdisc/tableofcontents.htm
McCarthy JJ, Canziani OF, Leary NA, Dokken DJ, White KS (2001) Climate change. In: McCarthy JJ et al (eds) Impacts, adaptation, and vulnerability. Cambridge University Press, Cambridge, MA, p 1032
Meehl J, Tebaldi C (2004) More intense, more frequent and longer lasting heat waves in the 21st century. Science 305:994–997
Meyer G, Pierce J (2003) Climatic controls on fire-induced sediment pulses in Yellowstone National Park and Central Idaho: a long-term perspective. For Ecol Manage 178:89–104
Moody J, Martin D (2001) Initial hydrologic and geomorphic response following a wildfire in the Colorado Front Range. Earth Surf Process Landf 26:1049–1070
Nakicenovic N, Swart R (eds) (2000) Special report on emissions scenarios (SRES). Cambridge University Press, New York, 612pp
NRC (2002) Inevitable surprise. Abrupt climate change. National Academy Press, Washington, DC
Potter C, Randerson J, Field C, Matson P, Vitousek P, Mooney H, Klooster S (1993) Terrestrial ecosystem production: a process model based on global satellite and surface data. Global Biogeochem Cycles 7:811–841
Ren D (2001) Scaling issues in the calculation of surface latent and sensible heat fluxes at Blue River Basin using SHEELS model. M.S. thesis, University of Oklahoma, Norman, OK, p 236
Ren D, Xue M (2004) An improved force-restore model for land-surface modeling. J Appl Meteorol 43:1768–1782
Ren D, Leslie LM, Karoly DJ (2008) Landslide risk analysis using a new constitutive relationship for granular flow. Earth Interact 12:1–16
Ren D, Wang J, Fu R, Karoly D, Hong Y, Leslie LM, Fu C, Huang G (2009) Mudslide caused ecosystem degradation following Wenchuan earthquake 2008. Geophys Res Lett 36, L05401. doi:10.1029/2008GL036702
Ren D, Fu R, Leslie LM, Dickinson R, Xin X (2010) A storm-triggered landslide monitoring and prediction system: formulation and case study. Earth Interact 14:12. doi:10.1175/2010EI337.1
Reneau S, Dietrich W (1987) The importance of hollows in debris flow studies; examples from Marin County, California. Geol Soc Am Rev Eng Geol 7:165–180
Richards LA (1931) Capillary conduction of liquids through porous mediums. Physics 1:318–333
Semenov V, Bengtsson L (2002) Secular trends in daily precipitation characteristic greenhouse gas simulation with a coupled AOGCM. Climate Dynam 19:123–140
Sidle R (1992) A theoretical model of the effects of timber harvesting on slope stability. Water Resour Res 28:1897–1910
Smith R, Smettem K, Broadbridge P, Woolhiser D (2002) Water resources monograph, 15. Infiltration theory for hydrologic applications. American Geophysical Union, Washington, DC
Wagner R, Nelson R (1961) Soil survey of the San Mateo Area, California. USDA, soil conservation service, series 1954, no. 13. USDA, Soil Conservation Service

Wells W (1981) Some effects of brushfires on erosion processes in coastal southern California. In: Davies T, Pearce A (eds) Erosion and sediment transport in pacific rim steeplands. International Association of Hydrological Sciences, Washington, DC, pp 305–342

Wilford D, Sakals M, Innes J, Sidle R (2005) Fans with forests: contemporary hydrogeomorphic processes on fans with forests in west central British Columbia, Canada. Geol Soc Lond (Spec Publ) 251:25–40

Wilson R (2000) Climatic variations in rainfall thresholds for debris-flow activity. In: Claps P, Wieczorek GW (eds) Proceedings of first Plinius conference on Mediterranean storms, Mareta, Italy, 14–16 Oct 1999. European Geophysical Union, Munich, pp 415–442

WMO (2002) WMO statement on the status of the global climate in 2002. World Meteorological Organisation Press Release, 17 Dec 2002. http://www.wmo.ch/web/Press/Press684.pdf

Works Bureau (1998) Information paper on slope safety, provisional Legco panel on planning lands and works. Hong Kong Legislative Council, Hong Kong

Zhang X, Kondragunta S (2006) Estimating forest biomass in the USA using generalized allometric models and MODIS land products. Geophys Res Lett 33, L09402. doi:10.1029/2006GL025879

Zhu J, Dabney S, Flanagan D (2001) Updating slope topography during erosion simulations with the water erosion prediction project. In: Stott D, Mohtar R, Steinhardt G (eds) Sustaining the global farm. pp 882–887. http://topsoil.nserl.purdue.edu/nserlweb-old/isco99/pdf/ISCOdisc/tableofcontents.htm

Chapter 10
Opportunity and Challenges in the Remote Sensing Era

In the remote sensing era, many opportunities exist that can potentially improve storm-triggered landslides studies (e.g., Ekstrom and Stark 2013). For example, for remote locations such as Alaska, the precipitation on snow packs adding to the melt-thaw cycle and many summer season landslides previous less well known because of the uninhabitated nature of the regions. In the tropical region, infrared and visible imageries make the track and intensity forecasting for tropical cyclones more accurate and the readiness in its flash floods and landslides warning. Increased using of realistic, full physics numerical weather prediction models, with the adding of remote sensing precipitation such as the NASA/TRMM, makes more and more feasible for quantitative precipitation forecasts (QPFs), the ability for numerical to be able to forecast the probabilities of extreme weather and heavy precipitation at specific times and locations, which has apparent geo-hazard consequences.

Historically, understanding of natural (large scale catagraphic) landslide dynamics are hindered by the lack of direct observations of the entire life cycle, due to the fact that landslide are rear events and some of the catagraphic ones occurred in remote areas. Remote sensing techniques provide the possibility of real-time detection of such events. Noticeably the Interferometric Synthetic-aperture Radar (InSAR) measurements. There are many providers of such data: see Jezek (2008) for Radarsat-1 of Canadian Space Agency; Rignot et al. (2011) for European Space Agency Earth Remote Sensing satellites ERS-1/2; and NASA's Making Earth Science Data Records for Use in Research Environments (MEaSUREs) for the Japanese Space Agency phased array l-band synthetic aperture radar palsar satellite. InSAR measurements can provide geometric constraints for the model simulated scars. With inverse modeling technique (e.g., adjoint based parameter retrieval), sensitive model parameters can be identified and improved. If the scarp geometry and the mass runout trajectory (both have direct remote sensing observations) are both simulated realistically, chances are that the landslide duration, momentum and potential energy loss are estimate realistically. The potential destructivity can then be estimated close to reality. In addition to this slope scale applications, remote sensing can also provide a diagnosis of the larger landslide

© Springer International Publishing Switzerland 2015

D. Ren, *Storm-triggered Landslides in Warmer Climates*,
DOI 10.1007/978-3-319-08518-0_10

environment. Following is a usage of gravity measurement satellites to evaluate the larger scale environments for landslide risks.

The Gravity Recovery And Climate Experiment (GRACE, Ivins and James 2005; Tapley et al. 2004) measurements (2003–present) over the peri-Himalayan shows systematic and 1,000 km spatial scale consistent signals of mass loss (blue color in Fig. 8.6a) and mass gain (red color shades in Fig. 8.6a). First, the significant mass loss from the Himalayan region is from the increased ice mass loss (may resulted from climate change). This melt water goes primarily to the rivers and discharged to the Indian and Pacific Oceans within a month (the general turnover time for those rivers are generally less than a week). The three surrounding domains all have significant mass losses, much larger than explainable by geological plate movements, which global wise only have a 1 GT magnitude, three orders of magnitudes smaller. Also, in this direction, there should be mass convergence and mass increases for domain 3. There also is no large scale population and animal migrations in the past decade. The only possible cause is in the water/fluids mass changes. Region 3, which is the primary agricultural region of China (crops composes the major vegetation over the region), may exhibit strong seasonal fluctuations in its biomass but annual variations still a good representation of the precipitation amount. Region 2 is arid region, which is clearly shown in the area total biomass (net primary production, NPP in Fig. 8.7). Region 2 has similar total area with Region 3 but the total NPP is two orders of magnitude smaller. Although the total mass in Region 2 significantly increased during the 2003–2012 period, the NPP did not; actually new data just received from MODIS indicate the same small decreasing trend. In Region 4, the precipitation showed a significant decrease during the past decade (2003–2012), in strong discord with the mass increase trend. The precipitation did not increase (actually reduced in region 4) for regions 2 and 4, the increased mass can only be explained by an increased proportion into groundwater reservation rather than into runoff (river flow). This can be a result of increased ground disintegration (crevasses of cracks in bed rocks). The reason is not clear but may also has a natural component after the 2008 Wenchuan earthquake. Whatever the casual factor's for the disintegration of the bedrock over the two domains, we should be on alert for possible subsequent natural hazards that is impending. As we reiterate the previously stated general rule: landslides partially are an upscaling processes. Local slope and geological features enhances its occurrence in a larger area predisposed for its development. The increased fractured bedrock and the accumulated fluids as ground water will work together make future landslides more severe and more frequent. If we look further ahead, the pattern of mass changes creates a saddle structure at the vicinity off region 2. The exerted stress may cause strain buildup and may cause further earthquake (reducing the natural occurrence period) and this composes a positive feedback to secondary geo-hazards.

Another example application of remote sensing is with landslide effects on the benthic ecosystems. Sediments generated by debris flows can have widespread impacts on aquatic environments and benthic ecosystems. In principle, all aquatic organisms are sensitive to granular particle concentration (particle stress, load

concentration, or particle pressure), especially corals, sea grasses, algae, and many filter feeders (e.g., sponges). Once intensity of pressure is high enough to cause sea grass fatality, sea turtles that feed on sea grass also are threatened. Generally, intensity of pressure, durations of exposure to these pressure intensities, and, more importantly, the frequency of exposure are key factors to evaluate ecosystem consequences. Apparently, an accurate dynamic core of landslide model helps answering these key questions. Future research need to focus on indicator species from each group selected on the basis that they cover the biogeographic range, are ecologically relevant and likely to span the range of responses that might be expected of each group of aquatic organisms (i.e., including both sensitive and resilient species). Relationships need to be established that allow pressure thresholds (particle concentration) associated with critical responses such as sublethal stress, recoverable impact, and mortality to be determined.

Although SEGMENT-Landslide has the ability to handling multiple rheology, it is not recommended to run the domain including rivers or ocean basins because simulating complicated ocean currents or river flow is not the emphasis of it. For evaluating the likely extent, severity, and persistence of ecosystem consequences associated with storm-triggered landslides/debris flows, or effectively and efficiently monitoring and managing environmental impacts, landslide models are required to provide the sediment source volume (the sliding material volume being dumped into waters), ingredients and source characteristics such as particle size distribution, density and mechanical properties such as drag coefficients against water. The following dispersion of the "flume" in turbulent water is handled by the same deposition/sedimentation scheme as in SEGMENT-Landslide, but applied to very low concentration of granular particles and turbulent ambient water flow. When sediments are transported through complex canopies such as corals and sea grass, the setting and resuspension also are sensitive to bottom bathymetric hydrodynamic conditions, primarily through the relevance to vertical diffusion coefficient. As remarked, the existing sediment transport schemes on settlement and resuspension still need significant improvement to be useful for predicting the fate of landslide generated sediments, applicable to a range of habitat types. Collecting validation data is a vital stage for model validation and optimization. MODIS data on water clarity (http://modis.gsfc.nasa.gov/) would be a useful source, albeit more robust schemes are still needed to decipher MODIS into particle size spectrum and concentration, to further improve the fidelity of sediment transport model. At present, it is possible to generate near-daily (excluding data contaminations from bad weather) total suspension sediment and light attenuation data suitable for validating plume models. Landsat Thematic Mapper (TM) and Enhanced TM data (ETM) are even more sensitive to cloud cover but are of better spatial resolution (Chipman et al. 2004). The historical data of Landsat are still valuable for dispersion model validation.

In order to make scientifically sound predictions of the likely extent, severity and persistence of marine environmental impacts associated with landslides, it is ideal to run the observational study for detecting species resilience synchronously with the MODIS measurements for suspension sediment for model validation.

Considering that the storm-triggered landslides associated with hurricanes (TCs) and cloudbursts nested in the monsoonal depressions occurring at locations close to oceans, establishing quantitative relationships between sediment concentration and the response from indicator species serve the overarching objectives of landslide hazard mitigation. At this stage, the information of landslide occurrence will be translated into tools and protocols to be used in real-world applications (e.g., for dredging sites design).

Thus, landslides hold a unique nexus location in the geomorphology research (joints the tectonic-climate-topography-erosion-river incision interlinks), unifying several disciplines on subjects ranging on many different spatial and temporal scales. Because complicated landforms are the products of deep Earth processes involving mantle convection and plumes producing plate tectonics, orogeny and epeirogeny, as well as the surficial processes of soil formation, denudation, and sedimentation, influenced by seismicity, climate change, and land cover change, with a recent (on geological scale) significant role for human agency. In addition, processes and rates of change vary with spatial and temporal scale in an interconnected hierarchy. As a result, the land surface become so complicated that there is no simple way to scaling up—processes that operate at small spatial scale will not provide either an adequate description or understanding of landforms at larger spatial scales. To handle the stability of slopes, only the full physics numerical model (e.g., SEGMENT-Landslide, a surface transport type of model in geomorphology term) is not adequate. Knowledge of the slope material (and its large enough neighboring region) properties is a prerequisite. The remote sensing era can assist in providing precipitation information, a component that is more volatile and also may be sensitive to climate change. The vegetation cover also affects slope stability (Chap. 5). Remote sensing products, such as MODIS, can also provide land cover information that can be assimilated by numerical model to improve the model skill in simulation as well as projection.

In summary, landslides are characterized by relatively small spatial and temporal scales of occurrence and hence the vulnerability of communities exposed to these events. Because the elements at risks are highly dispersed, the management of the storm-triggered landslides by means of structural measures (e.g., permanent infrastructure establishments) is difficult and often unsustainable in environmental or economic terms. Hence, forecasting, warning and emergency management are, by their nature, more suitable to cope with such risks. During landslides, the time available for communication is very limited and typically there is no time for learning as the landslide develops. The preparedness strategies should account for the multiple aspects that are associated with debris flows and landslides, taking advantage of improvements in landslide forecasting and warning and adapt to the large uncertainties affecting these forecasts. It is foreseeable that implementing emerging techniques for strom-triggered landslide enhance prediction and estimation of impacts in poorly gauges areas. The following research directions are worthwhile: (1) Use of remote sensing, real-time modeling and in-situ measurements to estimate soil moisture at the onset on an event; (2) Use of weather radar, lightning, satellite and storm tracking monitoring for rainfall estimation and now

casting during storm-triggered landslides; (3) Use of near real-time monitoring techniques (like GPS, mobile phone geo-positioning or online peer-to-peer communications technology) and quick response survey for inferring space-time patterns of human exposure, vulnerability and adaptive capacity; (4) Identifying the atmospheric and hydrologic controls on storm-triggered landslides, analyzing dominant processes transition with precipitation severity, threshold values and their relation to catchment characteristics; and (5) Geomorphological processes and sediment dynamics during such landslide events.

References

Chipman J, Lillesand T, Schmaltz J, Leale J, Nordheim M (2004) Mapping lake water clarity with Landsat images in Wisconsin, USA. Can J Rem Sens 30(1):1–7

Ekstrom G, Stark C (2013) Simple scaling of catastrophic landslide dynamics. Science 339:1416–1419

Ivins E, James T (2005) Antarctic glacial isostatic adjustment: a new assessment. Antarct Sci 17:541–553

Jezek K (2008) The RADARSAT-1 Antarctic Mapping Project. BPRC report no 22. Byrd Polar Research Center, The Ohio State University, Columbus, OH, p 64

Rignot E, Mouginot J, Scheuchl B (2011) Ice flow of the Antarctic ice sheet. Science 333:1427–1430

Tapley B, Bettadpur S, Ries J, Thompson P, Watkins M (2004) GRACE measurements of mass variability in the Earth system. Science 305:503–505

Chapter 11
The Path Forward: Landslides in a Future Climate

Natural hazards are an ever-present threat to human lives and infrastructure. The need for greater predictive capability has been identified as one of ten Grand Challenges in Earth Sciences (NRC 2008). For example, memories of geo-hazards which have impacted the activities of humans in China extend back several thousand years and represent an important complement to conventional scientific knowledge. While some records have long been captured in written form (or graphs), many in the form of folklore and oral traditions of preliterate cultures that sometimes today remain an important source of information for contemporary disaster risk reduction and climate-change adaptation. The efforts to provide rational explanations of these phenomena and ways of recognizing their precursors are the germane elements in modern efforts of prediction and forecasting based on better physics. In addition, many oral traditions and Chinese sayings incorporate advice about sustaining livelihoods in the face of natural challenges, advice that may be relevant to challenges arising from climate changes. As an effort toward the goal of a reliable landslide mapping and warning system, we present a modeling system that systematically estimates the potential for landslides over a regional area, rather than for a single slope. The process-based modeling system presented here (with SEGMENT-Landslide as a representative) has representation of the relevant physical processes and can be applied in a variety of environments. The promising performance of SEGMENT-Landslide is attributable to the use of a new, fully three-dimensional modeling framework based on a newly proposed granular rheology, and to the use of a land surface scheme that explicitly parameterizes the hydrological characteristics of macro-pores. Quantitative predictions of storm triggered landslides require a numerical modeling system like SEGMENT-Landslide. However, some of the requirements of model, especially the input and verification data, generally are not available even in current geological maps. These parameters include vegetation loading and root distributions in soils and weathered rocks. Applications of SEGMENT-Landslide to other regions are limited primarily by a lack of high-resolution input datasets. The new concepts implemented in SEGMENT-Landslide, if adopted by the relevant community, hopefully will

© Springer International Publishing Switzerland 2015

D. Ren, *Storm-triggered Landslides in Warmer Climates*,
DOI 10.1007/978-3-319-08518-0_11

encourage the collection of such vital information in future surveys. Recent advancements in meteorological forecasts have been particularly important in storm-triggered landslides situations. For example, estimates of total fallen precipitation, i.e., Quantitative Precipitation Estimates (QPEs), have improved because of the combination of spatially distributed radar data with accurate point measurements from rain gauges (Seo et al. 1999). In addition, estimates of immediate future precipitation, i.e., Quantitative Precipitation Forecasts (QPFs), have improved (especially at short lead times) because of increased ability of advanced numerical weather prediction models (NWPs) to assimilate remote sensing from radar, satellites, as well as gauged rainfall observations (e.g., Smith and Austin 2000) and to quantify uncertainties through ensemble predictions (e.g., Collier 2007). Improvements in landslide model's hydrologic submodel component to utilize these new hydrometeorological products are needed to further improve landslide model prediction skill.

There is a considerable and expanding body of opinion that suggests that the Earth may suffer marked temperature increases over the next 50–100 years (Rind 1984) due to heat retention by the atmosphere caused by increased levels of the greenhouse gases CO_2, CH_4, and oxides of nitrogen. These levels in the atmosphere have increased quite dramatically in the last 70 years and are expected to continue to rise. One consequence is an intensified hydrological cycle. Estimates of the effects vary widely but all predict some increase in storm-triggered landslides. The anticipated future climate warming has a significant influence on the occurrence of landslides caused by elevated water content in the ground. Changes in precipitation morphology are highly relevant for storm-triggered landslides and subsequent desertification, because the root system of vegetation has adapted to the current precipitation climatology and likely is not prepared for human-induced changes in climate. Under the current relatively stable astronomical boundary conditions there are natural "rhythms," whereas human induced changes are likely to produce a transition significantly in one direction, leading to a climate state not previously experienced by the existing terrestrial ecosystem. Microclimatic variations associated with slopes allow stands of an ecosystem type to exist far beyond their major zones of distribution (Chapin et al. 2002). These outliers act as important colonizing individuals during times of rapid climate change. Destroying these outlier species (the transitional belts on Holdridge's chart) by landslide burial accompanying extreme precipitation may slow down ecosystem migration in accord with climate change. Landslides are localized events. Advanced dynamical models with physical basis should be used as there is a need for prediction, rather than simply documenting the occurrence of landslides. SEGMENT-Landslide is an effort in this direction. Because there are biogeochemical submodels coupled in the SEGMENT-Landslide system, it also is a tool for investigating the environmental consequences of landslides, including deforestation and an associated decrease in productivity. The landslide environmental intelligence starts from data (information). Geological monitoring is primarily about strain deformation (relative movements between a set of locations) whereas the yielding/fracturing criteria is built on

the disparity in principal stress. A modeling approach such as SEGMENT-Landslides is needed to bridge the gap.

The occurrence of landslides as natural hazards and climate change are inevitable and unavoidable but their destructive financial and societal impacts can be reduced and/or eliminated by deploying "landslide mitigation and climate adaptation" strategies in the general form of international landslide intelligence system (Fig. 11.1). An advanced landslide model such as SEGMENT-Landslide is the core of such intelligence system. Support systems and tools must be better incorporated into preparedness paradigms at multiple scales: community, regions, nations and international collaborations. As remarked, landslides affect almost all mountain regions. However, different nations have different resilience. For example, eastern Australia also suffers landslides. Its limited population makes it possible to avoid all unstable regions. For most developing countries, it is impossible to take similar measures of avoiding unstable slopes as Australia. Actually, the primarily reason for landslides affecting developing countries disproportionately is because Human activities account for many of them. The construction of highways, hillside housing developments, dams, reservoirs, drainage and utility structures normally involve the movement of substantial amounts of soil and rock on slopes. If the operation involves addition of material to the top of slope or the removal of soil or rock from its base, then the slope is nudged toward failure. In the extreme cases, landslides take place immediately following or even during the construction process, but usually the effects tempers rather slowly and can be rather subtle in many circumstances. For example, the placement of fill material for a road across a hillside, may not, through its own weight, cause the hillside to fail, but may interfere with the natural regime of water flow and percolation through the soil or rock. Then the water pressure, as a horizontal stress component, increases in the rock interstices and can give rise to a slide one rainy season years after the construction. Similarly, when a dam is built across a valley and water impounded behind the dam to form a reservoir, slope failures along the valley sides can develop, caused by the saturation and consequent weakening of the material at the base of the slope, or by the wave erosion of the toe of the slopes if they are not protected. Material can be removed in this way in minor amounts until a large portion of the valley slope becomes unstable. The recharge and discharge of water in the reservoir also may cause repeated fatigue of the neighboring slopes, through perturbations on hydrostatic pressure and the fact that dynamic shear strength is smaller than the static value (Sect. 5.4). The presence of the man made "lake" also interfere with the hydrologic regime of rainfall, absorption and runoff (Fig. 11.1).

The biblical story of Noah and the Ark recounts an attempt to do something constructive about surviving in the face of impending disaster. Modern approaches of living with landslides are to undertake either corrective or preventative measures. All available measures, however, are essentially based on reducing surface runoff and/or conservation of soils. For example, engineering works endeavor to flatten a slope and improve the drainage are efforts on local scale helping stabilize a slope. On watershed scale, in addition to reduce watershed soil loss, the various measures minimize sand and silt movement and deposition in the downstream

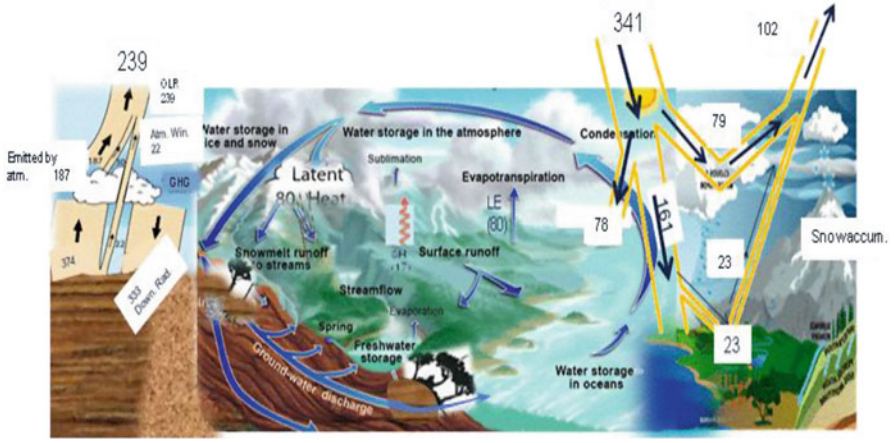

Fig. 11.1 Putting landslide intelligence system into the global hydrological and energy cycles. *Left portion* of this illustration is the long wave radiation budgets, *right portion* is the shortwave radiation budgets (solar radiation input is 341 W/m^2). At top of atmosphere, there is a general balance between the net incoming (solar radiation) and net outgoing (shortwave plus long wave radiations, or $239 + 102 = 341$) radiations. SH means sensible heat flux and LE means latent heat flux from surface. This is the global mean climate (long time mean) state. For both long wave and shortwave components, there are general poleward gradients and land surface heterogeneity caused disturbances. The longitudinal gradients of outgoing long wave radiation (OLR) is weaker than other components because there are poleward energy transport by atmospheric/oceanic circulation (general circulation). The general circulation is driven by the uneven geographical distribution of the radiative energy components and is an integral component of the global climate system. Central portion illustrates the global hydrological cycle. Evaporation from the Earth's surfaces adds water vapor into the atmosphere. As air cools, the water vapor in the air condenses to form cloud droplets. Eventually some of the moisture falls out of the clouds as precipitation. There are additional factors in the water cycle such as the transfer of water from plants directly into the air (transpiration), and the percolation of water downward through the soil. Some water is also stored temporarily in the tissues of living things, and for longer periods of time in underground reservoirs called aquifers. Some of the water that does not percolate into the soil flows along the surface to form streams, but some of that water also evaporates into the air. The (radiative) energy cycle and hydrological cycle is closely coupled, through land surface fluxes (LE and SH). Not shown but equally critical is the global atmospheric and oceanic circulations, which affects the spatial feature of the energy and water balances. Circulation-caused convective processes and the latent heat release warm the atmosphere and compose an important component of the outgoing long wave radiation from atmosphere. Landslide, just as wildfires, flashfloods, and windthrows, is a form of ecosystem disturbance. Partly adapted from USGS Web site. To investigate this form of ecosystem disturbance systematically, however, advanced modeling approach need to take all these components into consideration. In such a system, an atmospheric model is required to simulate the cyclic rain maker systems; a landslide modeling system to estimate aspects of landslides; and an ecosystem model to estimate the disturbances to the ecosystem. Because the critical role played by soil moisture, land surface submodels are required by all

channels and other structures help improve their (creeks) capacity to carry floods and avoid pore pressure buildup. The preventative measures involve planning for future developments of society, if we have to live with damaging landslides. International communities should realize that disaster prevention is better than

aftermath aid and reconstruction. Within a country, landslide mitigation and climate adaptation intelligence helps better mobilize the catastrophic risk management insurance resources to protect vulnerable community. The landslide mitigation and climate adaptation intelligence also is valuable for health and environmental security. Landslides in a warming climate have larger destabilizing impacts on national economy. The intelligence system provides guidelines for better plans and responses to those impacts. Economic benefits and apparent bankability of the intelligence system's services and products should revive interests in areas such as transportation, energy, health and emergency management. There are gaps to bridge because investors and scholars may not agree on what is bankable information. Some returns on interest for environmental associated savings are not so apparent for potential private/public partners. This review, placing landslides in the wider perspective of a disaster mitigation intelligence system, aims to facilitate synergies for moving the proposed collaborative initiative forward.

What likely lies ahead for storm-triggered landslides? A warmer climate, an amplified hydrological cycle, and more wild swings in weather all are expected. Preparing communities to deal with the future will require: critical landslide intelligence; and a society of informed citizens, communities, businesses, and emergency managers who know how to use the intelligence. The need to understand, predict, and manage responses to weather and climate extremes and the subsequent landslides exceeds the scope of any individual organization or government agency. Collaboration among academia, industry, federal agencies, and international communities is vital for successfully securing the proposed landslide ecosystem intelligence needed in the near future. For example, the smaller equatorial countries (e.g., Philippines) are prone to landslides but generally are southern countries with limited research ability and infrastructure. Industrialized countries can lead an initiative that better manage landslide information and develops international collaborations on the global landslide ecosystem intelligence system. This review focuses on the science perspective of the problem. Much effort is still needed to better frame the debate in international political circles about the nature of science—increase awareness of the landslide-ecosystem-under warming climate-intelligence system's role as one of the fuels for the growth engine for global economy. Scientist and managing agencies need to work together to promote dialogue and cooperation and to build an international accord just like the 1991 Rio de Janiero Climate Accord to address the evolving needs of the involved nations. In addition to effort that bridges the gap between science and planning, avoiding "science apart," the proposed intelligence system should have a physically based dynamic core. Successful projections of near future major landslide events from the dynamic core boost confidence and catalysts international collaborations. The road ahead is paved with uncertainty, under a future warming climate. Observation systems, research, and high performance computing are absolute prerequisites for producing reliable landslide projections.

Updating runs of the dynamic landslide system is necessary with improved scientific knowledge, better and extended geological databases, updated vegetation and land use datasets, and improved perceptions of future climate. Running the

landslide system efficiently and quickly is certainly a goal, however should not be achieved at the sacrifice of scientific strictness and loyalty to nature. Dynamic landslide model is always the scientific underpinning of the landslide intelligence system. With timely rerunning of the dynamic landslide model, the intelligence system provides services that are always up-to-date and is self-improving as science changes.

An operational landslides network may contain the following components:

11.1 Hydrometeorological Monitoring Networks

As landslide forecasting is data-intensive and highly dependent upon the timely processing of a variety of information before landslide events. Some types of data are available in real time through the internet and satellite downlinks. Most types of data, however, are region specific and are communicated using regional infrastructure. Since storms that cause landslides also tend to generate flashfloods. The two phenomena should be attended together, especially the weather radar networks and the satellite networks can and should be shared.

A primary function of a weather radar network is to provide high-resolution, real-time gridded rainfall estimation over a region of interest. Weather radars are powerful tools for hydrometeorological monitoring and forecasting (for example, being assimilated by weather models to better initialization), with the advantage of being able to characterize precipitation over a large area as oppose to the point measurement of an in situ gauge. Archival rada data also are precious in verifying QPF capability of weather models. Since landslides tend to occur in regions prone to intense rainfall, to avoid aliasing (artificial lowering of radar signal), polarimetric radars are preferred.

The mission of meteorological satellite is generally twofold: collection of observational data such as infrared and visible imagery, and dissemination of this data and other products that are uplinked from the meteorological service that controls the satellite. Additionally, these satellites perform a communications role in relaying data from various Data Collection Platforms (DCPs) such as stream flow and rain gauges. In many regions without sufficient radar coverage, satellite data are the primary means for making precipitation estimates. Several different satellite instruments are used in the process. Infrared sensors are probably the most familiar, with broad and consistent coverage from geostationary satellites. However, when clouds are present, infrared sensors observe only the temperature of the cloud tops. In contrast, passive microwave sensors on polar orbiting satellites observe emissions from water and ice within clouds to produce more reliable quantitative precipitation estimates, but they do so with less frequency. Finally, space-based active microwave (or radar) sensors have a role in the overall precipitation monitoring mission, producing the highest accuracy in both horizontal and vertical directions. Combining polar-orbiting microwave data and geostationary visible and infrared data provides opportunities to maximize the advantages of each

system. Each polar-orbiting satellite sensor views a location on the earth once every 12 h. However, multiple satellites currently operated jointly by the USA and Europe can provide passive microwave rain rate products for any given location every 3–4 h on average. Data from geostationary satellites arrives every half hour or even more often (~1 TB data per satellite per day data volume). Lacking microwave sensors, geostationary satellites can provide timely storm locations, but cannot produce reliable rain rates. Thus, researchers have developed synergistic precipitation products that combine the accuracy of the microwave rain rates with the temporal advantages of geostationary data. These high resolution products have been developed with an eye toward numerical modeling data assimilation, validation, and climate research. They are also promising with operational weather forecasting. For example, the previous mentioned TRMM multi-satellite precipitation analysis (TMPA) combines microwave estimates of precipitation with geostationary satellite infrared estimates. Microwave rain rates are used to "calibrate" the GOES estimates. The NOAA CPC Morphing Technique product is constructed entirely from passive microwave precipitation estimates. At times when polar-satellite microwave data are unavailable, the CPC Morphing Technique propagates the microwave estimates in the time gaps using trends observed in geostationary infrared data. This propagation is referred to as "morphing." To compute estimates using the Naval Research Laboratory Blended technique (NRL-Blended), passive microwave data from polar-orbiting satellites and TRMM radar data are used to calibrate the geostationary infrared data where the microwave and infrared data overlap. This information is retained and used to produce rain rates for continuing calibration of newly received geostationary satellite data. The NOAA/NESDIS (National Environmental Satellite, Data, and Information Service) Self-Calibrating Multivariate Precipitation Retrieval (SCaMPR) algorithm is yet another rain rate estimation technique that calibrates predictors from GOES data to rainfall rates from microwave instruments. The goal is to produce estimates at the frequency of GOES data but with an accuracy that is closer to that of the intermittently available microwave rainfall rates. SCaMPR is at present an experimental algorithm that is run in real time by the Center for Satellite Applications and Research (STAR), but very promising in natural hazard monitoring.

While the description of preprocessing of satellite data is beyond the scope of this book, it is important to remember that processing equipment needs to generate real-time, continental estimates of rainfall from satellite data for operational use. For example, the NOAA/NESDIS Center for Satellite Applications' Hydro-Estimator algorithm has automatically produced operational real-time rainfall estimates since 2002 from GOES-11 and -12 Imager band 4 (IR window) data. The final products are digital fields of instantaneous rainfall rate every 15 min. This would give a very good starting point for running the NWP model to produce reliable precipitation scenarios to drive landslide submodel.

The previous chapters make clear that forecasting landslides can be technology-intensive. This section summarizes the infrastructural requirements for implementing and operating a landslide early warning system. Since information technology is constantly changing, no attempts here are made to discuss specific

technology; instead, this section describe basic system capacities essential to predict storm-triggered landslide.

To ensure data availability and proceeding capability at all times, significant maintenance and proper redundancy. Under optimal conditions, all forecast centers would use the same hardware, operating systems, and applications. That way, development, maintenance, troubleshooting, and operations could be standardized, which saves resources.

This mainly concerns with creating and disseminating text and graphic products to customers and communication with peer forecast centers, in a timely fashion.

Alternate communication paths for data collection and also for product dissemination are needed by each center in the event of the failure of one of a center's primary communication links. Similarly, a center should not rely on a single source of input data, but utilize redundant networks. Then if their primary earth data network is unavailable, either through equipment failure or communications problems, the center still function using alternate networks. Finally, a well coordinated and support maintenance program is critical to the success of a forecast center.

11.2 Landslide Forecasting Subsystem Options

Storm-triggered landslides represent forecast and detection challenges because they are not always caused simply by meteorological phenomena, which is already very complicated. Storm-triggered landslides result when specific meteorological, hydrological and geological conditions coexist. Although heavy rainfall is usually a factor, a given amount and duration of rainfall may or may not result in a debris flow, depending on the hydrologic characteristics of the watershed where the rain is occurring and the geological conditions, as noted in Chap. 4. Magnitude, efficiency, and direction of runoff; antecedent slope conditions; precipitation intensity and duration; storm location, movement and evolution with respect to the slope; soil type, soil depth and antecedent soil moisture conditions; amount and type of vegetation covering the soil slope; land use characteristics including urbanization and deforestation; and the general topography and slope all bearing influence on the occurrence of landslides. While centers have options of choosing I.D., 2D stability model and full physics, distributed 3D models, it is recommended that landslide dynamic core implemented as distributed forecast models in the framework of a global landslide forecast system (GLFS). Landslide submodels with different complexity represent different rainfall-to-runoff relationship: the rainfall needed to produce a debris flow, given antecedent moisture conditions and other factors such as local terrain, land use, soil conditions, and vegetation characteristics.

Although it is true that at the present time even with the most robust of forecasting schemes employing dense radar coverage, satellite algorithms, high resolution computer models of atmospheric processes, and distributed landslide model, it is still beyond the state of science to accurately forecast with effective lead time where landslides occur from convective storms, improvements in QPE

certainty from advanced weather models and use of distributed landslide models are promising in further improving forecasting skills. Thus, the primary objective of a storm-triggered landslide system is to provide sufficient warning lead time and accuracy for users and emergency managers to take appropriate actions to mitigate loss of life, property and commerce. If observed hydrometeorological data are the sole basis for generating warnings then lead times may be so short that the forecast is of little value to user, because it also takes time to disseminate the warning to the users. By coupling meteorological forecasts with 3D landslide models, landslide forecasts can be extended hours or days into the future in the form of watches rather than warnings. This coupling of prediction models extends the lead time for users but also further increases the uncertainty in the forecast. Efforts in improving the landslide component submodel in its parameterization of hydrologic processes and mechanics, are correct direction for further reducing errors in forecasting accuracy. Storm-triggered landslides are hydrometeorological and geological phenomena. Given the importance of meteorological data and forecasts to the production of landslide forecasts, close collaborations among multidiscipline are necessary.

Society development is well into a new era, in which natural hazards, particularly weather and climate related hazards, are causing more damage than in the past (e.g., Kunreuther and Michel-Kerjan 2009; Pielke Jr. 2010). In recent years, society has faced a steep increase in economic and insured losses from weather and climate related hazards in general and flashfloods and debris flows in specific, likely due to significant increases in exposure (Hoppe and Pielke 2006). Projections of a continuing trend towards more intense systems (see Bender et al. 2010; Knutson et al. 2010 for the case of tropical cyclone) point to a possible further increase in societal vulnerability unless adequate planning and adaptation measures are implemented. More accurate information on high-impact events is thus a critical need for society.

This requires assessments of the statistics of high-impact events with regional clarity and on how they may change under climate variability and change together with estimates of associated uncertainties. This book focus on the dynamical process modeling of storm-triggered landslides. However, meeting these societal demands requires also a combination of dynamical and statistical components. The key component in understanding future risk in flashfloods and storm-triggered landslides resides with the understanding of extreme precipitation events (extreme events henceforth). The dynamical downscaling approach (in understanding extreme events) combines the capacity of regional high resolution model (e.g., regional atmospheric models and mesoscale models) to simulate weather events with the capacity of global coarse resolution model (e.g., GCMs) to simulate climate and large scale weather. To perform this downscaling, high-resolution regional model is embedded within the global mesh over regions of interest (e.g., Laprise et al. 2008).

It also is important to recognize that there are several types of dynamic downscaling as reported in Castro et al. (2005). Pielke and Wilby summarize them as follows. Type 1 downscaling is used for short-term, numerical weather prediction. In dynamic type 1 downscaling the regional model includes initial conditions from

observations. The regression relationships are developed from observed data and the type 1 type dynamic model predictions. Type 2 dynamic downscaling refers to regional weather (or climate) simulations (e.g., Feser et al. 2011) in which the regional model's initial atmospheric conditions are forgotten (i.e., the predictions do not depend on the specific initial conditions) but results still dependent on the lateral boundary conditions from a global numerical weather prediction where initial observed atmospheric conditions are not yet forgotten or are from a global reanalysis. Type 2 statistical downscaling uses the regression relationships developed for type 1 statistical downscaling except that the input variables are from the type 2 weather (or climate) simulation. Downscaling from reanalysis products (type 2 downscaling) defines the maximum forecast skill that is achievable with type 3 and type 4 downscaling.

Type 3 dynamic downscaling takes lateral boundary conditions from a global model prediction forced by specified realworld surface boundary conditions such as seasonal weather predictions based on observed sea surface temperatures, but the initial observed atmospheric conditions in the global model are forgotten (e.g., Castro et al. 2007). Type 3 statistical downscaling uses the regression relationships developed for type 1 statistical downscaling except using the variables from the global model prediction forced by specified real-world surface boundary conditions.

Type 4 dynamic downscaling takes lateral boundary conditions from an Earth system model in which coupled interactions among the atmosphere, ocean, biosphere, and cryosphere are predicted (e.g., Solomon et al. 2007). Other than terrain, all other components of the climate system are calculated by the model except for human forcings, including greenhouse gas emissions scenarios, which are prescribed. Type 4 dynamic downscaling is widely used to provide policy makers with impacts from climate decades into the future. Note that Type 4 statistical downscaling uses transfer functions developed for the present climate, fed with large scale atmospheric information taken from Earth system models representing future climate conditions. It is assumed that statistical relationships between real-world surface observations and large-scale weather patterns will not change. Type 4 downscaling has practical value but with the very important caveat that it should be used for model sensitivity experiments and not as predictions (e.g., Pielke 2002; Prudhomme et al. 2010).

The increase in computational capacity has enabled such simulations in unprecedented detail (Bender et al. 2010). For example, regional high resolution models can provide tractable weather systems on decadal time scales, physical insights into the variability, physical response of weather systems to climate variability and change. There remains, however, while for short term weather prediction this approach has shown prediction skill, a lack of demonstration of model skill at predicting changes in climate statistics on longer time periods. Thus, regional high resolutions can simulate weather systems on decadal and longer time scales, and provide physical insights into the variability, physical response of weather systems to climate variability and change, but we cannot assume they accurately represent what will occur in the future. Also, despite these accomplishments in downscaling,

finite (limited) computational resources and overwhelming data volumes require considerations of the appropriate balance between sufficient detail to resolve the relevant physical processes (extreme precipitations can be from mesoscale systems such as TCs as well as due to large scale weather features and planetary scale MJOs). There also needs to be a sufficiently long simulation to adequately sample the climatology and, most importantly, any changes in climate statistics over time, and sufficient ensemble size to sample associated model uncertainty. This, of course, often results in a truncation of the full distribution spectrum of the real world extreme precipitation. Even if regional models could capture the full distribution of the extreme events, then it still be necessary to treat error in location, occurrence frequency, and errors in physical parameterizations (parameterized physical mechanisms), as well as demonstrate that they actually have any skill on these longer time scales.

Realizing the limitations of the dynamical approach, a variety statistical approaches have been explored. Uses of empirical relationships between weather systems and the large scale environment have been successful in determining the weather system climate from climate model data (e.g., identifying blocking and cut-off systems from GCM output, identifying TC genesis and compose genesis potential indices), but only on short term weather scale. Statistical methods have also been used to post-process errors in frequency distributions of weather events from dynamical models (Katz 2010). These two statistical approaches can add value to the dynamical approach, if the parent global model has skill when compared with real world observations. Application of them in flashfloods and debris flows are limited on the one hand to the assumption of stationary in the statistical relationships. On the other hand, the geological and geographical parameters and land cover/land use changes defy simplified approaches.

Precisely because of the same reason that make statistical approaches difficult to apply to landslide research, projection of the future change in storm-triggered landslides are more demanding than estimating only future changes in weather extremes; a skill that has not yet been demonstrated. In another word, extreme precipitation is merely one factor among a series of factors such as land use/land cover, potential geological hazards such as earthquakes and eruption of major volcanos. Limiting only to land cover, climate warming may manifest drastically differently at different spatial scales (R. Pielke Sr., 2014, personal communication). It has been proposed to use a bottom-up perspective (i.e., a contextual vulnerability approach) in assessing the risks instead of downscaling for risk assessments (an outcome vulnerability approach) (Pielke Sr. et al. 2012). In terms of assessing the risk from landslides, this is a more inclusive approach to assess the threat from this type of environmental and societal issue.

Based primarily on the active downscaling research, the most recent IPCC report (chap. 7 in AR5 of Working Group I) uses very strong worded language about the increase in extreme precipitation events. We however need to pay a little bit attention that, the current knowledge level of downscaling are still very limited, especially in downscaling multi-decadal climate predictions is at best a kind of model sensitivity study. In certain cases, even the current climatology cannot be

adequately replicated. There still is a long way in predicting changes in regional climate statistics, such as changes in the frequency of extreme weather events (extreme rainfall for one).

Compared with preindustrial stable interglacial climate, future climate would be viewed as composed of natural variability and a trend of anthropogenic origin (greenhouse gases forced climate trend). Actually, the natural variability component is not identical to the preindustrial one. The frequency and amplitude will both be influenced by the warming trend. It is a challenging task to detect and properly attribute each component. Even though globally there are more extreme events, regional manifestation may likely vary. Thus, a contextual vulnerability assessment using the bottom-up, resource-based framework is more inclusive approach for policymakers to adopt effective mitigation and adaptation methodologies to deal with the complexity of the spectrum of social and environmental extreme events that will occur in the coming decades.

References

Bender M, Knutson T, Tuleya R, Sirutis J, Vecchi G, Garner S, Held I (2010) Modeled impact of anthropogenic warming on the frequency of intense Atlantic Hurricanes. Science 22:454–458

Castro CL, Pielke RA Sr, Leoncini G (2005) Dynamical downscaling: assessment of value retained and added using the Regional Atmospheric Modeling System (RAMS). J Geophys Res Atmos 110(D5):D05108, doi:10.1029/2004JD004721. http://pielkeclimatesci.wordpress.com/files/2009/10/r-276.pdf

Castro CL, Pielke RA Sr, Adegoke J, Schubert SD, Pegion PJ (2007) Investigation of the summer climate of the contiguous United States and Mexico using the Regional Atmospheric Modeling System (RAMS): Part II. Model climate variability. J Clim 20(15):3866–3887

Chapin F III, Matson P, Mooney H (2002) Principles of terrestrial ecosystem ecology. Springer, New York

Collier C (2007) Flash flood forecasting: what are the limits of predictability? Q J R Meteorol Soc 133:3–23

Feser F, Rockel B, von Storch H, Winterfeldt J, Zahn M (2011) Regional climate models add value to global model data—a review and selected examples. Bull Am Meteorol Soc 92:1181–1192. doi:10.1175/2011BAMS3061.1

Hoppe P, Pielke R Jr. (eds) (2006) Workshop on climate change and disaster losses: understanding and attributing trends and projections, final workshop report. Hohenkammer, Germany, 25–26 May

Katz R (2010) Statistics of extremes in climate change. Clim Change 100:71–76

Knutson T, McBride J, Chan J, Emanuel K, Holland G, Landsea C, Held I, Kossin J, Srivastava A, Sugi M (2010) Tropical cyclones and climate change. Nat Geogr 3:157–163

Kunreuther H, Michel-Kerjan E (2009) At war with the weather: managing large-scale risks in a new era of catastrophies. MIT Press, New York, p 416

Laprise R, De Elia R, Caya D, Biner S, Lucas-Picher P, Diaconescu E, Leduc M, Alexandru A, Separovic L (2008) Challenging some tenets of regional climate modelling. Meteorol Atmos Phys 100:3–22

NRC (2008) Origin and evolution of earth – research questions for a changing planet. National Academy Press, Washington, DC

Pielke RA Jr. (2010) The climate fix. http://rogerpielkejr.blogspot.com/2010/04/climate-fix.html

Pielke Sr. RA, Wilby R, Niyogi D, Hossain F, Dairaku K, Adegoke J, Kallos G, Seastedt T, Suding K (2012) Dealing with complexity and extreme events using a bottom-up, resource-based vulnerability perspective. Extreme events and natural hazards: the complexity perspective geophysical monograph series 196 © 2012. American Geophysical Union. All rights reserved. 10.1029/2011GM001086. http://pielkeclimatesci.files.wordpress.com/2012/10/r-3651.pdf

Rind D (1984) Global climate in the 21st century. Ambio 13:148–151

Seo D, Breodemnach J, Johnson E (1999) Real-time estimation of mean field bias radar rainfall data. J Hydrol 223:131–147

Smith K, Austin G (2000) Nowcasting precipitation – a proposal for a way forward. J Hydrol 239:34–45

Solomon S, et al. (Eds) (2007) Climate change 2007: the physical science basis. Contribution of Working Group I to the Fourth Assessment Report of the Intergovernmental Panel on Climate Change. Cambridge University Press, Cambridge, UK

Chapter 12
Mathematical Skills Required to Fully Understand SEGMENT-Landslide

12.1 Vector and Tensor Operations

In this book, we suppose the reader has basic vector concept and for the convenience, listed the basic vector operations in the Appendix D. In the following discussion, we stick to the right-hand system. Suppose the unit directional vectors of a Cartesian system is $\hat{e}_1$, $\hat{e}_2$ and $\hat{e}_3$. Position vector $\vec{x}$ (of a granular element), can be decomposed into the $\hat{e}_1$, $\hat{e}_2$ and $\hat{e}_3$ directions, so that $\vec{x} = x_1\hat{e}_1 + x_2\hat{e}_2 + x_3\hat{e}_3$. Now introduce a new Cartesian coordinate system, it is obtained by rotation of the original one. Unit vectors in the rotated system called $\hat{e}'_1$, $\hat{e}'_2$ and $\hat{e}'_3$. Then the same vector can be write in the new (rotated system) as: $\vec{x} = x'_1\hat{e}'_1 + x'_2\hat{e}'_2 + x'_3\hat{e}'_3 = \sum_{i=1}^{3} x'_i\hat{e}'_i$. Generally speaking, $x_i \neq x'_i$, $i = 1,2,3$. A natural question is how are the components of $\vec{x}$ in the new system related to its components in the original one? Take x'_2 for an example, $x'_2 = \vec{x} \bullet \hat{e}'_2 = \sum_{i=1}^{3} x_i\hat{e}_i \cdot \hat{e}'_2 = \sum_{i=1}^{3} x_i|\hat{e}_i||\hat{e}'_2|\cos\left(\hat{e}_i, \hat{e}'_2\right) = \sum_{i=1}^{3} x_i C_{i,2}$.

In the above, we define $C_{i,2} = \cos\left(\hat{e}_i, \hat{e}'_2\right)$. In general, for any component "j" in the new system,

$$x'_j = \sum_{i=1}^{3} x_i C_{i,j} \tag{12.1}$$

where i is "repeated" index and also called dummy index that can be any symbol, and directional cosine $C_{i,j} = \cos\left(\hat{e}_i, \hat{e}'_j\right)$.

"Einstein summation role" states that "whenever an index appears twice or more in the same term, a summation over that index is implied." Use this convenient role,

© Springer International Publishing Switzerland 2015

D. Ren, *Storm-triggered Landslides in Warmer Climates*,
DOI 10.1007/978-3-319-08518-0_12

we can omit the sigma sign in writing. For example, Eq. (12.1) can be written as $x_j^{'} = x_i C_{i,j} = x_k C_{k,j} = x_l C_{l,j}$. The above expression is actually three equations when j takes 1,2,3 in turn.

Exactly the same maneuver shows that

$$x_i = x_j^{'} C_{i,j} \tag{12.2}$$

Lets now consider Newton's law (2nd)

$$\vec{F} = m\vec{a}. \tag{12.3}$$

Consider the components of $\vec{F}$ in an original and a rotated coordinate system. In the original system,

$$F_i = ma_i = m\frac{d^2 x_i}{dt^2} \quad \text{(i.e., taking } \hat{e}_i \bullet \text{ Eq. 12.3).} \tag{12.4}$$

Multiply both sides of Eq. (12.4) by C_{ij} and take the summation,

$$C_{ij}F_i = m\frac{d^2\left(x_i C_{ij}\right)}{dt^2} = m\frac{d^2 x_j^{'}}{dt^2} \tag{12.5}$$

However, j-component of $\vec{F} = m\vec{a}$ in the rotated system should read

$$F_j^{'} = m\frac{d^2 x_j^{'}}{dt^2} \tag{12.6}$$

A comparison between Eqs. (12.5) and (12.6) yields

$$F_j^{'} = C_{ij}F_i \tag{12.7}$$

So, for $\vec{F} = m\vec{a}$ to hold in both coordinate system, or being rotationally invariant, the components of $\vec{F}$ must transform with the same rule as the components of position vector $\vec{x}$ with a rotation of coordinates.

More generally, any quantity $\vec{Q}$ is a vector if its components transform like the position vector $\vec{x}$ under rotation of coordinates $Q_j^{'} = C_{ij}Q_i$. Because vector possesses one free index (j), it is also known as 1st order tensor. Now lets introduce the concept of higher order tensors.

A quantity Q is a second order tensor if its components transformation under a rotation as

$$Q'_{mn} = C_{im}C_{jn}Q_{ij} \tag{12.8}$$

where m,n are free indices, and I,j are dummy indices. The m,n each takes 1,2,3, so there are 3 by 3 equals 9 equations all together. Written in matrix form,

$$Q'_{mn} = C^T_{mi}Q_{ij}C_{jn} \tag{12.9}$$

For example,

$$\begin{aligned} Q'_{23} = C_{2i}Q_{ij}C_{j3} = {} & C_{12}C_{13}Q_{11} + C_{12}C_{23}Q_{12} + C_{12}C_{33}Q_{13} \\ & + C_{22}C_{13}Q_{21} + C_{22}C_{23}Q_{22} + C_{22}C_{33}Q_{23} \\ & + C_{32}C_{13}Q_{31} + C_{32}C_{23}Q_{32} + C_{32}C_{33}Q_{33} \end{aligned}$$

Similarly, a quantity is a 4th order tensor if its components transform under a rotation as

$$Q'_{mnpq} = C_{im}C_{jn}C_{kp}C_{lq}Q_{ijkl} \tag{12.10}$$

It is a short hand for $3^4 = 81$ equations! In general, n^{th} order tensor contains 3^n equations.

Although tensor can be expressed by matrix, but not all matrix are tensors.

Following are two very useful tensors in stress and strain analysis: Kronecker substitution tensor and "alternating" tensor. In a certain sense, this section serves the general purpose as preparation for Chap. 4. The operators introduced here also helps understanding the derivations in Sect. 12.2.

Now consider a special quantity δ with components given by $\delta_{ij} = \vec{e}_i \cdot \vec{e}_j$. That is, $\delta_{11} = \delta_{22} = \delta_{33} = 1$, while the rest components are zeros. It is straightforward to proof that it is a tensor of second order.

An important 3rd order tensor is the "permutation tensor" or "alternating tensor," which has components:

$$\varepsilon_{i,j,k} = \begin{cases} 1, & \text{if i, j, k is cyclic order} \\ 0, & \text{any two of the three indices are equal} \\ -1 & \text{if i, j, k is anti} - \text{cyclic order} \end{cases}.$$

The important properties of the permutation tensor is listed in the Appendix D.

Higher order tensor can be obtained from lower order tensor by multiplication expansion and lower order tensor can be obtained from higher order tensor by contraction.

12.2 Orthogonal Curvilinear Coordinates

Enormous simplification can be achieved in solving partial differential equations if all boundaries correspond to coordinate surfaces, which are surfaces generated by holding one coordinate constant and varying the other two. Accordingly, many special coordinate systems are devised to solve problems in particular geometries. SEGMENT-Landslide is projected in earth spherical coordinate system, a special kind of orthogonal curvilinear coordinate system. To familiarize the readers with operators in the coordinate system, we would like to introduce the basic concepts of curvilinear coordinate system. In this section, a general discussion of orthogonal curvilinear system is given first, and then the relationships for spherical coordinates are described as a special case. With skills introduced in this subsection, readers will be able to follow the derivation from the governing equations into Eqs. (6.1)–(6.4).

12.2.1 Arc Length, Area Element, and Volume Element

In the following discussion, rectangular Cartesian system is characterized by unit directional vectors $\vec{i}$, $\vec{j}$ and $\vec{k}$ and a generic curvilinear system is characterized by unit vectors $\hat{e}_1$, $\hat{e}_2$ and $\hat{e}_3$. Right-handed system is followed in the following discussion. Position vector $\vec{r}$ (of a granular element), can be decomposed into the $\hat{e}_1$, $\hat{e}_2$ and $\hat{e}_3$ directions, so that $\vec{r} = q_1\hat{e}_1 + q_2\hat{e}_2 + q_3\hat{e}_3$, with q_1, q_2, and q_3 represent the three coordinates in a general, curvilinear system. In a standard Cartesian coordinate system, the same positional vector can be expressed as $\vec{x} = x\vec{i} + y\vec{j} + z\vec{k}$. For $\hat{e}_1$, $\hat{e}_2$ and $\hat{e}_3$ becoming a valid basis, it is required that

$$J = \frac{D(q_1, q_2, q_3)}{D(x, y, z)} \neq 0 \tag{12.11}$$

That means q_1, q_2, q_3 are functions of x, y, and z.

$$q_1 = q_1(x, y, z) \tag{12.12a}$$
$$q_2 = q_2(x, y, z) \tag{12.12b}$$
$$q_2 = q_3(x, y, z) \tag{12.12c}$$

Similarly, x, y, and z are also unique functions of q_1, q_2, and q_3.

$$x = x(q_1, q_2, q_3) \tag{12.13a}$$

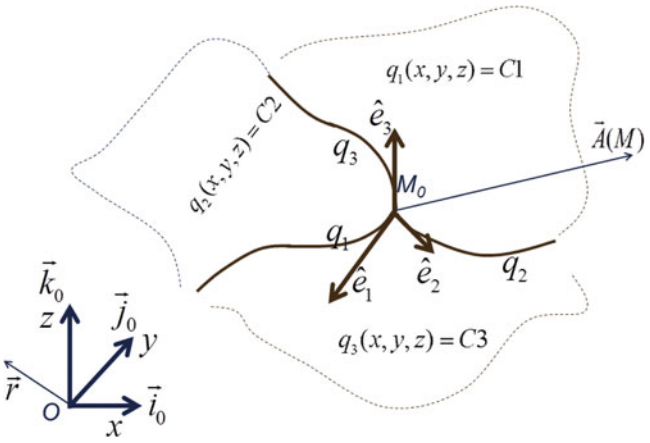

Fig. 12.1 Rectangle Cartesian coordinate and orthogonal curvilinear coordinate system. In the figure, i_0,j_0, and k_0 are unit vectors in the increasing direction of x, y, and z, respectively, in Cartesian coordinate. The r is a position vector in the Cartesian coordinate. Unit vectors (e_1,e_2, and e_3) passing through M_0 in an orthogonal curvilinear coordinate are shown. Each e_i is perpendicular to the surface defined by $q_i = \mathrm{C}(M_0)$ that passes M_0

$$y = y(q_1, q_2, q_3) \tag{12.13b}$$

$$z = z(q_1, q_2, q_3) \tag{12.13c}$$

Figure 12.1 is a comparison of Cartesian with a general curvilinear coordinate system.

When we let coordinate surfaces $q_1(x, y, z) = C_1$, $q_2(x, y, z) = C_2$, and $q_3(x, y, z) = C_3$, in turn, the intersectional lines form the general curvilinear coordinate system. In other words, a curve produced by varying q_i, with q_j ($j \neq i$) held constant, will be referred to as a "q_i curve." A unit vector along increasing q_i is defined as $\hat{e}_i$. Apparently, base vectors $\hat{e}_1$, $\hat{e}_2$ and $\hat{e}_3$ are unit vectors along increasing coordinate surfaces q_1, q_2, and q_3.

For example, the crossing line between $q_1(x, y, z) = C_1$, $q_2(x, y, z) = C_2$ actually is q_3 axis. The most wanted property from a coordinate system is orthogonality, that is, at any point in space the vectors aligned with the three coordinate directions are mutually perpendicular. In general, the variation of a single coordinate will generate a curve in space, rather than a straight line; hence the term curvilinear. Although the base vectors are each of constant (unit) magnitude, the fact that a q_i curve is not generally a straight line means that their direction is variable. In other words, e_i must be regarded as a function of position, in general. This discussion is restricted to coordinate systems in which ($\hat{e}_1$, $\hat{e}_2$, $\hat{e}_3$) is an orthonormal and right-handed set. At any point in space, such a set has the properties of the base vectors used in Sect. 12.1, namely,

$$\hat{e}_i \cdot \hat{e}_j = \delta_{ij} \tag{12.14}$$

$$\hat{e}_i \times \hat{e}_j = \sum_k \varepsilon_{ijk} \vec{e}_k \tag{12.15}$$

12.2.1.1 Differentials in Arc Length (l), Surface Area (S) and Volume (V)

The key to deriving expressions for curvilinear coordinates is to consider the arc length along a curve. In particular, let l_i represent arc length along a q_i curve.

The differential length of an arbitrary curve (with arc length l), by definition of the Euclidean norm, is

$$dl = \sqrt{dx^2 + dy^2 + dz^2} \tag{12.16}$$

From Eqs. (12.13a–12.13c),

$$dx = \frac{\partial x}{\partial q_1} dq_1 + \frac{\partial x}{\partial q_2} dq_2 + \frac{\partial x}{\partial q_3} dq_3 \tag{12.17a}$$

$$dy = \frac{\partial y}{\partial q_1} dq_1 + \frac{\partial y}{\partial q_2} dq_2 + \frac{\partial y}{\partial q_3} dq_3 \tag{12.17b}$$

$$dz = \frac{\partial z}{\partial q_1} dq_1 + \frac{\partial z}{\partial q_2} dq_2 + \frac{\partial z}{\partial q_3} dq_3 \tag{12.17c}$$

Applying Eqs. (12.17a–12.17c) specifically to q_1 curve ($dq_2 = dq_3 = 0$), and defining the incremental arc length in this direction as $\mathrm{d}l_1$.

$dx\big|_{q_1} = \frac{\partial x}{\partial q_1} dq_1$; $dy\big|_{q_1} = \frac{\partial y}{\partial q_1} dq_1$; and $dz\big|_{q_1} = \frac{\partial z}{\partial q_1} dq_1$. Substituting into Eq. (12.16),

$$dl_1 = \sqrt{dx\big|_{q_1}^2 + dy\big|_{q_1}^2 + dz\big|_{q_1}^2} = \sqrt{\left(\frac{\partial x}{\partial q_1}\right)^2 + \left(\frac{\partial y}{\partial q_1}\right)^2 + \left(\frac{\partial z}{\partial q_1}\right)^2} dq_1 = H_1 dq_1 \tag{12.18}$$

Similarly,

$$dl_2 = \sqrt{dx\big|_{q_2}^2 + dy\big|_{q_2}^2 + dz\big|_{q_2}^2} = \sqrt{\left(\frac{\partial x}{\partial q_2}\right)^2 + \left(\frac{\partial y}{\partial q_2}\right)^2 + \left(\frac{\partial z}{\partial q_2}\right)^2} dq_2 = H_2 dq_2, \text{ and} \tag{12.19}$$

$$dl_3 = \sqrt{dx\big|_{q_3}^2 + dy\big|_{q_3}^2 + dz\big|_{q_3}^2} = \sqrt{\left(\frac{\partial x}{\partial q_3}\right)^2 + \left(\frac{\partial y}{\partial q_3}\right)^2 + \left(\frac{\partial z}{\partial q_3}\right)^2} dq_3 = H_3 dq_3 \tag{12.20}$$

where scale factor $H_i = dl_i/dq_i = \sqrt{\left(\frac{\partial x}{\partial q_i}\right)^2 + \left(\frac{\partial y}{\partial q_i}\right)^2 + \left(\frac{\partial z}{\partial q_i}\right)^2}$ is called Lame operator.

Lame vector ($\hat{l}_i$), a vector that is tangent to corresponding q_i curve and directed toward increasing q_i is given by

$$\hat{l}_i = \frac{\partial \vec{r}}{\partial q_i} = H_i \hat{e}_i \tag{12.21}$$

Lame vectors are coordinate vectors (usually not of unit length) in a curvilinear coordinate system.

Letting S_i refer to a surface on which the coordinate q_i is held constant, we obtain, from orthogonality, its incremental can be expressed as:

$$dS_i = \left|\hat{l}_{i+1} \times \hat{l}_{i+2}\right| dq_{i+1} \cdot q_{i+2} = H_{i+1} H_{i+2} dq_{i+1} dq_{i+2} \tag{12.22}$$

In component form (for all three orthogonal surface elements):

$$dS_1 = H_2 H_3 dq_2 dq_3; \;\; dS_2 = H_1 H_3 dq_1 dq_3; \;\; dS_3 = H_1 H_2 dq_1 dq_2.$$

For a given coordinate system, the differential volume element dV corresponds to the volume of a parallelepiped with adjacent edges $\hat{e}_i dl_i$. The edges can be represented also as $\hat{l}_i dq_i$. As noted in connection with Eq. (A.22), the volume is given by the scalar triple product, or

$$dV = \hat{l}_1 dq_1 \times \hat{l}_2 dq_2 \cdot \hat{l}_3 dq_3 = H_1 H_2 H_3 dq_1 dq_2 dq_3 \tag{12.23}$$

We aim to establish the basis for transform of our partial differential equations from physical space (rectangle Cartesian coordinates) into calculational space. There involves scalar transfers as well as their various order derivatives with respect to directional coordinate variables. The basis for these transformation is the unit vector's derivatives.

12.2.1.2 Derivatives of Unit Vectors

As above-mentioned, one unique feature of orthogonal curvilinear coordinate is that, its unit vectors (of length equals unity) change directions in space. To effectively use the orthogonal curvilinear coordinates, we need to deduce their derivatives such as $\frac{\partial \hat{e}_j}{\partial q_k}(k \neq j)$, $\frac{\partial \hat{e}_j}{\partial q_j}$, $\nabla \hat{e}_j$, and $\nabla \times \hat{e}_j$.

(a) $\frac{\partial \hat{e}_j}{\partial q_k}(k \neq j)$

From Eq. (12.21), for an arbitrary positional vector $\vec{r}$, we have the following two expressions:

$\hat{l}_j = \frac{\partial \vec{r}}{\partial q_j} = H_j \hat{e}_j$ & $\hat{l}_k = \frac{\partial \vec{r}}{\partial q_k} = H_k \hat{e}_k$. Respectively taking derivatives with respect to q_k and q_k,we obtain

$\frac{\partial^2 \vec{r}}{\partial q_j \partial q_k} = \underline{\underline{\frac{\partial (H_j \hat{e}_j)}{\partial q_k} = \frac{\partial (H_k \hat{e}_k)}{\partial q_j}}}$. Expanding the underscored portion:

$$H_j \frac{\partial \hat{e}_j}{\partial q_k} + \hat{e}_j \frac{\partial H_j}{\partial q_k} = H_k \frac{\partial \hat{e}_k}{\partial q_j} + \hat{e}_k \frac{\partial H_k}{\partial q_j} \tag{12.24}$$

Rearranging according to each direction (j and k),

$$\left(H_j \frac{\partial \hat{e}_j}{\partial q_k} - \hat{e}_k \frac{\partial H_k}{\partial q_j} \right) + \left(\hat{e}_j \frac{\partial H_j}{\partial q_k} - H_k \frac{\partial \hat{e}_k}{\partial q_j} \right) = 0$$

Zero vector has all components being zero:

$$\left(H_j \frac{\partial \hat{e}_j}{\partial q_k} = \hat{e}_k \frac{\partial H_k}{\partial q_j} \right) \& \left(\hat{e}_j \frac{\partial H_j}{\partial q_k} = H_k \frac{\partial \hat{e}_k}{\partial q_j} \right)$$

Generally,

$$\frac{\partial \hat{e}_j}{\partial q_k} = \frac{\hat{e}_k}{H_j} \frac{\partial H_k}{\partial q_j} \ (j \neq k) \tag{12.25}$$

(b) $\frac{\partial \hat{e}_j}{\partial q_j} (j = 1, 2, 3)$

Because $\hat{e}_j = \hat{e}_{j+1} \times \hat{e}_{j+2}$ (orthogonality and right-hand system), thus

$$\begin{aligned}
\frac{\partial \hat{e}_j}{\partial q_j} = \frac{\partial}{\partial q_j} \left(\hat{e}_{j+1} \times \hat{e}_{j+2} \right) &= \frac{\partial}{\partial q_j} \left(\hat{e}_{j+1} \right) \times \hat{e}_{j+2} + \hat{e}_{j+1} \\
&\quad \times \frac{\partial}{\partial q_j} \left(\hat{e}_{j+2} \right) \underset{use \text{ Eq.}(11.24)}{=} \frac{1}{H_{j+1}} \frac{\partial H_j}{\partial q_{j+1}} \hat{e}_j \times \hat{e}_{j+2} \\
&\quad + \frac{1}{H_{j+2}} \frac{\partial H_j}{\partial q_{j+2}} \hat{e}_{j+1} \times \hat{e}_j \\
&= -\frac{1}{H_{j+1}} \frac{\partial H_j}{\partial q_{j+1}} \hat{e}_{j+1} - \frac{1}{H_{j+2}} \frac{\partial H_j}{\partial q_{j+2}} \hat{e}_{j+2} \\
&= -\sum_k \frac{1}{H_k} \frac{\partial H_j}{\partial q_k} \hat{e}_k (k \neq j)
\end{aligned}$$

Thus,

$$\frac{\partial \hat{e}_j}{\partial q_j} = -\sum_k \frac{1}{H_k}\frac{\partial H_j}{\partial q_k}\hat{e}_k (k \neq j) \tag{12.26}$$

(c) $\nabla \times \hat{e}_j$

From Eqs. (12.18)–(12.20), Hamilton operator's expression in the orthogonal curvilinear coordinate system is

$$\nabla = \sum_{j=1}^{3} \frac{\hat{e}_j}{H_j}\frac{\partial}{\partial q_j} \tag{12.27}$$

Therefore, $\nabla q_j = \frac{\hat{e}_j}{H_j}$. Take its vorticity, $0 = \nabla \times \nabla q_j = \nabla \times \frac{\hat{e}_j}{H_j} = \frac{1}{H_j}\nabla \times \hat{e}_j + \left(\nabla \frac{1}{H_j}\right) \times \hat{e}_j$

Thus,

$\frac{1}{H_j}\nabla \times \hat{e}_j = \hat{e}_j \times \left(\nabla \frac{1}{H_j}\right)$ using Eq. (69) $\hat{e}_j \times \sum_{k=1}^{3} \frac{\hat{e}_k}{H_k}\frac{\partial}{\partial q_k}\left(\frac{1}{H_j}\right) =$

$-\sum_{k=1}^{3} \frac{\hat{e}_j \times \hat{e}_k}{H_k}\frac{1}{H_j^2}\frac{\partial H_j}{\partial q_k}$

Finally, decompose into $k = j$, $k = j + 1$ and $k = j + 2$ components, with k = j part being zero,

$$\nabla \times \hat{e}_j = \frac{\hat{e}_{j+1}}{H_j H_{j+2}}\frac{\partial H_j}{\partial q_{j+2}} - \frac{\hat{e}_{j+2}}{H_j H_{j+1}}\frac{\partial H_j}{\partial q_{j+1}} \tag{12.28}$$

(d) $\nabla \cdot \hat{e}_j$

Similarly, using vector identity Eq. (A.11), or

$\nabla \cdot \left(\vec{a} \times \vec{b}\right) = \left(\nabla \times \vec{a}\right) \cdot \vec{b} - \vec{a} \cdot \left(\nabla \times \vec{b}\right)$, with $\vec{a} = \hat{e}_{j+1}$ and $\vec{b} = \hat{e}_{j+2}$, and the result obtained in Eq. (12.28), it is straight forward to obtain that

$$\nabla \cdot \hat{e}_j = \frac{1}{H_1 H_2 H_3}\frac{\partial}{\partial q_j}\left(H_{j+1} H_{j+2}\right) \tag{12.29}$$

With expressions in subsections (*a–d*), it is straightforward to obtain first order derivatives such as vorticity, divergence, gradient and second order derivatives such as scalar Laplacian terms across coordinates. Interested readers are referred to Hildebrand (1976). The following focusing on two unfamiliar terms that needs to be derived for a complete transformation of SEGMENT-Landslide across coordinates: the advection term and the vector Laplacian term.

Advection term is the primary source for nonlinearity and is an important term in the momentum equation as well as the entrainment/sediment processes.

$$\left(\vec{V}\cdot\nabla\right)\vec{V}=\sum_{j=1}^{3}\left(\sum_{k=1}^{3}\frac{u_k}{H_k}\frac{\partial u_j}{\partial q_k}+\sum_{k=1}^{3}\frac{u_k u_j}{H_j H_k}\frac{\partial H_j}{\partial q_k}-\sum_{k=1}^{3}\frac{u_k^2}{H_j H_k}\frac{\partial H_k}{\partial q_j}\right)\hat{e}_j \quad (12.30)$$

where $\vec{V}=(u_1,u_2,u_3)^T$ is the full 3D velocity.

Vector Laplacian terms only appear as diffusion terms in the momentum equations. However, the term is complicated and need special attention to avoid double counting. For that purpose, the generic form is listed here and, for specific, e.g., spherical coordinates, one need to calculate the Lame operators and substitute into the expression.

$$\begin{aligned}
\nabla^2\vec{V}=&\sum_{j=1}^{3}\frac{1}{\prod}\frac{\partial}{\partial q_j}\left(\frac{H_{j+1}H_{j+2}}{H_j}\right)\left(\frac{\partial u_1}{\partial q_j}\hat{e}_1+\frac{\partial u_2}{\partial q_j}\hat{e}_2+\frac{\partial u_3}{\partial q_j}\hat{e}_3\right)\\
&+\left(\frac{1}{H_j^2}\right)\left(\frac{\partial^2 u_1}{\partial q_j^2}\hat{e}_1+\frac{\partial^2 u_2}{\partial q_j^2}\hat{e}_2+\frac{\partial^2 u_3}{\partial q_j^2}\hat{e}_3\right)\\
&+\frac{2}{H_j^2}\left(\frac{\partial u_1}{\partial q_j}\frac{1}{H_1}\frac{\partial H_j}{\partial q_1}+\frac{\partial u_2}{\partial q_j}\frac{1}{H_2}\frac{\partial H_j}{\partial q_2}+\frac{\partial u_3}{\partial q_j}\frac{1}{H_3}\frac{\partial H_j}{\partial q_3}\right)\hat{e}_j\\
&+\frac{1}{\prod}\frac{\partial}{\partial q_j}\left(\frac{H_{j+1}H_{j+2}}{H_j}\right)\left(\frac{u_1}{H_1}\frac{\partial H_j}{\partial q_1}+\frac{u_2}{H_2}\frac{\partial H_j}{\partial q_2}+\frac{u_3}{H_3}\frac{\partial H_j}{\partial q_3}\right)\hat{e}_j\\
&-\frac{2}{H_j}\frac{1}{H_jH_{j+1}}\frac{\partial u_j}{\partial q_j}\frac{\partial H_j}{\partial q_{j+1}}\hat{e}_{j+1}-\frac{2}{H_j}\frac{1}{H_jH_{j+2}}\frac{\partial u_j}{\partial q_j}\frac{\partial H_j}{\partial q_{j+2}}\hat{e}_{j+2}\\
&+\frac{1}{H_j^2}\left\{\hat{e}_j\left[u_{j+1}\frac{\partial}{\partial q_j}\left(\frac{1}{H_{j+1}}\frac{\partial H_j}{\partial q_{j+1}}\right)+u_{j+2}\frac{\partial}{\partial q_j}\left(\frac{1}{H_{j+2}}\frac{\partial H_j}{\partial q_{j+2}}\right)\right.\right.\\
&\left.-\frac{u_j}{H_{j+1}}\frac{\partial H_j}{\partial q_{j+1}}\frac{1}{H_{j+1}}\frac{\partial H_j}{\partial q_{j+1}}-\frac{u_j}{H_{j+2}}\frac{\partial H_j}{\partial q_{j+2}}\frac{1}{H_{j+2}}\frac{\partial H_j}{\partial q_{j+2}}\right]\\
&+\hat{e}_{j+1}\left[-\frac{u_{j+1}}{H_{j+1}}\frac{\partial H_j}{\partial q_{j+1}}\left(\frac{1}{H_{j+1}}\frac{\partial H_j}{\partial q_{j+1}}\right)-\frac{u_{j+2}}{H_{j+2}}\frac{\partial H_j}{\partial q_{j+2}}\left(\frac{1}{H_{j+1}}\frac{\partial H_j}{\partial q_{j+1}}\right)\right.\\
&\left.-u_j\frac{\partial}{\partial q_j}\left(\frac{1}{H_{j+1}}\frac{\partial H_j}{\partial q_{j+1}}\right)\right]\\
&+\hat{e}_{j+2}\left[-\frac{u_{j+1}}{H_{j+1}}\frac{\partial H_j}{\partial q_{j+1}}\left(\frac{1}{H_{j+2}}\frac{\partial H_j}{\partial q_{j+2}}\right)-\frac{u_{j+2}}{H_{j+2}}\frac{\partial H_j}{\partial q_{j+2}}\left(\frac{1}{H_{j+2}}\frac{\partial H_j}{\partial q_{j+2}}\right)\right.\\
&\left.\left.-u_j\frac{\partial}{\partial q_j}\left(\frac{1}{H_{j+2}}\frac{\partial H_j}{\partial q_{j+2}}\right)\right]\right\}
\end{aligned} \quad (12.31)$$

where $\prod = H_1 H_2 H_3$.

For example, in the spherical coordinate system, with Eq. (12.13a–12.13c) in actual form:

$$\begin{cases} x = r\cos\lambda\cos\theta \\ y = r\cos\lambda\sin\theta \\ z = r\sin\lambda \end{cases} \tag{12.32}$$

Where r is radius of earth, λ is latitude, and θ is longitude, as depicted in Fig. 6.1.

Apparently, the Lame operator and unit vector derivatives are:

$$H_r = 1;\ H_\lambda = r;\ H_\theta = r\cos\lambda$$
$$\frac{\partial\vec{\theta_0}}{\partial\theta} = \sin\lambda\,\vec{\lambda}_0;\ \frac{\partial\vec{\lambda_0}}{\partial\lambda} = -\vec{r}_0;\ \frac{\partial\vec{r_0}}{\partial\lambda} = \vec{\lambda}_0;\ \frac{\partial\vec{r_0}}{\partial\theta} = \cos\lambda\ \vec{\theta}_0;\ \frac{\partial\vec{\lambda_0}}{\partial\theta} = -\sin\lambda\ \vec{\theta}_0 \tag{12.33}$$

Substituting Eq. (12.33) into Eq. (12.31), we obtain the vector Laplacian in spherical coordinate system as:

$$\begin{aligned}
\nabla^2\vec{V} = {} & \vec{\lambda}_0\left[\frac{1}{r^2\cos^2\phi}\frac{\partial^2 u_\lambda}{\partial\lambda^2} - \frac{2\sin\phi}{r^2\cos^2\phi}\frac{\partial u_\phi}{\partial\lambda} + \frac{2}{r^2\cos\phi}\frac{\partial u_r}{\partial\lambda} - \frac{tg^2\phi}{r^2}u_\lambda - \frac{u_\lambda}{r^2}\right. \\
& \left. + \frac{1}{r^2}\frac{\partial^2 u_\lambda}{\partial\phi^2} - \frac{tg\phi}{r^2}\frac{\partial u_\lambda}{\partial\phi} + \frac{\partial^2 u_r}{\partial r^2} + \frac{2}{r}\frac{\partial u_r}{\partial r}\right] \\
& + \vec{\phi}_0\left[\frac{2\sin\phi}{r^2\cos^2\phi}\frac{\partial u_\lambda}{\partial\lambda} - \frac{\sin^2\phi}{r^2\cos^2\phi}u_\phi + \frac{1}{r^2\cos^2\phi}\frac{\partial^2 u_\phi}{\partial\lambda^2} + \frac{1}{r^2}\frac{\partial^2 u_\phi}{\partial\phi^2}\right. \\
& \left. - \frac{tg\phi}{r^2}\frac{\partial u_\phi}{\partial\phi} + \frac{2}{r^2}\frac{\partial u_r}{\partial\phi} - \frac{1}{r^2}u_\phi + \frac{2}{r}\frac{\partial u_\phi}{\partial r} + \frac{\partial^2 u_\phi}{\partial r^2}\right] \\
& + \vec{r}_0\left[-\frac{2}{r^2\cos\phi}\frac{\partial u_\lambda}{\partial\lambda} - \frac{2}{r^2}\frac{\partial u_\phi}{\partial\phi} - \frac{2}{r^2}u_r + \frac{2}{r}\frac{\partial u_r}{\partial r} + \frac{2tg\phi}{r^2}u_\phi\right. \\
& \left. + \frac{1}{r^2\cos^2\phi}\frac{\partial^2 u_r}{\partial\lambda^2} + \frac{1}{r^2}\frac{\partial^2 u_r}{\partial\phi^2} - \frac{tg\phi}{r^2}\frac{\partial u_r}{\partial\phi} + \frac{\partial^2 u_r}{\partial r^2}\right]
\end{aligned}$$

$$\nabla^2\vec{V} = \vec{\theta}_0\left[\frac{1}{r^2\cos^2\lambda}\frac{\partial^2 u_\theta}{\partial\theta^2} - \frac{2\sin\lambda}{r^2\cos^2\lambda}\frac{\partial u_\lambda}{\partial\theta} + \frac{2}{r^2\cos\lambda}\frac{\partial u_r}{\partial\theta} - \frac{tg^2\lambda}{r^2}u_\theta - \frac{u_\theta}{r^2} + \frac{1}{r^2}\frac{\partial^2 u_\theta}{\partial\lambda^2}\right.$$
$$\left. - \frac{tg\lambda}{r^2}\frac{\partial u_\theta}{\partial\lambda} + \frac{\partial^2 u_r}{\partial r^2} + \frac{2}{r}\frac{\partial u_r}{\partial r}\right]$$
$$+ \vec{\lambda}_0\left[\frac{2\sin\lambda}{r^2\cos^2\lambda}\frac{\partial u_\theta}{\partial\theta} - \frac{\sin^2\lambda}{r^2\cos^2\lambda}u_\lambda + \frac{1}{r^2\cos^2\lambda}\frac{\partial^2 u_\lambda}{\partial\theta^2} + \frac{1}{r^2}\frac{\partial^2 u_\lambda}{\partial\lambda^2}\right.$$
$$\left. - \frac{tg\lambda}{r^2}\frac{\partial u_\lambda}{\partial\lambda} + \frac{2}{r^2}\frac{\partial u_r}{\partial\lambda} - \frac{1}{r^2}u_\lambda + \frac{2}{r}\frac{\partial u_\lambda}{\partial r} + \frac{\partial^2 u_\lambda}{\partial r^2}\right]$$
$$+ \vec{r}_0\left[-\frac{2}{r^2\cos\lambda}\frac{\partial u_\theta}{\partial\theta} - \frac{2}{r^2}\frac{\partial u_\lambda}{\partial\lambda} - \frac{2}{r^2}u_r + \frac{2}{r}\frac{\partial u_r}{\partial r} + \frac{2tg\lambda}{r^2}u_\lambda + \frac{1}{r^2\cos^2\lambda}\frac{\partial^2 u_r}{\partial\theta^2}\right.$$
$$\left. + \frac{1}{r^2}\frac{\partial^2 u_r}{\partial\lambda^2} - \frac{tg\lambda}{r^2}\frac{\partial u_r}{\partial\lambda} + \frac{\partial^2 u_r}{\partial r^2}\right] \tag{12.34}$$

12.2.2 The Model Grid

The continuous equations of SEGMENT described in the previous section are solved numerically using finite difference methods on a rectangular computational grid in a spherical coordinate system. The model variables are staggered on an Arakawa C-grid (Arakawa and Lamb 1977), with scalars defined at the center of the grid boxes and the normal velocity components defined on the corresponding box faces (Fig. 12.2). The coordinate variables x, y, and z are also staggered and are defined at the u, v, and w points, respectively. It follows that the (physical to computational space) transformation map factors need to be evaluated at half grid points of the horizontal vector points and vertical transformation coefficient simply at scalar points.

For the convenience of following discussion, we define the following notations for averaging and differencing (two basic operations for all numerical schemes), means to represent the governing equations in finite difference form.

$$\overline{q}^{ns} = 0.5[q(s + n\Delta s/2) + q(s - n\Delta s/2)] \tag{12.35}$$
$$\delta_{ns} q = [q(s + n\Delta s/2) - q(s - n\Delta s/2)]/(n\Delta s) \tag{12.36}$$

Where q is an interested quantity (dependent variable), Δs spatial interval (grid spacing), and n is integer counts.

As will soon be seen, the primary limitation in integration time step is the stiffness of the governing equations. Thus, to improve the model efficiency, the

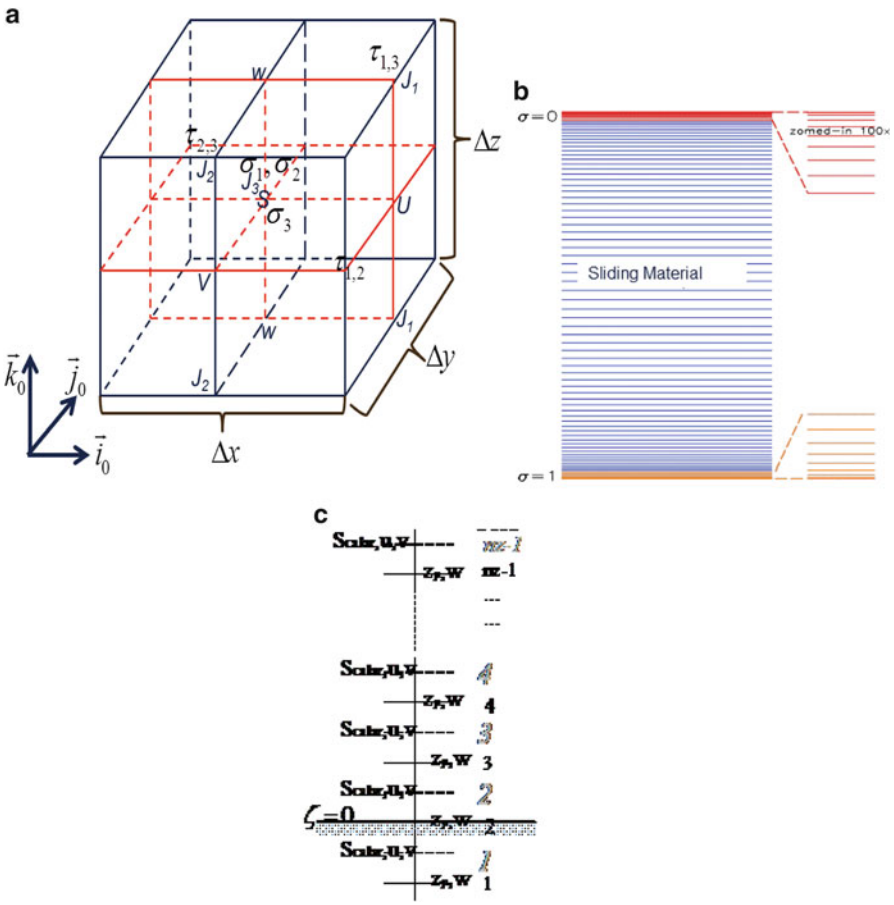

Fig. 12.2 A grid box depicting the staggering of the coordinate and dependent variables in SEGMENT-Landslide (**a**). Panel (**b**) is vertical grid stencil in numerical model. Vertical stretching using hyperbolic tangent function. $\Delta\mu_i = \Delta\mu_m + \frac{\Delta\mu_{\min} - \Delta\mu_m}{\tanh(2\alpha)} \tanh\left[\frac{2\alpha}{1-a}(1-a)\right]$ for i = 1, 2 , ... $n\,z/2$, where a = $(1 + \mathrm{nz})/2$. Schematic representation of the sigma coordinate system. Because slope hydrological processes are happening near surface but most strains are concentrated near bottom. SEGMENT-Landslide follows a symmetric stretching scheme that results in higher resolution at both the bottom and upper boundaries. Panel (**c**) shows the vertical staggering inside the simulation domain

mode-splitting time integration technique presented in Klemp and Wilhelmson (1978) is employed. For example, in the land surface sub-model component, the integration of the soil temperature equation using Crank–Nicolson (to be detailed in Sect. 12.3.4) scheme involves subdividing the time step into several small time steps.

Except for the advection term, the large time step integration uses a centered three-level (leapfrog) time differencing scheme (the associated numerical problems

such as "computational modes" will be addressed in Sect. 12.3.2). The advection, at the option of the user, can be either second- or fourth-order accurate. The large time step interval is limited by a stability condition based on advective flow speeds. For the small time step integration, there are full explicit forward–backward scheme and the absolutely stable but computationally more expensive (because a tridiagonal system needs to be solved at each small time step of integration) Crank–Nicolson scheme. For the forward–backward option, the momentum equations are first integrated one small time step using a forward scheme (relative to the stress forcing terms), then an integration using a backward scheme (relative to continuity equation which now is updated with the horizontal velocity components). In short build temporal interconnection and coherences to avoid domain separation. Also, in SEGMENT-Landslide, six types of boundary conditions are available for user selection. The most likely situations for realistic slopes are defaulted (such as stress free upper boundary condition).

12.3 Solving Partial Differential Equations

The physical principles discussed in earlier chapters form the basis for our ability to model the storm-triggered landslides numerically. Models of landslides can take many forms ranging from simple one-dimensional slope models to complex three-dimensional time-dependent models that conserve energy, mass and momentum of the entire system. The simpler mechanistic models are primarily aimed at providing insight into the relative roles of individual factors, while the more complex models are oriented toward the detailed simulation of observed phenomena. It is the latter class of the model hierarchy, the modern day full physics 3D landslide model, such as SEGMENT-Landslide, that we will discuss in this chapter. This type of model attempts to provide the most comprehensive mathematical description of the landslide ecosystem, and historically has been the most numerically complicated and computationally demanding of scientific simulation tools.

The scope of this book does not permit a complete theoretical development of all the relevant numerical and computational issues associated 3D dynamic modeling. Therefore, we will only introduce some of the more important numerical method concepts related to the construction of these models. Finally, we will address the computational challenges that will face future modeling efforts as we move into a satellite remote sensing era and widely available super computing architectures, particularly data assimilation and reverse modeling associated with forward landslide models.

Most, if not all, landslide models are based on the primitive equations (Eqs. 5.11–5.15). These highly nonlinear partial differential equations do not have closed form solutions, and must be integrated numerically. All numerical methods necessarily involve some type of discrete approximation to the continuous differential equations. These techniques generally fall into the broad categories of finite difference, spectral, and finite element methods. At present, finite difference

and spectral methods are the most dominant in landslide modeling. Here we limit our discussion to basic concepts associated with numerical solution techniques of SEGMENT-Landslide, particularly those relevant to current distributed memory parallel computing systems. We refer the interested reader to more complete developments of numerical methods in Mesinger and Arakawa (1976), Machenhauer (1979), and Haltiner and Williams (1980).

12.3.1 Numerical Approximation Concepts: Finite Difference Methods

Finite difference methods make use of a discrete set of regularly spaced points within the simulation domain of interest. The dependent variables are initially defined on this grid mesh or grid lattice and subsequently evaluated at these points. Most often, an Eulerian approach is used in which both space and time coordinates are chosen as independent variables where the spatial distribution of the finite difference grid remains fixed until re-gridded. Derivatives appearing in the governing equations are approximated using differences of dependent variables over finite space and time intervals, hence the term "finite difference method." These derivative approximations are used to construct a system of algebraic equations which are then solved using a computer.

Consider now an arbitrary function, f, of a single independent variable x,

$$f = f(x). \tag{12.37}$$

Which we want to approximate in some region $0 \leq x \leq L$. The simplest approach to the problem is to divide the range into an integer number of intervals I, of equal length Δx, called the grid length (size). Thus, the function f is approximated at the discrete points $x_i = i\Delta x$ where $i = 0,1,2,3,\ldots,I$. Thus, it is clear that the smallest feature (i.e., the shortest wavelength) that can be represented on such a discrete mesh is $2\Delta x$ in size. Figure 12.3 shows a function f(x) which has been sampled on a finite difference grid. Note how the smaller-scale features do not exist in the discrete representation, while the larger features are more faithfully approximated. Thus the interval $2\Delta x$ defines a lower resolution limit, although not necessarily a sufficient resolution for the proper treatment of such scales of motion, as we will demonstrate shortly.

Finite differences are discrete approximations to continuous derivatives and are calculated over one or more of the intervals Δx (or Δt if time is the independent variable). Formally, the first derivative of $f(x)$ at a point x_0 is defined as

$$\frac{df}{dx}|_{x=x0} \equiv f_x^{'}(x_0) = \lim_{\Delta x \to 0} \frac{f(x_0 + \Delta x) - f(x_0 - \Delta x)}{2\Delta x}. \tag{12.38}$$

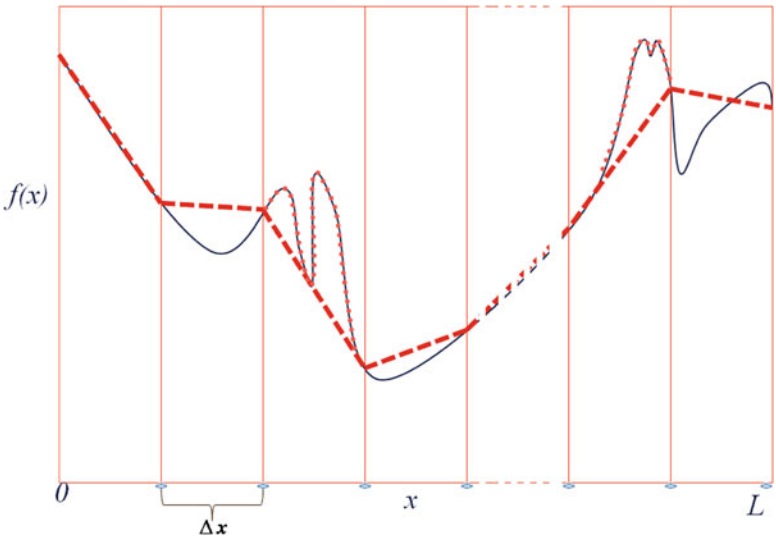

Fig. 12.3 Example of a discrete approximation (*thick dashed line*) of the continuous function f (x) (*solid black line*). Smaller features not represented by the grid mesh shown as *red dotted lines*

12.3.1.1 Numerical Accuracy Consideration

Finite difference approximations to the first derivative may be derived by using Taylor series expansions of f about a point x_0 such that

$$f(x_0 + \Delta x) = f(x_0) + f_x^{'}(x_0)\Delta x + \frac{1}{2} f_x^{''}(x_0)(\Delta x)^2 + O(\Delta x)^3 \tag{12.39}$$

$$f(x_0 - \Delta x) = f(x_0) - f_x^{'}(x_0)\Delta x + \frac{1}{2} f_x^{''}(x_0)(\Delta x)^2 + O(\Delta x)^3 \tag{12.40}$$

From Eqs. (12.39) and (12.40), uncentered difference operators may then be defined by

$$f_{x+}^{'}(x_0) = \frac{f(x_0 + \Delta x) - f(x_0)}{\Delta x} - \frac{1}{2} f_x^{''}(x_0)\Delta x + O(\Delta x)^2 \tag{12.41}$$

$$f_{x-}^{'}(x_0) = \frac{f(x_0) - f(x_0 + \Delta x)}{\Delta x} + \frac{1}{2} f_x^{''}(x_0)\Delta x + O(\Delta x)^2 \tag{12.42}$$

Where the terms following the leading term on the right-hand side define the truncation error for the scheme, a measure of the difference quotient accuracy for small values of Δx. The order of accuracy for the scheme is defined by the lowest power index of Δx appearing in the truncation error. For the uncentered operators defined above, the leading term in the truncation error is $O(\Delta x)$, which makes the

scheme first-order accurate. A centered difference operator can be derived by averaging the uncentered operators (Eqs. 12.39 and 12.40) such that

$$f_x^{'}(x_0) = \frac{f(x_0 + \Delta x) - f(x_0 - \Delta x)}{2\Delta x} + O(\Delta x)^2. \tag{12.43}$$

Now the leading term in the truncation error is much smaller for this second-order accurate scheme. This means using the same step size Δx, centered scheme is more accurate. For the one-dimensional centered case, the second derivative can be obtained by simply applying the first derivative twice

$$f_x^{''}(x_0) = \frac{f(x_0 + \Delta x) + f(x_0 - \Delta x) - 2f(x_0)}{\Delta x^2} + O(\Delta x)^2. \tag{12.44}$$

Another measure of the accuracy of a finite difference scheme can be illustrated by deriving what is sometimes referred to as the *response function* for the corresponding discrete operator. Lets assuming that

$$f(x) = A \sin\left(\frac{2\pi x}{L}\right), \tag{12.45}$$

For which the analytic derivative can be written as

$$f_x^{'}(x) = \frac{2\pi}{L} A \cos\left(\frac{2\pi x}{L}\right) \tag{12.46}$$

Using Eq. (12.43), the corresponding centered difference approximation of $f_x^{'}(x)$, can be written as

$$\delta_x f(x) = \frac{L}{2\pi\Delta x} \sin\left(\frac{2\pi\Delta x}{L}\right)\left[\frac{2\pi}{L} A \cos\left(\frac{2\pi x}{L}\right)\right] \tag{12.47}$$

The response function for this centered difference approximation to $f_x^{'}(x)$, defined as the ratio of the numerical to the analytic estimate, can then be derived as

$$R(L, \Delta x) = \frac{L}{2\pi\Delta x} \sin\left(\frac{2\pi\Delta x}{L}\right). \tag{12.48}$$

The solution, as graphically depicted in Fig. 12.4, clearly illustrates how the derivative estimates depend on the resolution of the finite difference grid, or how many discrete points are contained in a single wave. Despite the smooth and periodic nature of $f(x)$, 8 or more grid intervals are required for a reasonably accurate estimate of the first derivative using centered difference approximation ($R \rightarrow 1$). Even a cursory inspection of the governing system should underscore the importance of accurate derivative estimates in predicting the time evolution of granular flow.

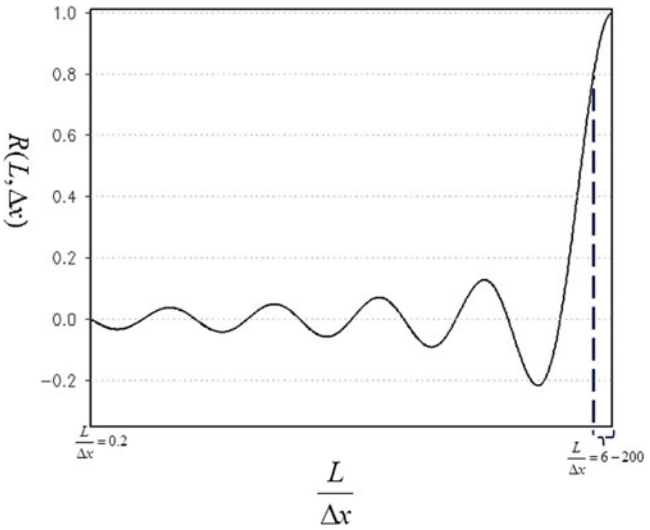

Fig. 12.4 Gain/response function. At least six grids are needed in one wave length to have a response function value higher than 0.8

12.3.1.2 Numerical Stability Consideration

We discussed different schemes can have different truncation errors in representing derivatives in the governing partial differential equations. There are two other very important issues related to numerical stability. To illustrate, we here make use of the one-dimensional non-linear advection equation. For simplicity, assume a sinusoidal function of the form

$$u(x,t) = U(t)\sin(kx) \tag{12.49}$$

Substitution into the nonlinear advection equation

$$\frac{\partial u}{\partial t} + u\frac{\partial u}{\partial x} = 0 \tag{12.50}$$

yields

$$\frac{\partial u}{\partial t} + 0.5U^2(t)k\sin(2kx) = 0 \tag{12.51}$$

As aforementioned, the shortest wave that can be represented on a finite difference grid is

$2\Delta x$ in length, which corresponds to a maximum wave number

$$k_{\max} = 2\pi/2\Delta x = \pi/\Delta x \tag{12.52}$$

The nonlinear advective term on the left-hand side of Eq. (12.50), however, can support a wave with twice the maximum wave number (or half the minimum wave length) that can be represented for the function u. Such a wave cannot be properly resolved on the finite difference grid and will be misrepresented in terms of permissible waves. The type of error is known as aliasing error (waves wrongly represented as constants in finite difference grids). The most serious consequence of aliasing errors is a spurious accumulation of energy in high wave number scales of motion. Over time, the energy at these scales grows beyond physically reasonable bounds, leading to nonlinear instability in the numerical integration. This is, in fact, the type of instability that was encountered by Lilly (1965) in his pioneering general circulation (climate and weather) modeling experiment. Phillips (1959a,b) correctly interpreted the nature of the instability and verified his explanation by periodically eliminating the high-frequency components of the vorticity field in a long integration of the non-divergent vorticity equation. It was later recognized that the same result could be accomplished by using a dissipative numerical integration scheme, or, even more flexibly, by including an adjustable dissipative term in the equations. More elegant approaches to the problem of nonlinear instability have since been developed by Arakawa (1984) who proposed finite difference schemes for the advective terms that are totally free of the spurious cascade of energy to smaller scales, thus eliminating the need for an artificial numerical dissipation.

The second stability concept involves the estimation of time steps can be used in actual integration. Because the complicity, we would like to use the linear advection equation (Eq. 12.50 with constant $u = c$). Assuming an initial condition of the form

$$f(x, 0) = Ae^{ikx} \tag{12.53}$$

where i means imaginary in a complex number, gives a time-dependent analytic solution:

$$f(x, t) = Ae^{ik(x-ct)}. \tag{12.54}$$

To see the time evolution of the magnitude, we assume the centered finite difference solution given in the form:

$$f(x, t + \Delta t) = f(x, t - \Delta t) - \frac{c\Delta t}{\Delta x}[f(x + \Delta x, t) - f(x - \Delta x, t)] \tag{12.55}$$

Substitution of the analytic solution Eq. (12.54) into the centered difference solution reveals that a numerically stable (i.e., nonamplifying) solution exists if and only if

$$\frac{c\Delta t}{\Delta x} \leq 1. \tag{12.56}$$

This stability bound is most commonly known as the Courant–Friedrichs–Lewy or CFL criterion. This relationship bounds the maximum time step by the ratio of the spatial resolution to the fastest signal propagating in the model (here, c). Thus, as the model resolution increases, the time step must necessarily decrease proportionally, further increasing the computational demand.

In simulating landslides, the CFL constraint is not that stringent. What limits the time step is the so-called "stiff" condition. In practical, the sensitive relationship between flow shear and the value of viscosity. In initializing the model run, for example, we may assume that the slope starts from standstill (with uniform velocity zero). With time, the gravity acceleration will accelerate granular material at every layer, relatively uniformly before the resistance from shear sets on. The shear at the lower boundary increases first and the layer above feel the effects gradually. If time step is too large, unrealistic resistive force may be generated at the lower boundary that may even yield a wrong direction of acceleration! This restraint on time step is the primary concern and reduces the upper limit of time step to 0.001 s.

12.3.2 Advection Schemes for Trace Element Deposition and Momentum Source/Sink

Advection transport is a dominant component of the evolution of flow and trace species (e.g., soil moisture) in the flow stage of landslides. Although the continuous prognostic equation describing advection of a quantity (a species for scalars) in a predetermined flow field assumes the simple form of a first-order partial differential equation, in general its explicit analytic solution is unavailable, and numerical techniques (advection schemes) must be involved in order to provide an approximate prognosis. Among a variety of existing methods there is no single, universal technique that can be recommended for all applications, and the choice of a method always compromises issues of overall accuracy, efficiency, and complexity of computations. We here only focus on the six-order monochromic (non-dissipative) scheme adapted in SEGMENT-Landslide and interested readers are referred to the monographs by e.g., Oran and Boris (1987) and Rood (1987) for practical currently used advection schemes in generic chemistry-transport models. Most of these advanced schemes are based on various improvements only a few elementary methods. Two basic operations: spatial averaging and staggering are commonly applied tricks. For illustration, we consider again the elementary one-dimensional advection equation

$$\frac{\partial q}{\partial t} + c\frac{\partial q}{\partial x} = 0 \tag{12.57}$$

Where c is constant (in space and time) flow velocity and *q(x,t)* is a generic quantity being advected, x and t are spatial and temporal variables.

The approximate solution to Eq. (12.57) can be obtained at time t_{n+1} and location x_i by employing one of the basic finite difference schemes. For example, the forward in time and centered in space (FTCS) approximation,

$$q_i^{n+1} = q_i^n - \frac{c\Delta t}{2\Delta x}\left(q_{i+1}^n - q_{i-1}^n\right) \tag{12.58}$$

Where $\Delta t = t_{n+1} - t_n$ is the time step and $\Delta x = x_{i+1} - x_i$ is the space interval between grid points. This scheme, although being explicit and therefore easy to carry out; however it is unconditionally unstable and therefore not useful for practical purpose. We use it here to illustrate what makes this scheme unstable and as an introduction for practical schemes. Expanding q_i^{n+1}, q_{i+1}^n and q_{i-1}^n in the second-order Taylor sum about q_i^n, and noting that, Eq. (12.57) also implies (further differentiate with respect to time)

$$\frac{\partial^2 q}{\partial t^2} - c^2\frac{\partial^2 q}{\partial x^2} = 0 \tag{12.59}$$

Shows that the FTCS scheme actually approximate the advection equation (Eq. 12.57, with formal solution $q = x - ct$) with the additional negative diffusion term $-c^2\frac{\Delta t}{2}\frac{\partial^2 q}{\partial x^2}$ appearing as a forcing term on the right-hand-side of the equation. This negative diffusion simulated by the FTCS scheme is responsible for the unconditional instability of the numerical solutions. If this defect can be corrected or mitigated, then practical schemes can be obtained. For example, the Lax scheme, where q_i^n is replaced by a spatial averaging of $i-1$ and $i+1$ points at current time level, i.e.,

$$q_i^{n+1} = 0.5\left(q_{i-1}^n + q_{i+1}^n\right) - \frac{c\Delta t}{2\Delta x}\left(q_{i+1}^n - q_{i-1}^n\right) \tag{12.60}$$

Can be interpreted as the FTCS scheme with the centered-in-space approximation to $c^2\frac{\Delta t}{2}\frac{\partial^2 q}{\partial x^2} \sim \frac{(\Delta x)^2}{2\Delta t}\frac{\partial^2 q}{\partial x^2}$, which is added to the right-hand side of the classical FTCS, a positive definiteness of the effective diffusion coefficient ensures it to cancel the negative diffusion, the source of unstable. It is easy to proof that if the CFL number satisfies the condition of

$$\left|\frac{c\Delta t}{\Delta x}\right| \leq 1. \tag{12.61}$$

Although the Lax scheme achieves stable solution, it is only first-order accurate and also suffers from excessive numerical dissipation, an unwanted property for tracer-transport and flow simulations.

The upwind differencing method (name gained because the scheme adapts to wind direction, derivatives always evaluated at upwind side), where Eq. (12.58) now is

$$\begin{aligned} q_i^{n+1} &= q_i^n - \frac{c\Delta t}{\Delta x}\left(q_{i+1}^n - q_i^n\right) \quad \text{for c} < 0 \\ &= q_i^n - \frac{c\Delta t}{\Delta x}\left(q_i^n - q_{i-1}^n\right) \quad \text{for c} > 0 \end{aligned} \tag{12.62}$$

The scheme is conditionally stable, preserves the sign of the initial condition but still is dissipative. The implicit diffusion of the upwind scheme is much less than the Lax scheme. There were efforts by introducing anti-diffusive velocity to achieve second-order accuracy for arbitrary flows.

Thus, both the Lax and the upwind schemes are first-order accurate and lead to smooth but overly diffusive solutions. Second- and higher-order methods improve the accuracy of approximations, but lose the smoothness of the first-order schemes. For example, the second order in time leapfrog method,

$$q_i^{n+1} = q_i^{n-1} - \frac{c\Delta t}{\Delta x}\left(q_{i+1}^n - q_{i-1}^n\right) \tag{12.63}$$

Is stable when CFL condition is satisfied, and also exhibits no implicit dissipation since the Taylor expansion of Eq. (12.63) contains no even-order terms. Disadvantages include excessive dispersion (due to the odd terms of the Taylor expansion), the memory requirements for storing values of q at two previous time levels to compute values at future time level, and the appearance of so-called computational modes related to the fact that odd and even mesh points are completely decoupled (mesh drifting).

The one-step Lax–Wendroff method

$$q_i^{n+1} = q_i^n - \frac{c\Delta t}{2\Delta x}\left(q_{i+1}^n - q_{i-1}^n\right) + \frac{1}{2}\left(\frac{c\Delta t}{\Delta x}\right)^2\left(q_{i+1}^n - 2q_i^n + q_{i-1}^n\right) \tag{12.64}$$

May be viewed as an elaboration of the classic FTCS scheme where the third term on the right-hand side of Eq. (12.64) compensates the negative diffusion implicit in the FTCS scheme. The method is conditional stable, and also free of the computational modes characteristic of the leapfrog scheme; however it is more difficult to

implement for 3D, arbitrary variable flows, in contrast with the leapfrog scheme where such generalizations are straightforward.

In the two-step Lax–Wendroff method (Appendix F), which also successfully avoids mesh drifting (by introducing neighboring grid connection) and only produces only limited dissipation, the advected variable at future time level and mesh center point i is calculated from introducing an intermediate time steps and mesh points (not detailed here; see Appendix F for the sample code). The advection scheme has direct relevance to Sect. 5.1.3.

In summary, the FTCS scheme is unstable, no matter how small the time step one uses. The solution obtained with the upwind method are positive and free of oscillations, but are strongly diffusive. The leapfrog method is not diffusive, but can result in non-physical (negative) q. This negative values, if not timely filtered out, will rapidly dominate the solution. The Lax–Wendroff method, compared with leapfrog, has moderate negative waves, and, compared with upwind scheme, moderate diffusion. But negative q still exists. The problem of unphysical negative mixing ratios is generally addressed by regularly applying numerical filters to the solution.

Specific methods in SEGMENT-Landslide.

12.3.3 *Smoothers and Filters for Stable and Accurate Numerical Integration*

Asselin (1972) time domain filter is crucial for a stable solution. Recent improvement from P. Williams also takes the conservative properties (of energetics of flow) into consideration.

Time domain filters are designed intend to control computational and high frequency physical (sound waves) modes arising in time integrations.

$$\overline{F_c(n)} = F(n) + 0.5\mu(F(n-1) + F(n+1) - 2F(n)) \tag{12.65}$$

μ is set to be between 0.1 and 0.3 in SEGMENT-Landslide and smooth solution is obtained. The filter very quickly removes the computational mode and also is very useful in damping high-frequency physical modes such as sound waves.

In addition, SEGMENT-Landslide offers numerical smoothing in the computational space. Computational smoothing is designed to remove the small scale noise of computational origin (e.g., advection-induced overshoots and undershoots described in Sect. 12.3.1; energy cascade towards small scales due to nonlinear instability). However, because of its non-physical origin, the computational smoothing should be applied least frequent to avoid affecting the physical solution. With the total mixing partitioned into separate parts, the conservation equations (for momentum, moisture and temperature) may be formally written as

$$\frac{\partial(\rho q)}{\partial t} \approx J\left(D_{q1} + D_{q2} + D_{q3}\right) \tag{12.66}$$

where $J = D(cal.\ Space\ dimensional\ variables)/D(physical\ space\ x,y,z)$ is three dimensional transformation Jacobian (map factor, smoothing is carried in calculation space), the D_{q1} represents physical mixing, D_{q2} the second and/or fourth order computational mixing and D_{q3} is upper-level Rayleigh type damping. Here q is one of u, v, w, T or moisture content.

SEGMENT-Landslide allows second- and fourth-order computational mixing/smoothing. Theoretically, the higher the smoothing order, the more efficient the short wavelength waves are damped. Hence, fourth order mixing is preferred because it damps out short wavelength noise more selectively than the second order mixing. Practically, however, high order smoothing is more difficult to implement, especially near the boundaries of staggered mesh grids.

In implementation, the fourth order computational mixing terms have the form

$$JD_{q2} = -K_{Hori}\left[\frac{\partial^4}{\partial x^4} + \frac{\partial^4}{\partial x^4}\right]\rho q - K_{Vertical}\left[\frac{\partial^4}{\partial z^4}\right]\rho q \tag{12.67}$$

To discretize Eq. (12.67) in the finite difference form, it is convenient to define a finite operator as

$$\delta_s^2 q = \frac{q_{i+1} + q_{i-1} - 2q_i}{(\Delta s)^2}, \tag{12.68}$$

where s denotes one of the independent spatial (computational space) variables x, y or z.

Because SEGMENT-Landslide is on staggered grids, the finite difference formulation of Eq. (12.67) for u,v, w and for a scalar (T) is different:

$$\begin{aligned} JD_{u2} = &-K_{Hori}\left[\delta_x^2\left(\delta_x^2(u\overline{\rho}^x)\right) + \delta_y^2\left(\delta_y^2(u\overline{\rho}^x)\right)\right] \\ &- K_{Vertical}\left[\delta_z^2\left(\delta_z^2(u\overline{\rho}^x)\right)\right], \text{ and} \end{aligned} \tag{12.69}$$

$$JD_{T2} = -K_{Hori}\left[\delta_x^2\left(\delta_x^2(T\overline{\rho}^s)\right) + \delta_y^2\left(\delta_y^2(T\overline{\rho}^s)\right)\right] - K_{Vertical}\left[\delta_z^2\left(\delta_z^2(T\overline{\rho}^s)\right)\right] \tag{12.70}$$

Note that the averaging is respectively at vector and scalar (s) grids.

Since the fourth-order terms cannot be directly evaluated at the first grid point inside the boundary. Prescribed boundary conditions are needed, or alternatively, a second order substitute is needed. The latter may introduce erroneous sources or sinks at the transition between the two schemes. In SEGMENT-Landslide, we try to overcome this difficulty by making further assumption of the intermediate terms such as $\left(\delta_y^2(u\overline{\rho}^x)\right)$ so that the mixing terms can be evaluated up to the first grid point

inside the boundary, and the formulation retains its conservative properties. In the case of periodic (or symmetric) boundary conditions, the assumption is unnecessary.

The 4th order smoothing given in Eq. (12.67) are computed in two steps (thus intermediate terms in round brackets of Eqs. 12.69 and 12.70). First, the intermediate terms are evaluated at interior grid points of the model domain, and their values at the boundaries are set based on additional assumptions. The mixing terms are then calculated from these intermediate terms, up to the first grid point inside the boundaries. Spliting the calculations into two steps also results in modular design, where each path through the operator involves only three grid points in each direction. This approach facilitates the massively parallel implementation of the SEGMENT code on distributed memory architectures (to be detailed in Sect. 12.4).

Finally, the fourth order horizontal smoothing coefficient K_{hori} can be expressed as $\alpha(\Delta x)^4/\Delta t$. Here α is a non-dimensional coefficient (usually on the order of 0.0001), Δx is horizontal grid scale magnitude (e.g., using a mathematically average over the two horizontal directions), and Δt is the time step size. It also important to note that the mixing/smoothing terms using forward in time integration schemes are only conditionally stable (Pielke 1984).

12.3.4 Diffusion Schemes

In many cases, the energy transport equations and water diffusion equations are diffusion equations. Also, in 3D models, diffusive terms accounts for subgrid mixing. For illustration, consider the one dimensional case given by

$$\frac{\partial q}{\partial t} = \frac{\partial}{\partial x}\left(D\frac{\partial q}{\partial x}\right) \tag{12.71}$$

where $D > 0$ is the diffusion coefficient. If, in a first case, D is assumed to be constant, Eq. (12.71) can be differenced and replaced by the FTCS expression

$$\frac{q_i^{n+1} - q_i^n}{\Delta t} = \frac{D}{(\Delta x)^2}\left(q_{i+1}^n - 2q_i^n + q_{i-1}^n\right). \tag{12.72}$$

The stability criterion for this scheme is

$$\frac{2D\Delta t}{(\Delta x)^2} \leq 1 \tag{12.73}$$

So that the number of time steps required to notice the effect of diffusion on a spatial scale significantly larger than the cell width Δx is usually prohibitive (D usually is 10^{-7} m^2 s^{-1}).

When a fully implicit scheme is used,

$$\frac{q_i^{n+1} - q_i^n}{\Delta t} = \frac{D}{(\Delta x)^2}\left(q_{i+1}^{n+1} - 2q_i^{n+1} + q_{i-1}^{n+1}\right) \tag{12.74}$$

The scheme can be unconditionally stable; a set of simultaneous linear equations has, however, to be solved at each time step t_{n+1}.

$$\alpha q_{i-1}^{n+1} + \beta q_i^{n+1} + \gamma q_{i+1}^{n+1} = q_i^n, \quad i = 1, I \tag{12.75}$$

Where $\alpha = \gamma = -D\Delta t/(\Delta x)^2, \beta = 1 - 2D\Delta t/(\Delta x)^2$, and I again is the number of mesh grids. Supplemented by appropriate boundary conditions at $i = 0$ and $i = I + 1$, this tridiagonal system can be easily solved. If you use large time step (to take advantage of its implicity), then you cannot expect accuracy for details of the small-scale (time) evolution from the initial condition but does yield the correct equilibrium solution for $\Delta t \to \infty$.

Stable solutions with greater accuracy can be obtained using the Crank–Nicholson scheme, in which the right-hand side of Eq. (12.71) is approximated by the average of the explicit and implicit formulation (hence there is a parameter determining the degree of implicitness). see Appendix G for the sample code of 1D.

12.3.4.1 3D Thermodynamic Equation Implicit Solver

The full form of thermodynamic equation in SEGMENT-Landslide reads:

$$\frac{\partial T}{\partial t} + \left(\vec{V} \bullet \nabla\right)T = \frac{1}{\rho_c}\left[\frac{\partial}{\partial x}\left(K_x \frac{\partial T}{\partial x}\right) + \frac{\partial}{\partial y}\left(K_y \frac{\partial T}{\partial y}\right) + \frac{\partial}{\partial z}\left(K_z \frac{\partial T}{\partial z}\right) + 2EA(T')f(\sigma)\sigma_{eff}^2\right] \tag{12.76}$$

Now define forcing $F = -\left(\vec{V} \bullet \nabla\right)T + \frac{E}{\rho_c \nu}\left[2\sigma_{eff}^2\right]$, where $\nu = 1/A(T)/f(\sigma)$. Then Eq. (12.76) can be formally written as

$$\frac{\partial T}{\partial t} = \frac{1}{\rho_c}\left[\frac{\partial}{\partial x}\left(K_x \frac{\partial T}{\partial x}\right) + \frac{\partial}{\partial y}\left(K_y \frac{\partial T}{\partial y}\right) + \frac{\partial}{\partial z}\left(K_z \frac{\partial T}{\partial z}\right)\right] + F \tag{12.77}$$

We now differentiate Eq. (12.77) as

$$\frac{T_i^{n+1} - T_i^n}{\Delta t} = \eta \frac{D_i \frac{T_{i+1}^{n+1} - T_i^{n+1}}{\Delta x_i} - D_{i-1} \frac{T_i^{n+1} - T_{i-1}^{n+1}}{\Delta x_{i-1}}}{\Delta \bar{x}\Big|_*^{n+1}} + (1-\eta) \frac{D_i \frac{T_{i+1}^n - T_i^n}{\Delta x_i} - D_{i-1} \frac{T_i^n - T_{i-1}^n}{\Delta x_{i-1}}}{\Delta \bar{x}\Big|_*^n} + F_i^n \tag{12.78}$$

Where $\Delta\overline{x} = 0.5(\Delta x_i + \Delta x_{i-1})$. The first part on the right-hand side of Eq. (12.78) is the implicit part and the second part is explicit part, with η the degree of implicitness. For example, when $\eta = 1$, Eq. (12.78) is unconditionally stable and the scheme is completely implicit. In general, stability requirement is

$$\Delta t \leq \frac{(\min(\Delta\overline{x}))^2}{4\max(D_i)} \tag{12.79}$$

where D_i is the diffusion coefficient on the ith spatial grid. Re-organizing (12.78) according to "time indices," it is easy to obtain,

$$AT_{i+1}^{n+1} + BT_i^{n+1} + CT_{i-1}^{n+1} = HT_{i+1}^n + GT_i^n + LT_{i-1}^n + F_i^n \Delta t \tag{12.80}$$

where $A = -\frac{\eta\Delta t}{\Delta\overline{x}} \frac{D_i}{\Delta x_i}$,

$$B = 1 + \frac{\eta\Delta t}{\Delta\overline{x}} \left(\frac{D_i}{\Delta x_i} + \frac{D_{i-1}}{\Delta x_{i-1}} \right),$$

$$C = \frac{\eta\Delta t}{\Delta\overline{x}} \left(\frac{D_{i-1}}{\Delta x_{i-1}} \right),$$

$$H = \frac{(1-\eta)\Delta t}{\Delta\overline{x}} \left(\frac{D_i}{\Delta x_i} \right),$$

$$G = 1 - \frac{(1-\eta)\Delta t}{\Delta\overline{x}} \left(\frac{D_i}{\Delta x_i} + \frac{D_{i-1}}{\Delta x_{i-1}} \right), \text{ and}$$

$$L = \frac{(1-\eta)\Delta t}{\Delta\overline{x}} \frac{D_{i-1}}{\Delta x_{i-1}}$$

If we further define $A = \frac{\eta\Delta t}{\Delta\overline{x}} \frac{D_i}{\Delta x_{i1}}$,

$$B = 1 + A + C,$$

$$C = \frac{\eta\Delta t}{\Delta\overline{x}} \frac{D_{i-1}}{\Delta x_{i-1}},$$

$$H = \frac{(1-\eta)\Delta t}{\Delta\overline{x}} \frac{D_i}{\Delta x_i},$$

$$F = \frac{(1-\eta)\Delta t}{\Delta\overline{x}} \frac{D_{i-1}}{\Delta x_{i-1}}$$

$$L = \frac{(1-\eta)\Delta t}{\Delta\overline{x}} \frac{D_{i-1}}{\Delta x_{i-1}}$$

The traditional tri-diagonal solver works this way, in matrix form,

$$\begin{pmatrix} B_1 & \mathbf{C_1} & & & & & & & & & \\ A_2 & B_2 & C_2 & & & & & & & & \\ & A_3 & B_3 & C_3 & & & & & & & \\ \cdots & \cdots & \cdots & \cdots & \cdots & \cdots & \cdots & \cdots & . & & \\ & & & A_{M-2} & B_{M-2} & C_{M-2} & & & & & \\ & & & & A_{M-1} & B_{M-1} & C_{M-1} & & & & \\ & & & & & A_M & B_M & & & & \end{pmatrix}^{n+1} \begin{pmatrix} T_1 \\ T_2 \\ T_3 \\ T_4 \\ \cdots \\ T_{M-1} \\ T_M \end{pmatrix}$$

$$= \begin{pmatrix} G_1 & H_1 & & & & & & & & & \\ L_2 & G_2 & H_2 & & & & & & & & \\ & L_3 & G_3 & H_3 & & & & & & & \\ \cdots & \cdots & \cdots & \cdots & \cdots & \cdots & \cdots & \cdots & . & & \\ & & & L_{M-2} & G_{M-2} & H_{M-2} & & & & & \\ & & & & L_{M-1} & G_{M-1} & H_{M-1} & & & & \\ & & & & & L_M & G_M & & & & \end{pmatrix}^{n} \begin{pmatrix} T_1 \\ T_2 \\ T_3 \\ T_4 \\ \cdots \\ T_{M-1} \\ T_M \end{pmatrix}$$

$$+ F \tag{12.81}$$

At a given time level, right-hand side is known. Using boundary conditions, an up-down process obtain all T's.

The numerical methods (Eq. 12.75) can be easily generalized to cases with variable diffusion coefficient *D(x)*. In this case, the right-hand side of Eq. (12.71) can be differenced as

$$\frac{\partial}{\partial x}\left(D\frac{\partial q}{\partial x}\right) \approx \left[D_{i+1/2}(q_{i+1}-q_i) - D_{i-1/2}(q_i - q_{i-1})\right]/(\Delta x)^2 \equiv D'' \tag{12.82}$$

If FTCS method is used, the stability criterion is

$\Delta t < \min\left[\frac{(\Delta x)^2}{2D_{i+1/2}}\right]$. Implicit scheme again is unconditionally stable.

When 3D diffusion is considered, a time splitting method (also called method of fractional steps) is an appropriate way to proceed. For example, in the alternating-direction implicit method, which is second-order accurate in time and space and is unconditionally stable, each time step is divided in K steps of size $\Delta t/K$, where K represents the spatial dimension (here 3) of the problem at hand. The idea is, at each substep, to treat a different dimension implicitly, while the others are treated explicitly.

$$\frac{\partial q}{\partial t} = \frac{\partial}{\partial x_1}\left(D_1\frac{\partial q}{\partial x_1}\right) + \frac{\partial}{\partial x_2}\left(D_2\frac{\partial q}{\partial x_2}\right) + \frac{\partial}{\partial x_3}\left(D_3\frac{\partial q}{\partial x_3}\right) \tag{12.83}$$

The solution at time t_{n+1} is obtained in three successive steps

$$\frac{q_i^{n+1/3} - q_i^n}{\Delta t/3} = \left(D_1^{''}\right)^{n+1/3} + \left(D_2^{''}\right)^n + \left(D_3^{''}\right)^n \tag{12.84a}$$

$$\frac{q_i^{n+2/3} - q_i^{n+1/3}}{\Delta t/3} = \left(D_1^{''}\right)^{n+1/3} + \left(D_2^{''}\right)^{n+2/3} + \left(D_3^{''}\right)^{n+1/3} \tag{12.84b}$$

$$\frac{q_i^{n+1} - q_i^{n+2/3}}{\Delta t/3} = \left(D_1^{''}\right)^{n+2/3} + \left(D_2^{''}\right)^{n+2/3} + \left(D_3^{''}\right)^{n+1} \tag{12.84c}$$

Where $(D_k^{\prime\prime})^n$ is evaluated from the corresponding *1D* diffusion term evaluated at time n. At each of the $K(=3)$ substeps, a tridiagonal system needs to be solved. Actually, operator splitting techniques are widely used in the SEGMENT-Landslide. For example, each physical process can be treated separately (advective and diffusion processes) and appropriate numerical techniques can be used for each of these processes.

12.3.4.2 3D Richards' Equation Numerical Solver

The numerical scheme is exactly parallel to the thermodynamic equation except that the distributed root transpiration and evaporation are treated as source terms. In addition, time step is minimized so that the wetting and drying processes are simulated accurately, rather than only the climatological states. A special simplified case will be further discussed in Sect. 12.5.2.

12.4 Parallel Computing and Parallelism in SEGMENT-Landslide

Parallel computing is use of multiple processors or computers working together on a common task. That is, each processor works on its section of the problem and processors can exchange information. Regional, high resolution run of SEGMENT-Landslide is demanding on memory and CPU time. Multiple instruction, multiple data (MIMD) type of parallel computing is an ideal option. Especially for real-time operational (landslide intelligence network) applications, parallel computating would be the only means at present technology level. There are different ways to organize multiple computers together (Fig. 12.5). They are different in their memory model: shared memory vs. distributed memory (nearly all parallel machines these days fall into one of the two). On shared memory machines, all processors have access (through bus or crossbar) to a pool of shared memory. On distributed machines, each (group) of processors has its own local memory. To exchange data between processors, message passing is needed. Processor/Memory units are organized together through various topological interconnects (networks).

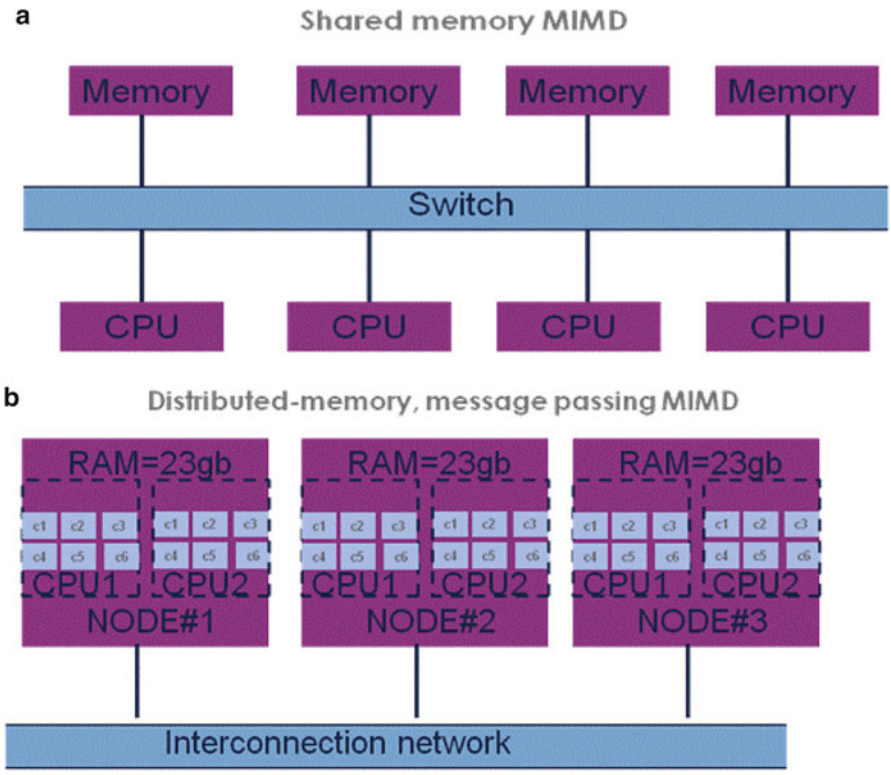

Fig. 12.5 Schematic illustration of shared-memory (**a**) and distributed-memory, message (**b**) multiple instruction/tasking multiple data (MIMD) architectures. In (**b**), nodes are connected by network cables for message passing. On each node, there are two CPUs, each of which has six cores. The 12 cores have access to the 23 Gb memory on each node. Memories are distributed on different nodes. Use massage passing, task is subdivided to nodes and processors. In coding, same piece of code is read by all nodes and each carry out different sections/segments of the task. SEGMENT-Landslide is designed using MPI strategy and suitable for execution on distributed memory architectures

SEGMENT-Landslide is designed for distributed memory systems according to the following strategy.

For a good performance (computational load balance), there are two general types of decompositions: functional and domain decomposition (Johnson et al. 1994). SEGMENT-Landslide chose the domain-decomposition strategy because this strategy is more suitable for current distributed memory system (to be elaborated below).

Domain decomposition involves assigning subdomains of the full computational grid to separate processors and solving all prognostic and diagnostic equations for that subdomain on that processor. No global information is required at any particular subdomain. Inter-processor communications are needed only at the boundaries of the subdomains. The inner border of a subdomain requires the outer border of the

adjacent subdomain during a time step because of spatial finite differences. The outer border data resident in the local memories of adjacent processors are supplied by passing messages between processors.

Even thorough all processors run the same set of code, domain decomposition is subject to load imbalances when the computational load is data dependent. As spatial –intermittent physical phenomena, landslides do not occur for many grids. Thus, many dynamic processes are not triggered for those spatial domains that are stable. In super computing, one situation needs to be avoided is that one node finishes later and other nodes have to wait it. Since it is impractical to divide spatial domain unevenly, SEGMENT-landslide makes the code scalable by making the calculational at all type of situations (all land cover types, slopes, and sliding material properties) identical, independent of what is actually occurring. The "operator" style of implementation minimizes work load difference due to data-dependent branching.

The most severe constraint on parallelism is the communication-to-computation ratio. Subdomains (computational) are with overlaps with neighbors. Or, the physical 3D cubes with necessary halos (because spatial differential schemes necessitates). The halo region needs inter-node communication at each integration time step. Too much inter-node communication reduces the supercomputing efficiency drastically. The ideal way of domain subdivision is to minimize the percentage of the halo region. So, one-dimensional (along the numerous dimension and fixed size in the model, e.g., the z-dimension of layered 3D models.) is a better strategy. However, for 3D landslide models, the most grid dimension is in the horizontal directions. Thus a two dimensional decomposing strategy of the computational domain is followed in SEGMENT-Landslide. Depending on network transmission rates (depending on the characteristics of the communication network linking the processors), proper weighing is needed in subdividing the calculational domain. The reason that the wall clock time can not be reduced linearly as processor numbers increase is primarily because message passing takes up increasing time (at least cannot be reduced linearly). So far, we have run SEGMENT-Landslide at OU-OSCAR, Curtin's iVEC and once on UT-Ranger, three different parallel architectures and gradually improved the performance of the model.

12.5 Variational Data Assimilation Ability of SEGMENT-Landslide

We are living in a data rich era, especially the remote sensing data. For example, one geostationary satellite can produce 1 Tb of observational data in its infrared and visible bands one single day. How to extract the most useful information from them is a challenge.

In numerical modeling context, there generally are two usages, one is for model verification and another is better initializing the model state variables. In both

procedures, model is adjusted in certain way to better fit the observational data. The data are assumed to have known uncertainty levels (error characteristics). Ensemble Kalman Filters (EnKF, a sequential data assimilation method), 3D data assimilation (an analysis of one time level of the fields), and 4D variational data assimilation (dealing with scattered observations over space and time) are different approaches for perform data assimilation.

The EnKF applies an ensemble of forward model states to represent the error statistics of the model estimate, it applies ensemble integrations to predict the error statistics forward in time, and it uses an analysis scheme which operates directly on the ensemble of model states when observations are assimilated. It has the advantage of being easy implementation (standardized procedures that do not involve changes to forward model itself) and efficient in executing. The next tier of complexity is 3D-Var data assimilation, which is an analysis procedure trying to produce an "optimal" estimate of the true atmospheric state at analysis time through iterative solution of a prescribed cost-function (Ide et al. 1997). 4D-Var data assimilation, being hard to code and resource consuming in execution, has the advantage of being able to utilize sparse information (observations) irregularly distributed spatially and temporally (e.g., there are missing data). The following section focuses on the 4D-Var data assimilation procedure of the SEGMENT-Landslide. In fact, the utility code of the 4D-Var is sufficient to perform 3D-Var and EnKF type of data assimilation. No extra modification to forward model is needed for performing 3D-Var and EnKF types of data assimilation. 4D-Var, however, involves complicated re-code of adjoint model strictly according to forward model. For landslide research, because the sliding stage is a relatively short stage of the entire slope evolving cycle, no reliable observations are four available during the movement stage. However, elevation changes before and after the sliding are collectable and can be used to deduce the material property of the slope. This improved understanding of the slope mechanical properties are valuable in make future predictions for the region. This idea also is the backbone for landslide information (intelligence) system elaborated in Chap. 10.

12.5.1 Basic Theory of Adjoint Based 4D-Var Procedure

12.5.1.1 A General Statement of Sensitivity Study and Data Assimilation Using Adjoint

Sensitivity studies and data assimilation may at first sight seem like rather different subjects. Using a variational optimization approach, adjoint model can however be developed for use for both (Errico 1997). In the following, a general variational framework is described, of which the adjoint sensitivity and variational data assimilation are special cases.

Consider a physical model that is represented in vector form by the following system of coupled nonlinear differential equations:

$$\frac{\partial U}{\partial t} = F(U, \alpha) \tag{12.85}$$

where $U(t)$ is an $N_s \times 1$ state vector (where N_s is the number of state variables augmented to include all spatial locations for a distributed physical system) and F is an $N_s \times 1$ nonlinear vector operator that is a function of the states themselves and the $N_p \times 1$ vector of time invariant spatially distributed model parameters α. Forcings such as the observed meteorological inputs are included in F.

We next define a scalar "measurement importance functional" (Backus and Gilbert 1970; Marchuk 1981) as

$$J = \iint_{\Sigma} \phi(U, \alpha) dx dt \tag{12.86}$$

where ϕ is a nonlinear function of the state variables and model parameters, x is the spatial variable, and t is time. In sensitivity study J may represent a quantity of interest (e.g., diurnally averaged evaporation), whereas for data assimilation it would represent the cost function, which is generally a least square performance metric that indicates the difference between model predictions and measurements. In either case, we are generally interested in obtaining sensitivity derivatives (Errico 1997). For sensitivity studies, these derivatives give the sensitivity of the model response to various model parameters. This gives insight into the relative sensitivities to different parameters as well as which physical processes are most important in the system. In data assimilation we generally need the derivatives of the least square cost function with respect to target parameters (also called control variables) as input to an optimization scheme.

With the above general task in mind, we first adjoint the model to the "measurement importance functional" using a vector of Lagrange multipliers (Yu and O'Brien 1991) λ^T:

$$L = J + \iint_{\Sigma} \lambda^T \left[\frac{\partial U}{\partial t} - F(U, \alpha) \right] dx dt \tag{12.87}$$

where T represents transpose operator, and L is the Lagrangian which transforms a constrained minimization problem into an unconstrained problem.

We now take the first order variation of L with respect to U and α.

$$\delta L = \iint_{\Sigma} \left\{ \left[-\frac{\partial \lambda^T}{\partial t} - \lambda^T \frac{\partial F}{\partial U} + \frac{\partial \phi}{\partial U} \right] \delta U + \left[\frac{\partial \phi}{\partial \alpha} - \lambda^T \frac{\partial F}{\partial \alpha} \right] \delta \alpha \right\} dt dx + \lambda^T \delta U \Big|_{t_0}^{t_1} \tag{12.88}$$

where we assumed that the assimilation period is $[t_0, t_1]$. If we denote the values of

the Lagrange multiplier at the initial and final time as λ_0 and λ_f, and assume $\lambda_f = 0$ (Thacker and Long 1988), Eq. (12.88) can be simplified as

$$\delta L = \iint_{\Sigma} \left\{ \left[-\frac{\partial \lambda^T}{\partial t} - \lambda^T \frac{\partial F}{\partial U} + \frac{\partial \phi}{\partial U} \right] \delta U + \left[\frac{\partial \phi}{\partial \alpha} - \lambda^T \frac{\partial F}{\partial \alpha} \right] \delta \alpha \right\} dt dx - \lambda_0^T \delta U(t_0). \tag{12.89}$$

A minimization of L requires that

$$\begin{cases} -\dfrac{\partial \lambda}{\partial t} - \dfrac{\partial F^T}{\partial U} \lambda + \dfrac{\partial \phi}{\partial U} = 0 \\ \dfrac{\partial L}{\partial \alpha} = \displaystyle\int \left[\frac{\partial \phi}{\partial \alpha} - \lambda^T \frac{\partial F}{\partial \alpha} \right] dt = 0 \\ \dfrac{\partial L}{\partial U(t_0)} = \lambda_0 = 0 \end{cases} \tag{12.90}$$

The Eq. (12.90a) is called adjoint system (of Eq. 12.85) because the Lagrange multipliers are called the adjoint variables. The adjoint model must be integrated backward in time as a terminal value problem. Note that the homogeneous part of the linear differential equation (the first two terms on the left-hand side of Eq. 12.90a) is totally determined by the Jacobian of the forward model with respect to U $\left(\text{i.e.}, \frac{\partial F^T}{\partial U}\right)$, while the forcing $\frac{\partial \phi}{\partial U}$ is dependent on the gradient of the model response. It is clear that the homogeneous adjoint model (so called adjoint system) can be constructed separately (see Chapter 3 of Ren 2004 Ph.D. Thesis) and then used in conjunction with different measurement importance functionals.

Our ultimate goal is $\frac{\partial L}{\partial \alpha}$, and $\frac{\partial L}{\partial U(t_0)}$ approach zero. However, once λ is known by the integrating of the adjoint model, Eqs. (12.90b) and (12.90c) do provide the way to find the gradient of L with respect to parameter α and initial condition of the control variable $U(t_0)$ during the minimization process. Herein exists one of the primary benefits of the adjoint method in that, once the adjoint model is developed, all of the derivatives can be obtained efficiently through a single forward model run and a single adjoint model run. This is possible by the fact that the adjoint model is developed from the forward model and propagates the sensitivity information backward in time over the model integration.

Closely related to the adjoint model is tangent linear model (TLM, will soon be defined in Eq. 12.92). For the convenience of the following discussion, the forward system is written in discrete integration form (evolution form) rather than in differential form as in Eq. (12.85). The conception of small perturbation can be found in Marchuk (1994), among many other sources. M is designated for the discrete system of F and x is designated for model control variable U.

Pick a control vector $c \in R^n$ and let $\overline{x}(0) = c$, the orbit can be computed using $x(k) = M(x(k-1), \alpha) = \ldots = M^{(k)}(c + \delta c, \alpha)$. The actual evolution of the perturbation is given by

$$x(k) - \overline{x}(k) = M^k(c + \delta c, \alpha) - M^k(c, \alpha). \tag{12.91}$$

Since the computation of $M^k(x, \alpha)$ is very difficult in general, this quantity is usually approximated using the first order Taylor series expansion:

$M(x(0), \alpha) = M\left(\overline{x(0)} + \delta c, \alpha\right) \approx M\left(\overline{x(0)}, \alpha\right) + \mathrm{J_M}\left(\overline{x(0)}, \alpha\right)\delta c$. Here $\mathrm{J_M}$ is the Jacobian of M with respect to x.

Similarly $\overline{x}(1) + \delta x(1)$ is an approximation to $x(1)$ to a first order accuracy. Thus, $M(x(1), \alpha) = M\left(\overline{x(1)} + \delta x(1), \alpha\right) \approx M\left(\overline{x(1)}, \alpha\right) + \delta x(1)\mathrm{J_M}\left(\overline{x(1)}, \alpha\right)$. By denoting $\delta x(2) = \delta x(1)\mathrm{J_M}\left(\overline{x(1)}, \alpha\right)$, $\overline{x}(2) + \delta x(2)$ is thus an approximation to $x(2)$.

Continuing this argument, inductively defining

$$\delta x(k+1) = \delta x(k)\mathrm{J_M}\left(\overline{x(k)}, \alpha\right), \tag{12.92}$$

results in $\overline{x}(k+1) + \delta x(k+1)$ as an approximation to $x(k+1)$.

Note that Eq. (12.92) is a non-autonomous linear dynamic system where the one step transition matrix $\mathrm{J_M}(\overline{x}(k), \alpha)$ is evaluated along the base state. Equation (12.92) is known as the tangent linear system (TLM). For convenience, introducing the following notation $\mathrm{J_M}(k) = \mathrm{J_M}(\overline{x}(k), \alpha)$, then Eq. (12.92) can be rewritten as $\delta x(k+1) = \delta x(k)\mathrm{J_M}(k) = \mathrm{J_M}(k)\mathrm{J_M}(k-1)\mathrm{J_M}(k-2)\ldots\mathrm{J_M}(1)\mathrm{J_M}(0)\delta c$. If one further defines, for $i \le j$, $\mathrm{J_M}(i:j) = \mathrm{J_M}(j)\mathrm{J_M}(j-1)\ldots\mathrm{J_M}(i)$, Eq. (12.92) can be further reduced to $\delta x(k+1) = \mathrm{J_M}(0:k)\delta c$, or $\delta x(k) = \mathrm{J_M}(0:k-1)\delta c$.

The iterative scheme that defines the TLM as in Eq. (12.92) can also be written in a matrix–vector form:

$$F\delta x = b, \tag{12.93}$$

where F is an N by N block partitioned matrix given by

$$F = \begin{bmatrix} I & O & O & & \\ -\mathrm{J_M}(1) & I & O & & \\ & -\mathrm{J_M}(2) & I & O & \\ O & & -\mathrm{J_M}(3) & I & O \\ \ldots\ldots & \ldots\ldots & & & \\ & O & & -\mathrm{J_M}(N-1) & I \end{bmatrix}, \quad \delta x = (\delta x(1), \delta x(2), \delta x(3), \quad \delta x(N))^T,$$

and b is a block partitioned vector given by $b = (J_M(0)\delta c, 0, 0, \ldots 0)^T$. Interestingly, homogeneous adjoint model is formally a transpose of the TLM model. For detailed derivations and explanations of the relationship between TLM and adjoint model (ADM), the reader is suggested to read Appendix B of Ren (2004).

As a review to 4DVAR data assimilation literature (e.g., LeDimet and Talagrand 1986; Courtier and Talagrand 1987), we conclude that: Applying the adjoint method, a model trajectory is brought as close as possible to the data by varying control variables. The closeness of model trajectory to a period of data is quantified by a cost function. An iterative algorithm is used to minimize the cost function: Starting from a first guess, the value of the cost function and its gradient with respect to the control variables are used to improve the estimation of the vector of the control variables. Under a series of forcing composed of the model-data misfits, a backward integration of the adjoint model provides the gradient vector of cost function with respect to control variables.

Sensitivity studies and data assimilation are actually closely related. McLaughlin (1995) generalized a framework that includes the cases of control variables (variables that have influence to cost function and usually is the objective of retrieval) are initial conditions, model parameters, and even model error (see also, Zupanski 1997). The adjoint (backward) method is a powerful tool for studying sensitivity. Using a nonlinear forward model and the adjoint of its tangent linear model (TLM), one can calculate the sensitivity of a chosen forecast metric (e.g., precipitation rate, accumulated precipitation, average temperature) to all model input variables at all grid points simultaneously (see, e.g., Errico 1997; Rabier et al. 1993). The sensitivity is expressed in terms of the gradient of the metric with respect to the input variables, and thus a single run of the forward model and its adjoint can reveal the sensitivity to different variables as well as the regions of maximum sensitivity.

Sensitivity studies using an adjoint model are not without limitations, the most important being the necessity of linearization. The adjoint based on the TLM may become invalid when the time period studied is long and/or when the initial perturbation is large so as to cause solution bifurcation (M. Xue, personal communication).

12.5.1.2 4DVAR Procedure and Definitions of a Cost Functions

Rewrite Eq. (12.71) as $x^f(t_i) = M_{i-1}(x^a(t_{i-1}))$ represents the (nonlinear) model forecast that advances from the previous analysis time t_{i-1} to the current t_i. Assume the observations distributed within a time interval $(t_0 - t_n)$ will be used. The cost function includes a term measuring the distance to the background at the beginning of the interval, and a summation over time of the cost function for each observational increment computed with respect to the model integrated to the time of the observation:

$$\begin{aligned} J(x(t_0)) = &\frac{1}{2}\left(x(t_0) - x^b(t_0)\right)^T B^{-1}\left(x(t_0) - x^b(t_0)\right) \\ &+ \frac{1}{2}\sum_{i=0}^{N}\left(H(x_i) - y_i^o\right)^T R_i^{-1}\left(H(x_i) - y_i^o\right) \end{aligned} \tag{12.94}$$

where N is the number of observational vectors y_i^o distributed over time. H is an operator through which model output is directly comparable with observations. B and R are relative uncertainty (standard deviations) of background estimates and observational errors.

In Eq. (12.94), we assume that the control variable (the variable with respect to which the cost function is minimized) is the initial state of the model at the beginning of the time interval, $x(t_0)$, whereas the analysis at the end of the interval is given by the model integration from the solution. In this sense, the model is used as a strong constraint, i.e., the analysis solution has to satisfy the model equations. In other words, 4D-Var seeks the initial condition such that the forecast best fits the observations within the assimilation interval. The fact that the 4D-Var method assumes a perfect model is a disadvantage since (for example) it will give the same credence to older observations at the beginning of the interval as to newer observations at the end of the interval

For parameter retrieval in SEGMENT-Landslide, the objective is to estimate the granular parameters that minimize the model-measurement misfit, where we assume no model error and perfect model parameters (i.e., model strong constraint in Zupanski 1997). For the granular-state variable retrieval problem using observed surface elevation changes observations as the constraint, the cost function is constructed as quadratic function of surface elevation. They are related through model dynamics to the granular mechanical properties. Define $U = (d, \rho, \psi, \mu)^T$,

$$J(U) = \sum_{i=1}^{N} \left(\frac{h_i^o - h_i^f(U)}{\sigma_h^o} \right)^2 + \left(U - \overline{U}\right)^T \sigma_a^{-2} \left(U - \overline{U}\right), \tag{12.95}$$

where N is the number of observations during an assimilation period, h represents surface elevation, superscript "O" means observation, superscript "f" means model forecast, superscript T means matrix transpose. σ^o's represent the relative confidence accredited to each observation and prediction pair (typically the standard deviation of the observational error). $\overline{U}$ is the prior estimate of the control variable vector and σ_a^2 is the prior error covariance. The two σ's weight the model–measurement misfit and prior estimate misfit, respectively, based on the uncertainty involved in each component. For example, if the measurement error was very small and the prior knowledge of the initial conditions was poor, then we would expect the estimation procedure to change greatly the initial guess U in an effort to fit the model output to the measurements. When many observations are available in the assimilation period or assimilation window, the background analysis term, i.e., the last term in Eq. (12.95), is less valuable since the situation of retrieval problem tends to be over-determined. This tends to be the case for our 1-D problem because of the relatively small degree of freedom. Also, for granular mechanical parameters, we usually lack proper background analyses.

Following a similar treatment as in Subsection 2.3.1 of Ren (2004), one obtains the adjoint model as

$$\frac{\partial \lambda}{\partial t} = -\frac{\partial F}{\partial U}\lambda - 2\frac{\partial h}{\partial U}\left(\sigma_h^o\right)^{-2}. \tag{12.96}$$

The adjoint model is integrated backward in time to obtain λ, the gradient of the objective function with respect to the initial conditions can then be computed as

$$\frac{\partial L}{\partial U(t_0)} = -\lambda_0 + 2\left(U - \overline{U}\right)\sigma_a^{-2} \tag{12.97}$$

Using this framework, the estimation procedure, or the procedure of optimally retrieving the initial state U, is as follows.

1. Based on the prior guesses of the initial conditions $\overline{U(t_0)}$, integrate the forward model over a chosen assimilation window in which observations are used. This forward integration yields *U(t)*, which is saved for use by the adjoint model integration.
2. Using the model-measurements misfit as forcing, integrate the adjoint Eq. (12.96) backward in time to obtain adjoint vector λ_0.
3. Compute the gradient of the objective function with respect to each initial condition according to Eq. (12.97).
4. Using certain optimization algorithm, such as the quasi-Newton methods (Shanno and Phua 1980; Gill and Murray 1979; Liu and Nocedal 1989; and Buckley and Lenir 1983), determine an optimal increment δU, which is added to the prior guess of U to obtain a new $U(t_0)$. This procedure is repeated until the convergence is reached. A forward model run with the obtained initial conditions will give quantities other than the control or analysis variables. Figure 12.6 is a flow chart of the 4DVAR data assimilation scheme.

We know see that 4D-Var is an optimal and relatively efficient (relative to e.g., Kalman filter[1]) assimilation algorithm. The evaluation of the 4D-Var observation cost function and its gradient, $J(U)$ and $\nabla J_0(U)$, requires one direct model integration from t_0 to t_n (data assimilation window) and one suitably modified (forced by the differences between observation and forward model) adjoint integration made of transposes of the tangent linear model time-stepping operators M_i (133). Although very powerful, 4D-Var procedure is not being able to "correct" forward

[1] Proof of the equivalent of an adjoint based 4D-Var and a Kalman filter.

The most important advantage of the 4D-Var is that if we assume that the forward model is perfect, and that the a priori error covariance at the initial time B_0 is correct, it can be shown that the 4D-Var analysis at the final time is identical to that of the extended Kalman Filter (Lorenc, 1986; Daley, 1991). This means that implicitly 4D-Var is able to evolve the forecast error covariance from B_0 to the final time.

Daley, R., 1991. Atmospheric data analysis. Cambridge University Press, Cambridge, P457.

Lorenc, A., 1986. Analysis methods for numerical weather prediction. Quart. J. Roy. Meteor. Soc., 112, 1177–1194.

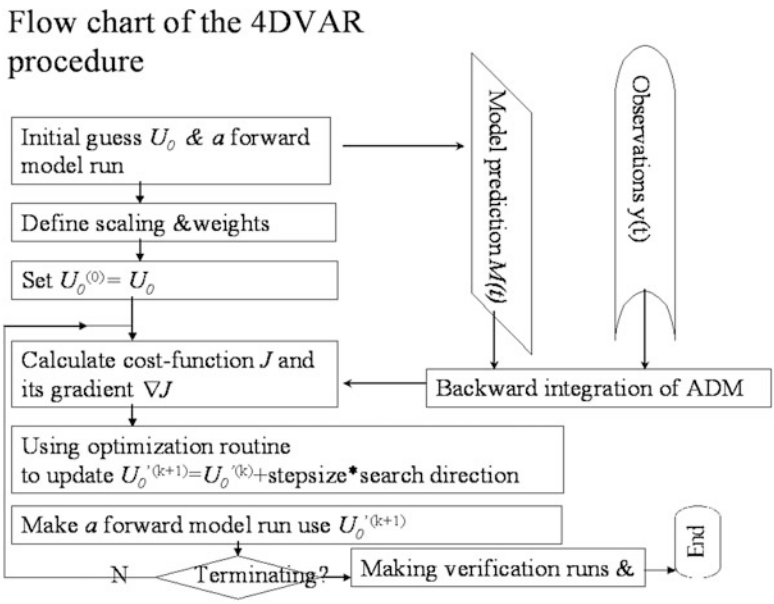

Fig. 12.6 Flow chart of the main minimization routine. The adjoint operation, which can also be viewed as a multidimensional application of the chain-rule for partial differentiation, permits efficient estimation of the gradients of the cost-function. Modern minimization techniques (e.g., quasi-Newton, preconditioned conjugate gradient methods) are available to efficiently coordinate cost function, gradient and the analysis information to optimize the control variables

model defects. It works only under the assumption that the model is perfect and problems can be expected if model errors are large. The model parameter tuning is data oriented. Most demandingly, it requires the implementation of the rather special adjoint model. This can be a lot of work if the forward model is complex. The adjoint model must be significantly recode if there are global changes to the forward modeling system. This is the major concern with the real-time application of SEGMENT-Landslide. If users improved the forward system, they need also update the corresponding adjoint system, which may be a challenging task for many.

Adjoint procedure can also be derived from governing equations. Using Richards equation as an example, we outline the procedure obtaining adjoint model from forward model.

12.5.2 Adjoint System of the Modified Richards' Equation

Lets start from a form of Richards equation as

$$\begin{cases} \dfrac{\partial \theta}{\partial t} = \dfrac{\partial}{\partial z}\left(K\dfrac{dh}{d\theta}\dfrac{\partial \theta}{\partial z}\right) - \dfrac{\partial K}{\partial z} - w\theta & \\ \theta(z \to \infty, t) = \theta_i & t \geq 0, \\ q_0\left(= -K\left(\dfrac{dh}{dz} - 1\right)\right) = const & t \geq 0,\ z = 0, \end{cases} \tag{12.98}$$

where z is depth with the origin at the land surface (m), and w is a weight aggregating the vegetation water extraction factors in Eq. (5.9) with its actual form to be defined later (s^{-1}), and θ_i is the initial soil moisture profile ($m^3\ m^{-3}$). In reality, the sink term ($-w\theta$ in Eq. 12.98) is a daytime phenomenon due to the stomata shutting down at dusk and opening at dawn. However, a strict implementation of this plant phonological phenomenon may cause difficulty in the adjoint system. Specifying a continuous transpiration rate does not harm our purposes in this study.

Richards' equation (Eq. 12.98) describes infiltration process with a constant flux at the soil surface. However, Eq. (12.98) may not be solved as it is, because it contains two unknowns θ and h, showing the duel dependency of the flow regime on both the soil hydraulic conductivity and water potential (a balance between retention and conduction). Here we chose to keep θ as the sole variable through the Brooks and Corey (1964) relationship.

$$\left(\frac{\theta - \theta_r}{\theta_s - \theta_r}\right) = \left(\frac{h_b}{h}\right)^{1/b}, \qquad h < h_b < 0 \tag{12.99}$$

$$\left(\frac{\theta - \theta_r}{\theta_s - \theta_r}\right) = \left(\frac{K}{K_s}\right)^{1/(2b+3)}, \qquad 0 < K < K_s \tag{12.100}$$

where θ_r is the residual water content which is the non-drainable water content and usually approximated as water retained at a rather high tension, e.g., 1.5 MPa (Sellers 1965). Here h_b is an air-entry value, K_s is the saturated hydraulic conductivity, b is a pore-size distribution index called the Clapp–Hornberger (Clapp and Hornberger 1978) parameter, and θ_s is the saturated water content.

In Eq. (12.98), water extraction rate w is given by:

$$w = \begin{cases} 0 & 0 < z < l_0, \text{ or } z > L + l_0 \\ w_0 \dfrac{L + l_0 - z}{L} & l_0 < z \leq L + l_0 \end{cases} \tag{12.101}$$

where L (m) is the depth of the root layer and w_0 ($m^3\ m^{-3}\ s^{-1}$) a constant water extraction rate (a multiplication of potential transpiration ($m\ s^{-1}$), a normalization factor $2/L$ (m^{-1}), and soil water availability constraint (unitless)). It is also assumed

that the transpiration process will not displace the water potential fields beyond the region between z = l_0 and z = $l_0 + L$.

Using Eqs. (12.99)–(12.101), Eq. (12.98) can be transformed into

$$\begin{cases} \dfrac{\partial \Theta}{\partial t} = -\dfrac{\partial}{\partial z}\left(K_s \Theta^{b+2} b h_b \dfrac{\partial \Theta}{\partial z}\right) - K_s \Theta^{2b+2}(2b+3)\dfrac{\partial \Theta}{\partial z} - w\psi\Theta \\ \Theta(z \to \infty, t) = \Theta_i & t \geq 0, \\ K_s \Theta^{b+2} b h_b \dfrac{\partial \Theta}{\partial z} + K_s \Theta^{2b+3} = q_0 & t \geq 0,\ z = 0 \end{cases} \tag{12.102}$$

In Eq. (12.102), after adjusting θ_r and normalizing by the saturated soil water content, Θ is the effective relative saturation and ψ is porosity.

Here, we outline a general form of adjoint equation to a nonlinear gravity assisted diffusion equation and the perturbation theory to tailor it to data assimilation purposes.

$$\begin{cases} \dfrac{\partial \Theta}{\partial t} + \dfrac{\partial}{\partial z}\left(K_1 \dfrac{\partial \Theta}{\partial z}\right) - K_2 \dfrac{\partial \Theta}{\partial z} + W\Theta = f(z,t) & z \geq 0,\ t \in (0, T] \\ \Theta(\infty, t) = \Theta_i & t \geq 0, \\ -K_1 \dfrac{\partial \Theta}{\partial z} - \dfrac{K_2}{2b+3}\Theta = q_0 & t \geq 0,\ z = 0 \\ \Theta(z, 0) = g(z) & z \geq 0 \end{cases} \tag{12.103}$$

Apparently, with $K_1 = K_s \Theta^{b+2} b h_b$, $K_2 = -K_s \Theta^{2b+2}(2b+3)$, $g(z) = \Theta_i$, and $f(z,t) = 0$, Equation (12.103) reduces to Eq. (5.9). We require that all derivative terms be quadratically summable on (0,T) × (0, ∞).

On assimilation domain $(0, T]$, consider the following integral:

$$\int_0^T dt \int_0^\infty \Theta^* \left[\frac{\partial \Theta}{\partial t} + \frac{\partial}{\partial z}\left(K_1 \frac{\partial \Theta}{\partial z}\right) - K_2 \frac{\partial \Theta}{\partial z} + W\Theta\right] dz = \int_0^T dt \int_0^\infty \Theta^* f dz. \tag{12.104}$$

Integration by part, for example, for the second term on the left-hand side,

$$\begin{aligned} \int_0^T dt \int_0^\infty \Theta^* \frac{\partial}{\partial z}\left(K_1 \frac{\partial \Theta}{\partial z}\right) dz &= \int_0^T dt \int_0^\infty \left[\frac{\partial}{\partial z}\left(\Theta^* K_1 \frac{\partial \Theta}{\partial z}\right) - K_1 \frac{\partial \Theta}{\partial z}\frac{\partial \Theta^*}{\partial z}\right] dz \\ &= \int_0^T \left[\Theta^* K_1 \frac{\partial \Theta}{\partial z} - \Theta K_1 \frac{\partial \Theta^*}{\partial z}\right]\Bigg|_0^\infty dt + \int_0^T dt \int_0^\infty \left[\Theta \frac{\partial}{\partial z}\left(K_1 \frac{\partial \Theta^*}{\partial z}\right)\right] dz. \end{aligned}$$

Rearrange, (146) becomes

$$\int_0^T dt \int_0^\infty \Theta \left[-\frac{\partial \Theta^*}{\partial t} + \frac{\partial}{\partial z}\left(K_1 \frac{\partial \Theta^*}{\partial z} \right) + K_2 \frac{\partial \Theta^*}{\partial z} + W\Theta^* \right] dz = \int_0^T dt \int_0^\infty \Theta^* f dz$$
$$- \int_0^\infty \Theta\Theta^* \Big|_0^T dz + \int_0^T dt \int_0^\infty \left[K_2 \frac{\partial}{\partial z}(\Theta^* \Theta) \right] dz$$
$$- \int_0^T K_1 \left[\Theta^* \frac{\partial \Theta}{\partial z} - \Theta \frac{\partial \Theta^*}{\partial z} \right] \Big|_0^\infty dt. \tag{12.105}$$

Thus, with the introduction of the adjoint system:

$$\begin{cases} -\dfrac{\partial \Theta^*}{\partial t} + \dfrac{\partial}{\partial z}\left(K_1 \dfrac{\partial \Theta^*}{\partial z} \right) + \dfrac{\partial K_2 \Theta^*}{\partial z} + W\Theta^* = p(z,t) & \\ \Theta^*(\infty, t) = 0 & t \geq 0, \\ \dfrac{\partial \Theta^*}{\partial z} = \Theta^* = 0 & t \geq 0,\ z = 0 \\ \Theta^*(z,T) = h(z) & z \geq 0 \end{cases}, \tag{12.106}$$

Equation (12.105) can be transformed into

$$\int_0^T dt \int_0^\infty \Theta p dz + \int_0^\infty \Theta(z,T) h(z) dz = \int_0^T dt \int_0^\infty \Theta^* f dz$$
$$- \int_0^\infty \Theta^*(z,0) g(z) dz \tag{12.107}$$

Equation (12.106) is the most generous form of the adjoint equation to Eq. (12.103), with the dual definition of the inner product (functional) as

$$J = \int_0^T dt \int_0^\infty \Theta p dz + \int_0^\infty \Theta(z,T) h(z) dz, \text{ and}$$
$$J = \int_0^T dt \int_0^\infty \Theta^* f dz - \int_0^\infty \Theta^*(z,0) g(z) dz. \tag{12.108}$$

Apply small perturbation to Eq. (12.103), use the adjoint unperturbed system (12.106), outstanding problems such as parameter retrieval (if K_1 and K_2 are left for variation), initial moisture retrieval (if only Θ is allowed to vary), or even the optimal design of the measurements (arbitrary measurements function $p(z,t)$ and $h(z)$ are varied) can be successfully addressed. For example, for data assimilation purpose, the second term on the right/left-hand side of Eq. (12.107) is zero simply because Θ^* is zero at $t = 0$ and T. The Lagrange identity is thus satisfied.

The following discussion is limited to the case of $f(z,t) = 0$ (the modified Richards' equation).

Perform a tangent linearization around the nonlinear trajectory of Θ (notice that K_1 and K_2 also has contributions to the perturbation), the tangent linear system is:

$$\frac{\partial \delta\Theta}{\partial t} + \frac{\partial}{\partial z}\left(K_1 \frac{\partial \delta\Theta}{\partial z}\right) + \delta\Theta \frac{\partial^2 K_1}{\partial z^2} - \frac{\partial K_2}{\partial z}\delta\Theta - K_2 \frac{\partial \delta\Theta}{\partial z} + W\delta\Theta = 0 \quad (12.109)$$

Multiply Eq. (12.109) by $\delta\Theta^*$ and integrate over the assimilation domain and the semi-infinite vertical domain, one get

$$\begin{aligned}
&\int_0^T dt \int_0^\infty \delta\Theta \left[-\frac{\partial \delta\Theta^*}{\partial t} + \frac{\partial}{\partial z}\left(K_1 \frac{\partial \delta\Theta^*}{\partial z}\right) + \frac{\partial^2 K_1}{\partial z^2}\delta\Theta^* + K_2 \frac{\partial \delta\Theta^*}{\partial z} + W\delta\Theta^* \right] dz = \\
&\quad - \int_0^\infty \delta\Theta\, \delta\Theta^* \Big|_0^T dz \\
&\quad + \int_0^T \left[K_2 \delta\Theta^*\, \delta\Theta\right] \Big|_0^\infty dt \\
&\quad - \int_0^T K_1 \left[\delta\Theta^* \frac{\partial \delta\Theta}{\partial z} - \delta\Theta \frac{\partial \delta\Theta^*}{\partial z} \right] \Big|_0^\infty dt
\end{aligned} \quad (12.110)$$

The first term on the right-hand side of Eq. (12.110) vanishes because the purpose of data assimilation is to fit the dynamics to observations lies between $t \in (0, T]$, the forcing/innovation outside this time domain is thus zero ($\delta\Theta^* = 0$). In order to eliminate the last term of Eq. (12.110), a natural choice for the lower boundary condition is very similar to the upper boundary condition of the forward model but with $q_0 = 0$. To eliminate the second term of Eq. (12.110), a further requirement for lower boundary condition is $\delta\Theta^*$ itself is zero. Thus, we propose the following form of adjoint system.

$$\begin{cases}
-\dfrac{\partial \delta\Theta^*}{\partial t} + \dfrac{\partial}{\partial z}\left(K_1 \dfrac{\partial \delta\Theta^*}{\partial z}\right) + \dfrac{\partial^2 K_1}{\partial z^2}\delta\Theta^* + K_2 \dfrac{\partial \delta\Theta^*}{\partial z} + W\delta\Theta^* = 0 & \\
\delta\Theta^*(\infty, t) = 0, & t \geq 0 \\
-K_1 \dfrac{\partial \delta\Theta^*}{\partial z} - \dfrac{K_2}{2b+3}\delta\Theta^* = 0,\ \delta\Theta^* = 0 \Leftrightarrow \left(\dfrac{\partial \delta\Theta^*}{\partial z} = \delta\Theta^* = 0\right), & z = 0,\ t \geq 0 \\
\delta\Theta^*(z, 0) = \delta\Theta^*(z, T) = 0, & z > 0
\end{cases} \quad (12.111)$$

In Eq. (12.111), $\delta\Theta^*$ is the adjoint variation of the state variable Θ, W is a short hand to $w\ \psi$, $K_1 = K_s\Theta^{b+2}bh_b$, and $K_2 = -K_s\Theta^{2b+2}(2b+3)$. The remaining symbols are as previously defined. Equations (12.102) and (12.111) enjoy many similarities except that the time integration in Eq. (12.111) is backward as signified by the minus sign preceding the time tendency term of the adjoint equation.

Similarly, let saturated hydraulic conductivity K_s vary and we will obtain a formula for updating K_s's value from an initial guess, following exactly the same derivation procedure. In reality, saturated hydraulic conductivity can vary by four orders of magnitudes (sandy end and clay end of soils). This requires that our retrieval be robust enough for initial guess error on K_s. To this end, the resulted adjoint system for parameter retrieval can be simplified according Ren (2004). The modified Richards equation signifies a stronger connection among different soil layers. Our derivations here have implications for land surface data assimilation, especially for observations that are indirectly related with soil moisture content.

12.6 Standstill Solution of SEGMENT-Landslide Indicating how Forces Are Balances When There Is No Motion

The governing Eqs. (6.1–6.11) in terrain following coordinate system (vertical dimension sigma coordinate system) reads (using vertical direction momentum equation as an example):

$$\rho\frac{dw}{dt} = \frac{\partial\Re_{xz}}{\partial x} + \frac{\Delta S_x}{H}\frac{\partial\Re_{xz}}{\partial S} + \frac{\partial\Re_{yz}}{\partial y} + \frac{\Delta S_y}{H}\frac{\partial\Re_{yz}}{\partial S} - \frac{1}{H}\frac{\partial\Re_{zz}}{\partial S} \tag{12.112}$$

At standstill, Eq. (12.112) becomes:

$$\frac{\partial\Re_{xz}}{\partial x} + \frac{\Delta S_x}{H}\frac{\partial\Re_{xz}}{\partial S} + \frac{\partial\Re_{yz}}{\partial y} + \frac{\Delta S_y}{H}\frac{\partial\Re_{yz}}{\partial S} - \frac{1}{H}\frac{\partial\Re_{zz}}{\partial S} = 0 \tag{12.113}$$

Assuming that sliding material is uniform in density and all mechanical properties, it is easy to demonstrate that Eq. (12.113) has the special solution

$$\Re_{xz} = L\frac{\partial h}{\partial x};\Re_{yz} = L\frac{\partial h}{\partial y};\Re_{zz} = L\left[\left(\frac{\partial h}{\partial x}\right)^2 + \left(\frac{\partial h}{\partial y}\right)^2\right] \tag{12.114}$$

Where $h(x,y)$ is surface elevation, L is lithostatic stress $L = -\rho gsH(x,y)$, and $H(x,y)$ is the sliding material thickness.

Substituting in the common factor $\left[1+\left(\frac{\partial h}{\partial x}\right)^2+\left(\frac{\partial h}{\partial y}\right)^2\right]$, the stress components can be related to the local slope directions. For example, the direction cosine of the slope surface is $\cos(\alpha)=1/\sqrt{\left[1+\left(\frac{\partial h}{\partial x}\right)^2+\left(\frac{\partial h}{\partial y}\right)^2\right]}$.

Thus,

$$\Re_{zz}=L\sin^2\alpha \tag{12.115}$$

As slope increases, $\Re_{xz}$ and $\Re_{yz}$ continue increase without upper limitation. However, $\Re_{zz}$, which is the bridging effects (how neighborhood contributes to the balance) has an upper limit (the repose angle $\alpha\le\phi$). Once slope angle exceeds the repose angle ϕ, balance is broken and sliding initiates. Notice that, when reducing to two-dimension, for example, keeping only the x dependence, $\Re_{xz}=L\cos\alpha.$, a balance is in the form of $tg(\alpha)\le\mu=tg\phi$, the basis of all present 2D slope stability models.

From the above analysis, it is clear that, when sliding material is not in motion, lithostatic balance is a viable solution/explanation of the spherical part of internal stress tensor. But it is not a proper measure for the slope stability. $\Re_{zz}$, which is proportional to $\Re_{xz}$ and $\Re_{yz}$, is a proper measure. When material is in motion, depending on material rheology, $\Re_{zz}$ can significantly deviate from the lithostatic form of expression. Note that Rzz is a diagnostic in the SEGMENT-Landslide and is updated regularly using an integral form of expression based on Eq. (12.112). Equation (12.115), however, provides some clue for initializing R_{zz} in model forward marching.

Note again, inside solids, the lithostatic balance may be a good approximation in the vertical direction. However, the stress in horizontal direction can be minimal so that slopes at upper surface does not necessarily cause "down-slope" motion tendency. Actually, the degree of closeness of spherical components of internal stress tensor to hydrostatic/lithostatic stress is the measure of fluidity. Granular material has certain degree of fluidity, as described in Appendix A. The existence of a maximum repose angle is a direct manifestation of such semi-fluidity (true fluids has zero degree of repose angle). Shaking and adding fluids help increase the granular material's fluidity. This is the rudimentary reason why earthquake and storms can cause slope instability.

The success of SEGMENT-Landslide also relies on its fluid viscosity analogous in parameterizing granular granular viscosity in Eq. (5.13). In SEGMENT-Landslide, the generic relationship between deviatoric stress τ and strain rate is implemented as

$$\tau=\eta\left(,\dot{\varepsilon},S\right)\dot{\varepsilon} \tag{12.116}$$

Where effective viscosity η is a function of strain rate $\dot{\varepsilon}$ and an isotropic confining pressure S. The way viscosity is parameterized in Eq. (5.13) is equivalent to a Kevin–Voigt assumption at the slow deforming stage. At very small deforming rate, the stress is composed of a term that is no longer dependent on strain rate (Eq. 5.13 in the limit of $\dot{\varepsilon} \to 0$). At the other extreme when $\dot{\varepsilon} \to \infty$, deviatoric stresses are dominated by strain rates. As strain rate increases, the granular viscosity decreases but the resistive stress increases, because the decreasing rate is slower than the increasing rate of strain rate. This way, a steady state is eventually reachable for granular material sliding down a "sticky" slope (flow is no-slip at the lower interface/boundary and free of stress at the upper boundary). The effective viscosity increases with confining pressure because of the increase in inter-particle friction. Granular viscosity decreases as shear rate increases can be understood through the analogous to the energy-trap well. Viscosity of granular material is determined by particle size, shape, and the strength of inter-particle bonding. The strain rate does not change the particle geometrical characteristics. But the rate of variation in flow shear results from the competing between two effects: the tendency the granular domain to return to its equilibrium configuration (restructuring) and the continuous breakage as a result of flow (motion relative to neighboring granular particles, or destructuring of equilibrium state). Flow involves particles/elements jump out of their potential well. Under high shear rates, the material does not have enough time to restructure and the potential wells are much shallower and easier to overcome. In the viscosity parameterization, we assumed that granular material has no memory of previous strain history. This is close to reality for uniform, non-cohesive granular material. The parameterization in Eq. (5.13) also guarantees a smooth transition from the standstill state to motion state (agreeing with Eq. 12.115). In other words, the proposed constitutive law insures that a yielding criterion exists in the form of $|\tau| \underset{\text{in Appendix 4}}{\overset{\text{invariant I2 in Eq. (4.67)}}{=}} \sqrt{0.5(\tau_{ij})^T \tau_{ij}} = \mu_0 S_p$.

If under tensile, granular viscosity is set to a small constant. This is of the generic yielding criteria form introduced in Sect. 5.1.1 (Coulomb–Navier criteria), with cohesion relegated to spherical stress tensor.

References

Arakawa A, Lamb V (1977) Computational design of the basic dynamical processes of the UCLA general circulation model. In: Chang J (ed) Methods in computational physics, vol 17. Academic, New York, NY, pp 174–264

Arakawa A (1984) Boundary conditions in limited-area model. Department of Atmospheric Sciences, University of California, Los Angeles, CA, 28 pp

Asselin R (1972) Frequency filter for time integration. Mon Weather Rev 100:487–490

Brooks R, Corey W (1964) Hydraulic properties of porous media, Hydrology Paper 3. Colorado State University, Fort Collins, CO

Backus G, Gilbert F (1970) Uniqueness in the inversion of inaccurate gross earth data. Phil Trans R Soc A 266:123–192

Buckley A, LeNir A (1983) QN-like variable storage conjugate gradients. Math Prog 27:155–175
Clapp RB, Hornberger GM (1978) Empirical equations for some soil hydraulic properties. Water Resour Res 14:601–604
Courtier P, Talagrand O (1987) Variational assimilation of Meteorological observations with the adjoint equation. Part II: numerical results. Q J Roy Meteor Soc 113:1329–1347
Errico R (1997) What is an adjoint model? Bull Am Meteorol Soc 78:2577–2591
Gill PE, Murray W (1979) The numerical solution of a problem in the calculus of variations. In: Bell DJ (ed) Recent mathematical developments in control. Academic, London, pp 97–122
Haltiner GJ, Williams RT (eds) (1980) Numerical weather prediction and dynamic meteorology, vol 2. John Wiley and Sons, Inc., New York, NY
Hildebrand F (1976) Advanced calculus for applications, 2nd edn. Prentice-Hall, Englewood Cliffs, NJ
Ide K, Courtier P, Ghil M, Lorenc A (1997) Unified notation for data assimilation: operational, sequential and variational. J Meteor Soc Jpn 75:181–197
Johnson KW, Bauer J, Riccardi GA, Droegemeier KK, Xue M (1994) Distributed processing of a regional prediction model. Mon Weather Rev 122:2558–2572
Klemp JB, Wilhelmson R (1978) The simulation of three-dimensional convective storm dynamics. J Atmos Sci 35:1070–1096
LeDimet FX, Talagrand O (1986) Variational algorithms for analysis and assimilation of meteorological observations-Theoretical aspects. Tellus 38A:97–110
Lilly DK (1965) On the computational stability of numerical solutions of timedependent nonlinear geophysical fluid dynamics problems. Mon Weather Rev 93:11–26
Liu D, Nocedal J (1989) On the limited memory BFGS method for large scale optimization. Math Prog 45:503–528
Machenhauer B (1979) The spectral method. Numerical methods used in atmospheric models, Vol. II, GARP publications series no. 17, WMO/ICSU, Geneva, 502 pp. [Available from Secretariat of WMO, Case Postale No. 5, CH-1211 Geneva 20, Switzerland.]
Marchuk GI (1981) Methods of computational mathematics. Springer, New York, NY
Marchuk GI (1994) Adjoint equations and analysis of complex systems, vol 295, Mathematics and its applications. Kluwer Academic Press, Dordrecht
McLaughlin D (1995) Recent developments in hydrologic data assimilation. Rev Geophys 33 (suppl):977–984
Mesinger F, Arakawa A (1976) Numerical methods used in atmospherical models, vol 17, GARP Publication Series. WMO/ICSU Joint Organizing Committee, Geneva, pp 53–54
Oran E, Boris J (1987) Numerical simulation of reactive flow. Elsevier, New York, NY
Phillips N (1959a) An example of nonlinear computational instability, The atmosphere and sea in motion, Rossby memorial volume. Rockefeller Institute Press, New York, NY, pp 501–504
Phillips N (1959b) Numerical integration of the prime equations. Mon Weather Rev 87:333–345
Pielke R (1984) Mesoscale meteorological modeling. Academic, Orlando, FL, 611 pp
Rabier F, Courtier P, Pailleux J, Talagrand O, Vasiljevic D (1993) A comparison between four-dimensional variational assimilation and simplified sequential assimilation relying on three-dimensional variational analysis. Q J Roy Meteor Soc 119:845–880
Ren D (2004) 4DVAR retrieval of prognostic land surface model variables for ARPS. University of Oklahoma, Norman, OK, p 236
Rood R (1987) Numerical advection algorithms and their role in atmospheric transport and chemistry models. Rev Geophys 25:71–100
Sellers WD (1965) Physical climatology. University of Chicago Press, Chicago, IL, 272 pp
Shanno D, Phua K (1980) Remark on algorithm 500: minimization of unconstrained multivariate functions. ACM Trans Math Soft 6:618–622
Thacker W, Long RB (1988) Fitting dynamics to data. J Geophys Res 93:1227–1240
Yu L, O'Brien JJ (1991) Variational Estimation of the wind stress drag coefficient and the oceanic eddy viscosity profile. J Phy Ocean 21(709–719):1991
Zupanski D (1997) A general weak constraint applicable to operational 4DVAR data assimilation systems. Mon Weather Rev 125:2274–2292

Appendix A
Pressure Fields Within Simple Granular Media—A Comment on a Recent *Science* Article on Locomotor Running Over Sand

A.1 Multi-body Problem

Granular material is a multi-body, loose lump of solid granules (i.e., the solid particles that have same chemical composition and physical properties as their non-fractured mother material). Because of the increased degree of freedom, the inter-particle interactions can through collisions as well as interfacial actions, manifesting macroscopically as have fluidity while being solids individually. However, the mean free path (in analogous to the Prandtl mixing length model in fluid dynamics), measured by granule average size, is much smaller than liquid molecules (measured by molecule size). For loosely packed granular material, shaking can increase the mean path of the granular particle and make it more like fluids. This limited fluidity explains that a load (a solid body being placed on top of a lump of granular substance) can be placed anywhere inside the granular media and find an equilibrium. There simply is no hydrostatic pressure concept inside granular material's internal stress fields. Put more technically, the pressure field inside the granular material is anisotropic. The relationships among stresses in different principal directions are loosely confined only by certain form of yielding criteria for compression conditions (Timoshenko and Gere 1963). Although granular material is not true fluids, in separating the granules (e.g., putting a wedge into them), the resistance forces experienced primarily originate from gravity of the granular material involved, whereas the cohesive bonding is weak or non-existent. There are wide applications of granular material rheology, for example in geosciences for landslides (Iverson 1997) and in designing vehicles to be used in deserts (e.g., Li et al. 2013).

© Springer International Publishing Switzerland 2015

D. Ren, *Storm-triggered Landslides in Warmer Climates*,
DOI 10.1007/978-3-319-08518-0

A.2 Non-hydrostatic but Has Definite Range of Influence

This is a compliment to the model introduced in Li et al. (2013). All idealized (imaginary) experiments are based on a 3D full Navier–Stokes framework (SEGMENT-Landslides, Ren et al. 2008) with granular viscosity parameterized as in Jop et al. (2006). To simplify the problem, we follow the same assumption on granular material as they made. In summary, there is no cohesion among granular particles. This means that all shear stress is proportional to the normal stress by internal friction coefficient. This is also equivalent to the assumption that "if no normal press, there is no friction." As Li et al. (2013) put it "friction-dominated forces are proportional to the hydrostatic-like pressure in granular media." Put in another more salient way, particles are in point-to-point interaction rather than area-to-area interaction as in reality. Before analyzing the effects of striking angle and frequency, it is necessary to examine the basic problem of putting a load on a lump of such ideal granular substance (Fig. A.1).

In Fig. A.1, a cylindrical load (aspect ratio and density as labelled) is overlying a lump of dry, ideal spherical granular particles of 2 mm diameter and of 26° repose angle. The influence on the stress field is shown as the white contour lines of pressure in vertical direction. If the dots, where two vertically adjacent isolines become parallel and no longer being unevenly affected by the load, are connected, an oval spherical surface is obtained (cross section as the bold blue line in Fig. A.1a). The space inside this half oval sphere is defined as "influence domain" (ID). The ID is a conservative quantity and, using this concept, it is easy to explain the energetics involved in the load's motion inside the granular media.

The pattern of the isolines of the compressive stress moves with the load body if it goes further down. There is only a minimum intruder depth, while no upper limit. That means the load can be placed at arbitrary depths below the sands while stay standstill. This is unlike a solid body floating in liquids, and the free board-depth is not applicable. The influence (or mobilization) domain is a proper concept for granular material under loading. Although the load can stay at force-balance at any depth deeper than the minimum depth (shown in Fig. A.1a), motion within granular involves energy loss through irreversible heat dissipation. The rate of energy loss is nonlinearly proportional to the ID volume, the motion speed, and the granular viscosity. The seemingly simple process of slowly putting the load on granular media (and it gradually sets in and reaches balance at the minimum intrude depth) actually involves the gradual increasing of the ID domain, transfer of potential energy into heat, and the generation of lifts (as shown in Fig. A.1a), the full spectrum.

Back to the problem of interest, at which depth a wheel (or leg) stays when a locomotors is in motion depends on the weight of the locomotors, the touching area (i.e., footprint) of the legs and the frequency of striking (for legged ones, or, for wheeled locomotors, the wheel rotating frequency). If the granular material is deep enough and has no horizontal boundary (or boundary is far away), the momentum of striking exerted on granules and the stance of the legs all affect the "intruder depth."

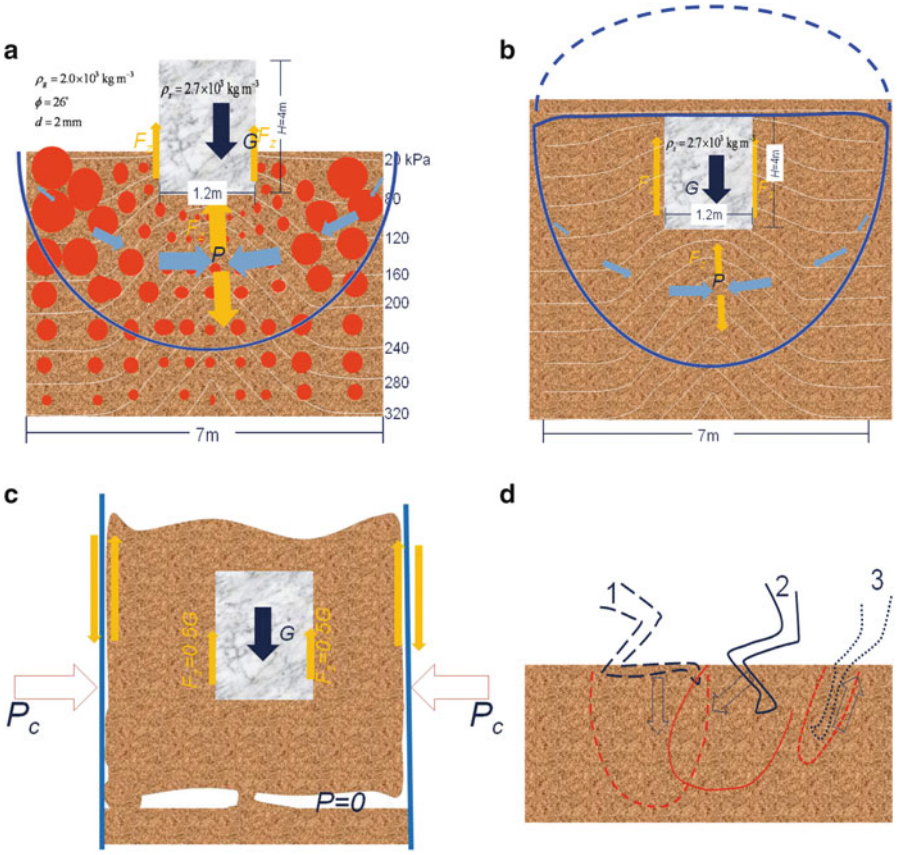

Fig. A.1 Granular responses to loading. This diagram illustrates how the "lift" is generated and the minimum intruder depth and domain of influence (ID, or the region confined by the deflected isolines). Panel (**a**) is a cross-sectional view of a load of density 2.7×10^3 kg/m^3 of labelled aspects placed on sands (mechanical properties labelled). The *contour lines* are vertical component of compressive stress within granular lump. The vertical gradients of the curve, after adjusting the shelf-weight, are lift contribution. *Red blobs* indicate elastic granules that should be of identical size when not being compressed. *Bold arrows* are forces: *black arrow* is the load's gravity, *yellow arrows* are lifts, and *cyan arrows* are confining stress generated within the ID, which (ID boundary) is outlined using a *bold blue curve*. Granules have certain degree of elasticity, with modulus similar to its un-fractured mother material. Granule compression is exaggerated in the illustration (*red bubbles* of different sizes intend to show different degrees of compression). Other assumptions are of the granular media are taken from Li et al. (2013), such as non-cohesive point-to-point contact. Panel (**b**) is identical to (**a**) except that it shows the force balance and range ID after a complete submersion of the load. The ID of a cylindrical load resembles a downward-pointing half-oval. The eccentricity (e) of this half-oval depends on weight of the load, the footprint area, the dry repose angle of the granular material and the fractional coefficients between load and granular material. The e is also an indicator of the ratio of lateral lift to bottom lift. When the load is moving inside the granular material, its ID follows. For example, when it moves downward, there will be an egg-shaped ID surrounding the load (*dotted blue curve* shows the tracing section). The spatial variations of the resistive force are shown as *bold arrows*. The smaller confining pressure at the boundary of ID gets enhanced in-directly by the weight of the granular material within the influence domain and contributes a lift to balances the weight of the load. Not only the forces are balanced within the ID, the kinetic energy of the intruder also loses to overcome

We here emphasize that the footprint of the wheel or leg is critical for the size and shape of the ID. There are rule of thumb that the smaller the touch area, the deeper the intruder depth but no linear relationship. This simply is because that the weight of the granular material within the ID cannot be translated directly to lifts that balances the weight of the load body, it must be transformed through the shear stress (friction) and normal stress (compression of granules). The filled arrows in Fig. A.1a shows the confining pressure originating from the boundary wall of the ID being gradually amplified by the weight of overlying granular material in the influence domain and because of the concaved configuration of the compressed granules, this force become a lift to balance the load body's weight. Another important source of lift is lateral frictional forces exerted on the load by surrounding granules. As the footprint reduces, the influence region reduces faster in a nonlinear manner. That explains why lizards change the leg stances for pushing stage and retracting phase of a step on sands (fig. 1 of Li et al. 2013). If the granular material is compacted (Fig. A.1c), bridging effects may totally annihilate the vertical pressure and this further invalidate the hydrostatic assumption. However, the ID concept always holds.

Fig. A.1 (continued) the internal friction within ID and eventually as heat dissipation, when it moves around in the granular media. In another way, work has to be done to reconfigure the granular assembly as ID changes location and involves new comer granules (it is a dynamic processes of new granules get involved and some original granules go out of the ID). There is a minimum set-in depth because work has to be done to reconfigure the granular assembly as ID expands and involves new comer granules. The internal stress (granular materials usually do not bear tensile stress, only compressive and shear stresses. So we use pressure for the compressive stress and friction for the shear stress) within granular material is highly anisotropic and there usually is no "hydrostatic" relationship. Double the weight of the load does not double the minimum set-in depth. This is rooted in that fact that the free-path for the granules is relatively short compared with true fluids, relative to their respective particle dimensions and interchange of locations of granules needs energy input. Macroscopically, it manifests as there is no free-board level for a lighter load. No matter the shapes and densities, a load can find a balance at arbitrary depth within granular media. The pressure filed inside the granular media is highly anisotropic and it is not necessarily true that the vertical pressure is greater than the horizontal component, especially when dry repose angle is large or the ID intercept the lateral boundary of the container. Pressure components in different directions are only weakly constrained by yielding criteria such as von Mise criteria (Jaeger 1969a). In this study, we assume that individual granules are not further crashed into smaller particles. This is a rather wide pressure range for normally seen loading material (except extremely small or large densities of the load, in that case, the very heavy load will settle to the bottom and the extremely light load will float to surface). Panels (**a**) and (**b**) are the case without horizontal confinement, or the case with lateral boundary far away. For the case with very high confinement pressure ($P_c > Gtg\phi$, G the total gravity of the granular material being confined, and ϕ is repose angle), "bridging" effects can cause voids/fissures/crevasses of 0 vertical pressure inside the granular (**c**). In the case of (**c**), lateral frictions completely balance the weight of the load. In the voids (tunnels), the pressure is zero. Panel (**d**) is a pose of a hind foot of zebra-tailed lizard. *Dashed*, *solid*, and *dotted* tracings are leg positions at early, mid-, and late stance. *Hollow arrows* indicate local movement directions of the leg elements. *Red lines* of the corresponding styles indicate the influence domain at that stance

At standstill state, the minimum set-in (intruding) depth increases monotonously with decreasing footprint area (but nonlinearly). If the intruder (load) has a footprint comparable with granular particle size, there exists large uncertainty in the resistance it may meet in down-ward intruding. It is theoretically possible to go through the inter-particle voids without any resistance. In this study, we consider cases with footprints 10^6 times larger than average granule size. As is clearly shown that, even for this very idealized case (Fig. A.1a), force is non-local and nonlinear with respect to all the labelled dimensions of the load. So, in addition to angle of attack, the hrdrostatic-like formula (eq. (1) of Li et al. 2013) needs to include striking frequency as a factor in α, because the nonuniqueness nature of the intruder depth.

A.3 Granular Viscosity Should be Factored in to Address Robot-Granular Material Interactions

Another point we would like to point out is that, the static properties of dry repose angle and particle size is insufficient to describe the interaction of leg/wheel with granular media. Granular viscosity must be parameterized. For example, poppy seeds may have same repose angle with certain-sized hollow plastic beads that also have the same density (as poppy seeds). This is feasible because repose angle is very weakly related to density and only sensitive to particle size and surface properties. So, for certain material, first decide the particle size that will yield a repose angle identical to the poppy seeds. Then determine the void portion so that the gross density matches. But when put in motion (e.g., setting on a slope slanting steeper than the repose angle and let go), they will behave very differently! Granular viscosity is not mentioned in the present study (Li et al. 2013), but the first author (personal communication with C. Li, 2013) admits that, when running at higher frequency, the granular material becomes "tardy." As frequency gets higher, the repelled granular material simply have no time to response rheologically before the legs actually moved ahead. Under this situation, the granular ground actually provides much rigid support for the overlain load and the robot vehicle should run more efficiently. Using of robot and granular material parameters listed in Fig. A.2's legend, the numerical experiments with SEGMENT-Landslide reproduces the observed maximum attainable velocity vs. frequency relationship for the 0–5 Hz range. Observational data are unavailable for higher frequency. From Fig. A.2, Li et al. (2013) experiments actually cover only a limited portion/segment of the full-range sigmoidal curves. The thick black curve indicates the ideal case of robot (vehicle) running on rigid, elastic, and non-slip track. Because significant amount of the kinematic energy is transformed into heat (through internal friction as wheels passing through viscous granular media), none of the cases is close to the ideal case of rigid, elastic, and non-slip ground. Counterintuitively, as striking frequency gets higher, the repelled granules simply

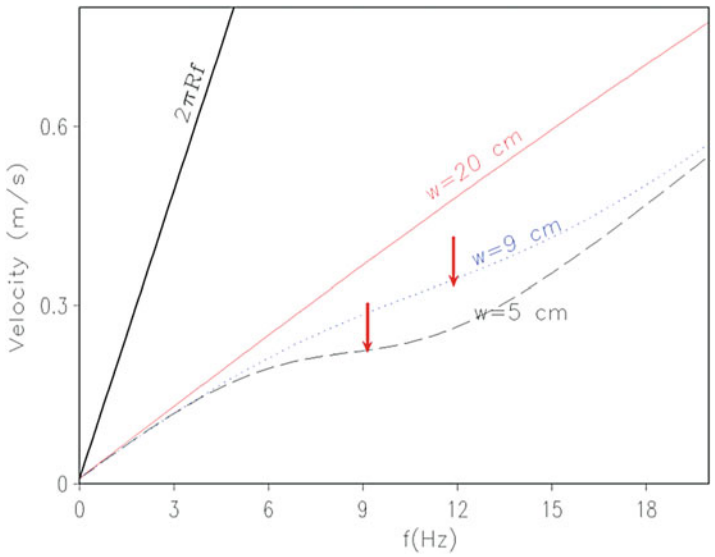

Fig. A.2 Vehicle performance illustrated using maximum attainable translational speed as a function of wheel/leg striking frequencies. The turning points (*red arrows* pointed locations) of these sigmoidal curves satisfy this constraint: $f_c = C_1/(C_2/w - 1)$, where C_1 (Hz) and C_2 (m) are constants for the same intruder moving inside the same granular media. The performance curves for all experiments are sigmoidal but with variant transition turning points. Generally, all else being the same, the transition is at higher frequency with increasing wheel width. The turning point separates two flow regime: frictional angle dominated regime at low leg-rotating frequency and viscosity dominated regime at high leg-rotating frequency. The parameter setting as in Li et al. (2013): $G = 0.15$ kg; at $w = 1$, $A = 3 \times 10^{-4}$ m^2 (case not shown in the figure for clarity); leg length $R' = 2.05$ cm; dry repose angle for loosely packed situation $\phi = 36°$; degree of compactness can be retrieved from the fact that "slowly set the robot on top of flat upper surface get a dent of ~0.5 cm when three C-legs are pointing downward" (C. Li, personal communication)

have no time to response (granular viscosity usually are 10^4 Pa S) and acts much rigid than at lower striking frequency. Figure A.2 also indicates that the turning points are sensitive to leg-width, with wider leg-width has higher performance efficiency and the transitional point comes at higher striking frequency. So increase the leg-width is one safe way increasing performance efficiency for a robot running on granular ground. Wheels/legs bearing different track depths encounter granular media of different viscosities, because granular viscosity, unlike true fluids, are also normal pressure dependent. Without detailed granular viscosity parameterization, the portion of kinetic energy lost as heat dissipation is hard to estimate and generalize.

A.4 A More Suitable Scaling Invariant

Because the complicated internal stress fields within granular media, resistive forces to intruder (load) cannot be described using the hydrostatic relationship. A universal feature is that, within a certain domain surrounding the intruder, granules experience different degrees of elastic compression (once the intruder moves away, granules can restore previous unperturbed conditions). Viewing from another angle, the granules are loosely organized (can only bear compression and not tension), the perturbation caused by the intruder (load) cannot be localized, instead, all granules within the ID are mobilized and work in synergy to resist the intruder. Actually, considerable portion of kinetic energy of a moving intruder is lost to overcome internal friction and dissipates as heat inside the ID The fact that the envelop of the ID follows the loading intruder if it moves around indicates that the size of the ID is a proper invariant for evaluating the performance of a locomotors with wheel (legs) partially set in granular media.

Based on the ID conception of granular material, we feel a more suitable scaling is an invariant based on a unit-less combination of the weight of the locomotor (G), the footprint area (A), and rotation frequency of the legs (f). For the turning points of the maximum attainable steady speed (V_{max}) of robot as a function of rotating frequency, we here propose the $A^2f\rho/GV_{\max}$ is a unit-less property as a scaling invariant that constrain the wheel (leg) rotating frequency and maximum attainable steady velocity at lower frequency range. Another unit-less combination, $Gf/(\rho AV)$, is suitable scaling invariant for high frequency range where dynamic granular viscosity, instead of the dry repose angle, becoming the dominant factor for resistance to intruder's motion. The turning points of the sigmoidal curves signify the regime transition. The two unit-less properties vary only according to granular material's mechanical properties. Critical frequencies (the two red arrows in Fig. A.2) are estimated based on the continuity requirement of these two expressions at the critical frequencies. Once the same robot walking on the same granular media, weight G and density ρ are further fixed. Different footprint area is linearly proportional to leg width (w). We here only show the results of the C-leg configuration in Li et al. (2013). Other leg configurations are qualitatively similar.

The same reason reptiles walking on sands adjust the stance in pushing and retracting stages of a step also implies the close relationship between the wheel (legs) width in the maximal attainable speed of the locomotor. For a fair comparison, different wheel radius (curvature should, at standstill, have the same footprint size). From Their fig. 4c, it seems unlikely. The full C-leg case gain an edge because it has the largest footprint. The retracting styles of the C-legs of different radius are similar and makes no qualitative differences. The counter-C legs dig deeper and waste more energy in pulling out and thus is the least efficient among the leg shapes experimented. This scaling scheme also is a nexus for two Science articles on the same volume (Li et al. 2013; Ekstrom and Stark 2013).

In reality, legged locomotor has advantages in reducing payload when being used in scientific research in outer space. So this study (Li et al. 2013) is very useful.

But, as the wheels (legs) running over granular dirt, the granules are set into motion. Only standstill analysis is insufficient to fully comprehend the problem. The viscosity of granular must be properly implemented to simulate the kinematic energy loss in stroking and passing-through the granular media. Here we reexamined the experiments using an advanced Navier–Stokes framework with parameterized granular viscosity. It is found that The performance efficiency of the robot, if measured by the maximum speed attainable, follow a six-parameter sigmoid curve against frequency. A proper scaling for the turning point of the sigmoid curve involves the footprint size, rotation frequency and weight of the robot. Our proposed granular response to a load, or the "influencing domain" concept points out that there is no hydrostatic balance within granular material. Their balance is a synergic action of multi-body solids. A solid (of whatever density) may stay in equilibrium at an arbitrary depth inside a lump of granular material. For top load, there exist only a minimum set-in depth and there is no maximum or optimal depth. What set-in depth a moving vehicle takes is a combination of its weight, footprint, thrusting/stroking frequency, surface property of the vehicle against granular material (that is in direct contact), and internal mechanical properties of the granular material. If vehicle's working environment is known, the wheel-granular interaction and the granular mechanical properties can be lumped together. The unitless combination of the other three can form invariants to scale the performance of various designs of wheels/legs/legs. Once a design is chosen, the wider the wheel, the higher the maximum achievable speed, everything else the same.

References

Ekstrom G, Stark D (2013) Simple scaling of catastrophic landslide dynamics. Science 339:1416–1419

Li C, Zhang T, Goldman D (2013) A terradynamics of legged locomotion on granular media. Science 339:1408–1412

Iverson R (1997) The physics of debris flows. Rev Geophy 35:245–296

Jop P, Forterre Y, Pouliquen O (2006) A constitutive law for dense granular flows. Nature 441:727–730

Ren D, Leslie LM, Karoly DJ (2008) Landslide risk analysis using a new constitutive relationship for granular flow. Earth Interact 12:1–16

Timoshenko S, Gere J (1963) Theory of elastic stability, 2nd edn. McGraw-Hill, New York

Appendix B
Cluster Analysis

The cluster analysis of the landslide positions involved a multivariate kernel density estimation (KDE) method, with a Gaussian kernel. The univariate KDE approximates the probability density function of a point x as:

$$f(x) = \frac{1}{n}\sum_{i=1}^{n} K_h(x - x_i), \tag{A.1}$$

where n is the number of observations, h is a smoothing variable (the bandwidth), and K_h is a kernel function. There is a number of possible choices of kernel function. For this study the Gaussian (normal) kernel is used, defined as:

$$K_h(x - x_i) = \frac{1}{h\sqrt{2\pi}} e^{\frac{-(x-x_i)^2}{2h^2}}. \tag{A.2}$$

A 2-dimensional KDE can be represented by:

$$f(x) = \frac{1}{n}\sum_{i=1}^{n} \left[K_{h_1}\left(x^{(1)} - x^{(1)}{}_i\right)\right]\left[K_{h_2}\left(x^{(2)} - x^{(2)}{}_i\right)\right], \tag{A.3}$$

where $x = (x^{(1)}, x^{(2)})$, and with separate bandwidths for each dimension. Here, multiple bandwidth pairs (h_1, h_2) were used for comparison, as well as the bandwidth pair determined by the normal reference rule for a multivariate KDE given in Scott (1992):

$$h_j^* = \left(\frac{4}{n(d+2)}\right)^{\frac{1}{d+4}} \sigma_j, \tag{A.4}$$

© Springer International Publishing Switzerland 2015

D. Ren, *Storm-triggered Landslides in Warmer Climates*,
DOI 10.1007/978-3-319-08518-0

where d is the number of dimensions. In this study, $d = 2$ and thus

$$h_j^* = \left(\frac{1}{n}\right)^{\frac{1}{6}} \sigma_j = n^{-1/6}\sigma_j. \tag{A.5}$$

Reference

Scott D (1992) Multivariate density estimation. Wiley, New York

Appendix C
Scarp Size Distribution: Who Are the Players?

How much sliding material can be mobilized on an unstable slope is co-determined by slope hydrology and precipitation morphological characteristics (total amount as well as intensity distribution). For thoroughly fractured slopes, how much rainfall is infiltrated or drained into ground is a key parameter for estimating the landslide magnitude. For example, suppose two rain events have the same precipitation amount (e.g., 10 mm). In one case, the rain lasted only 10 min, whereas it lasted 40 min in another case (Fig. A.3). The dry soil hydrological properties of a slope are a characteristic quantity of the slope. For example, the infiltration rate is assumed to be 0.05 m/s. For the case of intense burst that lasted only 10 min, time is insufficient to infiltrate. The surface runoff, when meets crevasses, percolated into deeper depth, creating a shear zone much deeper than uniform wetting can reach. The crevasses here can be a result of weathering processes or caused by live vegetation activities. In case the two mechanisms both function, the rainfall water percolates even deeper. The landslide magnitude thus is much larger for the intense storm case (cf. Fig. A.3a, b). Also, it is possible that the root reinforcements effects do not work simply because the shear zone is far deeper then the root zone and there is a decoupling of the two. The rainwater may find a roundabout to saturated shear zone that does not intersect with root networks. This supports the findings in Sects. 7.4.3 and 7.4.4. Figure A.3 illustrates how rainfall distribution within the slope affects the landslide magnitude. The weight of rainfall is negligible in aiding the driving stress. However, if it can be effectively channelled into the interface between non-fracture bedrock and the overlain granular lump, the effect on reducing the maximum resistive stress is significant. In addition, the concentrated water column inside the crevasses will exert a hydrostatic horizontal direction differential pore pressure, aiding the driving stress in overcoming the resistive stress. Once the driving stress and the differential pore pressure together overtake the reduced (by drainage lubrication) maximum available resistive stress, the entire layer is set into motion; even through most the soil inside this layer still is dry. In contrast, if the precipitation is retained entirely in the upper shallow layer and did not discharge into deeper layer, only a very shallow layer is mobilized and this layer, by entrain

© Springer International Publishing Switzerland 2015

D. Ren, *Storm-triggered Landslides in Warmer Climates*,
DOI 10.1007/978-3-319-08518-0

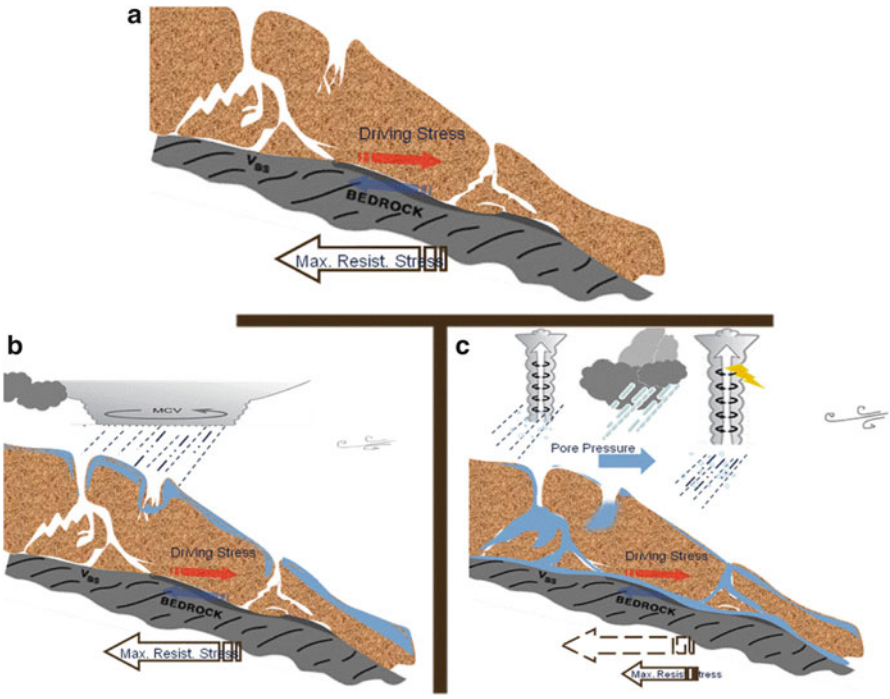

Fig. A.3 Rainfall characteristics and landslide magnitudes. *Cyan color* indicates wet soil and accumulated ground water. (**a**) illustrates a vertical cross section of a fractured slope, under dry condition. Driving stress is exactly balanced by resistive stress and their magnitudes are smaller than the maximum resistive stress the bedrock can provide, or $\tau_R = \tau_D < \tau_{D\max}$ by several kPa. (**b**) illustrates the situation under stratiform precipitation, where rainfall intensity is small but lasting longer time. Most rainfall are uniformly infiltrated to the near surface layer. (**c**) is the situation under convective cloudbursts, which have intense precipitation that generate runoff and percolation. Most rainfall is either drained into crevasses or simply lost as surface runoff. In case (**b**), only the surface layer is mobilized. In case (**c**), the water discharged to the bottom reduces the maximum resistive stress significantly. In addition, there is an extra pore water caused horizontal stress (pointing down slope) aiding the driving stress and the entire deep layer is set into motion: $\tau_R = \tau_{D\max} < \tau_D + P_s$. Thus, same amount of precipitation, come in different morphology, result into different rainfall distribution within slope and mobilize drastically different amount of sliding material

drier material, quickly loss its fluidity and may stop mid-slope. The above two cases correspond respectively to intense convective precipitation and stratiform precipitation.

There are also cases that medium-followed by severe rainfall intensity maximizes the sliding material gain. For example, for nonuniform graded slopes, at medium rainfall rate, sliding material cannot slide all the way to toe, and it stops mid-slope. The following intense rainfall is capable to send then to the toe, entraining along the way at significantly larger entraining rate, because entrainment process is nonlinearly related to instantaneous amount of the sliding material.

Only for enough slow thawing cycle, the landslide scarp size is proportional to slope length dimension (Ekstrom 2013). Compared to the speed of washout, the accumulation speed of granular sliding material is much slower. Availability of granular material on slopes is the first prerequisite for landslides. Thus, steep slopes are on one end and the fractured granular mantle is on another end. The above-discussed is for well-weathered slopes.

Appendix D
Basic Tensor and Vector Operations

The following tensor and vector operations are useful for readers interested in following the derivations of governing equations in the numerical modeling system.

D.1 Identities

Suppose ϕ and ψ are scalar functions and ϕ and ψ are vector functions, we have the following ten identities:

$$\nabla(\phi\psi) = \psi\nabla\phi + \phi\nabla\psi \tag{A.6}$$

$$\nabla\left(\phi\vec{f}\right) = \nabla\phi\cdot\vec{f} + \phi\left(\nabla\cdot\vec{f}\right) \tag{A.7}$$

$$\nabla\times\left(\phi\,\vec{f}\right) = \nabla\phi\times\vec{f} + \phi\left(\nabla\times\vec{f}\right) \tag{A.8}$$

$$\begin{aligned}\nabla\left(\vec{g}\cdot\vec{f}\right) = {} & \vec{f}\times\left(\nabla\times\vec{g}\right) + \vec{g}\times\left(\nabla\times\vec{f}\right) + \left(\vec{f}\cdot\nabla\right)\vec{g} \\ & + \left(\vec{g}\cdot\nabla\right)\vec{f}\end{aligned} \tag{A.9}$$

$$\nabla\times\left(\vec{f}\times\vec{g}\right) = \vec{f}\left(\nabla\cdot\vec{g}\right) - \vec{g}\left(\nabla\cdot\vec{f}\right) + \left(\vec{g}\cdot\nabla\right)\vec{f} - \left(\vec{f}\cdot\nabla\right)\vec{g} \tag{A.10}$$

$$\nabla\cdot\left(\vec{f}\times\vec{g}\right) = \left(\nabla\times\vec{f}\right)\cdot\vec{g} - \vec{f}\cdot\left(\nabla\times\vec{g}\right) \tag{A.11}$$

© Springer International Publishing Switzerland 2015

D. Ren, *Storm-triggered Landslides in Warmer Climates*,
DOI 10.1007/978-3-319-08518-0

$$\nabla \times \nabla \phi = 0 \tag{A.12}$$

$$\nabla \cdot (\nabla \phi) = \nabla^2 \phi \equiv \Delta \phi \tag{A.13}$$

$$\nabla \cdot \left(\nabla \times \vec{f} \right) = 0 \tag{A.14}$$

$$\nabla \times \left(\nabla \times \vec{f} \right) = \nabla \left(\nabla \cdot \vec{f} \right) - \nabla^2 \vec{f} \tag{A.15}$$

And the following four vector identities (vector sign omitted because all involved are vectors):

$$A \times (B \times C) = (A \cdot C)B - (A \cdot B)C \tag{A.16}$$

$$(A \times B) \times C = -C \times (A \times B) = (C \cdot A)B - (C \cdot B)A \tag{A.17}$$

$$(A \times B) \cdot (C \times D) = (A \cdot C) \cdot (B \cdot D) - (A \cdot D)(B \cdot C) \tag{A.18}$$

$$\begin{aligned} (A \times B) \times (C \times D) &\overset{applying\ (A4.11)}{=} B[A \cdot (C \times D)] - A[B \cdot (C \times D)] \\ &= C[A \cdot (B \times D)] - D[A \cdot (B \times C)] \end{aligned} \tag{A.19}$$

D.2 Opertators

(a) Kronecker substitution tensor (second order tensor)

$$\delta_{i,j} = \vec{e}_i \cdot \vec{e}_j = \begin{cases} 1, & \mathrm{i} = \mathrm{j} \\ 0, & \mathrm{i} \neq \mathrm{j} \end{cases} \tag{A.20}$$

For example, $\delta_{i,j} u_j = u_i$, $\nabla \cdot \vec{a} = \frac{\partial a_i}{\partial x_i}$, and $\vec{a} \cdot \vec{b} = a_i b_j \delta_{i,j}$ are all various uses of this operator.

(b) Alternating/permutation (third order tensor operator)

$$\varepsilon_{i,j,k} = \begin{cases} 1, & \text{if i, j, k is cyclic order} \\ 0, & \text{any two of the three indices are equal} \\ -1 & \text{if i, j, k is anti-cyclic order} \end{cases} \tag{A.21}$$

Example usages of this operator include take one component from a vector such as

$$\left[\vec{a} \times \vec{b} \right]_k = \varepsilon_{ijk} a_i b_j$$

$\left[\nabla \times \vec{a} \right]_k = \varepsilon_{ijk} \frac{\partial a_j}{\partial x_i}$, and a very useful relationship: epsilon-delta relationship

(c) Epsilon-delta relationship

$$\varepsilon_{ijk}\varepsilon_{klm} = \delta_{il}\delta_{jm} - \delta_{im}\delta_{jl} \tag{A.22}$$

(d) Matrix expression of vector/tensor operations

As we are familiar, $\vec{a} \cdot \vec{b} = \left|\vec{a}\right| \cdot \left|\vec{b}\right| \cos\left(\hat{\vec{a}, \vec{b}}\right)$. In matrix form of expression, it is

$$\vec{a} \cdot \vec{b} = \begin{pmatrix} a_1 \\ a_2 \\ a_3 \end{pmatrix}^T \begin{pmatrix} b_1 \\ b_2 \\ b_3 \end{pmatrix}$$

For $\left|\vec{a} \times \vec{b}\right| = \left|\vec{a}\right| \cdot \left|\vec{b}\right| \sin\left(\hat{\vec{a}, \vec{b}}\right)$, matrix expression of the vector cross product is

$$\vec{a} \times \vec{b} = \begin{vmatrix} \vec{i} & \vec{j} & \vec{k} \\ a_1 & a_2 & a_3 \\ b_1 & b_2 & b_3 \end{vmatrix}$$

$$\vec{a} \cdot \vec{b} \times \vec{c} = \begin{vmatrix} a_1 & a_2 & a_3 \\ b_1 & b_2 & b_3 \\ c_1 & c_2 & c_3 \end{vmatrix}$$

D.3 Stress as Force per Unit Area Exerted Across Areal Element $\vec{dA}$

In contrast to body forces that action at distance (e.g., gravity) and is proportional to volume of a parcel, stress if "surface force" or "contact force" that is forces exerted on the surface of a parcel or element by its immediate surroundings. In general, stress force depends on orientation of the surface boundering the parcel.

A more strict definition of stress or traction: Suppose δF (Fig. A.4) is the resultant of all forces exerted by the material on the positive side of area element δA upon the material on the other side of δA. The limit of the ratio $\delta F/\delta A$ as δA tends to zero is called the stress at the point O across the plane whose normal is the direction OP.

$\vec{\tau}_{op} = \lim_{\delta A \to 0} \frac{\delta \vec{F}}{\delta A}$. $\vec{\tau}_{op}$ is sometimes called a "stress vector" or "traction."

In a rectangular right-handed Cartesian coordinates, force in i direction,

$$\vec{F}_i = \left(\tau_{i,1}\vec{e}_1 + \tau_2\vec{e}_2 + \tau_{i,3}\vec{e}_3\right) = \tau_{i,j}\vec{e}_j dA = \tau_{i,j}dA_j = (\tau \bullet dA)_i \tag{A.23}$$

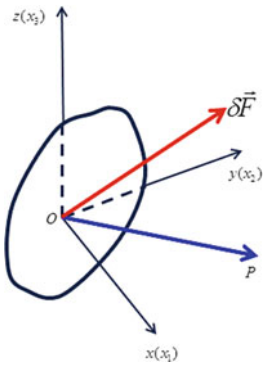

Fig. A.4 Illustration of an areal element and the stress tensor

Here stress τ is a second order tensor. The first suffix index denotes the orientation of the surface (the direction of the normal to the small area δA), while the second suffix the direction in which the component acts (direction of force). When the two indices are the same, τ_{ii} is the normal force per unit area on x_i face (also is noted as σ_i for convenience). This type of stress is "direct" or "normal" stress. If the normal component of the stress across a surface is positive it is called a tensile stress, and if it is negative it is called a compressive stress. When the two indices are different, τ_{ij} is force exerted per unit area on i surface in the j direction. These types of stress components are called "transverse" or "shear stress."

For example, τ_{12} and τ_{13} are shear stress forces per unit area on x_1 face. Eq. (A.23) is the master equation in constructing momentum equations for the sliding material. Similarly, the stress at O across a plane whole normal is in the direction of oy will have τ_{yx}, τ_{yy} and τ_{yz} and that across a plane whose normal is in the oz direction will have components τ_{zx}, τ_{zy} and τ_{zz}. The above nine expressions are called stress-components at the point O. And matrix

$$\begin{pmatrix} \tau_{xx} & \tau_{xx} & \tau_{xx} \\ \tau_{yx} & \tau_{yy} & \tau_{yz} \\ \tau_{zx} & \tau_{zy} & \tau_{zz} \end{pmatrix} \tag{A.24}$$

can give a complete specification of the stress at point O, because stress across any plane through O can be expressed in terms of them. Actually, because $\tau_{ij} = \tau_{ji}$,[1] only six of them suffices: $\tau_{xx}, \tau_{yy}, \tau_{zz}, \tau_{xy}, \tau_{xz}, \tau_{yz}$.

[1] Proof of the symmetry of shear stress using force couple equilibrium. Consider the force on a very small square of material OABCO whose side length OA = OC = a is very small (Fig. A.5). The force on the face AB (per unit length perpendicular to the plane of the paper) are $a\tau_{xx}$, and $a\tau_{yx}$. Those on the face CD, remembering that they are those exerted by the material to the left on the material on the right, are $-a\tau_{xx}$, and $-a\tau_{xy}$, and so on. Considering the equilibrium of the square as a whole, it appears that the forces are in equilibrium, but there is a couple of magnitude $a^2(\tau_{yx} - \tau_{xy})$ that trying to rotate the square clockwise. Since the system is in equilibrium this couple must vanish so we must have $\tau_{yx} = \tau_{xy}$.

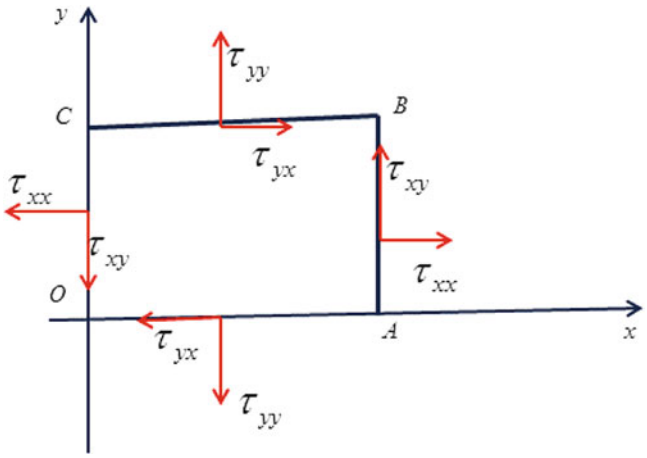

Fig. A.5 Equilibrium of a 2D box

For an arbitrary stress, we have the following symmetric properties of stress tensor:

$$\tau_{.j} = -\tau_{._j};\ \tau_{i.} = -\tau_{\_i},\ \text{and}\ \tau_{ij} = \tau_{ji}.$$

The following intend to help the readers in understanding the yielding criteria and the developing of the mathematical theory of the landslide modeling. The two dimensional, which usually has more easy comprehensible physical meaning, are presented first before introducing the general 3D case.

D.3.1 Maximum Normal Stress Angle θ *for General 2D Situation*

Because of the symmetric property, out of the four stress components in 2D case, only three are independent. Next, we show that the stress across any plane through O whose normal OP is inclined at θ to the OX (Fig. A.6) can be expressed in terms of τ_{xx}, τ_{yy} andτ_{xy}.

To do this, we calculate the normal and shear stress stresses σ and τ across a plane AB near to O: these will differ very little from those across a parallel plane through O. as shown by the arrow in Fig. A.6. τ is reckoned positive when it is directed towards the left of OP (i.e., right-handed system, τ is measured positive in the direction to the left of the outward normal).

Considering the equilibrium of the triangle OAB (or rather a prism of unit height on this as base), resolving in the direction of OP, write a for the length AB, and remembering that to get the force across any face the stress must be multiplied by the area of the face, we get (remember that anticlock is positive)

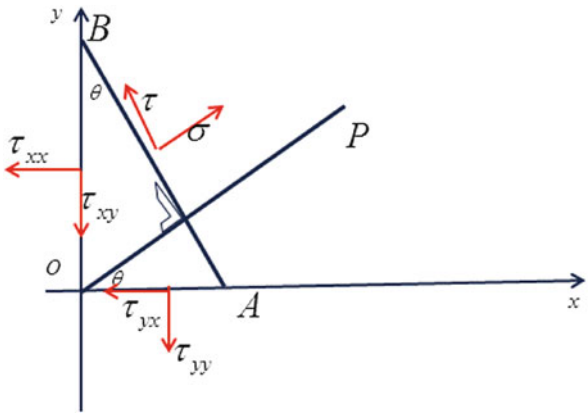

Fig. A.6 2D setting of stress expression

$$a\sigma = a\sin\theta\left(\tau_{xy}\cos\theta + \tau_{yy}\sin\theta\right) + a\cos\theta\left(\tau_{xx}\cos\theta + \tau_{xy}\sin\theta\right) \tag{A.25}$$

And, resolving in direction AB,

$$a\tau = a\sin\theta\left(-\tau_{xy}\sin\theta + \tau_{yy}\cos\theta\right) + a\cos\theta\left(-\tau_{xx}\sin\theta + \tau_{xy}\cos\theta\right) \tag{A.26}$$

Equations (A.25) and (A.26) can be rewritten as

$$\begin{aligned}\sigma &= \tau_{xx}\cos^2\theta + 2\tau_{xy}\sin\theta\cos\theta + \tau_{yy}\sin^2\theta \\ &= \tau_{xx}\cos^2\theta + \tau_{xy}\sin 2\theta + \tau_{yy}\sin^2\theta\end{aligned} \tag{A.27}$$

And, resolving in direction AB,

$$\begin{aligned}\tau &= \left(\tau_{yy} - \tau_{xx}\right)\sin\theta\cos\theta + \tau_{xy}\left(\cos^2\theta - \sin^2\theta\right) \\ &= \left(\tau_{yy} - \tau_{xx}\right)\sin\theta\cos\theta + \tau_{xy}\cos 2\theta\end{aligned} \tag{A.28}$$

Equations (A.27) and (A.28) may be used to give the stress-components $\tau_{y'y'}$, $\tau_{x'x'}, \tau_{x'y'}$ relative to axes OX′, OY′ rotated from OX and OY. $\tau_{x'y'}$ is given by Eq. (A.28), and using Eq. (A.27) for angles θ and $\theta + \pi/2$, respectively, yields

$$\tau_{x'x'} = \tau_{xx}\cos^2\theta + \tau_{xy}\sin 2\theta + \tau_{yy}\sin^2\theta \tag{A.29}$$

$$\tau_{y'y'} = \tau_{xx}\sin^2\theta - \tau_{xy}\sin 2\theta + \tau_{yy}\cos^2\theta \tag{A.30}$$

Adding Eqs. (A.29) and (A.30) gives

$$\tau_{x'x'} + \tau_{y'y'} = \tau_{xx} + \tau_{yy} \tag{A.31}$$

That is, if the axes are rotated, this quantity $\tau_{xx} + \tau_{yy}$ remains unchanged or invariant though both τ_{xx} and τ_{yy} themselves change. Such invariants are of great

importance in the development of the creeping and yielding theories. Eqs. (A.27) and (A.28) give a complete description of the way in which the stress at a point varies with direction. We now discuss this behavior in detail and obtain some simple geometrical representations of it.

Differentiating Eq. (A.27) gives

$$\begin{aligned}\frac{d\sigma}{d\theta} &= -2\tau_{xx}\cos\theta\sin\theta + 2\tau_{xy}\cos 2\theta + 2\tau_{yy}\cos\theta\sin\theta \\ &= 2\tau_{xy}\cos 2\theta + \sin 2\theta\left(\tau_{yy} - \tau_{xx}\right)\end{aligned} \tag{A.32}$$

It follows from Eq. (A.32) that the normal stress is a minimum or maximum when θ is given by

$$\begin{aligned}0 = \frac{d\sigma}{d\theta} &= 2\tau_{xy}\cos 2\theta + \sin 2\theta\left(\tau_{yy} - \tau_{xx}\right) \\ \Rightarrow tg\,2\theta &= \frac{2\tau_{xy}}{\left(\tau_{xx} - \tau_{yy}\right)} = \frac{2\tau_{xy}}{\left(\sigma_x - \sigma_y\right)}\end{aligned} \tag{A.33}$$

Note that if we set $\tau = 0$ in Eq. (A.28), same result is obtained. Eq. (A.33) defines two directions at right angle such that the normal stress over them are greatest and least at the point and the shear stress over them are zero. These directions are called principal axes of stress and the stresses over them are called the principal stresses.

The notation σ_1 and σ_2 will be used for the principal stresses, σ_1 being assumed the algebraically greatest, and, as always, tensile stresses being reconed positive. From Eq. (A.33), if the (state of stress at a point) is known, the directions of the principal axes and the values of the principal stresses can be found immediately. When these are known, it is much simpler to take the principal axes as axes of reference: thus, if we take these as new x and y axes, we have $\sigma_x = \sigma_1, \sigma_y = \sigma_2$, $\tau_{xy} = 0$. From Eqs. (A.27) and (A.28), the normal and shear stresses across a plane whose normal is inclined at θ to the (principal) x-axis becomes:

$$\sigma = \sigma_1\cos^2\theta + \sigma_2\sin^2\theta \overset{\left(\begin{smallmatrix}\text{using } \cos 2\theta = 1 - 2\sin^2\theta \\ = 2\cos^2\theta - 1\end{smallmatrix}\right)}{=} \frac{1}{2}(\sigma_1 + \sigma_2) + \frac{1}{2}(\sigma_1 - \sigma_2)\cos 2\theta \tag{A.34}$$

$$\tau = (\sigma_2 - \sigma_1)\sin\theta\cos\theta = -\frac{1}{2}(\sigma_1 - \sigma_2)\sin 2\theta \tag{A.35}$$

Another representation which is of greatest theoretical importance is obtained by taking a line from the origin in the direction θ of the normal and choosing a point P on it whose distance r from the origin is

$$r = k\sigma^{-0.5}, \text{ so that } \sigma = k^2/r^2, \tag{A.36}$$

where σ is the normal stress across the plane and k is a constant.

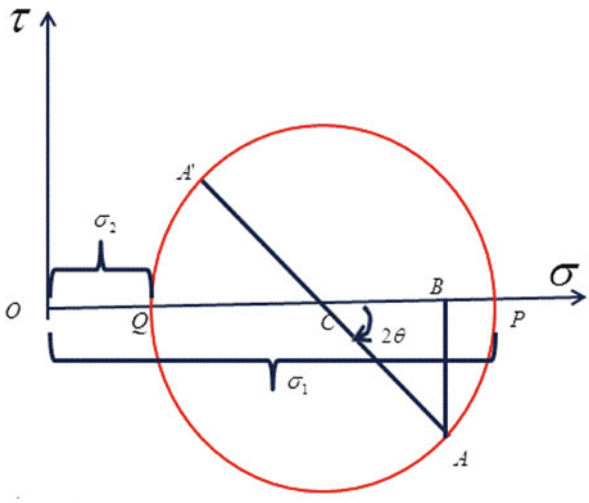

Fig. A.7 Mohr's circle diagram for 2D cases

Putting Eq. (A.36) into Eq. (A.34) gives

$$\sigma_1 r^2 \cos^2\theta + \sigma_2 r^2 \sin^2\theta = k^2 \tag{A.37}$$

Since $x = r\cos\theta, y = r\sin\theta$ are the coordinates of the point P, it lies on the conic

$$\sigma_1 x^2 + \sigma_2 y^2 = k^2 \tag{A.38}$$

This is called a stress conic: it is an ellipse if σ_1 and σ_2 have the same sign, and an hyperbola if they have opposite signs. The same conic, rooted through an angle given by Eq. (A.33), would have been found if we had discussed Eq. (A.27) in the same way, and the principal axes and principal stresses could have been found from it: this is, in fact, a common approach and one which can be used in three dimensions. In the same way, using

$\tau = k^2/r^2$ in Eq. (A.35), the shear stress in principal axes can be represented by a point on the hyperbola:

$$(\sigma_2 - \sigma_1)xy = k^2 \tag{A.39}$$

D.3.2 Mohr's Circle Diagram in 2D

Yet another representation of Eq. (A.27), Mohr's circle diagram, is the simplest and most useful of all.

Suppose that, as in Fig. A.7, we mark off lengths $OP = \sigma_1$ and $OQ = \sigma_2$ on a line and draw a circle on PQ as diameter with center C. Apparently, $OC = (\sigma_1 + \sigma_2)/2$. Then, if A is a point on the circle such that the angle PCA measured clockwise is 2θ

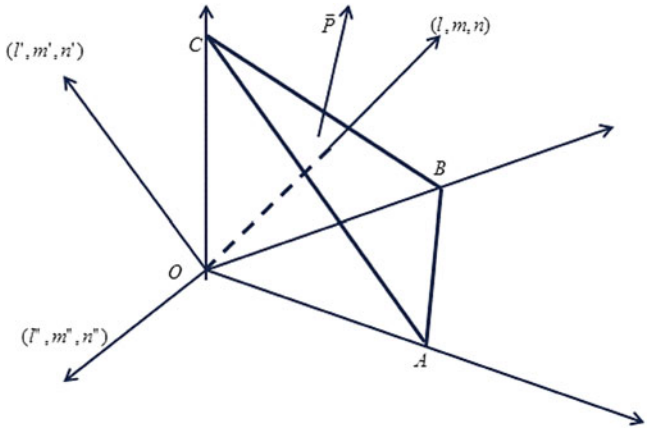

Fig. A.8 Principal stress components in 3D

and AB is perpendicular to PQ, it follows from Equations (A.34) and (A.35) that $OB = \sigma$ and $AB = \tau$. That is A represents the normal and shear stresses across the plane θ plotted on a (σ, τ) plane, and the circle of center C is their locus as θ changes. It is straightforward to see that shear stress has its greatest magnitude when $\theta = 45^\circ$ or 135° (in principal axes).

D.3.3 Stress in Three Dimensions

Suppose that $\sigma_x(\tau_{xx}), \sigma_y(\tau_{yy}), \sigma_z(\tau_{zz}), \tau_{xy}, \tau_{xz}, \tau_{yz}$ are three dimensional stress components at point O, it can be proof (by considering the equilibrium of a small rectangular parallelepiped) the symmetric properties of shear stresses:

$$\tau_{xy} = \tau_{yx}, \tau_{yz} = \tau_{zy}, \tau_{xz} = \tau_{zx} \tag{A.40}$$

Now, lets estimate the stress across a plane through O whose normal has direction cosine (l, m, n) relative to the axes ox, oy, oz.

To do this we consider the equilibrium of the small tetrahedron $OABC$ whose face ABC is normal to (l, m, n) and has area w so that the areas of the faces OAB, OBC, and OCA are nw, lw, mw, respectively (Fig. A.8).

Suppose that P_x, P_y, P_z are the components of the stress across the face ABC in the direction of the axes ox, oy, oz. Then, resolving in the direction of ox, we get

$$wP_x = wl\sigma_x + wm\sigma_{xy} + wn\sigma_{xz}, \text{ or } P_x = l\sigma_x + m\tau_{xy} + n\tau_{xz} \tag{A.41}$$

And, similarly,

$$P_y = l\tau_{xy} + m\sigma_y + n\tau_{yz} \tag{A.42}$$

$$P_x = l\tau_{xz} + m\tau_{yz} + n\sigma_z \tag{A.43}$$

In vector form,

$$\vec{P} = \begin{pmatrix} \sigma_x & \tau_{xy} & \tau_{xz} \\ \tau_{yx} & \sigma_y & \tau_{yz} \\ \tau_{zx} & \tau_{zy} & \sigma_z \end{pmatrix} \begin{pmatrix} l \\ m \\ n \end{pmatrix} = \vec{\tau}\vec{P}^0 \tag{A.44}$$

Equations (A.41)–(A.43) specify stress across the plane whose normal has direction (l, m, n) but they are not very directly related to this plane since they refer to the coordinate directions ox, oy, oz. The most interesting quantities are the normal stress σ and shear stress τ across the plane.

$$\sigma = \vec{P} \cdot \vec{n} = l^2\sigma_x + m^2\sigma_y + n^2\sigma_z + 2lm\tau_{xy} + 2\ln\tau_{xz} + 2mn\tau_{yz} \tag{A.45}$$

In the same way, the shear stress across the plane could be resolved into its components τ' in the direction (l', m', n') and τ'' in the direction (l'', m'', n'')

$$\tau' = \left(l', m', n'\right) \begin{pmatrix} \sigma_x & \tau_{xy} & \tau_{xz} \\ \tau_{yx} & \sigma_y & \tau_{yz} \\ \tau_{zx} & \tau_{zy} & \sigma_z \end{pmatrix} \begin{pmatrix} l \\ m \\ n \end{pmatrix} = \left(l', m', n'\right)(\tau_{ij}) \begin{pmatrix} l \\ m \\ n \end{pmatrix} \tag{A.46}$$

$$\tau'' = \left(l'', m'', n''\right)(\tau_{ij}) \begin{pmatrix} l \\ m \\ n \end{pmatrix} \tag{A.47}$$

where direction (l', m', n') and (l'', m'', n'') are two perpendicular directions in the plane. Thus, resolving in the direction (l', m', n') gives

$$\tau' = ll'\sigma_x + mm'\sigma_y + nn'\sigma_z + \left(l'm + lm'\right)\tau_{xy} + \left(l'n + n'l\right)\tau_{xz} + \left(mn' + m'n\right)\tau_{yz} \tag{A.48}$$

With a similar formula for τ''

$$\tau'' = ll''\sigma_x + mm''\sigma_y + nn''\sigma_z + \left(l''m + lm''\right)\tau_{xy} + \left(l''n + n''l\right)\tau_{xz} + \left(mn'' + m''n\right)\tau_{yz} \tag{A.49}$$

Now lets introduce the following cosine directions:

$$\hat{e}_1 = (l,m,n)\begin{pmatrix}\vec{i}\\ \vec{j}\\ \vec{k}\end{pmatrix}; \hat{e}_2 = \left(l',m',n'\right)\begin{pmatrix}\vec{i}\\ \vec{j}\\ \vec{k}\end{pmatrix}; \hat{e}_3 = \left(l'',m'',n''\right)\begin{pmatrix}\vec{i}\\ \vec{j}\\ \vec{k}\end{pmatrix} \tag{A.50}$$

The three compose a right-handed coordinates with directional cosine matrix as

$$M = \begin{pmatrix} l & l' & l'' \\ m & m' & m'' \\ n & n' & n'' \end{pmatrix} \tag{A.51}$$

Thus, $MM^T = M^TM = I$ is a direct result from the orthogonal relationship.

Expressions in Eqs. (A.45), (A.48), and (A.49) may also be regarded as formulae for change of axes which gives the stress components for the new coordinates of rectangular axes $\hat{e}_1$, $\hat{e}_2$ and $\hat{e}_3$, in terms of those for the system O_{xyz}. Now we demonstrate that the extreme normal stress is in the principal direction $\left(\text{an } \hat{e}_1 \text{ that is aligned with } \begin{pmatrix}P_x\\ P_y\\ P_z\end{pmatrix}\right)$.

Because there are only 2 degree of freedom of the three base vector ($\hat{e}_1$, $\hat{e}_2$ and $\hat{e}_3$), suppose $l(\hat{e}_1)$ and $m(\hat{e}_2)$ directions are independent, or $\frac{\partial l}{\partial m} = \frac{\partial m}{\partial l} = 0$.

From Eq. (A.51), there is a constraint among the base vectors as

$$l^2 + m^2 + n^2 = 1 \tag{A.52}$$

Thus, through differentiating Eq. (A.52) with respect to l and m, respectively, we have

$$l + n\frac{\partial n}{\partial l} = 0 \Rightarrow \frac{\partial n}{\partial l} = -\frac{l}{n} \text{ and } \frac{\partial n}{\partial m} = -\frac{m}{n} \tag{A.53}$$

The conditions for σ to be stationary are

$$\frac{\partial \sigma}{\partial m} = \frac{\partial \sigma}{\partial l} = 0 \tag{A.54}$$

From Eq. (A.45),

$$\begin{aligned}\frac{\partial \sigma}{\partial l} &= P_x + l\frac{\partial P_x}{\partial l} + m\frac{\partial P_y}{\partial l} + n\frac{\partial P_z}{\partial l} + P_z\frac{\partial n}{\partial l} \\ &= P_x + P_z\frac{\partial n}{\partial l} + l\left(\sigma_x + \frac{\partial n}{\partial l}\tau_{xz}\right) + m\left(\tau_{xy} + \frac{\partial n}{\partial l}\tau_{zy}\right) + n\left(\tau_{xz} + \frac{\partial n}{\partial l}\sigma_z\right) \\ &\underset{\text{using definition}}{=} 2\left(P_x + P_z\frac{\partial n}{\partial l}\right)\end{aligned} \tag{A.55}$$

So $\frac{\partial \sigma}{\partial l} = 0$ means

$$\left(P_x + P_z \frac{\partial n}{\partial l}\right) = 0 \tag{A.56}$$

similarly
$\frac{\partial \sigma}{\partial m} = 0$ means

$$\left(P_y + P_z \frac{\partial n}{\partial m}\right) = 0 \tag{A.57}$$

Using Eqs. (A.53), (A.56), and (A.57) yield

$$\frac{P_x}{l} = \frac{P_y}{m} = \frac{P_z}{n} \tag{A.58}$$

Physically, this expression tells us that a plane through O can be properly oriented so that on this plane, there is only normal stress and shear stress disappears.

Now, let construct the principal axes and examine the topological structure of the principal stresses. If σ is the value of this (remainder) normal stress acting on surface (l, m, n), Eq. (A.58) may be written as

$$P_x = \sigma l \tag{A.59}$$

However, from Eq. (A.41),

$$P_x = l\sigma_x + m\tau_{xy} + n\tau_{xz}, \text{ thus}$$

$$(\sigma - \sigma_x)l - m\tau_{xy} - n\tau_{xz} = 0 \tag{A.60}$$

Similarly, from $P_y = \sigma m$; and $P_z = \sigma n$, we get

$$l\tau_{xy} + m(\sigma_y - \sigma) + n\tau_{yz} = 0 \tag{A.61}$$

and

$$l\tau_{xz} + m\tau_{yz} + n(\sigma_z - \sigma) = 0 \tag{A.62}$$

The Eqs. (A.60)–(A.62) are a set of three homogeneous linear equations for (l, m, n). From algebraic theory that they have a non-trite (zero) solution for (l, m, n) only when σ is a root of the equation

$$\begin{vmatrix} \sigma_x - \sigma & \tau_{xy} & \tau_{xz} \\ \tau_{xy} & \sigma_y - \sigma & \tau_{yz} \\ \tau_{xz} & \tau_{yz} & \sigma_z - \sigma \end{vmatrix} = 0 \tag{A.63}$$

Expand form is

$$\sigma^3 - I_1\sigma^2 - I_2\sigma - I_3 = 0 \tag{A.64}$$

where invariants I_1, I_2, and I_3 are, respectively:

$$I_1 = \left(\sigma_x + \sigma_y + \sigma_z\right) \tag{A.65}$$

$$I_2 = -\left(\sigma_y\sigma_z + \sigma_x\sigma_z + \sigma_x\sigma_y\right) + \tau_{xy}^2 + \tau_{xz}^2 + \tau_{yz}^2, \tag{A.66}$$

$$I_3 = \sigma_x\sigma_y\sigma_z + 2\tau_{xy}\tau_{xz}\tau_{yz} - \sigma_x\tau_{yz}^2 - \sigma_y\tau_{xz}^2 - \sigma_z\tau_{xy}^2. \tag{A.67}$$

These quantities I_1, I_2, and I_3 apparently depend upon the initial choice of the x-, y-, and z-axes, but the roots of Eq. (A.64) which are the principal stresses are independent of this choice and so the coefficients I_1, I_2, and I_3 must also be independent of the choice of coordinates. Out in another way, the quantities I_1, I_2, and I_3 must remain unchanged or "invariant" if the axes are changed.

$$\left(\sigma_x + \sigma_y + \sigma_z\right) = \sigma_1 + \sigma_2 + \sigma_3 \tag{A.68}$$

I_2, which is fundamental for the theory of viscoplasticity (e.g., ice), follows

$$\left(\sigma_y\sigma_z + \sigma_x\sigma_z + \sigma_x\sigma_y\right) + \tau_{xy}^2 + \tau_{xz}^2 + \tau_{yz}^2 = \sigma_1\sigma_2 + \sigma_2\sigma_3 + \sigma_1\sigma_3 \tag{A.69}$$

Similarly, by taking a square of Eq. (A.65) and using the expression of I_2 in Eq. (A.66), it is straightforward to obtain

$$\left(\sigma_x^2 + \sigma_y^2 + \sigma_z^2\right) + 2\tau_{yz}^2 + 2\tau_{xz}^2 + 2\tau_{xy}^2 = \sigma_1^2 + \sigma_2^2 + \sigma_3^2 \tag{A.70}$$

Since Eq. (A.64) is a cubic in σ, it has three (real) roots σ_1, σ_2 and σ_3, and corresponding to each of these gives a set of direction cosines (l_1, m_1, n_1), (l_2, m_2, n_2), and (l_3, m_3, n_3), respectively. These directions are, in fact, mutually perpendicular.

Readers can omit the following advanced derivatives and discussions without affecting the understanding of the chapters in the book.

So there are three mutually perpendicular directions called the principal axes of stress in which the stress is purely normal and has values σ_1, σ_2 and σ_3 which are called the principal stresses. We should always use the convention $\sigma_1 > \sigma_2 > \sigma_3$, and, since the normal stress has been proved to be stationary (with maximum and minimum values) in the direction of the principal axes, it follows that σ_1 is the algebraically greatest, and σ_3 the least, normal stress at the point of interest. If the six stress components at the point are given numerically, it is possible by the above analysis to determine the principal axes and stresses; needless to say, it is rarely necessary to do this. The importance of the present discussion is that it gives a complete picture of the way in which the normal stress varies.

Parallel to the 2D stress conic (Eq. A.38), in the case of 3D, there is a stress quadric concept. If we plot a point with distance $k/\sqrt{\sigma}$ from the origin in the direction (l, m, n), its coordinates will be

$$x = \frac{lk}{\sqrt{\sigma}}, y = \frac{mk}{\sqrt{\sigma}}, z = \frac{nk}{\sqrt{\sigma}} \tag{A.71}$$

But, from Eq. (A.45),
$\sigma = l^2\sigma_x + m^2\sigma_y + n^2\sigma_z + 2lm\tau_{xy} + 2nl\tau_{xz} + 2mn\tau_{yz}$. Substitute in the expressions of l, m, n from Eq. (A.71), we get

$$x^2\sigma_x + y^2\sigma_y + z^2\sigma_z + 2xy\tau_{xy} + 2xz\tau_{xz} + 2yz\tau_{yz} = k^2 \tag{A.72}$$

This surface spanned by Eq. (A.72) is called a stress quadric. It is known from pure geometry that it has a set of three mutually perpendicular axes referred to which the terms of type yz, xy, xz in Eq. (A.72) disappear. These are exactly the principal axes found above. It should be mentioned that the determination of principal axes is unique only if none of σ_1, σ_2, σ_3 are equal. If two of them are equal, there is rotational symmetry about the third axis. If the three are all equal (hydrostatic pressure or tension), the stress quadric is a sphere and any set of mutually perpendicular axes may be taken as principal axes.

In the following discussion, we take the axes of reference to be principal axes. Suppose now, that ox, oy, oz are the principal axes and σ_1, σ_2, σ_3 the associated principal stresses with, as usual, $\sigma_1 > \sigma_2 > \sigma_3$. Then the components of the stress across a plane whose normal is in the direction (l, m, n) are

$$\vec{P}_x = \sigma_1 l\hat{\sigma}_1^0; \quad \vec{P}_y = \sigma_2 m\hat{\sigma}_2^0; \quad \vec{P}_z = \sigma_3 n\hat{\sigma}_3^0 \tag{A.73}$$

It follows immediately from Eq. (A.52) that

$$\left(\frac{P_x}{\sigma_1}\right)^2 + \left(\frac{P_y}{\sigma_2}\right)^2 + \left(\frac{P_z}{\sigma_3}\right)^2 = 1 \tag{A.74}$$

Note that Eq. (A.74) is independent of the direction. In fact, the components of the stress across any plane lie on an ellipsoid sometimes called the ellipsoid of stress.

The normal stress σ across the plane is

$$\sigma = \vec{P} \cdot \begin{pmatrix} l\hat{\sigma}_1^0 \\ m\hat{\sigma}_2^0 \\ n\hat{\sigma}_3^0 \end{pmatrix} = l^2\sigma_1 + m^2\sigma_2 + n^2\sigma_3 \tag{A.75}$$

The magnitude of the stress across the plane, R, is

$$R = \left|\vec{P}\right| = \sqrt{p_x^2 + p_y^2 + p_z^2} = \left(l^2\sigma_1^2 + m^2\sigma_2^2 + n^2\sigma_3^2\right)^{0.5} \tag{A.76}$$

The above discussion focuses on the normal stress. The shear stress and its magnitude also hold a critical role in yielding theories. The magnitude of the shear stress is easier to obtain by resolving the total stress $\vec{P}$ across the plane into its component in (τ), and perpendicular to, the plane (σ).

$$\tau^2 = R^2 - \sigma^2 = (\sigma_1 - \sigma_2)^2 l^2 m^2 + (\sigma_2 - \sigma_3)^2 m^2 n^2 + (\sigma_3 - \sigma_1)^2 n^2 l^2 \tag{A.77}$$

In the case in which $\sigma_1 = \sigma_2 = \sigma_3 = -p$, we have by Eq. (A.77) and (A.75), $\tau = 0, \sigma = -p$ for all directions. This is the case of hydrostatic pressure. To understand the direction of shear stress, more detailed analyses are needed that helps better understand the stress structure within in material. Suppose the two direction cosines (unit normal vectors) in the two shear stress directions are:

$\begin{pmatrix} l'\hat{\sigma}_1^0 \\ m'\hat{\sigma}_2^0 \\ n'\hat{\sigma}_3^0 \end{pmatrix}$ and $\begin{pmatrix} l''\hat{\sigma}_1^0 \\ m''\hat{\sigma}_2^0 \\ n''\hat{\sigma}_3^0 \end{pmatrix}$. The projection of full stress vector $\vec{P}$ in these two directions are, respectively

$$\begin{aligned}
\vec{\tau}' &= \left(l\sigma_1\hat{\sigma}_1^0, m\sigma_2\hat{\sigma}_2^0, n\sigma_3\hat{\sigma}_3^0\right)\begin{pmatrix} l'\hat{\sigma}_1^0 \\ m'\hat{\sigma}_2^0 \\ n'\hat{\sigma}_3^0 \end{pmatrix}\left(l'\hat{\sigma}_1^0, m'\hat{\sigma}_2^0, n'\hat{\sigma}_3^0\right) \\
&= \left(ll'\sigma_1 + mm'\sigma_2 + nn'\sigma_3\right)\left(l'\hat{\sigma}_1^0, m'\hat{\sigma}_2^0, n'\hat{\sigma}_3^0\right) \\
&= \left(ll'l'\sigma_1 + l'mm'\sigma_2 + l'nn'\sigma_3\right)\hat{\sigma}_1^0 + \left(ll'm'\sigma_1 + mm'm'\sigma_2 + nn'm'\sigma_3\right)\hat{\sigma}_2^0 \\
&\quad + \left(ll'n'\sigma_1 + mm'n'\sigma_2 + nn'n'\sigma_3\right)\hat{\sigma}_3^0
\end{aligned} \tag{A.78}$$

Similarly, in the second shear direction,

$$\begin{aligned}
\vec{\tau}'' &= \left(l\sigma_1\hat{\sigma}_1^0, m\sigma_2\hat{\sigma}_2^0, n\sigma_3\hat{\sigma}_3^0\right)\begin{pmatrix} l''\hat{\sigma}_1^0 \\ m''\hat{\sigma}_2^0 \\ n''\hat{\sigma}_3^0 \end{pmatrix}\left(l''\hat{\sigma}_1^0, m''\hat{\sigma}_2^0, n''\hat{\sigma}_3^0\right) \\
&= \left(ll''\sigma_1 + mm''\sigma_2 + nn''\sigma_3\right)\left(l''\hat{\sigma}_1^0, m''\hat{\sigma}_2^0, n''\hat{\sigma}_3^0\right) \\
&= \left(ll''l''\sigma_1 + l''mm''\sigma_2 + l''nn''\sigma_3\right)\hat{\sigma}_1^0 + \left(ll''m''\sigma_1 + mm''m''\sigma_2 + nn''m''\sigma_3\right)\hat{\sigma}_2^0 \\
&\quad + \left(ll''n''\sigma_1 + mm''n''\sigma_2 + nn''n''\sigma_3\right)\hat{\sigma}_3^0
\end{aligned} \tag{A.79}$$

Reorganizing $\vec{\tau}'' + \vec{\tau}''$ in all three $\hat{\sigma}_*^0$ direction, we have

$$\vec{\tau}'' + \vec{\tau}'' = l\left[m^2(\sigma_1 - \sigma_2) + n^2(\sigma_1 - \sigma_3)\right]\vec{\sigma}_1^0 + m\left[l^2(\sigma_2 - \sigma_1) + n^2(\sigma_2 - \sigma_3)\right]\vec{\sigma}_2^0 + n\left[l^2(\sigma_3 - \sigma_1) - m^2(\sigma_2 - \sigma_3)\right]\vec{\sigma}_3^0$$

The right hand side also clearly indicates the direction cosine of the shear stress direction is

$$\left\{l[m^2(\sigma_1 - \sigma_2) + n^2(\sigma_1 - \sigma_3)]; m\left[l^2(\sigma_2 - \sigma_1) + n^2(\sigma_2 - \sigma_3)\right]; n\left[l^2(\sigma_3 - \sigma_1) - m^2(\sigma_2 - \sigma_3)\right]\right\} \tag{A.80}$$

Corresponding geometric representation of shear stress also is much more complicated than the normal stress. To get a geometrical representation of Eq. (A.77), we may plot a point distance $k/\sqrt{\tau}$ from the origin in the direction (l, m, n), its coordinates will be

$$x = \frac{lk}{\sqrt{\tau}}, y = \frac{mk}{\sqrt{\tau}}, z = \frac{nk}{\sqrt{\tau}} \tag{A.81}$$

Eq. (A.77) now becomes a fourth degree surface in place of the simpler second degree surface for normal stress:

$$x^2y^2(\sigma_1 - \sigma_2)^2 + y^2z^2(\sigma_2 - \sigma_3)^2 + x^2z^2(\sigma_3 - \sigma_1)^2 = k^4 \tag{A.82}$$

Note that the coefficients are always positive. Because of the importance of shear in the failure of material, it is obviously necessary to discuss the variation of τ with l, m, n in great details.

First, lets address the problem when τ is a maximum. Using the property of direction cosine (e.g., Eqs. A.52 and A.53), remove n and only leave l, m in the expression of τ.

$$\tau^2 = l^2\left(\sigma_1^2 - \sigma_3^2\right) + m^2\left(\sigma_2^2 - \sigma_3^2\right) + \sigma_3^2 - \left\{\sigma_3 + l^2(\sigma_1 - \sigma_3) + m^2(\sigma_2 - \sigma_3)\right\}^2 \tag{A.83}$$

In Eq. (A.83), l and m may vary independently and the condition for τ to be stationary is

$$\frac{\partial \tau}{\partial l} = 0 \text{ and } \frac{\partial \tau}{\partial l} = 0 \tag{A.84}$$

Now, from Eq. (A.83),

$$\begin{aligned}\tau\frac{\partial\tau}{\partial l} &= l\left(\sigma_1^2-\sigma_3^2\right)-2l(\sigma_1-\sigma_3)\left\{\sigma_3+l^2(\sigma_1-\sigma_3)+m^2(\sigma_2-\sigma_3)\right\}^2 \\ &= l(\sigma_1-\sigma_3)\left[(\sigma_1+\sigma_3)-2\left\{\sigma_3+l^2(\sigma_1-\sigma_3)+m^2(\sigma_2-\sigma_3)\right\}\right]\end{aligned} \tag{A.85}$$

$$\tau\frac{\partial\tau}{\partial m} = m(\sigma_2-\sigma_3)\left[(\sigma_2+\sigma_3)-2\left\{\sigma_3+l^2(\sigma_1-\sigma_3)+m^2(\sigma_2-\sigma_3)\right\}\right] \tag{A.86}$$

To make both Eqs. (A.85) and (A.86) vanish as required by Eq. (A.84), we may take $l=0$ so that Eq. (A.85) is readily satisfied, and using this value of l in Eq. (A.86) we have:

$$0 = m\left(1-2m^2\right)(\sigma_2-\sigma_3)^2 \tag{A.87}$$

Because m $\neq 0$ and σ_2 and σ_3 freely varies, $2m^2=1$ is required.

Thus, if $m=n=\sqrt{2}/2, l=0$, τ is stationary and by Eq. (A.77), its value is $(\sigma_2-\sigma_3)/2$. Since the status of l, m, n is equal, similarly, we have

If $l=n=\sqrt{2}/2, m=0, \tau$ is stationary and by Eq. (A.77), its value is $(\sigma_1-\sigma_3)/2$.

If $m=l=\sqrt{2}/2, n=0, \tau$ is stationary and by Eq. (A.77), its value is $(\sigma_1-\sigma_2)/2$. These stationary values of the shear stress are called the principal shear stress and are denoted by τ_1, τ_2, τ_3, so that

$$\tau_1=\frac{1}{2}(\sigma_2-\sigma_3), \tau_2=\frac{1}{2}(\sigma_1-\sigma_3), \tau_3=\frac{1}{2}(\sigma_1-\sigma_2) \tag{A.88}$$

Since, by our convention, $\sigma_2>\sigma_2>\sigma_3$, the greatest of (A.88) is τ_2. The normal stresses corresponding to τ_1, τ_2, τ_3 are $\frac{1}{2}(\sigma_2+\sigma_3), \frac{1}{2}(\sigma_1+\sigma_3), \frac{1}{2}(\sigma_1+\sigma_2)$.

The most important result is that the greatest shear is $\frac{1}{2}(\sigma_1-\sigma_3)$ and is across a plane whose normal bisects the angle between the direction of greatest and least principal stresses.

Mohr's representation of stress in three dimensions aiming an elegant representation of the variation of normal and shear stresses in three dimensions.

Recall the definition expression in Eqs. (A.75) and (A.77), and the direction cosine orthogonal properties, solving for l^2, m^2, and n^2, yields:

$$l^2=\frac{(\sigma_2-\sigma)(\sigma_3-\sigma)+\tau^2}{(\sigma_2-\sigma_1)(\sigma_3-\sigma_1)} \tag{A.89}$$

$$m^2=\frac{(\sigma_3-\sigma)(\sigma_1-\sigma)+\tau^2}{(\sigma_3-\sigma_2)(\sigma_1-\sigma_2)} \tag{A.90}$$

$$n^2=\frac{(\sigma_1-\sigma)(\sigma_2-\sigma)+\tau^2}{(\sigma_1-\sigma_3)(\sigma_2-\sigma_3)} \tag{A.91}$$

Now suppose that one direction cosine, say n, is fixed; this implies that the normal to the plane considered makes a fixed angle $\cos^{-1} n$ with the z-axis. Then, by (A.91), σ and τ for such a plane are related by

$$(\sigma_1 - \sigma)(\sigma_2 - \sigma) + \tau^2 = n^2(\sigma_1 - \sigma_3)(\sigma_2 - \sigma_3) \tag{A.92}$$

or

$$\tau^2 + [\sigma - 0.5(\sigma_1 + \sigma_2)]^2 = \frac{1}{4}(\sigma_1 - \sigma_2)^2 + n^2(\sigma_1 - \sigma_3)(\sigma_1 - \sigma_3) \tag{A.93}$$

That is, plotted on the (σ, τ) plane, σ and τ lie on a circle whose center is at (0.5 $(\sigma_1 + \sigma_2)$, 0) and whose radius is $\frac{1}{2}\sqrt{(\sigma_1 - \sigma_2)^2 + n^2(\sigma_1 - \sigma_3)(\sigma_1 - \sigma_3)}$. Other families of circles can be obtained by rotatingly fixing l and m. The reduced special cases are the 2D Mohr' representation. However, spatial shape can be complicated donuts shape for full 3D situation.

D.4 Three Theorems

(a) *Stokes' Theorem*

If S is an open surface bounded by a simple closed curve C and if A has continuous derivatives, then

$$\oint_C \vec{A} \cdot d\vec{r} = \int_S \left(\nabla \times \vec{A}\right) \cdot \vec{n} \cdot dS \tag{A.94}$$

where C is traversed in the positive (counterclockwise) direction.

(b) *Divergence Theorem of Gauss*

If V is a volume bounded by a closed surface S and if A is a vector function of position with continuous derivatives, then

$$\iiint_V \left(\nabla \cdot \vec{A}\right) \cdot dv = \int_S \vec{A} \cdot \vec{n} \cdot dS \tag{A.95}$$

where $\vec{n}$ is unit vector drawn normal to S.

(c) *Green's Theorem*

Green's theorem in a plane states that if R is a closed region in the x-y plane bounded by a simple closed curve C and if M and N are continuous functions of x and y having continuous partial derivatives in the region R, then

$$\oint_C M \cdot dx + N \cdot dy = \int_R \left(\frac{\partial N}{\partial x} - \frac{\partial M}{\partial y} \right) \cdot dxdy \tag{A.96}$$

Apparently, this is a more general form of the Stokes Theorem. We have Green's first identity as

$$\iiint_V \left(\phi \nabla^2 \rho + \nabla \phi \nabla \rho \right) \cdot dv = \int_S \phi \nabla \rho \cdot dS \tag{A.97}$$

and Green's second identity

$$\iiint_V \left(\phi \nabla^2 \rho - \rho \nabla^2 \phi \right) \cdot dv = \int_S \left(\phi \nabla \rho - \rho \nabla \phi \right) \cdot dS \tag{A.98}$$

D.5 Leibnitz Formula

As granular lump has tremendous degree of freedom, we are not intended to follow each granule. Rather, the group behavior is usually desired. Leibnitz formula is one fundamental such relationship governing sliding material's time variation in properties.

$$\frac{d}{dt} \iiint_V F\left(\vec{x}, t\right) dV = \iiint_{V(fct \text{ of time } t)} \frac{\partial}{\partial t} F\left(\vec{x}, t\right) dV + \int_{A(t)} F \vec{U}_A \vec{n} dA \tag{A.99}$$

where V is a time (t) varying volume holding the sliding material of interest, $\vec{n}$ is out normal of the surface/boundary A, $\vec{U}_A$ is the local velocity at area element ($d\vec{A}$) at the boundary of the volume V. The first term on the right hand side is the source and think, the second term is from flux, or the convergence or divergence of flow. Certainly, we can also perceive the $\vec{U}_A \vec{n}$ as the outward expansion of the volume through the motion of the boundary.

In Fig. A.9, Panel (a) is a Lagrangian parcel (i.e., following a parcel, or "material volume"), and (b) is an imaginary Eulerian Box (i.e., "fixed volume box").

For a fixed volume, $\vec{U}_A = 0$ so that

$$\frac{d}{dt} \iiint_V F\left(\vec{x}, t\right) dV = \iiint_{V(fct \text{ of time } t)} \frac{\partial}{\partial t} F\left(\vec{x}, t\right) dV \tag{A.100}$$

Whereas for a material volume, $\vec{U}_A = U$, the fluid velocity. In this case, we can also write $\frac{d}{dt}$ as $\frac{D}{Dt}$, total derivative following the parcel.

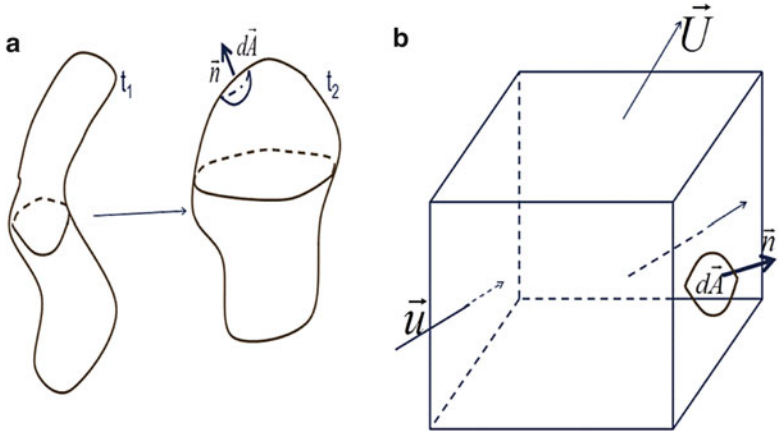

Fig. A.9 A Lagrangian parcel (**a**) and an imaginary Eulerian box (**b**) to illustrate the granular fluxes across the boundary (U) and spatially distributed flow (u). In the illustration, $\vec{n}$ is out normal of the surface/boundary A, $\vec{U}_A$ is the local velocity at area element ($d\vec{A}$) at the boundary of the volume V

$$\frac{D}{Dt}\iiint_V F\left(\vec{x},t\right)dV = \iiint_{V(fct\ \text{of time}\ t)} \frac{\partial}{\partial t}F\left(\vec{x},t\right)dV + \int_{A(t)} F\vec{U}_A\vec{n}dA = \text{applying Stokes theorem}$$

$$\times\iiint_V \left[\frac{\partial}{\partial t}F\left(,\vec{x},t\right) + \nabla\cdot\left(F\vec{u}\right)\right]dV$$

$$\times \overset{(A4.2):}{=} \overset{\nabla\left(F\vec{u}\right)=F\nabla\cdot\vec{u}+\nabla F\vec{u}}{} \iiint_V \left[\underline{\underline{\left(\frac{\partial}{\partial t}F\left(,\vec{x},t\right) + \vec{u}\nabla F\right)}} + F\nabla\cdot\vec{u}\right]dV$$

$$= \iiint_V \left[\underline{\underline{\left(\frac{D}{Dt}F\left(,\vec{x},t\right)\right)}} + F\nabla\cdot\vec{u}\right]dV \tag{A.101}$$

Application in the SEGMENT-Landslide system includes the estimation of upper free surface elevation change.

$$\frac{\partial h(x,y)}{\partial t} = \frac{dh}{dt} - \left(\vec{v}\cdot\nabla\right)h = w\big|_{top} - u\big|_{top}\frac{\partial h}{\partial x} - v\big|_{top}\frac{\partial h}{\partial y} \tag{A.102}$$

This expression had been used in several places in the main text.

Appendix E
GPD Analysis of Extreme Precipitation

There are two prevailing extreme precipitation analysis techniques: the Generalized Extreme Value (GEV, chapter 4 of Wilks (2011)) analysis and the generalized Pareto distribution (GPD) analysis. The GEV picks one (the largest precipitation from a given year) value to represent a year's precipitation. The annual values are assumed to obey a Weibull distribution and the shape factor and scale factor are determined based on existing observations. Advantage of this approach is easy of implementation (Coles 2001). Here we focus on the GPD, which is more demanding for implementation but has the advantage of fully using the daily precipitation observations.

We aim to model the behavior of the daily rainfall series at a grid point (Fig. A.10) at extreme levels, that is, above the chosen threshold (u). Because we have no specified model for the underlying distribution of daily rainfall, and it is the tail behavior that is of interest for storm-triggered landslides, we appeal to an asymptotic approach (Coles and Tawn 1996). The GPD has an interpretation as a limiting distribution of observations that lie above a given threshold. This idea was first suggested by Pickands (1971) and has been developed by, among others, DuMouchel (1983), Davison (1984), Smith (1984, 1985, 1987), Hosking and Wallis (1987), and Joe (1987). In particular, Davison and Smith (1990) use the GDP as a modeling distribution for exceedance over high thresholds, which is similar to our application here.

E.1 Fitting a GPD to Rainfall Series

In this sub-section we illustrate how to model extreme daily rainfall behavior via a GPD. The focus is on modeling extreme daily rainfall at Enshi (30° 18′ °N; 109° 29′ °E), China. For ease of presentation, let $X_1, \ldots, X_n$ be a series of identically distributed random variables with an unknown underlying distribution $F(x)$. Here, random variable X_i denotes a daily rainfall observation. Our interest lies in estimating the behavior of rainfall over a given high threshold u. This can be approached by estimating the excess distribution defined by

© Springer International Publishing Switzerland 2015

D. Ren, *Storm-triggered Landslides in Warmer Climates*,
DOI 10.1007/978-3-319-08518-0

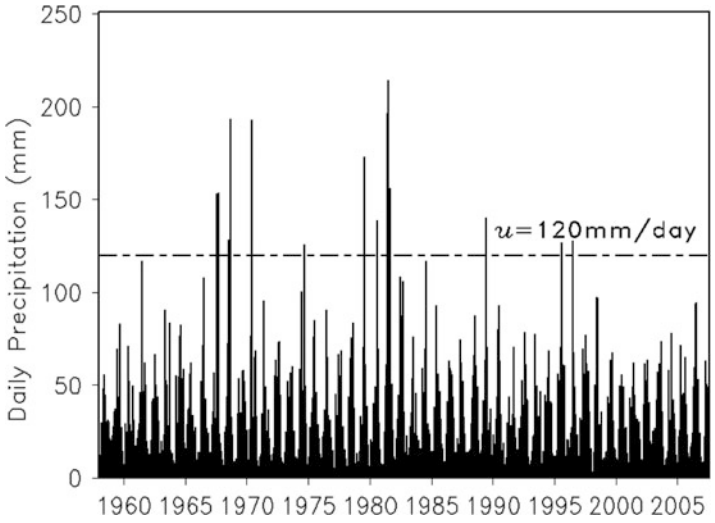

Fig. A.10 Times series of daily rainfall (mm) from 1 Jan 1959 to 30 Dec 2008 EnShi, China

$$F_u(y) = P\{X_i \le y + u | X_i > u\} = \frac{P\{(X_i \le y + u) \cap (X_i > u)\}}{P\{X_i > u\}}$$
$$= \frac{F(u+y) - F(u)}{1 - F(u)} \tag{A.103}$$

where $0 \le y < r_F - u$, and $r_F = \inf\{y{:}F(y) = 1\} \le \infty$ is the right endpoint of $F(y)$. The excess distribution represents the probability that an extreme rainfall event that has a value of X_i exceeds the threshold u by at most an amount of y, given that it exceeds the threshold u. The following limit theorem is a key result about the asymptotic form of $F_u(y)$, and was first given by Balkema and de Haan (1974) and Pickands (1975).

For a large class of underlying distributions we can find a function $\beta(u)$ such that

$$\lim_{u \to r_F} \sup_{0 \le y < r_F - u} \left| F_u(y) - G_{\xi,\beta(u)}(y) \right| = 0 \tag{A.104}$$

where

$$G_{\xi,\beta(u)}(y) = \begin{cases} 1 - \left(1 + \xi \frac{y}{\beta}\right)^{-1/\xi} & \xi \ne 0 \\ 1 - \exp\left(-\frac{y}{\beta}\right) & \xi = 0 \end{cases} \tag{A.105}$$

Equation (A.105) is the generalized Pareto distribution with parameters $\beta > 0$, and $y \geq 0$ when $\xi \geq 0$, as well as $0 \leq y \leq -\beta/\xi$ when $\xi < 0$; ξ is the *shape* parameter of the distribution and β is the *scaling* parameter. That is, for a large class of the underlying distributions $F(y)$, as the threshold u progressively becomes large, the excess distribution $F_u(y)$ converges to a GPD. This limit theorem is, of course, not mathematically complete because it fails to convey what exactly is meant by "a large class of distributions." Fortunately, it is known (e.g., McNeil 2000) that the class contains all of the common continuous distributions of statistics and climate science (normal, lognormal, χ^2, t, F, gamma, exponential, uniform, beta, etc.). The precipitation events generally believed to occur according to gamma distribution.

Following McNeil (2000), our model for a rainfall value X_i, having a distribution $F(x)$, assumes that for a certain u the excess distribution over the threshold may be taken as an exact GPD for some ξ and β, that is,

$$F_u(y) = G_{\xi,\beta(u)}(y) \tag{A.106}$$

To make assumption (A.106) more realistic, it is important to choose a proper threshold u. The choice of the threshold u usually proceeds from a compromise between choosing a sufficiently high threshold so that Eq. (A.106) is essentially satisfied and choosing a sufficiently low threshold so that we have enough excess data to estimate the parameters ξ and β. After choosing a threshold u, ξ and β in Eq. (A.106) can be estimated. It is known that if the sample size is large, the maximum likelihood estimation (MLE) is to be preferred because of its efficiency (Hosking and Wallis 1987; Smith 1985). This is the case in extreme precipitation application. The underlying assumption of MLE is that the realization series as a whole has the largest occurrence possibility. By definition, the probability density

$$f(y) = \frac{dF_u}{dy} = \frac{dG_{\xi,\beta(u)}}{dy} = \frac{1}{\beta}\left(1 + \frac{\xi}{\beta}y\right)^{-\left(1+\frac{1}{\xi}\right)} \tag{A.107}$$

Suppose that N_u excesses, out of a total of n data points, exceed the threshold u; the GPD is fitted to the N_u excesses by the MLE method to obtain estimates $\hat{\xi}$ and $\hat{\beta}$, which are chosen by maximizing the log-likelihood function

$$\begin{aligned} L(\xi,\beta) &= \sum_{i=1}^{N_u} \ln f(y_i) = \sum_{i=1}^{N_u} \ln\frac{1}{\beta} - \left(1 + \frac{1}{\xi}\right)\sum_{i=1}^{N_u} \ln\left(1 + \frac{\xi}{\beta}y_i\right) \\ &= -N_u \ln\beta - \left(1 + \frac{1}{\xi}\right)\sum_{i=1}^{N_u} \ln\left(1 + \frac{\xi}{\beta}y_i\right) \end{aligned} \tag{A.108}$$

provided that $(1 + \xi Y_i/\beta) > 0$ for $i = 1, \ldots, N_u$; otherwise, $L(\xi, \beta) = -\infty$, where Y_1, $\ldots$, Y_{Ni} denote the points over the threshold u in $\{X_1, \ldots, X_n\}$. See Davison and Smith (1990), McNeil (2000), and Coles (2001) for details.

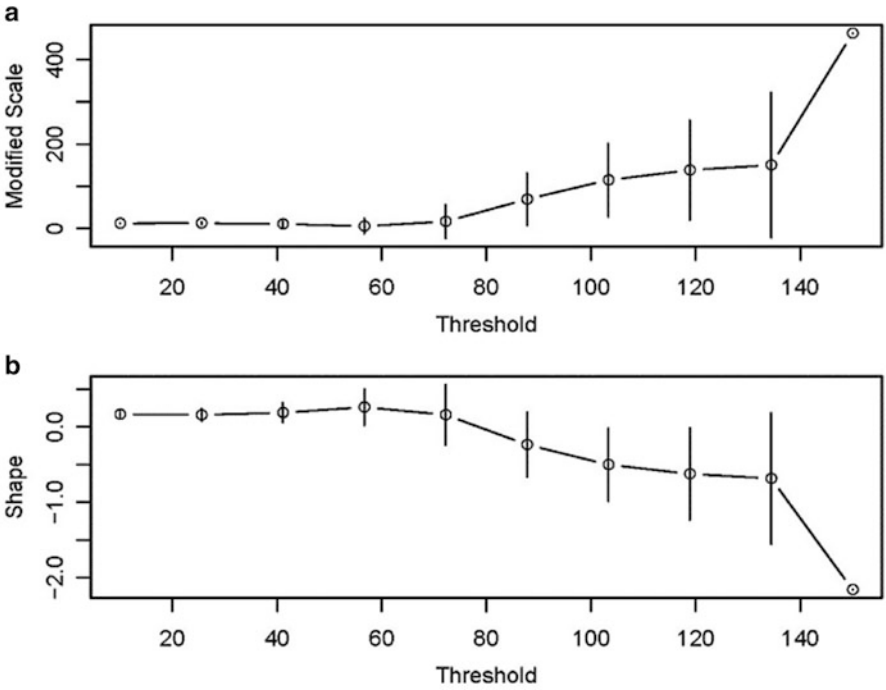

Fig. A.11 Shape (**a**) and modified scale parameter (**b**) estimates an against the threshold for Enshi daily rainfall data. It is evident that both estimates ξ (lower panel) and β (upper) are near constant for $30 \leq u \leq 35$. Hence, we choose the threshold of $u = 30$ mm

Thus, for a given threshold u, the maximum likelihood estimates of parameters for ξ and β can be obtained from Eq. (A.108). The threshold u can be obtained following a procedure developed by Coles (2001, p. 83). It is based on the fact that the GPD shape parameter ξ and the re-parameterizing scale parameter $\beta_u = \beta - \xi u$ are constant with $u > u_0$, if u_0 is a valid threshold for excesses (above u_0) that follow the GPD. This argument suggests that plotting the maximum likelihood estimates $\hat{\xi}$ and $\hat{\beta}_u$ together with confidence intervals for each of these quantities is useful for selecting the threshold, and the threshold should be chosen as the lowest value of u for which the estimates $\hat{\xi}$ and $\hat{\beta}_u$ remain near constant. The confidence intervals of $\hat{\xi}$ and $\hat{\beta}_u$ were derived by Coles (2001, p. 83). Figure A.11 gives the parameter estimates against the threshold for Enshi daily rainfall data. It is evident that both estimates $\hat{\xi}$ and $\hat{\beta}_u$ are nearly constant for $30 \leq u \leq 35$. Moreover, using a goodness-of-fit test (Choulakian and Stephens 2001), we can accept the following hypothesis: Enshi daily rainfall over 30 mm follows a GPD at a highly significant level (p-value > 0.05). Hence, we choose the threshold $u = 30$ mm. Note that we have used the assumption that individual rainfall excesses are independent, leading to the log-likelihood (Eq. A.108). This is because the temporal dependence in the daily rainfall series at extreme levels is typically weak (Coles 1994), and the theoretical

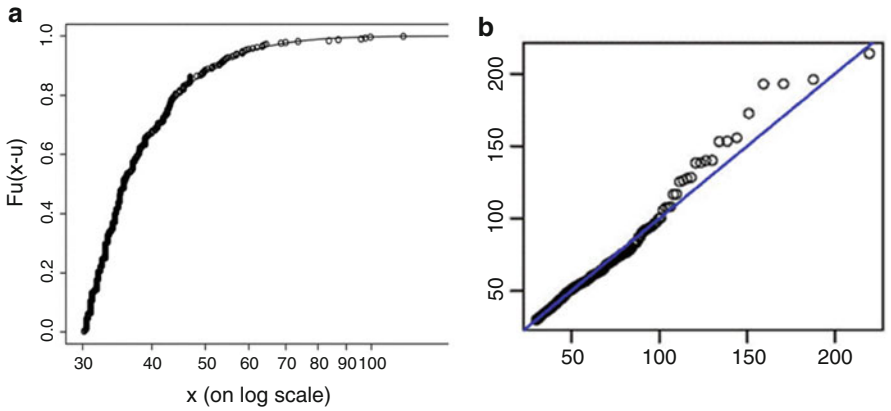

Fig. A.12 Modeling the excess distribution of rainfall series at Enshi in 1889–2001 by the GPD with parameter $\xi = 0.16$ and $\beta = 18.87$. In (**a**) the estimated GPD model for the excess distribution is shown as a *smoothed solid curve*. The empirical distribution of the 351 excesses is shown as *points*. It is evident that the GPD model fits these excesses well. In (**b**), the 90 % quantile plot indicates that for <120 mm/day cases are very well modeled. The skill are less for cases between 150 and 200 mm/day

analysis by Katz (1998) also indicates that temporal correlation is not crucial for estimates of the probability of extreme rainfall events. In addition, we have checked the daily rainfall over the threshold of 30 mm and find there are no two threshold excesses within 3 days, which implies that these are approximately independent excesses.

Having chosen the threshold $u = 30$ mm we have, for our rainfall data in 1959–2008, $n = 41{,}271$ observations and $N_u = 351$ excesses. On the basis of these rainfall data, estimates of the shape $\hat{\xi}$ and scale $\hat{\beta}_u$ are obtained as 0.126 and 8.313, with standard errors of 0.057 and 0.65, respectively. Figure A.12 gives the fitted excess distribution $F_u(y-u)$ by the GPD $G_{\xi,\beta}(y-u)$ with the above estimates. In this figure the estimated GPD model for the excess distribution is shown as a smooth, solid curve. The empirical distribution of the 351 excesses is shown as points. It is evident that the GPD model fits these excesses very well.

Because the extreme rainfall (>30 mm) behavior is governed by the tail of the unknown distribution $F(x)$, we need to construct the tail estimate $F_u(x)$ based on the excess distribution $F_u(x-u)$. By setting $x = u + y$ and combining Eqs. (A.103) and (A.106) we have

$$F(y) = [1 - F(u)]G_{\xi,\beta}(y-u) + F(u) \tag{A.109}$$

for $y > u$. Now, substituting $F(u)$ with its empirical estimator $(n - N_u)/n$, and ξ and β with their MLE $\hat{\xi}$ and scale $\hat{\beta}$, respectively, we get the tail estimate

$$\hat{F}(y) = 1 - \frac{N_u}{n}\left[1 + \frac{\hat{\xi}(y-u)}{\hat{\beta}}\right]^{-1/\hat{\xi}} \tag{A.110}$$

for $y > u$. This function can be viewed as an asymptotic and partially nonparametric estimate of the upper tail of an unknown distribution based on the extreme value theory. Equation (A.110) can always be used to construct the tail of $F(y)$ when we believe that data come from a common distribution, although its statistical properties are best understood when data are also assumed to be independent or only weakly dependent (McNeil 2000).

Similarly, we can give an estimate of the mean $E(Y)$ based on the tail of $F(y)$, where Y denotes an arbitrary daily rainfall. Depending on $Y > u$, the rainfall excess $Y - u$ follows a GPD with shape ξ and scale β, where

$$E\big(Y - u \big| Y > u\big) = \frac{\sigma}{1-\xi}, \tag{A.111}$$

provided that $\xi < 1$. It can be easily seen that

$$E(Y) = u + E\big(Y - u \big| Y > u\big)[1 - F(u)] + E\big(Y - u \big| Y \le u\big)F(u), \tag{A.112}$$

Note that $E(Y - u|Y \le u)$ is simply the mean of the belowness of u, for which the sample mean B_u of the threshold belowness of u provides a good empirical estimate because of the large number of observations below the threshold u. Accordingly, the estimate of the mean $E(Y)$ is

$$\hat{E}(Y) = u + \frac{\hat{\sigma}}{1-\hat{\xi}}\frac{N_u}{n} + B_u\left(1 - \frac{N_u}{n}\right), \tag{A.113}$$

Equation (A.113) gives an estimate of the mean $E(Y)$ based on the estimated tail of $F(y)$. It provides a way to explore the role of the changes at extreme tails of the distribution for the changes in mean precipitation. This has clear relevance in a future warming climate.

For our rainfall series in 1959–2008, $F(u)$ is estimated by (41,271–351)/41,271 = 0.991. Combining this with the earlier parameter estimates, the tail estimate $\hat{F}(y)$ for $y > 30$ mm is shown in Fig. A.13. In this figure, the y axis is the tail probability $1 - F(x)$ (log scale) and the x axis denotes the rainfall values (log scale). The top-left corner of the graph shows that the threshold $u = 30$ has a tail probability of 0.0085 [empirical estimator $1 - (41{,}271 - 351)/41{,}271 = 0.008505$]. The points in the graph represent the empirical distribution of the 351 extreme rainfall events over 30 mm, and the solid curve shows how tail estimation in Eq. (A.110) allows extrapolation into the area where the data become sparse, that is, we can read off the probabilities of extreme rainfall from the solid curve in the graph. This is very important for risk management, such as for flashfloods and storm-triggered landslides.

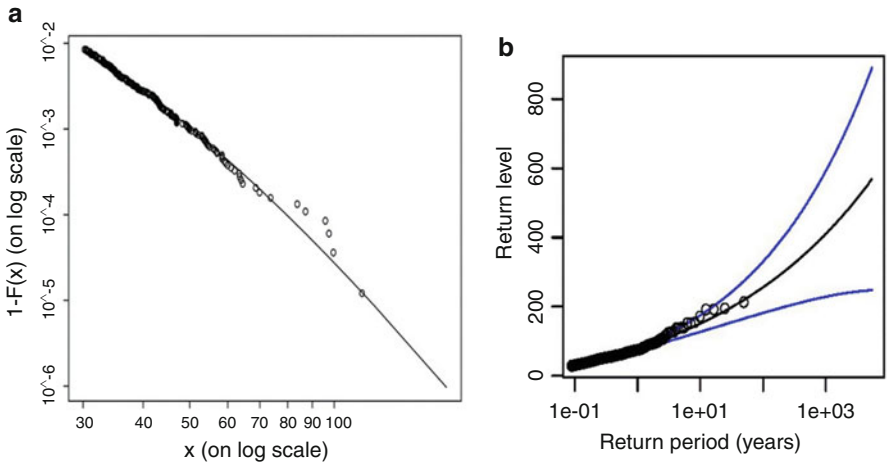

Fig. A.13 Modeling the tail of the underling distribution for rainfall series at Enshi for the period of 1959–2008. Here, the y axis is the tail probabilities $1 - F(x)$ (on log scale) and the x axis denotes the rainfall values (on log scale). The *points* in (**a**) represent empirical distribution of the 351 extreme rainfall events over 30 mm and the *solid curve* shows how the tail estimation formula (Eq. A.110) allows extrapolation into the area where the data become sparse. Panel (**b**) is viewing in another angle from the return level estimates (e.g., 120 mm in Fig. A.10 corresponds a ~70 year return period). The uncertainty (confidence interval confined by the two *blue curves*) increases with the return period. For example, for extreme precipitation of 100 year return period, the actual daily precipitation is allowed to vary between 180 and 320 mm/day

E.2 Quantifying the Recurrence Frequency in Extreme Rainfall

One of the advantage of GPD vs. GEV is that in estimating the return period of extreme events, the GPD utilizes more information (daily rainfall). From Eq. (A.105), it is straightforward to obtain the rainfall intensity of a given return period as $y = \frac{\beta}{\xi}\left[1 - \left(\frac{1}{365.25T}\right)^{-\xi}\right]$. Similarly, specify an intensity, the return period T_R (in year) based on these two-tail distributions, is $\{T_R = 1/[365.25 \times (1 - \hat{F}(y))]\}$.

References

Balkema A, de Haan L (1974) Residual lifetime at great age. Ann Probab 2:792–804

Choulakian V, Stephens M (2001) Goodness-of-fit tests for the generalized Pareto distribution. Technometrics 43:478–484

Coles S (2001) An introduction to statistical modeling of extreme values. Springer Series in Statistics, p 224, ISBN-10:1852334592

Coles S (1994) A temporal study of extreme rainfall. In: Barnett V, Turkman KF (eds) Statistics for the environment 2: water related issues. Wiley, New York, pp 61–78

Coles S, Tawn J (1996) A Bayesian analysis of extreme rainfall data. Appl Stat 45:463–478
Davison A (1984) Modelling excesses over high thresholds, with an application. In: Tiago de Oliveira J (ed) Statistical extreme and applications. Reidel, Dordrecht, pp 461–482
Davison A, Smith R (1990) Models for exceedances over high thresholds (with discussion). J Roy Stat Soc B 52:393–442
DuMouchel W (1983) Estimating the stable index α in order to measure tail thickness. Ann Stat 11:1019–1036
Hosking J, Wallis J (1987) Parameter and quantile estimation for the generalized Pareto distribution. Technometrics 29:339–349
Joe H (1987) Estimation of quantile of the maximum of N observations. Biometrika 74:347–354
Katz R (1998) Extreme value theory for precipitation: Implication for climate change. Preprints, ninth symp. on global change studies, Phoenix, AZ. Am Meteorol Soc, pp J11–J15
McNeil A (2000) Extreme value theory for risk managers. In: Embrechts P (ed) Extreme and integrated risk management. UBS Warbug, Basel, pp 1–35
Pickands J (1971) The two-dimensional Poisson process and extremal process. J Appl Probab 8:745–756
Pickands J (1975) Statistical inference using extreme order statistics. Ann Stat 3:119–131
Smith R (1984) Threshold methods for sample extremes. In: Tiago de Oliveira J (ed) Statistical extreme and applications. Reidel, Dordrecht, pp 621–638
Smith R (1985) Maximum likelihood estimation in a class of nonregular cases. Biometrika 72:67–90
Smith R (1987) Estimating tails of probability distributions. Ann Stat 15:1174–1207
Wilks D (2011) Statistical methods in the atmospheric sciences, 3rd edn. International geophysics series, V100, Elsevier, San Diego, CA, p 676

Appendix F
Lax–Wendroff Scheme of Various Order of Accuracy (1D Followed by a Higher Order Scheme Implemented in SEGMENT-Landslide)

Usage: untar the adv.tar.gz; gfortran adv.f90 (compile only once); vi AdjustParameter.input (edit name list input parameters to set up the initial fields of F (q in Eq. 12.57) and U (c in Eq. 12.57); a.out (to execute and produce the binary file for graphic plots).

In subroutine "KICKstart" you may redefine the wind/flow field that advects the F field, using parameters UM and UV and NPER (or you can introduce new parameters). For sinusoidal form, NPER means wave number within the spatial domain, UV means the amplitude of the sine/cosine waves, and UM is the mean flow magnitude. The initial field of F also is defined in this routine. One can also modify and pick any form they would like to (e.g., square wave, bell-shape wave, or sine/cosine waves). The default form is a triangle form. IORD controls the scheme accuracy. There are six options available. DT is time step size, XL and XR specify the boundary of the spatial domain. NSTEP means how many steps of time marching will be performed. Other utility routines are self-explanatory (Fig. F.1).

Code: *adv.f90* (Various schemes for the one dimensional, time-dependent, advection Eq. (12.57) in Sect. 12.3.2).

© Springer International Publishing Switzerland 2015

D. Ren, *Storm-triggered Landslides in Warmer Climates*,
DOI 10.1007/978-3-319-08518-0

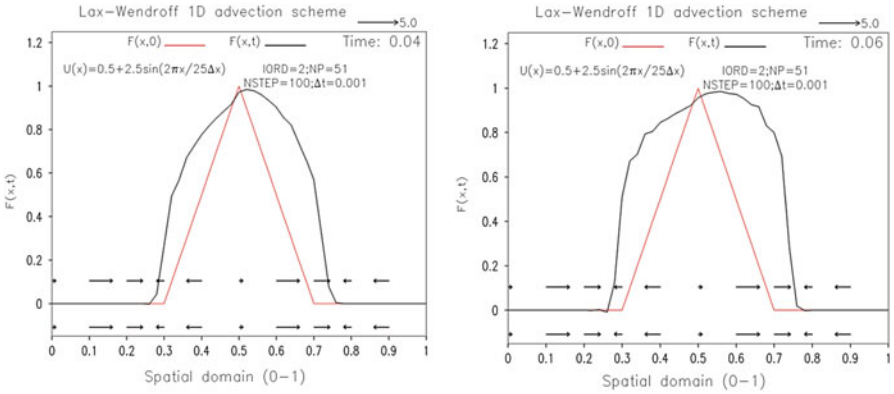

Fig. F.1 Illustration of the Lax–Wendroff advection scheme. Spatial variation of flow (U, or c in Eq. 12.57) are labelled. Wind vectors are duplicated for clarity. Initial values of q (F in the panels) are shown as *red triangles*. Corresponding animation shows the gradual evolution of the *black curves* ($F(x, t)$)

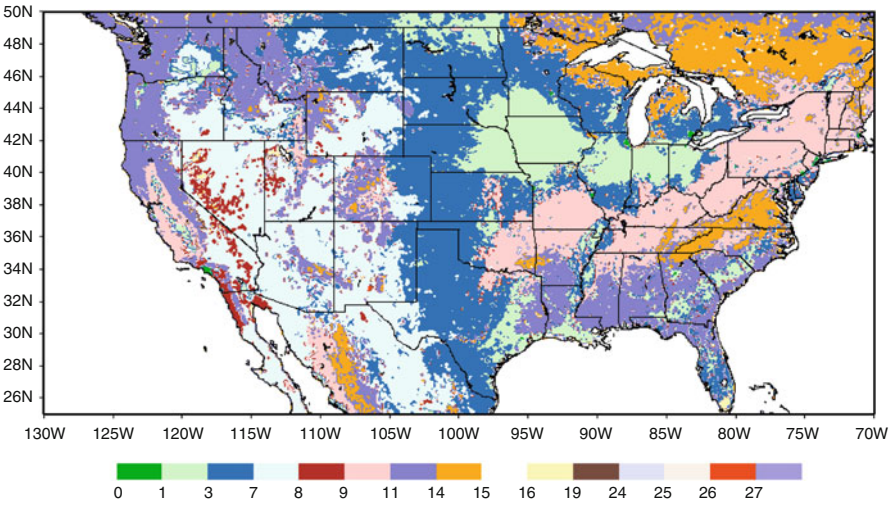

Sample output (images from selected time levels):
The advection code in SEGMENT: *adv3D.f90*

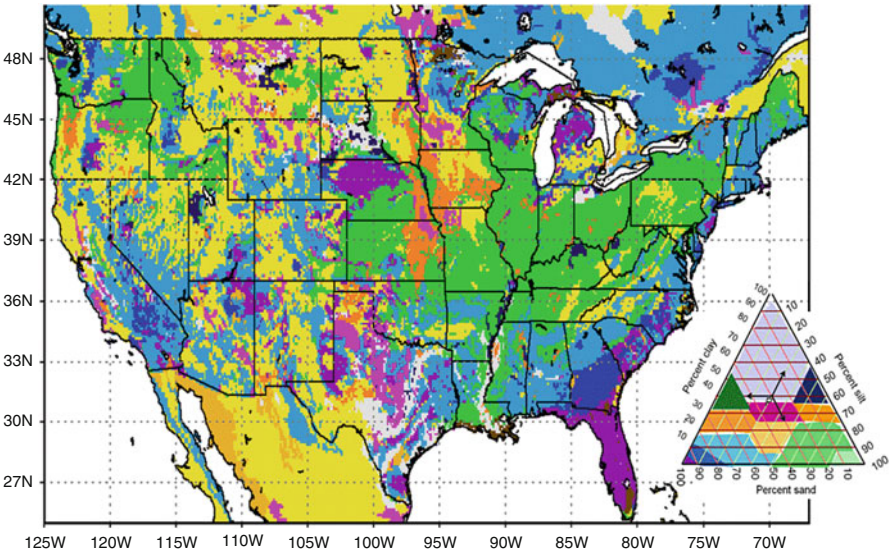
48N
45N
42N
39N
36N
33N
30N
27N
125W
120W
115W
110W
105W
100W
95W
90W
85W
80W
75W
70W
Percent clay
Percent silt
Percent sand

Appendix G
1D Thermal Equation Solver (Semi-implicit C-N Scheme)

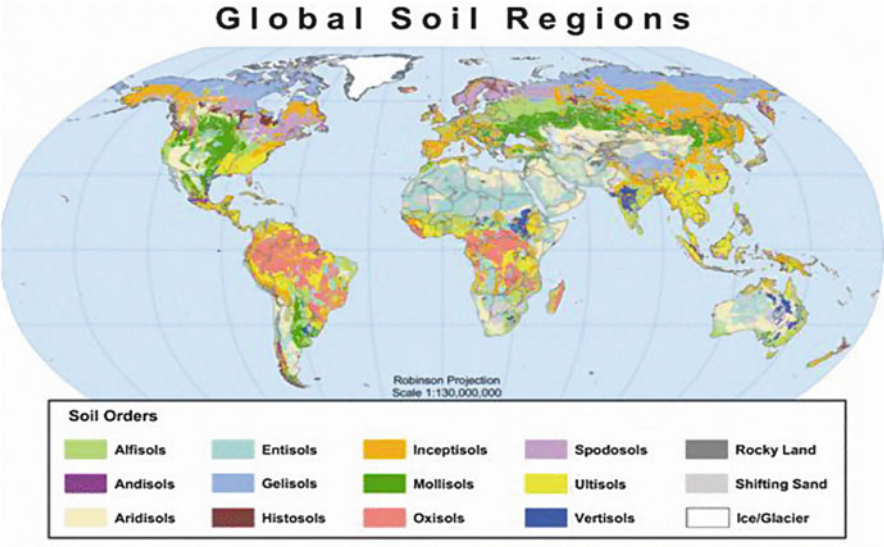

© Springer International Publishing Switzerland 2015

D. Ren, *Storm-triggered Landslides in Warmer Climates*,
DOI 10.1007/978-3-319-08518-0